Universidade do Porto

Faculdade de Engenharia

Computer Modelling of Atmospheric Flows in Wind Energy Applications

Carlos Alberto Veiga Rodrigues

Dissertation submited to the University of Porto
in partial satisfaction of the requirements for the
degree of Doctor in Mechanical Engineering.

June 2013

Abstract

A study was conducted towards the improvement of methodologies for wind power forecasting and prediction of the wind resource in mountainous terrain, based on non-linear flow models.

The electrical power of two wind farms was forecasted employing a transfer function, generated from a set of computational fluid dynamics (CFD) simulations. The atmospheric flow was solved assuming neutral stratification, using the Reynolds averaged Navier-Stokes (RaNS) formulation and the $k - \epsilon$ turbulence model. The transfer function was used to generate time series of the wind speed at wind turbine locations, from weather forecasts at a reference location, obtained through a chain composed of a mesoscale coupled with a global circulation model. The results were compared against one year of field measurements of wind speed and electrical power, yielding an agreement with 15% of mean absolute error when normalized by the wind farm rated power.

The CFD model was changed to solve flows with thermal stratification. To validate the code, a set of idealized cases was made to reproduce gravity waves over axisymmetric mountains. Under the assumption of inviscid flow, linear and non-linear mountain wave regimes were simulated, namely breaking waves and flow splitting. The results obtained were found to be in agreement with both analytical and numerical works in the literature. The simulations were repeated assuming turbulent flow and surface friction at the lower boundary. The same regimes were reproduced with a decrease of the waves amplitude, favouring splitted flows and large mountain wakes.

A new model chain was established where the stratified CFD model was used as a microscale model to downscale results from a mesoscale model, using its full tridimensional time-dependent solutions. Operational analyses from global circulation models were used to drive the mesoscale model, acting as a compromise between producing forecasts or virtual wind time series from re-analyses. The flow was downscaled in four sites, two of these with wind farms, encompassing 10 meteorological masts. A total of four weeks were simulated, two during summer and two at the end of autumn. Based on the wind speed forecast, the electrical power of the wind turbines was estimated using the manufacturer's power curve. The mesoscale model yielded a better prediction of the electrical power, with 14% improvements over the microscale in the summer. Regarding the wind speed, the microscale model yielded on 65% of the set of masts and periods considered, with positive skill scores around 0.3 on average. The predicted turbulence intensity and vertical wind shear yielded a good agreement with the characteristic values found in the measurements, conversely to the results obtained with the neutral stratification model.

Resumo

Foi realizado um estudo para o desenvolvimento de metodologias de previsão da geração elétrica de origem eólica e de avaliação do recurso eólico em terreno montanhoso, com base em modelos não-lineares para simulação de escoamentos.

A previsão a curto prazo da potência elétrica de dois parques eólicos foi obtida utilizando uma função de transferência, gerada a partir de um conjunto de simulações de mecânica dos fluidos computacional (MFC). A solução do escoamento atmosférico foi obtida assumindo estratificação neutra, a formulação das equações de Navier-Stokes com médias de Reynolds (RaNS) e o modelo de turbulência $k - \epsilon$. A função de transferência foi utilizada para gerar séries temporais da velocidade do vento em locais com turbinas eólicas, a partir de previsões meteorológicas num local de referência, obtidas através de uma cadeia formada por um modelo de mesoescala acoplado a um modelo de circulação global. Os resultados foram comparados com um ano de dados de medições de campo da velocidade do vento e potência elétrica, resultando numa concordância com 15% de erro absoluto médio, quando normalizado pela potência nominal do parque.

O modelo de MFC foi alterado por forma a ter a capacidade de resolver escoamentos estratificados. Para validar o código, foram resolvidos vários casos idealizados com o objectivo de gerar ondas gravíticas sobre montanhas axisimétricas. Assumindo escoamento invíscido foram simulados regimes lineares e não-lineares de ondas de montanhas, nomeadamente o regime de quebra de onda e separação do escoamento a montante. Verificou-se que os resultados obtidos estão em acordo com soluções analíticas e numéricas encontradas na literatura. As simulações foram repetidas assumindo escoamento turbulento e fricção superficial na parede. Foram reproduzidos regimes semelhantes mas com um decréscimo da magnitude das ondas gravíticas, favorecendo a separação do escoamento a montante e o aumento da esteira da montanha.

Uma nova cadeia de modelos foi estabelecida onde o código de MFC estratificado foi utilizado como modelo de microescala, acoplado ao modelo de mesoescala por forma a refinar os resultados deste, fazendo uso da sua solução instacionária e tri-dimensional. Análises operacionais de modelos de circulação global foram utilizadas para alimentar o modelo de mesoescala, atuando como um compromisso entre a previsão a curto prazo e a geração de séries virtuais de condições de vento a partir de reanálises. O escoamento foi resolvido para quatro locais, dois destes com parques eólicos, abrangendo um total de 10 estações meteorológicas. Foram simuladas quatro semanas, duas para um período de verão e outras duas no final do outono. A partir da previsão da velocidade do vento, a potência eléctrica nas turbinas eólicas foi estimada utilizando a curva de potência do fabricante. O modelo de mesoescala obteve uma melhor previsão da potência elétrica, com melhorias de 14% em relação aos resultados da microescala no verão. Relativamente à velocidade do vento, o modelo de microescala trouxe melhorias em 65% do conjunto de estações e períodos envolvidos, com indicadores de precisão (*skill scores*) na ordem de $0,3$, em média. Para a intensidade da turbulência e tensão de corte vertical, foi registada uma boa concordância com os valores característicos das medições, contrariamente aos resultados obtidos com o modelo de estratificação neutra.

Résumé

Une étude a été réalisée pour développer des méthodologies de prévision de production électrique d'origine éolienne et de léstimation de la ressource du vent en terrain montagneux, basée sur des modèles d'écoulement non-linéaires.

La production éléctrique de deux parcs éoliens a été prévue en utilisant une fonction de transfert, produite a partir d'un groupe de simulations de mécanique des fluides numérique (MFN). La solution de l'écoulement atmosphérique a été obtenue en assumant un régime de stratification neutre, une formulation des équations de Navier-Stokes en moyennes de Reynolds (RaNS) et un modèle de turbulence $k - \epsilon$. La fonction de transfert fournit une série temporel de la vitesse du vent aux positions des éoliennes, en ayant comme source une prévision météorologique dans une localisation de référence, celle-là obtenue par un modèle de méso-échelle couplé a un modèle de circulation générale. Les résultats ont été comparés face à des mesures locales du vent et production d'éléctricité, provenant d'une année de données, en produisant une erreur moyenne absolute de 15%, normalisée par la puissance installée du parc éolien.

Le modèle de MFN a été modifié pour résoudre écoulements en régime stratifié. Pour valider le code, un groupe de cas idéalisés ont été produits pour simuler des ondes gravitiques sur monts axissimétriques. En supposant un écoulement inviscide, ondes de montagne lineaires et non-lineaires ont été simulés, nommément le déferlement des ondes et la séparation de l'écoulement en amont. On a constaté que les résultats obtenus sont en accord avec les solutions analytiques et numériques publiés dans la littérature. Les simulations ont été répétées pour écoulements turbulents avec frottement sur la paroi. Les mêmes régimes ont été réproduits, mais avec une baisse de l'amplitude des ondes, en favorisant la séparation de l'écoulement a montant et l'augmentation de la sillage du mont.

Une nouvelle chaine de modèles a été créée où le modèle MFN stratifié il a été utilisé comme modèle de micro-échelle, couplé au modèle à méso-échelle, à fin de perfectionner ses résultats, en utilisant ses solutions tri-dimensionelles instationnaires. Des analyses opérationnelles d'un modèle de circulation générale forcent le modèle de mésoéchelle, a compromis entre production de prévisions à court therme et la génération de séries virtuelles de vent a partir de reanalyses. L'écoulement a été raffiné en quatre sites, dont deux s'agissent de parcs éoliens, en tenant en compte un total de 10 mâts de mésure. Quatre semaines ont été simulées, dont deux pendant l'été et deux à la fin de l'automne. Basée sur la prévision de la vitesse du vent, la puissance électrique des éoliennes a été estimé en utilisant la courbe de puissance du fabricant. Le modèle de méso-échelle a produit une meilleure prévision de la production électrique, en apportant une amélioration de 14% versus le modèle de micro-échelle pour les périodes estivales. En ce qui concerne la vitesse du vent, le modèle MFN a eu une meilleure performance en 65%, en tenant en compte tous les mâts et périodes, avec des indicateurs de precison (*skill scores*) de $0,3$, en moyenne. L'intensité de la turbulence et le cisaillement vertical du vent ont montré une bonne concordance avec les valeurs characteristiques mésurées, contrairement aux résultats obtenus avec le modèle de stratification neutre.

Contents

List of Figures

List of Tables

Nomenclature

Abbreviations

3FTI	Three time-level implicit scheme
ABL	Atmospheric boundary-layer
AGL	Above ground level
BIAS	Average of signed errors
CBL	Convective boundary-layer
CFD	Computational fluid dynamics
CV, CVs	Control volume(s)
FDDA	Four-dimensional data assimilation
GCM	Global circulation model
GDAS	Global Data Assimilation System
ST	Standard time, without daylight saving
MAE	Mean absolute errors
MM5	Fifth-generation Penn State/NCAR mesoscale model
MOST	Monin-Obukhov similarity theory
MRE	Mean of relative errors
MSE	Mean squared errors
MSRE	Mean of squared relative errors
NWP	Numerical weather prediction
PICTURE	Proper interpolation for a collocated treatment of the unsteady Reynolds-averaged equations

PWIM	Pressure weighted interpolation method
QUICK	Quadratic upwind interpolation scheme
RaNS	Reynolds averaged Navier-Stokes
RBIAS	Average of signed relative errors
RMSE	Root mean squared errors
RMSRE	Root mean of squared relative errors
RMS	Root mean squares
RRTM	Rapid radiative transfer model
SCADA	Supervisory control and data acquisition
SIMPLE	Semi-implicit method for pressure-linked equations
SSBL	Stably-stratified boundary-layer
SS	Skill score
TDMA	Tri-diagonal matrix algorithm
UDS	Upwind discretization scheme
uRaNS	Unsteady Reynolds averaged Navier-Stokes
WRF	Weather Research and Forecast, regional mesoscale model

Dimensionless parameters

Fr	Froude number
Pr	Prandtl number
Re	Reynolds number
Ri	Richardson gradient number
Ri_b	Bulk Richardson number
Ri_c	Critical Richardson number
Rf	Richardson flux number
Rf_c	Critical Richardson flux number
St	Strouhal number

Greek symbols

α	Shear factor, exponent of a power law for the vertical velocity profile	
α_t	Turbulent thermal diffusivity	$\mathrm{L}^2\,\mathrm{T}^{-1}$
δ	Boundary-layer depth	L
ϵ	Turbulence energy dissipation	$\mathrm{L}^2\,\mathrm{T}^{-3}$
γ	Ratio of specific heats	
κ	von Kármán constant	
λ	Thermal conductivity	$\mathrm{M}\,\mathrm{L}^2\,\mathrm{T}^{-3}\,\Theta^{-1}$
λ_t	Turbulent thermal conductivity	$\mathrm{M}\,\mathrm{L}^2\,\mathrm{T}^{-3}\,\Theta^{-1}$
μ	Dynamic viscosity	$\mathrm{M}\,\mathrm{L}^{-1}\,\mathrm{T}^{-1}$
μ_t	Turbulent dynamic viscosity	$\mathrm{M}\,\mathrm{L}^{-1}\,\mathrm{T}^{-1}$
ν	Kinematic viscosity	$\mathrm{L}^2\,\mathrm{T}^{-1}$
ν_t	Turbulent kinematic viscosity	$\mathrm{L}^2\,\mathrm{T}^{-1}$
ω	Angular speed of the Earth	T^{-1}
$\vec{\Omega}$	Rotation vector of the Earth	T^{-1}
Ω	Volume of bounded region of space	L^3
φ	Latitude angle	
Π	Exner function	
ϕ_h	Stability function for heat	
ϕ_m	Stability function for momentum	
ψ_h	Integral function of $\phi_h$for the diabatic thermal boundary-layer	
ψ_m	Integral function of $\phi_m$for the diabatic velocity boundary-layer	
σ_u, σ_v, σ_w	Standard deviation of velocity, for each component of $\vec{u}$	$\mathrm{L}\,\mathrm{T}^{-1}$
σ_V	Standard deviation of the horizontal velocity	$\mathrm{L}\,\mathrm{T}^{-1}$
σ_ϵ	Turbulent Prandtl number, ratio of momentum and ϵ diffusivities	
$\underline{\underline{\sigma}}$	Stress tensor, for a newtonian fluid is the sum of the hydrostatic and deviatoric stresses, $\underline{\underline{\sigma}} = -p\mathrm{I} + \underline{\underline{\tau}}$	$\mathrm{M}\,\mathrm{L}^{-1}\,\mathrm{T}^{-2}$

σ_k	Turbulent Prandtl number, ratio of momentum and k diffusivities	
σ_θ	Turbulent Prandtl number, ratio of momentum and θ diffusivities	
$\sigma_{\theta N}$	Turbulent Prandtl number σ_θ under neutral stratification	
$\underline{\underline{\tau}}$	Deviatoric stress tensor	$\mathrm{M\,L^{-1}\,T^{-2}}$
τ'_{w}	Wall shear stress due to turbulent stresses	$\mathrm{M\,L^{-1}\,T^{-2}}$
θ_*	Temperature turbulence scale for the thermal boundary-layer	Θ
θ	Potential temperature	Θ
Θ	Temperature representative of the surface-layer	Θ
$\vec{\xi} = \{\xi, \eta, \zeta\}$	Computational domain coordinate system	L
ζ	Stability parameter based on the Monin-Obukhov length	

Roman symbols

$\vec{a}_c$	Coriolis acceleration vector	$\mathrm{L\,T^{-2}}$
$\mathcal{B}$	Acceleration due to buoyancy	$\mathrm{L\,T^{-2}}$
$C_{\epsilon 1}$, $C_{\epsilon 2}$, $C_{\epsilon 3}$	Constants in the turbulence model equation for ϵ	
C_m	Bulk transfer coefficient for momentum	
C_μ	Turbulent viscosity constant in the $k-\epsilon$ model	
c_p	Isobaric specific heat capacity	$\mathrm{L^2\,T^{-2}\,\Theta^{-1}}$
C_θ	Bulk transfer coefficient for heat	
c_v	Isochoric specific heat capacity	$\mathrm{L^2\,T^{-2}\,\Theta^{-1}}$
R_d	Specific gas constant for dry air	$\mathrm{L^2\,T^{-2}\,\Theta^{-1}}$
$\mathcal{D}_\epsilon$	Rate of dissipation of k in the model equation for ϵ	$\mathrm{M\,L^{-1}\,T^{-3}}$
e_I	Internal energy of a system, per unit of mass	$\mathrm{L^2\,T^{-2}}$
$\mathcal{E}_\mathcal{I}$	Total energy of a system	$\mathrm{M\,L^2\,T^{-2}}$
$e_\mathcal{I}$	Total energy per unit of mass	$\mathrm{L^2\,T^{-2}}$
f_c	Coriolis frequency	$\mathrm{T^{-1}}$
g	Acceleration due to gravity	$\mathrm{L\,T^{-2}}$

$\mathcal{G}$	Production of k due to buoyancy	$\mathrm{M\,L^{-1}\,T^{-3}}$
k	Turbulence kinetic energy	$\mathrm{L^2\,T^{-2}}$
$\mathcal{L}$	Monin-Obukhov length	L
l_*	Mixing-length, characteristic length scale for turbulent eddies	L
N	Brunt-Väisälä frequency, or buoyancy frequency	$\mathrm{T^{-1}}$
p	Pressure field	$\mathrm{M\,L^{-1}\,T^{-2}}$
$\mathcal{P}_\epsilon$	Production of k in the turbulence model equation for ϵ	$\mathrm{M\,L^{-1}\,T^{-3}}$
$\mathcal{P}_k$	Production of k in the turbulence model equation for k	$\mathrm{M\,L^{-1}\,T^{-3}}$
$\mathcal{P}$	Production of k due to mechanical shear	$\mathrm{M\,L^{-1}\,T^{-3}}$
$\mathcal{Q}$	Energy transferred under the form of heat	$\mathrm{M\,L^2\,T^{-2}}$
$\vec{q}$	Heat flux vector, rate of energy per unit area	$\mathrm{M\,T^{-3}}$
q	Heat per unit of mass	$\mathrm{L^2\,T^{-2}}$
S	Surface area of bounded region of space	$\mathrm{L^2}$
t	Time coordinate	T
TI	Turbulence intensity	
$\mathcal{T}_k$	Diffusive transport term in the equation for k	$\mathrm{M\,L^{-1}\,T^{-3}}$
t_*	Characteristic time scale for turbulent eddies	T
$\vec{u} = \{u, v, w\}$	Velocity field, vector form and x, y and z component	$\mathrm{L\,T^{-1}}$
U	Velocity representative of inlet or free-stream conditions	$\mathrm{L\,T^{-1}}$
$\vec{u}_\tau$	Velocity tangential to the wall for the first grid point	$\mathrm{L\,T^{-1}}$
u_*	Friction velocity, scale for the turbulent boundary-layer	$\mathrm{L\,T^{-1}}$
R_v	Specific gas constant for water vapour	$\mathrm{L^2\,T^{-2}\,\Theta^{-1}}$
$\mathcal{W}$	Energy transferred under the form of work	$\mathrm{M\,L^2\,T^{-2}}$
w	Work per unit of mass	$\mathrm{L^2\,T^{-2}}$
$\vec{x} = \{x, y, z\}$	Position vector and respective streamwise, spanwise and vertical coordinates	L
z_{h0}	Wall roughness length for the thermal boundary-layer	L

z_{m0} , z_0	Wall roughness length for the momentum boundary-layer	L

Subscripts and superscripts

$\widehat{A}$	Perturbation to quantity A
A_r	Reference state of quantity A, such that $A_r = A - \widehat{A}$
A_H	Reference state of quantity A, when it also refers to hydrostatic equilibrium, such that $A_H = A - \widehat{A}$
A_w	Value of quantity A at the ground surface
A_0	Value of quantity A at the average sea surface level
A_{00}	Value of quantity A at the isobaric surface corresponding to a reference pressure of 100 kPa

Operators and mathematical symbols

$\{\hat{\boldsymbol{\imath}}, \hat{\boldsymbol{\jmath}}, \hat{\boldsymbol{k}}\}$	Standard basis vectors for the Cartesian coordinate system
$\hat{\mathbf{e}}_i$	Representation of the standard basis, such that: $\{\hat{\mathbf{e}}_1, \hat{\mathbf{e}}_2, \hat{\mathbf{e}}_3\} \equiv \{\hat{\boldsymbol{\imath}}, \hat{\boldsymbol{\jmath}}, \hat{\boldsymbol{k}}\}$
$\hat{\mathbf{a}}$	Versor or unit vector, first rank tensor
$\vec{a}$	Vector, first rank tensor
$\underline{\underline{A}}$	Matrix, second rank tensor
$\underline{\underline{C}} = \vec{a} \otimes \vec{b}$	Dyadic product of vectors, equivalent to tensor $\underline{\underline{C}}$ where $C_{ij} = a_i\, b_j$
$\underline{\underline{A}} : \underline{\underline{B}}$	Double inner product, equivalent to $\sum_i \sum_j A_{ij}\, B_{ij}$
δ_{ij}	Kronecker delta
ε_{ijk}	Levi-Civita symbol
$\dfrac{\partial A}{\partial b}$, $\partial_b (A)$	Partial derivative of variable A in respect to b
$\dfrac{\partial^2 A}{\partial b^2}$, $\partial_b^2 (A)$	Second derivative of variable A in respect to b
$\dfrac{\partial^2 A}{\partial b\, \partial c}$	Second order mixed derivatives of variable A in respect to b and c
$\dfrac{DA}{Dt}$, $D_t (A)$	Lagrangian derivative of quantity A, equivalent to $\dfrac{\partial A}{\partial t} + \vec{u} \cdot \nabla A$
∇a	Gradient operator: $\nabla a = \sum_i \dfrac{\partial a}{\partial x_i} \hat{\mathbf{e}}_i$, $\nabla \vec{a} = \sum_i \sum_j \dfrac{\partial a_j}{\partial x_i} \hat{\mathbf{e}}_i \hat{\mathbf{e}}_j$

$\nabla \cdot \vec{a}$	Divergence of vector $\vec{a}$, equivalent to $\sum_i \frac{\partial a_i}{\partial x_i}$
$\nabla \times \vec{a}$	Curl of vector $\vec{a}$, equivalent to $\sum_i \sum_j \sum_k \varepsilon_{ijk} \frac{\partial a_k}{\partial x_j} \hat{\mathbf{e}}_i$
$\det(\underline{\underline{A}})$	Determinant of matrix $\underline{\underline{A}}$
$\mathrm{inv}(\underline{\underline{A}})$	Matrix inverse of $\underline{\underline{A}}$
$\dot{a}$	Rate of change of quantity a with time
$\langle a \rangle$	Ensemble average of quantity a
$\overline{a}$	Time average of quantity a
a'	Turbulent fluctuation of quantity a
$\overset{e\leftarrow}{\overline{\{a_P,\, a_E\}}}$	Interpolation of quantity a to position $\vec{x}_e$, using values of the field $a(\vec{x})$ at positions $\vec{x}_P$ and $\vec{x}_E$
$\overset{e\leftarrow}{\overline{\{a\}}}$	Interpolation of quantity a to position $\vec{x}_e$, using nearby values of the field $a(\vec{x})$

Chapter 1

Introduction

1.1 Motivation

The harvest of wind energy has continuously increased in the last 20 years. The global installed wind capacity is currently 282 GW, with an annual growth close to 19% (GWEC, 2013). In several countries, wind resource assessment is paramount as these have less detailed meteorological records and the wind potential is still largely unexplored. In Europe, however, the annual growth has decreased from 18% to 13% between 2007 and 2012 (EWEA, 2013). The amount of wind power in Europe represents 11% of the electrical share, roughly one-quarter of the electricity converted from fossil fuels. Additionally, the intermittent nature of wind makes it non-dispatchable by electricity operators. Hence, the need of an efficient management of the electrical network has pushed for the development of wind power forecast methodologies.

Generally, wind resource assessment begins with a 5 year field measurement campaign (Landberg *et al.*, 2003). This is very restrictive and in practice shorter time spans are used, some with less than 2 years. The measurements are often correlated with a longer time series gathered at old meteorological stations which, depending on the correlation obtained, is used to extrapolate the wind resource.

Because data obtained from the measurement campaign is limited to the locations of the measurement masts, the wind characteristics are mapped for the surrounding area using linear models, based on the seminal work of Jackson and Hunt (1975), and non-linear computational fluid dynamics (CFD) models. Linear models are unable to predict flow separation and are not suitable for terrain with slopes higher than 17°. Nevertheless, these models have become the standard in wind resource assessment and are often used in complex terrain, even when slopes around 25° exist (Bowen and Mortensen, 2004).

During the last decade, non-linear models have proved to be a reliable complement to linear models and are currently used by wind farm promoters and turbine manufacturers. Besides the estimation of the wind energy potential, these allow to identify high turbulence regions, excessive shear in the wind velocity profile and unsteady flow features (Palma *et al.*, 2008). These factors may impair the operation of a wind turbine, depending on their occurrence and intensity.

These engineering models are commonly employed considering neutrally stratified flow. One argument is that neutral stratification comprehends the average of the several states of atmospheric stability. Landberg *et al.* (2003) argues that thermal stability should only be taken into account when its effects are deemed important. Regarding the boundary-layer, this usually happens for low wind speeds, below $10\,\mathrm{m\,s^{-1}}$. However, stratification exists on a daily basis and changes between diurnal and nocturnal periods. It also allows for thermal circulations to happen, which may induce considerable seasonal changes on the flow field, *e.g.*, the occurrence of sea and valley breezes during summer (Whiteman, 2000). The neglect of stratification is mainly related with the increased computational cost it entails and the lack of field data, as most measurement masts are not equipped to provide an estimation of the atmospheric stability.

Presently, two applications of numerical models in wind energy have gained importance: the short-term forecasting of wind power and simulation of virtual wind atlases for resource assessment. Both applications share similar methodologies: several numerical models are coupled, constituting a model chain, such that results from a global circulation model (GCM) are downscaled to the mesoscales by a regional model (Warner, 2011), whose results are further downscaled to the microscales that characterize wind farms, below 1 km. The difference lies in the purpose and the input of the model chain. Short-term forecasting is focused on the prediction of the power output of a wind farm for the next 3 days, requiring weather forecasts as initial and boundary conditions to the regional model. The goal is to assist electricity operators in the management of the electrical grid. The simulation of virtual atlases and masts employs the same model chain, only using analyses and re-analyses from global models to predict the flow field for a period in the past. The focus is not on the power forecasting for small time scales, but the prediction of the average power and wind characteristics, including turbulence and shear. As stated by Landberg *et al.* (2003), this approach is an alternative to measurement field campaigns.

Mesoscale modelling alone has been used to produce virtual wind atlases for a region. Frank and Landberg (1997) have estimated the wind power density over Ireland and more recently, (Larsén *et al.*, 2010) produced virtual wind maps for Northern Europe down to horizontal resolutions of 10 km, using re-analysis data downscaled with a mesoscale model. Landberg and Watson (1994; 1999) employed a model chain that combined a regional model with a linear model and statistical methods. The linear model was used to generate a transfer function to correct the mesoscale prediction for local effects, *i.e.*, orography and roughness. Stratification was neglected in the microscale model, resulting in a decrease of performance when thermal circulations dominate the flow. Kunz *et al.* (2000) developed a model chain where a non-linear CFD solver was included as a microscale model, but coupled with the regional model, using its output as initial and boundary conditions. Although such methodology is more expensive than the use of transfer functions, both unsteady phenomena and atmospheric stratification are considered.

1.2 Objectives

The purpose of this thesis was the development of CFD models for the forecast of wind characteristics in wind farms, located in complex sites. Two methodologies were used to downscale the results from weather predictions to the microscales: (i) employing transfer functions and (ii) using a model chain, where a microscale model is coupled to a mesoscale model. Both methodologies were used to predict the flow field characteristics and the power output of wind farms, having been compared against field measurements from mountainous terrain sites in Portugal.

The transfer function method was used in the short-term forecasting of wind power for two wind farms. The flow over the sites was characterized with the non-linear CFD model VENTOS® (Castro *et al.*, 2003) and a database of simulations was made encompassing the full range of directions of the incoming flow, at different velocities. The transfer function was created from these results, by relating the wind conditions at the turbines and a reference location. The wind conditions in the vicinity of the wind turbines was predicted by applying the transfer function to the weather forecast at the respective reference location. The power curve of the turbines was used to estimate the electrical output. The results refer to one year of data, which was compared against the measured power output of the wind farms.

The second method incorporated VENTOS® into the model chain as a microscale model, coupled with the mesoscale model. This implied changes to the code to consider the atmospheric stability and extract initial and boundary conditions from the mesoscale model output. Besides the two wind farms studied with the transfer function method, two other sites were used, comprising of 7 measurement masts and without wind turbines. Due to the required computational cost only 4 weeks of predictions were made: two in the summer and two in the end of autumn. The transfer function methodology was also applied to compare both methods against the measurements of the wind farms output. Several other quantities were analysed to assess the improvement that the microscale model provided when inserted into the model chain and its use as a tool to predict virtual time series.

The VENTOS® upgrade to work under non-neutral stratification regimes demanded for a validation of the code. With this purpose, the stably-stratified flow over an isolated axisymmetric mountain was investigated. A set of simulations were made to generate mountain waves under linear and non-linear flow regimes. Both inviscid and turbulent flow results were compared with predictions by analytic solutions and other reference numerical results in the literature.

1.3 Contributions of the thesis

This work started with the use of the VENTOS® code to perform simulations of the neutral flow over complex terrain. VENTOS® was initiated by Castro (1997) and its development continued, having been used in wind resource assessment to model atmospheric flows over complex terrain and forests (Lopes da Costa *et al.*, 2006; Palma *et al.*, 2008). It is currently used in wind resource studies by wind energy consultants,

Renewable Energy Systems Ltd. and Natural Power, under licence. The transfer functions used in Chapter 4 were made from the results obtained with VENTOS®, allowing for the short-term forecasting of wind power. This work was part of project EPREV (Previsão da Produção Eléctrica de Base Eólica), having been published under the following conference articles:

- Veiga Rodrigues C, Silva Santos CM, Palma JMLM, Castro FA, Miranda PMA, Rodrigues AH. 2008. Short-term Forecasting of a Wind Farm Output using CFD. In: *Proceedings of the European Wind Energy Conference and Exhibition*. European Wind Energy Association: Brussels, Belgium, ISBN 978-1-61567-115-1, pp. 675–684
- Veiga Rodrigues C, Matos JC, Paiva LT, Palma JMLM. 2010. Analysis of the Similarity in Turbulence Intensity and Wind Shear as Function of the Wind Velocity: Field Measurements and Numerical Results. In: *Proceedings of the European Wind Energy Conference and Exhibition*. European Wind Energy Association: Warsaw, Poland, ISBN 978-1-61782-310-7, pp. 2742–2751

and a chapter in a technical report, produced for the EPREV consortium:

- Rodrigues AH, Matos JC, Bessa RJ, Sousa JN, Monteiro C, Lopes JA, Veiga Rodrigues C, Silva Santos C, Castro FA, Palma JMLM, Dutra E, Martins JPA, Tomé R, Miranda PMA. 2008. *EPREV - Previsão da Produção Eléctrica de Base Eólica*. Contract report for the EPREV companies consortium, INEGI, INESC-Porto, CEsA, CGUL/IDL. 339 pp

An extension to this work was submitted to a journal and has been accepted for publication:

- Paiva LT, Veiga Rodrigues C, Palma JMLM. 2013. Determining a wind turbine power curve based on operating conditions. *Wind Energy* (manuscript ID: WE-10-0113.R6, in press)

On Chapter 3 and 5, the VENTOS® code was changed to include stratification and to allow its coupling with the regional model WRF (Weather Research and Forecast, Skamarock *et al.*, 2008). The first efforts to develop the coupled version are described in Castro *et al.* (2008), namely the parallelization technique. Two versions were made to validate the stratified code: one for inviscid flow and another for turbulent flow. Castro (1997) also made simulations with an inviscid code but this has several differences with the one used in Chapter 3, *e.g.*, the stratification was imposed through a density perturbation instead of using temperature. From the work done in the validation process, the coupled version suffered further changes, being later named VENTOS®/M. Among the changes made to develop both the stratified version of VENTOS® and VENTOS®/M, the most important were:

1. New geographic coordinate conversion routines to the FORTRAN routines written by Daly (1999), due to problems arising when different UTM (Universal Transverse Mercator) zones are present in the same map. Moreover, a Molodensky transformation was implemented in the code to reduce the error between global and local datums.
2. Re-evaluation of the procedure used to extract the wind conditions from the mesoscale model output and interpolate to the VENTOS®/M grid. To enforce mass conservation, the previous procedure changed the velocity values at one domain

boundary only, which sporadically led to unrealistic speeds. The new procedure enforces mass conservation by changing all domain boundaries. The interpolation routines were also changed to fit wall functions for grid nodes in the surface-layer, instead of a linear interpolation.

3. The pressure weighted interpolation scheme (Appendix A, §A.3) did not store the cell-face velocities from past time-steps, interpolating these instead from the nodal velocity fields, to reduce cache memory. It was verified that this yielded non-physical solutions of the pressure field when the flow was stably-stratified. The Rhie and Chow (1983) scheme was changed such that the cell-face velocities are kept. Furthermore, the PICTURE scheme of Pascau (2011) was implemented into the code, having been selected to perform the simulations from Chapter 3 and 5.

4. Initially the computation of surface fluxes was made only for momentum, using a zero gradient boundary condition for the heat flux at the wall. Such solution neglected the existence of a thermal boundary-layer. This was changed and both momentum and heat fluxes at the surface are computed using an iterative procedure (Chapter 5, §5.3.5), to have both the momentum and thermal boundary-layers in equilibrium with the velocity and temperature values above the wall.

5. Several outflow boundary conditions were tested for the stratified VENTOS® version. A brief description of these tests is found in Appendix C.

Part of the work developed in this thesis was used in the following publications, where the VENTOS®/M code was employed to downscale results from the WRF regional model:

- Ely A, Stuart P, Zhu M, Palma JMLM, Veiga Rodrigues C, Chertovskih R. 2012. Mesoscale and CFD Coupling: An Improved Technique for Predicting Microscale Wind. In: *Proceedings of the EWEA annual Conference and Exhibition*. European Wind Energy Association: Copenhagen, Denmark. 10 pp

- Ely A, Stuart P, Zhu M, Donnet V, Feeney S, Palma JMLM, Veiga Rodrigues C, Chertovskih R. 2013a. Comparisons of Coupled Mesoscale-CFD Model Predictions with Atmospheric Stability Measurements. In: *Proceedings of the EWEA annual Conference and Exhibition*. European Wind Energy Association: Vienna, Austria. 11 pp

- Ely A, Stuart P, Zhu M Chertovskih R, Palma JMLM, Veiga Rodrigues C. 2013b. Mesoscale and CFD coupling: an improved technique for predicting microscale wind. *Wind Energy* (submitted)

1.4 Outline of the thesis

This thesis is divided in six chapters. The introduction to the thesis is made in Chapter 1, where a brief state of the art is made and the objectives of the present work are referred.

In Chapter 2, the fundamental equations that govern fluid flow and their application to the atmospheric surface-layer are described. An overview of the computer model and its numerical techniques is made, both for incompressible neutrally stratified flow and anelastic flow where atmospheric stratification is considered.

Chapter 3 describes the numerical simulation of the stably-stratified flow over an isolated mountain. This work was made to serve as a validation of the computer model under non-neutral stratification, but also to study gravity waves phenomena and their interaction with a surface boundary-layer.

Chapter 4 deals with the short-term forecasting of the power output of two wind farms. The forecast method used a transfer function, built from the results of neutral flow simulations of several possible wind directions.

The coupling between mesoscale and microscale model to predict the wind conditions in complex terrain is presented in Chapter 5. The model chain is used for both power forecasting and the generation of virtual time series of wind conditions.

The conclusions of the thesis are presented in Chapter 6, where a synthesis is made to link the most important findings. Suggestions for future work are included in the end.

Chapter 2

Mathematical model and numerical techniques

In this chapter, the fundamental equations and mathematical models used in this work are presented. A description of the main physical processes in atmospheric flows is made, namely the conservation of mass, momentum and energy; and the models used for turbulence and thermal stratification. The techniques used to numerically solve the fluid flow equations and for simulating the atmospheric boundary layer are shown.

2.1 Fundamental equations

The equation for the conservation of mass, commonly designated as continuity, is:

$$\frac{\partial \rho}{\partial t} + \nabla\cdot(\rho\,\vec{u}) = 0\,, \tag{2.1}$$

with ρ as the fluid density, $\vec{u}$ the velocity vector and $\nabla\cdot()$ is the divergence operator. Following Lions (1996), the equations for the conservation of momentum for a compressible fluid are:

$$\frac{\partial}{\partial t}(\rho\,\vec{u}) + \nabla\cdot(\rho\,\vec{u}\otimes\vec{u}) = -\nabla p + \nabla\cdot\underline{\underline{\tau}} + \rho\,\vec{g} + \rho\,\vec{f}_b\,. \tag{2.2}$$

for each component of the velocity vector. In these, p is the absolute pressure acting on the boundaries of an infinitesimal parcel of fluid and $\vec{f}_b$ is the sum of any forces acting in its volume. In a Cartesian coordinate system where z is aligned with the vertical direction, the gravity acceleration vector $\vec{g}$ has only the vertical component $-g\,\hat{\mathbf{e}}_3$. In the second term, named the advection term, the result of $\vec{u}\otimes\vec{u}$ is a second rank tensor with the operator $\otimes$ representing the dyadic product.* Considering that the fluid is Newtonian, *i.e.*, stress varies linearly with the rate-of-strain, the deviatoric stress tensor $\underline{\underline{\tau}}$ is defined as:

$$\underline{\underline{\tau}} = \mu\,\left[\nabla\,\vec{u} + (\nabla\,\vec{u}\,)^{\mathsf{T}}\right] - \mathrm{I}\,\mu\,\frac{2}{3}\,\nabla\cdot\vec{u}\,, \tag{2.3}$$

*The divergence of $\nabla\cdot(\vec{u}\otimes\vec{u})$ is equivalent to write $\sum_i\sum_j \frac{\partial}{\partial x_j}\left(u_j\,u_i\right)\hat{\mathbf{e}}_i$, using Gibb's notation.

where μ is the fluid dynamic viscosity and I is the identity matrix. It should be noted that the gradient of the velocity vector is a second rank tensor:

$$\nabla \vec{u} \equiv \nabla \otimes \vec{u} = \sum_i \sum_j \frac{\partial u_i}{\partial x_j} \hat{\mathbf{e}}_i \hat{\mathbf{e}}_j \,.$$

For a fluid at rest, the eqs. (2.2) become,

$$-\nabla p + \rho \vec{g} = 0 \quad \Rightarrow \quad \frac{dp_{\text{H}}}{dz} = -\rho_{\text{H}} g \,, \tag{2.4}$$

meaning that the pressure gradient is not null, in order to compensate the acceleration due to gravity. The pressure resulting from this vertical gradient can be used as a reference state, *i.e.* an hydrostatic pressure and density, p_{H} and ρ_{H}. With these, a perturbed state for a fluid in motion is defined by subtraction from the total values:

$$\begin{cases} p = p_{\text{H}} + \widehat{p} \,, \\ \rho = \rho_{\text{H}} + \widehat{\rho} \,. \end{cases} \tag{2.5}$$

By substituting p with p_{H} and $\widehat{p}$ in the pressure gradient term on eqs. (2.2), these yield the convenient form:

$$\frac{\partial}{\partial t}(\rho \vec{u}) + \nabla \cdot (\rho \vec{u} \otimes \vec{u}) = -\nabla \widehat{p} + \nabla \cdot \underline{\underline{\tau}} + \rho \vec{f}_b \,. \tag{2.6}$$

The presented conservations equations are said to be in the Euleurian frame of reference, *i.e.*, these are focused on a fixed spatial location and the fluid motion that passes through that location, as function of time. The equations can be rearranged to obtain a Lagrangian frame of reference, tracking instead an individual fluid parcel as it travels through space and time. For this purpose the operator $D_t(\,)$, known in the literature as the substantial derivative or Lagrangian derivative, is defined as:

$$D_t(\,) = \frac{\partial}{\partial t}(\,) + \vec{u} \cdot \nabla(\,) \,. \tag{2.7}$$

Thus, in a Lagrangian perspective, the equations for conservation of mass (2.1) and momentum (2.6) become:

$$D_t(\rho) + \rho \nabla \cdot \vec{u} = 0 \,, \tag{2.8}$$

$$D_t(\rho \vec{u}) + \rho \vec{u} \, \nabla \cdot \vec{u} = -\nabla \widehat{p} + \nabla \cdot \underline{\underline{\tau}} + \rho \vec{f}_b \,. \tag{2.9}$$

Note that the equation for conservation of mass can itself be used to simplify the advective term of the momentum equations. By straightforward algebraic manipulation:

$$\begin{aligned} D_t(\rho) \;&=\; \frac{\partial}{\partial t}(\rho) + \vec{u} \cdot \nabla \rho \;=\; -\rho \nabla \cdot \vec{u} \,, \\ \Rightarrow \quad D_t(\rho \vec{u}) + \rho \vec{u} \, \nabla \cdot \vec{u} \;&=\; \rho \, D_t(\vec{u}) + \vec{u} \, D_t(\rho) + \rho \vec{u} \, \nabla \cdot \vec{u} \\ &\equiv\; \rho \, D_t(\vec{u}) \;=\; \rho \frac{\partial \vec{u}}{\partial t} + \rho \vec{u} \cdot \nabla \vec{u} \,. \end{aligned} \tag{2.10}$$

2.1.1 Thermodynamic relations and states

In the atmosphere, dry air behaves approximately as an ideal gas, thus the ideal gas law may be used to model how its observable thermodynamic properties relate,

$$p = \rho R_d T \quad \Rightarrow \quad \frac{dp}{p} = \frac{d\rho}{\rho} + \frac{dT}{T} \,. \tag{2.11}$$

In this equation the pressure, p, is proportional to the gas density, ρ, and temperature, T. The proportionality constant R_d is known as the specific gas constant, with the value of 287.052 $\mathrm{J\,kg^{-1}\,K^{-1}}$ for dry air.

As a parcel of air is displaced vertically in the atmosphere, the internal energy of the parcel will balance the heat and work exchange between the environment and the parcel. This balance is given by the 1$^{\text{st}}$ law of thermodynamics which states that the energy of a system is conserved:

$$de_I = dq + dw \,, \tag{2.12}$$

where de_I is the variation of internal energy of the system, where the quantities are specific to one unit mass of fluid. The internal energy, e_I, is the sum of the kinetic energy of all the molecules which compose the air parcel. All variation of e_I happens due to the addition of sensible heat, q, or work, w, done on the parcel from its environment. Though the potential energy related to molecular forces can change the internal energy, like the chemical potential and latent heat due to phase changes, these will not be considered. The internal energy is difficult to quantify, being related to other properties of the system by eq. (2.12).

For a process happening at constant pressure, $\left(\partial q/\partial T\right)_p = c_p$, where c_p is known as the isobaric specific heat capacity and its variation with temperature is small, allowing to be treated as a constant. Likewise, for a process at constant volume, $\left(\partial q/\partial T\right)_v = c_v$, with c_v as the isochoric specific heat capacity. Many processes in the atmosphere are often assumed to be adiabatic, *i.e.*, there is no heat transfer to or from the system. This implies that the following relations hold:

$$\begin{cases} \dfrac{c_p}{R_d}\dfrac{dT}{T} = \dfrac{dp}{p} \\[2ex] \dfrac{c_v}{R_d}\dfrac{dT}{T} = \dfrac{d\rho}{\rho} \end{cases} \quad \Rightarrow \quad \frac{T}{T_0} = \left[\frac{p}{p_0}\right]^{\frac{R_d}{c_p}} = \left[\frac{\rho}{\rho_0}\right]^{\frac{R_d}{c_v}} \,. \tag{2.13}$$

When an air parcel is convected from its original position, it may not be in thermodynamical equilibrium with its environment. Assuming that the parcel's pressure balances its surroundings much faster than any other processes, the parcel will only be in thermodynamical equilibrium if ρ or T are also balanced. Because the atmosphere is in hydrostatic equilibrium (as stated in eq. (2.4)), if a parcel rises it must also expands, balancing its temperature by performing work, without any heating or cooling. Thus, in an adiabatic atmosphere any displaced parcel will be in equilibrium. By combining eqs. (2.4) and (2.13), this adiabatic temperature gradient is estimated as:

$$\frac{dT_{\mathrm{H}}}{dz} = -\frac{g}{c_p} \,. \tag{2.14}$$

This linear decay is known as the adiabatic temperature lapse rate. For a dry atmosphere in hydrostatic equilibrium, this would be the reference state for neutral stability, *i.e.*, any vertical displacement of an air parcel is neither damped nor accelerated by buoyant forces, as these are null because the parcel is in thermal equilibrium with its environment.

Depending on the existence of heat transfer between the horizontal layers of the atmosphere, a convected parcel where its ρ and T differs from its surroundings will experience a buoyancy force (acting accordingly to the Archimedes' principle):

(i) Buoyant forces will result in a restoring force, dampening vertical motions for temperature gradients greater than $-\,g/c_p$. This is designated as stable stratification.

(ii) Otherwise, a parcel with a vertical motion will tend to continue its movement because of the increasingly density unbalance with its environment. This is known as an unstable or convective stratification.

This is mainly influenced by the ground heating or cooling due to the existence of radiation, as well as other phenomena like moist stratification.

To assess the stability of the atmospheric stratification in a more expedite way, a potential temperature, θ, is defined based on the adiabatic relations in eq. (2.13):

$$\theta = T \left[\frac{p_{00}}{p}\right]^{\frac{R_d}{c_p}} . \tag{2.15}$$

The quantity p_{00} is a reference pressure and is usually given a value of 100 kPa. Likewise, it is useful to define a variable Π, such that,

$$\Pi = \left[\frac{p}{p_{00}}\right]^{\frac{R_d}{c_p}} \quad \Rightarrow \quad \theta\,\Pi = T\,. \tag{2.16}$$

This adiabatic pressure ratio is named in the literature as the Exner function. These definitions and the equation of state can be manipulated to obtain the following mathematical expressions:

$$\frac{d\theta}{\theta} + \frac{d\Pi}{\Pi} = \frac{dT}{T}\,, \tag{2.17}$$

$$\frac{d\Pi}{\Pi} = \frac{R_d}{c_p}\frac{dP}{P}\,, \tag{2.18}$$

$$\frac{1}{\Pi}\frac{d\Pi}{dz} = -\frac{g}{c_p\,T} \quad \Rightarrow \quad \frac{d\Pi}{dz} = -\frac{g}{c_p\,\theta}\,, \tag{2.19}$$

$$\rho = \frac{p_{00}\,\Pi^{\frac{c_v}{R_d}}}{R_d\,\theta}\,. \tag{2.20}$$

The stability at a certain height above the mean sea level is simply inferred from the

sign of the gradient of θ:

$$\begin{cases} \dfrac{d\theta}{dz} < 0 \quad \Rightarrow \quad \dfrac{dT}{dz} < -\dfrac{g}{c_p}\,, & \text{unstably stratified} \\ \dfrac{d\theta}{dz} = 0 \quad \Rightarrow \quad \dfrac{dT}{dz} = -\dfrac{g}{c_p}\,, & \text{neutral} \\ \dfrac{d\theta}{dz} > 0 \quad \Rightarrow \quad \dfrac{dT}{dz} > -\dfrac{g}{c_p}\,, & \text{stably stratified} \end{cases} , \tag{2.21}$$

A measure based on the gradient of θ is the static stability parameter, defined as:

$$s = \frac{g}{\theta}\frac{d\theta}{dz} = \frac{g}{T}\left[\frac{dT}{dz} + \frac{g}{c_p}\right] . \tag{2.22}$$

In a stably stratified environment, a vertically displaced air parcel will tend to return to its original position, producing oscillations from the balance between buoyancy and gravity forces. These are known as gravity waves, characterized by their frequency of oscillation:

$$N = \sqrt{\frac{g}{\theta}\frac{d\theta}{dz}} = \sqrt{s}\,, \tag{2.23}$$

also named as Brunt-Väisälä frequency or buoyancy frequency.

For details on the definitions and mathematical manipulations of the equations describing thermodynamical processes, refer to Fermi (1956).

Common atmospheric states and profiles of thermodynamical quantities

The base state of the atmosphere is described by knowing its thermodynamical properties and how they vary with height. Such is difficult to obtain and without any information by field measurements, it must be specified under idealized conditions.

1. Adiabatic atmosphere, corresponding to a null vertical gradient of θ, thus a neutrally stratified atmosphere.
2. Isothermal atmosphere, corresponding to a constant temperature profile. This yields a stable stratified atmosphere.
3. Constant temperature gradient, corresponding to a linear vertical profile. The solution allows for stable, neutral and unstable stratification regimes, depending on the value prescribed for the gradient.
4. Isopycnic atmosphere, corresponding to a constant density profile, based on the considerations used for the simulation of incompressible fluids. This assumption, together with the hydrostatic equilibrium, yields a state that is unstably stratified.
5. Constant Brunt-Väisälä frequency. Such condition only allows for stable stratified solutions for real values of N.
6. Constant gradient of θ, corresponding to a linear vertical profile. This condition allows solutions for any stratification regime.

Table 2.1: Reference states for an atmosphere in hydrostatic equilibrium.

1. Adiabatic	2. Isothermal	3. Constant $\frac{dT}{dz}$	4. Isopycnic	5. Constant N	6. Constant $\frac{d\theta}{dz}$
$\frac{d\theta}{dz} = 0$	$\frac{dT}{dz} = 0$	$\frac{dT}{dz} = \Gamma$	$\frac{d\rho}{dz} = 0$	$\frac{1}{\theta}\frac{d\theta}{dz} = \frac{N^2}{g}$	$\frac{d\theta}{dz} = \Gamma_\theta$
$\theta(z) = \theta_0$	$T(z) = T_0$	$T(z) = T_0 + z\,\Gamma$	$\rho(z) = \rho_0$	$\theta(z) = \theta_0 \exp\left(\frac{z\,N^2}{g}\right)$	$\theta(z) = \theta_0 + z\,\Gamma_\theta$
$\frac{d\Pi}{dz} = -\frac{g}{c_p\,\theta_0}$	$\frac{1}{p}\frac{dp}{dz} = -\frac{g}{R_d\,T_0}$	$\frac{1}{p}\frac{dp}{dz} = -\frac{g}{R_d\,T}$	$\frac{dp}{dz} = -\rho_0\,g$	$\frac{d\Pi}{dz} = -\frac{g}{c_p\,\theta}$	$\frac{d\Pi}{dz} = -\frac{g}{c_p\,\theta}$
$\Pi = \Pi_0 - z\frac{g}{c_p\,\theta_0}$	$p = p_0 \exp\left(-\frac{z\,g}{R_d\,T_0}\right)$	$p = p_0\left[\frac{T}{T_0}\right]^{-\frac{g}{R_d\Gamma}}$	$p = p_0 - z\,\rho_0\,g$	$\Pi = \Pi_0 + \frac{g^2}{c_p N^2}\left[\frac{1}{\theta} - \frac{1}{\theta_0}\right]$	$\Pi = \Pi_0 - \frac{g}{c_p\,\Gamma_\theta}\log\left(\frac{\theta}{\theta_0}\right)$
$\frac{dT}{dz} = -\frac{g}{c_p}$	$\frac{1}{\rho}\frac{d\rho}{dz} = \frac{1}{p}\frac{dp}{dz}$	$\frac{1}{\rho}\frac{d\rho}{dz} = -\frac{1}{T}\left[\frac{g}{R_d} + \Gamma\right]$	$\frac{dT}{dz} = -\frac{g}{R_d}$	$\frac{1}{p}\frac{dp}{dz} = \frac{c_p}{R_d\,\Pi}\frac{d\Pi}{dz}$	$\frac{1}{p}\frac{dp}{dz} = \frac{c_p}{R_d\,\Pi}\frac{d\Pi}{dz}$
$T = T_0 - z\frac{g}{c_p}$	$\rho = \rho_0 \exp\left(-\frac{z\,g}{R_d\,T_0}\right)$	$\rho = \rho_0\left[\frac{T}{T_0}\right]^{-1-\frac{g}{R_d\Gamma}}$	$T = T_0 - z\frac{g}{R_d}$	$p = p_{00}\,\Pi^{\frac{\gamma}{\gamma-1}}$	$p = p_{00}\,\Pi^{\frac{\gamma}{\gamma-1}}$
$\frac{1}{p}\frac{dp}{dz} = -\frac{g}{R_d\,T}$	$\frac{1}{\theta}\frac{d\theta}{dz} = \frac{g}{c_p\,T_0}$	$\frac{1}{\theta}\frac{d\theta}{dz} = \frac{1}{T}\left[\frac{g}{c_p} + \Gamma\right]$	$\frac{1}{\theta}\frac{d\theta}{dz} = -\frac{g}{R_d\,\gamma\,T}$	$\frac{dT}{dz} = -\frac{g}{c_p} + \frac{T\,N^2}{g}$	$\frac{dT}{dz} = -\frac{g}{c_p} + \Gamma_\theta\,\Pi$
$p = p_0\left[\frac{T}{T_0}\right]^{\frac{\gamma}{\gamma-1}}$	$\theta = \theta_0 \exp\left(\frac{z\,g}{c_p\,T_0}\right)$	$\theta = \theta_0\left[\frac{T}{T_0}\right]^{1+\frac{g}{c_p\Gamma}}$	$\theta = \theta_0\left[\frac{T}{T_0}\right]^{\frac{1}{\gamma}}$	$T = \theta\,\Pi$	$T = \theta\,\Pi$
$\frac{1}{\rho}\frac{d\rho}{dz} = \frac{1}{T}\left[\frac{g}{c_p} - \frac{g}{R_d}\right]$	$\frac{1}{\Pi}\frac{d\Pi}{dz} = -\frac{g}{c_p\,T_0}$	$\frac{1}{\Pi}\frac{d\Pi}{dz} = -\frac{g}{c_p\,T}$	$\frac{1}{\Pi}\frac{d\Pi}{dz} = -\frac{g}{c_p\,T}$	$\frac{1}{\rho}\frac{d\rho}{dz} = -\frac{g}{\gamma\,R_d\,T} - \frac{N^2}{g}$	$\frac{1}{\rho}\frac{d\rho}{dz} = -\frac{g}{\gamma\,R_d\,T} - \frac{\Gamma_\theta}{\theta}$
$\rho = \rho_0\left[\frac{T}{T_0}\right]^{\frac{1}{\gamma-1}}$	$\Pi = \Pi_0 \exp\left(-\frac{z\,g}{c_p\,T_0}\right)$	$\Pi = \Pi_0\left[\frac{T}{T_0}\right]^{1-\frac{g}{c_p\Gamma}}$	$\Pi = \Pi_0\left[\frac{T}{T_0}\right]^{1-\frac{1}{\gamma}}$	$\rho = \frac{p_{00}\,\Pi^{\frac{1}{\gamma-1}}}{R_d\,\theta}$	$\rho = \frac{p_{00}\,\Pi^{\frac{1}{\gamma-1}}}{R_d\,\theta}$

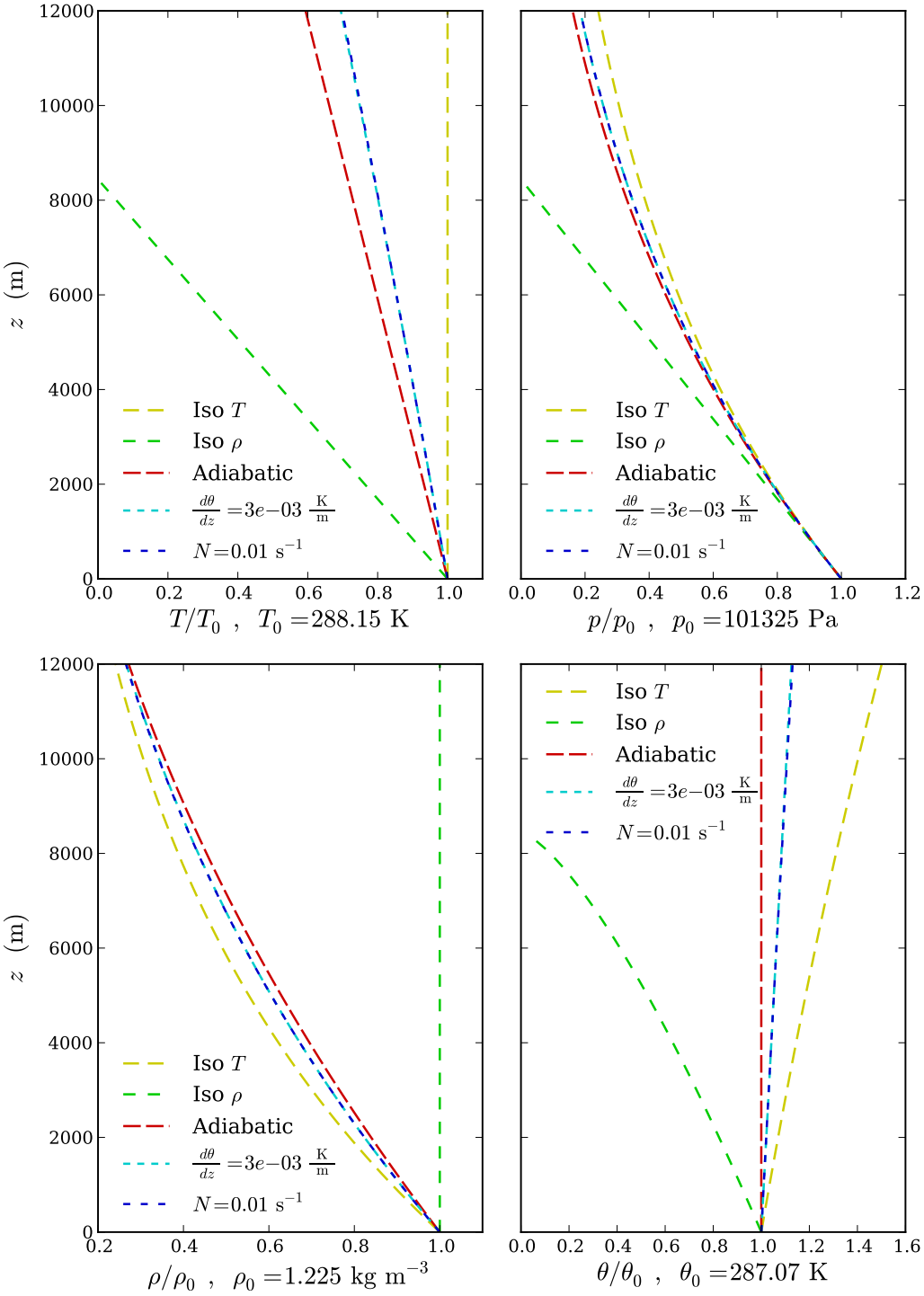

Figure 2.1: Comparison of several idealized states for the vertical profiles of the thermodynamical quantities of the atmosphere. The values at $z = 0\,\mathrm{m}$ are assumed as $T_0 = 288.15\,\mathrm{K}$, $p_0 = 101325\,\mathrm{Pa}$ and $\rho_0 = 1.225\,\mathrm{kg\,m^{-3}}$.

Table 2.2: Scales for an isothermal hydrostatic atmosphere at $T = 288.15\,\mathrm{K}$.

Pressure scale-height	$H_p = \left\lvert \frac{1}{p}\frac{dp}{dz} \right\rvert^{-1} = \frac{R_d\, T_0}{g}$	$\sim 8440\,\mathrm{m}$
Density scale-height	$H_\rho = \left\lvert \frac{1}{\rho}\frac{d\rho}{dz} \right\rvert^{-1} \equiv H_p$	$\sim 8440\,\mathrm{m}$
Potential temperature scale-height	$H_\theta = \left\lvert \frac{1}{\theta}\frac{d\theta}{dz} \right\rvert^{-1} = \frac{c_p\, T_0}{g} = \frac{c_p}{R_d} H_p$	$\sim 29541\,\mathrm{m}$
Buoyancy frequency	$N = \sqrt{\frac{g}{\theta}\frac{d\theta}{dz}} = \sqrt{g/H_\theta}$	$\sim 0.0182\,\mathrm{s}^{-1}$
Gravity waves speed	$C_{gw} = H_\rho\, N = \sqrt{g\, H_\rho^2 / H_\theta}$	$\sim 154\,\mathrm{m\,s}^{-1}$
Sound speed	$C_{gw} = \sqrt{\gamma\, p/\rho} = \sqrt{\gamma\, R_d\, T_0}$	$\sim 340\,\mathrm{m\,s}^{-1}$

For each of these states, the equations for the vertical profiles and gradients of T, ρ, p, θ and Π can be found in Table 2.1. In Figure 2.1 these profiles are presented, using reference values usually found in the literature.

Characteristic scales in the atmosphere

To perform a dimensional analysis of the fundamental equations in order to determine what are the relevant physical processes to be modelled, scales that characterize the troposphere must be estimated. Following Ogura and Phillips (1962) and more recently Klein (2010), these are estimated considering an isothermal atmosphere at rest, thus in hydrostatic equilibrium as stated in eq. (2.4).

From the thermodynamical relations given in the second collumn of Table 2.1, numerical values for the scale-heigths of p, ρ and θ are presented in Table 2.2, considering a sea level temperature of $T_0 = 288.15\,\mathrm{K}$. Additionally, the corresponding value for the Brunt-Väisälä frequency, the speed of propagation of internal gravity waves and sound waves are given.

2.1.2 Equation for the conservation of energy

A parcel of fluid that is in motion is a thermodynamical system whose energy is the sum of its internal energy, kinetic energy and potential energy. When applying the 1st law of thermodynamics in eq. (2.12) to such a system, it is the total energy of the system that should be considered, thus:

$$D_t\left(\mathcal{E}_\mathcal{I}\right) = \dot{\mathcal{Q}} + \dot{\mathcal{W}}\,. \tag{2.24}$$

The total energy, $\mathcal{E}_\mathcal{I}$, will increase with the amount of heat transferred into the system, $\mathcal{Q}$, as well as the work done from the forces exerted on it, $\mathcal{W}$. Because the Lagrangian

derivative is being used (eq. (2.7)), the mass of the parcel of fluid being tracked is constant, such that:

$$D_t\left(\mathcal{E}_\mathcal{T}\right) \equiv \rho\,\Omega\,D_t\left(e_\mathcal{T}\right) = \rho\,\Omega\,D_t\left(e_I + \frac{\vec{u}\cdot\vec{u}}{2} - \vec{g}\cdot\vec{x}\right)$$
$$= \rho\,\Omega\left[D_t\left(e_I\right) + \vec{u}\cdot D_t\left(\vec{u}\right) - \vec{g}\cdot\vec{u}\right] , \tag{2.25}$$

where $e_\mathcal{T}$ and e_I are the total and internal energy, both in $\mathrm{J\,kg^{-1}}$, and Ω is the volume of the parcel. For the potential energy term, only the gravitational potential was considered. $\mathcal{Q}$ is the net heat transfer by conduction and radiation into the parcel by its boundaries. Thus, using Fourier's law and the divergence theorem:

$$\dot{\mathcal{Q}} = -\oiint_S \vec{q}\cdot\hat{\mathbf{n}}\,dS = -\int_\Omega \nabla\cdot\vec{q}\,d\Omega = \int_\Omega \nabla\cdot\left(\lambda\nabla T\right)d\Omega - \int_\Omega \nabla\cdot\vec{q}_r\,d\Omega ,$$

where S refers to the surface formed by the boundaries of the parcel, $\hat{\mathbf{n}}$ is the outward unit vector field of surface S, $\vec{q}$ is the heat flux in $\mathrm{J\,s^{-1}\,m^{-2}}$, $\vec{q}_r$ is the thermal radiation flux in the same units and λ is the thermal conductivity of the medium in $\mathrm{J\,s^{-1}\,m^{-1}\,K^{-1}}$. Similarly, the net work $\mathcal{W}$ generated by the forces acting on the boundaries of the parcel. Thus, integrating the stress tensor, $\underline{\underline{\sigma}} = -p\,\mathrm{I} + \underline{\underline{\tau}}$, over surface S:

$$\dot{\mathcal{W}} = \oiint_S \left(\vec{u}\cdot\underline{\underline{\sigma}}\right)\cdot\hat{\mathbf{n}}\,dS = \int_\Omega \nabla\cdot\left(\vec{u}\cdot\underline{\underline{\sigma}}\right)d\Omega$$
$$= -\int_\Omega \nabla\cdot\left(p\,\vec{u}\right)d\Omega + \int_\Omega \nabla\cdot\left(\vec{u}\cdot\underline{\underline{\tau}}\right)d\Omega .$$

Substituting in eq. (2.24) yields the equation for conservation of total energy:

$$\rho\,D_t\left(e_\mathcal{T}\right) = \nabla\cdot\left(\lambda\,\nabla T\right) - \nabla\cdot\left(p\,\vec{u}\right) + \nabla\cdot\left(\vec{u}\cdot\underline{\underline{\tau}}\right) - \nabla\cdot\vec{q}_r . \tag{2.26}$$

Using the momentum equation (2.2), the kinetic energy term in eq. (2.25) is given as,

$$\rho\,\vec{u}\cdot D_t\left(\vec{u}\right) \equiv -\vec{u}\cdot\nabla p + \vec{u}\cdot\left(\nabla\cdot\underline{\underline{\tau}}\right) + \rho\,\vec{u}\cdot\vec{g} , \tag{2.27}$$

Substitution of eqs. (2.26) and (2.27) into (2.25) returns the equation for conservation of internal energy:

$$\rho\,D_t\left(e_I\right) = \nabla\cdot\left(\lambda\,\nabla T\right) - p\,\nabla\cdot\vec{u} + \underline{\underline{\tau}} : \nabla\,\vec{u} - \nabla\cdot\vec{q}_r , \tag{2.28}$$

where the operator : represents the double inner product.[†] The last term is known as the dissipation function and in indicial notation becomes:

$$\underline{\underline{\tau}} : \nabla\,\vec{u} = \frac{1}{2}\,\mu\sum_i\sum_j\left[\frac{\partial\,u_i}{\partial\,x_j} + \frac{\partial\,u_j}{\partial\,x_i}\right]^2 - \frac{2}{3}\,\mu\left[\sum_k \frac{\partial\,u_k}{\partial\,x_k}\right]^2 .$$

[†]For the second rank tensors $\underline{\underline{A}}$ and $\underline{\underline{B}}$, the double inner product is given by $\underline{\underline{A}} : \underline{\underline{B}} \equiv \sum_i\sum_j A_{ij}\,B_{ij}$.

By using the isobaric specific heat capacity, the internal energy can be related to temperature. From the definition of enthalpy (*cf.* Fermi, 1956),

$$\begin{aligned} & D_t\left(e_I + p\,\rho^{-1}\right) = c_p\,D_t\left(T\right) \quad \Leftrightarrow \\ \Leftrightarrow \quad & \rho\,D_t\left(e_I\right) + D_t\left(p\right) - p\,\rho^{-1}\,D_t\left(\rho\right) = \rho\,c_p\,D_t\left(T\right) \quad \Leftrightarrow \\ \Rightarrow \quad & \rho\,D_t\left(e_I\right) = \rho\,c_p\,D_t\left(T\right) - D_t\left(p\right) - p\,\nabla\cdot\vec{u}\;. \end{aligned} \tag{2.29}$$

Substitution of eq. (2.29) into (2.28) gives the temperature transport equation,

$$\rho\,c_p\,D_t\left(T\right) = \nabla\cdot\left(\lambda\,\nabla T\right) + D_t\left(p\right) + \underline{\underline{\tau}} : \nabla\,\vec{u} - \nabla\cdot\vec{q}_r\;. \tag{2.30}$$

Instead, if the isochoric specific heat capacity is used,

$$\rho\,D_t\left(e_I\right) \equiv \rho\,c_v\,D_t\left(T\right) = \nabla\cdot\left(\lambda\,\nabla T\right) - p\,\nabla\cdot\vec{u} + \underline{\underline{\tau}} : \nabla\,\vec{u} - \nabla\cdot\vec{q}_r\;. \tag{2.31}$$

These equations are all different ways to describe the energetic balance in eq. (2.24), whose derivation found in most fluid dynamics textbooks is similar (*e.g.* Schlichting and Gersten, 2000). However, when applying the conservation of energy to atmospheric flows, it is more convenient to use the potential temperature θ, because it remains constant for adiabatic processes. Using expressions (2.17-2.20),

$$\begin{aligned} \rho\,c_p\,D_t\left(T\right) \;&\equiv\; \rho\,c_p\,\frac{T}{\theta}D_t\left(\theta\right) + D_t\left(p\right)\;, \\ \Rightarrow \quad \rho\,D_t\left(\theta\right) \;&=\; \frac{\theta}{c_p\,T}\left[\nabla\cdot\left(\lambda\,\nabla T\right) + \underline{\underline{\tau}} : \nabla\,\vec{u} - \nabla\cdot\vec{q}_r\right]. \end{aligned} \tag{2.32}$$

Although eqs. (2.30) and (2.32) can be found on works like Lafore *et al.* (1998) and Alinot and Masson (2005), most authors in the literature substitute the energy conservation by a transport equation for θ, like,

$$D_t\left(\rho\,\theta\right) \;=\; 0\;, \tag{2.33}$$

or, accounting for diffusive transport,

$$D_t\left(\rho\,\theta\right) \;=\; \nabla\cdot\left(\frac{\lambda}{c_p}\,\nabla\theta\right) + S_\theta\;. \tag{2.34}$$

Following Lynch and Cassano (2006), by modelling all motion of an air parcel as an adiabatic process, potential temperature is conserved. This reasoning is also found in the books of Stull (1988), Pielke (2002) and Holton (2004).

2.1.3 Buoyancy-driven flows and the Boussinesq approximation

Changes in the fluid density act as a driving force in the flow. This force is known as buoyancy and is mathematically modelled by the principle of Archimede's, *i.e.*, for a body immersed in a fluid, an upward force is exerted that equals the weight of the volume of fluid which was displaced by that body.

Considering an air parcel with temperature, T_{pa}, and density, ρ_{pa}, which is advected vertically through a surrounding atmosphere in hydrostatic equilibrium with temperature, T_{atm}, and density, ρ_{atm}, the application of the equations of continuity (2.1) and vertical momentum (2.2) in a Lagrangian frame of reference yields:

$$\begin{cases} D_t\left(\rho_{\text{pa}}\right) + \rho_{\text{pa}} \dfrac{\partial w_{\text{pa}}}{\partial z} = 0 \,, \\ D_t\left(\rho_{\text{pa}}\, w_{\text{pa}}\right) + \rho_{\text{pa}}\, w_{\text{pa}} \dfrac{\partial w_{\text{pa}}}{\partial z} = -\dfrac{\partial p_{\text{pa}}}{\partial z} - \rho_{\text{pa}}\, g + \dfrac{\partial \tau_{33}}{\partial z} \,. \end{cases} \tag{2.35}$$

This system of equations is obtained considering that the velocity vector of the parcel, $\vec{u}_{\text{pa}}$, consists only of the vertical component w_{pa}. Because,

$$D_t\left(\rho_{\text{pa}}\, w_{\text{pa}}\right) = \rho_{\text{pa}}\, D_t\left(w_{\text{pa}}\right) + w_{\text{pa}}\, D_t\left(\rho_{\text{pa}}\right) = \rho_{\text{pa}}\, D_t\left(w_{\text{pa}}\right) - w_{\text{pa}}\, \rho_{\text{pa}} \frac{\partial w_{\text{pa}}}{\partial z} \,,$$

the system in (2.35) simplifies to:

$$\rho_{\text{pa}}\, D_t\left(w_{\text{pa}}\right) = -\frac{\partial p_{\text{pa}}}{\partial z} - \rho_{\text{pa}}\, g + \frac{\partial \tau_{33}}{\partial z} \,. \tag{2.36}$$

Neglecting the effects of the viscous term, τ_{33}, and following the assumption postulated on §2.1.1, that the parcel's pressure balances its surroundings much faster than any other processes, p_{pa} will always equal p_{atm} , hence:

$$\frac{\partial p_{\text{pa}}}{\partial z} \equiv \frac{\partial p_{\text{atm}}}{\partial z} = -\rho_{\text{atm}}\, g \,.$$

Equation (2.36) thus becomes:

$$D_t\left(w_{\text{pa}}\right) = \frac{\rho_{\text{atm}} - \rho_{\text{pa}}}{\rho_{\text{pa}}}\, g \equiv \mathcal{B} \,. \tag{2.37}$$

The result in eq. (2.37) defines the buoyancy force per unit mass, $\mathcal{B}$, which ultimately is given by the difference in density between the air parcel and its surrounding fluid. Applying the equation of state (2.11) and the definition of θ in eq. (2.15),

$$\begin{aligned} & p_{\text{pa}} = p_{\text{atm}} \quad \Leftrightarrow \quad \rho_{\text{pa}}\, R_d\, T_{\text{pa}} = \rho_{\text{atm}}\, R_d\, T_{\text{atm}} \,, \\ & \Pi_{\text{pa}} = \Pi_{\text{atm}} \quad \Leftrightarrow \quad T_{\text{pa}}/\theta_{\text{pa}} = T_{\text{atm}}/\theta_{\text{atm}} \,, \\ & \Rightarrow \quad \mathcal{B} = \frac{\rho_{\text{atm}} - \rho_{\text{pa}}}{\rho_{\text{pa}}}\, g = \frac{T_{\text{pa}} - T_{\text{atm}}}{T_{\text{atm}}}\, g = \frac{\theta_{\text{pa}} - \theta_{\text{atm}}}{\theta_{\text{atm}}}\, g \,. \end{aligned} \tag{2.38}$$

When reviewing the result of eq. (2.38) from an Eulerian perspective, the following field variables can be partitioned into a reference hydrostatic state and a perturbation:

$$\begin{cases} \rho_{\text{pa}} \equiv \rho \,, \quad \rho_{\text{atm}} \equiv \rho_{\text{H}} & \Rightarrow \quad \rho = \rho_{\text{H}} + \widehat{\rho} \,, \\ T_{\text{pa}} \equiv T \,, \quad T_{\text{atm}} \equiv T_{\text{H}} & \Rightarrow \quad T = T_{\text{H}} + \widehat{T} \,, \\ \theta_{\text{pa}} \equiv \theta \,, \quad \theta_{\text{atm}} \equiv \theta_{\text{H}} & \Rightarrow \quad \theta = \theta_{\text{H}} + \widehat{\theta} \,. \end{cases} \tag{2.39}$$

yielding:

$$\mathcal{B} = -\frac{\widehat{\rho}}{\rho}\, g = \frac{\widehat{T}}{T_{\text{H}}}\, g = \frac{\widehat{\theta}}{\theta_{\text{H}}}\, g \,. \tag{2.40}$$

The momentum equations for buoyancy-driven flows

Considering the equations for conservation of momentum, eqs. (2.6), an atmosphere in hydrostatic equilibrium providing a reference state, eq. (2.4), and the partitioning of the thermodynamic states as presented in (2.39):

$$\begin{aligned}
&\nabla p_{\text{H}} = \rho_{\text{H}}\,\vec{g}\,,\\
&\nabla p = \nabla p_{\text{H}} + \nabla \widehat{p} = \rho_{\text{H}}\,\vec{g} + \nabla \widehat{p}\,,\\
&\Rightarrow \quad \rho\, D_t\,(\vec{u}) = -\nabla p + \nabla\cdot\underline{\underline{\tau}} + \rho\,\vec{g} = -\nabla \widehat{p} + \nabla\cdot\underline{\underline{\tau}} + \left[\rho - \rho_{\text{H}}\right]\,\vec{g}\,.
\end{aligned} \tag{2.41}$$

It should be noted that in this derivation, it was allowed the existence of a pressure perturbation, $\widehat{p}$, from the reference state, p_{H}. However, by defining buoyancy using the parcel theory as expressed in eq. (2.38), the pressure of a convected air parcel p_{pa} is assumed to equal p_{atm}. Hence the perturbation $\widehat{p}$ is such that it will not result from any buoyant effect, *i.e.*, it will be decoupled from anything related to buoyancy.

Following these considerations, approximating the buoyancy term in eq. (2.41) using the relations in eq. (2.38) yields:

$$\begin{aligned}
&\widehat{\rho}\,\vec{g} \;\approx\; -\rho\,\frac{\widehat{T}}{T_{\text{H}}}\,\vec{g} \;=\; -\rho\,\frac{\widehat{\theta}}{\theta_{\text{H}}}\,\vec{g}\,,\\
&\Rightarrow \quad \rho\, D_t\,(\vec{u}) \;=\; -\nabla \widehat{p} + \nabla\cdot\underline{\underline{\tau}} - \rho\,\frac{\widehat{\theta}}{\theta_{\text{H}}}\,\vec{g}\,.
\end{aligned} \tag{2.42}$$

The Boussinesq approximation

If the perturbations from the hydrostatic state are small, yet a motion due to buoyancy is significant, the Boussinesq approximation is commonly applied. The objective is to decouple the density perturbations from the terms in the momentum eqs. (2.42) which are not related to buoyancy. Following Turner (1973), this is equivalent to assume:

$$\widehat{\rho}\Big/_{\rho_{\text{H}}} \;\approx\; 0\,. \tag{2.43}$$

Consequently, for any arbitrary term ξ,

$$\rho\,\xi \;=\; \rho_{\text{H}}\left[1 + \frac{\widehat{\rho}\!\!\!/}{\rho\!\!\!/_{\text{H}}}\right]\,\xi \;\approx\; \rho_{\text{H}}\,\xi\,,$$

while for the pressure and gravity terms,

$$-\frac{\nabla p}{\rho} + \vec{g} = -\frac{\overbrace{\nabla p_{\text{H}}}^{=\rho_{\text{H}}\vec{g}}}{\rho} - \frac{\nabla \widehat{p}}{\rho_{\text{H}}\left[1 + \dfrac{\widehat{\rho}\!\!\!/}{\rho\!\!\!/_{\text{H}}}\right]} + \vec{g} = \frac{\rho - \rho_{\text{H}}}{\rho}\,\vec{g} - \frac{\nabla \widehat{p}}{\rho_{\text{H}}}\,.$$

Direct application to the momentum equations yields:

$$\rho_{\text{H}}\, D_t\,(\vec{u}) \;=\; -\nabla \widehat{p} + \nabla\cdot\underline{\underline{\tau}} + \rho_{\text{H}}\,\frac{\widehat{\rho}}{\rho}\,\vec{g} \;=\; -\nabla \widehat{p} + \nabla\cdot\underline{\underline{\tau}} - \rho_{\text{H}}\,\frac{\widehat{\theta}}{\theta_{\text{H}}}\,\vec{g}\,. \tag{2.44}$$

A more extensive analysis on the derivation of the buoyancy force acting on a parcel of air and the Boussinesq approximation can be found in Batchelor (1953).

Remarks on the definition of buoyancy as a relative quantity

As stated in eq. (2.37), the Archimede's principle assumes that the air parcel gets its buoyancy solely from the difference in density or temperature with the surrounding fluid. Thus buoyancy is a relative quantity as it can only be computed if ρ, T or θ of the surrounding fluid is known. This reference state is estimated from the thermodynamic properties of the fluid at rest, presumed to be in hydrostatic equilibrium, eq. (2.4). Recent literature reviews how buoyancy is usually imposed in the momentum equations, concluding that it is not a relative quantity and it should not be dependent on an arbitrary reference state (Davies-Jones, 2003; Doswell and Markowski, 2004). Following these works, a non-Archimedian approach would incorporate the effect of a vertical pressure gradient, such that:

$$\mathcal{B} \equiv D_t\left(w\right) = -\frac{1}{\rho}\frac{\partial\,\widehat{p}_b}{\partial\,z} - \frac{\widehat{\rho}}{\rho}\,g\,, \tag{2.45}$$

where $\widehat{p}_b$ is a pressure perturbation which is exclusively consequence of buoyancy. Although the fundamental questions raised are important, this approach was not pursued in the present work.

2.1.4 Incompressible and anelastic approximations

The continuity equation (2.1) allows the existence of acoustic waves (*cf.* §3.3 in Holton, 2004). However, with the Boussinesq approximation of eq. (2.43), the system of equations cannot produce these waves because density perturbations are disregarded.

In engineering applications in the field of subsonic flows, it is common to use the continuity and momentum equations assuming that the fluid is incompressible, *i.e.*, the fluid density is constant. This yields that the divergence of the velocity vector is null, $\nabla\cdot\vec{u} = 0$. Despite its common use in the numerical simulation of neutral atmospheric flows, when applied to the atmosphere, the assumption of a constant ρ is closer to an isopycnic than of an adiabatic atmospheric reference state. In fact, unless the equation of state (2.11) is dropped, there is no solution for an isopycninc hydrostatic atmosphere that is also adiabatic.

Batchelor (1953) defines how the equations of continuity and momentum can be simplified for an ideal-gas atmosphere where $\rho_{\mathrm{H}} = \rho_{\mathrm{H}}\left(z\right)$. This work was continued by Ogura and Phillips (1962) which, through a formal scale analysis, arrived to the same results. Following these works, two main simplifications are possible to discard acoustic waves, yet remain with internal gravity-waves: the *incompressible* and *anelastic* approximations to the continuity equation. While similar works by Dutton and Fichtl (1969) and Gough (1969) introduced small modifications, Durran (1989) establishes the *pseudo-incompressible equation*, an alternative continuity equation that improves the accuracy of the anelastic approximation and the energetic consistency of the system. A review of these models is given in §3.1 of Pielke (2002).

Assuming that the vertical scale of convection is lower than the density scale-height,

i.e., $L_z \ll H_\rho$, with these defined as:

$$L_z \sim \left| \frac{1}{w} \left(\frac{dw}{dz} \right) \right|^{-1} \sim \left| \frac{1}{\widehat{\rho}} \left(\frac{d\widehat{\rho}}{dz} \right) \right|^{-1} , \quad H_\rho \sim \left| \frac{1}{\rho_{\text{H}}} \left(\frac{d\rho_{\text{H}}}{dz} \right) \right|^{-1} ,$$

the continuity equation is simplified to yield the incompressible (or shallow convection) approximation:

$$\nabla \cdot \vec{u} = 0 \, . \tag{2.46}$$

This implies that the air density can be treated as a constant as far as mass balances are concerned. However this does not mean that ρ_{H} should be considered constant everywhere, rather the temporal and spatial derivatives of ρ_{H} can be dismissed.

Considering instead that atmospheric motions can be large enough as the density scale-height, $L_z \sim H_\rho$, the anelastic approximation is obtained:

$$\nabla \cdot (\rho_{\text{H}} \, \vec{u}) = 0 \, , \tag{2.47}$$

also known as the deep convection continuity equation.

To conclude, the alternative pseudo-incompressible continuity equation developed by Durran (1989), is given as:

$$\nabla \cdot (\rho_{\text{r}} \, \theta_{\text{r}} \, \vec{u}) = \rho_{\text{r}} \, \frac{\theta_{\text{r}}}{\theta} \frac{q}{c_p \, \Pi_{\text{r}}} \, , \tag{2.48}$$

where the subscript $()_{\text{r}}$ refers to a reference state, which may or may not be in hydrostatic equilibrium, and q is the rate of heating in $\text{J}\,\text{kg}^{-1}\,\text{s}^{-1}$.

2.2 Turbulence model

An analytical solution for the equations of continuity (2.1) and momentum (2.2) is only obtainable for very simple flows and geometries. For the generality of applications numerical techniques must be used, yielding an approximate solution of the flow field.

Although the equations may be solved directly, even applying several simplifications specific of the flow being investigated, *e.g.*, eqs. (2.40, 2.43, 2.46, 2.47), the range of spatial and temporal flow scales due to turbulence is so large that the solution becomes unfeasible due to the amount of time and computer resources. This method, known as DNS (direct numerical simulation), is constrained by the Taylor microscales of the flow, *i.e.*, the largest length scales at which viscosity affects the turbulent eddies. Even for simple geometries and scales well below the ones found in the atmosphere, DNS is highly resource consuming on both computer processing and memory requirements. An estimation (Choi and Moin, 2012) of the amount of grid nodes necessary to perform a DNS of a turbulent boundary-layer developing over a flat plate, where $\text{Re}_x \in [5 \times 10^5, \, 10^7]$, leads to $\sim 10^{14}$ grid nodes.

The alternative is to modify the conservation equations introducing turbulence models. There are two main approaches for turbulence modelling: LES (large eddy simulation) and RaNS (Reynolds averaged Navier-Stokes).

LES attempts to compute the details of the large scales of motion (the resolved field) yet modelling the small scales which cannot be resolved by the computational grid (the sub-filter field). A filter function is used to set apart both scales. By filtering the momentum equations, extra stress terms appear representing the influence of the sub-filter field on the large scales. Smagorinsky (1963) laid the foundations of the technique and the sub-filter scale model, having been extended in works such as Germano *et al.* (1991). The computational requirements of LES are lower than those of DNS, especially when wall functions are applied to avoid resolving the inner layer (linear and logarithmic sub-layers). However, the use of LES is still beyond the scope of common engineering applications. Following the estimate by Choi and Moin (2012), to solve a turbulent boundary-layer over a flat plate encompassing $\mathrm{Re}_x \in [5 \times 10^5, 10^7]$, a grid size of $\sim 10^8$ would be required using a modelled wall layer and $\sim 10^9$ if the wall is resolved. The application of LES to solve atmospheric flows has been geared to describe the flow under specific inflow conditions (*e.g.*, the flow field when winds originate from northwest) than to be used in weather forecasting (Chow and Street, 2009).

In RaNS, an average operator is applied to the momentum equations and all of the fields which describe the flow, *e.g.*, velocity, pressure and density. Similarly to LES, extra stress terms appear representing the covariances of the turbulent fluctuations. However, all of the turbulent scales are being modelled in the equations employed to compute these terms. The turbulent stresses are related to the gradients of the mean flow through a diffusion coefficient, known as turbulent viscosity, μ_t. The problem is diverted from the estimation of individual turbulent stresses to the computation of μ_t, in order to close the set of equations. For this purpose a variety of models have been proposed (Rodi, 1984), namely algebraic models; models which include transport equations for one or several turbulent quantities; to models which have a transport equation for each of the turbulent stresses. In terms of grid nodes, employing a similar analysis as in Choi and Moin (2012) to flat plate flow up to Re_x of 10^7 yields a grid size of $\sim 4 \times 10^5$, two orders of magnitude lower than for LES.

Following the above considerations and the limitations of the available numerical resources, a RaNS approach was used for turbulence modelling.

2.2.1 Unsteady Reynolds averaged Navier-Stokes equations

The method proposed by Reynolds (1895) is based on decomposing the instantaneous value of flow variable into its mean value and a fluctuation due to turbulence. For instance, the decomposition of the x component of the velocity vector yields:

$$u\left(t,\vec{x}\right) \;=\; \overline{u}\left(t,\vec{x}\right) + u'\left(t,\vec{x}\right) \;, \qquad \overline{\overline{u}} \;\equiv\; \overline{u} \;, \qquad \overline{u'} \;=\; 0 \;, \tag{2.49}$$

where the operator $\overline{()}$ and $()'$ respect to the mean and turbulent fluctuation components. When the purpose is to find a steady solution for a specific flow, the mean operator $\overline{()}$ represents a time average over an integration time, $T \to \infty$, such that:

$$\overline{u}\left(t,\vec{x}\right) \equiv \overline{u}\left(\vec{x}\right) = \lim_{T\to\infty} \frac{1}{T} \int_{t-\frac{T}{2}}^{t+\frac{T}{2}} u\left(t,\vec{x}\right)\, dt \;. \tag{2.50}$$

Applying this decomposition, any temporal derivative term in the flow equations is dropped. Instead, if the flow is such that its solution is expected to be unsteady or quasi-stationary, the mean component of the flow is itself function of time. In unsteady regimes, the mean operator $\overline{()}$ represents an ensemble average, where for a number N of hypothetical experiments:

$$\overline{u}\,(t,\vec{x}) \equiv \lim_{N\to\infty} \frac{1}{N} \sum_{n=1}^{N} u\,(n,t,\vec{x}) \quad , \quad n = 1,2,\ldots,N\,. \tag{2.51}$$

For details on the algebraic properties of time and ensemble averaging, as well as the application of the Reynolds decomposition, refer to §16 and §21 in Schlichting and Gersten (2000).

To apply Reynolds averaging to an equation, first the variables are decomposed according to eq. (2.49) and subsequently the equation is averaged in order to eliminate most of the turbulent fluctuation terms. The equations of continuity and momentum, after Reynolds averaging, yield a system that will be time dependent according to the kind of averaging performed: if it is a time average (2.50) or an ensemble average (2.51). The latter yields a more generic formulation, because it reverts to the stationary equations just by dropping the time derivatives. The resulting set of equations is known as uRaNS (unsteady Reynolds averaged Navier-Stokes).

Applying the Reynolds averaging to the variables in the equation of state (2.11):

$$\begin{aligned} \overline{p} \;&=\; R_d\left[\overline{\rho}\,\overline{T} + \overline{\rho'\,T'}\right] \;=\; R_d\,\overline{\rho}\,\overline{T}\left[1 + \underbrace{\frac{\overline{\rho'\,T'}}{\overline{\rho}\,\overline{T}}}_{\approx 0}\right] \quad \Leftrightarrow \\ \Rightarrow \quad \overline{p} \;&=\; \overline{\rho}\,R_d\,\overline{T} \quad \wedge \quad \frac{p'}{\overline{p}} \;=\; \frac{\rho'}{\overline{\rho}} + \frac{T'}{\overline{T}}\,, \end{aligned} \tag{2.52}$$

considering R_d constant and $|\overline{\rho'\,T'}| \ll \overline{\rho}\,\overline{T}$. By also assuming that $|p'| \ll \overline{p}$, the Exner function (2.16) and potential temperature (2.15) becomes:

$$\overline{\Pi} \;=\; \overline{\left[\frac{\overline{p}+p'}{p_{00}}\right]^{R_d/c_p}} \;=\; \overline{\left[\frac{\overline{p}}{p_{00}}\left[1+\frac{p'\!\!\!/}{\overline{p}\!\!\!/}\right]\right]^{R_d/c_p}} \;\approx\; \left[\frac{\overline{p}}{p_{00}}\right]^{\frac{R_d}{c_p}}\,, \tag{2.53}$$

$$\frac{\Pi'}{\overline{\Pi}} \;\approx\; 0 \quad \Rightarrow \quad \overline{\Pi}\,\overline{\theta} \;=\; \overline{T} \quad \wedge \quad \frac{\theta'}{\overline{\theta}} \;=\; \frac{T'}{\overline{T}} \;=\; -\frac{\rho'}{\overline{\rho}} + \frac{p'\!\!\!/}{\overline{p}\!\!\!/}\,. \tag{2.54}$$

The application to the incompressible continuity eq. (2.46) yields, after averaging:

$$\nabla\cdot\overline{\vec{u}} = 0 \quad \Rightarrow \quad \nabla\cdot\vec{u}\,' = 0\,. \tag{2.55}$$

Similarly, the anelastic continuity eq. (2.47) returns:

$$\nabla\cdot\left(\rho_{\text{H}}\,\overline{\vec{u}}\right) = 0 \quad \Rightarrow \quad \nabla\cdot\left(\rho_{\text{H}}\,\vec{u}\,'\right) = 0\,. \tag{2.56}$$

When decomposing θ, the hydrostatic part θ_{H} is associated with the mean component. Hence, only the perturbation $\widehat{\theta}$ is partitioned into $\overline{\widehat{\theta}}$ and a turbulent fluctuation θ'. Thus the buoyancy acceleration given in eq. 2.40 yields,

$$\overline{\frac{(\theta-\theta_{\text{H}})}{\theta_{\text{H}}}}\,g = \overline{\frac{(\theta\!\!\!/_{\text{H}} + \widehat{\theta} + \theta' - \theta\!\!\!/_{\text{H}})}{\theta_{\text{H}}}}\,g = \frac{\overline{\widehat{\theta}}}{\theta_{\text{H}}}\,g\,. \tag{2.57}$$

After Reynolds averaging, the momentum equations (2.44) become,

$$\rho_{\mathrm{H}} \frac{\partial \overline{u}_i}{\partial t} + \rho_{\mathrm{H}} \sum_j \frac{\partial \left(\overline{u}_j \, \overline{u}_i\right)}{\partial x_j} + \rho_{\mathrm{H}} \sum_j \frac{\partial \, \overline{u_i' \, u_j'}}{\partial x_j} = -\frac{\partial \, \overline{\widehat{p}}}{\partial x_i} + \sum_j \frac{\partial \, \overline{\tau}_{ij}}{\partial x_j} + \rho_{\mathrm{H}} \frac{\overline{\widehat{\theta}}}{\theta_{\mathrm{H}}} g \, \delta_{i3} \,, \tag{2.58}$$

using Gibb's indicial notation. The resulting equations are identical to the original ones, with the exception of the term involving $\overline{u_i' \, u_j'}$. These covariances arise from the non-linearity of the advection term. As these resemble apparent stresses acting on the fluid parcel, they are known as Reynolds stresses. They represent momentum fluxes and must be modelled in order to close the system of equations.

Considering a reference state that is constant or changes in timescales much larger than those being modelled, the potential temperature transport (2.34), after decomposing and averaging yields:

$$\frac{\partial}{\partial t}\left(\rho_{\mathrm{H}} \, \overline{\widehat{\theta}}\right) + \sum_j \frac{\partial}{\partial x_j}\left(\rho_{\mathrm{H}} \, \overline{u}_j \, \overline{\widehat{\theta}}\right) + \sum_j \frac{\partial}{\partial x_j}\left(\rho_{\mathrm{H}} \, \overline{\theta' \, u_j'}\right) + \frac{\partial}{\partial z}\left(\rho_{\mathrm{H}} \, \overline{w} \, \theta_{\mathrm{H}}\right) = \sum_j \frac{\partial}{\partial x_j}\left(\frac{\lambda}{c_p} \frac{\partial \overline{\theta}}{\partial x_j}\right). \tag{2.59}$$

Similarly to eq. (2.58), extra terms appear with the covariances $\overline{\theta' \, u_j'}$, representing turbulent heat fluxes.

2.2.2 The gradient-diffusion and turbulence-viscosity hypotheses

To model the covariances appearing in the Reynolds averaged equations of momentum and potential temperature, (2.58) and (2.59), the hypotheses of gradient-diffusion and turbulence-viscosity were employed (*cf.* §4.4 in Pope, 2000).

The gradient-diffusion hypothesis postulates that $\overline{(\theta' \, u_j')}$ is related to the mean gradient of the conserved scalar θ. Analogously to the Fourier's law of heat conduction and Fick's law of molecular diffusion,

$$q_j' = \rho_{\mathrm{H}} \, c_p \, \overline{\theta' \, u_j'} \approx -\rho_{\mathrm{H}} \, c_p \, \alpha_t \, \frac{\partial \overline{\theta}}{\partial x_j} = -\lambda_t \, \frac{\partial \overline{\theta}}{\partial x_j} \,. \tag{2.60}$$

where q_j' is the turbulent heat flux, α_t the turbulent thermal diffusivity in $\mathrm{m}^2 \cdot \mathrm{s}^{-1}$ and λ_t is the turbulent thermal conductivity, in $\mathrm{J} \cdot \mathrm{s}^{-1} \cdot \mathrm{m}^{-1} \cdot \mathrm{K}^{-1}$.

Akin to gradient-diffusion, the Reynolds stresses $\overline{(u_i' \, u_j')}$ are modelled in analogy to the Newtonian fluid proportionality between stress and the rate-of-strain. Thus the turbulent momentum diffusion coefficient is like a viscosity that is not a property of the fluid, but of the flow. This is known as the turbulence-viscosity hypothesis and was postulated by Boussinesq (1877). Hence,

$$\begin{aligned} {\tau_{ij}}' = -\rho_{\mathrm{H}} \, \overline{u_i' \, u_j'} &\approx 2 \, \rho_{\mathrm{H}} \, \nu_t \, \overline{S}_{ij} - \delta_{ij} \, \rho_{\mathrm{H}} \, \frac{2}{3} \, k \\ &= \mu_t \left[\frac{\partial \overline{u}_i}{\partial x_j} + \frac{\partial \overline{u}_j}{\partial x_i} - \delta_{ij} \, \frac{2}{3} \underbrace{\sum_k \frac{\partial \overline{u}_k}{\partial x_k}}_{=\nabla \cdot \vec{u}} \right] - \delta_{ij} \, \rho_{\mathrm{H}} \, \frac{1}{3} \sum_k \overline{(u_k' \, u_k')} \,, \end{aligned} \tag{2.61}$$

where τ' is the Reynolds stress tensor, $\overline{S}$ is the mean rate-of-strain tensor, ν_t is the turbulent momentum diffusivity in $\mathrm{m}^2 \cdot \mathrm{s}^{-1}$ (also known as turbulent kinematic viscosity), μ_t the turbulent dynamic viscosity in $\mathrm{kg} \cdot \mathrm{s}^{-1} \cdot \mathrm{m}^{-1}$ and k is the turbulence kinetic energy, defined as:

$$k = \frac{\overline{u'u'} + \overline{v'v'} + \overline{w'w'}}{2} \,. \tag{2.62}$$

For both incompressible and anelastic approximations in §2.1.4, the velocity divergence term, $\nabla \cdot \vec{u}$, is dropped.

Is common to find in the literature the momentum and thermal turbulent diffusivities, ν_t and α_t, represented as K_m and K_h. For consistency with reference fluid mechanics books (*e.g.* Pope, 2000; Schlichting and Gersten, 2000), the notation in eqs. (2.60) and (2.61) is preferred.

By applying both hypotheses, the system is closed if the turbulent diffusivities and the turbulence kinetic energy are computed or prescribed. To further simplify the problem, a dimensionless quantity akin to the Prandtl number is introduced: the turbulent Prandtl number, σ_θ, defined as:

$$\sigma_\theta = \frac{\nu_t}{\alpha_t} = c_p \frac{\mu_t}{\lambda_t} \,. \tag{2.63}$$

From σ_θ, the thermal turbulent diffusivity α_t is obtained from the turbulent viscosity ν_t. According to Kaimal and Finnigan (1994), the experimental value of σ_θ is approximately 0.95, although a value of 1 is commonly assumed.

2.2.3 The $k - \epsilon$ turbulence model

With the concepts of turbulent viscosity and turbulent thermal diffusivity, the variables that remain unknown are the variances $\overline{u'u'}$, $\overline{v'v'}$ and $\overline{w'w'}$, the turbulence kinetic energy, k, and the positive scalar turbulent viscosity, ν_t. From dimensional analysis, ν_t can be described by two parameters, a velocity scale $u_\wedge$ and a length scale $l_\wedge$:

$$\nu_t = u_\wedge \, l_\wedge \,. \tag{2.64}$$

Both $u_\wedge$ and $l_\wedge$ are local scales representative of the turbulent eddies in the flow, with the subscript $\wedge$ designating this. Also, the length scale $l_\wedge$ is usually named as the mixing-length. The turbulence kinetic energy is also related to this velocity scale, such that $u_\wedge = c\sqrt{k}$, with c as a constant (Pope, 2000). Thus, the turbulent viscosity can be alternatively described as,

$$\nu_t = c \, l_\wedge \sqrt{k} \,. \tag{2.65}$$

By knowing k and $l_\wedge$, the system of equations (2.60, 2.61) is closed. For this purpose, a transport equation for k is derived from the RaNS equations (*cf.* §4.1 in Wilcox, 1994):

$$\frac{\partial}{\partial t}(\rho_\mathrm{H} \, k) + \nabla \cdot (\rho_\mathrm{H} \, \vec{u} \, k) = \nabla \cdot \left(\left[\mu + \frac{\mu_t}{\sigma_k} \right] \nabla k \right) + \underbrace{\mathcal{P} + \mathcal{G}}_{\mathcal{P}_k} - \rho_\mathrm{H} \, \epsilon \,, \tag{2.66}$$

where ϵ is the rate of dissipation of turbulence kinetic energy and σ_k is a turbulent Prandtl number that relates the turbulent diffusivity of k with μ_t, being a coefficient of the model. The terms $\mathcal{P}$ and $\mathcal{G}$ are the production of turbulence by mechanical shear and due to buoyancy, defined as:

$$\mathcal{P} = -\sum_i \sum_j \rho_{\text{H}} \overline{u_i' u_j'} \frac{\partial \overline{u_i}}{\partial x_j} = \sum_i \sum_j \tau_{ij}' \frac{\partial \overline{u_i}}{\partial x_j} \approx \sum_i \sum_j \mu_t \left[\frac{\partial \overline{u_i}}{\partial x_j} + \frac{\partial \overline{u_j}}{\partial x_i} \right] \frac{\partial \overline{u_i}}{\partial x_j}, \tag{2.67}$$

$$\mathcal{G} = \rho_{\text{H}} \frac{g}{\theta_{\text{H}}} \overline{w'\theta'} = -\frac{g}{\theta_{\text{H}}} \frac{\mu_t}{\sigma_\theta} \frac{\partial \overline{\theta}}{\partial z}. \tag{2.68}$$

According to Detering and Etling (1985), the energy dissipation ϵ is usually modelled from the Kolmogorov relation, as well from dimensional analysis:

$$\epsilon \approx c_d \frac{k^{3/2}}{l_\wedge} \approx \frac{u_\wedge^3}{l_\wedge}, \tag{2.69}$$

with c_d as another constant. Simple models for turbulence specify $l_\wedge$ as a function of space and time, by means of algebraic expressions, *e.g.* the expression commonly found in the literature given by Blackadar (1962):

$$l_\wedge = l_\wedge(z) = \frac{1}{\dfrac{1}{\kappa z} + \dfrac{1}{l_{\max}}}, \tag{2.70}$$

where κ is the von Kármán constant, z is the vertical direction and $l_{\max}$ is the maximum value intended for $l_\wedge$. Approaches such as this are referred in the literature as one-equation models. For complex flows it is difficult to establish algebraic laws the mixing-length $l_\wedge$ or the dissipation ϵ, hence these models are insufficient.

By establishing a second transport equation for one of the variables that characterize turbulence, better results are expected. This is referred as a two-equation model, being the common approach found in the literature and industry. Although there are several choices for the second equation, the preferred is to model the transport of the turbulence energy dissipation, ϵ, as first proposed by Launder and Spalding (1974). This procedure is extensively found in the literature and is known as the $k-\epsilon$ turbulence model. Details on the derivation of this equation can be found on §4.3.2 of Wilcox (1994), although the model is well described in §10.4 of Pope (2000).

From expressions (2.64), (2.65) and (2.69), k, ϵ and ν_t are related by:

$$\nu_t = C_\mu \frac{k^2}{\epsilon}, \tag{2.71}$$

where C_μ is a constant, being linked to the other constants defined previously in this section as $C_\mu \equiv c^4 \equiv c_d^{4/3}$. In the $k-\epsilon$ model, relation (2.71) is considered valid at every spatial location. The model equation for the transport of ϵ is:

$$\frac{\partial}{\partial t}(\rho_{\text{H}}\,\epsilon) + \nabla\cdot(\rho_{\text{H}}\,\vec{u}\,\epsilon) = \nabla\cdot\left(\left[\mu + \frac{\mu_t}{\sigma_\epsilon}\right]\nabla\epsilon\right) + \frac{\epsilon}{k}\left[\underbrace{C_{\epsilon 1}\,[\mathcal{P}+\mathcal{G}]}_{\mathcal{P}_\epsilon} \underbrace{-C_{\epsilon 2}\,\rho_{\text{H}}\,\epsilon}_{\mathcal{D}_\epsilon}\right], \tag{2.72}$$

where $C_{\epsilon 1}$ and $C_{\epsilon 2}$ are two new coefficients, together with a second turbulent Prandtl number, σ_ϵ, for the diffusivity of ϵ. Besides the advective and diffusive term, this equation has both a production and dissipation term, $\mathcal{P}_\epsilon$ and $\mathcal{D}_\epsilon$, similarly to the equation for k (2.66). The several coefficients of the model are determined through the behaviour of k and ϵ equations for several flows and specific situations, like homogeneous and decaying turbulence. When analysing how the equations become in a boundary-layer characterized by a logarithmic velocity profile, assuming constant shear stress in the surface-layer and neutral stratification, then $\mathcal{P} \approx \rho_{\mathrm{H}}\, \epsilon$, resulting in the expression:

$$\kappa^2 = \sigma_\epsilon \sqrt{C_\mu}\, (C_{\epsilon 2} - C_{\epsilon 1})\,. \tag{2.73}$$

The standard values given in Launder and Spalding (1974) to the several coefficients of the model are:

$$\kappa = 0.43\,,\;\; C_\mu = 0.09\,,\;\; C_{\epsilon 1} = 1.44\,,\;\; C_{\epsilon 2} = 1.92\,,\;\; \sigma_k = 1\,,\;\; \sigma_\epsilon = 1.3\,. \tag{2.74}$$

While these values are the reference in engineering applications and for many types of flows, to model atmospheric turbulence several alternatives were proposed in the literature. Detering and Etling (1985) derived new values for the coefficients,

$$\kappa = 0.4\,,\;\; C_\mu = 0.026\,,\;\; C_{\epsilon 1} = 1.13\,,\;\; C_{\epsilon 2} = 1.9\,,\;\; \sigma_k = 0.74\,,\;\; \sigma_\epsilon = 1.3\,. \tag{2.75}$$

In the works related to the Askervein Hill project, Beljaars *et al.* (1987) and Raithby *et al.* (1987), the changes are mainly on the value of C_μ based on the experimental values established for the $k/{u_*}^2$ ratio in the atmospheric surface layer:

$$\kappa = 0.4\,,\;\; C_\mu = 0.033\,,\;\; \sigma_\epsilon = 1.85\,. \tag{2.76}$$

In a previous work by Wyngaard (1975) the turbulent atmospheric boundary layer is simulated with a 2$^{\text{nd}}$ order closure, where each component of the Reynolds-stress tensor and the turbulent heat flux, $\overline{u_i' u_j'}$ and $\overline{\theta' u_j'}$, has its own transport equation. An equation for ϵ was derived where the way how the $\mathcal{G}$ term was modelled into $\mathcal{P}_\epsilon$ differs, introducing a square term and coefficient for stable stratification:

$$\mathcal{P}_\epsilon = \begin{cases} C_{\epsilon 1}\,[\mathcal{P} + \mathcal{G}]\;,\; C_{\epsilon 1} = 1.5\,,\; C_{\epsilon 2} = 2\,, & \text{neutral or unstable,} \\ C_{\epsilon 1}\,\mathcal{P} + C_{\epsilon 3}\,\mathcal{G} + \mathcal{G}^2/\epsilon\;,\; C_{\epsilon 1} = 1.75\,,\; C_{\epsilon 2} = 2\,,\; C_{\epsilon 3} = 0.5\,, & \text{stable.} \end{cases} \tag{2.77}$$

Duynkerke (1988) reviews the former works and establish a new set of coefficients:

$$\kappa = 0.4\,,\;\; C_\mu = 0.033\,,\;\; C_{\epsilon 1} = 1.46\,,\;\; C_{\epsilon 2} = 1.83\,,\;\; \sigma_k = 1\,,\;\; \sigma_\epsilon = 2.38\,, \tag{2.78}$$

proposing also a different production term for the ϵ equation that approximately matches the one obtained by Wyngaard, eq. (2.77):

$$\mathcal{P}_\epsilon = C_{\epsilon 1}\,[\mathcal{P} + \max(0, \mathcal{G})]\;, \tag{2.79}$$

where the function max suppresses all negative contributions from $\mathcal{G}$. Additionally, it is argued that the contribution from the diffusive transport of k, $\mathcal{T}_k$, should also be accounted for:

$$\mathcal{P}_\epsilon = C_{\epsilon 1}\,[\mathcal{P} + \max(0, \mathcal{G}) + \max(0, \mathcal{T}_k)]\;,\quad \mathcal{T}_k = \nabla\cdot\left(\left[\mu + \frac{\mu_t}{\sigma_k}\right]\nabla k\right). \tag{2.80}$$

Later works keep the reference values given by the standard model, with just slight changes related to the value of the von Kármán constant, κ. In Apsley and Castro (1997), only the turbulent Prandtl numbers for ϵ and θ are changed,

$$\kappa = 0.4\,, \quad \sigma_\epsilon = 1.11\,, \quad \sigma_\theta = 0.9\,. \tag{2.81}$$

2.3 Physics of the atmospheric surface layer

The atmospheric boundary layer can be divided into two regions:

1. A surface layer where, due to the mixing and wall proximity, the vertical turbulent fluxes are nearly constant. The depth of this layer is around 10 % of the total boundary layer height.
2. An outer layer where the turbulent fluxes vary with height and the wind characteristics are influenced by the surface fluxes, the thermal stability and the Coriolis acceleration due to earth's rotation. These factors also influence the total height of the boundary layer.

For the surface layer the following expressions for the turbulent fluxes can be written,

$$\tau'_{\mathrm{w}} = -\rho_{\mathrm{w}}\,\overline{(u'\,w')}_{\mathrm{w}} = \rho_{\mathrm{w}}\,\nu_t\,\frac{\partial\,\overline{u}}{\partial\,z}\,, \tag{2.82}$$

$$q'_{\mathrm{w}} = \rho_{\mathrm{w}}\,c_p\,\overline{(\theta'\,w')}_{\mathrm{w}} = -\rho_{\mathrm{w}}\,c_p\,\alpha_t\,\frac{\partial\,\overline{\theta}}{\partial\,z}\,, \tag{2.83}$$

These are simplified forms of the gradient-diffusion and turbulence-viscosity hypotheses (§2.2.2), where the x spatial coordinate is aligned with the main direction of the wind velocity, the average vertical velocity $\overline{w}$ is disregarded and the flow is both horizontally homogeneous and incompressible, *i.e.*, velocity divergence is null.

In the CBL (convective boundary-layer) the unstable stratification favours turbulence production, thus the thermal and mechanical production of turbulence are combined. Conversely, in the SSBL (stably stratified boundary-layer) buoyancy tends to restore advected air parcels, dampening and suppressing turbulent motions. To characterize the relative importance of buoyancy and shear in turbulence production, the Richardson number was introduced. This parameter was first defined with the gradients of θ and $\vec{u}$, commonly designated as the gradient Richardson number, Ri. To characterize turbulent flows, Ri was redefined to account for turbulent fluxes instead of gradients, known as the flux Richardson number, Rf:

$$\mathrm{Ri} = \frac{\dfrac{g}{\theta_{\mathrm{H}}}\dfrac{\partial\,\overline{\theta}}{\partial\,z}}{\left(\dfrac{\partial\,\overline{u}}{\partial\,z}\right)^2 + \left(\dfrac{\partial\,\overline{v}}{\partial\,z}\right)^2}\,, \tag{2.84}$$

$$\mathrm{Rf} = \frac{\dfrac{g}{\theta_{\mathrm{H}}}\,\overline{\theta'\,w'}}{\overline{u'\,w'}\,\dfrac{\partial\,\overline{u}}{\partial\,z} + \overline{v'\,w'}\,\dfrac{\partial\,\overline{v}}{\partial\,z}} \equiv -\frac{\mathcal{G}}{\mathcal{P}}\,. \tag{2.85}$$

The definition of Rf is directly related with the terms $\mathcal{P}$ and $\mathcal{G}$ from eqs. (2.67) and (2.68), although in most definitions found in the literature horizontal gradients and the vertical velocity $\overline{w}$ are disregarded. Applying the gradient-diffusion hypothesis, the following relation is established:

$$\mathrm{Rf} = \frac{\alpha_t}{\nu_t}\,\mathrm{Ri}\,. \tag{2.86}$$

In the surface layer, the vertical profiles of the physical quantities are described by the Monin-Obukhov similarity theory (MOST). It states that the relevant scales are:

$${u_*}^2 = \sqrt{\overline{(u'\,w')}_{\mathrm{w}}^2 + \overline{(v'\,w')}_{\mathrm{w}}^2}\,, \quad \theta_* = \frac{-\overline{(\theta'\,w')}_{\mathrm{w}}}{u_*}\,, \quad l_* = \kappa\, z\,, \quad \frac{g}{\Theta} \approx \frac{g}{\theta_{\mathrm{HW}}}\,, \tag{2.87}$$

where u_* is the turbulence velocity scale, also known as friction velocity, θ_* is the turbulence temperature scale, l_* is the surface mixing-length and g/Θ is the buoyancy parameter with Θ as the temperature representative of the surface layer. These are scales that are measured at the surface and are constant, unlike local scales such as $u_\wedge$ or $l_\wedge$. When using these scales to normalize the gradients of velocity and potential temperature, MOST states that these will obey the following similarity laws:

$$\frac{l_*}{u_*}\frac{\partial\,\overline{u}}{\partial\,z} = \phi_m\,, \tag{2.88}$$

$$\frac{l_*}{\theta_*}\frac{\partial\,\overline{\theta}}{\partial\,z} = \phi_h\,, \tag{2.89}$$

where ϕ_m and ϕ_h are dimensionless similarity functions known in the literature as stability functions. These are function of the dimensionless height AGL (above the ground level) normalized by the Obukhov length, $z/\mathcal{L}$. The Obukhov length is the height at which the ratio between the mechanical turbulence production equals the buoyancy turbulence production, however as in MOST the surface turbulent fluxes are considered constant, these are used to define $\mathcal{L}$ instead of local fluxes. Thus,

$$\begin{aligned} \mathrm{Rf}_{\mathrm{w}} = 1 \;&\Rightarrow\; \mathcal{P}_{\mathrm{w}} = -\mathcal{G}_{\mathrm{w}} \\ &\Rightarrow\; \mathcal{L} = -\frac{{u_*}^3\,\Theta}{\kappa\, g\,\overline{(\theta'\,w')}_{\mathrm{w}}} \equiv \frac{{u_*}^2\,\Theta}{\kappa\, g\,\theta_*}\,. \end{aligned} \tag{2.90}$$

The sign of $\mathcal{L}$ is contrary to the direction of the surface heat flux, ${q'}_{\mathrm{w}}$, such that:

1. For stable stratification, $\mathcal{L} > 0$, where $\mathcal{L}$ is the AGL height above which the buoyancy effects counteract the vertical turbulent motions, suppressing the turbulence of the flow.
2. For unstable conditions, $\mathcal{L} < 0$. In this case $\mathcal{L}$ can be understood as the AGL height above which convection due to unstable stratification becomes more important than mechanical shear in producing turbulence.

From expressions (2.82), (2.83), (2.88) and (2.89) one derives that the turbulent diffusivities of momentum and temperature in the surface layer should obey:

$$\nu_t = \frac{u_*\,l_*}{\phi_m}\,, \quad \alpha_t = \frac{u_*\,l_*}{\phi_h}\,, \quad \frac{\nu_t}{\alpha_t} = \frac{\phi_h}{\phi_m}\,. \tag{2.91}$$

It follows that the Richardson numbers Ri and Rf in the surface layer are also related by,

$$\mathrm{Rf} = \frac{\phi_m}{\phi_h}\,\mathrm{Ri}\,. \tag{2.92}$$

For neutral stability, *i.e.*, only forced convection, function $\phi_m = 1$, while the gradient of $\overline{\theta}$ is null. Integrating eq. (2.88) for these conditions yields the logarithmic law for atmospheric flows,

$$\overline{u} = \frac{u_*}{\kappa}\ln\left(\frac{z}{z_0}\right)\,, \tag{2.93}$$

where z_0 is an integration constant known as the roughness length, being related with the amount and dimension of the roughness elements in the topography. For diabatic conditions, $\phi_m = \phi_m\left(z/\mathcal{L}\right)$ and the profile of $\overline{u}$ becomes the same logarithmic law plus a deviation from it:

$$\begin{aligned}
&\frac{\partial\,\overline{u}}{\partial\,z} = \frac{u_*}{l_*} + \frac{u_*\left[\phi_m - 1\right]}{l_*} \quad \Leftrightarrow \\
&\Leftrightarrow \int_{\overline{u}(z_0)=0}^{\overline{u}(z)} d\overline{u} = \frac{u_*}{\kappa}\left[\int_{z_0}^{z}\frac{dz}{z} - \int_{z_0}^{z}\frac{(1-\phi_m)}{z}dz\right] \quad \Leftrightarrow \\
&\Leftrightarrow \quad \overline{u} = \frac{u_*}{\kappa}\left[\ln\left(\frac{z}{z_0}\right) - \int_{\zeta(z_0)}^{\zeta(z)}\frac{\left[1-\phi_m\right]}{\zeta}\,d\zeta\right] \quad \Leftrightarrow \\
&\Leftrightarrow \quad \overline{u} = \frac{u_*}{\kappa}\left[\ln\left(\frac{z}{z_0}\right) - \int_{0}^{\zeta(z)}\frac{\left[1-\phi_m\right]}{\zeta}\,d\zeta + \int_{0}^{\zeta(z_0)}\frac{\left[1-\phi_m\right]}{\zeta}\,d\zeta\right] \quad \Leftrightarrow \\
&\Leftrightarrow \quad \overline{u} = \frac{u_*}{\kappa}\left[\ln\left(\frac{z}{z_0}\right) - \psi_m\left(\frac{z}{\mathcal{L}}\right) + \psi_m\left(\frac{z_0}{\mathcal{L}}\right)\right]\,,
\end{aligned} \tag{2.94}$$

where $\zeta = \zeta\left(z\right) = z/\mathcal{L}$ and $\psi_m(\zeta)$ is function of the integral of $\phi_m(\zeta)$. Likewise, from the integration of eq. (2.89) a profile for θ can be derived,

$$\overline{\theta} = \overline{\theta}_{\mathrm{w}} + \frac{\theta_*}{\kappa}\left[\ln\left(\frac{z}{z_0}\right) - \psi_h\left(\frac{z}{\mathcal{L}}\right) + \psi_h\left(\frac{z_0}{\mathcal{L}}\right)\right]\,, \tag{2.95}$$

where similarly $\psi_h(\zeta)$ is function of the integral of $\phi_h(\zeta)$.

Because in the limit $z \to 0 \;\Rightarrow\; \ln(z/z_0) \to -\infty$, it is usual to displace vertically the referential by z_0 such that $\overline{u}\left(z=0\right) = 0$, thus preventing numerical indetermination. Additinally, the roughness lengths for both velocity and temperature logarithmic laws may differ, being represented instead as z_{m0} and z_{h0}. With these considerations, the logarithmic profiles become:

$$\overline{u} = \frac{u_*}{\kappa}\left[\ln\left(\frac{z}{z_{\mathrm{m0}}}+1\right) - \psi_m\left(\frac{z+z_{\mathrm{m0}}}{\mathcal{L}}\right) + \psi_m\left(\frac{z_{\mathrm{m0}}}{\mathcal{L}}\right)\right]\,, \tag{2.96}$$

$$\overline{\theta} = \overline{\theta}_{\mathrm{w}} + \frac{\theta_*}{\kappa}\left[\ln\left(\frac{z}{z_{\mathrm{h0}}}+1\right) - \psi_h\left(\frac{z+z_{\mathrm{h0}}}{\mathcal{L}}\right) + \psi_h\left(\frac{z_{\mathrm{h0}}}{\mathcal{L}}\right)\right]\,. \tag{2.97}$$

Table 2.3: Constants for the stability functions ϕ_m and ϕ_h.

			Unstable				Stable		
Author	κ	$\sigma_{\theta N}$	b_{mu}	c_m	b_{hu}	c_h	b_{ms}	b_{hs}	$z/\mathcal{L}$ range
Dyer and Hicks (1970)	0.41	1	16	$-1/4$	16	$-1/2$			$[-1, 0]$
Businger *et al.* (1971)	0.35	0.74	15	$-1/4$	9	$-1/2$			$[-1, 0]$
							4.7	4.7	$[0, 2]$
Carl *et al.* (1973)	0.41		16	$-1/3$					$[-10, -2]$
			16	$-1/4$					$[-2, 0]$
Dyer (1974)	0.41	1	16	$-1/4$	16	$-1/2$			$[-\infty, 0]$
							5	5	$[0, +\infty]$
Hicks (1976)	0.41	1	16	$-1/4$					$[-1, 0]$
							5		$[0, 1]$
Dyer and Bradley (1982)	0.40	1	28	$-1/4$	14	$-1/2$			$[-4, 0]$
Högström (1988)	0.40	0.95	19.3	$-1/4$	11.6	$-1/2$			$[-2, 0]$
							4.8	7.8	$[0, 0.5]$
	0.40	1	19.3	$-1/4$	12	$-1/2$			$[-2, 0]$
							4.8	8	$[0, 0.5]$
Högström (1996)	0.40	0.95	19	$-1/4$	11.6	$-1/2$			$[-2, 0]$
		1					5.3	8	$[0, 0.5]$

2.3.1 Stability functions

To evaluate the turbulent fluxes, gradients and profiles of $\overline{u}$ and $\overline{\theta}$ in the surface layer, the stability functions ϕ_m and ϕ_h must be known. Albeit these functions must obey some assumptions laid out by dimensional analysis, they are empirical fittings to experimental field measurements whose objective is to characterize the atmospheric turbulence in the surface layer.

Several formulations exist in the literature, some described in works such as Panofsky (1963), Yaglom (1977) and Högström (1988). However, it was the expressions proposed by Businger and Dyer that became accepted as the state-of-the-art. Following Dyer and Hicks (1970), Businger *et al.* (1971) and Businger (1988), ϕ_m is given by,

$$\phi_m\left(\frac{z}{\mathcal{L}}\right) = \begin{cases} \left[1 - b_{mu}\,\dfrac{z}{\mathcal{L}}\right]^{c_m}, & \text{for} \quad \dfrac{z}{\mathcal{L}} < 0 \\ 1 + b_{ms}\,\dfrac{z}{\mathcal{L}}, & \text{for} \quad \dfrac{z}{\mathcal{L}} \geq 0 \end{cases}, \tag{2.98}$$

where b_{mu}, b_{ms} are constants determined from surface layer measurements. According to

the Businger-Dyer formulation, the value of the exponent becomes $c_m = -1/4$. Similarly,

$$\phi_h\left(\frac{z}{\mathcal{L}}\right) = \begin{cases} \sigma_{\theta N}\left[1 - b_{hu}\frac{z}{\mathcal{L}}\right]^{c_h}, & \text{for} \quad \frac{z}{\mathcal{L}} < 0 \\ \sigma_{\theta N} + b_{hs}\frac{z}{\mathcal{L}}, & \text{for} \quad \frac{z}{\mathcal{L}} \geq 0 \end{cases}, \tag{2.99}$$

where b_{hu}, b_{hs} are also empirically determined constants. For unstable conditions the exponent $c_h = -1/2$. For ϕ_h to be consistent with relation (2.91), it is function of the turbulent Prandtl number under neutral conditions, $\sigma_{\theta N}$. The numerical values for the constants b_{mu}, b_{ms}, b_{hu} and b_{hs} were collected in Table 2.3. The values used in the present work are the ones given by Dyer (1974) and suggested in reference textbooks (Kaimal and Finnigan, 1994; Arya, 2001):

$$\sigma_{\theta N} = 1\,, \quad b_{mu} = b_{hu} = 16\,, \quad b_{ms} = b_{hs} = 5\,, \tag{2.100}$$

thus $\phi_h \equiv \phi_m$ for stable conditions and $\phi_h \equiv {\phi_m}^2$ in unstable conditions.

Regarding the integral functions ψ_m and ψ_h, while in stable conditions their derivation is trivial, for negative values of $\mathcal{L}$ analytical solutions were given by Paulson (1970) and reviewed by Benoit (1977). Thus, using the expression in (2.98),

$$\psi_m(\zeta) = \int_0^{\zeta(z)} \frac{[1 - \phi_m(\zeta)]}{\zeta}\, d\zeta \quad \Leftrightarrow$$

$$\Leftrightarrow \quad \psi_m(\zeta) = \begin{cases} \ln\left(\frac{[1+\eta^2][1+\eta]^2}{8}\right) - 2\arctan(\eta) + \frac{\pi}{2}, & \text{for} \quad \zeta < 0 \\ -b_{ms}\,\zeta\,, & \text{for} \quad \zeta \geq 0 \end{cases},$$

$$\text{with:} \quad \zeta = \frac{z}{\mathcal{L}}\,, \quad \eta = \sqrt[4]{1 - b_{mu}\frac{z}{\mathcal{L}}}\,. \tag{2.101}$$

For the θ profile, using the expression in (2.99),

$$\psi_h(\zeta) = \int_0^{\zeta(z)} \frac{[1 - \phi_h(\zeta)]}{\zeta}\, d\zeta \quad \Leftrightarrow$$

$$\Leftrightarrow \quad \psi_h(\zeta) = \begin{cases} (1 - \sigma_{\theta N})\ln(z) + \sigma_{\theta N}\, 2\ln\left(\frac{1+\xi}{2}\right), & \text{for} \quad \zeta < 0 \\ (1 - \sigma_{\theta N})\ln(z) - b_{hs}\,\zeta\,, & \text{for} \quad \zeta \geq 0 \end{cases},$$

$$\text{with:} \quad \zeta = \frac{z}{\mathcal{L}}\,, \quad \xi = \sqrt{1 - b_{hu}\frac{z}{\mathcal{L}}}\,. \tag{2.102}$$

The second integral may be neglected. However, following Benoit (1977), one can obtain numerically robust expressions by keeping $\psi_m(z_{m0}/\mathcal{L})$ and $\psi_h(z_{h0}/\mathcal{L})$:

$$-\psi_m(\zeta)+\psi_m(\zeta_0)=\begin{cases}\ln\left(\dfrac{[1+\eta_0^2][1+\eta_0]^2}{[1+\eta^2][1+\eta]^2}\right)\ \cdots & \\ \quad\ldots+2\left[\arctan(\eta)-\arctan(\eta_0)\right] & \text{for}\quad \zeta<0\\ b_{ms}\left[\zeta-\zeta_0\right], & \text{for}\quad \zeta\geq 0\end{cases},$$

$$\text{with:}\quad \zeta=\frac{z}{\mathcal{L}},\quad \zeta_0=\frac{z_{\mathrm{m0}}}{\mathcal{L}},\quad \eta=\sqrt[4]{1-b_{mu}\frac{z}{\mathcal{L}}},\quad \eta_0=\sqrt[4]{1-b_{mu}\frac{z_{\mathrm{m0}}}{\mathcal{L}}}.$$

$$-\psi_h(\chi)+\psi_h(\chi_0)=\begin{cases}(\sigma_{\theta N}-1)\ln\left(\dfrac{z}{z_{\mathrm{h0}}}\right)+\sigma_{\theta N}2\ln\left(\dfrac{1+\xi_0}{1+\xi}\right), & \text{for}\quad \chi<0\\ (\sigma_{\theta N}-1)\ln\left(\dfrac{z}{z_{\mathrm{h0}}}\right)+b_{hs}\left[\chi-\chi_0\right], & \text{for}\quad \chi\geq 0\end{cases},$$

$$\text{with:}\quad \chi=\frac{z}{\mathcal{L}},\quad \chi_0=\frac{z_{\mathrm{h0}}}{\mathcal{L}},\quad \xi=\sqrt{1-b_{hu}\frac{z}{\mathcal{L}}},\quad \xi_0=\sqrt{1-b_{hu}\frac{z_{\mathrm{h0}}}{\mathcal{L}}}.$$

The use of these expressions is straightforward when the referential is displaced vertically as in eqs. 2.96 and 2.97, by shifting the following quantities accordingly with z, leaving the ones related to z_0 unaltered:

$$\zeta=\frac{z+z_{\mathrm{m0}}}{\mathcal{L}},\quad \zeta_0=\frac{z_{\mathrm{m0}}}{\mathcal{L}},\quad \eta=\sqrt[4]{1-b_{mu}\frac{z+z_{\mathrm{m0}}}{\mathcal{L}}},\quad \eta_0=\sqrt[4]{1-b_{mu}\frac{z_{\mathrm{m0}}}{\mathcal{L}}},$$
$$\chi=\frac{z+z_{\mathrm{h0}}}{\mathcal{L}},\quad \chi_0=\frac{z_{\mathrm{h0}}}{\mathcal{L}},\quad \xi=\sqrt{1-b_{hu}\frac{z+z_{\mathrm{h0}}}{\mathcal{L}}},\quad \xi_0=\sqrt{1-b_{hu}\frac{z_{\mathrm{h0}}}{\mathcal{L}}}.$$

2.4 Numerical model for the simulation of the neutral flow

The analytical solution of a system of partial differential equations may be difficult to find, if not impossible, unless some assumptions are made to simplify the system and if the geometry of the problem is also simple. For atmospheric flows and several problems involving the Navier-Stokes equations, analytical solutions are only possible for simple flows or under several restrictive assumptions. The state of the art is to employ numerical methods to obtain an approximate solution, yielding results that describe the physics within the equations.

Although there are several methods to obtain numerical solutions of partial differential equations, the most used are the finite differences, finite volume and finite element methods. In these, the governing equations are discretized to form a set of algebraic equations where the values are calculated at discrete places on a computational grid that resembles the physical domain. A description of these methods can be found in Ferziger and Perić (2002).

The computer code used throughout this thesis is VENTOS® initially developed by Castro (1997) in his doctoral work, having been extensively used in research related to

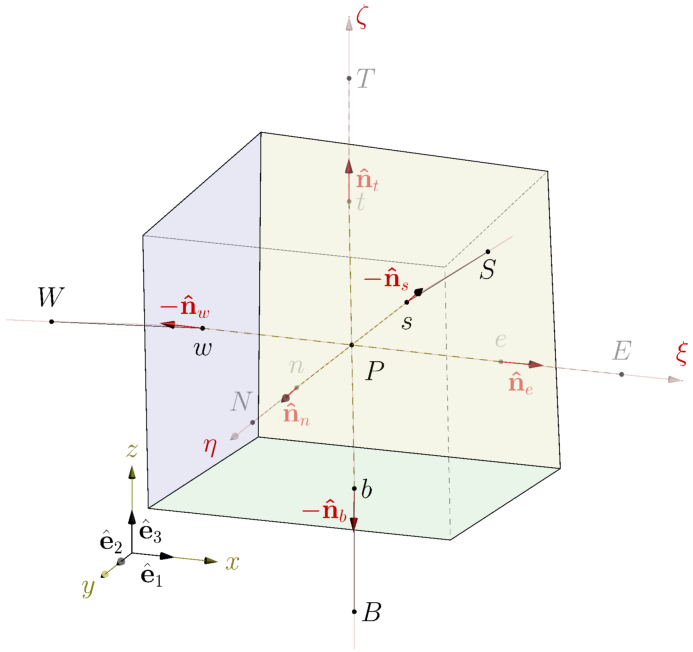

Figure 2.2: Example of a control volume.

wind energy resource assessment, *e.g.*, Castro *et al.* (2003), Lopes da Costa *et al.* (2006) and Palma *et al.* (2008). In VENTOS® the governing equations are discretized in a structured mesh using the finite volume method, with a collocated arrangement of the primitive variables . The algebraic equations are solved in a segregated approach, using the semi-implicit method for pressure-linked equations (SIMPLE) in Patankar (1980) to maintain the pressure-velocity coupling.

Throughout this section, the numerical techniques implemented in VENTOS® for solving neutral atmospheric flows in mountainous topography are briefly described.

2.4.1 Computational grid and transformation to generalized curvilinear coordinates

In the finite volume method, the governing equations are discretized by evaluating surface and volume integrals over control volumes (CV). For structured grids each CV adopts a rectangular cuboid shape, as shown in Figure 2.2. Because these are arranged in three directions, for a specific CV at point P, its neighbours are identified as the east (E), west (W), north (N), south (S), top (T) and bottom (B), respectively connected by the e, w, n, s, t and b faces. For each face the normal vectors must be defined, as this is needed to evaluate the fluxes entering and exiting the CV.

In order for the computational domain to have CVs arranged in an irregular way that follows a complex topography composed of mountains and valleys, *i.e.*, arranged in a non-orthogonal computational grid, a new system of coordinates $\vec{\xi} = \{\xi, \eta, \zeta\}$ is created such that its coordinate lines,

$$\xi^1 \equiv \xi = \xi\left(x,y,z\right) \ , \qquad \xi^2 \equiv \eta = \eta\left(x,y,z\right) \ , \qquad \xi^3 \equiv \zeta = \zeta\left(x,y,z\right) \ , \tag{2.103}$$

follow the computational CVs. A detailed description of this technique, its definitions and applications can be found in Thompson *et al.* (1985). To define this curvilinear

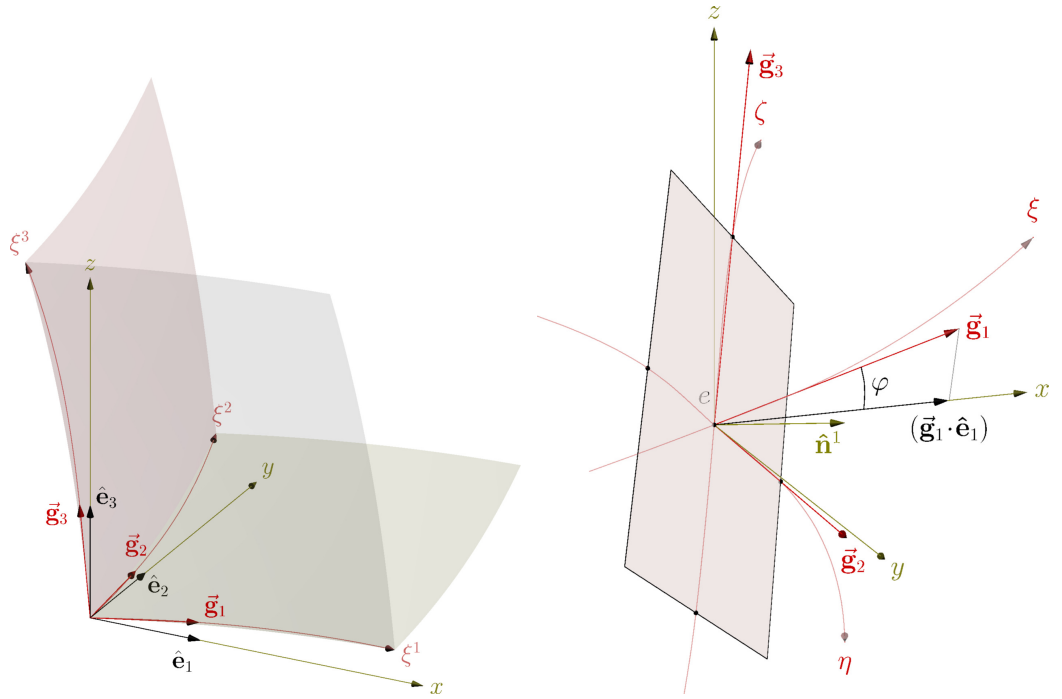

Figure 2.3: Generalized curvilinear coordinates: (a) correspondence between the physical domain Cartesian referential $\{x, y, z\}$ and the computational domain non-orthogonal coordinates $\{\xi, \eta, \zeta\}$; (b) difference between covariant and contravariant base vectors, $\vec{\mathbf{g}}_1$ and $\vec{\mathbf{n}}^1$, for a surface of constant ξ and relation between the ratio of the coordinate axes, x and ξ, given by the cosine of angle φ.

system, a new set of base vectors known as covariant base vectors, $\vec{\mathbf{g}}_1$, $\vec{\mathbf{g}}_2$ and $\vec{\mathbf{g}}_3$, is established such that these are tangent to the coordinate lines, respectively ξ, η and ζ:

$$\vec{\mathbf{g}}_i = \frac{\partial \vec{x}}{\partial \xi^i} = \sum_k \frac{\partial x_k}{\partial \xi^i} \hat{\mathbf{e}}_k \,, \quad \text{and} \quad \hat{\mathbf{e}}_i = \sum_k \frac{\partial \xi^k}{\partial x_i} \vec{\mathbf{g}}_k \,, \tag{2.104}$$

where the unitary vectors $\hat{\mathbf{e}}_i$ are the Cartesian basis vectors:

$$\hat{\mathbf{e}}_1 = \begin{Bmatrix} 1 \\ 0 \\ 0 \end{Bmatrix} \,, \qquad \hat{\mathbf{e}}_2 = \begin{Bmatrix} 0 \\ 1 \\ 0 \end{Bmatrix} \,, \qquad \hat{\mathbf{e}}_3 = \begin{Bmatrix} 0 \\ 0 \\ 1 \end{Bmatrix} \,. \tag{2.105}$$

From Figure 2.3a the derivatives between the Cartesian and curvilinear coordinate lines are related to the angle φ between them, such that:

$$\vec{\mathbf{g}}_i \cdot \hat{\mathbf{e}}_k = \|\vec{\mathbf{g}}_i\| \cos\varphi \equiv \frac{\partial x_k}{\partial \xi^i} \,. \tag{2.106}$$

If the grid is arranged in such a way that the curvilinear coordinates are non-orthogonal between themselves, another set of base vectors can be defined, $\vec{\mathbf{n}}_1$, $\vec{\mathbf{n}}_2$ and $\vec{\mathbf{n}}_3$ that, instead of being tangent, are normal to surfaces of constant ξ, η and ζ, being known as the contravariant basis:

$$\vec{\mathbf{n}}^i = \nabla \xi^i = \sum_k \frac{\partial \xi^i}{\partial x_k} \hat{\mathbf{e}}_k \,, \quad \text{and} \quad \hat{\mathbf{e}}_i = \sum_k \frac{\partial x_i}{\partial \xi^k} \vec{\mathbf{n}}^k \,. \tag{2.107}$$

The indexes in $\vec{\mathbf{n}}^i$ are superscripted to agree with the nomenclature usually found in the literature. Both sets of base vectors, $\vec{\mathbf{g}}_i$ and $\vec{\mathbf{n}}^i$ are locally defined, as shown in the Figure 2.3b. Because the covariant basis is tangent to the coordinate lines and the contravariant is orthogonal to the surfaces formed by these, they are respectively orthogonal, thus:

$$\vec{\mathbf{g}}_i \cdot \vec{\mathbf{n}}^j = \begin{cases} 1\,, & \text{if} \quad i = j \\ 0\,, & \text{if} \quad i \neq j \end{cases} . \tag{2.108}$$

By knowing the Cartesian position vector, $\vec{x}$, and its values in the curvilinear system, $\vec{\xi}$, each partial derivative $\partial x_i / \partial \xi^k$ can be computed, defining a transformation matrix:

$$\underline{\underline{\mathsf{J}}} = \begin{bmatrix} \frac{\partial x}{\partial \xi} & \frac{\partial x}{\partial \eta} & \frac{\partial x}{\partial \zeta} \\ \frac{\partial y}{\partial \xi} & \frac{\partial y}{\partial \eta} & \frac{\partial y}{\partial \zeta} \\ \frac{\partial z}{\partial \xi} & \frac{\partial z}{\partial \eta} & \frac{\partial z}{\partial \zeta} \end{bmatrix} \quad \Rightarrow \quad \text{inv}(\underline{\underline{\mathsf{J}}}) = \begin{bmatrix} \frac{\partial \xi}{\partial x} & \frac{\partial \xi}{\partial y} & \frac{\partial \xi}{\partial z} \\ \frac{\partial \eta}{\partial x} & \frac{\partial \eta}{\partial y} & \frac{\partial \eta}{\partial z} \\ \frac{\partial \zeta}{\partial x} & \frac{\partial \zeta}{\partial y} & \frac{\partial \zeta}{\partial z} \end{bmatrix} . \tag{2.109}$$

To describe the governing equations in a referential of curvilinear coordinates, the inverse transformation matrix, $\text{inv}(\underline{\underline{\mathsf{J}}})$, must be known. However, when a computational grid is specified it is easier to compute $\underline{\underline{\mathsf{J}}}$ with finite differences. The inverse matrix, $\text{inv}(\underline{\underline{\mathsf{J}}})$, can be obtained applying Cramer's rule *i.e.*, from the transpose of the cofactor matrix of $\underline{\underline{\mathsf{J}}}$, normalized by the determinant $\det(\underline{\underline{\mathsf{J}}})$:

$$\mathsf{J} = \det(\underline{\underline{\mathsf{J}}}) = \frac{1}{\det(\text{inv}(\underline{\underline{\mathsf{J}}}))} = \vec{\mathbf{g}}_1 \cdot (\vec{\mathbf{g}}_2 \times \vec{\mathbf{g}}_3) \ . \tag{2.110}$$

For the sake of simplicity, the cofactors of $\text{inv}(\underline{\underline{\mathsf{J}}})$ will be represented by the symbol β, such that:

$$\beta_i^k = \mathsf{J} \frac{\partial \xi^k}{\partial x_i} \,, \tag{2.111}$$

thus, the elements of matrix $\text{inv}(\underline{\underline{\mathsf{J}}})$ are:

$$\begin{aligned}
&\beta_1^1 = \frac{\partial y}{\partial \eta}\frac{\partial z}{\partial \zeta} - \frac{\partial y}{\partial \zeta}\frac{\partial z}{\partial \eta} \,, \quad \beta_2^1 = -\frac{\partial x}{\partial \eta}\frac{\partial z}{\partial \zeta} + \frac{\partial x}{\partial \zeta}\frac{\partial z}{\partial \eta} \,, \quad \beta_3^1 = \frac{\partial x}{\partial \eta}\frac{\partial y}{\partial \zeta} - \frac{\partial x}{\partial \zeta}\frac{\partial y}{\partial \eta} \,, \\
&\beta_1^2 = -\frac{\partial y}{\partial \xi}\frac{\partial z}{\partial \zeta} + \frac{\partial y}{\partial \zeta}\frac{\partial z}{\partial \xi} \,, \quad \beta_2^2 = \frac{\partial x}{\partial \xi}\frac{\partial z}{\partial \zeta} - \frac{\partial x}{\partial \zeta}\frac{\partial z}{\partial \xi} \,, \quad \beta_3^2 = -\frac{\partial x}{\partial \xi}\frac{\partial y}{\partial \zeta} + \frac{\partial x}{\partial \zeta}\frac{\partial y}{\partial \xi} \,, \\
&\beta_1^3 = \frac{\partial y}{\partial \xi}\frac{\partial z}{\partial \eta} - \frac{\partial y}{\partial \eta}\frac{\partial z}{\partial \xi} \,, \quad \beta_2^3 = -\frac{\partial x}{\partial \xi}\frac{\partial z}{\partial \eta} + \frac{\partial x}{\partial \eta}\frac{\partial z}{\partial \xi} \,, \quad \beta_3^3 = \frac{\partial x}{\partial \xi}\frac{\partial y}{\partial \eta} - \frac{\partial x}{\partial \eta}\frac{\partial y}{\partial \xi} \,.
\end{aligned}$$

With $\underline{\underline{\mathsf{J}}}$ and $\text{inv}(\underline{\underline{\mathsf{J}}})$ defined, both sets of base vectors can be computed applying the following relations:

$$\begin{aligned}
&\vec{\mathbf{g}}_i = \underline{\underline{\mathsf{J}}}\, \hat{\mathbf{e}}_i \,, \qquad \vec{\mathbf{n}}^i = \text{inv}(\underline{\underline{\mathsf{J}}})^{\mathsf{T}}\, \hat{\mathbf{e}}_i \,, \qquad \hat{\mathbf{e}}_i = \underline{\underline{\mathsf{J}}}^{\mathsf{T}}\, \vec{\mathbf{n}}^i \,, \qquad \hat{\mathbf{e}}_i = \text{inv}(\underline{\underline{\mathsf{J}}})\ \vec{\mathbf{g}}_i \,, \\
&\vec{\mathbf{n}}^i = \frac{\vec{\mathbf{g}}_j \times \vec{\mathbf{g}}_k}{\mathsf{J}} \,, \quad \text{with} \quad \{i,j,k\} = \{1,2,3\} \vee \{2,3,1\} \vee \{3,1,2\} \,.
\end{aligned} \tag{2.112}$$

The arc length increment $\Delta x|_{\xi^i}$ for a coordinate line ξ^i is given by the covariant base vectors:

$$\Delta x|_{\xi^i} = \|\vec{\mathbf{g}}_i\| \, \Delta\xi^i \,, \tag{2.113}$$

while the area ΔS_{ξ^i} for a surface where ξ^i is constant can be obtained from the contravariant set:

$$\Delta S_{\xi^i} = \mathrm{J} \left\| \vec{\mathbf{n}}^i \right\| \Delta\xi^j \, \Delta\xi^k = \left\| \vec{\mathbf{g}}_j \times \vec{\mathbf{g}}_k \right\| \Delta\xi^j \, \Delta\xi^k \,, \quad \text{with} \quad i \neq j \neq k \,. \tag{2.114}$$

The volume for a curvilinear rectangular cuboid element is directly obtained from the jacobian J:

$$\Delta\Omega = \mathrm{J} \, \Delta\xi \, \Delta\eta \, \Delta\zeta \,. \tag{2.115}$$

Applying definition (2.104) to a Cartesian vector $\vec{u}$ yields:

$$\begin{aligned} \vec{u} = & \; u_1 \, \hat{\mathbf{e}}_1 + u_2 \, \hat{\mathbf{e}}_2 + u_3 \, \hat{\mathbf{e}}_3 \\ = & \sum_i \sum_k u_i \frac{\partial \, \xi^k}{\partial \, x_i} \, \vec{\mathbf{g}}_k \; = \; \sum_i \sum_k u_i \, \frac{\beta_i^k}{\mathrm{J}} \, \vec{\mathbf{g}}_k \; = \; \sum_k \left(\vec{u} \cdot \vec{\mathbf{n}}^k \right) \, \vec{\mathbf{g}}_k \,. \end{aligned} \tag{2.116}$$

This derivation serves as an example how a vector, or any other tensor, may be represented in the curvilinear referential using the covariant base vectors. Likewise, using instead the contravariant base vectors:

$$\vec{u} = \sum_i \sum_k u_i \frac{\partial \, x_i}{\partial \, \xi^k} \, \vec{\mathbf{n}}^k \; = \; \sum_k \left(\vec{u} \cdot \vec{\mathbf{g}}_k \right) \, \vec{\mathbf{n}}^k \,. \tag{2.117}$$

The differential operators present in the governing equations are the gradient of a scalar, $\nabla\phi$, the divergence of a vector, $\nabla\cdot\vec{u}$, the divergence of a second rank tensor, $\nabla\cdot\underline{\underline{\tau}}$, and a generic diffusion term, $\nabla\cdot(\Gamma\nabla\phi)$. Restating these using curvilinear coordinates yields:

$$\nabla\phi = \frac{1}{\mathrm{J}} \sum_i \frac{\partial}{\partial \, \xi^i} \left(\mathrm{J} \, \vec{\mathbf{n}}^i \phi \right) = \frac{1}{\mathrm{J}} \sum_i \frac{\partial}{\partial \, \xi^i} \left(\sum_k \beta_k^i \, \phi \right) \, \hat{\mathbf{e}}_i \,, \tag{2.118}$$

$$\nabla\cdot\vec{u} = \frac{1}{\mathrm{J}} \sum_i \frac{\partial}{\partial \, \xi^i} \left(\mathrm{J} \, \vec{\mathbf{n}}^i \cdot \vec{u} \right) = \frac{1}{\mathrm{J}} \sum_i \frac{\partial}{\partial \, \xi^i} \left(\sum_k \beta_k^i \, u_k \right) \,, \tag{2.119}$$

$$\nabla\cdot\underline{\underline{\tau}} = \frac{1}{\mathrm{J}} \sum_i \sum_j \sum_k \frac{\partial}{\partial \, \xi^j} \left(\mathrm{J} \, (\vec{\mathbf{n}}^j \cdot \hat{\mathbf{e}}_k) \, \tau_{ik} \right) \hat{\mathbf{e}}_i = \frac{1}{\mathrm{J}} \sum_i \sum_j \frac{\partial}{\partial \, \xi^j} \left(\sum_k \beta_k^j \, \tau_{ik} \right) \hat{\mathbf{e}}_i \,. \tag{2.120}$$

$$\nabla\cdot(\Gamma\nabla\phi) = \frac{1}{\mathrm{J}} \sum_i \sum_j \frac{\partial}{\partial \, \xi^i} \left(\Gamma \vec{\mathbf{n}}^i \cdot \frac{\partial}{\partial \, \xi^j} \left(\mathrm{J} \, \vec{\mathbf{n}}^j \phi \right) \right) = \frac{1}{\mathrm{J}} \sum_i \sum_j \sum_k \frac{\partial}{\partial \, \xi^i} \left(\Gamma \frac{\beta_k^i \beta_k^j}{\mathrm{J}} \frac{\partial \, \phi}{\partial \, \xi^j} \right) . \tag{2.121}$$

In the derivation of these relations, the following metric identity was used:

$$\sum_i \frac{\partial \left(\mathrm{J} \, \vec{\mathbf{n}}^i \right)}{\partial \, \xi^i} = \sum_i \frac{\partial \left(\vec{\mathbf{g}}_j \times \vec{\mathbf{g}}_k \right)}{\partial \, \xi^i} = \sum_i \frac{\partial \, \vec{\mathbf{g}}_j}{\partial \, \xi^i} \times \vec{\mathbf{g}}_k + \sum_i \vec{\mathbf{g}}_j \times \frac{\partial \, \vec{\mathbf{g}}_k}{\partial \, \xi^i} = 0 \,,$$

$$\text{with} \quad \{i,j,k\} = \{1,2,3\} \vee \{2,3,1\} \vee \{3,1,2\} \,. \tag{2.122}$$

2.4.2 Governing equations in generalized curvilinear coordinates

With the relations obtained to describe the several differential operators in a set of general curvilinear coordinates, the equations for conservation of mass and momentum (2.56, 2.58), assume the following form:

$$\sum_j \frac{1}{\mathsf{J}} \frac{\partial}{\partial \xi^j} \left(\sum_k \rho_{\mathrm{H}} \, \overline{u}_k \, \beta_k^j \right) = 0 \,, \tag{2.123}$$

$$\frac{\partial}{\partial t}(\mathsf{J} \, \rho_{\mathrm{H}} \overline{u}_i) + \sum_j \frac{\partial}{\partial \xi^j} \left(\rho_{\mathrm{H}} \sum_k \overline{u}_k \, \beta_k^j \, \overline{u}_i \right) = - \sum_j \frac{\partial \left(\overline{\widehat{p}} \, \beta_i^j \right)}{\partial \xi^j} + \sum_j \sum_k \frac{\partial}{\partial \xi^j} \left(\left[\overline{\tau}_{ik} + \tau'_{ik} \right] \beta_k^j \right) \,, \tag{2.124}$$

where the viscous and Reynolds stress tensors become:

$$\overline{\tau}_{ik} = \sum_m \frac{\mu}{\mathsf{J}} \left[\beta_k^m \frac{\partial \, \overline{u}_i}{\partial \, \xi^m} + \beta_j^m \frac{\partial \, \overline{u}_k}{\partial \, \xi^m} \right] \,, \tag{2.125}$$

$$\tau'_{ik} = \sum_m \frac{\mu_t}{\mathsf{J}} \left[\beta_k^m \frac{\partial \, \overline{u}_i}{\partial \, \xi^m} + \beta_j^m \frac{\partial \, \overline{u}_k}{\partial \, \xi^m} \right] - \delta_{ik} \, \rho_{\mathrm{H}} \, \frac{2}{3} \, k \,. \tag{2.126}$$

The transformed equations for the $k - \epsilon$ turbulence model (2.66, 2.72), are given by:

$$\begin{aligned} \frac{\partial}{\partial t}(\mathsf{J} \, \rho_{\mathrm{H}} \, k) + \sum_j \frac{\partial}{\partial \xi^j} \left(\rho_{\mathrm{H}} \sum_k \overline{u}_k \, \beta_k^j \, k \right) = \; & \ldots \\ \ldots \sum_j \sum_k \sum_m \frac{\partial}{\partial \xi^j} \left(\left[\mu + \frac{\mu_t}{\sigma_k} \right] \frac{\beta_k^m \, \beta_k^j}{\mathsf{J}} \, \frac{\partial \, k}{\partial \, \xi^m} \right) + \mathsf{J} \left[\mathcal{P} - \rho_{\mathrm{H}} \, \epsilon \right] \,, \end{aligned} \tag{2.127}$$

$$\begin{aligned} \frac{\partial}{\partial t}(\mathsf{J} \, \rho_{\mathrm{H}} \, \epsilon) + \sum_j \frac{\partial}{\partial \xi^j} \left(\rho_{\mathrm{H}} \sum_k \overline{u}_k \, \beta_k^j \, \epsilon \right) = \; & \ldots \\ \ldots \sum_j \sum_k \sum_m \frac{\partial}{\partial \xi^j} \left(\left[\mu + \frac{\mu_t}{\sigma_\epsilon} \right] \frac{\beta_k^m \, \beta_k^j}{\mathsf{J}} \, \frac{\partial \, \epsilon}{\partial \, \xi^m} \right) + \mathsf{J} \, \frac{\epsilon}{k} \left[C_{\epsilon 1} \, \mathcal{P} - C_{\epsilon 2} \, \rho_{\mathrm{H}} \, \epsilon \right] \,, \end{aligned} \tag{2.128}$$

with a transformed mechanical turbulence production term:

$$\mathcal{P} = \sum_i \sum_k \sum_m \tau'_{ik} \, \frac{\beta_k^m}{\mathsf{J}} \, \frac{\partial \, \overline{u_i}}{\partial \, \xi^m} \,. \tag{2.129}$$

2.4.3 Application of the finite volume method for non-orthogonal grids

The finite volume method uses the divergence theorem to evaluate volume integrals as an algebraic sum of the quantities in the faces of the computational element. With general curvilinear coordinates, the faces of the CV are constant surfaces of ξ for the

east and west, η for north and south, ζ for top and bottom faces. Exemplifying for the advection term of a scalar ϕ:

$$\iiint_{\Omega} \nabla\cdot(\rho\,\vec{u}\,\phi)\,d\Omega \;=\; \oiint_{S} \rho\,\phi\,\vec{u}\cdot\hat{\mathbf{n}}\,dS \;\approx\; \sum_{f} \rho_f\,\phi_f\,\vec{u}_f\cdot\hat{\mathbf{n}}_f\,\Delta S_f\;, \qquad (2.130)$$

$$\text{with :} \quad f = e,\, w,\, n,\, s,\, t,\, b\;.$$

In the preceding notation, the subscript f indicates the face of the CV, *i.e.*, east, west, north, south, top or bottom. $\hat{\mathbf{n}}_f$ is the face normal vector. The density ρ_f, velocity $\vec{u}_f$ and scalar ϕ_f are the respective quantities averaged over face f. The face normal vector and area, $\hat{\mathbf{n}}_f$ and ΔS_f, are given by the contravariant basis vectors, related to the cofactors defined in eq. (2.111). Thus:

$$\hat{\mathbf{n}}_e\,\Delta S_e = (\,\mathsf{J}\,\vec{\mathbf{n}}^1)_e\,\Delta\eta\,\Delta\zeta = \begin{Bmatrix}\beta^1_{1e}\\ \beta^1_{2e}\\ \beta^1_{3e}\end{Bmatrix}\;, \quad \hat{\mathbf{n}}_w\,\Delta S_w = -(\,\mathsf{J}\,\vec{\mathbf{n}}^1)_w\,\Delta\eta\,\Delta\zeta = -\begin{Bmatrix}\beta^1_{1w}\\ \beta^1_{2w}\\ \beta^1_{3w}\end{Bmatrix}\;,$$

$$\hat{\mathbf{n}}_n\,\Delta S_n = (\,\mathsf{J}\,\vec{\mathbf{n}}^2)_n\,\Delta\xi\,\Delta\zeta = \begin{Bmatrix}\beta^2_{1n}\\ \beta^2_{2n}\\ \beta^2_{3n}\end{Bmatrix}\;, \quad \hat{\mathbf{n}}_s\,\Delta S_s = -(\,\mathsf{J}\,\vec{\mathbf{n}}^2)_s\,\Delta\xi\,\Delta\zeta = -\begin{Bmatrix}\beta^2_{1s}\\ \beta^2_{2s}\\ \beta^2_{3s}\end{Bmatrix}\;,$$

$$\hat{\mathbf{n}}_t\,\Delta S_t = (\,\mathsf{J}\,\vec{\mathbf{n}}^3)_t\,\Delta\xi\,\Delta\eta = \begin{Bmatrix}\beta^3_{1t}\\ \beta^3_{2t}\\ \beta^3_{3t}\end{Bmatrix}\;, \quad \hat{\mathbf{n}}_b\,\Delta S_b = -(\,\mathsf{J}\,\vec{\mathbf{n}}^3)_b\,\Delta\xi\,\Delta\eta = -\begin{Bmatrix}\beta^3_{1b}\\ \beta^3_{2b}\\ \beta^3_{3b}\end{Bmatrix}\;.$$

The grid spacing is chosen such that the numeric values of $\Delta\xi$, $\Delta\eta$ and $\Delta\zeta$ are 1, thus these are omitted throughout the remainder of this text.

The advective flux for the east and west faces is:

$$\rho_e\,\phi_e\,\vec{u}_e\cdot\hat{\mathbf{n}}_e\,\Delta S_e \;=\; \rho_e\,\phi_e\,\sum_k \left(u_k\,\beta^1_k\right)_e\;. \qquad (2.131)$$

Analogously, the discretization of a diffusive term is:

$$\iiint_{\Omega} \nabla\cdot(\,\Gamma\,\nabla\phi)\,d\Omega \;=\; \oiint_{S} \Gamma\,\nabla\phi\cdot\hat{\mathbf{n}}\,dS \;\approx\; \sum_{f} \Gamma_f\;(\nabla\phi)_f\cdot\hat{\mathbf{n}}_f\,\Delta S_f\;, \qquad (2.132)$$

where Γ refers to the diffusion coefficient of the scalar ϕ. With an orthogonal grid, the normal vectors of the faces coincide with the Cartesian basis vectors, simplifying the computation of this term because only the normal derivative needs to be evaluated. However for non-orthogonal grids, all of the components of $\nabla\phi$ need to be evaluated at each face. Exemplifying for the east face:

$$\Gamma_e\;(\nabla\phi)_e\cdot\hat{\mathbf{n}}_e\,\Delta S_e \;=\; \Gamma_e\sum_k\left(\frac{\partial\,\phi}{\partial\,x_k}\beta^1_k\right)_e \;=\; \Gamma_e\sum_k\sum_m\left(\frac{\partial\,\phi}{\partial\,\xi^m}\frac{\partial\,\xi^m}{\partial\,x_k}\beta^1_k\right)_e \;\ldots$$

$$\ldots \;=\; \Gamma_e\sum_k\sum_m\left(\frac{\beta^m_k\,\beta^1_k}{\mathsf{J}}\frac{\partial\,\phi}{\partial\,\xi^m}\right)_e\;. \qquad (2.133)$$

A body force, $\mathcal{B}$, is evaluated as a volume integral, being approximated by the nodal value for the CV:

$$\iiint_{\Omega} \mathcal{B}\, d\Omega \;\approx\; \mathcal{B}_P\, \Delta\Omega_P \;, \tag{2.134}$$

where $\Delta\Omega_P$ is volume of the CV and subscript P denotes its centre.

Approximation of the values of variables at the faces

To compute the advective and diffusive fluxes, both the scalar ϕ and its gradient $\nabla\phi$ have to be known. In a collocated arrangement these quantities are only available at the nodes of each CV, thus they are evaluated numerically by interpolation and finite differences. Having Figure 2.2 as reference, the value at the east face can be obtained by linear interpolation from the values at P and E nodes:

$$\phi_e = c_{1P}\,\phi_P + (1 - c_{1P})\,\phi_E \;, \qquad c_{1P} = \frac{\|\vec{x}_e - \vec{x}_P\|}{\|\vec{x}_P - \vec{x}_e\| + \|\vec{x}_e - \vec{x}_E\|} \;. \tag{2.135}$$

The interpolation coefficient c_1 is computed using the Cartesian distances between the nodes and the face, to account for the grid non-orthogonality. This is done to compute ρ_e and Γ_e, however to compute ϕ_e, a 1$^{\text{st}}$ order upwind scheme (UDS) is used, where the value at the face is estimated from the upstream value, according to the direction of the flow:

$$\phi_e = \text{UDS}\,(\phi) = \begin{cases} \phi_P \;, & \vec{u}_e \cdot \hat{\mathbf{n}}_e \geq 0 \\ \phi_E \;, & \vec{u}_e \cdot \hat{\mathbf{n}}_e < 0 \end{cases} \;. \tag{2.136}$$

Although this approximation does not produces oscillatory solutions as it fully satisfies the boundedness criterion, it does so by introducing high numerical diffusion. To improve the approximation, a deferred-correction approach is implemented by computing ϕ_e explicitly with a higher-order scheme, being inserted as a source term:

$$\phi_e\, \vec{u}_e \cdot \hat{\mathbf{n}}_e \;\approx\; \vec{u}_e \cdot \hat{\mathbf{n}}_e\, \text{UDS}\,(\phi)^{m+1} + \vec{u}_e \cdot \hat{\mathbf{n}}_e \left[\text{QUICK}\,(\phi)^{m} - \text{UDS}\,(\phi)^{m}\right] \;. \tag{2.137}$$

The function $\text{UDS}\,(\phi)$ refers to the computation of ϕ_e with the upwind scheme. The subscript $m+1$ refers to the iteration for which ϕ is being implicitly computed while m is the value at the previous iteration. The function $\text{QUICK}\,(\phi)$ is the explicit high-order scheme used to compute ϕ_e, which in VENTOS® is the quadratic upwind interpolation scheme by Leonard (1979):

$$\phi_e = \text{QUICK}\,(\phi) = \begin{cases} c_{2uu}\,\phi_W + c_{2u}\,\phi_P + c_{2d}\,\phi_E \;, & \vec{u}_e \cdot \hat{\mathbf{n}}_e \geq 0 \\ c_{2uu}\,\phi_{EE} + c_{2u}\,\phi_E + c_{2d}\,\phi_P \;, & \vec{u}_e \cdot \hat{\mathbf{n}}_e < 0 \end{cases} \;. \tag{2.138}$$

This is also an upwind scheme as it computes the face value using always two nodes upstream and one downstream. For the case when the mass flux through the east face

is positive, the coefficients are given as:

$$\begin{cases} c_{2uu} = \dfrac{\left\|-\overrightarrow{eP}\right\| \left\|\overrightarrow{eE}\right\|}{\left(\left\|\overrightarrow{Ww}\right\| + \left\|\overrightarrow{wP}\right\|\right)\left(\left\|\overrightarrow{Ww}\right\| + \left\|\overrightarrow{wP}\right\| + \left\|\overrightarrow{Pe}\right\| + \left\|\overrightarrow{eE}\right\|\right)} , \\ c_{2d} = \dfrac{\left\|\overrightarrow{eP}\right\| \left(\left\|\overrightarrow{eP}\right\| + \left\|\overrightarrow{Pw}\right\| + \left\|\overrightarrow{wW}\right\|\right)}{\left(\left\|\overrightarrow{Ee}\right\| + \left\|\overrightarrow{eP}\right\|\right)\left(\left\|\overrightarrow{Ee}\right\| + \left\|\overrightarrow{eP}\right\| + \left\|\overrightarrow{Pw}\right\| + \left\|\overrightarrow{wW}\right\|\right)} , \\ c_{2u} = 1 - c_{2uu} - c_{2d} . \end{cases} \tag{2.139}$$

For a negative flux instead, the coefficients are computed similarly, but the positions are shifted to evaluate instead the two upstream nodes, *e.g.*, nodes EE, E and P are used instead of W, P and E.

Approximation of derivatives at the faces

A derivative is decomposed using chain rule defined in eq. (2.118). Considering the east face and the x_i direction:

$$\left.\frac{\partial \phi}{\partial x_i}\right|_e = \left.\frac{\partial \phi}{\partial \xi}\right|_e \frac{\beta^1_{ie}}{\mathrm{J}_e} + \left.\frac{\partial \phi}{\partial \eta}\right|_e \frac{\beta^2_{ie}}{\mathrm{J}_e} + \left.\frac{\partial \phi}{\partial \zeta}\right|_e \frac{\beta^3_{ie}}{\mathrm{J}_e} .$$

For derivatives in the direction normal to the face, the values at the node centres are used directly, applying a central difference scheme (CDS):

$$\left.\frac{\partial \phi}{\partial \xi}\right|_e \approx \left.\frac{\Delta \phi}{\Delta \xi}\right|_e = \phi_E - \phi_P .$$

Derivatives in the other directions require the values of ϕ at the faces locations, obtained through interpolation:

$$\begin{aligned} \left.\frac{\partial \phi}{\partial \eta}\right|_e &\approx c_{1P} \left.\frac{\Delta \phi}{\Delta \eta}\right|_P + [1 - c_{1P}] \left.\frac{\Delta \phi}{\Delta \eta}\right|_E = c_{1P}[\phi_n - \phi_s] + [1 - c_{1P}][\phi_{En} - \phi_{Es}] \ \ldots \\ \ldots &= c_{1P}\Big[c_{2P}\,\phi_P + [1 - c_{2P}]\,\phi_N - c_{2S}\,\phi_S - [1 - c_{2S}]\,\phi_P\Big] \ \ldots \\ \ldots &+ [1 - c_{1P}]\Big[c_{2E}\,\phi_E + [1 - c_{2E}]\,\phi_{EN} - c_{2ES}\,\phi_{ES} - [1 - c_{2ES}]\,\phi_E\Big] , \end{aligned} \tag{2.140}$$

$$\begin{aligned} \left.\frac{\partial \phi}{\partial \zeta}\right|_e &\approx c_{1P} \left.\frac{\Delta \phi}{\Delta \zeta}\right|_P + [1 - c_{1P}] \left.\frac{\Delta \phi}{\Delta \zeta}\right|_E = c_{1P}[\phi_t - \phi_b] + [1 - c_{1P}][\phi_{Et} - \phi_{Eb}] \ \ldots \\ \ldots &= c_{1P}\Big[c_{3P}\,\phi_P + [1 - c_{3P}]\,\phi_T - c_{3B}\,\phi_B - [1 - c_{3B}]\,\phi_P\Big] \ \ldots \\ \ldots &+ [1 - c_{1P}]\Big[c_{3E}\,\phi_E + [1 - c_{3E}]\,\phi_{ET} - c_{3EB}\,\phi_{EB} - [1 - c_{3EB}]\,\phi_E\Big] , \end{aligned} \tag{2.141}$$

where c_1, c_2 and c_3 are interpolation coefficients in the ξ, η and ζ directions. These are defined following the method presented in eq. (2.135).

Time integration for unsteady flow simulation

In a steady-state simulation the time rate of change is discarded. For an unsteady computation, the time derivative is approximated using a three time-level implicit scheme (3FTI scheme in Fletcher, 1991):

$$\frac{\partial}{\partial t}\left(\iiint_{\Omega} \rho\,\phi\,d\Omega\right) \approx \left[3\,(\rho\,\phi)_P^{n+1} - 4\,(\rho\,\phi)_P^{n} + (\rho\,\phi)_P^{n-1}\right]\frac{\Delta\Omega_P}{2\,\Delta t}\,, \tag{2.142}$$

with index n referring to the time vector discretized with evenly spaced Δt intervals. With this scheme, the field of ϕ at time t^{n+1} is computed from the values at the two previous time-steps, with the remaining terms of the transport equation being evaluated at time t^{n+1}, *i.e.*, advection, diffusion and source terms.

Pressure-velocity coupling

In the discretization of the momentum equations, the pressure gradient term is handled as a surface integral. Exemplifying for the pressure derivative in the x direction:

$$\begin{aligned}\iiint_{\Omega} \frac{\partial\,\widehat{p}}{\partial\,x}\,d\Omega \;\equiv\; \iiint_{\Omega} \nabla\cdot(\widehat{p}\,\hat{\mathbf{e}}_1)\,d\Omega \;=\; \oiint_{S} \widehat{p}\;\hat{\mathbf{e}}_1\cdot\hat{\mathbf{n}}\,dS \;\approx\; \sum_f \widehat{p}_f\,\hat{\mathbf{e}}_1\cdot\hat{\mathbf{n}}_f\,\Delta S_f \;\ldots \\ \ldots \;=\; \widehat{p}_e\,\beta_{1e}^1 - \widehat{p}_w\,\beta_{1w}^1 + \widehat{p}_n\,\beta_{1n}^2 - \widehat{p}_s\,\beta_{1s}^2 + \widehat{p}_t\,\beta_{1t}^3 - \widehat{p}_b\,\beta_{1b}^3\,.\end{aligned} \tag{2.143}$$

For the derivatives in the y and z directions, the unitary vectors $\hat{\mathbf{e}}_2$ and $\hat{\mathbf{e}}_3$ are used instead.

The velocity and pressure fields are solved using the SIMPLE algorithm of Patankar (1980). Due to the non-staggered arrangement of variables in the grid, the pressure-weighted interpolation method (PWIM) of Rhie and Chow (1983) is used to ensure that the pressure and velocity fields remain coupled at the CV faces. In the simulation of unsteady flows, the treatment of the time integration terms in eq. (2.142) allows for different equations for the PWIM. The PICTURE scheme of Pascau (2011) was implemented as this ensures that the PWIM remains independent of the integration time-step.

Details on the implementation of the SIMPLE algorithm are in the Appendix A, namely the presure-correction equation (A.31) and the expressions for the PWIM (§A.3).

Linear system of equations and solver

After the application of the finite volume method to the transport equation for a scalar ϕ, its discretized form may be arranged as:

$$A_P^{\phi}\,\phi_P + A_E^{\phi}\,\phi_E + A_W^{\phi}\,\phi_W + A_N^{\phi}\,\phi_N + A_S^{\phi}\,\phi_S + A_T^{\phi}\,\phi_T + A_B^{\phi}\,\phi_B = S^{\phi}\,, \tag{2.144}$$

where A_F^{ϕ} represents all of the terms which multiply variable ϕ at the nodal location of control volume F (with F being either P, E, W, N, S, T, B). All of the terms which have no explicit value of ϕ_F go to the independent term S^{ϕ}.

Table 2.4: Position of control volumes in grid and matrix index notations.

Nodal location	Grid location	Matrix location
B	$\{i, j, k-1\}$	$\{l, l-N_i N_j\}$
S	$\{i, j-1, k\}$	$\{l, l-N_i\}$
W	$\{i-1, j, k\}$	$\{l, l-1\}$
P	$\{i, j, k\}$	$\{l, l\}$
E	$\{i+1, j, k\}$	$\{l, l+1\}$
N	$\{i, j+1, k\}$	$\{l, l+N_i\}$
T	$\{i, j, k+1\}$	$\{l, l+N_i N_j\}$

By establishing an equation for ϕ arranged as in eq. (2.144) for each CV belonging to the computational grid, a system of algebraic equations is formed such that:

$$\underline{\underline{A}}^{\phi} \cdot \vec{\phi} = \vec{S}^{\phi} \ , \tag{2.145}$$

whose matrix of coefficients, $\underline{\underline{A}}^{\phi}$, is composed by the several A_F^{ϕ} values. This is a septa-diagonal matrix with dimensions $(N_i \times N_j \times N_k)^2$ where N_i, N_j and N_k are the number of nodes in the ξ, η and ζ directions, respectively. The matrix index l is related to the grid indices by:

$$l = i + (j-1)\, N_i + (k-1)\, N_i\, N_j \ ,$$

whilst the grid indices may be obtained from index l by:

$$\begin{aligned} i &= 1 + (l-1) \bmod N_i \ , \\ j &= 1 + \left\lfloor \frac{l-i}{N_i} \right\rfloor \bmod N_j \ , \\ k &= 1 + \left\lfloor \frac{l-i-(j-1)\, N_i}{N_i\, N_j} \right\rfloor \bmod N_k \ . \end{aligned}$$

Each diagonal of $\underline{\underline{A}}^{\phi}$ corresponds to a specific nodal location where B, S and W are the lower diagonals, P is the central diagonal and E, N and T are the upper diagonals, forming the structure presented in Table 2.4.

The structure established in eq. (2.144) and its corresponding system of algebraic equations are valid for all fields, namely: (i) the velocity, defined in each of the momentum eqs. (2.58), (ii) the pressure-correction (A.31), (iii) the turbulence model variables (2.66, 2.72), and (iv) the potential temperature (2.59), if applicable. Each of the respective fields are solved in a segregated approach, using the tri-diagonal matrix algorithm (TDMA) in a line-by-line manner, alternating the sweep direction. The coefficient matrix $\underline{\underline{A}}^{\phi}$ is modified to solely have three diagonals, adding the remaining four to the independent vector $\vec{S}^{\phi}$, assuming that the respective ϕ values are temporarily known. This process is iteratively repeated, alternating the diagonals which are kept in $\underline{\underline{A}}^{\phi}$ to solve for lines in the direction of ξ, η and ζ (Castro *et al.*, 2008).

2.4.4 boundary conditions

Velocity wall boundary conditions

The wall boundary conditions make use of the logarithmic wall law (2.93), to estimate the tangential wall stresses from the velocity values at the first grid cell above the wall. The component of the velocity vector that is tangent to the wall, $\vec{u}_\tau$, is obtained from:

$$\vec{u}_\tau = \vec{u_P} - (\vec{u_P} \cdot \hat{\mathbf{n}}_b)\ \hat{\mathbf{n}}_b \,,$$

where $\hat{\mathbf{n}}_b$ is the normal vector of the bottom wall. A bulk transfer coefficient for momentum, C_m, is defined such that:

$$C_m = \kappa\ \ln^{-1}\left(\frac{\Delta z}{z_{\mathrm{m0}}} + 1\right) , \tag{2.146}$$

where Δz is the distance to the wall for the cell centre of the first CV above the wall,

$$\Delta z = [\vec{x}_P - \vec{x}_{\mathrm{w}}] \cdot \hat{\mathbf{n}}_b \,.$$

Additionally, a shifted z coordinate is used such that $\overline{u}(z = 0) = 0$, like in eq. (2.96). The wall shear stress is thus related with $\vec{u}_\tau$, C_m and u_*, through eqs. (2.82) and (2.87):

$$\begin{aligned} &\tau'_{xw} = \rho_{\mathrm{w}}\, u_*\, C_m\, u_\tau \ , \quad \tau'_{yw} = \rho_{\mathrm{w}}\, u_*\, C_m\, v_\tau \ , \quad \tau'_{zw} = \rho_{\mathrm{w}}\, u_*\, C_m\, w_\tau \ , \\ &\left|\tau'_{\mathrm{w}}\right| = \rho_{\mathrm{w}}\, u_*\, C_m\ \|\vec{u}_\tau\| \ . \end{aligned} \tag{2.147}$$

With this formulation, the boundary condition is split into an implicit and explicit part, *e.g.*, while solving the momentum equation for u, the wall stress terms containing u_P are treated implicitly and the remaining terms go to the independent vector.

The friction velocity, u_*, could be obtained from the value of the wall shear stress, $|\tau'_{\mathrm{w}}|$, or related to C_m and $\|\vec{u}_\tau\|$. This would rely on the values obtained at the previous iteration. Instead, u_* is obtained from the value of k at the wall, assuming an equilibrium between the turbulence production terms and its dissipation, yielding:

$$u_* = {C_\mu}^{1/4}\, k_{\mathrm{w}}^{1/2} \ . \tag{2.148}$$

Turbulence model wall boundary conditions

The turbulence production and dissipation terms of the k eq. (2.66) near the wall are obtained assuming a surface layer with constant shear. The production $\mathcal{P}$ is specified by the wall shear stress and the velocity gradient, applying expressions (2.82, 2.87, 2.88):

$$\mathcal{P} \approx \left|\tau'_{\mathrm{w}}\right| \ \frac{{C_\mu}^{1/4}\, k_{\mathrm{w}}^{1/2}}{\kappa\,[\Delta z + z_{\mathrm{m0}}]} \ . \tag{2.149}$$

The $\mathcal{P}$ term is approximated by the value at the CV centre and added to the independent vector. Assuming that production is in equilibrium with the dissipation:

$$\mathcal{P} = \rho_{\mathrm{H}}\, \epsilon_P \quad \Leftrightarrow \quad \epsilon_P \approx \frac{{C_\mu}^{3/4}\, k_{\mathrm{w}}^{3/2}}{\kappa\,[\Delta z + z_{\mathrm{m0}}]} \ . \tag{2.150}$$

As this term is of opposite sign to $\mathcal{P}$, it is treated implicitly, using $k_w \equiv k_P$ as the first CV is in the surface layer.

In the transport equation of ϵ (2.72), by solving the k field first, the ϵ value at the first CV centre is directly obtained from condition (2.150). Thus, the value of ϵ_P is prescribed:

$$A_E^\epsilon = A_W^\epsilon = A_N^\epsilon = A_S^\epsilon = A_T^\epsilon = A_B^\epsilon = 0\,,$$
$$A_P^\epsilon = \Delta\Omega_P\, 10^3\,, \quad S_P^\epsilon = A_P^\epsilon \frac{{C_\mu}^{3/4} k_w^{3/2}}{\kappa\,[\Delta z + z_{m0}]}\,. \tag{2.151}$$

Symmetry conditions

At domain boundaries where there is no mass transfer, *e.g.*, the top, north and south boundaries; a symmetry condition is used. The gradient normal to the domain boundary is set to zero, thus,

$$\nabla\phi \cdot \hat{\mathbf{n}} = 0\,, \tag{2.152}$$

where $\hat{\mathbf{n}}$ is the normal vector to the boundary. For a scalar field ϕ and the velocity field on a CV near the boundary, condition (2.152) yields:

$$\phi_{boundary} = \phi_P\,, \quad \vec{u}_\tau|_{boundary} = \vec{u}_\tau|_P\,, \quad \vec{u}_\perp|_{boundary} = 0\,.$$

This imply that a symmetry condition acts as a stress-free plane for the flow.

Outflow conditions

If the flow field which exits the domain is completely known, the values at the outflow boundary are prescribed as a Dirichlet boundary condition. As this information is rarely available, the exit flow is extrapolated from the neighbouring nodes. In a steady-state formulation, the velocity is extrapolated such that:

$$\frac{\partial \vec{u}}{\partial \mathsf{n}} = 0 \;\Rightarrow\; \vec{u}_{out} = \vec{u}_P\,, \tag{2.153}$$

where n represents the direction normal to the boundary, the subscript *out* is the node at the boundary and P the centre of the CV next to it. For an unsteady formulation, a convective condition is used instead:

$$\frac{\partial \vec{u}}{t} + C\frac{\partial \vec{u}}{\partial n} = 0 \;\Rightarrow\; \vec{u}_{out}^{\,n+1} = \vec{u}_{out}^{\,n} - C\frac{\Delta t}{\Delta \mathsf{n}}\left[\vec{u}_{out}^{\,n} - \vec{u}_P^{\,n}\right]\,, \tag{2.154}$$

where the subscript n indicates the time-step, representing Δt time units. Length $\Delta\mathsf{n}$ is the distance between P and the outlet. The advection velocity C is estimated as the average velocity of the inward mass flow at the other boundaries.

As the pressure is not known at the exit, it is extrapolated from the adjacent nodes of the inner pressure field (details in Appendix A, §(A.4)). As such, these outflow conditions do not guarantee overall mass conservation. To prevent this, mass conservation is enforced by scaling the normal velocity vector:

$$\vec{u}_\perp|_{out}^{\,corr} = \vec{u}_\perp|_{out}\frac{\sum \dot{m}_{in}}{\sum \dot{m}_{out}}$$

where $\sum \dot{m}_{in}$ is the mass flow that enters into the computational domain and $\sum \dot{m}_{out}$ is the mass flow leaving the computational domain, estimated from the uncorrected velocities at the outlet.

For all the other scalar quantities at the outflow boundary, a zero gradient condition is used, like eq. (2.152). To be accurate, these outflow conditions rely on the smoothness of the exiting flow and, thus, the outlet boundary should be placed far downstream to be away from any perturbed region, *e.g.*, a recirculating zone. In the simulation of atmospheric flow over complex terrain this is difficult to obtain. The common practice is to place the region of interest at the middle of the domain, disregarding the flow near the outflow boundaries as it will not be representative of the real flow conditions.

Inlet and initial conditions

The flow conditions at the inlet are imposed as Dirichlet boundary conditions. Usually neither the velocity nor turbulence quantities are know, as field measurements do not provide enough data at a sufficient height above the ground. As such, the inlet conditions have to be idealized.

The velocity is set using the logarithmic law for neutral flow, eq. (2.93), up to a distance δ above the wall. For this, both u_*, z_{m0} and δ have to be specified prior to the simulation start. The computational domain is aligned to have the longitudinal direction coincide with the direction of the inlet flow. The eastern face of the domain is set as an outflow boundary and the other faces are symmetry planes.

The inlet profiles for k and ϵ are estimated from the respective values at the wall, obtained from u_*:

$$k(z) = \frac{{u_*}^2}{\sqrt{C_\mu}} \left[1 - \frac{\min(z,\, 0.99\,\delta)}{\delta}\right]^2 , \tag{2.155}$$

$$\epsilon(z) = \frac{{u_*}^3}{\kappa\, \min(z,\ 0.99\,\delta)} \left[1 - \frac{\min(z,\, 0.99\,\delta)}{\delta}\right]^3 , \tag{2.156}$$

where z represents the vertical distance above the wall. Further details on the development of these profiles are referred in Appendix B.

2.4.5 Consideration of Coriolis terms in the momentum equations

The Cartesian coordinate system to which the conservation equations are referenced is usually aligned such that $\hat{\boldsymbol{\imath}}$, $\hat{\boldsymbol{\jmath}}$ and $\hat{\boldsymbol{k}}$ point to the east, north and in the upward direction, respectively. From the viewpoint of an observer in such reference frame, an object in motion will be subjected to a Coriolis force due to the rotation of the Earth. The Rossby number, Ro, is a measure of the relative weight between the Coriolis and the inertial forces of the flow,

$$\mathrm{Ro} = \frac{U}{f_c\, L} , \tag{2.157}$$

where U and L are characteristic values for speed and length. The parameter f_c is the Coriolis frequency, defined as:

$$f_c = 2\,\omega\,\sin\varphi\,, \tag{2.158}$$

where ω is the angular speed of the Earth and φ is the latitude. For flows at the microscales, where $L < 10\,\text{km}$, then $\text{Ro} \gg 1$, and the Coriolis force is usually neglected.

For flows where the Coriolis force is considered, a body force is added to the momentum eqs. (2.159),

$$\frac{\partial}{\partial t}(\rho\,\vec{u}) + \nabla\cdot(\rho\,\vec{u}\otimes\vec{u}) = -\nabla\widehat{p} + \nabla\cdot\underline{\underline{\tau}} + \rho\,\vec{a}_c\,, \tag{2.159}$$

where the acceleration $\vec{a}_c$ is the Coriolis force per unit of mass. It is related to both the fluid velocity, $\vec{u}$, and the rotation vector of the Earth, $\vec{\Omega}$, such that:

$$\vec{a}_c = -2\,\vec{\Omega}\times\vec{u} = -2\,\omega\begin{Bmatrix}0\\ \cos\varphi\\ \sin\varphi\end{Bmatrix}\times\begin{Bmatrix}u\\ v\\ w\end{Bmatrix} = f_c\begin{Bmatrix}v - w\,\cot\varphi\\ -u\\ u\,\cot\varphi\end{Bmatrix}. \tag{2.160}$$

The existence of the Coriolis force has another important consequence. For an ABL (atmospheric boundary-layer) whose horizontal velocity is constant above the boundary-layer, the vertical shear stresses decrease with height until these become zero (Garrat, 1992). In such conditions, the pressure gradient is balanced by the Coriolis force. It is suitable to represent the pressure gradient by the geostrophic wind, as this is the velocity for a height sufficiently high to have the diffusion terms neglected. By disregarding the Coriolis term, an alternative balance for momentum must happen, leading to the following modelling assumptions:

(i) A shear stress condition is applied at the top boundary of the domain, such that the streamwise pressure gradient is practically zero. However, such yields a vertical stress profile which will not tend to zero, resembling a constant stress layer instead.

(ii) A null shear stress condition is applied at the top. Although a decreasing vertical profile of the shear stress is obtained, a streamwise pressure gradient must exist.

For the simulation of flows where the representation of the ABL is confined to the surface-layer, condition (i) should be applied. In the more common situation of a flow with an ABL developing over a terrain, whose topography elements may protrude the surface-layer and the ABL itself, condition (ii) becomes a more reasonable assumption.

2.5 Numerical model for the simulation of stratified flow

When stratification is considered, one more transport equation must be solved, eq. (2.59), to compute the potential temperature field. Applying the relations in eqs. (2.60) and (2.63), the turbulent diffusion may be described as:

$$\sum_j \frac{\partial}{\partial x_j}\left(\rho_{\text{H}}\,\overline{\theta'\,u_j'}\right) \equiv \sum_j \frac{\partial}{\partial x_j}\left(\frac{q_j'}{c_p}\right) = -\sum_j \frac{\partial}{\partial x_j}\left(\frac{\mu_t}{\sigma_\theta}\,\frac{\partial\left(\theta_{\text{H}} + \overline{\widetilde{\theta}}\right)}{\partial x_j}\right).$$

The transport equation for the potential temperature perturbation becomes:

$$\frac{\partial}{\partial t}\left(\rho_{\mathrm{H}}\,\widehat{\overline{\theta}}\right)+\sum_j\frac{\partial}{\partial x_j}\left(\rho_{\mathrm{H}}\,\overline{u}_j\,\widehat{\overline{\theta}}\right)=\sum_j\frac{\partial}{\partial x_j}\left(\left[\frac{\lambda}{c_p}+\frac{\mu_t}{\sigma_\theta}\right]\frac{\partial\overline{\theta}}{\partial x_j}\right)-\frac{\partial}{\partial z}\left(\rho_{\mathrm{H}}\,\overline{w}\,\theta_{\mathrm{H}}\right)\,. \tag{2.161}$$

2.5.1 Boundary conditions

Velocity wall boundary conditions

The formulation for the wall shear stress is the same as in eq. (2.147), using instead the logarithmic diabatic law (2.96) to establish the bulk transfer coefficient C_m:

$$C_m=\kappa\,\left[\ln\left(\frac{\Delta z}{z_{\mathrm{m0}}}+1\right)-\psi_m\left(\frac{\Delta z+z_{\mathrm{m0}}}{\mathcal{L}}\right)+\psi_m\left(\frac{z_{\mathrm{m0}}}{\mathcal{L}}\right)\right]^{-1}\,. \tag{2.162}$$

The friction velocity, u_*, is estimated as in eq. (2.148). However, a dependency on $\mathcal{L}$ and ϕ_m appears when the z coordinate is shifted as in eq. (2.96):

$$u_*=\frac{{C_\mu}^{1/4}\,k_{\mathrm{w}}^{1/2}}{\left[1-\dfrac{z_{\mathrm{m0}}}{\mathcal{L}\,\phi_m(z_{\mathrm{m0}}/\mathcal{L})}\right]^{1/4}}\approx{C_\mu}^{1/4}\,k_{\mathrm{w}}^{1/2}\,. \tag{2.163}$$

It may be neglected however, as the influence on the value of u_* is below 0.3% for $|\mathcal{L}|\sim 10$ and $z_{\mathrm{m0}}\sim 0.1$, and 3% if $z_{\mathrm{m0}}\sim 1$.

Boundary conditions when the Monin-Obukhov length is prescribed

If $\mathcal{L}$ is known or prescribed during the simulation, the bulk transfer coefficient C_m is directly computed. After the velocity field is solved, u_* is obtained from $|\tau'_{\mathrm{w}}|$:

$${u_*}^2=|\tau'_{\mathrm{w}}|/\rho_{\mathrm{w}}\ \,, \tag{2.164}$$

and the surface heat flux is computed as:

$$q'_{\mathrm{w}}=-\frac{c_p\,\Theta\,|\tau'_{\mathrm{w}}|^{3/2}}{\rho_{\mathrm{w}}^{1/2}\,\kappa\,g\,\mathcal{L}}\,. \tag{2.165}$$

The flux q'_{w} is applied as a Neumann type boundary condition to close the set of algebraic equations and solve for $\widehat{\theta}$.

As for momentum, a bulk transfer coefficient for heat, C_θ, is defined as:

$$C_\theta=\kappa\,\left[\ln\left(\frac{\Delta z}{z_{\mathrm{h0}}}+1\right)-\psi_h\left(\frac{\Delta z+z_{\mathrm{h0}}}{\mathcal{L}}\right)+\psi_h\left(\frac{z_{\mathrm{h0}}}{\mathcal{L}}\right)\right]^{-1}\,. \tag{2.166}$$

After the linear system is solved, the perturbation temperature at the wall, $\widehat{\theta}_{\mathrm{w}}$, is obtained from the inner θ field:

$$q'_{\mathrm{w}}=-\rho_{\mathrm{w}}\,c_p\,u_*\,C_\theta\,\left[\overline{\theta}-\overline{\theta}_{\mathrm{w}}\right]\quad\Rightarrow\quad\widehat{\theta}_{\mathrm{w}}=\overline{\theta}-\theta_{\mathrm{Hw}}-\frac{|\tau'_{\mathrm{w}}|\,\Theta}{\rho_{\mathrm{w}}\,\kappa\,g\,\mathcal{L}\,C_\theta}\,. \tag{2.167}$$

Boundary conditions when the surface heat flux is prescribed

In a mesoscale-microscale dynamical coupling, the surface heat flux is known from the output of the regional model. Hence, a Neumann boundary condition is directly applied using q'_{w}. The difficulty lies in the computation of a value for $\mathcal{L}$ such that the surface fluxes are in agreement with the thermal and momentum logarithmic profiles. A solution for $\mathcal{L}$ is found iteratively, whose procedure is described in Chapter 5, §5.3.5.

After $\mathcal{L}$ is known, the perturbation temperature at the wall is obtained after the temperature field is solved, using eq. (2.167).

Turbulence model wall boundary conditions

For stratified flow, the k equation has the extra term, $\mathcal{G}$, representing the production of k due to buoyancy. From the definition in eq. (2.68), the following boundary condition is constructed:

$$\mathcal{G} = -\frac{g}{\theta_{\mathrm{H}}}\,\frac{\mu_t}{\sigma_\theta}\,\frac{(\overline{\theta}-\overline{\theta}_{\mathrm{w}})}{C_\theta\,\kappa\,[\Delta z + z_{\mathrm{h0}}]}\,\phi_h\ , \tag{2.168}$$

where ϕ_h is the stability function for heat, eq. (2.99), and C_θ is the bulk transfer coefficient defined in eq. (2.166).

The remaining terms are similar to the ones used in the neutral model, with the difference that the momentum stability function, eq. (2.98), is also considered. For the mechanical production term, $\mathcal{P}$:

$$\mathcal{P} = \left|\tau'_{\mathrm{w}}\right|\,\frac{{C_\mu}^{1/4}\,k_{\mathrm{w}}^{1/2}}{\kappa\,[\Delta z + z_{\mathrm{m0}}]}\,\phi_m\ . \tag{2.169}$$

The ϵ_P is obtained assuming that the production terms are balanced with the dissipation, and by applying the definition for Rf, eq. (2.85), for the surface layer:

$$\mathcal{P}+\mathcal{G} = \rho_{\mathrm{H}}\,\epsilon_P \quad \Leftrightarrow \quad \epsilon_P \approx \frac{{C_\mu}^{3/4}\,k_{\mathrm{w}}^{3/2}}{\kappa\,[\Delta z + z_{\mathrm{m0}}]}\left[\phi_m - \frac{\Delta z + z_{\mathrm{m0}}}{\mathcal{L}}\right]\ . \tag{2.170}$$

As in the neutral model, the ϵ values for the first CV above the wall are directly computed after solving the k field, as in expression (2.151).

Outflow conditions

Regarding conditions at outlet boundaries, condition (2.154) for unsteady flow is replaced by a formulation based on Durran and Klemp (1983), employing the same time integration scheme used by the unsteady solver (3FTI scheme in Fletcher, 1991). Further details are given in Appendix C, §C.2.8, together with an evaluation of the performance of other outflow conditions. The outflow velocities correction to enforce domain mass conservation and the zero gradient extrapolation for scalar quantities are the same as for the neutral model.

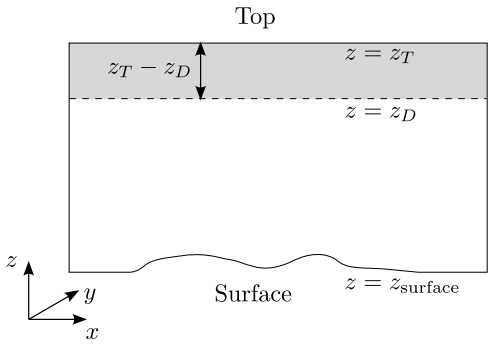

Figure 2.4: Representation of a damping layer placed at the top boundary.

Inlet and initial conditions

When idealized profiles at the inlet are required, the diabatic logarithmic laws for velocity (2.94) and potential temperature (2.95) are used. These require the specification of the Monin-Obukhov length, $\mathcal{L}$, or the surface heat flux. Additionally, the potential temperature at the surface must be specified. Regarding the roughness length for heat, z_{h0}, a good approximation is given by $0.1 z_{\text{m0}}$ (Garrat, 1992).

For the inlet profiles of turbulent quantities, although some changes may be applied based on the appearance of the buoyancy turbulence production term and eq. (2.170) of the wall value for ϵ, this leads to inconsistent results (described in §B.3). As such, the inlet profiles for k and ϵ are the same as used for neutral flow, eqs. (2.155) and (2.156).

Besides the inlet profiles, initial conditions for the thermodynamical reference state of the atmosphere must be given. One of the formulations in Table 2.1 can be used for this purpose.

2.5.2 Rayleigh damping layer

Without a special treatment of the top boundary conditions, any gravity wave which is propagating upward can be reflected downward by the domain top boundary. This reflection is unphysical and can alter the results. To avoid this, an absorbing layer known as Rayleigh damping was used at the top boundary. Following the formulation in Durran and Klemp (1983), an extra dissipative term is placed in the conservation equations such that:

$$\partial_t \left(\rho_{\text{H}}\, \phi\right) = f\left(\rho_{\text{H}}\, \phi,\, \vec{x}\right) - \rho_{\text{H}}\, R_D\left(z\right) \left[\phi - \widetilde{\phi}\right] , \tag{2.171}$$

where ϕ is the damped variable. This is usually the vertical velocity $\overline{w}$ but it can also be any of the other system variables: $\overline{u}$, $\overline{v}$, θ, k and ϵ. The damping, $R_D\left(z\right)$, is such that the value of ϕ near the boundary will be relaxed to a reference value $\widetilde{\phi}$. This function is

defined as:

$$R_D(z) = \begin{cases} 0\,, & \text{for } z \leq z_D \\ \alpha_D \sin^2\left(\dfrac{\pi}{2}\dfrac{z - z_D}{z_T - z_D}\right), & \text{for } z_D < z < z_T \end{cases} . \tag{2.172}$$

In this formulation, z_T is the height of the top boundary, z_D is the vertical height at which the damping layer starts and α_D is a coefficient that controls the damping strength. Through the ratio, $(z - z_D)/(z_T - z_D)$, the damping R_D is function of the distance to the boundary, decreasing the further it is away from it.

For one-way coupling simulations, the regional model provides the values at the boundaries. These become the reference values of the damping term. Additionally, damping layers can also be specified for the lateral boundaries using a similar formulation. The only difference is on the direction that will be used to define the damping function R_D, which is normal to that boundary.

Chapter 3

Simulation of mountain waves over idealized topography

In this chapter, numerical solutions of stably stratified flow over idealized hills are presented. Inviscid flow results show the generation of mountain waves for several flow regimes. These are compared with results found in the literature and analytical solutions given by linear theory. The same conditions are repeated for turbulent flow, considering surface friction and a boundary-layer, to study their effect on the dampening of the waves.

3.1 Introduction

In the present chapter, results of simulations of stably stratified flow over axisymmetric mountains are presented. The purpose was to assess how the code is able to reproduce gravity waves in the lee of mountains. These are dependent on the dimensionless mountain height parameter, $h^* = Nh/U$, where N is the Brunt-Väisälä frequency, U is the inlet free-stream velocity and h is the mountain height. For $h^* \ll 1$, the linear theory of Smith (1980; 2007) is valid and describes the mountain waves. For $h^* > 1$, non-linear phenomena such as wave breaking, flow splitting and vortex shedding may occur.

A first set of simulations was done considering inviscid flow, a frictionless bottom surface (free-slip condition) and a background stratification with constant N. These were realized for h^* ranging from 0.5 to 4.5. The mountain length was set such that $a^* = Na/U = 10$. The simulations where run up to dimensionless times of 40 to 160. To compare with numerical results from Smolarkiewicz and Rotunno (1989), simulations with $h^* = 4.5$ and $a^* = 38$ were also produced.

The simulations where repeated considering turbulence and a no-slip condition at the bottom surface, thus the existence of a boundary layer. The boundary layer height, δ, was set as $0.2\,U/N$. This dampened the non-linear effects of breaking waves and splitting flow, changing considerably the flow topology near the surface. Another set of simulations were made for a topography with $a^* = h^*$, to compare with the numerical results from Eidsvik (2008) and the laboratory experiments of Hunt and Snyder (1980).

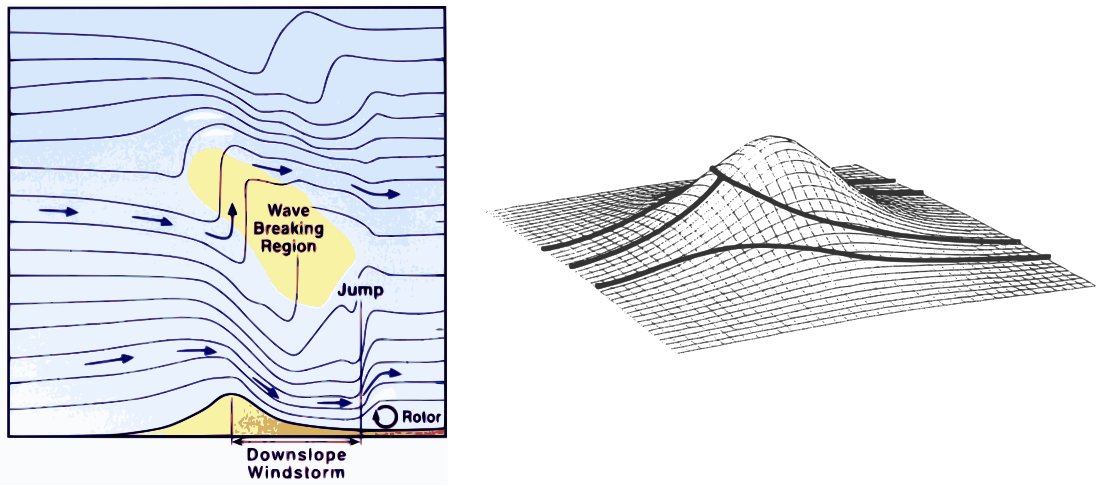

Figure 3.1: Illustrations of non-linear phenomena associated with stably stratified flows over mountains. *Left*: formation of an hydraulic jump with wave breaking (from Whiteman (2000)). *Right*: upstream splitting of flow streamlines (from Smith (1989))

Table 3.1: Description of the relevant parameters.

Dimensional parameters	
N	Brunt-Väisälä frequency (s^{-1})
U	Inlet free-stream velocity ($m\,s^{-1}$)
h	Mountain height, used in eq. (3.1) (m)
a	Characteristic mountain length from eq. (3.1) (m)
$\lambda_z = 2\pi U/N$	Vertical wavelength of gravity waves (m)
D_{lin}	Streamwise pressure drag predicted by linear theory, eq. (3.5) (N)
δ	Depth of the boundary-layer for turbulent flow (m)
δ_t	Boundary-layer displacement thickness, eq. (3.12) (m)
Θ_t	Boundary-layer momentum thickness, eq. (3.12) (m)
U_b	Velocity for the step-function of Smith (2007) ($m\,s^{-1}$)
H_b	Depth for the step-function of Smith (2007) (m)
Dimensionless parameters	
$h^* = N\,h/U$	Dimensionless mountain height
$a^* = N\,a/U$	Dimensionless mountain length
$\mathrm{Fr}_h = 1/h^*$	Froude number based on h
$\mathrm{Fr}_a = 1/a^*$	Froude number based on a
$t^* = t\,U/a$	Dimensionless time unit
$T^* = T\,U/a$	Dimensionless period, with T representing the period
$D^* = D_x/D_{lin}$	Pressure drag normalized by the linear theory prediction

For the sake of clarity, Table 3.1 shows the main parameters and symbols used throughout this chapter.

3.1.1 Definition of the problem and summary of linear theory solutions

The simulated topography is an Agnesi shape mountain, defined as:

$$f_h\,(x,y) = h\,\left[1+\left(\frac{x}{a}\right)^2+\left(\frac{y}{a}\right)^2\right]^{-\frac{3}{2}}\,, \tag{3.1}$$

where h and a are the mountain height and horizontal scale. The $3/2$ exponent is commonly chosen to study three-dimensional stratified flow because of its Fourier transform:

$$\widetilde{f_h}\,(k,l) = \frac{1}{4\,\pi^2}\int\limits_{-\infty}^{\infty}\int\limits_{-\infty}^{\infty} f_h\,(x,y)\;e^{-i(kx+ly)}\,dx\,dy = \frac{h\,a^2}{2\,\pi}\,e^{\left(-a\,\sqrt{k^2+l^2}\right)}\,, \tag{3.2}$$

for the wavenumbers k and l.

Smith (1980) developed a linear theory to obtain analytical solutions of the hydrostatic stratified inviscid flow over the hill shape in eq. (3.1). This theory was first applied to axisymmetric mountains, being later extended to elliptical obstacles by Phillips (1984). From the solution for the perturbation pressure at the surface,

$$\widehat{p}\,(x,y) = -\rho_{\text{H}}\,N\,U\,\frac{h\,x}{a}\,\left[1+\left(\frac{x}{a}\right)^2+\left(\frac{y}{a}\right)^2\right]^{-\frac{3}{2}}\,, \tag{3.3}$$

the horizontal pressure drag exerted on the mountain is estimated by:

$$\vec{D} = \int\limits_{-\infty}^{\infty}\int\limits_{-\infty}^{\infty}\widehat{p}\,(x,y)\;\nabla f_h(x,y)\,dx\,dy\,, \tag{3.4}$$

yielding for the inlet streamwise direction,

$$D_{lin} = D_x = \frac{\pi}{4}\rho_{\text{H}}\,N\,U\,h^2\,a\,. \tag{3.5}$$

When discretizing eq. (3.4) to compute the drag from a flow field returned by a simulation, the metrics from the matrix of transformation in eq. (2.111) can be used. Thus:

$$\begin{aligned}
&\frac{\partial\,f_h(x,y)}{\partial\,x} = \tan(\alpha_x) = -\frac{\beta^3_{1b}}{\beta^3_{3b}}\,, \qquad \frac{\partial\,f_h(x,y)}{\partial\,y} = \tan(\alpha_y) = -\frac{\beta^3_{2b}}{\beta^3_{3b}}\,,\\
&D_x = -\sum_{i,j}\left[\widehat{p}\,\frac{\beta^3_{1b}}{\beta^3_{3b}}\,\Delta S_b\right]_{i,j}\,, \qquad D_y = -\sum_{i,j}\left[\widehat{p}\,\frac{\beta^3_{2b}}{\beta^3_{3b}}\,\Delta S_b\right]_{i,j}\,,
\end{aligned} \tag{3.6}$$

where i and j are indices mapping the computational bottom surface, with slopes in the x and y directions defined by the angles α_x and α_y.

The thermodynamic reference profile is set such that the Brunt-Väisälä frequency, N, is constant with height:

$$\begin{aligned} \theta_{\text{H}} &= \theta_0 \exp\left(\frac{N^2}{g} z\right) , & \frac{d\theta_{\text{H}}}{dz} &= \frac{N^2}{g}\theta_{\text{H}} , \\ \Pi &= \Pi_0 + \frac{g^2}{c_p N^2}\left[\frac{1}{\theta} - \frac{1}{\theta_0}\right] , & \rho_{\text{H}} &= \frac{p_{00}\,\Pi^{\frac{1}{\gamma-1}}}{R_d\,\theta_{\text{H}}} , \end{aligned} \tag{3.7}$$

where p_{00} is a reference pressure value, usually taken as 100 kPa.

For inviscid flow the initial velocity field is constant and equal to U, while the potential temperature perturbation is null, *i.e.*, $\widehat{\theta} = 0$. For turbulent flow, due to the presence of surface friction these conditions are inappropriate. As diffusion terms are not neglected the surface heat flux, q_{w}, may exist and be unrelated with the value of N and the stable hydrostatic profile above the boundary layer. One way to consider q_{w} and relate it with N is to assume that $\overline{\overline{\theta}} = 0$, thus $\overline{\theta} = \theta_{\text{H}}$. The heat flux would be constant and equal to the amount of energy transferred from the atmosphere to the surface required to maintain the hydrostatic temperature profile. From the reference profiles in eq. (3.7):

$$q_{\text{w}} = -\lambda \frac{\partial\,\theta_{\text{H}}}{\partial\, z} = -\lambda \frac{N^2}{g}\theta_{\text{H}} , \tag{3.8}$$

where λ is the thermal conductivity of air. However this procedure was questionable as it implies a non-equilibrium thermal boundary layer and the profiles for the turbulence kinetic energy and dissipation, k and ϵ, remained unknown. A better approach was to consider a neutral boundary layer as an initial condition, yielding for the velocity:

$$\overline{u}\,(\Delta z) = \frac{u_*}{\kappa} \ln\left(\frac{\min(\Delta z,\, \delta)}{z_{\text{m0}}} + 1\right) , \qquad \text{where:} \quad \overline{u}\,(\delta) \equiv U , \tag{3.9}$$

where $\Delta z = z - f_h(x,y)$, *i.e.*, the height above the bottom surface. The neutral thermal boundary layer becomes constant inside the boundary layer, representing a well mixed temperature field, thus:

$$\begin{cases} \overline{\theta}(x,y,z) = \overline{\theta}(x,y,\delta + f_h) , & z < \delta + f_h \\ \overline{\theta}(x,y,z) = \theta_{\text{H}}(x,y,z) , & z \geq \delta + f_h \end{cases} , \quad \Rightarrow \quad \overline{\overline{\theta}}\,(x,y,z) = 0 \text{ , for } z \geq \delta + f_h$$

meaning that:

$$\begin{aligned} &\overline{\theta}(x,y,\delta + f_h) = \theta_{\text{H}}(x,y,\delta + f_h) , \\ &\overline{\overline{\theta}}\,(x,y,z) = \theta_{\text{H}}(x,y,\delta + f_h) - \theta_{\text{H}}(x,y,z) , \quad \text{for } \; z < \delta + f_h . \end{aligned} \tag{3.10}$$

For turbulent flow the surface drag contains also the normal stress arising from the Reynolds stress tensor, eq. (2.61), which also contributes to the force acting on the surface:

$$D_x = -\sum_{i,j}\left[\left(\widehat{p} + \frac{2}{3}\rho_{\text{H}} k\right)\frac{\beta_{1b}^3}{\beta_{3b}^3}\,\Delta S_b\right]_{i,j} , \quad D_y = -\sum_{i,j}\left[\left(\widehat{p} + \frac{2}{3}\rho_{\text{H}} k\right)\frac{\beta_{2b}^3}{\beta_{3b}^3}\,\Delta S_b\right]_{i,j} . \tag{3.11}$$

Smith (2007) revised his linear theory to account for the interaction between a boundary layer and mountain waves. It uses a step-function that attempts to describe the upstream boundary layer, relating it to the displacement and momentum thickness of the unperturbed velocity profile upstream, δ_t and Θ_t:

$$\delta_t = \int_0^\delta \left[1 - \frac{\overline{u}(z)}{U}\right] dz \,, \qquad \Theta_t = \int_0^\delta \frac{\overline{u}(z)}{U}\left[1 - \frac{\overline{u}(z)}{U}\right] dz \,. \tag{3.12}$$

The velocity and depth of the step-function boundary-layer, U_b and H_b, are defined as:

$$U_b = U\frac{\Theta_t}{\delta_t} \,, \qquad H_b = \frac{\delta_t^2}{\delta_t - \Theta_t} \,. \tag{3.13}$$

From these, two parameters are computed: the surface friction coefficient, C_b, and the friction coefficient at $z = H_b$, C_t:

$$C_b = \frac{2\,{u_*}^2}{H_b\,U_b} \,, \qquad C_t = C_b\frac{\Theta_t}{\delta_t - \Theta_t} \,.$$

The pressure (normalized by ρ_{H}) is computed for each wavenumber k and l:

$$\widetilde{\widehat{p}}\,(k,l) = \frac{i\,N\,U\,\widetilde{f_h}(k,l)}{1 - B(k,l)}\frac{k}{\sqrt{k^2+l^2}} \,, \tag{3.14}$$

where the function B is defined as:

$$B(k,l) = \left[\frac{i\,k\,U + C_t}{i\,k\,U_b + C_b + C_t}\right]\frac{i\,N\,H_b}{U_b}\frac{\sqrt{k^2+l^2}}{k} \,.$$

The drag is obtained by taking the inverse Fourier transform of the pressure. Alternatively it may be computed directly in wavenumber space by applying Parseval's relation:

$$D_x = \int_{-\infty}^{\infty}\int_{-\infty}^{\infty} \widehat{p}(x,y)\,\frac{\partial f_h}{\partial x}\,dx\,dy = 4\,\pi^2 \int_{-\infty}^{\infty}\int_{-\infty}^{\infty} \mathrm{conj}\left(\widetilde{\widehat{p}}\,(k,l)\right)\,i\,k\,\widetilde{f_h}(k,l)\,dk\,dl \,. \tag{3.15}$$

3.1.2 Description of the numerical simulations

The characteristics of the computational domains used in the simulations are summarized in Table 3.2. These are grouped into sets labelled from I to IV, as shown in the first column. For all simulations, the Brunt-Väisälä frequency, N, was set to $0.01\,\mathrm{s}^{-1}$ and the freestream inlet velocity, U, to $5\,\mathrm{m\,s}^{-1}$, leading to an hydrostatic vertical wavelength of $\lambda_z = 3142\,\mathrm{m}$. The vertical domain height was set to $12\,\mathrm{km} \approx 4\,\lambda_z$.

The grids in group I cover several values for h^*, keeping a^* constant and equal to 10. A first set of simulations considered inviscid flow while a second set has both turbulence and a boundary-layer, due to friction at the bottom wall. The size of the horizontal domain was the same in the spanwise, with $y/a \in [-10, 10]$. For lower values of h^* the domain size in the streamwise direction was set $x/a \in [-10, 15]$. For larger h^*, the domain downstream of the mountain was increased to accommodate for the larger wake produced. On the standard grid each horizontal layer of the mesh is composed

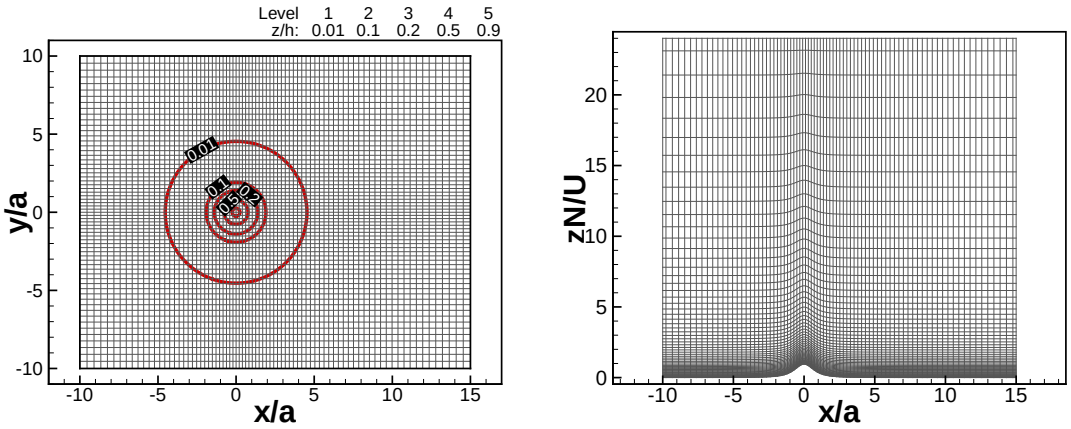

Figure 3.2: Computational grid used in the simulation of flows where $h^* = 1$ and $a^* = 10$. The computational grid for other values of a has the same expansion ratios and the same horizontal domain, $x/a = [-10, 15]$ and $y/a = [-10, 10]$. For other values of h the vertical discretization was similar to the presented grid. The height of the first control volume was set to $0.01\,U/N$.

Table 3.2: Description of the computational domain. $\min(\Delta x)$ and $\min(\Delta z)$ refers to the minimum horizontal length and vertical height of the grid elements. The parameters $\max(f_x)$ and $\max(f_z)$ are the maximum expansion factors for the geometric progression used, in the horizontal and vertical.

	h^*	a^*	Grid	x/a	y/a	$\min(\Delta x)$	$\max(f_x)$	$\min(\Delta z)$	$\max(f_z)$
I	0.1	10	$80 \times 80 \times 70$	$[-10, 10]$	$[-10, 10]$	$0.16\,a$	1.0216	$0.01\frac{U}{N}$	1.0776
	0.2								
	0.3								
	0.5	10	$100 \times 80 \times 70$	$[-10, 15]$	$[-10, 10]$	$0.16\,a$	1.0216	$0.01\frac{U}{N}$	1.0776
	0.8								
	1.0								
	1.2	10	$120 \times 80 \times 70$	$[-10, 20]$	$[-10, 10]$	$0.16\,a$	1.0216	$0.01\frac{U}{N}$	1.0776
	1.4								
	1.5								
	1.6								
	2.0	10	$140 \times 80 \times 70$	$[-10, 25]$	$[-10, 10]$	$0.16\,a$	1.0216	$0.01\frac{U}{N}$	1.0776
	3.0								
	4.5								
II	4.5	10	$96 \times 64 \times 70$	$[-10, 20]$	$[-10, 10]$	$0.2\,a$	1.0272	$0.01\frac{U}{N}$	1.0776
	4.5		$192 \times 128 \times 70$			$0.1\,a$	1.0133		
III	4.5	10	$112 \times 64 \times 60$	$[-10, 25]$	$[-10, 10]$	$0.2\,a$	1.0272	$0.06\,h$	1.0126
	4.5		$140 \times 80 \times 60$			$0.16\,a$	1.0216		
	4.5	38	$96 \times 64 \times 60$	$[-10, 20]$	$[-10, 10]$	$0.2\,a$	1.0272	$h/12$	1.0021
	4.5		$120 \times 80 \times 60$			$0.16\,a$	1.0216		
IV	1.0	1.0	$100 \times 64 \times 70$	$[-10, 15]$	$[-8, 8]$	$0.16\,a$	1.0272	$0.01\frac{U}{N}$	1.0776
	1.25	1.25	$140 \times 64 \times 70$	$[-10, 25]$					
	2.5	2.5							
	5.0	5.0							

of 100×80 elements, whose minimum length was set to $0.16\,a$ at the location of the mountain hilltop, $(x, y) = (0, 0)$. From this location, the CV length expands until the boundary is reached, following a geometric progression with expansion ratios below 1.03. The vertical domain was discretized with 70 levels where the height for the bottommost elements was set to $0.01\,U/N = 5\,\mathrm{m}$. A geometric progression was used in the vertical to have a higher mesh concentration near the bottom surface, with a maximum vertical expansion ratio of 1.08. This low value for the bottommost elements height was chosen to have at least 13 elements below the boundary layer height. Although inviscid simulations do not have a boundary-layer, the mesh was kept the same for better comparison.

The grids in group II were used to verify the grid dependence of the numerical results, having been compared with the $h^* = 4.5$ simulations in group I. The group III grids refer to simulations with different horizontal mesh spacing and height of the bottommost elements. These were made for validation purposes, to mimic numerical results from the literature (Smolarkiewicz and Rotunno, 1989; Ólafsson and Bougeault, 1996; Castro, 1997). The group IV grids were used in turbulent flow simulations where a^* was set equal to h^*. These were compared with both experimental and numerical results (Hunt and Snyder, 1980; Eidsvik, 2008).

To prevent wave reflection, a Rayleigh damping layer was applied as described in §2.5.2. The value of the damping coefficient was set to $3.5\,U/a$ such that $2 < \alpha_D\, a/U < 5$, following the recommendations in Durran and Klemp (1983). Several tests were made to choose: (i) what domain boundaries should have a damping layer, (ii) to which variables should the damping be applied, (iii) should the values of $\vec{u}$, k and ϵ at the boundary be used as reference values. Regarding the use of boundary values as reference (iii), the numerical solution would never reach a steady-state, even for large t^*. On most simulations where an approximately steady solution was obtained, for different arrangements of boundaries (i) and variables (ii) to which damping was applied, the integrated value of the surface drag would differ from a similar simulation with no damping, even for low h^* (where non-linear effects are small). On simulations considering turbulent diffusion and surface friction, the arrival to a steady state required always large simulation times ($t^* > 100$), being much more sensitive to the damping layer set-up. The conclusion was that a damping layer at the top boundary and affecting only the $\overline{w}$ velocity component was enough.

A review of outflow boundary conditions and their implementation in the numerical model is included in Appendix C. The condition used at the outlet boundary is based on the formulation in Durran and Klemp (1983), modified to use the 3FTI implicit scheme (Fletcher, 1991) instead of explicit Euler for the time integration. Further details concerning this outflow condition are given in §C.2.8.

3.2 Grid dependence study

To check how grid refinement affected the solution, simulations were made with different number of computational nodes and element size in the horizontal. The mountain parameters were $h^* = 4.5$ and $a^* = 10$, a highly non-linear regime with flow splitting

Table 3.3: Evaluation of grid dependence for simulations of inviscid flow at a dimensionless mountain height of $N\,h/U = 4.5$ and length of $N\,a/U = 10$. The height of the bottommost control volume is $0.01\,U/N$.

Time ($t\,U/a$)	5			9			16		
$\min(\Delta x)$	$0.2\,a$	$0.16\,a$	$0.1\,a$	$0.2\,a$	$0.16\,a$	$0.1\,a$	$0.2\,a$	$0.16\,a$	$0.1\,a$
Grid	$96 \times 64 \times 70$	$140 \times 80 \times 70$	$192 \times 128 \times 70$	$96 \times 64 \times 70$	$140 \times 80 \times 70$	$192 \times 128 \times 70$	$96 \times 64 \times 70$	$140 \times 80 \times 70$	$192 \times 128 \times 70$
upstr. $\min(u)/U$	-0.52	-0.43	-0.37	-0.45	-0.33	-0.35	-0.48	-0.28	-0.35
position S_u (x/a)	-1.00	-0.98	-1.04	-1.21	-1.37	-1.31	-1.26	-1.72	-1.81
position N_u (x/a)	-0.89	-0.81	-0.70	-0.95	-1.12	-1.13	-1.04	-1.32	-1.03
position N_{uf} (x/a)	-0.17	-0.19	-0.20	-0.16	-0.20	-0.23	-0.17	-0.22	-0.23
downstr. $\min(u)/U$	-1.19	-1.14	-1.23	-1.57	-1.68	-1.56	-1.80	-1.83	-1.83
position S_{d1} (x/a)	0.33	0.66	0.56	0.49	0.56	0.63	‡	‡	0.50
position S_{d*} (x/a)	1.47	1.51	1.42	1.99	1.98	1.71	1.63	1.89	1.99
dist. lee vort. (Δ/a)	1.72	1.79	1.61	1.64	2.58	1.57	2.79	2.85	†† 2.27
position S_{df} (x/a)	3.39	3.43	3.44	4.65	4.53	4.53	6.58	6.46	6.53
N. saddles	5	5	8	5	7	6	8	10	11
N. nodes & focus	5	5	8	5	7	6	8	10	11
** Drag (D_x/D_{lin})	0.65	0.65	0.67	0.53	0.54	0.55	0.47	0.49	0.50

** The pressure drag is normalized by the one predicted by linear inviscid theory. The numeric value is the average over one dimensionless time unit $\Delta t^* = a/U$.

†† The lee vortices are characterized by more points than a pair of focus. The numeric value is the greatest distance between points in the spanwise direction.

‡ Downstream saddle point S_{d1} and S_{d*} are the same.

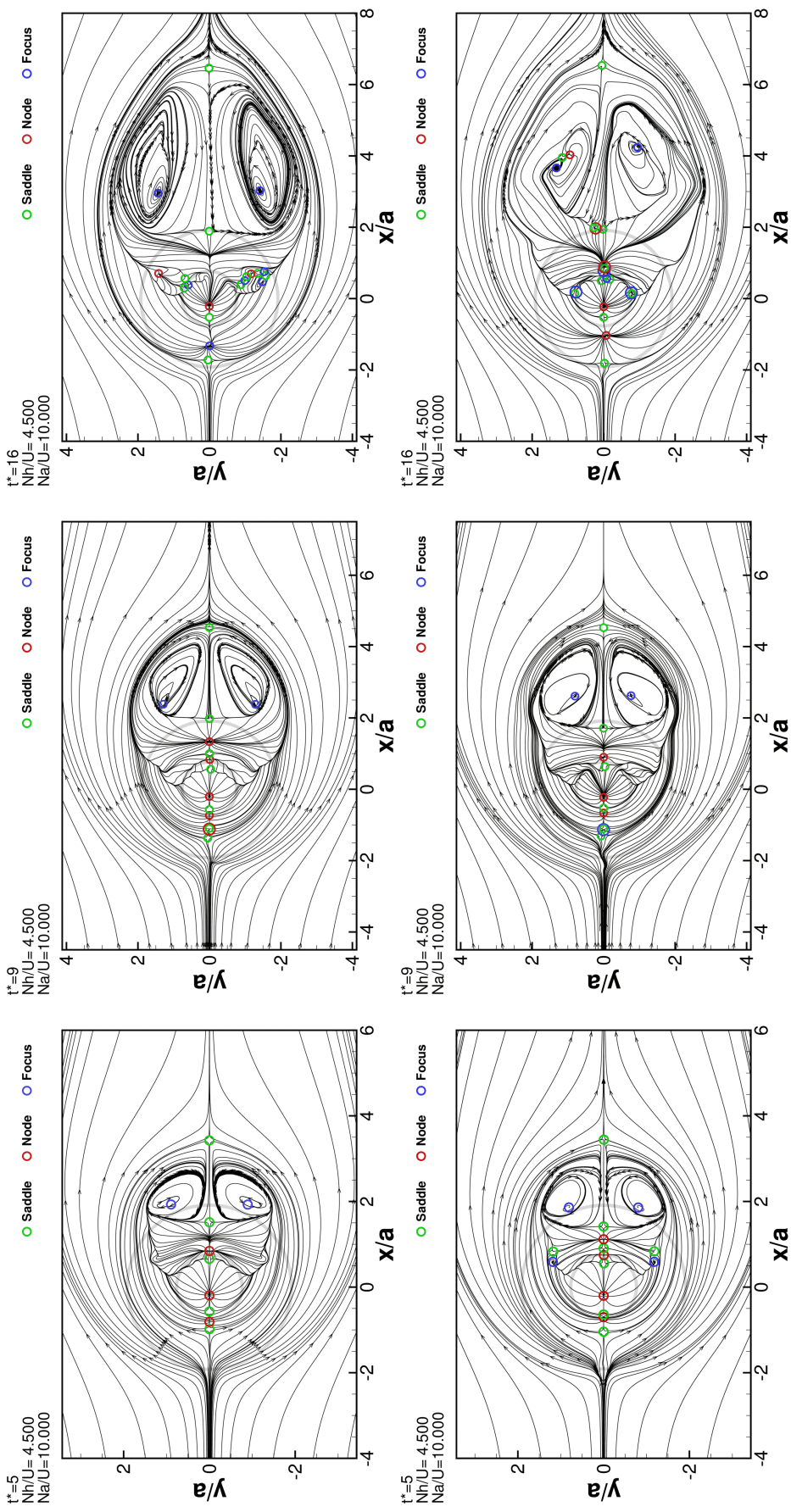

Figure 3.3: Results of inviscid flow simulations to verify grid dependence, for $h^* = 4.5$ and $a^* = 10$. The topmost figures refer to the $140 \times 80 \times 70$ grid. The bottommost figures refer to the most refined grid, with $192 \times 128 \times 70$ elements. The streamlines of the surface flow are shown for the dimensionless times of 5, 9 and 16. The circles in green, red and blue represent saddle, nodes and focus points. The grey circles are contours of the surface height at $0.1\,h$ and $0.5\,h$.

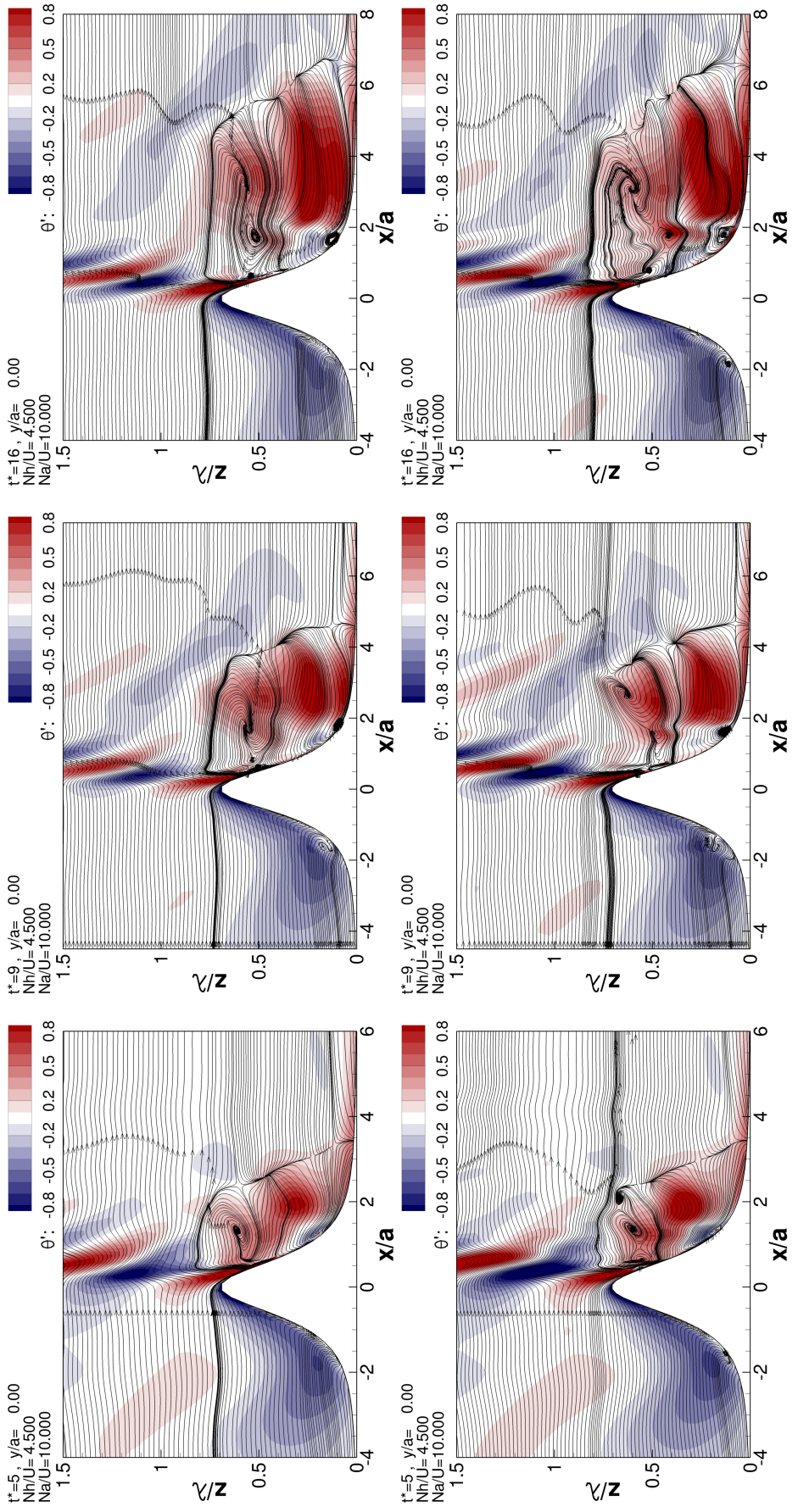

Figure 3.4: Results of inviscid flow simulations to verify grid dependence, for $h^* = 4.5$ and $a^* = 10$. The topmost figures refer to the $140 \times 80 \times 70$ grid. The bottommost figures refer to the most refined grid, with $192 \times 128 \times 70$ elements. The results shown are vertical slices of the $y = 0$ plane with streamlines and contours of the perturbation of potential temperature, for the dimensionless times of 5, 9 and 16.

and vortex formation. The simulations were run up to a dimensionless time t^* of 16 for the following grid sizes:

- $96 \times 64 \times 70$ with $\min(\Delta x) = 0.2\,a$ and $x/a \in [-10, 20]$,
- $140 \times 80 \times 70$ with $\min(\Delta x) = 0.16\,a$ and $x/a \in [-10, 25]$,
- $192 \times 128 \times 70$ with $\min(\Delta x) = 0.1\,a$ and $x/a \in [-10, 20]$.

Other characteristics are given in Table 3.2. The outlet boundary of the $140 \times 80 \times 70$ grid was placed further downstream than the other grids, as this was run for higher t^*, requiring an increased domain due to the wake formed.

Figure 3.3 shows the streamlines of the surface flow for the $140 \times 80 \times 70$ and $192 \times 128 \times 70$ grids, at the dimensionless times of 5, 9 and 16. These reveal the topological features of the surface vector field, namely the critical points where the velocity vector is zero, *i.e.*, saddle, nodes and focus. The comparison of the solutions for the $140 \times 80 \times 70$ and $192 \times 128 \times 70$ grids show that a truly grid independent solution was not obtained. As more control volumes are added more flow structures are produced. Some of these are highly dependent on time, moving and disappearing fast. However other structures are more steady and although their position changes, it does so slowly. These appear on all grids tested and can be used to compare how the solutions differ, by quantifying their position for a particular t^*. Although not being grid independent, the solutions may be equivalent in describing these steady features.

For $h^* \gg 1$ the flow is characterized by a saddle point upstream of the hill, S_u, usually followed by a node, N_u. If more critical points exist upstream, these will usually terminate with a node before the hilltop, N_{uf}. The first critical point after the hilltop is usually a saddle, S_{d1}. Downstream the flow is more complex with several structures being formed in the sides of the hill. However, there are two large vortices that end the wake, characterized by their spanwise distance, Δ. These lie in between two saddle points, S_{d*} and S_{df}, with this last ending the wake. The values for the position of these points are presented in Table 3.3, together with the integral of the surface drag (x component as defined in eq. (3.6)) and the minimum centreline streamwise velocity ($y = 0$), upstream and downstream. Additionally, contours of $\widehat{\theta}$ on the central cross-section are displayed in Figure 3.4, together with streamlines of the flow in that plane.

Most values agree with relative differences below 15%, with better results given by the $140 \times 80 \times 70$ grid. The largest discrepancy is found in the spanwise distance between the lee vortices, Δ, which is off by 64% and 26% for t^* of 9 and 16, respectively. For $t^* = 9$ this quantity was better estimated by the coarsest grid. Despite this, both the streamwise and spanwise size of the vortices are similar and differ less than the location of the focus points, as it can be observed in Figure 3.3. For $t^* = 16$ the most refined solution is clearly distorted, contrarily to the other grids which retain some symmetry due to numeric diffusion.

The same simulations were repeated for turbulent flow with surface friction. The locations of the critical points, flow topology near the surface and contours of $\widehat{\theta}$ are show in Table 3.4 and Figures 3.5 and 3.6. As for the inviscid case, the increase in grid refinement translates into an higher number of fast dissipating structures, particularly on the sides of the hill. The same steady features found in the inviscid case are present,

Table 3.4: Evaluation of grid dependence for simulations of turbulent flow with surface friction at a dimensionless mountain height of $Nh/U = 4.5$ and length of $Na/U = 10$. The height of the bottommost control volume is $0.01\,U/N$ and the boundary layer depth is $0.2\,U/N$.

Time (tU/a)	5			9			16		
$\min(\Delta x)$	$0.2\,a$	$0.16\,a$	$0.1\,a$	$0.2\,a$	$0.16\,a$	$0.1\,a$	$0.2\,a$	$0.16\,a$	$0.1\,a$
Grid	$96 \times 64 \times 70$	$140 \times 80 \times 70$	$192 \times 128 \times 70$	$96 \times 64 \times 70$	$140 \times 80 \times 70$	$192 \times 128 \times 70$	$96 \times 64 \times 70$	$140 \times 80 \times 70$	$192 \times 128 \times 70$
upstr. $\min(u)/U$	-0.18	-0.20	-0.23	-0.15	-0.17	-0.19	-0.14	-0.17	-0.20
position S_u (x/a)	-2.66	-2.65	-2.64	-2.95	-2.94	-2.94	-3.09	-3.12	-3.10
position N_u (x/a)	-1.56	-1.56	-1.52	-1.57	-1.57	-1.53	-1.44	-1.39	-1.38
position N_{uf} (x/a)	-0.25	-0.23	-0.24	-0.25	-0.25	-0.26	-0.26	-0.26	-0.26
downstr. $\min(u)/U$	-1.18	-1.22	-1.28	-1.17	-1.23	-1.28	-1.18	-1.24	-1.28
position S_{d1} (x/a)	0.45	0.50	0.44	0.46	0.52	0.43	0.47	0.51	0.43
position S_{d*} (x/a)	1.52	1.56	1.50	1.88	1.90	1.85	2.04	2.02	1.95
dist. lee vort. (Δ/a)	1.96	1.90	1.89	2.27	2.25	2.20	2.63	2.59	2.58
‡‡ position P_{df} (x/a)	3.88	3.85	3.86	5.35	5.30	5.24	7.26	7.24	7.26
¶ Lee topology shape	$N+2S$	$N+2S$	$S+2N+2S$	$S+2N+2S$	$N+4S+2N$	$N+4S+2N$	$N+2S$	$N+2S$	$N+2S$
N. saddles	10	9	20	15	19	27	16	13	29
N. nodes & focus	10	9	20	15	19	27	16	13	29
** Drag (D_x/D_{lin})	0.57	0.58	0.59	0.49	0.51	0.51	0.42	0.42	0.43

** The pressure drag is normalized by the one predicted by linear inviscid theory. The numeric value is the average over one dimensionless time unit $\Delta t^* = a/U$.

†† The lee vortices are characterized by more points than a pair of focus. The numeric value is the greatest distance between points in the spanwise direction.

‡‡ Instead of a single saddle point downstream of the vortex pair, there is a more complex topology. Position of last point near $y = 0$.

¶ Shape of topology downstream of the vortex pair. Class of point near $y = 0$ (S for saddle, N for node), followed by the class and number of remaining points.

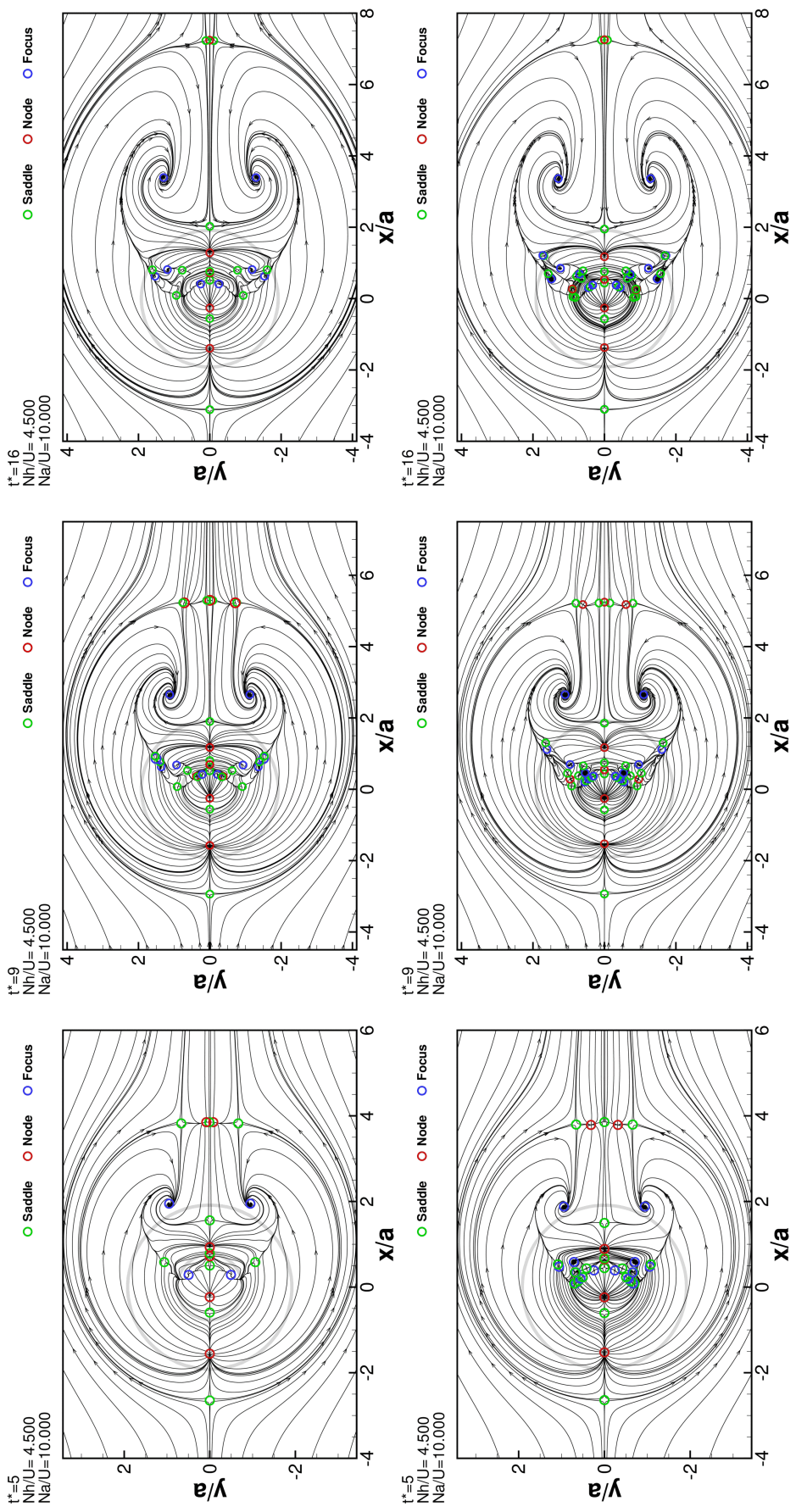

Figure 3.5: Results of turbulent flow simulations to verify grid dependence, for $h^* = 4.5$ and $a^* = 10$. The topmost figures refer to the $140 \times 80 \times 70$ grid. The bottommost figures refer to the most refined grid, with $192 \times 128 \times 70$ elements. The streamlines of the surface flow are shown for the dimensionless times of 5, 9 and 16. For further details, refer to the caption of Figure 3.3.

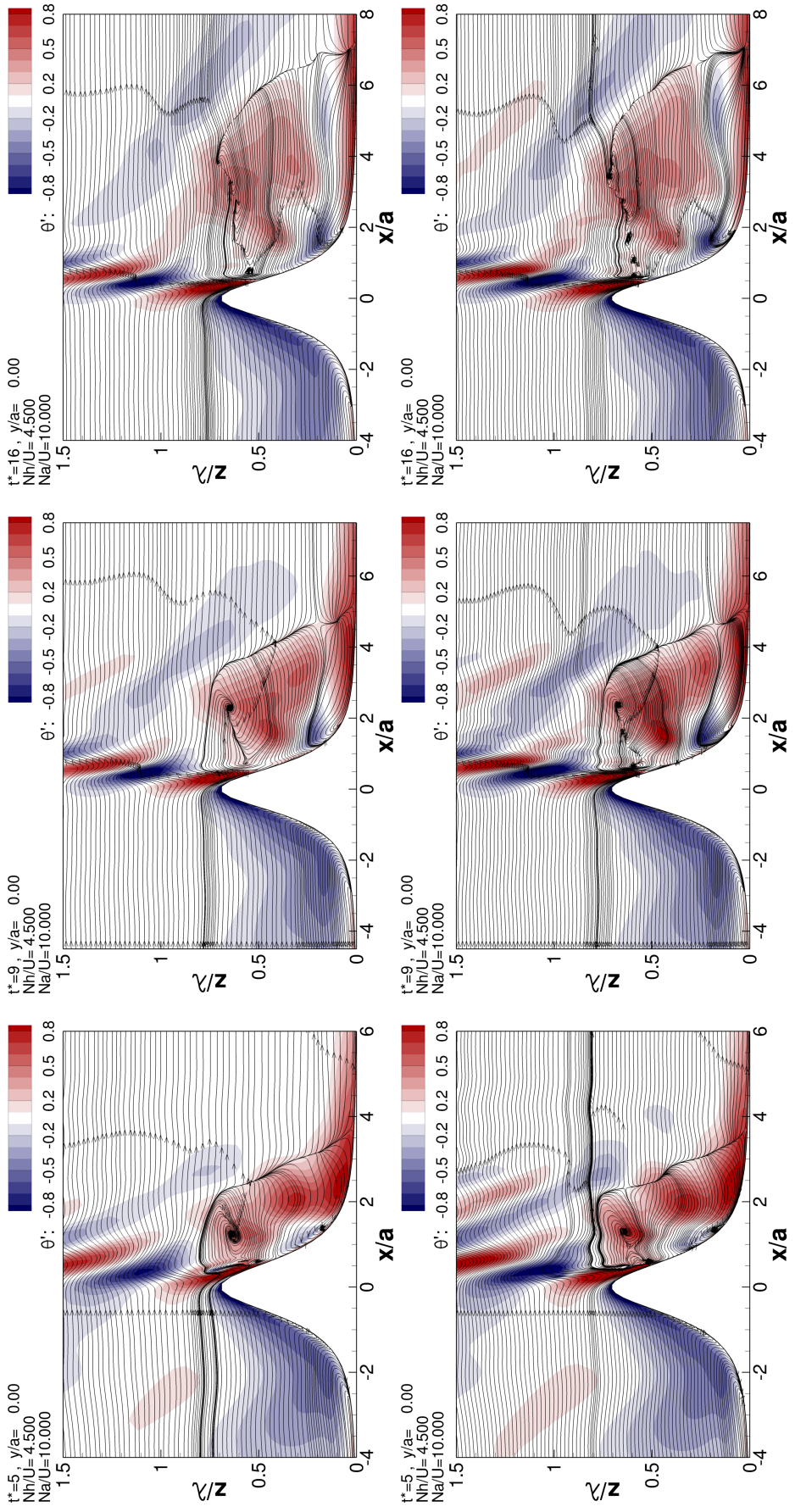

Figure 3.6: Results of turbulent flow simulations to verify grid dependence, for $h^* = 4.5$ and $a^* = 10$. The topmost figures refer to the $140 \times 80 \times 70$ grid. The bottommost figures refer to the most refined grid, with $192 \times 128 \times 70$ elements. The results shown are vertical slices of the $y = 0$ plane with streamlines and contours of the perturbation of potential temperature, for the dimensionless times of 5, 9 and 16.

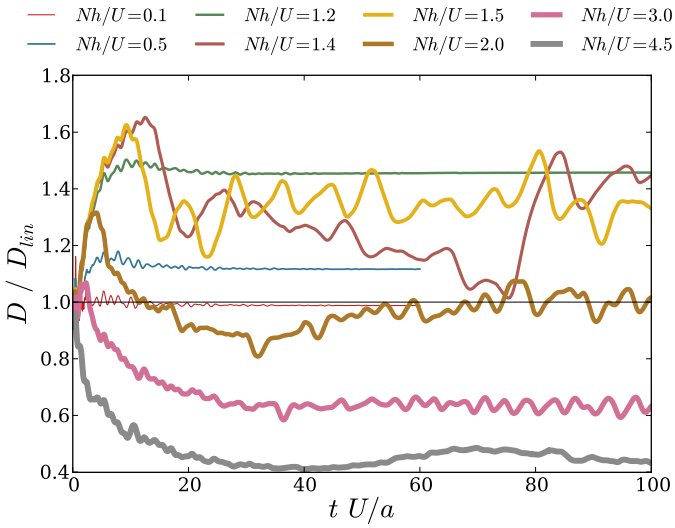

Figure 3.7: Inviscid flow longitudinal pressure drag for several values of $h*$, normalized by the linear theory prediction, eq. (3.5).

with the exception of the points that end the lee wake. In the inviscid case this was characterized by a saddle point, S_{df}, located after the vortex pair. For the turbulent flow simulations, the lee topology is more complex and more saddle-node pairs appear. This is found in Table 3.4, where the $140 \times 80 \times 70$ grid predicts better than the coarsest grid. The overall agreement is better than in the inviscid case, with relative differences below 5% in most values.

Comparing all solutions, the inviscid flow field is very different from the turbulent flow. The wake becomes much wider as the flow splits much more upstream than in the inviscid case. Also the distortions verified in the inviscid case are not present, due to the diffusion which endures the symmetry of the lee flow. Although the surface drag is nearly grid independent on both inviscid and turbulent cases, the last presents lower values.

3.3 Flow regimes observed in the inviscid simulations

Figure 3.7 shows the evolution of the pressure drag with time, for several simulations. The behaviour and patterns found in the time series are enough to reveal different regimes, showing the dependence of the flow on h^*:

1. For $h^* \ll 1$, value of the drag is close to the linear prediction given in eq. (3.5). As h^* increases the drag also increases, presenting small oscillations and converging to a constant value as time progresses ($t^* \sim 30$).

2. For $h^* \approx 1.4$ the amplitude of the waves over the mountain is such that these break. Hydraulic jumps and large structures are generated on the leeward side. For this breaking wave regime the drag does not converge, oscillating with a period defined by instants where the lee surface flow is blocked or not, related with the height at which the wave breaking occurs.

3. For $h^* > 2$ the flow lacks the energy to overcome the mountain, starting to split upstream and going around it. This effect is contrary to wave breaking as it lessens the wave amplitude, decreasing the drag. In this regime the leeward flow is characterized by a large wake with two vortices. The drag decreases fast during the first time-steps ($t^* < 10$) and may converge to a stationary value. The drag for $h^* = 4.5$ is shown as an example.

4. As a consequence of flow splitting and the high non-linear regime at $h^* > 2$, the vortices which compose the mountain wake may be released and advected in an asymmetrical way, known as vortex shedding. Unless the initial field for a simulation is set to promote flow asymmetries, this is observed only for high values of t^*. An example was the drag for $h^* \geq 3$ which was characterized first by flow splitting and afterwards by vortex shedding.

5. For values of h^* that lie in between the breaking wave and flow splitting regimes, such as $h^* = 2$, a chaotic pattern may emerge that does not converge to a constant value nor presents a well defined oscillation frequency. Flows in this regime share several characteristics pertaining to both breaking wave and flow splitting, being at some instances dominated by one of these effects.

3.3.1 Linear and quasi-linear regime

For values of $h^* \ll 1$ and $a^* > 2\pi$ the flow is described by the linear theory of Smith (1980). To verify how the code reproduces the linear regime, simulations were performed for h^* of 0.1, 0.5 and 0.8 at mountain lengths of $a^* = 10$.

For $h^* = 0.1$, the drag differs only by 1.2% from the linear prediction in eq. (3.5) (Figure 3.7). This difference is attributed to the finite dimensions of the domain and the grid discretization, including mismatches between the topography and the analytical function describing the surface, in eq. (3.1).

As h^* is increased to 0.5 the difference with D_{lin} rises to 12%. Nonetheless, the flow field shows a high agreement with the linear theory. Figure 3.8 shows the isentropic displacement, normalized by h, for four horizontal planes of constant zN/U: $\pi/8$, $\pi/4$, $\pi/2$ and π. The results were taken at $t^* = 60$, although the drag value becomes steady from $t^* > 20$ (Figure 3.7). When comparing with the linear theory (*cf.* Figure 1 in Smith, 1980, p. 352) the agreement is very good. It should be noted that in Smith (1980), the results are given in metre. When normalized by the respective mountain height ($h = 10\,\mathrm{m}$) the scale used to define the isolines becomes $[-0.4, -0.2, -0.1, -0.05, 0.05, 0.1, 0.2, 0.4]$, the same as in Figure 3.8.

Figure 3.9 shows the field of the pressure coefficient, C_p, together with a slice at the centre plane, $y = 0$. The simulation results of C_p (represented as filled contours) is in agreement with the linear theory prediction (represented as isolines), both qualitatively and quantitatively, apart from some discrepancies for $|C_p| < 0.05$.

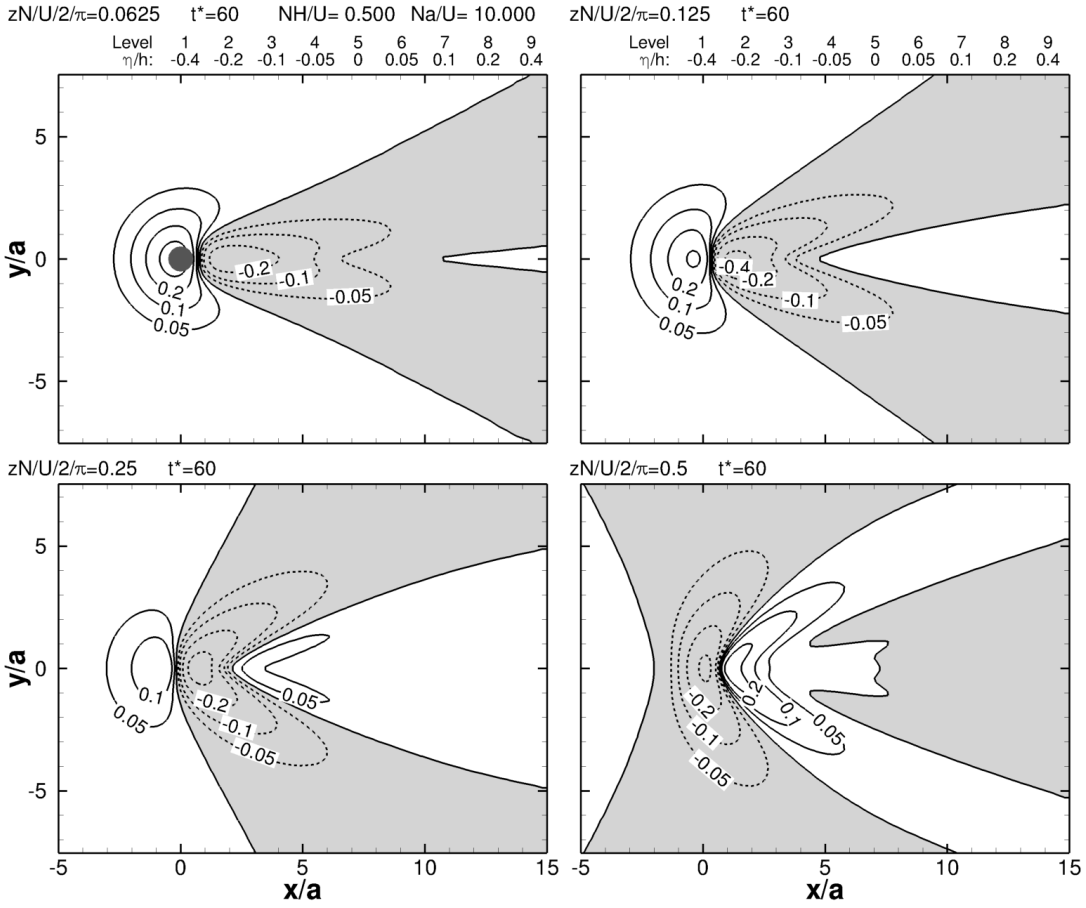

Figure 3.8: Isentropic displacement for $h^* = 0.5$ and $a^* = 10$, normalized by h.

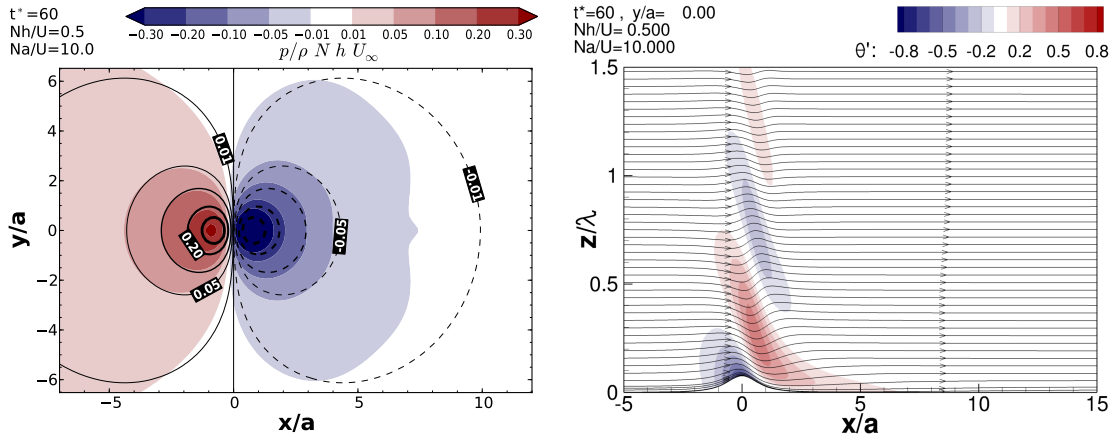

Figure 3.9: Results for $h^* = 0.5$ and $a^* = 10$. *Left*: contours of pressure coefficient field, defined as $C_p = \widehat{p}/\rho UNh$. The isolines respect to the C_p predicted by Smith (1980) linear theory. *Right*: the flow streamlines and perturbation of potential temperature at the centre $y = 0$ plane.

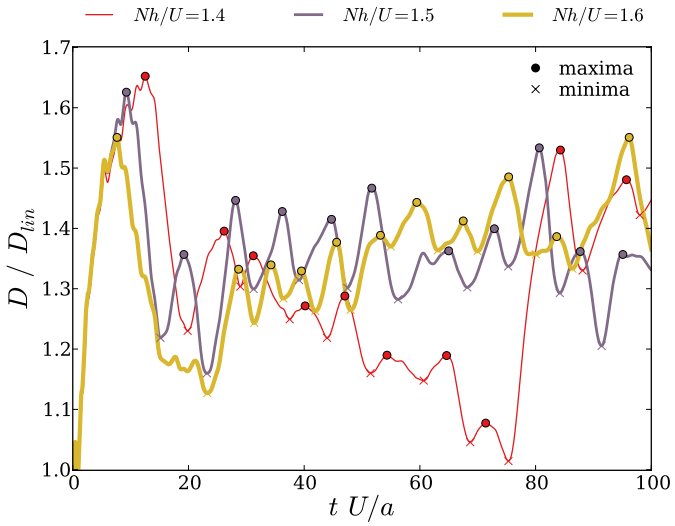

Figure 3.10: Normalized form drag for simulations with oscillatory drag, associated with breaking wave phenomena.

3.3.2 Breaking wave regime

For $h^* > 1$ the lee waves steepen, breaking if the amplitude is beyond a critical level. This non-linear phenomena is associated with high wave drag. Although the maximum drag produced by the simulations was obtained for $h^* = 1.4$, 1.5 and 1.6, a stationary value was impossible to reach as the drag presented severe oscillations. This is in agreement with the literature, *cf.* Smolarkiewicz and Rotunno (1989) and Miranda and James (1992). The evolution of the form drag with time is displayed in Figure 3.10. After the simulation start the drag, D^*, increases until it achieves a local maxima. The values of D^* at this point are the highest obtained for the simulated time span, around 1.6 times the drag predicted by linear theory, D_{lin}. Afterwards the drag decreases reaching a local minima, subsequently entering into an oscillating signal with a roughly constant period and amplitude. In Table 3.5 are gathered measures that characterize these drag oscillations: the maximum and minimum values of D^*, the slope of the local maxima and minima points, the average period of the oscillations and the main frequencies found in the power spectrum. This last was obtained by applying the discrete Fourier transform to the data, after detrending and zero padding.

For $h^* = 1.4$ there is the first maximum at $t^* = 12.5$, followed by several oscillations that show a trend with a decreasing slope (estimated as -6.5×10^{-3} drag units per time). However, for $t^* = 84.3$ this trend is broken by a maxima with $D^* = 1.53$. This suggests a low frequency that could not be determined by the discrete Fourier transform (due to the limited simulation time) with a period around $T^* = 70$. For $h^* = 1.5$ there is no discernible trend in the data, while for $h^* = 1.6$ there is a trend again but with a positive slope (around 2.6×10^{-3}). Also, the values of the first maximum decrease as h^* increases.

Figures 3.11 and 3.12 illustrate the flow patterns at consecutive local maximum and minimum occurrences, for h^* of 1.4 and 1.5. Focusing on the instants where D^* is maximum, the hydraulic jump is located at $x \approx 1.5\,a$, with a height of $0.3\,\lambda_z$. The

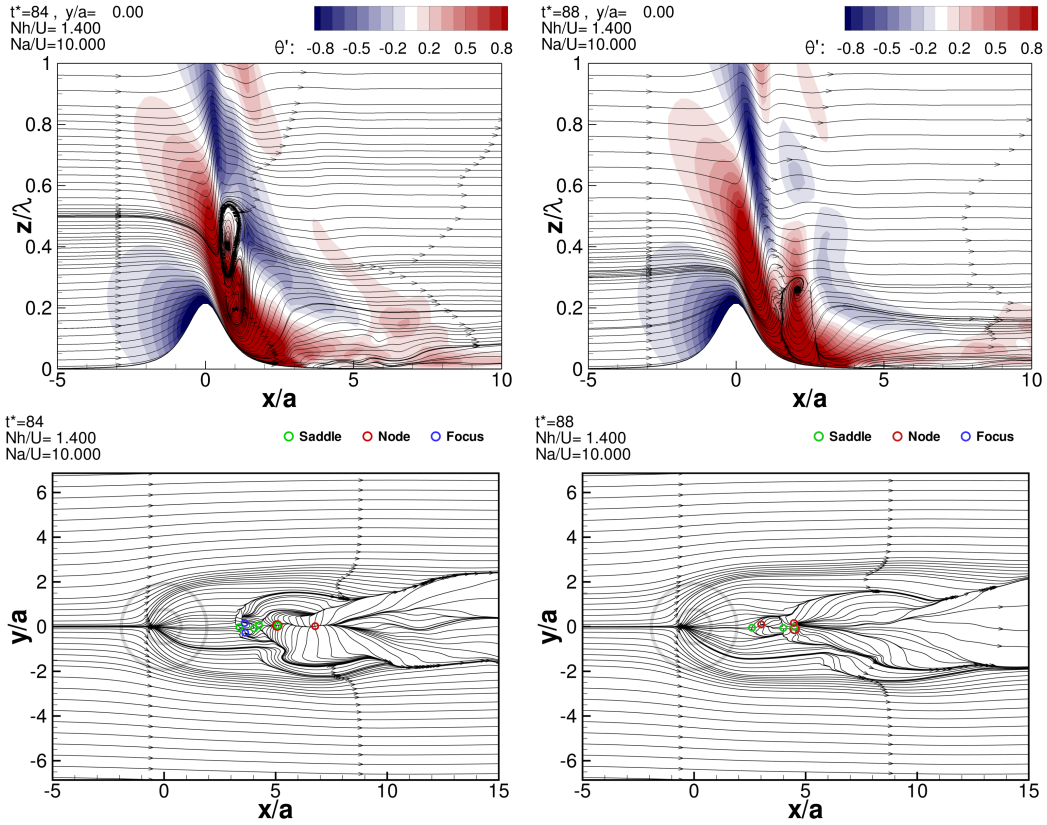

Figure 3.11: Results of breaking waves under inviscid flow for $h^* = 1.4$ and $a^* = 10$: streamlines and contour of the perturbation of potential temperature in the $y = 0$ vertical plane (*top*) and surface flow streamlines (*bottom*). The leftmost plots refer to a local maximum of the drag, the rightmost to a local minimum. For further details, refer to Fig. 3.3 and 3.4.

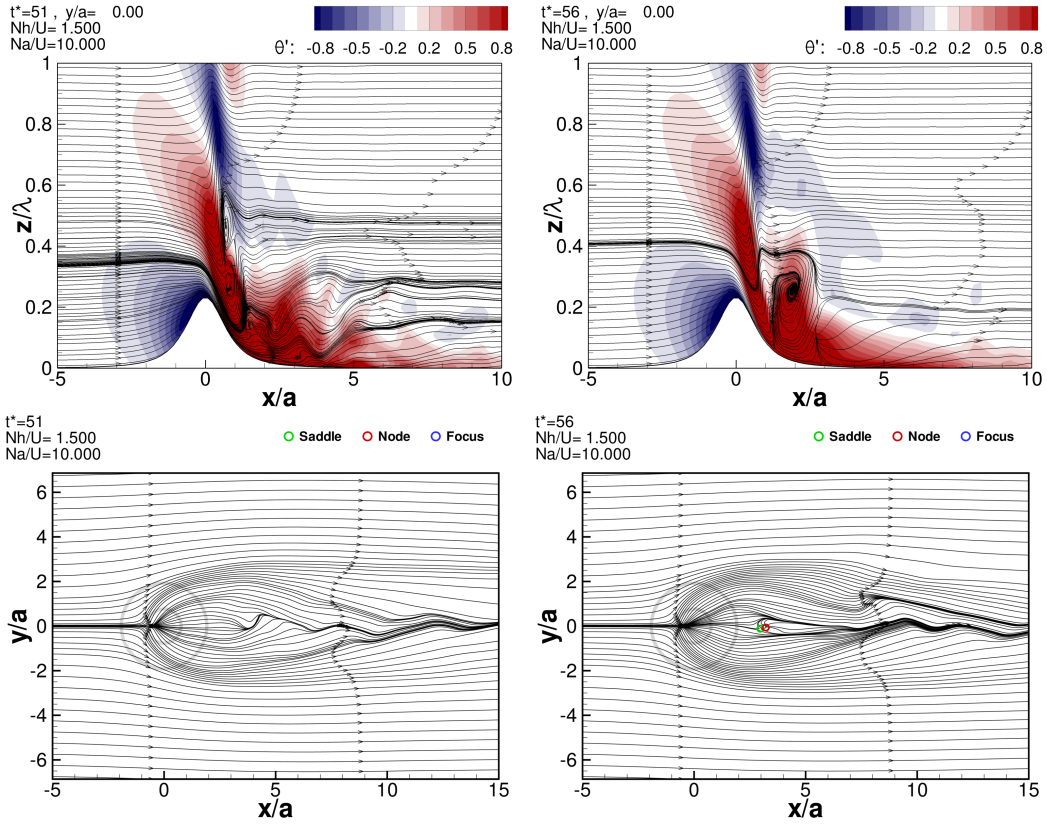

Figure 3.12: Same as Figure 3.11, for $h^* = 1.5$ and $a^* = 10$.

Table 3.5: Description of the frequency content found in the time evolution of the form drag under the breaking wave regime. The slope refers to the increase in drag of the local maxima and minima points, obtained through linear regression. The average period was estimated dividing the time span by the number of maxima and minima.

	Drag		Slope	Period	Power spectrum (relevant frequencies)		
h^*	max.	min.	$\Delta D^*/\Delta t^*$	avg(T^*)	Main peaks	Period T^*	Amplitude
1.4	1.65	1.01	-6.5×10^{-3}	8.4	1st	7.9	0.025
					2nd	16.3	0.024
					Long period	~ 70	~ 0.22
1.5	1.63	1.22	~ 0	8.5	1st	8.1	0.051
					2nd	16.6	0.039
					3rd	22.7	0.039
					4th	35.4	0.046
1.6	1.55	1.13	2.6×10^{-3}	6.8	1st	5.6	0.022
					2nd	7.3	0.021
					3rd	21.5	0.025

breaking wave region is contiguous to the hilltop, extending to a height of $z = 0.6\,\lambda_z$. It contains two large rotating structures, the lower with a counter-clockwise motion. Underneath these structures lies unblocked flow where the downslope speed reaches $2\,U$. This dynamic pressure implies a low static pressure which favours the drag integral in eq. (3.6), as this happens on the lee side. These two large structures posteriorly merge together and are advected downstream, following the direction of the downslope flow. The resulting structure is impinged towards the wall obstructing the surface flow, hence increasing the pressure as the stagnation occurs. Such event results in a decrease of the drag, corresponding to the local minima of D^*. As shown in Figure 3.11, there is a saddle point in the lee wake near $x \approx -2\,a$ when D^* is minimum (surface streamlines), corresponding to a large lee vortex blocking the surface flow (vertical cross-section streamlines). Later, as this structure is advected farther downstream, the downslope flow becomes unblocked. As the downward flow accelerates, the amplitude of the waves over the hill increases until these break and the process repeats again. At the local minima events, although the streamlines after the hilltop are almost vertical, the height of the jump is less than $0.2\,\lambda_z$.

These results are comparable to the ones of Smolarkiewicz and Rotunno (1989, Figures 1(b) and 2(b), §3, pp. 1157–9) for $h^* = 1.515$ and $a^* = 12.626$. Although the streamlines at the central cross-section do not show the two structures above the hilltop, the surface flow is in agreement, *i.e.*, there is no upstream flow splitting and no vortex pair in the lee wake was found. In their work, this vortex pair is found only for $h^* > 1.8$, while in the present results flow splitting starts for $h^* = 2$ and the lee vortex pair exists only for $h^* \geq 3$.

3.3.3 Splitting flow regime

At higher dimensionless mountain heights, $h^* > 2$, the flow splits upstream as it lacks energy to overcome the mountain. This reduces both the wave drag and the vertical displacement of the streamlines above the mountain. The flow for $h^* = 4.5$ is of particular interest as it is documented in the works of Smolarkiewicz and Rotunno (1989) (SR), Miranda and James (1992) (MJ), Ólafsson and Bougeault (1996) (OB) and Castro (1997). These provide information regarding the location of saddle and nodal points for the surface flow.

To compare with the simulations of SR and OB, the mountain length was set to $a^* = 38$ (grids in group III from Table 3.2). The vertical discretization mimics the height of the bottommost control volumes in SR, $h/12 = 187.5$m. The comparisons were made using the flow fields at the dimensionless times of 9 and 16. The results are shown in Figure 3.13. To characterize the flow topology, the following quantities were computed: (i) upstream and downstream minimum velocity in the $y = 0$ plane; (ii) position of the first saddle and nodal point upstream of the mountain, S_u and N_u; (iii) position of the first saddle point on the lee side, S_{d1}; (iv) position of the last saddle point delimiting the downstream wake, S_{df}; (v) spanwise distance of the lee vortex pair centres. These quantities are shown in Table 3.6.

The agreement is good both qualitatively and quantitatively. When comparing the quantities in Table 3.6, the present results fall within the scatter shown by the several reference values. The main differences are in the upstream points, S_u and N_u, which are closer to the hilltop. S_u is located 25% closer than SR and 11% than Castro, with similar numbers for N_u. Both minimum velocities upstream and downstream lie in between SR and OB results. The downstream points agree with SR and Castro, whereas OB returns higher values for S_{d1}. The value with the best accord by all results is distance between the lee vortices, suggesting a good prediction of the wake width. The increase of S_{df} in time results in a larger wake, as expected. For $t^* = 16$ the end of the wake was composed of a set of a nodal point flanked by two saddles, different from the termination with a single saddle. This set of points started at $t^* = 11$ and persisted until the simulation was terminated, at $t^* = 20$.

MJ published numerical results for $h^* = 4.56$ and $a^* = 11.4$, which were compared with results for $h^* = 4.5$ and $a^* = 10$ in Castro. Simulations were made to compare with these results (Table 3.2, group III grids), where the height of the bottommost elements was set to $0.06\,h = 135$m, The results are displayed in Figure 3.14. In Table 3.7 are shown the locations of saddle and nodal points for the surface flow, with the same information as in Table 3.6. Although S_u is consistent with MJ and Castro, both N_u and S_{d1} are closer to the hilltop by 20% and 50% respectively. The distance between the vortices is also closer than in the reference values, however the end of the wake is well predicted. Other simulations were made with different parameters (not included in the text), showing that the position of the lee vortex centres are sensitive to the mesh resolution and simulation time. These may not be representative of the wake width, which was much more dependent on the position of S_{df}. Similar to the results for $h^* = 38$, for $t^* > 9$ the wake ends with a node flanked by two saddles, later becoming a set of 3 saddles and 2 nodes when $t^* > 13$. For coarser simulations with $\min(\Delta x) = 0.2\,a$, this only happens for $t^* > 11$.

Table 3.6: Results of inviscid flow at a dimensionless mountain height of $h^* = 4.5$ and length of $a^* = 38$. Reference values from Smolarkiewicz and Rotunno (1989) (SR), Ólafsson and Bougeault (1996) (OB) and Castro (1997).

	SR	OB		Castro		present results	
Nh/U	4.54(54)	4.545		4.5		4.5	
Na/U	37.87(87)	40		27		38	
Time (tU/a)	9	8.1	16.2	9	16	9	16
upstr. $\min(u)/U$	-0.02	-0.06	-0.08	-0.02	-0.02	-0.05	-0.07
position S_u (x/a)	-1.9	-2.3	-1.9	-1.6	-1.6	-1.42	-1.51
position N_u (x/a)	-1.1	-1.4	-1.4	-1.0	-1.0	-0.87	-0.83
downstr. $\min(u)/U$	-1.45	-1.12	-0.73	-	-	-1.25	-1.30
position S_{d1} (x/a)	0.4	0.7	0.7	0.3	0.4	[†] 0.41	0.40
dist. lee vort. (Δ/a)	2.2	2.1	2.1	2.0	2.1	1.95	2.16
position S_{df} (x/a)	4.5	5.0	6.3	5.0	7.0	4.82	[‡] 6.94

[†] The first critical point appearing in the lee side is a node with two saddles (at the north and south of the node), instead of a single saddle. Position of the nodal point.
[‡] Set of 2 saddles and 1 node instead of 1 final saddle. The numeric value is the position of the node.

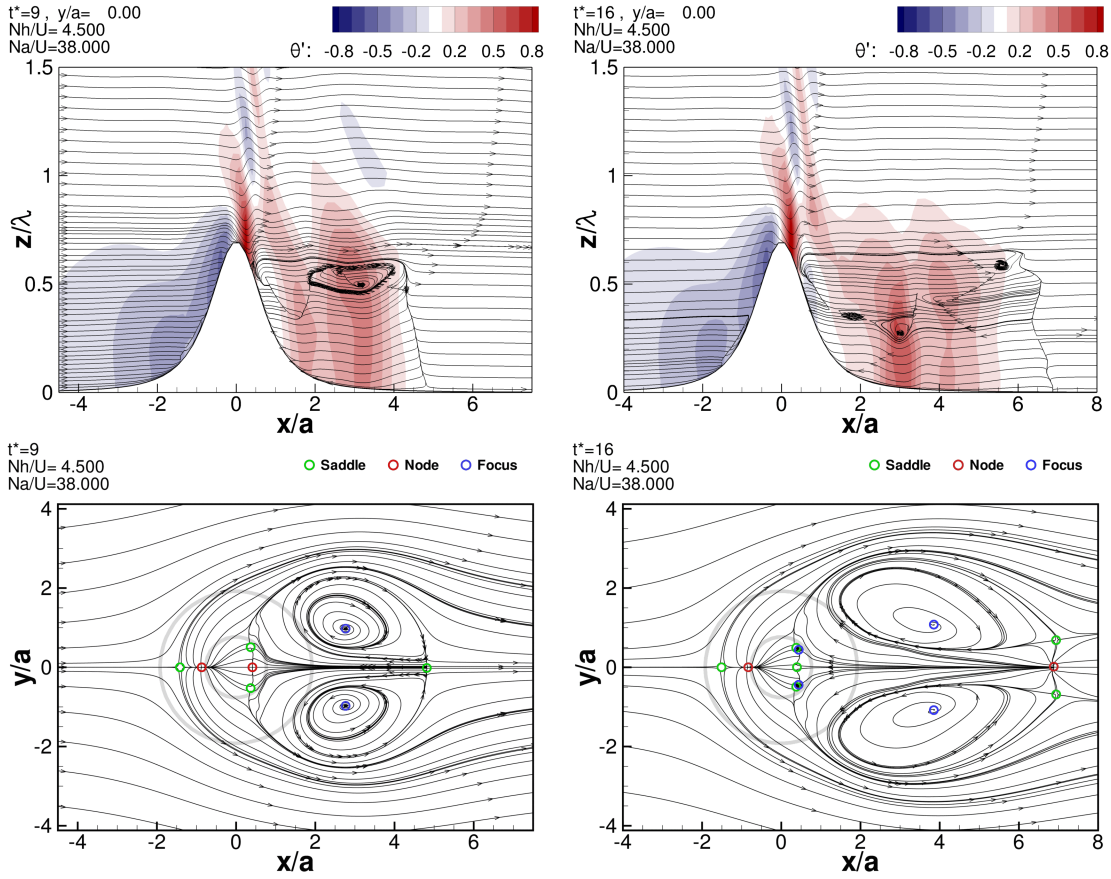

Figure 3.13: Results of inviscid flow for $h^* = 4.5$ and $a^* = 38$, at t^* of 9 and 16: streamlines and contour of the perturbation of potential temperature in the $y = 0$ vertical plane (*top*) and surface flow streamlines (*bottom*). For further details, refer to Fig. 3.3 and 3.4.

Table 3.7: Results of inviscid flow at a dimensionless mountain height of $h^* = 4.5$ and length of $a^* = 10$. Reference values from Miranda and James (1992) (MJ) and Castro (1997).

	MJ	Castro		present results	
Nh/U	4.558	4.5		4.5	
Na/U	11.4	10		10	
Time (tU/a)	5.2	5	9	5	9
position S_u (x/a)	−2.0	−1.9	−2.0	−2.03	−2.36
position N_u (x/a)	−0.7	−0.8	−0.8	−0.54	−0.55
position S_{d1} (x/a)	0.7	0.5	0.5	0.36	0.46
dist. lee vort. (Δ/a)	2.0	2.0	2.0	1.47	1.82
position S_{df} (x/a)	3.5	3.4	5.0	3.48	‡ 4.85

‡ Set of 2 saddles and 1 node instead of one final saddle. The numeric value is the position of the node.

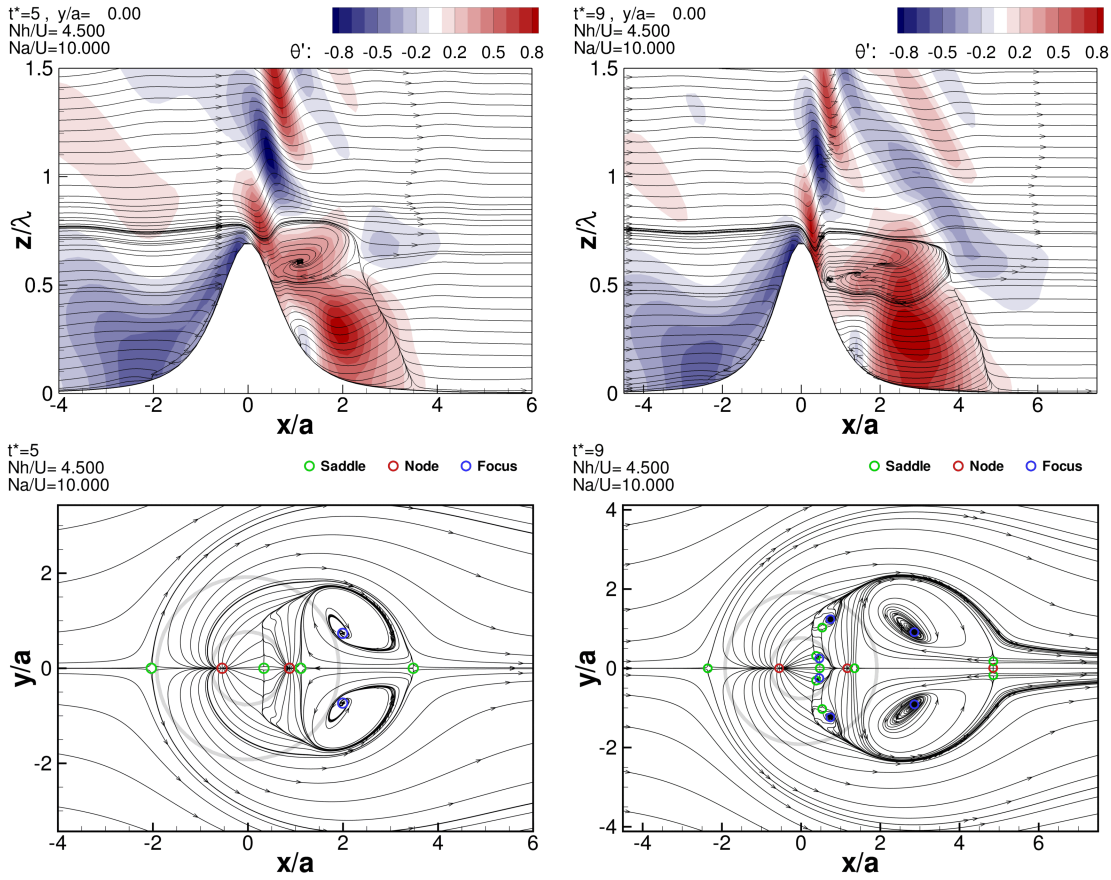

Figure 3.14: Results of inviscid flow for $h^* = 4.5$ and $a^* = 10$, at t^* of 5 and 9: streamlines and contour of the perturbation of potential temperature in the $y = 0$ vertical plane (*top*) and surface flow streamlines (*bottom*). For further details, refer to Fig. 3.3 and 3.4.

In all simulations the number of saddle points equalled the nodes, including focus and vortex centres. This is in agreement with the rules dictated by Hunt *et al.* (1978) for this kind of obstacle.

Influence of the height of bottommost control volumes

To compare the inviscid and turbulent flow simulations, the same computational grid was used. The vertical mesh was changed to match the grid used for the simulations considering turbulence. Due to the boundary-layer these required a lower height of the elements near the ground, set-up to $0.01\,U/N = 5\,\mathrm{m}$. This refinement yielded significant differences for the inviscid results, when compared to the results in Figure 3.14. In Table 3.8 are shown the values of critical points for t^* of 5, 9 and 16. Figure 3.15 shows the streamlines of the surface flow at $t^* = 9$, for different heights of the bottommost control volumes.

The flow topology is remarkably different. There are more critical points near the $y = 0$ plane for the $\min(\Delta z) = 5\,\mathrm{m}$ solution. Additionally, there is a lack of saddle-focus pairs on the sides of the hill. The position of the upstream points is much closer to the hilltop for the vertically refined mesh, while S_{d1} is further downstream. Although differences appear in the spanwise distance of the lee vortex centres, from the figures one concludes the width of the wake does not change drastically, being $\approx 4\,a$. Likewise, the end of the wake remains almost unchanged.

Flow field for large t^*

For a large simulation time the symmetry in the leeward flow is lost. These asymmetries eventually develop into vortex shedding and the lee wake is characterized by periodic phenomena, as shown in Figure 3.16 for $h^* = 3$ and $h^* = 4.5$. For both cases the period of the vortex shedding (inverse of the Strouhal number) was estimated around $12 \sim 15$ dimensionless time units, starting at $t^* > 35$.

3.4 Simulations of turbulent flow for $a^* = 10$

In several numerical investigations (Miranda and James (1992), Schär and Durran (1997), Bauer *et al.* (2000)) turbulence was considered but with a free-slip condition at the wall. Richard *et al.* (1989) simulated the 2D flow over a ideal hill shape with turbulence and surface friction, initializing their model using data from atmospheric soundings. They concluded that the inclusion of surface friction decreased both the surface pressure drag and the velocity magnitude in the lee, resulting in more realistic values. Ólafsson and Bougeault (1997) simulated the flow over elliptical and axisymmetric mountain shapes for a free-slip wall, with and without rotation due to Coriolis forces. These were compared with simulations under no-slip conditions but with rotation, having not isolated the effect of surface-friction and a boundary-layer alone. They concluded that the inclusion of surface-friction resulted in a reduction of the wave amplitude and complete

Table 3.8: Influence of the height of bottommost elements, $\min(\Delta z)$, on the surface topology for inviscid flow with $h^* = 4.5$ and $a^* = 10$.

Time ($t\,U/a$)	5		9		16	
$\min(\Delta z)$	$0.06\,h$	$0.01\,\frac{U}{N}$	$0.06\,h$	$0.01\,\frac{U}{N}$	$0.06\,h$	$0.01\,\frac{U}{N}$
position S_u (x/a)	-2.03	-0.98	-2.36	-1.37	-2.57	-1.72
position N_{uf} (x/a)	-0.54	-0.19	-0.55	-0.20	-0.57	-0.22
position S_{d1} (x/a)	0.36	0.66	0.46	0.56	0.46	1.89
dist. lee vort. (Δ/a)	1.47	1.79	1.82	2.58	2.34	2.85
position S_{df} (x/a)	3.48	3.43	‡ 4.85	4.53	§ 6.80	6.46

‡ Set of 2 saddles and 1 node instead of one final saddle. The numeric value is the position of the node.
§ Set of 3 saddles and 2 nodes instead of one final saddle. The numeric value is the position of the saddle near $y = 0$.

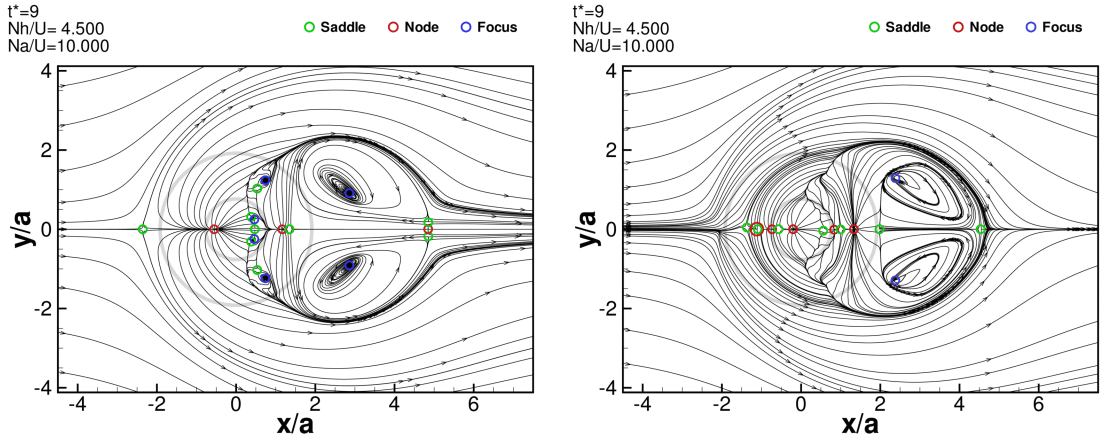

Figure 3.15: Influence of the height of bottommost elements, $\min(\Delta z)$, on the surface flow topology. The figures show the inviscid surface flow streamlines for $h^* = 4.5$ and $a^* = 10$ at $t^* = 9$, with $\min(\Delta z) = 0.06\,h = 135\,\mathrm{m}$ (*left*) and $\min(\Delta z) = 0.01\,U/N = 5\,\mathrm{m}$ (*right*). For further details, refer to Fig. 3.3.

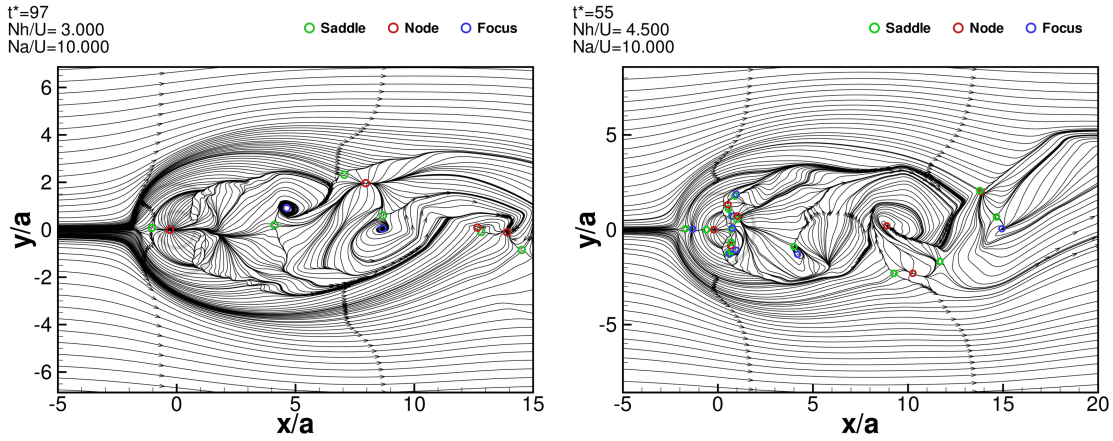

Figure 3.16: Vortex shedding at large t^* for inviscid flow with $h^* = 3$ (*left*) and $h^* = 4.5$ (*right*), both with $a^* = 10$. The figures show the surface flow streamlines. For further details, refer to Fig. 3.3.

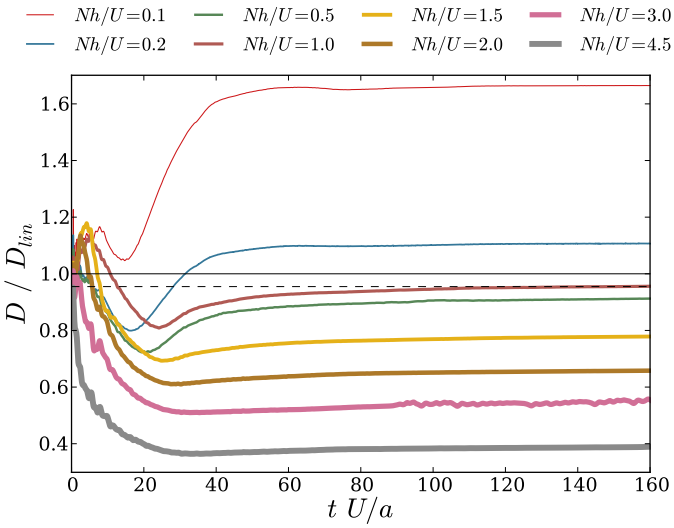

Figure 3.17: Turbulent simulations form drag for several values of $h*$. The drag was normalized by the inviscid linear theory prediction, eq. (3.5). The dashed line refers to the step-function model of Smith (see Table 3.9).

Table 3.9: Application of the linear theory of Smith (2007).

Boundary-layer parameters			Step-function parameters			Pressure drag		
U	=	$5\,\mathrm{m\,s^{-1}}$	H_b	=	50.5 m	$\Delta x/a$	=	0.01
δ	=	$0.2\,U/N$	U_b	=	$3.70\,\mathrm{m\,s^{-1}}$	$\Delta y/a$	=	0.01
u_*	=	$0.263\,\mathrm{m\,s^{-1}}$	C_b	=	$7.40\times10^{-4}\,\mathrm{s^{-1}}$	x/a	$\in$	$[-25, 25]$
δ_t	=	13.1 m	C_t	=	$2.11\times10^{-3}\,\mathrm{s^{-1}}$	y/a	$\in$	$[-25, 25]$
Θ_t	=	9.71 m	$U_b/a\,C_b$	=	1.35	D_{trb}/D_{lin}	=	0.9548

suppression of wave breaking. Jiang *et al.* (2006) investigated how a boundary-layer acts as an dissipation layer for trapped lee waves using 2D ridges.

Albeit the literature on mountain waves is extensive, there is not much work that focus on the effect of surface friction without rotation on vertically propagating waves, induced by 3D idealized broad mountains. In this section are shown results where $a^* = 10$, matching the numerical work in §3.3. The existence of a boundary-layer implies a new parameter based on its height, δ, set to the constant value of $0.2\,U/N = 100\,\mathrm{m}$ for all simulations. A constant value was preferred over a ratio of h^* because for low heights the value of δ would become unrealistic. It is also a value close to the empirical height of the nocturnal boundary-layer.

For a prediction of the pressure drag, the model of Smith (2007) was used. After computing the step-function parameters for the boundary-layer used in these simulations, eq. 3.14 was used to obtain the surface pressure field and the drag, D_{trb}. This value is independent of the mountain height h^* when is normalized with the drag predicted by inviscid linear theory, eq. (3.5). Table 3.9 summarizes the values obtained for the Agnesi mountain shape, eq. (3.1). The analytic prediction of the boundary-layer effect on the drag is a reduction of $\sim 5\%$ on the value given by inviscid theory.

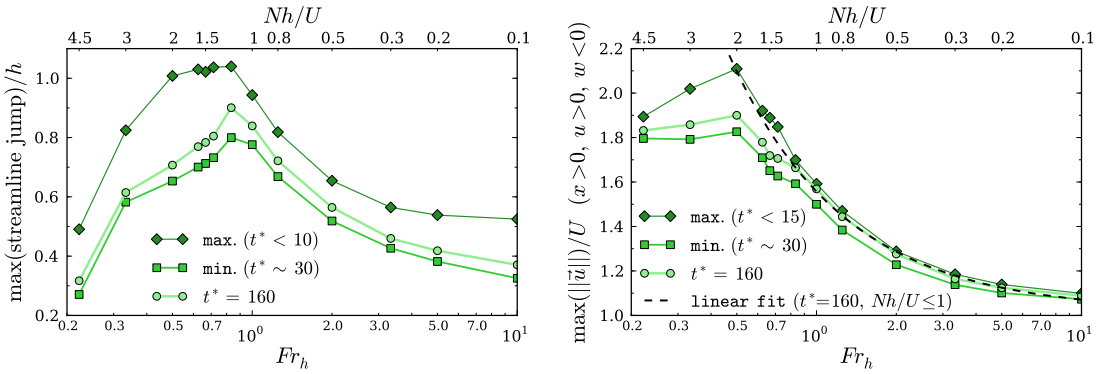

(a) Maximum streamline jump.

(b) Leeward maximum downslope speed.

Figure 3.18: Maximum jump in the streamlines over the hill, in $y = 0$ plane (a) and leeward maximum downslope speed (b). The values are shown as function of $h*$ and for several values of t^*: at the simulation start, when the drag is minimum, and at the end (convergence).

3.4.1 Flow features and their evolution with time

Figure 3.17 shows the pressure drag for turbulent flow, as function of time and h^* The evolution of the drag is much different from the inviscid results (Figure 3.7). The most striking is the difference between the drag for $h* < 0.2$ and the respective analytical predictions.

The same characteristics are found in all simulations. First, there is an increase until $t^* \sim 5$ where the maximum drag is reached. This state corresponds to the highest wave amplitude. Although hydraulic jumps are present for $h^* \geq 1.2$, wave breaking was found only for $h^* \geq 3$. Afterwards, the drag decreases, reaching its minimum value when t^* is $20 \sim 30$. This minimum corresponds to the instant when the wake achieves its highest width, remaining approximately the same throughout onwards. Throughout the remainder of the simulation the drag converges to a steady value. Separation at the leeward side exists for $h^* \geq 1.2$, while flow splitting is present only for $h^* \geq 2$. Another main difference is the absence of oscillatory solutions, as opposed to the inviscid case in §3.3.2.

Figure 3.18a shows the maximum jump found in the streamlines over the hilltop, representative of the amplitude of the waves. This quantity was defined as the highest upward deflection undergone by a streamline, after its lowest value on the leeward side. The trend is related to the evolution of the drag and is similar for all h^*: (i) at the start of the simulation the deflection has its maximum values, (ii) the jump becomes minimum at a t^* related with the lowest drag, and (iii) for large t^* the values converge to an intermediate value, albeit closer to the minimum values. The same evolution is seen in the magnitude of the downslope winds at the lee side, shown at Figure 3.18b. The location of the maximum downslope winds was always found close to the hilltop and the central cross-section. For $h^* \in [1, 1.6]$ the displacement of the jump is higher than for $h^* \geq 2$. Additionally, the maximum downslope wind curves show an trend for $h^* < 2$ where the values are increasing proportionally with h^*, being destroyed for $h^* > 2$. Both of these behaviours are indicators that flow splitting develops for $h^* \geq 2$, as this is the mechanism responsible for the damping of wave amplitude.

3.4.2 Attached flow and small mountain heights

For $h^* \leq 1$ the flow remains attached to the hill in the leeward side and no stagnant region was found, *e.g.*, Figures 3.19 and 3.20 for $h^* = 0.5$. Although the streamlines at the central cross-section (Figure 3.20) and the surface flow (not shown) are similar to their inviscid counterpart, the flow differs from the results in §3.3.1: the displacement of isentropic surfaces (Figure 3.19) only bear resemblance to the inviscid one for $z \geq 0.25\,\lambda_z$. The height of the first surface, $z = 1/16\,\lambda_z$, is twice the δ, piercing it only near the hilltop.

The pressure at the surface in Figure 3.20 shows a clear pressure gradient of -0.04 units of dimensionless drag per mountain length, contrarily to the inviscid results (Figure 3.9). Because of surface friction, an energy loss is introduced under the form of pressure head. Without tangential stresses at the top boundary, Coriolis forces or any other counteracting mechanism, the simulation evolves into a channel flow. This explains the differences of the isentropic displacement and drag values in Figure 3.17. For very low values of h^*, the pressure gradient is much stronger than the perturbation imposed by the mountain on the flow, resulting in the increased drag seen for $h^* = 0.1$, near 1.7 times $D_{lin,x}$. This effect is less noticeable for $h^* = 0.3$ and onwards. The drag value is lower than the inviscid counterpart, as surface friction decreases the waves amplitude.

The vertical profiles of $\overline{u}$ are displayed in Figures 3.21a and 3.21c for inviscid and turbulent flow. In these the inlet boundary-layer height is located at $z = (10\,\pi)^{-1}\,\lambda_z$. For $z > 0.2\,\lambda_z$ the velocity profiles match, with no noticeable differences found. Below this height the boundary-layer remains superficial up to $x < a$. At the hilltop, the speed-up is ~ 0.5 for both cases. The main differences start at $x = a$, where due to the lack of a boundary-layer the inviscid maximum velocity is $\sim 15\%$ higher. Although the flow remains attached, there is a velocity deficit on the lee side, deeper than in the upstream profiles, which propagates to the remainder of the computational domain.

3.4.3 Flow with leeward separation

For $h^* \in [1.2, 1.6]$ the flow is characterized by separation and a wake forming downstream. Due to its slow growth with time, the simulations of turbulent flow required much more time to stabilize than the inviscid ones, around $\Delta t^* = 100$. As the results are similar, only the flow field for $h^* = 1.5$ is shown (Figure 3.22). The simulation start corresponds to the highest drag. Flow separation is already present although with a small wake constituted by a saddle point, a set of points terminating the wake with a reattachment saddle at the centre line and a vortex pair in between. For higher $t*$ the topology changes such that this vortex pair dissipates and the wake is composed solely by a separation saddle and a reattachment node.

The position of these points as function of h^* is shown in Figure 3.24, together with the wake width. The wake increases with h^*, both in is width and length, verified by the shift downstream of the reattachment point, N_{df}. The separation point, S_{d1}, shows a decreasing trend however, moving closer to the hilltop except for $h^* = 2$

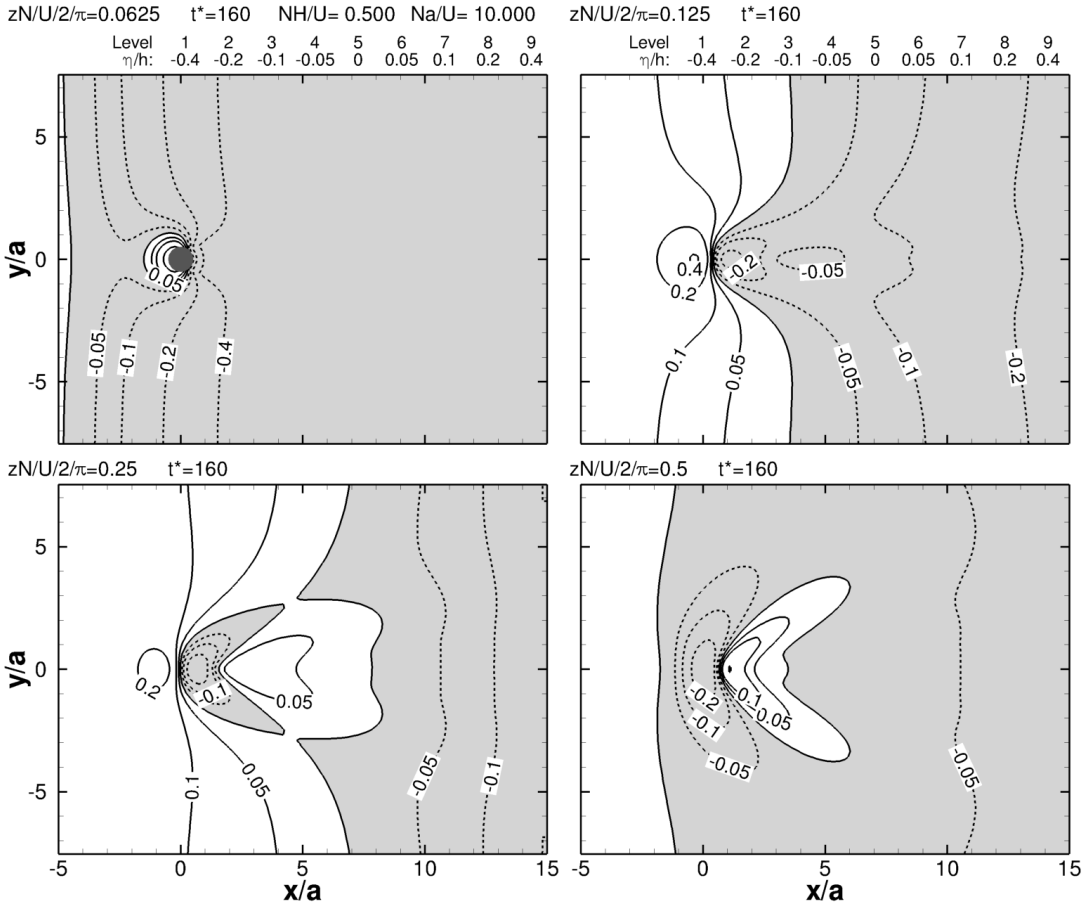

Figure 3.19: Isentropic displacement in turbulent flow for $h^* = 0.5$ and $a^* = 10$, normalized by h.

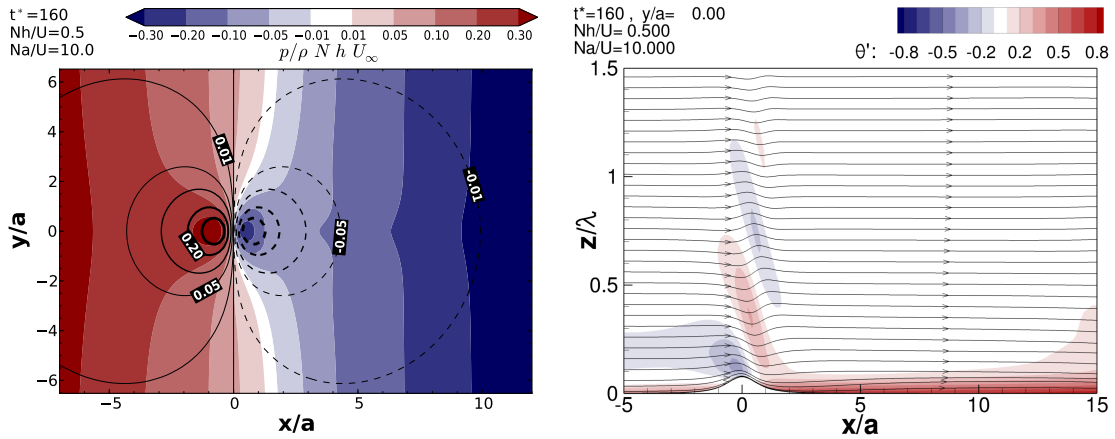

Figure 3.20: Results of turbulent flow for $h^* = 0.5$ and $a^* = 10$. For further details, refer to Figure 3.9.

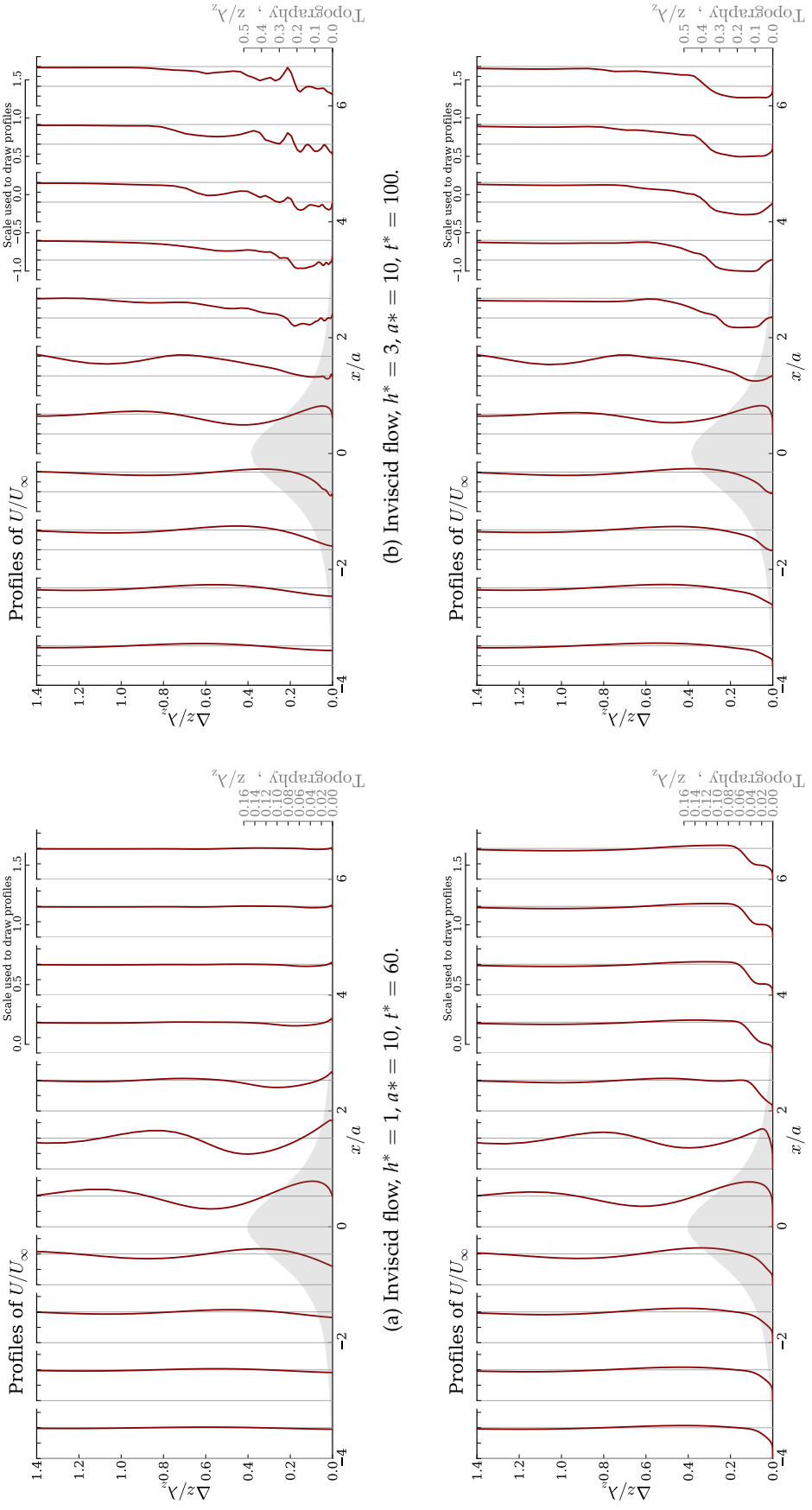

(a) Inviscid flow, $h^* = 1, a* = 10, t^* = 60$.

(b) Inviscid flow, $h^* = 3, a* = 10, t^* = 100$.

(c) Turbulent flow, $h^* = 1, a* = 10, t^* = 160$.

(d) Turbulent flow, $h^* = 3, a* = 10, t^* = 160$.

Figure 3.21: Vertical profiles of the streamwise velocity along the centre plane ($y = 0$).

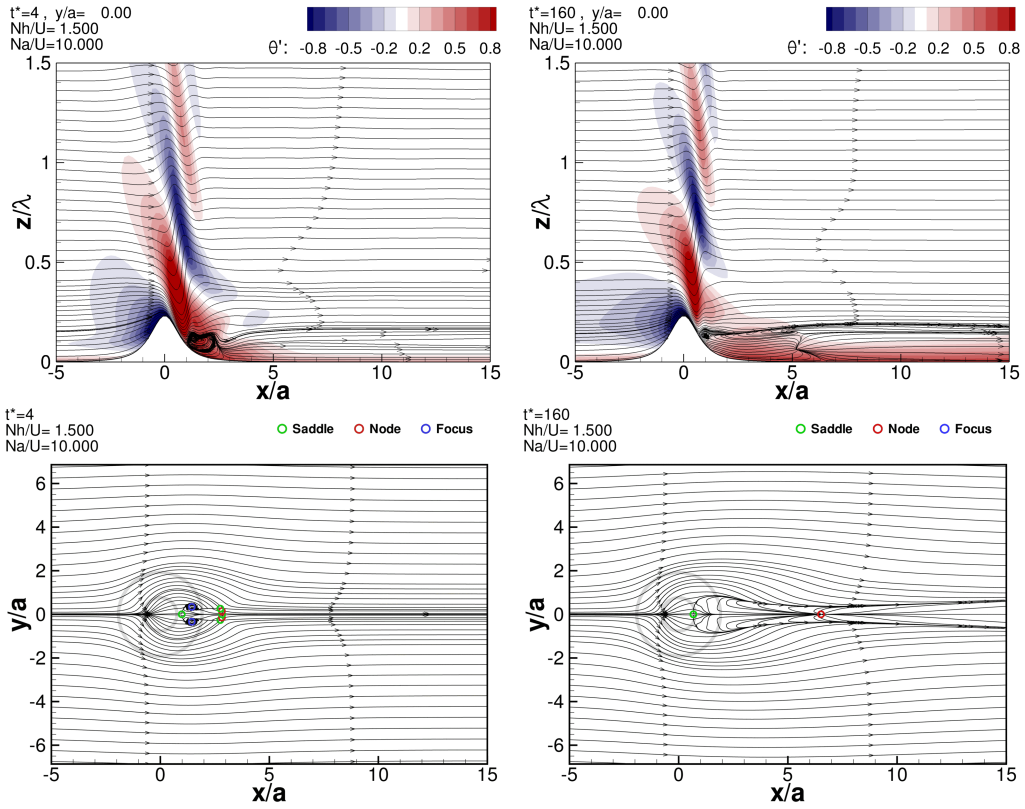

Figure 3.22: Results of turbulent flow for $h^* = 1.5$ and $a^* = 10$, at t^* of 4 and 160, respectively the time of the local maximum and the simulation end, when it may be considered that the simulation has converged. For further details, refer to Fig. 3.11.

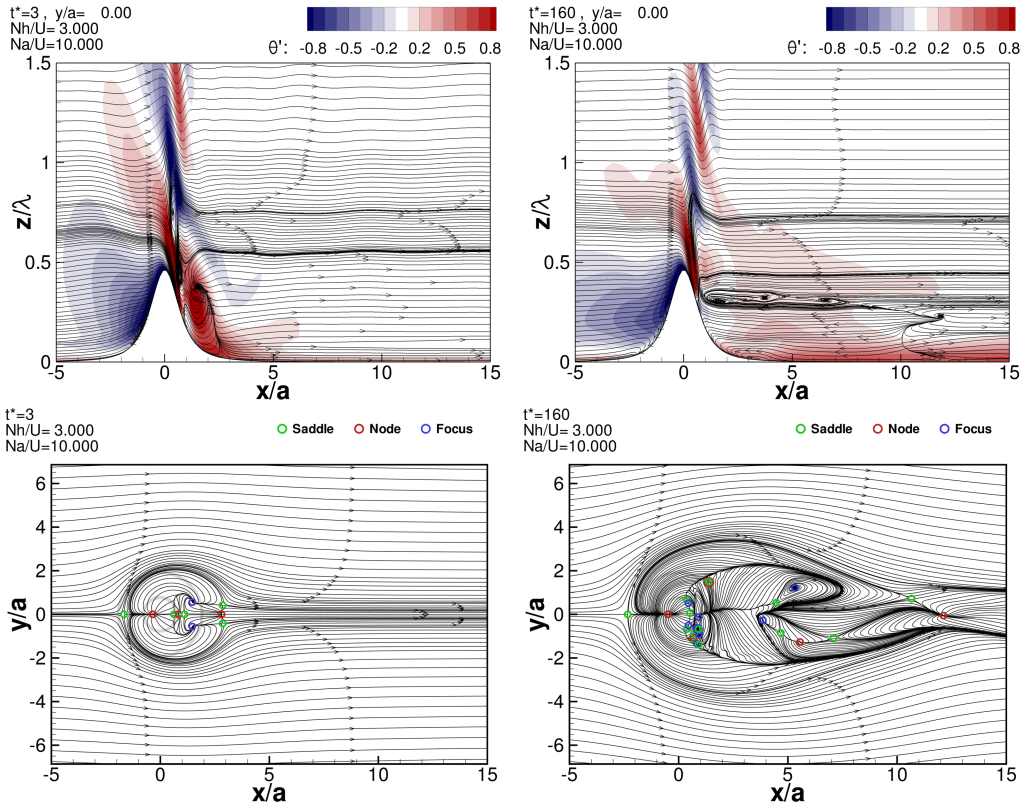

Figure 3.23: Same as Figure 3.22, for $h^* = 3$ and $a^* = 10$.

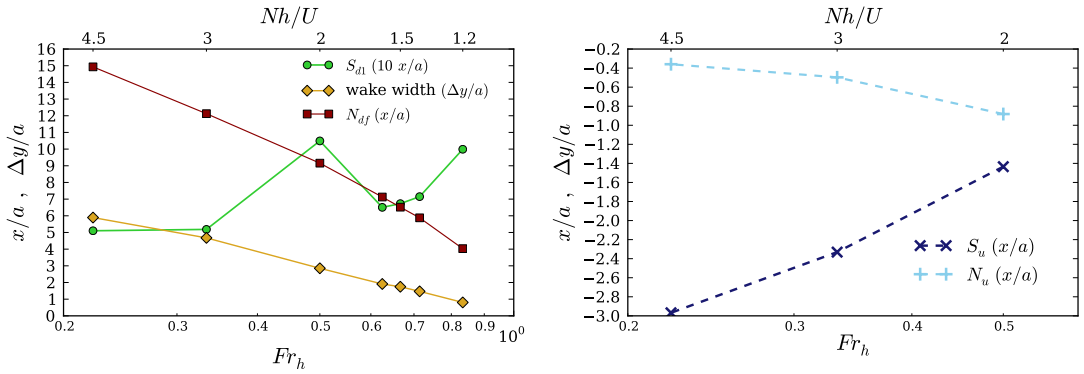

Figure 3.24: Position of critical points and wake width of the surface flow topology as function of $h*$ for $t^* = 160$. Leeward wake characterized by the position of first saddle, S_{d1}, nodal point that terminates the wake, N_{df}, and width of the wake (*left*); position of the upstream saddle point and node, S_u and N_u (*right*).

3.4.4 Breaking waves, splitting flow and vortex shedding

Figure 3.23 shows results for $h^* = 3$ for the first drag maximum and for $t^* = 160$. This is representative of the simulations where $h^* \geq 2$. Upstream flow splitting is present from the start, as is verified in the surface flow streamlines by the stagnant region on the windward side, delimited by a saddle and nodal point, S_u and N_u. Their position is shown in Figure 3.24, as function of h^*. The recirculation area increases as their distance increases, S_u positioning further upstream and N_u closer to the hilltop. The lee topology is altered by the existence of flow splitting, as it becomes characterized also by the vortex pair which endures throughout the simulation, until asymmetries arise for $t^* > 100$.

Contrarily to Ólafsson and Bougeault (1997) events of breaking waves were found, albeit it is present only for low t^* when the drag maximum is reached. When $h^* = 3$, asymmetry is found for $t^* > 140$ while for $h^* = 4.5$ it happens sooner, for $t^* > 100$. These do not develop to a well defined vortex shedding, but a complex wake is clearly present as shown in Figure 3.23.

A detailed comparison between the turbulent and inviscid cases was already made in the grid dependency study of §3.2. The flow over the mountain with $h^* = 4.5$ was used to compare both the surface flow topology (Figures 3.3 and 3.5), the streamlines and contours of $\widehat{\theta}$ at the central cross-section (Figures 3.4 and 3.6) and the location of the main features and critical points (tables 3.3 and 3.4).

For $x < a$ the vertical profiles of $\overline{u}$ for both inviscid and turbulent flow are very similar, with the same speed-up found for $h^* = 1$ (Figures 3.21b and 3.21d). Due to the asymmetries at high t^* these results are not directly comparable in the wake region. However the shapes of both profiles are similar, with the turbulent profiles resembling a smoother version of the inviscid ones. For $x = a$ the amount of separated flow is higher for the turbulent case, a trait that endures throughout the remainder of the wake, even at $x = 6\,a$.

3.4.5 Turbulence kinetic energy field and comparison between normal and shear stresses

The turbulence kinetic energy field, k, is shown in Figure 3.25 for $h^* = 1$ and 3, representative of attached and separated split flow. For $h^* = 1$ the maximum values are found in the lee side, with values of 0.18 for the turbulence intensity, $\sqrt{k}/U$. In the upstream, the maximum values are one order of magnitude lower, around 0.08. The leeward k is mainly generated by the downslope winds. Their higher speed ($\approx U$) results in an increased wall shear stress, thus k is mainly generated due to the interaction with the surface. Due to the leeward jump in the streamlines, k is advected, creating the patch saw in Figure 3.25. Although not shown, for $h^* = 1.5$ the conclusion is the same, with higher downslope winds ($\approx 1.6\,U$).

The presence of upstream splitting for $h^* = 3$ significantly changes the upstream k field. In the upstream the turbulence intensity values become ~ 0.12, however this is due to the higher gradients found than to the tangential speeds near the wall, which are $\sim 0.2\,U$. After the hilltop the downslope speeds ($\approx 1.6\,U$) result in an increase of k, also due to the wall shear stress. Another difference is the leeward advection of k which is much lower than in attached flow. As the wave amplitude becomes higher and the streamlines more vertical, k is advected upwards losing its intensity.

The surface values of the normal and longitudinal shear stresses are compared in Figure 3.26. The first is mainly due to pressure as the k contribution is negligible. To compare both, only the streamwise component of the vector is used. The values of the ratio between pressure and shear stresses are thus shown in Figure 3.26, meaning that for absolute values of $|\sigma_{n,x}/\tau_{w,x}| > 1$ the pressure drag will be higher. As the flow remains attached for $h^* = 0.1$ and 1, no negative region exists (given by the blue colour). For $h^* = 0.1$ the values are lower than 0.5, meaning that the drag due to shear stresses is dominant over the pressure drag. For $h^* = 1$ the pressure is clearly dominant for flow near the mountain, becoming the main mechanism in drag production. These observations are in agreement with the analysis made in §3.4.2.

For higher values of h^* where separation occurs the normal stresses are also dominant over the tangential ones, even in zones of reversed flow. The upstream recirculation for $h^* = 4.5$ is clearly verified, implying a change of sign in the ratio but not of intensity, as the pressure force magnitude remains unchanged.

3.5 Regime diagrams for the inviscid and turbulent flow simulations

Stratified flow over mountains is strongly dependent on the dimensionless mountain height, h^*. There are several measurable quantities that may be used to characterize the flow, as these vary with h^* and serve to diagnose if breaking wave or flow splitting exist.

The maximum velocity magnitude of the downslope winds, shown in Figure 3.27a, is measure of the strength of the wave amplitude and high drag states. It was computed considering only the velocity values for $x > 0$ where $\overline{u} > 0$ and $\overline{w} < 0$. For $h^* < 1$ the values are similar for both inviscid and turbulent flow. These grow until $h^* \sim 2$, when due to flow splitting the wave activity becomes reduced. In the inviscid simulations

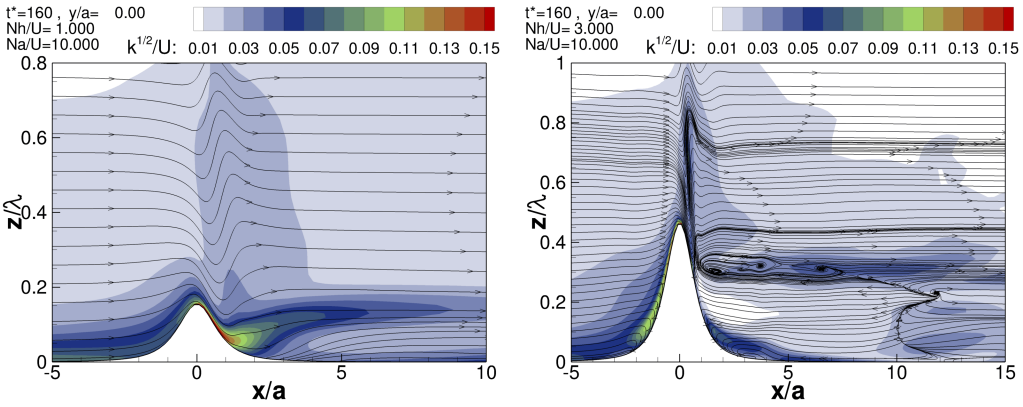

Figure 3.25: Contours of turbulence kinetic energy for h^* of 1 and 3, at the $y = 0$ plane.

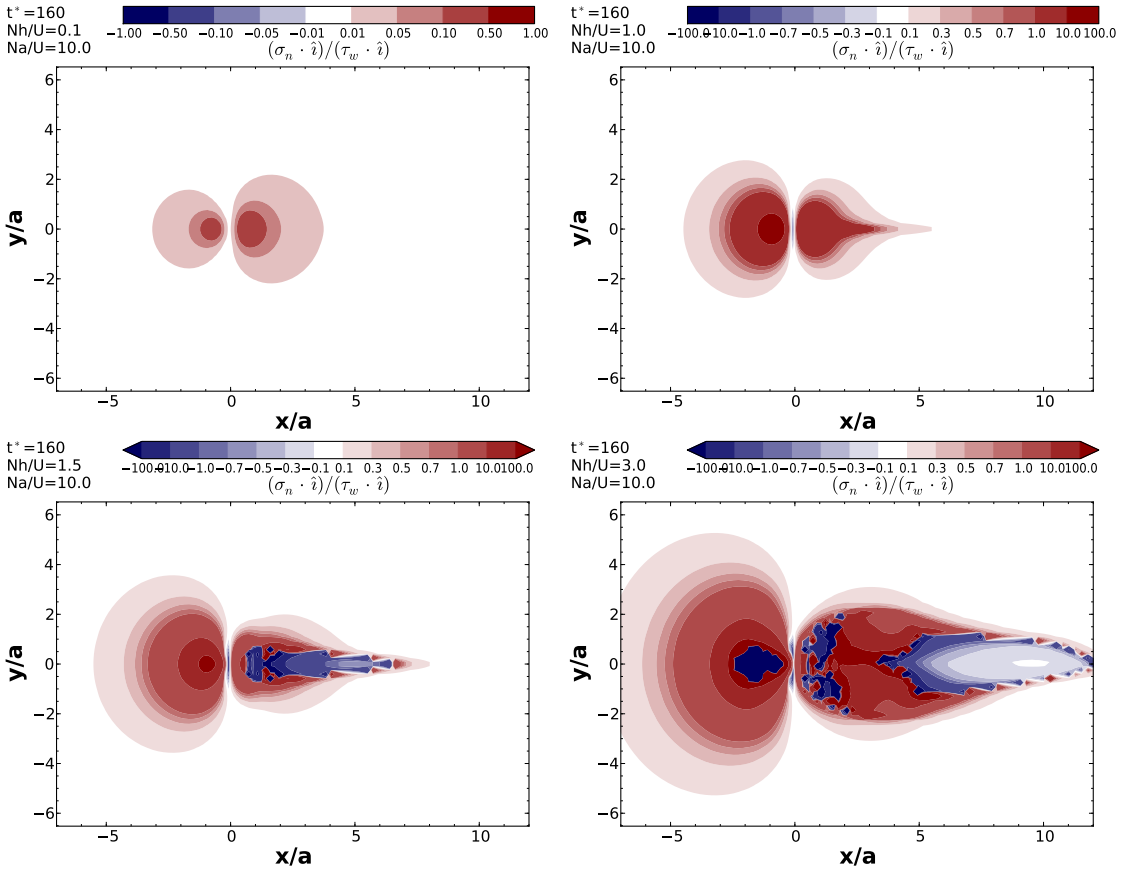

Figure 3.26: Ratio between the normal and tangential stresses for h^* of 0.1, 1.0, 1.5 and 3.0. The streamwise component is used to compare both quantities. The colour scale is not the same for all plots.

the span between the maxima and minima (delimiting the coloured patch) is high for $h^* = 1.5$, when the flow solution is oscillatory due to wave breaking. The values for turbulent flow are lower for $h^* > 1$ than the inviscid ones, because the boundary-layer decreases the downslope winds speed, as these are located near the hill surface.

The minimum velocity magnitude in the leeward side (Figure 3.27b) may be used to diagnose if separation occurs. To identify if there is reversed flow this quantity must allow negative values, thus it was computed as the minimum of $\text{sgn}(\overline{u}) \cdot \|\vec{u}\|$ for $x > 0$. For low h^* the values are positive as the flow remains attached. The values decrease with increasing h^* until separation occurs, for $h^* = 1.4$ and 1.2 for inviscid and turbulent flow respectively. For turbulent flow the velocities are closer to 0 due to the boundary-layer. Similar to the minimum leeward velocity, the minimum windward velocity is an indicator for the existence of flow splitting (Figure 3.27c). It is computed in the same way, $\text{sgn}(\overline{u}) \cdot \|\vec{u}\|$, albeit for $x < 0$. This shows that upstream separation occurs for $h^* \geq 2$ only.

A measure of the amplitude of the waves may be attained by measuring the maximum absolute displacement of the streamlines. This was computed by integrating a finite number of streamlines at different heights above the hilltop. For each streamline, its height at the inlet is subtracted to get the displacement. The results are shown in Figure 3.27d. For inviscid flow the displacement is close to unity when the displacement is normalized by h. The occurrence of wave breaking is related higher amplitudes, up to $h^* \leq 1.6$. For $h^* \geq 2$ the displacement substantially decreases due to flow splitting. Regarding the turbulent flow results, there is also a decrease in wave amplitude as h^* is increased and flow splitting starts, however the differences are subtler and for $h^* < 1$ the normalized displacement continuously increases, up to 1.4 when $h^* = 0.1$. Because the boundary-layer height grows with the streamwise distance, a vertical motion is introduced. The streamlines are thus affected, showing a positive slope which is more pronounced at the inlet. This results in a displacement which is a sum of both the deflection due to the mountain height, h, and the boundary-layer growth, related with its depth, δ. For $h^* = 0.1$, the ratio δ/h is equal to 2 and the displacement is influenced by this effect. As h is increased, δ/h decreases and this effect becomes negligible.

A better measure to describe the influence of h^* on the wave amplitude is the maximum vertical jump in the leeward streamlines (Figure 3.27e). This quantity was defined as the highest upward deflection undergone by a streamline, after its lowest value on the leeward side. The values are lower for turbulent flow, denoting the effect of surface friction in dampening the waves. For $h^* \geq 3$ both inviscid and turbulent cases yield similar values, as both have upstream splitting. The inviscid flow at $h^* \sim 1.5$ is characterized by wave breaking events, resulting in the large deviation found for the maximum and minimum extremes. Although increased values are observed for turbulent flow, these are not characterized by wave breaking, thus the deviation is much lower.

Figure 3.27f shows how turbulence kinetic energy varies with h^*. It shows the maximum turbulence intensity values found, defined as $\sqrt{k}/U$. As discussed in §3.4.5 for attached flow, turbulence is mainly generated by the downslope lee speeds near the surface, thus by the increase of the wall shear stress. This corresponts to values of turbulence intensity around 12%. The k increases with h^*, having a narrow difference between its maximum and minimum values. For $h^* \geq 2$ the maximum and minimum extremes

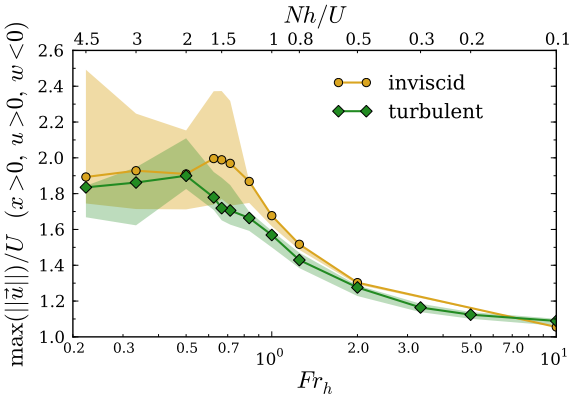

(a) Maximum intensity in leeward downslope wind.

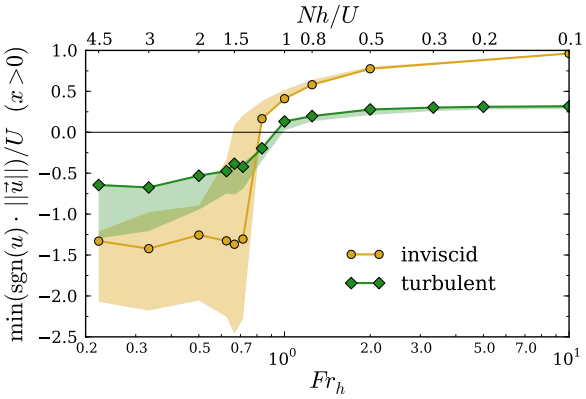

(b) Minimum magnitude in leeward velocities.

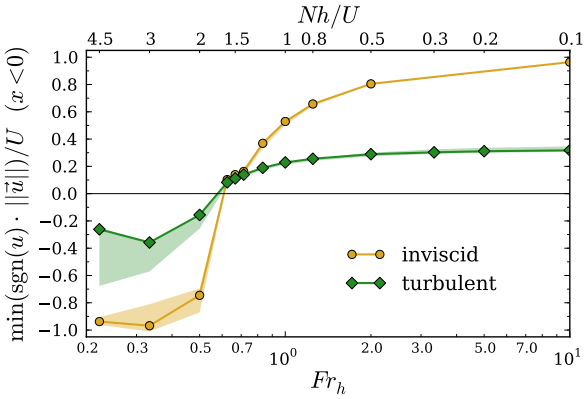

(c) Minimum magnitude in upstream velocities.

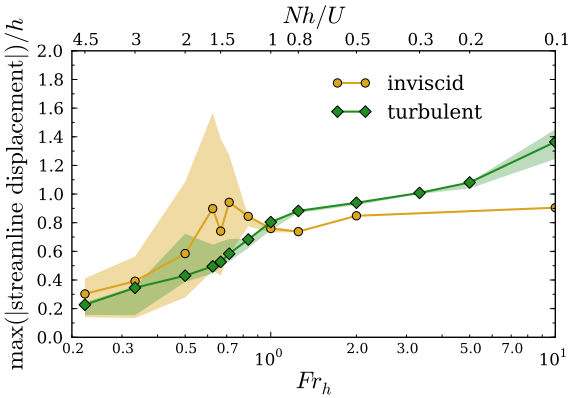

(d) Maximum streamline displacement.

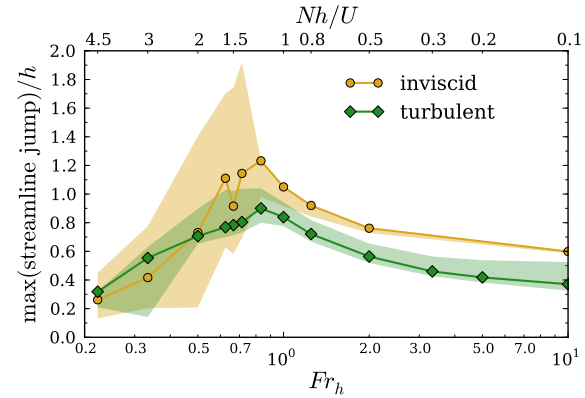

(e) Maximum jump in the leeward streamlines.

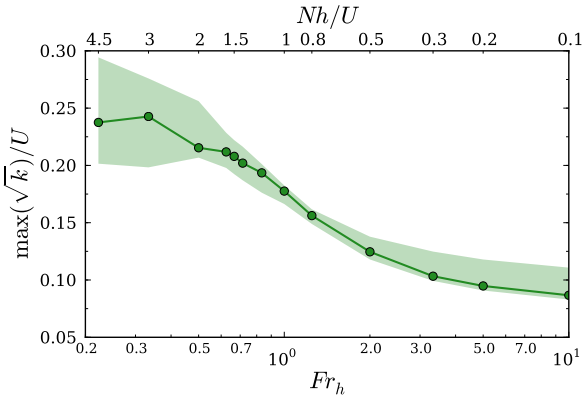

(f) Maximum turbulence intensity.

Figure 3.27: Dependence on the value of h^* for several quantities found in the simulations of inviscid and turbulent flow. The coloured patch is delimited by the minimum and maximum values (for $t^* \geq 5$). The lines with symbols refer to the values found near convergence, taken as the average of the last 10 units of t^*. As the inviscid results for $h^* \in [1.4, 2]$ have an oscillatory solution, the average for $t^* > 5$ is taken instead.

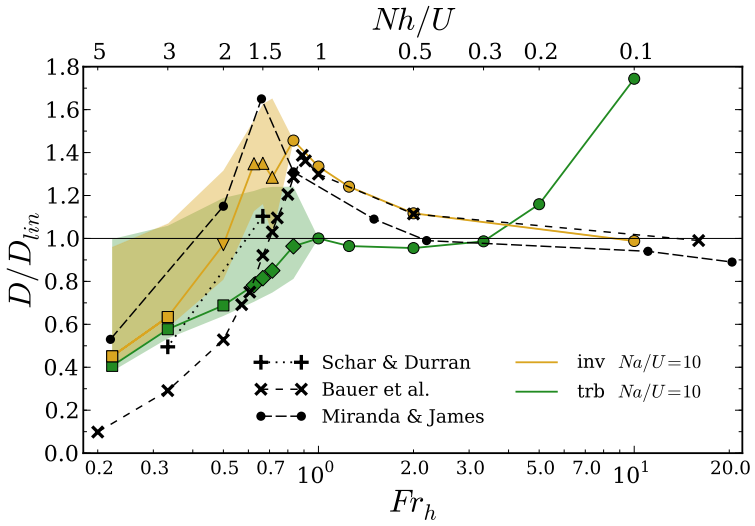

Figure 3.28: Dependence of the normalized pressure drag with h^*. The solid lines with symbols show the drag value near convergence or its average value, depending if the drag converges or is oscillatory. The coloured patch show the maximum and minimum values attained by the drag as the simulation evolved. Symbols used: ○, linear and quasi-linear regime, drag converges; ◇, leeward flow separation, drag converges (turbulent); △, wave breaking, oscillatory drag; ▽, wave breaking and flow splitting, oscillatory drag; □, flow splitting, drag converges despite small oscillations due to vortex shedding. The inviscid and turbulent drag are normalized by the Smith (1980) and Smith (2007) linear models, respectively. The dashed and dotted lines refer to the numerical results of Miranda and James (1992), Schär and Durran (1997) and Bauer *et al.* (2000), shown for comparison.

increase, related with the existence of flow splitting These high values of k occurr at a very thin shear layer after the hilltop and before the lee wake starts, characterized by high downslope wind speeds.

The surface pressure drag is the diagnose variable commonly used to characterize the non-linear flow regimes. It was obtained from the numerical simulations by applying the integration in eq. 3.6, being shown in Figure 3.28. For comparison with the data in the literature, the results of Miranda and James (1992) (MJ), Schär and Durran (1997) (SD) and Bauer *et al.* (2000). are also displayed. To normalize the drag, the linear theory prediction was used, *i.e.*: the result of eq. 3.5 for inviscid flow and the value computed using eq. 3.14 (shown in Table 3.9) for turbulent flow. Similar to the maximum streamline jump, the drag also evidences $h^* \sim 1.5$ has a high drag state due to wave breaking occurrences, while for $h^* > 2$ the drag decreases sharply due to flow splitting. As discussed in §3.4.1, for high h^* the highest drag events are obtained during the first time-steps, before flow splitting becomes dominant. The drag later decreases with time, as the solution reaches a converged state. This happens for both inviscid and turbulent flow, explaining the large deviation found between the observed maxima and minima values. For $h^* < 0.3$ the inviscid flow drag is in agreement with the linear theory prediction, while for turbulent flow it clearly diverges, reaching $D \approx 1.8\, D_{lin}$ for $h^* = 0.1$. From the analysis of §3.4.2 it was concluded that this is caused by the pressure gradient, produced due to surface friction, which becomes more dominant than the effect of the topography shape.

For $h^* < 1$ the inviscid drag values are in perfect agreement with the results from Bauer *et al.* (2000) and over predicting the MJ curve by $\sim 10\%$. For $h^* > 1$ however, it is the MJ curve which better agrees with the present results, both on the highest drag value reached (by the maximum and for $h^* = 1.5$) and lowest value for $h^* = 4.5$. The average drag curve lies in between the literature results, 80% above Bauer *et al.* (2000) and 15% below MJ results. The Schär and Durran (1997) results, altough consisting only of two points, provide a similar agreement as MJ, albeit under-predicting.

3.6 Simulations of turbulent flow over hills with $h^* = a^*$

To investigate turbulent boundary-layer flows over mountains, Eidsvik (2008) produced a set of numerical results using the experimental work of Hunt and Snyder (1980) as reference. To verify the agreement with both numerical and experimental results, simulations were performed to replicate the same dimensionless parameters, but under atmospheric conditions using the same profiles and conditions described in §3.1.1.

The shape of the topography was an inverted 4^{th} order polynomial:

$$f_h(r) = h \left[\frac{1.04}{1 + \left(\frac{r}{a}\right)^4} - \frac{0.083}{1 + \left(\frac{r - 0.203}{0.076}\right)^2} - 0.03 \right] , \quad a = h , \tag{3.16}$$

where $r^2 = x^2 + y^2$. The mountain height and characteristic width are the same, thus, $h^* = a^*$. In §3.3 and 3.4 the mountain width was set such that $a^* = 10$, thus the energy propagation was mainly upward. For values of $h^* = a^* \sim 1$, the decrease of the mountain width allows for the horizontal propagation of the waves downstream. Additionally, the presence of the boundary-layer introduces variations in the Scorer parameter,

$$l^2(z) = \frac{N^2}{\overline{u}^2(z)} - \frac{1}{\overline{u}(z)} \frac{\partial^2 \overline{u}(z)}{\partial z^2} ,$$

such that it decreases with height while $z \leq \delta$. A significant decrease of $l^2(z)$ may lead to resonance in the lee waves (Durran, 2002). Following Eidsvik (2008), the inlet velocity profile was a neutral logarithmic law, eq. (3.9), and the thermal boundary layer is non-existent, with its depth set to zero. These profiles yield:

$$l^2(z) = \begin{cases} \dfrac{N^2 \kappa}{u_* \ln\left(\dfrac{z}{z_{\text{m0}}} + 1\right)} + \dfrac{1}{\ln\left(\dfrac{z}{z_{\text{m0}}} + 1\right) z_{\text{m0}}^2 \left[\dfrac{z}{z_{\text{m0}}} + 1\right]^2} , & z < \delta , \\ N^2 / U^2 , & z > \delta . \end{cases} \tag{3.17}$$

Although the variation of $l^2(z)$ within the boundary-layer cannot be described by a single value, the $l^2(z)$ values are 10 to 10^5 times higher than on the upper layer above it.

It was verified that the presence of waves near the domain outlet would hinder the solution for simulation times $t^* > 60$. To avoid these a damping layer was placed at the

Table 3.10: Parameters from the Hunt and Snyder (1980) experiments.

h^*	a^*	Fr_h	$U\ (\mathrm{m\,s^{-1}})$	$\lambda_z\ (\mathrm{m})$	$z_{\max}/\lambda_z$
1	1	1	0.305	1.44	0.8
2.5	2.5	0.4	0.122	0.58	2.1
5	5	0.2	0.061	0.29	4.2

outlet, similar to the top damping referred in §2.5.2. In addition to the damping of $\overline{w}$, the SIMPLE pressure correction field was also damped to avoid large velocity corrections. Apart from these considerations, the simulations are similar to those realized for turbulent flow over mountains with $h^* = 10$.

The present simulations, as those of Eidsvik (2008), have several differences from the experimental apparatus of Hunt and Snyder (1980). The tank width corresponded to $10.5\,a$, smaller than the width of $16\,a$ of the computational domain used in the present simulations. The vertical depth of the tank was $5.2\,h$. In Table 3.10 are displayed the values for λ_z and $z_{\max}/\lambda_z$, obtained from the several experimental parameters. Only for $h^* = 5$ the water tank is deeper than the computational domain (set to $4\,\lambda_z$), while for $h^* = 1$ is less than $1/4$. The maximum t^* possible is 98, thus ~ 50 for any measurement taken halfway. No information was found regarding the time at which the experimental measurements were taken, being presented as steady-state results. From the numerical simulations, although the flow streamlines and most of its characteristics present little variation past $t^* > 20$, a steady converged solution was not found for $t^* < 100$. As in these experiments stratification is imposed by a salinity profile, it differs from the atmospheric stratification used in the simulations as the thermodynamic reference profiles were established from the ideal gas law.

In Figure 3.29 are presented the results for the mountain heights simulated: 1, 1.25, 2.5 and 5. As expected, the waves propagate in the horizontal direction for $a^* \leq 2.5$. This favours the appearance of leeward rotors, even for $h^* = 1$. At some point in time, all of the simulated flow fields developed both upstream flow splitting and leeward separation. The positions of the critical points which characterize the surface flow topology are in Table 3.11.

The $h^* = 1$ flow field (Figure 3.29) is in disagreement with Hunt and Snyder (1980) results, which show a simpler flow topology and no upstream splitting. However, when visualizing the flow near the start of the simulation (for $t^* = 4$, Figure 3.30), the solution resembles the experimental results (Figure 15(c) in Hunt and Snyder, 1980, p. 692). There is no flow splitting and a recirculation zone exists in the lee slope, although small. The separation saddle point is located at $x = 0.65\,a$, over-predicting the experimental result by 30%, while the reattachment is in agreement ($\sim$ 3%). The lee vortices are located closer to the hilltop (-33%) and the farther away (75% on the spanwise) than in the experiments.

The $h^* = 1.25$ flow field (Figure 3.29) shows close resemblance with the results of Eidsvik (2008, Figure 9 and 10, p. 165). There is separation at the lee side only at the start of the simulation ($t^* \leq 8$) and close to the end ($t^* \geq 87$). Eidsvik results show two rotors, each producing a stagnant region underneath. The present results are

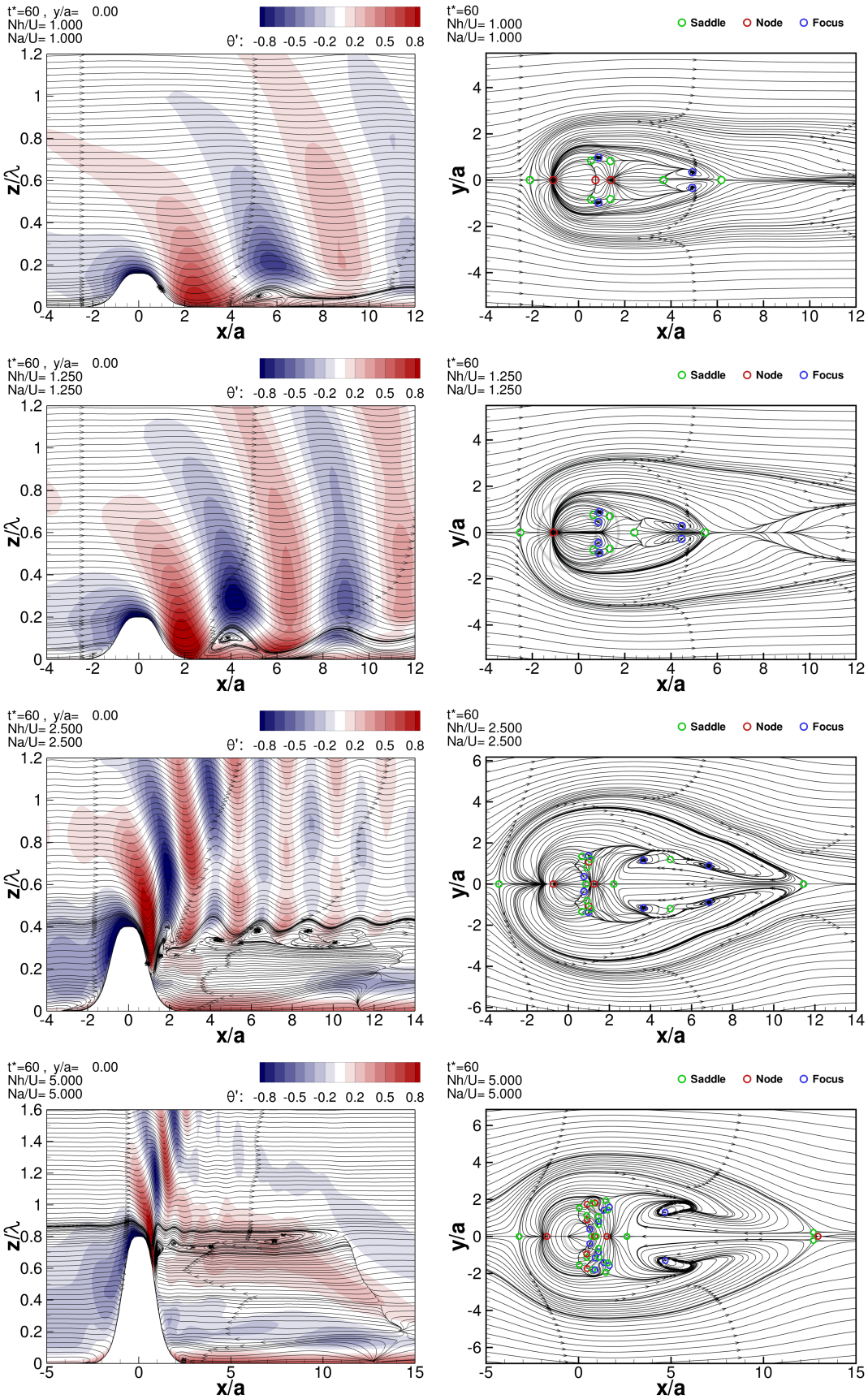

Figure 3.29: Results of turbulent flow over the Hunt and Snyder (1980) topography, for values of $h^* = a^*$ of 1, 1.25, 2.5 and 5. All results were taken at $t^* = 60$. The plots refer to: streamlines and contours of the potential temperature perturbation at the $y = 0$ plane (*left*), surface flow streamlines (*right*). For further details, refer to Fig. 3.3 and 3.4.

Table 3.11: Critical points in the simulations with $h^* = a^*$. Reference values from Hunt and Snyder (1980) (HS) and Eidsvik (2008). For nomenclature details refer to Table 3.6 and §3.3.3.

$h^* = 1$	$S_u\,(\frac{x}{a})$	$N_u\,(\frac{x}{a})$	$S_{d1}\,(\frac{x}{a})$	$S_{df}\,(\frac{x}{a})$	dist. lee vort. $(\frac{\Delta y}{a})$
Hunt and Snyder	n/a	n/a	0.5	1.6	0.8
present $t^* = 4$	n/a	n/a	0.65	1.56	1.4
$t^* = 60$	-2.10	-1.10	0.74	1.41	1.94

			1st rotor	
$h^* = 1.25$	$S_u\,(\frac{x}{a})$	$N_u\,(\frac{x}{a})$	start $(\frac{x}{a})$	end $(\frac{x}{a})$
Hunt and Snyder			~ 3	
Eidsvik	-1.7	-1.3	2.9	5.2
present $t^* = 5$	-2.01	-1.08	2.89	3.27
$t^* = 60$	-2.52	-1.08	2.41	5.47

$h^* = 2.5$	$S_u\,(\frac{x}{a})$	$N_u\,(\frac{x}{a})$	$S_{d1}\,(\frac{x}{a})$	$S_{df}\,(\frac{x}{a})$	dist. lee vort. $(\frac{\Delta y}{a})$
Hunt and Snyder	-1.8	-1.0	1.0	3.0	1.0
Eidsvik	< -2	-1.0	1.4	> 6	
present $t^* = 5$	-2.90	-1.18	1.02	3.44	1.70
$t^* = 60$	-3.37	-0.73	0.86	11.45	2.30

$h^* = 5$	$S_u\,(\frac{x}{a})$	$N_u\,(\frac{x}{a})$	$S_{d1}\,(\frac{x}{a})$	$S_{df}\,(\frac{x}{a})$	dist. lee vort. $(\frac{\Delta y}{a})$
Hunt and Snyder	-2.4	-0.4	0.4	5.8	1.8
present $t^* = 5$	-3.21	-1.54	0.72	3.18	2.24
$t^* = 60$	-3.21	-1.71	0.70	12.95	2.60

in agreement with the first rotor, albeit predicting a larger recirculation starting 17% upstream and ending 5% downstream. Regarding the second rotor, although there is a wave crest with a similar size and location, there is no further stagnation after the first rotor. Hunt and Snyder does not show results for $h^* = 1.25$, referring only that there is an hydraulic jump peak near $x = 3\,a$, which is close to the position of the first rotor.

For $h* = 2.5$ a large wake develops which is much larger, 5 times greater than the one observed by Hunt and Snyder. Despite this, the Eidsvik results show similar agreement. Although the exact value of the end the wake is not specified, it is referred to be further than $6\,a$. Throughout the simulation the wake grown up to $t^* = 80$, reaching $S_{df} = 12.1\,a$. As for $h = 1$, the flow field at smaller time-steps ($t^* = 5$) shows better agreement with the experimental values, appart from position of the flow splitting which is 60% farther upstream. The propagation of the waves has become much more vertical, but still producing a streak of rotors in the interface between the wake and the upper flow.

For $h^* = 5$, because the value of the mountain length is $a \approx 0.8\,\lambda_z$, the direction of propagating waves becomes nearly vertical, with lower streamwise oscillations. The wake is the largest, reaching $S_{df} = 16.8\,a$ at the end of the simulation ($t^* = 100$). The position of the critical points which characterize the upstream splitting and the start of the wake are nearly constant throughout the simulation. The windward stagnant region is 15% smaller and located 70% farther upstream than in the experimental results, while

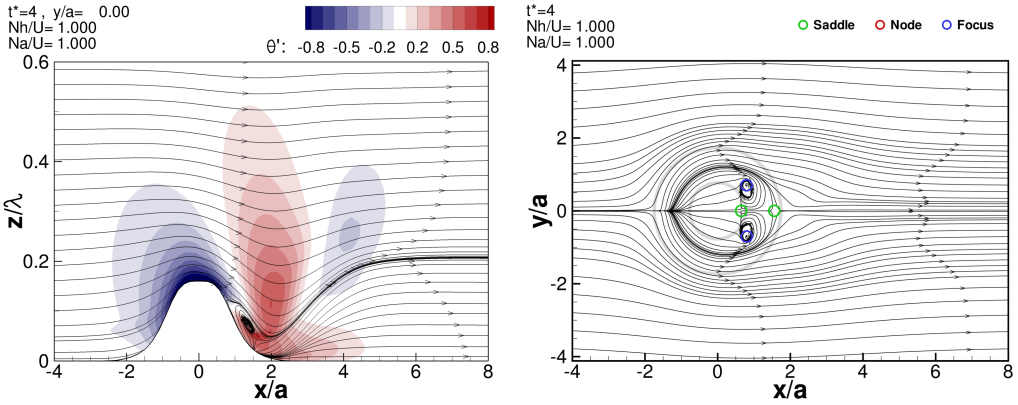

Figure 3.30: Results of turbulent flow over the Hunt and Snyder (1980) topography, for $h^* = a^* = 1$ at $t^* = 4$. For further details, refer to Fig. 3.3 and 3.4.

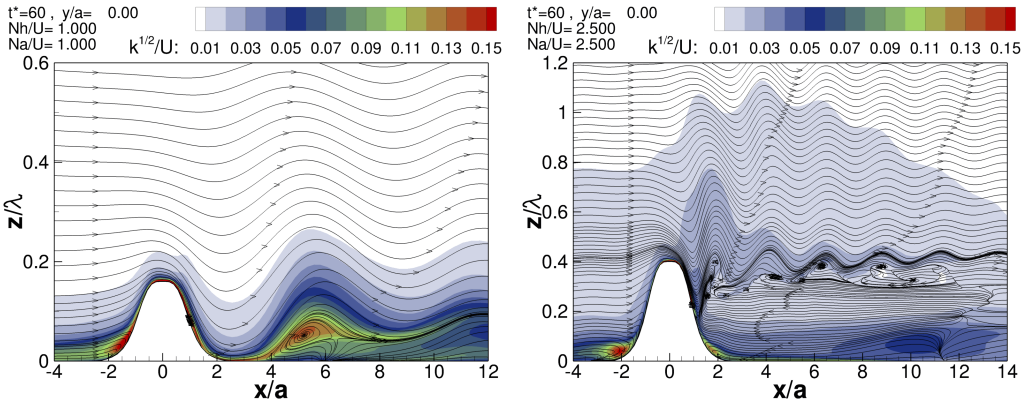

Figure 3.31: Contours of turbulence intensity in $y = 0$ plane, for $h^* = 1$ and 2.5 at $t^* = 60$.

the wake at $t^* = 60$ is 2.3 times larger.

Contour plots of turbulence intensity are shown in Figure 3.31 for $h^* = 1$ and 2.5, representative of the other simulations. For $h^* = 1$ there are high turbulence levels on the leeward wake and in zones where separation happens, different from the results in §3.4.5. When strong rotors are formed due to resonance, these become a significant source of k production. For $h^* \leq 1.25$ the maximum turbulence intensity reaches ~ 0.25, shown in the regime diagram of Figure 3.32a. These refer to the $\sqrt{k}/U$ at the wall shear layer over the hilltop and the lee side. Inside the rotors $\sqrt{k}/U$ may reach 0.14. On the recirculation zone where flow splitting occurs the values are also high, ~ 0.18. For $h^* \geq 2.5$ the turbulence inside the rotors is much lower, ~ 0.03. Although the maximum values are higher than for lower h^*, it is solely due to the shear layer region and the downslope wind speeds. When comparing the values obtained by Eidsvik (2008), also shown in Figure 3.32a, these are $\sim 40\%$ lower. In his work, several remarks were made on the turbulence model (also a two equation $k - \epsilon$), in which turbulence intensity might have beeen under-predicted, especially on the rotors.

The horizontal wavelength is shown on Figure 3.32b. This value should close to λ_z for small a^* and $\delta/h \ll 1$. Because the mountain length is set such that $a^* = h^*$, as both increases the propagation of the waves becomes more vertical and the ratio λ_x/λ_z

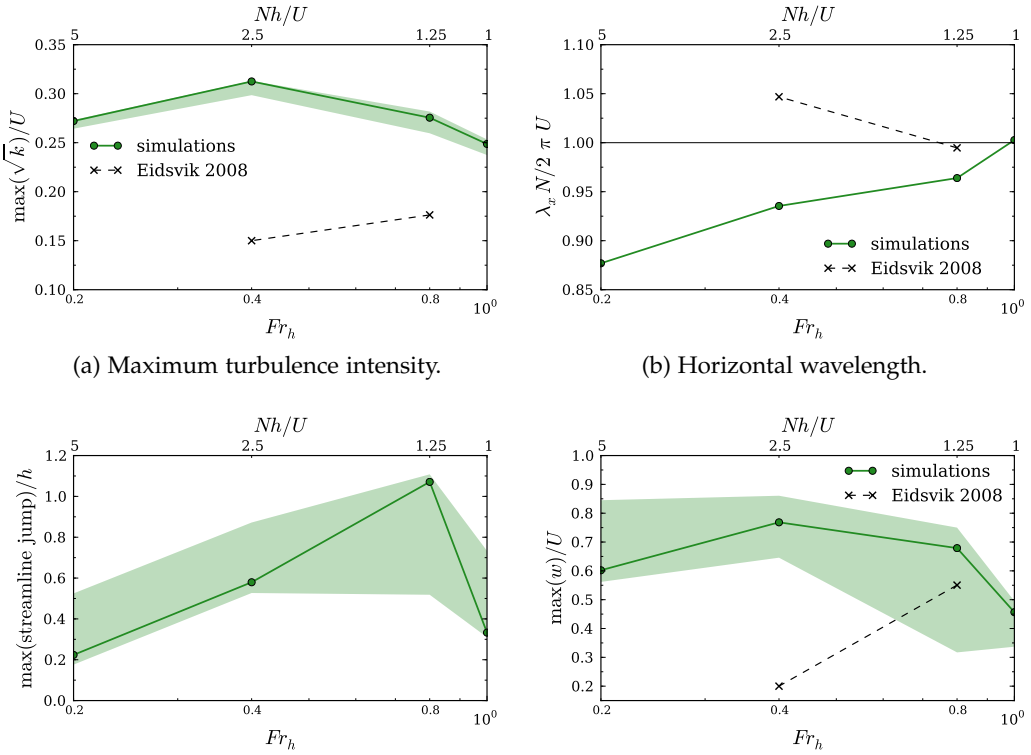

(a) Maximum turbulence intensity.

(b) Horizontal wavelength.

(c) Maximum streamline jump.

(d) Maximum lee vertical velocity.

Figure 3.32: Regime diagrams for the simulations of turbulent flow over Hunt and Snyder (1980) topography. The results of Eidsvik (2008) are also displayed for comparison.

should reduce. This is in agreement with the negative trend shown by the results. The maximum jump in the streamlines over the hilltop (Figure 3.32c) shows that the wave activity is higher for $h^* \sim 1.25$, in agreement with the previous results in §3.5. Figure 3.32d shows the comparison between the maximum vertical velocity found in the lee side and the result from Eidsvik (2008). While for $h^* = 1.25$ the values agree, for $h^* = 2.5$ the present simulations return a maximum 3 times higher. Both curves for the $\max(\sqrt{k}/U)$, $\max(w/U)$ and maximum leeward streamline jump show the same trend, decreasing as flow splitting becomes more dominant.

3.7 Conclusions

Simulations of mountain waves were performed in order to validate the numerical model. These were first made assuming inviscid flow and with stable stratification based on a constant Brunt-Väisälä frequency. The simulations covered several dimensionless mountain heights ranging from 0.1 to 4.5, for a constant dimensionless mountain width of 10. The same case was simulated with turbulent flow and surface friction, thus requiring a boundary-layer whose dimensionless depth was set as constant, equal to 0.2.

The main conclusions of this work were:

1. The inviscid flow simulations in the linear and quasi-linear regime yielded excellent agreement with the linear theory of Smith (1980). Separation at the leeward

side was observed first at $Nh/U = 1.4$, always occurring for higher mountain heights. This dimensionless mountain height was also related with high streamline displacement, resulting in wave breaking and oscillatory solutions. At mountain heights where $h^* \geq 2$, flow splitting occurs and the amplitude of the waves decreased. Vortex shedding was obtained for simulations where $h^* \geq 3$, beginning only for $t^* > 35$.

2. The inclusion of turbulent dissipation resulted on a overall dampening of the wave activity. For $h^* \leq 1$, the flow field was similar to the respective inviscid flow counterpart, aside from the presence of the boundary-layer. Separation in the leeward flow happens for $h^* \geq 1.2$. As the wave amplitude is lessened, there is no wave breaking nor oscillatory solutions in the simulations where $h^* \sim 1.5$. Simulations where $h^* \geq 2$ were characterized by flow splitting and large wakes with complex flow topology. Wave breaking was found to occur for $h^* \geq 2$, however only for few dimensionless times after the start of the simulation. Asymmetry in the leeward flow was found for $h^* \geq 3$ and large dimensionless time, above 100. The flow, however, did not developed into a well defined vortex shedding.

3. The pressure drag is a good indicator of the wave regime, unless there is a streamwise pressure gradient. In the turbulent flow simulations a pressure gradient developed to balance the wall shear stress, as there were both surface friction and a stress-free condition at the top. In the simulations with low hills ($h^* \leq 0.2$) the pressure gradient influence on the longitudinal pressure drag was comparable to that of the mountain shape. This led to high values of the normalized drag in respect to the inviscid flow results.

4. The simulations performed where $a^* \sim 1$ were successful in generating lee waves with a strong horizontal component in the direction of propagation. These waves showed several rotors downstream whose horizontal wavelength agreed with the theoretical value. As a^* was increased to 5, the waves tilted until their direction was nearly vertical. The simulations showed a good agreement with the experiments of Hunt and Snyder (1980) up to 10 dimensionless time units, but significant differences at higher time, namely on the location where flow splitting occurred and the size of the leeward wake. Such disagreements were also present in the Eidsvik (2008) numerical results. Despite this, the main features of the flow were similar in both the simulations and the experimental results.

Chapter 4

Wind power forecast using transfer functions

This chapter concerns wind power prediction using weather forecasts and transfer functions. Firstly, results from numerical simulations of the atmospheric flow under conditions of neutral stratification are presented and discussed. These are simulations where the objective is to describe the flow over real topography, for which the amount of information and experimental data are the same as found on typical engineering applications. A procedure is established to numerically describe the flow for the complete range of azimuthal sectors at different velocities, such that the wind over the site is fully characterized. From these simulations, the wind conditions at the locations of wind turbines are gathered in discrete transfer functions, which relate these with the wind direction and speed at a reference location. Lastly, a comparison is made with real measurements to assess the quality of these transfers functions in estimating wind power when driven by weather forecasts.

4.1 Introduction

The ability to forecast the power production up to 72 hours ahead is of increasing importance in the management of wind power production and distribution. The state of the art comprises two approaches:

1. A chain of physical models, starting on global circulation models (GCM) and regional mesoscale models to obtain a numerical weather prediction (NWP). These supply data to microscale models working at smaller scales and higher spatial resolution. An application of this approach is given by Landberg (1999). One drawback is the need to relate wind speed with the electrical power converted by the turbines, usually applying a power curve which may have a considerable error.

2. Instead of relying on physical models for the microscale flow, a statistical method is employed such as autoregressive models (as in Sánchez, 2006). Although these relate directly the electrical power to the wind speed given by the weather forecast, most of these models must be trained before they can be used, with measurements of the wind farm power output.

From a physical standpoint, wind power prediction can be divided into two tasks: forecasting the wind conditions at each turbine and converting these into electrical power. The addition of a microscale model to this sequence can bring improvements, in particular when complex topographies weaken the correlation between NWP and the local wind conditions.

To forecast the electrical power converted by wind farms in complex terrain, a procedure based on physical models was established such that for a specific site, several numerical simulations where performed to characterize the steady neutral atmospheric flow by mapping ranges of wind velocities and directions. These were performed with the computer code VENTOS®, following the works of Castro *et al.* (2003) and Lopes da Costa *et al.* (2006). The results were gathered in a transfer function, where a given wind direction and speed at a reference location was translated into wind conditions for every turbine of the wind farm. This velocity matrix was corrected to account for wake effects, being subsequently converted into power using the turbine manufacturer power curve.

4.2 Methodology

Figure 4.1 illustrates the methodology adopted. Weather forecasts, obtained from numerical simulation with a mesoscale regional model, are related to the power output of each turbine using a transfer function and a power curve.

The wind speed and direction from the NWP are referred to a reference location within the wind farm (step A → B). A transfer function establishes the relation between the wind conditions at the reference location, with those at each turbine location (B → C). This transfer function was obtained from a large set of CFD simulations of the flow field, covering several wind directions and velocities. The power output for each turbine was then obtained by applying a power curve (C → D), being this the one provided by the turbine manufacturer.

4.2.1 Procedure to characterize the flow field from numerical simulations

The numerical simulations were performed using VENTOS®, described in §2.4. The computational domain was based on the terrain topography, which was rotated in order to have the x coordinate aligned with the flow direction. The velocity at the top and lateral boundaries was allowed only to have tangential components, while the lower boundary was modelled as a rough surface with z_0 estimated from the kind of roughness elements in the topography map.

The simulations where performed to estimate the wind speed and direction at a reference location and for each turbine in the wind farm. This reference location was chosen to coincide with the location of the wind farm meteorological mast, whose data is used for the control system of the turbines. The range of possible wind directions at the reference location was divided into sectors. The inlet conditions where changed by setting different values for the friction velocity, u_*, thus creating different classes of velocity, as u_* acts as a scale factor. The inlet flow direction was iteratively adjusted so

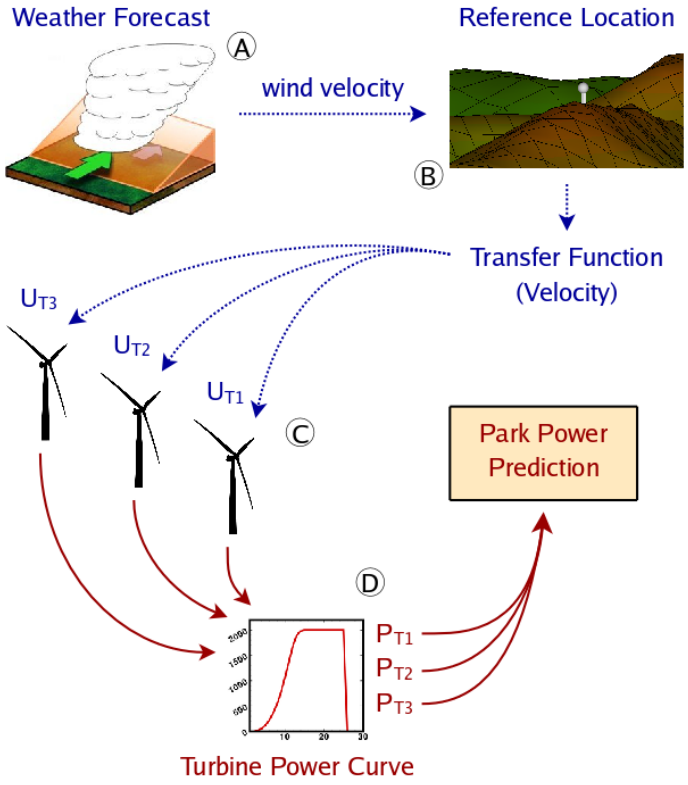

Figure 4.1: Methodology for wind power forecasting, based on a transfer function.

that the direction at the reference mast location (interpolated from the flow field), would match the average sector direction. This procedure is summarized in figure 4.2.

For the sake of simplicity, neutral stratification was always considered for the atmospheric flow. This compromise was made due to the increase of the number of simulations that would be needed to cover all combinations of stratification, direction and velocity classes. On the basis of these simplification lies the fact that the flow, at the scales of interest, is mainly dominated by the surface roughness and the orography complexity, ensuring that turbulence production due to shear is high even in stably stratified conditions. Moreover, the available data was insufficient to determine the stratification regime, as there were no measurements of the heat flux nor for the temperature gradient.

For a set of simulations belonging to the same direction group (*i.e.* having the same wind direction at the reference location), a linear relation was observed between the interpolated speeds at the turbines and the reference location. These locations are usually at elevated places where the wind speed-up is expected to be the highest, thus are prone for such similarity. This bears resemblance with the dimensionless wall shear stress for a turbulent boundary-layer flow over a flat plate. When the surface roughness is such that the flow is at a fully rough regime, the skin friction coefficient becomes independent of the Reynolds number (Schlichting and Gersten, 2000). In contrast, locations at the bottom of valleys or ridges will probably have recirculation bubbles that will impose strong non-linear features to the flow. For the directional groups where a linear relation is verified, the number of velocity classes to simulate may be reduced to 3 or 4

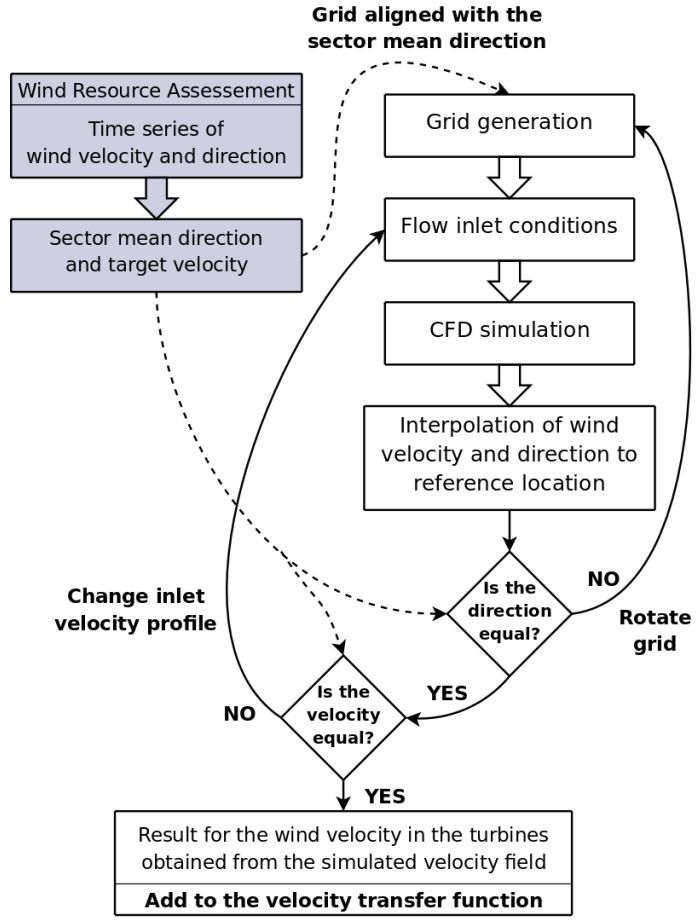

Figure 4.2: Procedure used to obtain a numerical solution for a specific wind direction sector and target velocity.

simulations.

4.2.2 Building the transfer function and producing the forecast

In the present section are described the procedures used to generate a transfer function and use it to produce a velocity and power prediction, from a weather forecast wind condition. As most of the symbols used throughout this section are not referred again, their nomenclature is presented in Table 4.1.

Having previously generated a repository of numerical simulations of the flow field following the methodology in Figure 4.2, these were organized into direction groups. Each direction group has several simulations with the same wind direction at the reference location (subscript R), but each with a different wind speed. The way how the numerical data from the 3D fields was extracted and organized is summarized in Algorithm 1, written in pseudo-code.

When a weather forecast is performed, only the values for the wind speed and direction at the reference location, $\mathscr{V}$ and φ, are needed to make a prediction of the wind speed at a turbine location, $\mathscr{V}_T$. This is achieved through the use of a transfer function

Table 4.1: Nomenclature specific to Chapter 4.

Indexing variables	
d	Index representing direction in the transfer function arrays.
Nd	Number of simulated direction groups.
s	Index representing the different inlet speeds in the transfer function arrays. Each simulation has a different speed at the inlet.
$Ns(d)$	Array with number of simulations for direction group d. Each simulation has a different speed at the inlet.
Symbols related with the transfer function	
$\mathbf{Gv}$	Transfer function for the horizontal wind speed, relating the wind conditions at a reference location and a turbine.
φ	Arbitrary value for the wind direction at the reference location.
$\mathscr{V}$	Arbitrary value for horizontal wind speed at the reference location.
$\mathscr{V}_T$	Wind speed at the turbine location, related with the wind conditions at the reference location through the transfer function $\mathbf{Gv}$.
a, b, c	Interpolation coefficients in the transfer function.
l, ld, lu, r, rd, ru	Indices needed to find interpolating values.
Variables at the reference location from the numerical simulations	
$\overline{\phi}_R(d)$	Angle mean of the azimuths for the simulations in direction group d.
$\phi_R(d,s)$	Azimuth angle of the wind vector, measured clockwise from North, for direction group d and simulation s.
$V_R(d,s)$	Magnitude of the wind horizontal velocity vector, for direction group d and simulation s.
$u_R(d,s)$	x component of the wind velocity vector, for direction group d and simulation s.
$v_R(d,s)$	y component of the wind velocity vector, for direction group d and simulation s.
$w_R(d,s)$	z component of the wind velocity vector, for direction group d and simulation s.
$k_R(d,s)$	Turbulence kinetic energy for direction group d and simulation s.
Variables at the turbine location from the numerical simulations	
$\phi_T(d,s)$	Azimuth angle of the wind vector, measured clockwise from North, for direction group d and simulation s.
$V_T(d,s)$	Magnitude of the wind horizontal velocity vector, for direction group d and simulation s.
$u_T(d,s)$	x component of the wind velocity vector, for direction group d and simulation s.
$v_T(d,s)$	y component of the wind velocity vector, for direction group d and simulation s.
$w_T(d,s)$	z component of the wind velocity vector, for direction group d and simulation s.
$k_T(d,s)$	Turbulence kinetic energy for direction group d and simulation s.

Algorithm 1 Generating the velocity transfer function

Require: Data from simulations must be organized into direction groups. Each group is composed of simulations with different speeds at the inlet, but with the same wind direction at the reference location.
Output: The interpolated values at the reference and turbine locations, organized in the 2D arrays $V_R(d,s)$, $\phi_R(d,s)$, $u_R(d,s)$, $v_R(d,s)$, $w_R(d,s)$, $k_R(d,s)$, $V_T(d,s)$, $\phi_T(d,s)$, $u_T(d,s)$, $v_T(d,s)$, $w_T(d,s)$, $k_T(d,s)$ and the 1D array $\overline{\phi}_R(d)$.

procedure MPVEL
  for $d = 1, Nd$ **do** *# For each direction group*
    $Ns(d) =$ number of simulations in the group
    for $s = 1, Ns(d)$ **do** *# For each inlet speed*
      Read fields from simulation SIM(d,s)
      # Interpolate values at reference location
      From SIM(d,s) interpolate $u_R(d,s)$, $v_R(d,s)$, $w_R(d,s)$, $k_R(d,s)$
      # Interpolate values at turbine location
      From SIM(d,s) interpolate $u_T(d,s)$, $v_T(d,s)$, $w_T(d,s)$, $k_T(d,s)$
      # Compute horizontal velocity magnitude and direction
      $V_R(d,s)$, $\phi_R(d,s) \leftarrow u_R(d,s)$, $v_R(d,s)$
      $V_T(d,s)$, $\phi_T(d,s) \leftarrow u_T(d,s)$, $v_T(d,s)$
    end for
    # Compute average group direction at reference location
    $\overline{\phi}_R(d) =$ ANGLEMEAN$(\phi_R(d, 1 : Ns(d)))$
  end for
end procedure

Gv that relates the wind conditions at the reference and turbine locations. **Gv** is an abstract function that is in fact a procedure to interpolate $\mathscr{V}_T$ from the discrete values of the 2D array $V_T(d,s)$; $d = 1, \ldots, Nd$; $s = 1, \ldots, Ns(d)$. As the number of simulations, Ns, can differ between the several direction groups, thus $Ns = Ns(d)$ and the arrays obtained with Algorithm 1 are unstructured. In Algorithm 2 the function **Gv** is described using pseudo-code.

To obtain a discrete matrix of values of the wind speed at a turbine, $\mathscr{V}_T$, as a function of the conditions at the reference location, $\mathscr{V}_T(\mathscr{V}, \varphi)$, structured by direction and velocity classes, one simply has to generate two vectors:

$$\mathscr{V} = \{\mathscr{V}_1, \mathscr{V}_2, \ldots, \mathscr{V}_{Ni}\} \ ,$$

$$\varphi = \{\varphi_1, \varphi_2, \ldots, \varphi_{Nj}\} \ ,$$

using them afterwards as input to **Gv**, such that:

$$\mathscr{V}_{T\,i,j} = \mathbf{Gv}(\mathscr{V}_i, \varphi_j)\,; \quad i = 1, \ldots, Ni\,; \quad j = 1, \ldots, Nj\,. \tag{4.1}$$

In this way, a lookup table is obtained for plotting or simply to perceive how the transfer function is structured and its values distributed. An example is given in Figure 4.3a

Algorithm 2 Velocity transfer function

Input: The wind conditions at the reference location, $\mathscr{V}$ for the wind speed and φ for the wind direction.
Output: The wind speed $\mathscr{V}_T$ at the turbine T, related with the wind conditions at the reference location.

function $\mathscr{V}_T$ = **Gv** ($\mathscr{V}$, φ)
Use procedure MPVEL to get $\overline{\phi}_R(d)$, $V_R(d,s)$, $\phi_R(d,s)$ and $V_T(d,s)$
 # Get direction groups closest to φ
if ($\varphi < \min[\overline{\phi}_R]$) $\vee$ ($\varphi \geq \max[\overline{\phi}_R]$) **then**
Find r such that $\overline{\phi}_R(r) \equiv \min[\overline{\phi}_R]$
Find l such that $\overline{\phi}_R(l) \equiv \max[\overline{\phi}_R]$
else
Find r that minimizes the positive value of $[\overline{\phi}_R(r) - \varphi]$
Find l that minimizes the positive value of $[\varphi - \overline{\phi}_R(l)]$
end if
 # For direction group at left of φ get the velocities closest to $\mathscr{V}$
if ($\mathscr{V} < \min[V_R(l,:)]$) **then**
Find ld such that $V_R(l,ld) \equiv \min[V_R(l,:)]$
Find lu such that $V_R(l,lu)$ is lowest value after $V_R(l,ld)$
else if ($\mathscr{V} \geq \max[V_R(l,:)]$) **then**
Find lu such that $V_R(l,lu) \equiv \max[V_R(l,:)]$
Find ld such that $V_R(l,ld)$ is highest value after $V_R(l,lu)$
else
Find ld that minimizes the positive value of $[\mathscr{V} - V_R(l,ld)]$
Find lu that minimizes the positive value of $[V_R(l,lu) - \mathscr{V}]$
end if
 # Repeat the last procedure for direction group at right of φ
...
Find rd that minimizes the positive value of $[\mathscr{V} - V_R(r,rd)]$
Find ru that minimizes the positive value of $[V_R(r,ru) - \mathscr{V}]$
...
 # Compute angle differences to φ
$\Delta\varphi_{ld}$ = AngleDifference(φ, $\phi_R(l,ld)$)
$\Delta\varphi_{lu}$ = AngleDifference(φ, $\phi_R(l,lu)$)
$\Delta\varphi_{rd}$ = AngleDifference(φ, $\phi_R(r,rd)$)
$\Delta\varphi_{ru}$ = AngleDifference(φ, $\phi_R(r,ru)$)
 # Get interpolation coefficients

$$a = \frac{\mathscr{V} - V_R(l,ld)}{V_R(l,lu) - V_R(l,ld)}$$

$$b = \frac{\mathscr{V} - V_R(r,rd)}{V_R(r,ru) - V_R(r,rd)}$$

$$c = \frac{-a\Delta\varphi_{lu} - [1-a]\Delta\varphi_{ld}}{b\Delta\varphi_{ru} + [1-b]\Delta\varphi_{rd} - a\Delta\varphi_{lu} - [1-a]\Delta\varphi_{ld}}$$

 # Interpolate

$$\mathscr{V}_T = [1-c]\Big[[1-a]\,V_T(l,ld) + a\,V_T(l,lu)\Big] + c\Big[[1-b]\,V_T(r,rd) + b\,V_T(r,ru)\Big]$$

return $\mathscr{V}_T$
end function

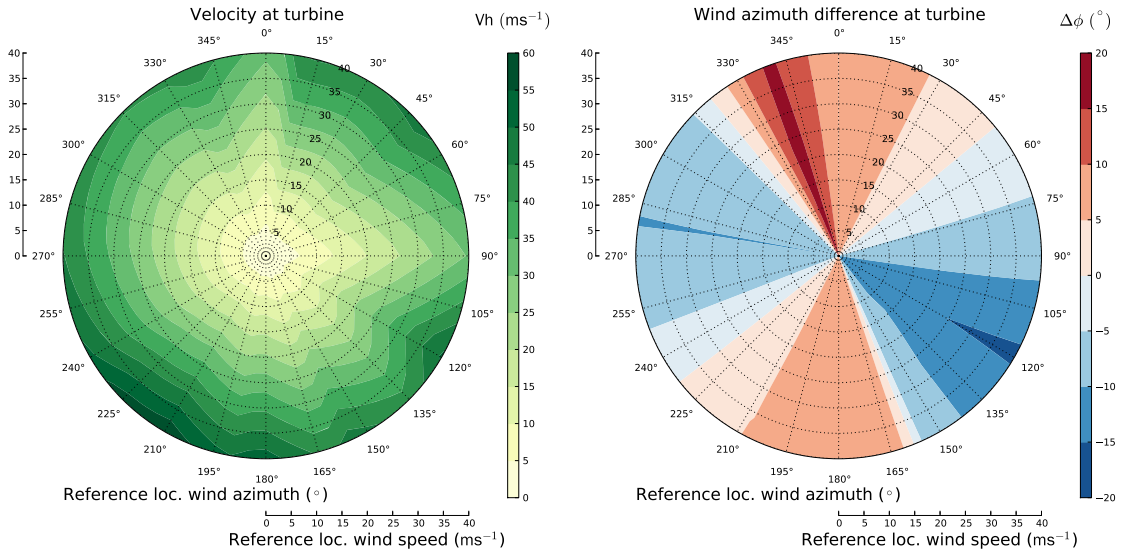

(a) (b)

Figure 4.3: Polar contour plot of a transfer function for (a) wind speed; (b) wind direction. The radial axis represents the wind speed at the reference location, whereas the angular axis is the wind azimuth.

where the velocity at a turbine is plotted as function of the wind speed and direction at a reference location. Other variables besides the wind speed are interpolated by changing the source array from where the value is interpolated (in Algorithm 2 this is the array V_T at the last portion of the code). Exemplifying, to interpolate the wind direction at a turbine as displayed in Figure 4.3b, one needs only to apply the same interpolation coefficients for both components of the unit vector ($\sin\phi$ and $\cos\phi$) of each value ϕ in the direction array ϕ_T. The interpolated angle ϕ_{int} is obtained applying the arctangent trigonometric function:

$$\phi_{\text{int}} = 2 \arctan\left(\frac{1+\cos\phi}{-\sin\phi}\right) , \quad \forall \ \sin\phi \neq 0 .$$

4.2.3 Turbine wake model

To account for wake effects, a velocity deficit was applied as a post-processing to the velocity field, using the analytical model of Jensen (Katic *et al.*, 1986). Other models found in later works, *e.g.* Frandsen *et al.* (2006) and Barthelmie *et al.* (2006), follow the same reasoning and considerations.

With this model, the wake effect of a wind turbine is estimated by assuming that the flow is steady, incompressible and neglecting the rotation of the wake. This last assumption is reasonable considering that the rate of rotation is high enough that becomes averaged by the measurements and one is only interested in characterizing the far wake, instead of the near wake. Likewise, the viscous terms are discarded and only the velocity component in the direction of the wake axis is considered, simplifying the

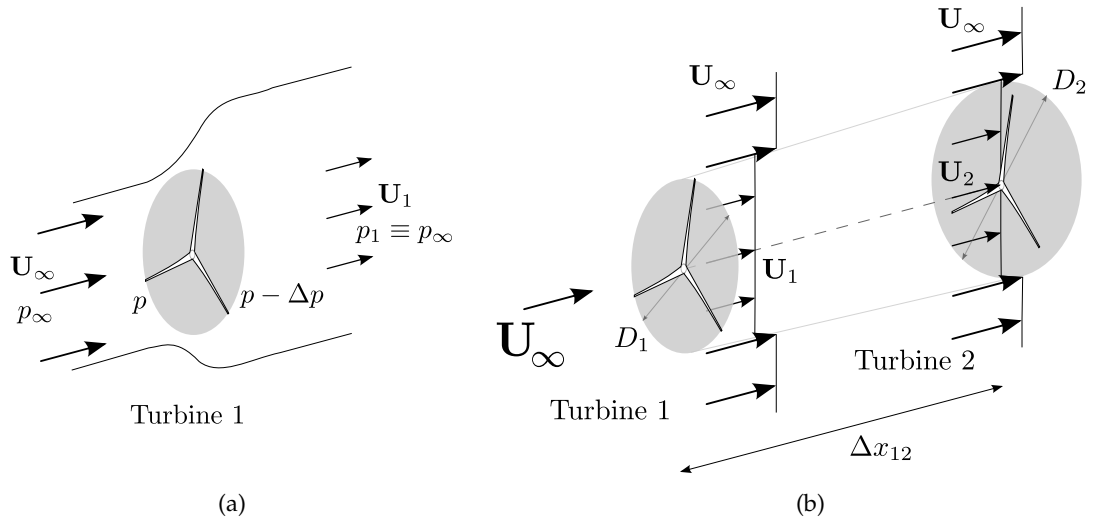

Figure 4.4: Analytic wake model of Jensen: (a) flow velocity and pressure near an idealized turbine; (b) the wake effect of turbine 1 on turbine 2 modelled as a velocity deficit estimated from the linear expansion of the far wake.

momentum eqs. (2.9):

$$\rho\, u \frac{\partial\, u}{\partial\, x} = -\frac{\partial\, p}{\partial\, x} \quad \Leftrightarrow \quad \frac{\partial}{\partial\, x}\left(\rho\, \frac{u^2}{2} + p\right) = 0 \quad \Rightarrow \quad \rho \frac{u^2}{2} + p = C\,, \tag{4.2}$$

which is a simplified form of the energy equation with C as the total pressure, constant along a streamline. By considering the velocity and pressure upstream of the turbine rotor, U_∞ and p_∞, and defining the location x_1, downstream of the rotor, where the pressure p_1 becomes equal to p_∞ and the flow velocity is U_1, then:

$$\begin{cases} \rho\, \dfrac{U_\infty^2}{2} + p_\infty = \rho\, \dfrac{u^2}{2} + p \\ \rho\, \dfrac{u^2}{2} + p - \Delta p = \rho\, \dfrac{U_1^2}{2} + \underbrace{p_1}_{\equiv\, p_\infty} \end{cases} \quad \Rightarrow \quad \Delta p = \rho\, \frac{\left[U_\infty^2 - U_1^2\right]}{2}\,, \tag{4.3}$$

where p and u represent the pressure and velocity at an arbitrary distance between the turbine and x_1. Figure 4.4a shows a schematic of the idealized pressure and velocity fields past a turbine. The energy loss due to the turbine operation is given by the pressure drop Δp, which is related with the axial thrust force T exerted on the turbine:

$$T = \Delta p\, S_{\text{rotor}} = C_T\, \rho\, \frac{U_\infty^2}{2}\, S_{\text{rotor}}\,, \tag{4.4}$$

where S_{rotor} is the rotor swept area and C_T is the thrust coefficient. The information for both is retrieved from the specifications given by the turbine manufacturer (*e.g.* Figure 4.6). From eqs. 4.3 and 4.4 a relation between U_∞ and U_1 is obtained:

$$U_1 = U_\infty\, \sqrt{1 - C_T}\,. \tag{4.5}$$

Having defined a way to quantify the wake in the proximity of a turbine, its evolution downstream can be determined. The Jensen model assumes the wake geometry expands

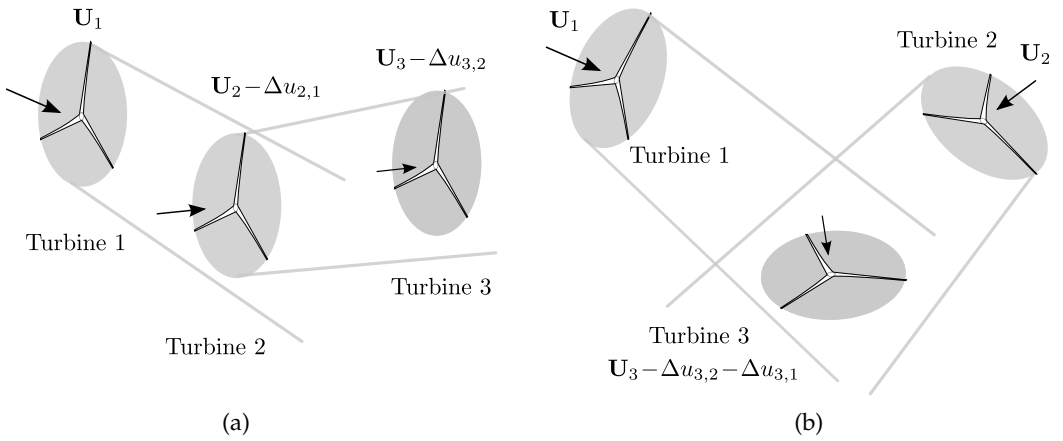

Figure 4.5: Aplication of the Jensen model to multiple wakes: (a) situation where the wake of one turbine is influencing a second turbine that is influenciating another; (b) situation where a turbine is influenced by two independent wakes.

linearly with the distance to the rotor, taking the shape of a cone (Figure 4.4b). The diameter growth is modelled by,

$$D_2 = D_1 + 2\,\alpha_{\text{wake}}\,\Delta x_{12}\,, \tag{4.6}$$

where D_1 is the rotor diameter of the turbine generating the wake, D_2 is the wake diameter at position x_2 downstream, at a distance Δx_{12}. The constant α_{wake} is the wake decay coefficient, assuming values between 0.04 for water surfaces ($z_0 = 0.0002\,\text{m}$), $0.063 \sim 0.075$ for rough terrain ($z_0 = 0.03 \sim 0.05\,\text{m}$) and ≥ 0.1 for forested areas. The wake is thus characterized by a velocity deficit, Δu, function of Δx_{12} and the wake diameter by:

$$\begin{aligned} &\Delta u_{2,1} = U_\infty - U_2\,, \qquad [U_\infty - U_2]\; D_2^2 = [U_\infty - U_1]\; D_1^2\,, \\ &\Rightarrow \quad \Delta u_{2,1} = U_\infty \left[1 - \sqrt{1 - C_T}\right] \left[\frac{D_1}{D_1 + 2\,\alpha_{\text{wake}}\,\Delta x_{12}}\right]^2 . \end{aligned} \tag{4.7}$$

Throughout the derivation of this expression it was assumed that the flow outside of the wake has a constant velocity equal to U_∞, which is hardly true either in numerical simulations or reality. However, when deriving using velocities for the free flow such that $U_{1\infty} = U_\infty(x_1)$ and $U_{2\infty} = U_\infty(x_2)$, *i.e.*, with different velocities for the flow unperturbed by the wake, eq. (4.7) remains the same by redefining $\Delta u_{2,1} = U_{2\infty} - U_2$ and $U_\infty = U_{1\infty}$.

The application of the Jensen wake model to several turbines is dependent on the layout of the wind farm. The procedure developed is described using pseudo-code in Algorithm 3. The reasoning behind this algorithm is that the turbine $T1$ wake is influencing turbine $T2$ and this is accounted in the velocity deficit $\Delta u_{2,1}$. However if $T2$ is influencing turbine $T3$, but this is not affected by the wake of $T1$, then one should account for the deficit $\Delta u_{3,2}$ and not $\Delta u_{3,1}$. Nevertheless care must be taken to compute $\Delta u_{3,2}$ using a velocity for $T2$ that is itself reduced by $T1$, thus:

Algorithm 3 Wake model implementation – Part 1

program MAIN

Require: The velocity at each turbine location, as given by procedure MPVEL (in Algorithm 1), after being run for every turbine in the wind farm.
Output: The velocity at each turbine location considering the wake effect of the turbines, structured in the same way as the input.

call procedure WAKE_EVAL to get **WEVAL** # *Algorithm 4, page 106*
call procedure WAKE_INFLUENCE to get **WINFLU** # *Algorithm 5, page 107*

 # Establish the order in which the turbine wakes are evaluated
for $i = 1, Nt$ **do** *# For each turbine*
  $\mathbf{WSUM}(i) = \sum_{j=1}^{Nt} \mathbf{WINFLU}(i, j)$
end for
 # For turbine i, the lower $\mathbf{WSUM}(i)$ *is, less is the influence this turbine suffers from the remaining. A value of* 0 *means i is not under any wake. Sort the order as the turbines are evaluated such that the first is the one with the lowest value in* **WSUM**. *Store the indexes in the array* **WORDER**.
WORDER = SORT_INDEXES(**WSUM**)

 # Compute the velocity deficit
for $k = 1, Nt$ **do** $i = \mathbf{WORDER}(k)$
  if $\mathbf{WEVAL}(i, k) = 1$ **then**
    Rotate and translate horizontal vectors $\vec{x}_i$ and $\vec{x}_k$ to a referential with the x coordinate in the direction of the horizontal velocity vector $\vec{u}_k$, centred in $\vec{x}_k$
    # Compute wake diameter at turbine i location
    $D_{\text{wake}} = D_k + \alpha_{\text{wake}} \Delta x_{ki}$
    Compute Overlap from intersection of $\text{Area}_{\text{rotor, i}}$ and $\text{Area}_{\text{wake, k}}$
    if Overlap > 0 **then**
      $C_T = \text{INTERPOLATE}(V_k)$ *# From the manufacturer curve* $C_T = f(u)$
      Compute velocity deficit $\Delta u_{i,k}$
      $V_i = V_i \left[1 - \dfrac{\text{Overlap}}{\text{Area}_{\text{rotor, i}}}\right] + [V_i - \Delta u_{i,k}] \left[\dfrac{\text{Overlap}}{\text{Area}_{\text{rotor, i}}}\right]$
    end if
  end if
end for
end program

Continued in Algorithm 4 at page 106 ...

Algorithm 4 Wake model implementation – Part 2

... continuation from Algorithm 3 in page 105.

procedure WAKE_EVAL

Output: A square matrix of boolean numbers with the size given by the number of turbines Nt^2. A value of 1 in $\mathbf{WEVAL}(i, j)$ means that the turbine i is influenced by the wake of turbine j, not caring if the wake of other turbines is more significant or not.

for $i = 1, Nt$ **do** # *For each turbine*
  for $j = 1, Nt$ **do** # *For the other turbines*
    if $i = j$ **then**
      $\mathbf{WEVAL}(i, j) = 0$
    else
      Rotate and translate horizontal vectors $\vec{x}_i$ and $\vec{x}_j$ to a referential with the x coordinate in the direction of the horizontal velocity vector $\vec{u}_j$, centred in $\vec{x}_j$
      if (turbine j is upwind of i) $\wedge$ ($\text{Area}_{\text{rotor, i}}$ overlaps $\text{Area}_{\text{rotor, j}}$) **then**
        $\mathbf{WEVAL}(i, j) = 1$
      end if
    end if
  end for
end for
end procedure

Continued in Algorithm 5 at page 107 ...

Algorithm 5 Wake model implementation – Part 3

... continuation from Algorithm 4 in page 106.

procedure WAKE_INFLUENCE

Require: The square matrix **WEVAL** as given by procedure WAKE_EVAL.
Output: A square matrix of boolean numbers with the size given by the number of turbines Nt^2. A value of 1 in **WINFLU**(i, j) means that the turbine i is influenced by the wake of turbine j, where this may be a direct influence (i in the wake of j) or an indirect influence (i not in the wake of j, but j is in the wake of k thus i is influenced by k).

```
for i = 1, Nt do                                   # For each turbine
    for j = 1, Nt do                               # For the other turbines
        if WEVAL(i, j) = 1 then
            WINFLU(i, j) = 1
            WINFLU = WAKE_RECUR(WEVAL, i, j, 0)
        end if
    end for
end for
```

 # WAKE_RECUR is a recursive function that checks if another turbine k has its wake influencing turbine j, thus indirectly influencing turbine i. Note that the wake of turbine k may be directly influencing i or not. Integer Nr exists to stop the recursion.

```
function WINFLU = WAKE_RECUR(WEVAL, i, j, Nr)
    if Nr < Nt then
        for k = 1, Nt do
            if WEVAL(j, k) = 1 then
                WINFLU(i, k) = 1
                WINFLU = WAKE_RECUR(WEVAL, i, k, Nr + 1)
            end if
        end for
    end if
end function
end procedure
```

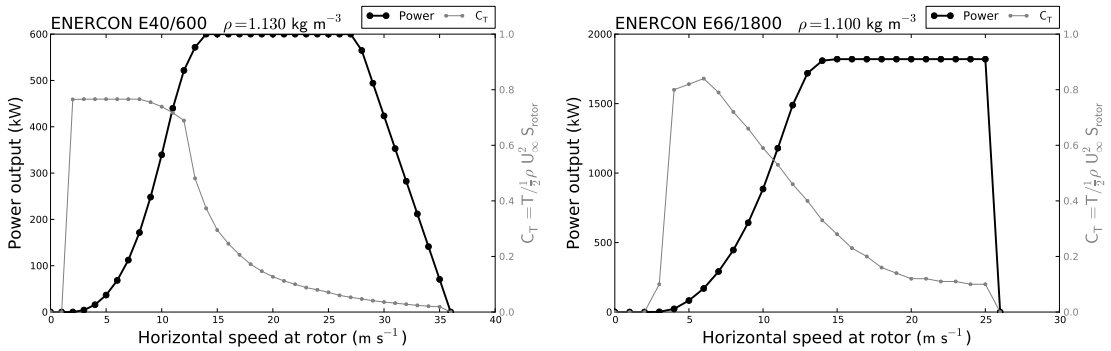

Figure 4.6: Power output and thrust coefficient curves for the ENERCON wind turbines E40/600 and E66/1800.

$$\Delta u_{2,1} = U_{1\infty}\left[1-\sqrt{1-C_T}\right]\left[\frac{D_1}{D_1+2\,\alpha_{\text{wake}}\,\Delta x_{12}}\right]^2, \qquad U_{2\text{wake}} = U_{2\infty} - \Delta u_{2,1}\,,$$

$$\Rightarrow \quad \Delta u_{2,3} = U_{2\text{wake}}\left[1-\sqrt{1-C_T}\right]\left[\frac{D_2}{D_2+2\,\alpha_{\text{wake}}\,\Delta x_{23}}\right]^2.$$

In Figure 4.5a this turbine layout is displayed. Considering now the layout in Figure 4.5b, turbine $T3$ is in the wake of $T1$ and also in the wake of $T2$, but $T2$ is not in the wake of $T1$, then both deficits $\Delta u_{3,1}$ and $\Delta u_{3,2}$ will have an influence on $\vec{u}_2$.

Albeit the algorithm developed for the Jensen wake model takes into account some interaction between turbines, it remains simple when compared to more complex methodologies such as Ainslie (1988), or those that model directly sink terms in the momentum equations to account for the velocity deficit, *e.g.* El Kasmi and Masson (2008) or Réthoré *et al.* (2009). Even so, to have a more complex model would imply a high number of simulations to cover all the possible situations where the turbine layout changes due to turbines out-of-operation, to the extreme of becoming unfeasible to manage or compute in acceptable time. A flaw in this model is that the direction of the wake is given by the direction of the horizontal velocity vector at the location of the turbine generating it. An upgrade would consider the streamline instead, forcing the wake geometry to follow it. However this would turn an inexact, yet simple model, into a much more complex and of difficult programming.

4.2.4 Conversion from velocity to electrical power

Having generated a transfer function and produced a wind speed forecast, the power output from the turbine is obtained from a power curve, relating these two quantities. This information is supplied by the turbine manufacturer, as presented in Figure 4.6. For a wind farm with different turbine models, where some may be out-of-operation due to malfunctions or scheduled maintenance, the wind speeds are still predicted at each location and rotor height. The respective power curve is used to interpolate the velocities into the turbine electrical output. Ultimately, the wind farm power is obtained by summing the power from each operational turbine.

The manufacturer power curve is often given considering a specific value for the air density. When there is information on the density from the field measurements or from the weather forecast, the interpolated power is corrected according to §8 of the IEC 61400-12 standard (IEC, 1998). Considering that the power coefficient, C_P, remains constant:

$$P = C_P \, \tfrac{1}{2} \, \rho \, V_\infty^3 \, S_{rotor} \quad \Rightarrow \quad \left[\frac{P}{\rho \, V_\infty^3} \right]_{curve} = \left[\frac{P}{\rho \, V_\infty^3} \right]_{atm} , \tag{4.8}$$

where P is the power output, u_∞ is the horizontal wind speed at the rotor and S_{rotor} is the area swept by the turbine blades. The subscripts *curve* and *atm* refer to the values given by the power curve and the value considering the actual dry air density ρ_{atm} at a specific condition. For a stall-regulated wind turbine the power correction is proportional to the density ratio,

$$P_{atm} = P_{curve} \, \frac{\rho_{atm}}{\rho_{curve}} , \tag{4.9}$$

while on a pitch-regulated turbine the correction is performed by correcting the wind speed instead, interpolating the power for that value:

$$V_{\infty,atm} = V_{\infty,curve} \left[\frac{\rho_{atm}}{\rho_{curve}} \right]^{\frac{1}{3}} \quad \Rightarrow \quad P_{atm} = f \left(V_{\infty,atm} \right) . \tag{4.10}$$

4.2.5 Remarks on the influence of the integration time in the power curve

When comparing predictions and measurements of a turbine power output, these regard average values instead of instantaneous events. As such, even if the power curve is a perfect relation between the instantaneous values of velocity and power and no other sources of error exist, the variation of the wind speed within the integration time will result in discrepancies between the average power and the value obtained after converting the average velocity into power. This is caused by the non-linear shape which characterizes the power curve itself.

Considering that a velocity average is the result from several events in the integration time, each event is related to the PDF (probability distribution function) of the wind speed. Assuming this may be characterized by a Gaussian function, its shape is symmetric and function of its average and variance. If the velocity PDF is converted by the power curve, due to its non-linearity the power PDF may be distorted and asymmetric. This is observed in Figure 4.7, where this effect is sketched for different regions of the power curve:

1. For low wind speeds, near the cut-in, the power output is limited by 0 resulting in a positively skewed distribution.
2. For wind speeds between the cut-in and the rated output, the blending between the shapes of the power curve and the Gaussian distribution determine the skewness, which varies from positive to negative.
3. For wind speeds close to the rated output the distribution is negatively skewed, limited by the nominal turbine power.

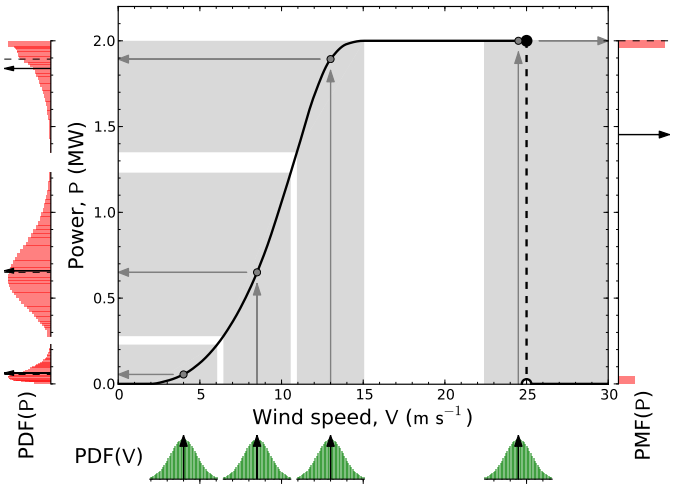

Figure 4.7: Schematic of the conversion of a PDF (probability distribution function) of wind speed into power using the power curve of the manufacturer (ENERCON E66/2000 wind turbine). The wind speed distribution was assumed normal (in green), analogous to the result of a 10 minutes measurement. For several values of the velocity average the power PDF differs considerably (in red), according to the respective power curve region. The black arrows show the true average from the PDF, instead of the direct conversion from the velocity average into power, represented by the dashed line.

4. If the cut-off speed is reached the distribution will be severely distorted, as there will be events at both the nominal power and no power at all.

The worse the distortion is, the higher will be the mismatch between the measured power and the power curve. Conversely, if the wind speed lies between rated output and below the cut-off, the power values will be close to the nominal power with very little dispersion.

4.3 Neutral flow and transfer functions for Pinheiro and Rainha sites

To test the transfer function methodology for forecasting the power output of wind farms, two sites where studied: Pinheiro and Cabeço da Rainha wind farms. Measurements of the wind conditions and power output were available for several periods throughout 2004 to 2006. This work was developed under project EPREV (Previsão da Produção Eléctrica de Base Eólica).

4.3.1 Description of the wind farms

Pinheiro (Figure 4.8a) is located on a plateau. Although in the wind farm region the terrain does not present complex features nor high slopes, these are present on the surroundings. It is composed of twelve 1.82 MW E66 wind turbines with a hub height positioned at 65 m AGL, a rotor radius of 35 m, pitch-regulated and a cut-off speed at 25 m s^{-1}. The respective power function is presented at Figure 4.6. As the turbines are spatially distributed in a shape resembling a closed ring, wake effects are predominant

in all directions. There were two measurement masts available, PORT071 and PORT214, however the later is too close to the turbines, thus subjected to wake effects from the turbines. As such, PORT071 was chosen as the reference location for the transfer functions. The Ruggedness Index (RIX, Mortensen and Petersen 1997) in the wind farm area varies between 7.2% and 17.1%.

The Cabeço da Rainha site is more complex than Pinheiro (Figure 4.8b), resulting in highly complex flow fields. The wind farm is located along a ridge, hence wake effects are predominant for winds from the northeast or southwest. The park is composed of seventeen E40 600 kW turbines with 46 m height and 21 m radius, pitch-regulated with a storm control mechanism. This allows continuous operation up to 35 m s^{-1}, linearly decreasing the power output (Figure 4.6). It has also three E66 2 MW turbines at 65 m height, similar to the turbines installed in Pinheiro, with a cut-off speed of 25 m s^{-1}. This site has two measurement masts, Cabeço da Rainha (Ecra) and Lontreira (Elnt), being the first chosen for the reference location. The RIX inside the wind farm area varies between 18.5% and 29.6%.

4.3.2 Description of the available data

The data available from the measurement stations consisted of time series of the wind speed and direction azimuth. These were averaged throughout integration times of 10 minutes, with a sampling frequency of $1/2$ Hz, as standard practice in wind energy. Some datasets additionally had the minimum, maximum and standard deviation of the wind speed. Measurements of the power output of each turbine were acquired by the wind farm SCADA (supervisory control and data acquisition). The average, minimum and maximum power are available in the datasets for the same integration time. The wind velocity was recorded also at the cup anemometer on the nacelle of each turbine. These

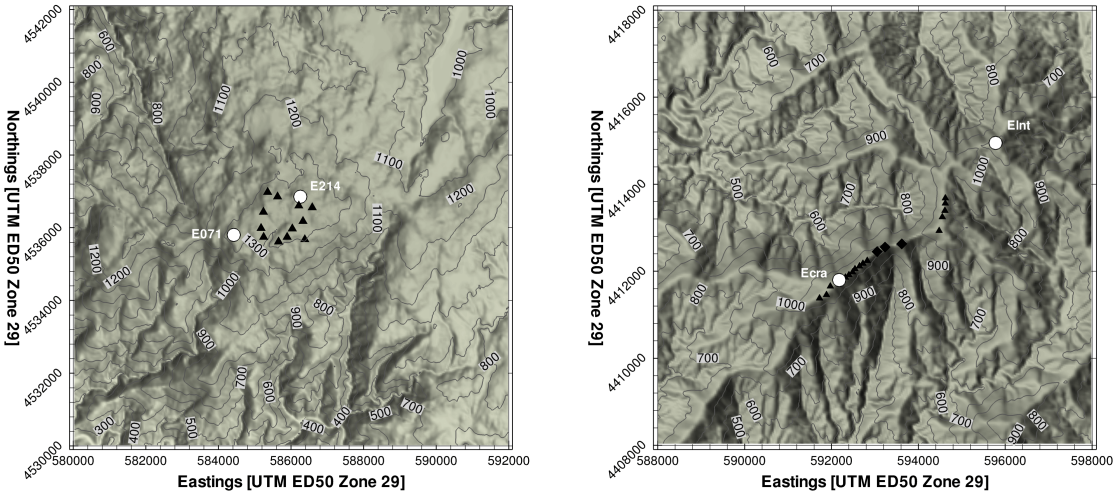

(a) Pinheiro wind farm. Location of the masts (○) and the 1.8 MW turbines (▲).

(b) Cabeço da Rainha wind farm. Location of the masts (○), the 600 kW turbines (▲) and the 2 MW turbines (⧫).

Figure 4.8: Topographies of the investigated sites. Contour lines are spaced by 100 m.

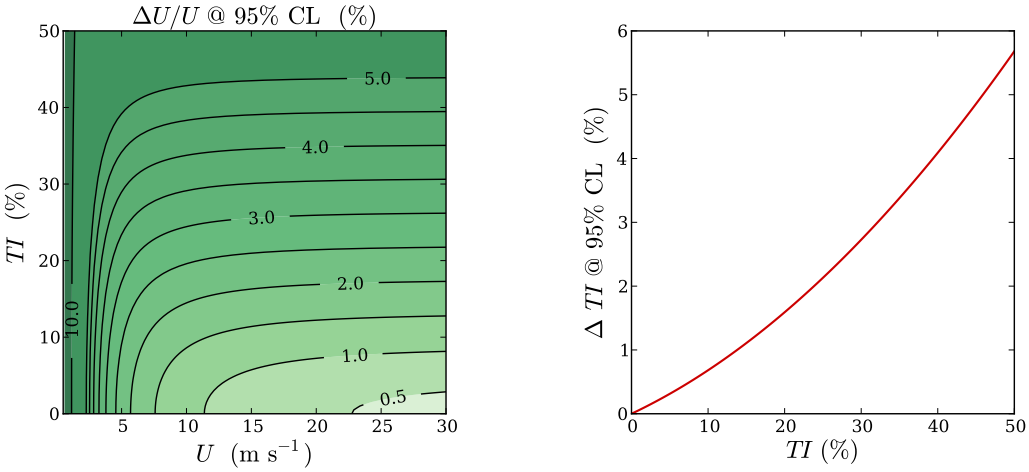

Figure 4.9: Estimation of the uncertainty in the cup anemometer measurements, using the calibration information for the PORT071 mast. *Left*: the relative uncertainty in the mean value, $\overline{u}$, as function of the turbulence intensity, $TI = \sigma(u)/\overline{u}$, and $\overline{u}$. *Right*: the uncertainty in the estimation of $TI = \sigma(u)/\overline{u}$, as function of the value of TI.

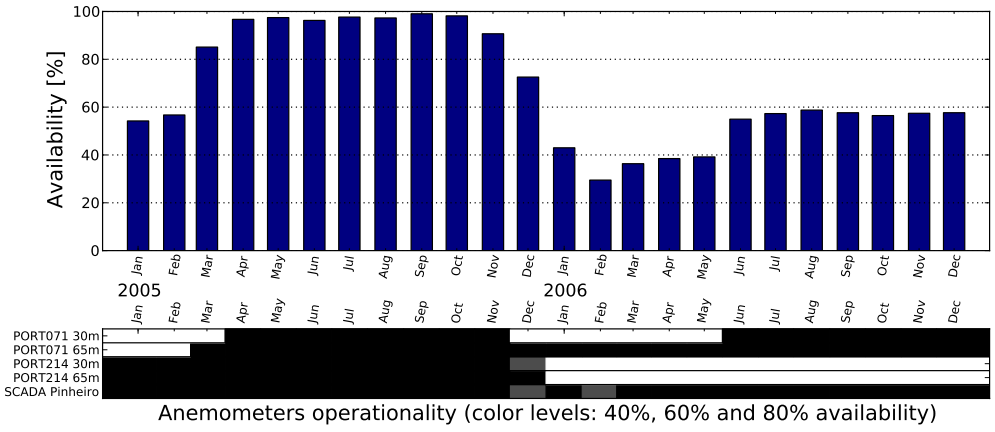

(a) Availability for Pinheiro wind farm.

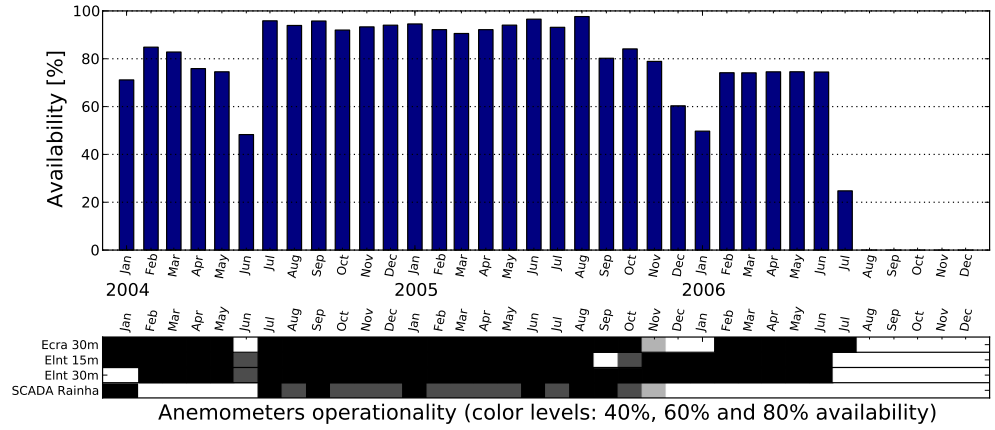

(b) Availability for Cabeço da Rainha wind farm.

Figure 4.10: Availability of the wind measurements and the turbines output power from the SCADA data. For each figure, the topmost plot is the percentage of valid data, for all the measurements combined. In the bottommost plot the availability is given for each dataset, using a colour code where black means $\geq$ 80%, dark grey for [60%, 80%[, light grey for [40%, 60%[and white for $<$ 40%.

were not used, as they may be unreliable due to the proximity to the turbine blades.

The uncertainty in the wind speed measurement was estimated for PORT071 (shown in Figure 4.9). This result was obtained considering a number of 300 samples for each integration time and a resolution of $0.05\,\mathrm{m\,s^{-1}}$. Additionally, the uncertainty given in the calibration certificate was $0.11\,\mathrm{m\,s^{-1}}$. Regarding the wind vanes, the equipment resolution is limited to 1°, with an accuracy of ±2°.

At Pinheiro there were also measurements of the atmospheric pressure, temperature and humidity. These were taken at one height only and for the purpose of computing the air density to estimate the wind energy potential. The density of humid air, ρ_h, was computed as:

$$\rho_h = \frac{p}{R_d\,T} + \frac{H_R\,p_{\mathrm{sat}}}{T}\left[\frac{1}{R_v} - \frac{1}{R_d}\right]\,,\; p_{\mathrm{sat}} = 611.2\,\exp\left(\frac{17.62\,T - 4812.903}{T - 30.03}\right)\,, \quad (4.11)$$

where R_d and R_v are the gas constants for dry air and water vapour, T the absolute temperature, p the atmospheric pressure, H_R the relative humidity and p_{sat} the saturation vapour pressure, computed following the recommendations in the WMO guide, Annex 4.B (WMO, 2008). The obtained air density was used to correct the power interpolated from the turbine power curve, by applying the expressions in §4.2.4.

Besides the error codes which were found within the datasets, the following conditions were used to discard outliers:

1. The time tag must be valid, unique throughout the whole series and must fall within evenly spaced intervals, defined by the integration time used.
2. The average wind magnitude must be higher than $0.3\,\mathrm{m\,s^{-1}}$ and lower than $99\,\mathrm{m\,s^{-1}}$. The lower limit is set because the anemometer may freeze during the winter.
3. If the minimum and maximum velocities were recorded, the following relation must hold: $\min(V) \leq \mathrm{mean}(V) \leq \max(V)$.
4. Negative power values were discarded, as these refer to situations where the wind turbines are out-of-operation, however their control mechanisms are consuming energy.
5. Besides the average power, the minimum and maximum values must be available. Thus the following relation must hold: $\min(P) \leq \mathrm{mean}(P) \leq \max(P)$.
6. If either $|\max(P) - \mathrm{mean}(P)|$ or $|\mathrm{mean}(P) - \min(P)|$ were higher than $1/3$ of the nominal power for that wind turbine, the record was discarded. This condition was used to filter situations where, under that integration time, the turbine was both operating and out-of-operation (due to the cut-off velocity being reached). This results in records which are outliers, as these are unable to be modelled by the power curve.
7. Only situations where all turbines were operational were considered. Records which did not met this criteria were discarded. A turbine which is out-of-operation is considered to be operational, *i.e.*, fully functional, even if its average power is zero.

Table 4.2: List of simulations performed to generate the Pinheiro transfer function, organized by direction classes. The direction of the wind set at the inlet is compared with the wind direction obtained at the locations of PORT071 and PORT214.

ϕ inlet (°)	3	40	62	90	110	148	180	217	245	270	295	339
ϕ PORT071 (°)	355	33	60	92	118	153	180	212	241	272	301	338
ϕ PORT214 (°)	358	36	60	92	115	151	177	214	244	273	299	338
Number simulations	4	4	7	5	5	7	8	4	7	7	4	5

The data availability for the Pinheiro and Cabeço da Rainha are displayed in Figures 4.10a and 4.10b with outliers removed, in addition to the error codes and data gaps.

The topographic and roughness maps were provided by the Institute of Mechanical Engineering and Industrial Management (INEGI). These were produced using data from the Army Geographic Institute (IGeoE), the Shuttle Radar Topography Mission project and the CORINE Land Cover 2000 project.

4.3.3 Numerical simulation results and generation of the transfer functions

To obtain a transfer function for Pinheiro wind farm, 67 simulations were produced. These spread over 12 sectors, covering a velocity range equal to the turbines operational range. For the set of simulations produced for each sector, a linear relation was observed between the velocities at the turbines and the reference location. This means that for a particular direction group d, composed of $s = 1, \ldots, Ns(d)$ simulations, the velocity at a turbine V_T can be approximated by $V_T(s) \approx a_1 V_R(s) + a_0$, where a_0 and a_1 are the coefficients of a 1st degree polynomial and V_R is the velocity at the reference location. This allowed the reduction of the number of velocity classes to simulate, resulting in a minimum of 4 simulations per sector. Figure 4.11 shows the squared correlation coeffi-

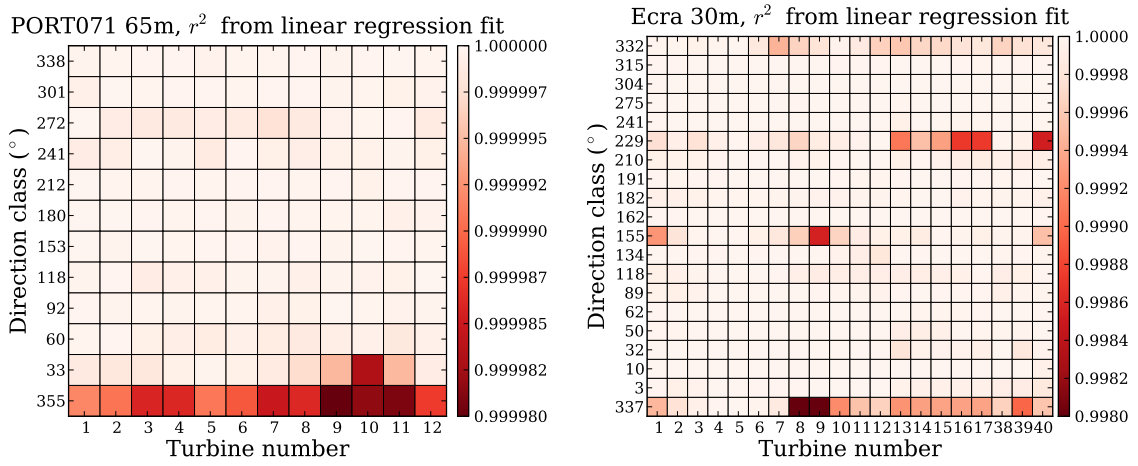

Figure 4.11: Linearity in the transfer functions. The contour field refers to the squared correlation coefficient, or coefficient of determination, r^2, between the velocities simulated at the reference location and at each turbine. This is presented for each turbine and direction class. *Left*: Pinheiro site using PORT071 as reference. *Right*: Cabeço da Rainha site using Ecra as reference.

Table 4.3: List of simulations performed to generate the Cabeço da Rainha transfer function, organized by direction classes. The direction of the wind set at the inlet is compared with the wind direction obtained at the locations of Ecra and Elon.

ϕ inlet (°)	8	17	31	45	56	62	77	93	117	149
ϕ Ecra (°)	337	3	10	32	50	62	89	118	134	155
ϕ Elon (°)	357	10	30	48	61	68	82	94	116	150
Number simulations	6	6	6	6	7	6	7	6	8	5
ϕ inlet (°)	180	202	211	225	236	241	260	281	297	333
ϕ Ecra (°)	162	182	191	210	229	241	275	304	315	332
ϕ Elon (°)	180	203	211	232	244	246	270	290	303	329
Number simulations	6	5	6	6	7	5	6	6	7	6

cient, r^2, as function of the turbine and direction sector. For all sectors and turbine sets, $r^2 > 0.99998$, hence the error of applying a 1^{st} degree polynomial is negligible. Table 4.2 shows the number of simulations per sector and the direction of the inlet flow.

In the case of Cabeço da Rainha, due to its complex topography 123 simulations were needed for its transfer function. Because the flow suffers severe changes with small rotations of the inlet flow direction, the number of directional sectors had to be increased to 20. Due to the extended operational range given by the Storm Control (up to 35 m s^{-1}), the minimum number of simulations per sector was 5. As shown in Figure 4.11, the linear relation found in Pinheiro results was also present, with $r^2 > 0.998$.

The majority of the simulations were performed with a steady state formulation, with the exception of sectors 149° and 333° in Cabeço da Rainha. For high speeds set at the inlet (speeds above 20 m s^{-1} at Ecra), no steady state solutions could be found for these azimuths. This further increased the computational cost of generating the transfer function. Although these simulations where unsteady, the fields where averaged after the simulation time was long enough for patterns in the velocity time series to repeat themselves, as displayed in Figure 4.12. The effect of these simulations on the linearity between velocities at the turbines and the reference location was negligible. These

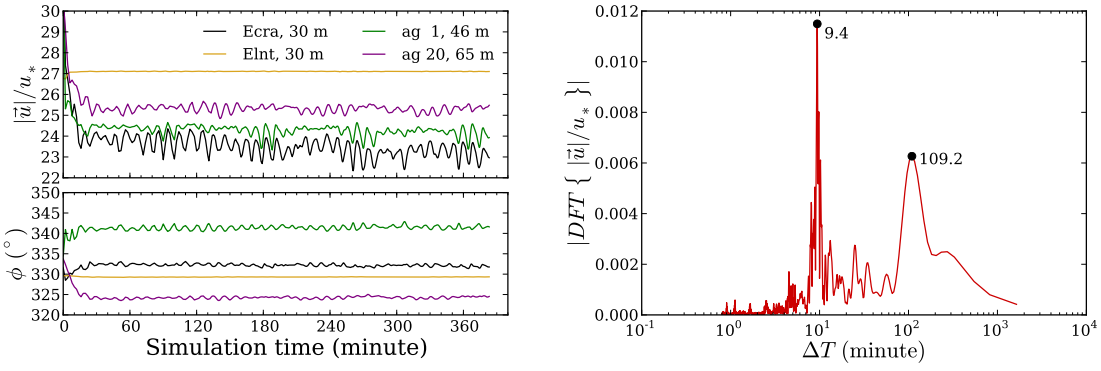

Figure 4.12: *Left*: time evolution of velocity magnitude and direction for unsteady simulations. *Right*: Discrete Fourier transform of the velocity magnitude signal from the reference location (Ecra), to identify the main frequencies.

sectors correspond to wind directions at Ecra of 155° and 332°. From Figure 4.11, the lowest values of r^2 are observed for 229° and 337°.

The simulations were produced on the NxPy cluster, an IBM eServer 1350 composed of 32 nodes. Each node has two Intel® Xeon® CPU at 3.00 GHz clock speed, with 2 MB cache and 64 bit instruction set. The compiler used was the Intel® Fortran Compiler 9.

4.3.3.1 Flow characteristics for the Pinheiro site

Figures 4.13 and 4.14 show contour maps from the velocity and turbulence kinetic energy fields, obtained from the available set of simulations. This is presented for each direction sector, normalizing the velocity field using the horizontal wind speed at the reference location. The turbulence intensity, TI, was estimated as:

$$\sigma_u \approx \sigma_v \approx \sigma_w \quad \Rightarrow \quad TI = \frac{\sigma_u}{V} \approx \frac{\sqrt{\frac{2}{3}k}}{V}, \tag{4.12}$$

where σ_u, σ_v and σ_w are the standard deviations for each component of the velocity vector, k is the turbulence kinetic energy and V is the average of horizontal wind speed.

Northern sectors [339°, 40°]

Both direction and velocity magnitude are the same on PORT071 as at the turbines. There are recirculation of the flow to the south of the wind farm, together with a large decrease of the velocity magnitude. The TI values are low in the wind farm area, close to 7%. The vertical component in the wind is also low, lesser than 5°.

Eastern sectors [62°, 110°]

The velocity at the turbines is higher than at PORT071, although the direction is the same. There are no recirculation zones upwind or downstream, except for the valley to the southeast which channels part of the flow through that direction. There is a gradual increase in TI as the flow direction becomes closer to the south, where there are values near 12%.

Southern sectors [148°, 217°]

The wind direction and speed are nearly the same in the turbines as in PORT071. There are no recirculation zones in the vicinity of the wind farm. TI decreases to values between 4% and 8%.

Western sectors [245°, 295°]

As the flow direction changes to 245°, large gradients in the wind speed are observed upstream, due to the valley located northwest from PORT071. The wind speed at the turbines is higher than at PORT071 by 1.2 times, There are several recirculation zones due to the valleys to the south and southeast from the park. Even so there are no noticeable differences in the wind direction on the plateau where the wind farm is installed.

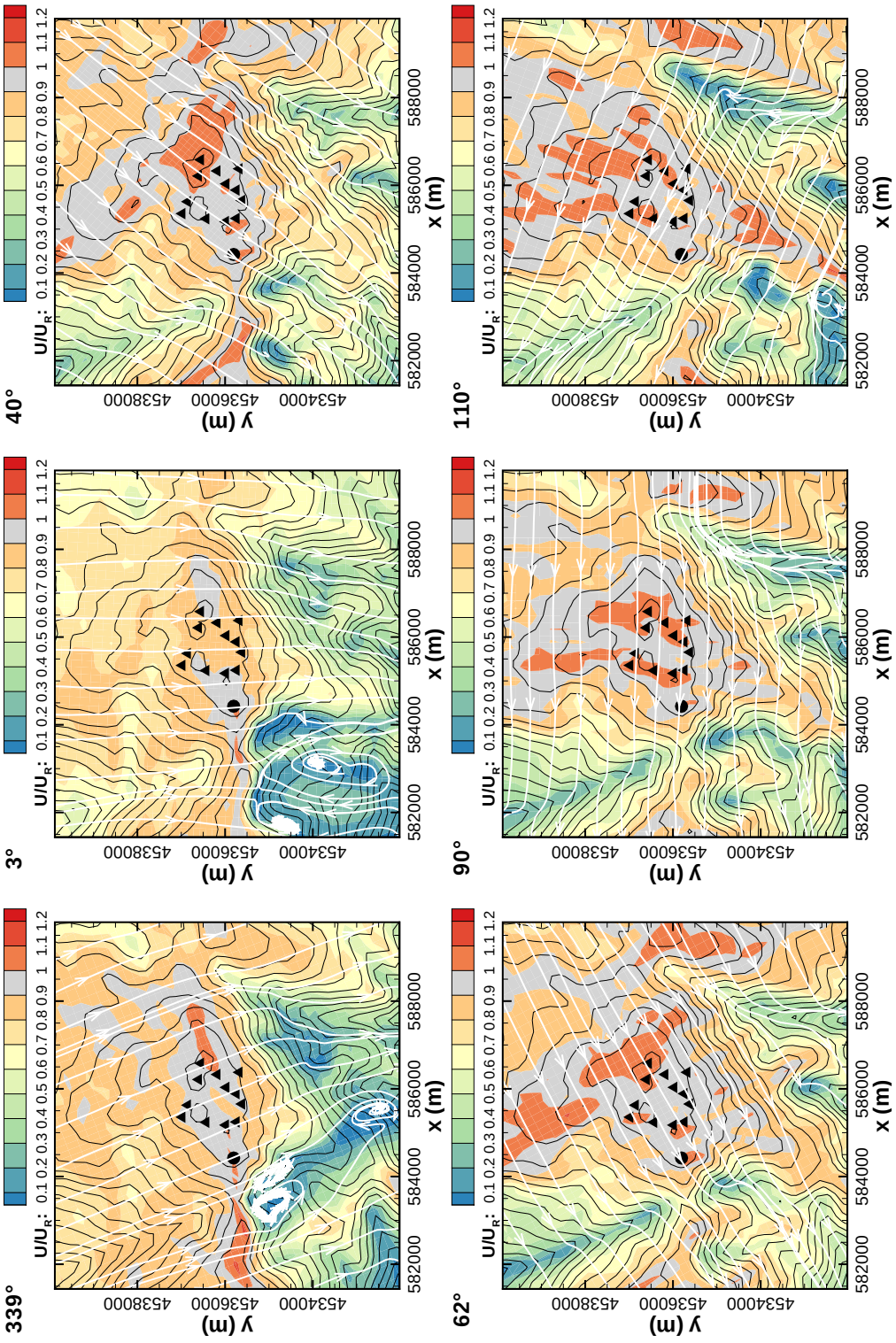

Figure 4.13: Flow maps for Pinheiro site. Contour of the horizontal velocity magnitude and streamlines, at 65 m height AGL. The velocity was normalized using the value at the reference mast, represented by the filled circle (●). The location of the turbines are represented by the black triangles (▲). The topography is represented by the contour lines, each spaced by 50 m.

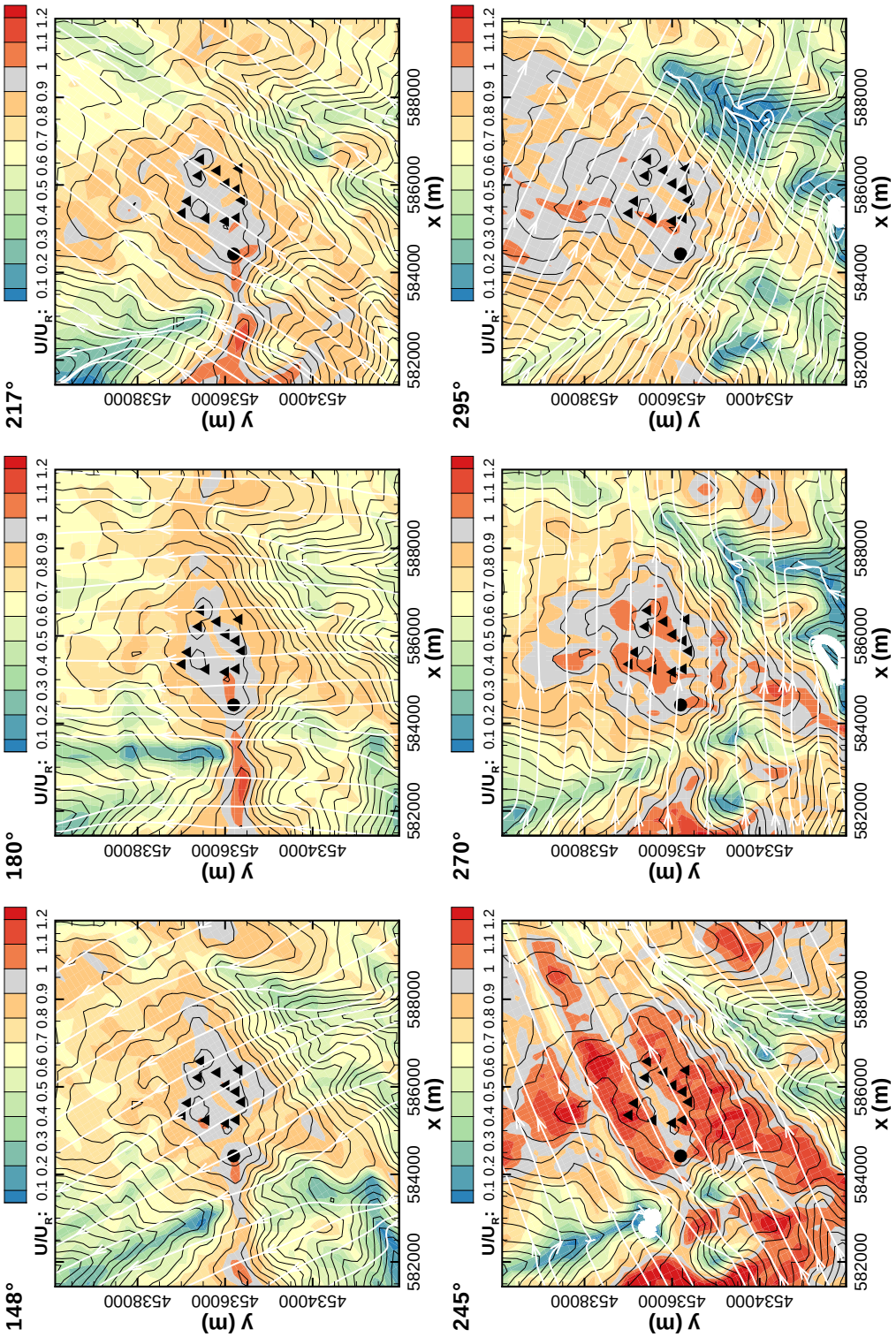

Figure 4.13: Flow maps for Pinheiro site (*continuation from page 117*).

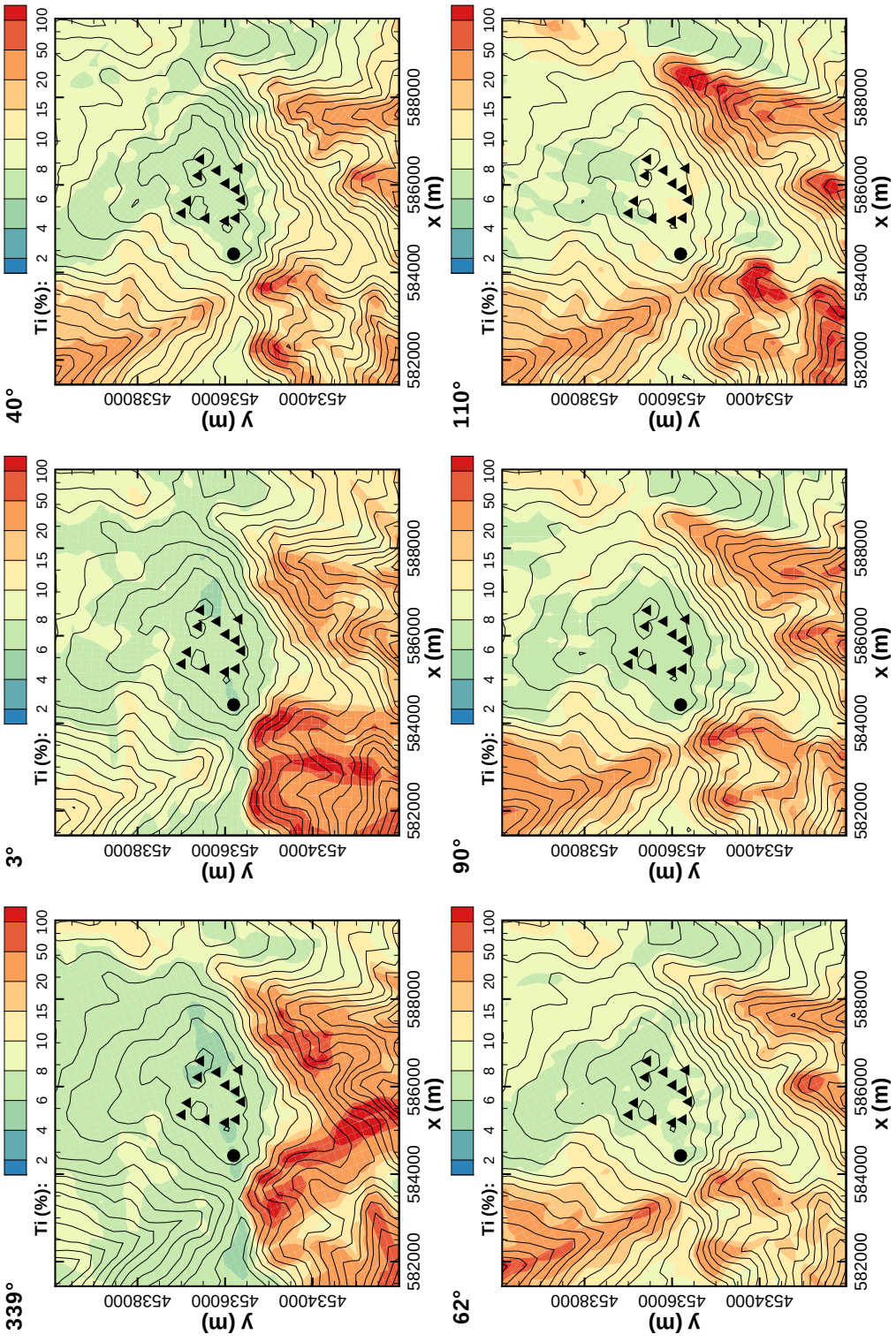

Figure 4.14: Turbulence maps for Pinheiro site. Turbulence intensity contours at 65 m height AGL. For a detailed description refer to Figure 4.13.

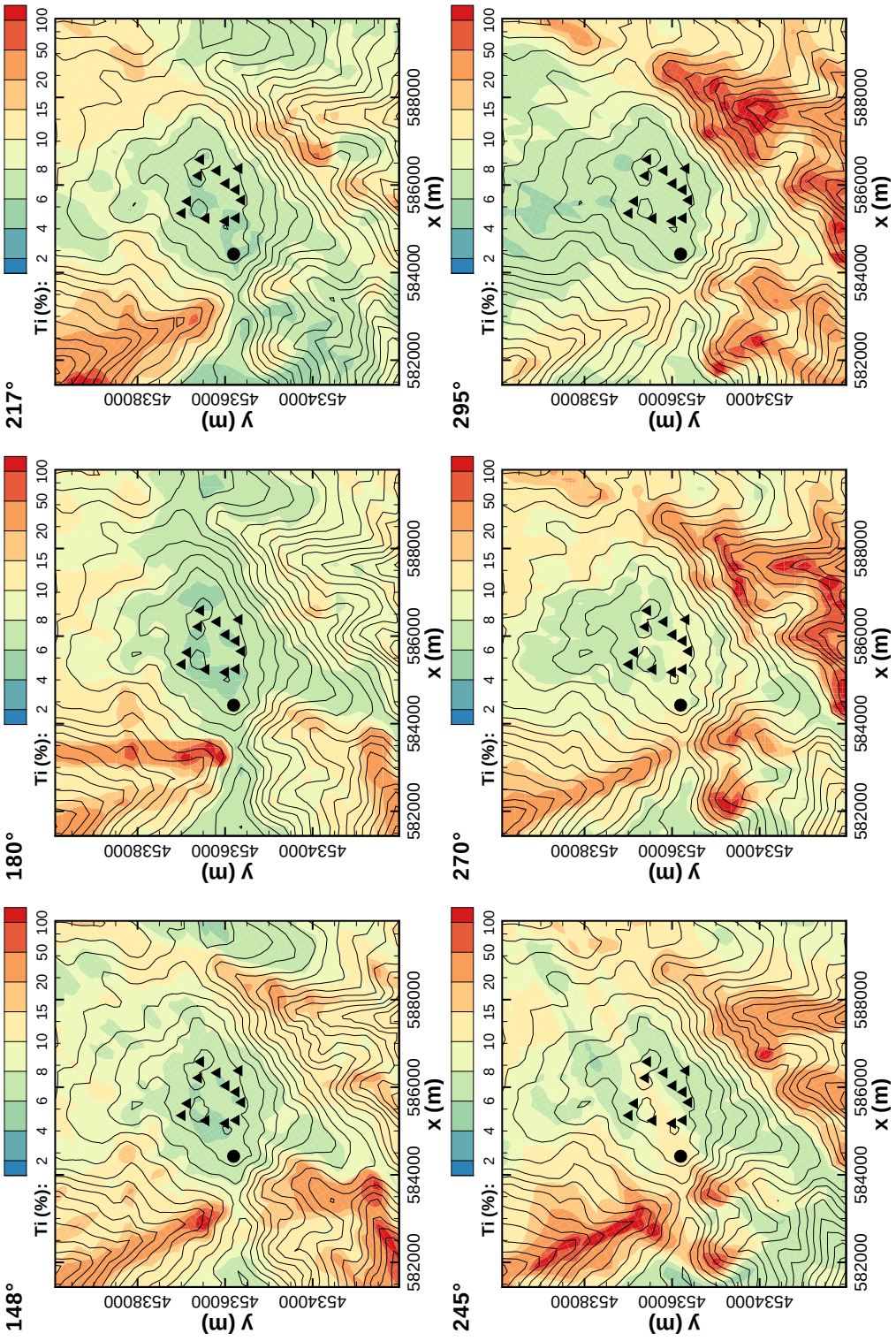

Figure 4.14: Turbulence maps for Pinheiro site. (*continuation from page 119*).

4.3.3.2 Flow characteristics for the Cabeço da Rainha site

Figures 4.15 and 4.16 show the wind flow field for the Cabeço da Rainha site Due to the increase in the number of directions from 12 to 20, these are grouped in a different order as some directional sectors have required more simulations than others.

Northern sectors [333°, 31°]

The upstream flow is characterized by large recirculating zones. These form on the valley at the north-northwest from the wind farm. The wind direction changes over the ridge where the turbines are, shifting to the west. The velocity is generally higher on some turbines than on Ecra, except for the eastern group where is 80% lower. The TI is around 10% on the ridge, increasing to $\sim$ 50% on the valleys in the vicinity.

Eastern sectors [45°, 117°]

The velocities at the eastern turbines are higher than the western group and Ecra. The wind direction is generally the same, despite few sudden changes. For northeast wind there is only one recirculation zone, between the eastern and western groups of turbines in the mountain pass. As the inlet wind direction shifts from the east to the south recirculation zones appear, both upwind and downstream. The TI near the turbines is low however, around 8%.

Southern sectors [149°, 217°]

The recirculation zones lie downstream of the turbines with severe changes in the wind direction. The wind at the eastern group of turbines is mainly influenced by the flow climbing from the valley northwest of the wind farm. This results in wind speeds lower for the eastern group than for Ecra and the western turbines. This also affects the values of TI which are higher in the eastern group.

Western sectors [225°, 297°]

The wind speeds are lower on the 2 MW turbines in the middle than on the remainder turbines and on Ecra, particularly for flow near 240°. There are no recirculation zones upstream and there are only few downstream, except for 297°. TI is also generally lower, below 8%.

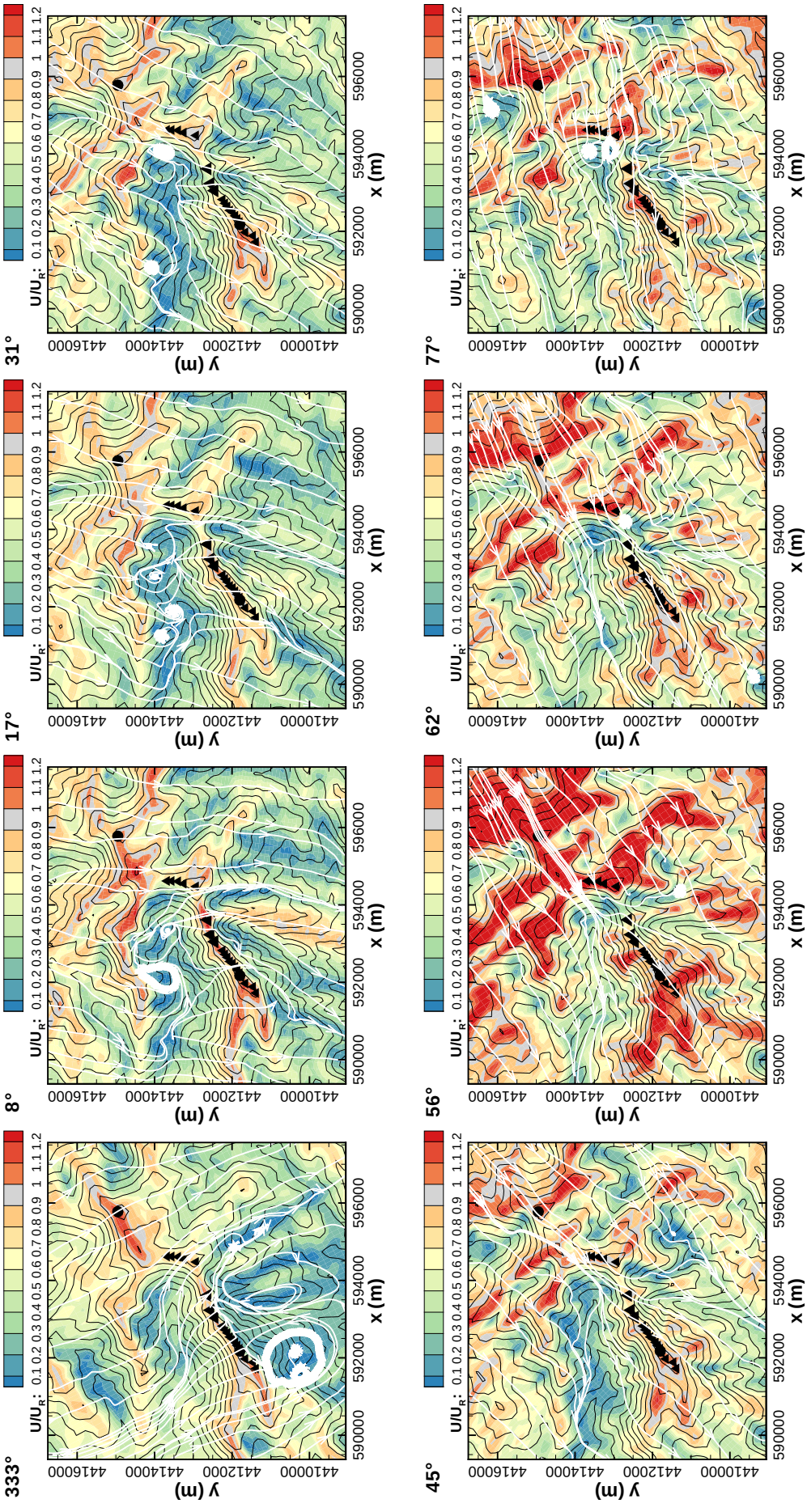

Figure 4.15: Flow maps for the Cabeço da Rainha site. Contour of the horizontal velocity magnitude and streamlines, at 30 m height AGL. The velocity was normalized using the value at the reference mast, represented by the filled circle (●). The location of the turbines are represented by the black triangles (▲). The topography is represented by the contour lines, each spaced by 50 m.

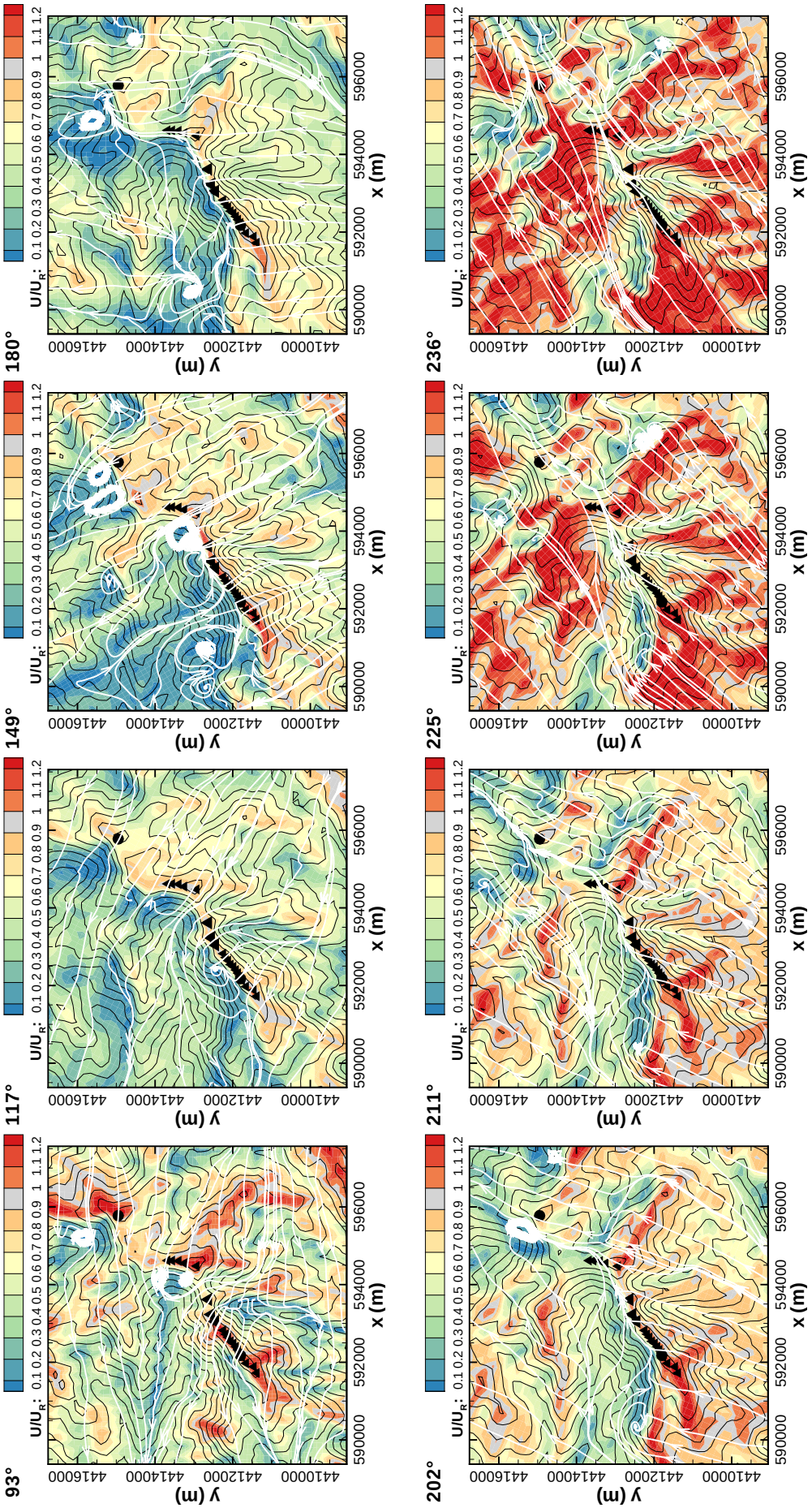

Figure 4.15: Flow maps for Cabeço da Rainha site (*continuation from page 122*).

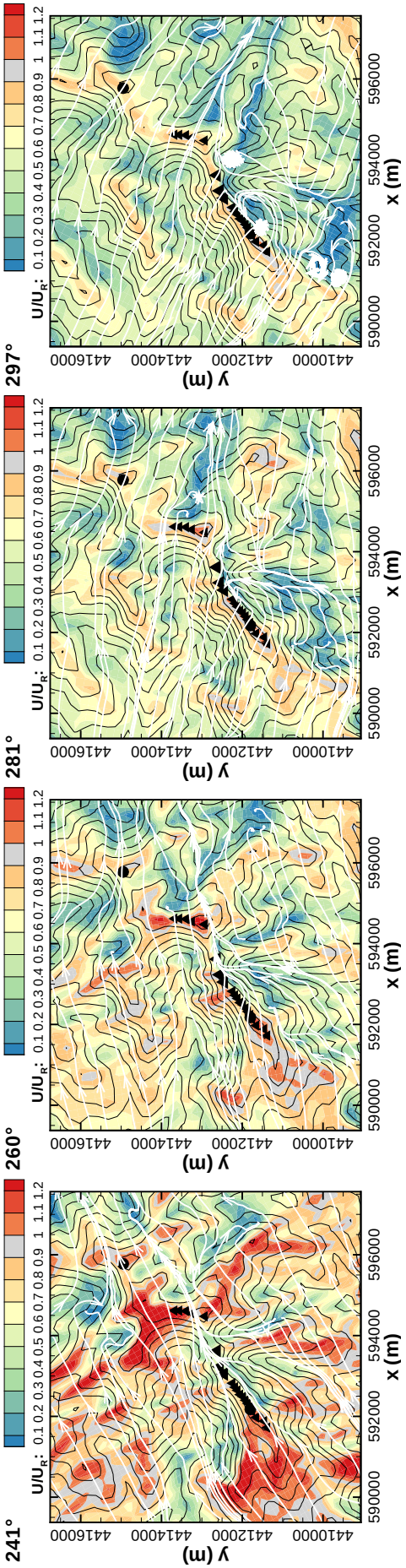

Figure 4.15: Flow maps for the Cabeço da Rainha site (*continuation from page 123*).

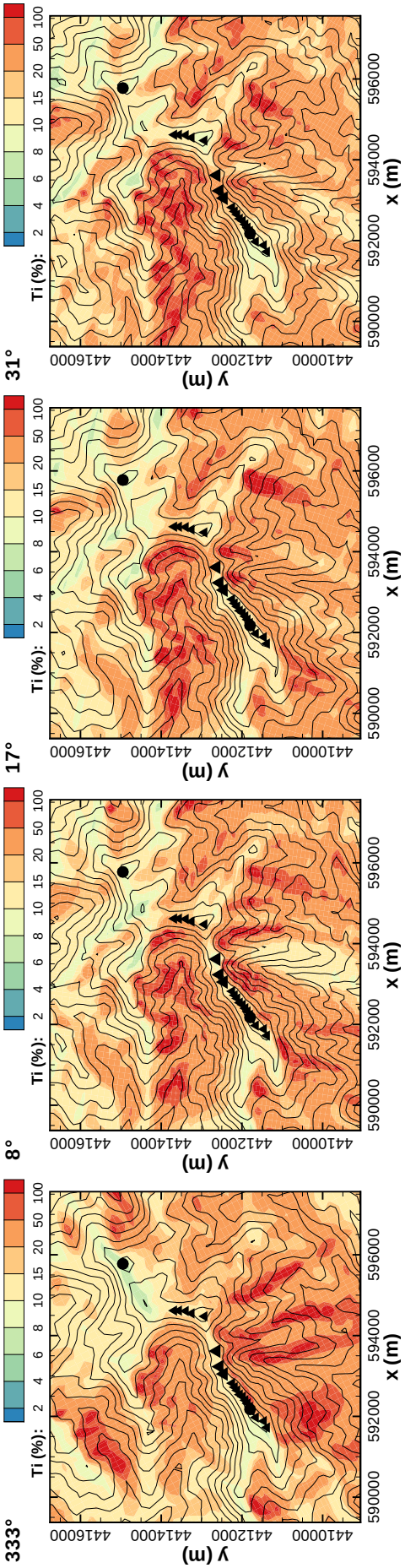

Figure 4.16: Turbulence maps for the Cabeço da Rainha site. Turbulence intensity contours at 30 m AGL. Refer to Figure 4.15 for a detailed description.

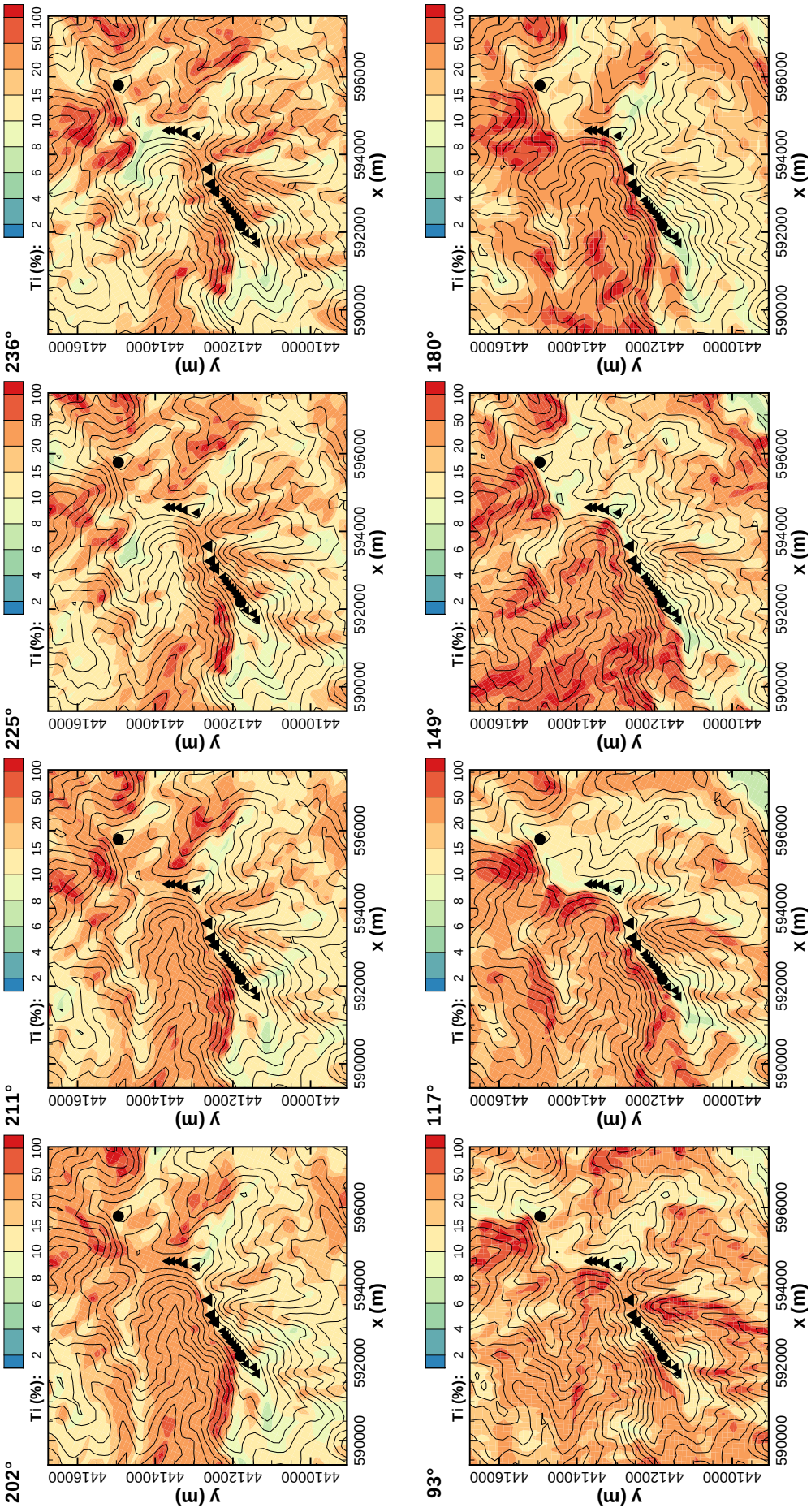

Figure 4.16: Turbulence maps for the Cabeço da Rainha site. (*continuation from page 124*).

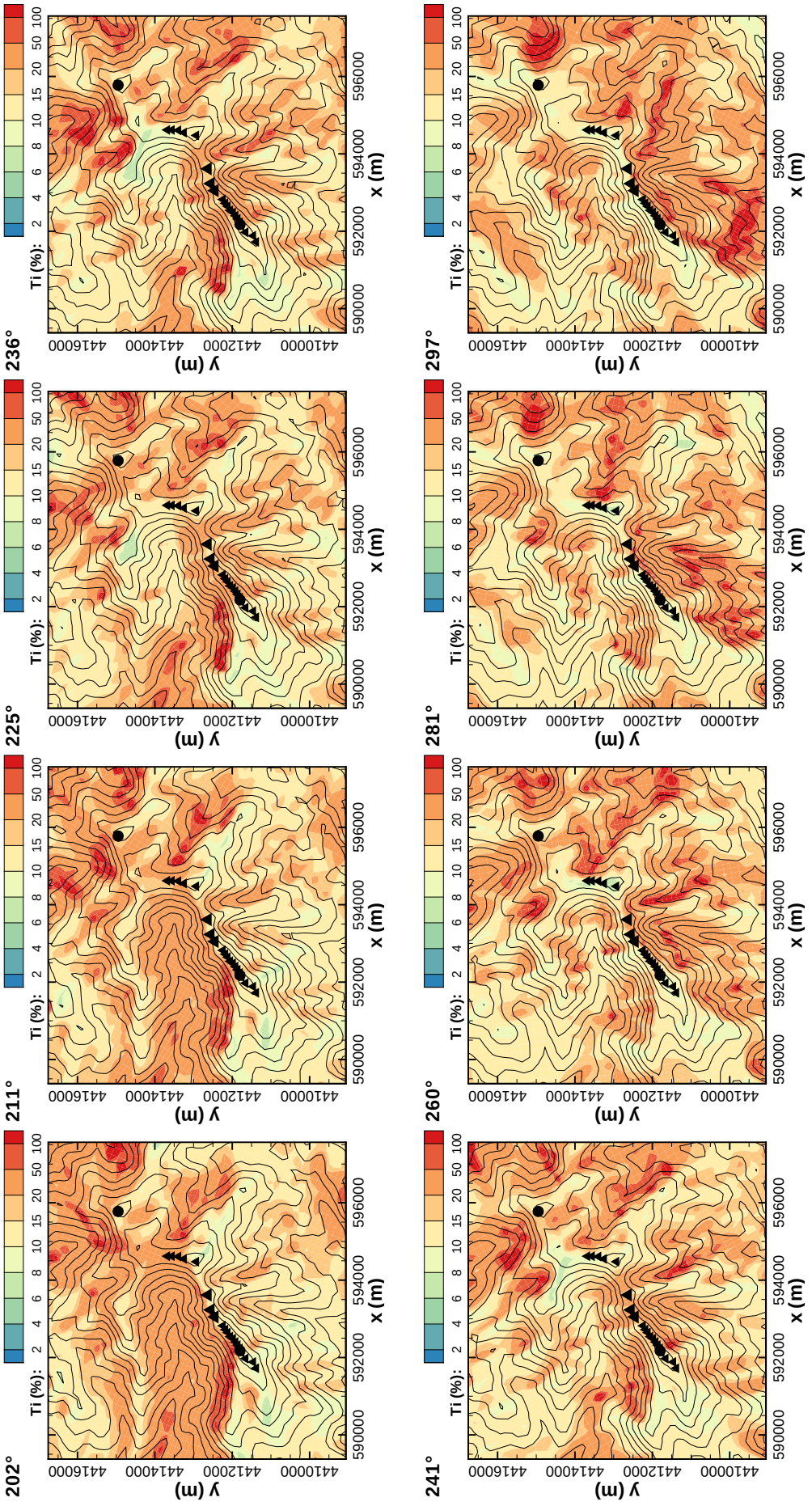

Figure 4.16: Turbulence maps for the Cabeço da Rainha site. (*continuation from page 125*).

4.3.3.3 Influence of thermal stratification

As referred in §4.2.1, from the available data it was not possible to obtain a measure for the atmospheric stability. To infer, although qualitatively, how strong were the effects due to stratification the measurements were separated into two datasets:

1. Summer day: the hours between 12:00 to 18:00 hours of the months between May to September. It is expected that most of these instances are related with a convective atmosphere.
2. Winter night: the hours between 00:00 to 06:00 hours of the months between November to March, thus the typical winter night. It is expected that these instances represent stably stratified conditions.

In Figure 4.17 the turbulence intensity, TI, is shown as function of the wind speed, as measured at PORT071 of Pinheiro. The information is displayed for four direction sectors, all for different quadrants. The raw data was grouped into $1\,\mathrm{m\,s^{-1}}$ bins. The data in each bin is displayed using box-plots (Tukey, 1977), showing the minimum, 25^{th} percentile, the median (black line), 75^{th} percentile and maximum values. Any record which its value is $3/2$ times above or below the interquartile range (length between the 75^{th} and 25^{th} percentiles) is deemed an outlier and dismissed from the sample. The average TI was computed for each bin, resulting in the green curve. This curve follows the median given by the box-plots, which may indicate small or no skewness. Additionally both the summer day and the winter night datasets are shown as the red and blue curves, respectively.

The TI results from the CFD for the several wind velocities simulated are presented for comparison, for the respective sector. Cup anemometers measure the magnitude of horizontal wind speed. Although not able to measure vertical components, these have some parasitic influence on the measurements (H. *et al.*, 2001). The variance of the wind speed is, thus, related to the magnitude of horizontal speed instead of a particular component. This makes it difficult to estimate how the measured variance relates to the numerical results in the CFD flow field. The standard way is to make TI to be representative of the longitudinal fluctuations, as given in eq. (4.12). Alternatively:

$$\begin{cases} \sigma_u^2 \approx \sigma_v^2 \approx \sigma_w^2 \\ \sigma_V^2 = \sigma_u^2 + \sigma_v^2 + \overline{u}^2 + \overline{v}^2 - \overline{V}^2 \approx \sigma_u^2 + \sigma_v^2 \end{cases} \quad \Rightarrow \quad 2\,k = \sigma_V^2 + \frac{\sigma_V^2}{2}\,,$$

$$\Rightarrow \quad TI = \frac{\sqrt{\frac{4}{3}\,k}}{V}\,, \tag{4.13}$$

obtained considering instead the fluctuation of the horizontal magnitude of velocity, V. Although it is difficult to pinpoint what should be the value of the variance measured by the anemometers, the value should lie between both of these measures. If the average of the lateral component, $\overline{v}$, was zero in the 10 minutes time span, then $\overline{u} \equiv \overline{V}$ and the measure in eq. (4.12) should correspond to the measurement. If instead both components are not null, $\overline{u}$ and $\overline{v}$, the measured variance may be given by eq. (4.13). As such, both values are shown in the plots as an horizontal grey patch. Although both CFD curves for TI were obtained for several wind speeds, the differences are negligible and the TI values lie on an horizontal line (*cf.* discussion in §4.2.1 and Figure 4.11).

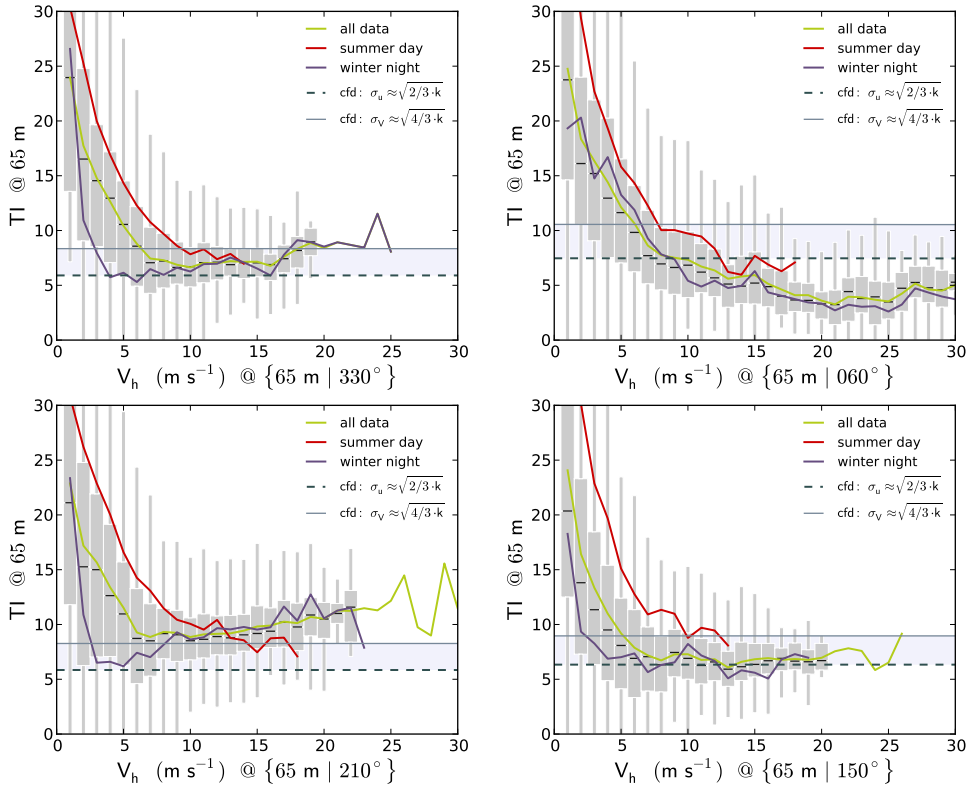

Figure 4.17: Turbulence intensity, TI, as function of the wind speed, from the PORT071 measurements at 65 m. The data is displayed using box-plots (see text). The TI average at each bin is shown by the green, red and blue lines for all data, the summer day and the winter night, respectively. Equivalent results from the CFD simulations are shown for comparison, given by the grey horizontal patch.

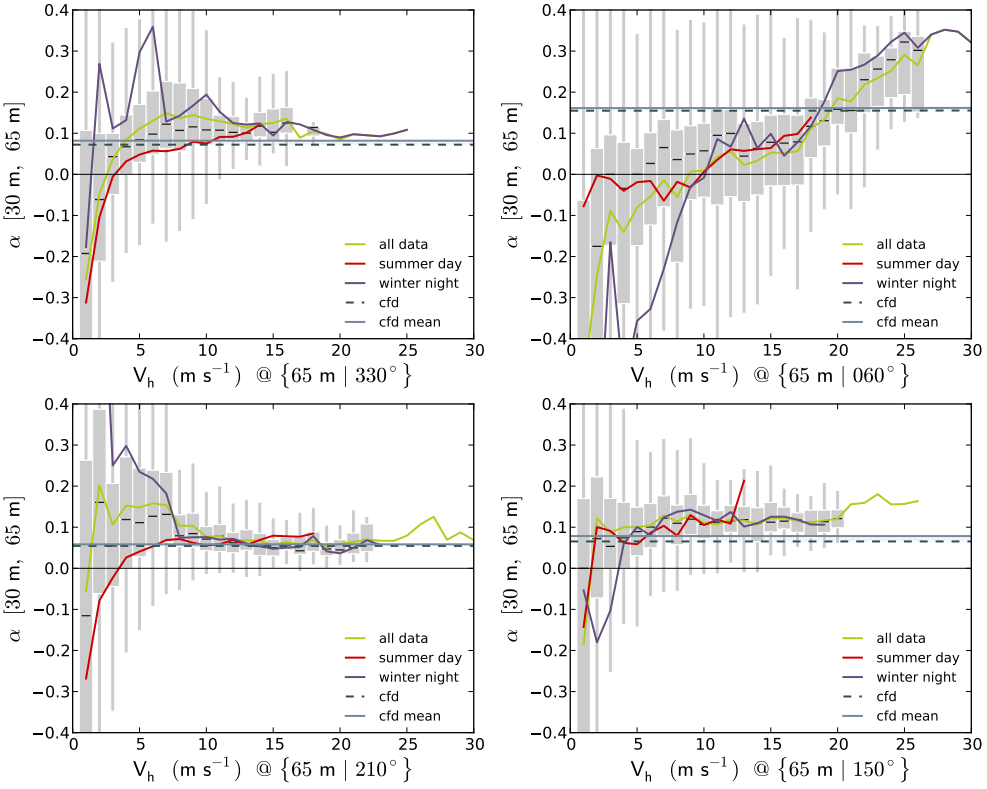

Figure 4.18: Shear factor, α, as function of the wind speed, from the PORT071. Computed using simultaneous data at 30 m and 65 m. For further details, refer to the caption of Fig. 4.17

For wind speeds above $\sim 7\,\mathrm{m\,s^{-1}}$ there is a good agreement between the CFD and the measurements. For high wind speeds there are less records available, thus the green, red and blue curves cease to be representative. The agreement is particularly good for 150° and 330° directions, which lie opposite to each other. For the 60° sector, the CFD results over-predict while for 210° these under-predict. The influence of stratification effects may be present when the blue and red curves detach from the mean value. This happens at speeds $< 7\,\mathrm{m\,s^{-1}}$, where the blue and red curves yield lower and higher values. While the green curve agrees with the median, the blue and red curves follow the 25^{th} and 75^{th} percentile. The first is consistent with the expected behaviour for a stable atmosphere, in which turbulence is damped, thus TI should be lower, whereas for the red curve the opposite happens, which is also consistent with what is expected in a convective surface layer. It may be concluded that, while for low wind speeds an influence from atmospheric stability is clear, for higher speeds the production of turbulence due to mechanical shear is higher, thus buoyancy effects are less discernible.

Figure 4.18 shows the same information, but for the shear factor, α, defined from the empirical power law for the wind profile as:

$$\frac{V(z_1)}{V(z_2)} = \left[\frac{z_1}{z_2}\right]^{\alpha} \quad \Rightarrow \quad \alpha = \frac{\ln\left(V(z_1)/V(z_2)\right)}{\ln\left(z_1/z_2\right)}\,, \tag{4.14}$$

where z_1 and z_2 are the two measurement heights at PORT071, 30 m and 65 m. Again, the measurements were divided into the summer day and winter night datasets. From the CFD results, two different measures of α were computed: (i) using the interpolated values at both heights and (ii) by averaging the shear factors found between those heights. The differences between these measures are small. The best agreement is found for the 210° sector, whilst for 150° and 330° the results are also good. The wind speed at which the measurements and the curves stabilize are lower than for the TI plot, around $5\,\mathrm{m\,s^{-1}}$. The 60° sector presents a continuous increase of α with the wind speed, not reproduced by the numerical results. For low wind speeds, while the summer day curve is closer to zero, mostly beneath the green curve, the opposite is verified for the winter night dataset. This is not discernible, however, for the 60° and 150° sectors. This behaviour agrees with the shape of the velocity profiles expected for convective and stable boundary-layers. Lower values for α agree with low values for the shape factor, thus flatter profiles, common of turbulent boundary-layers. For the winter night data, the values for α are higher, indicating that the wind gradient is higher. In a high stably-stratified situation, turbulence would be damped so much that the wind profile could resemble the one of a laminar boundary-layer. For very low wind speeds, $< 3\,\mathrm{m\,s^{-1}}$, a high number of occurrences of negative shear factors are observed, indicating that there is a speed-up of the wind profile. However, this does not indicates any presence of nocturnal low-level jets, as it is the summer day dataset which presents more negative α.

This information was not produced for Cabeço da Rainha as the variance of the wind speed was lacking in the measurements. Although the Lontreira mast had two heights of measurements, these were very close to the ground (15 m and 30 m). This resulted in negative shear factors for all directions, which the numerical simulations were not able to replicate.

4.3.4 Assessment of the error in the transfer functions

When transfer functions are used to translate a weather forecast into the power output of a wind farm, through the method described in §4.2, three sources of error can be distinguished:

1. The weather forecast at the reference location.
2. The transfer function, *i.e.*, the CFD velocity fields.
3. The conversion from velocity to the power output through the power curve.

Regarding the last two sources, there was no way to separate them. Wind velocity measurements at the turbine locations would be needed and nacelle anemometers are not reliable for this purpose. The presence of the mere turbine itself perturbs the velocity field, whereas such a measurement of velocity, if made, should be free of both downstream and upstream influences from the turbine.

It was possible, however, to separate the error introduced by the weather forecast by instead using the velocity measured at the reference mast. In essence, this represents what the method would return if the NWP forecast at the reference location was perfect, *i.e.*, error free. Albeit this *ideal forecast* is not a forecast itself, it serves as a way to evaluate the transfer function quality.

4.3.4.1 Definition of error measures

The indicators used to assess the error are defined in this section. Although some of the names vary throughout the literature, these are well known quantities and their definitions may be found in works such as Gyalistras (2003) or Madsen *et al.* (2005). In the following equations, the quantities F and M respectively refer to a forecast and a measured value of some quantity, the later taken as the true value. As both are given as a time series, F and M are function of a discrete time array, t, such that t_n, $n = 1, \ldots, N_t$. Both the forecast and the measurement are thus referenced to each instant t_n, $F_n = F(t_n)$ and $M_n = M(t_n)$. The absolute and relative errors, EA and ER, may be defined for each index n as:

$$\mathrm{EA}_n = F_n - M_n \,, \tag{4.15}$$

$$\mathrm{ER}_n = \frac{F_n}{M_n} - 1 \,, \quad M_n > 0 \,. \tag{4.16}$$

With this definition for both errors, a positive value indicates that the forecast is over-predicting the observation and otherwise for a negative value.

From the absolute error, the following measures may be defined:

$$\mathrm{BIAS} = \frac{1}{N_t}\sum_{n=1}^{N_t} \mathrm{EA}_n \,, \quad \mathrm{MAE} = \frac{1}{N_t}\sum_{n=1}^{N_t} |\mathrm{EA}_n| \,, \quad \mathrm{MSE} = \frac{1}{N_t}\sum_{n=1}^{N_t} \mathrm{EA}_n^2 \,. \tag{4.17}$$

The BIAS is a signed quantity, indicating if a forecast consistently is over or under-predicting on average. The other quantities are the Mean Averaged Error (MAE) and

the Mean Squared Error (MSE). While the BIAS and MAE have the same units as M and F, the MSE has these squared.

Similar quantities may be defined for the relative error:

$$\text{RBIAS} = \frac{1}{N_t}\sum_{n=1}^{N_t}\text{ER}_n\,, \quad \text{MRE} = \frac{1}{N_t}\sum_{n=1}^{N_t}|\text{ER}_n|\,, \quad \text{MSRE} = \frac{1}{N_t}\sum_{n=1}^{N_t}\text{ER}_n^2\,, \tag{4.18}$$

where MRE is the Mean Relative Error, MSRE is the Mean Squared Relative Error and RBIAS stands for relative bias. These quantities are dimensionless, usually given as a percentage. As they are based on ER and this is normalized by M_n, a higher weight is given when M_n is small. This may be undesirable if one is more concerned about the error values when F_n and M_n are high. This is the case when computing the error in a wind power prediction, *e.g.*, for a 2 MW turbine, an error of 200% in a power forecast when $M_n = 20\,\text{kW}$ corresponds to an over-prediction by 40 kW, which is much less important than an error of 25% when $M_n = 1600\,\text{kW}$, as it corresponds to an over-prediction by 400 kW. To remove some of the effect due to small values of M, instead of computing ER for $M > 0$, a threshold was defined such that $M >$ threshold. This threshold is chosen as a fraction of some known quantity, such as the nominal power of a turbine.

Another way is to use the absolute measures, BIAS, MAE and MSE, as these weight in equal form all the values of M and F. To present them in a dimensionless form, they may be normalized using some known quantity, *e.g.*, for wind power, the turbine nominal power. If the quantity is such that a value is difficult to prescribe, the mean value of the time series or the range between maximum and minimum may be used. Additionally to the measures in eqs. 4.17 and 4.18, the square root of the MSE and MSRE is widely used:

$$\text{RMSE} = \sqrt{\text{MSE}}\,, \quad \text{RMSRE} = \sqrt{\text{MSRE}}\,, \tag{4.19}$$

where RMSE is the Root Mean Squared Error and RMSRE is the Root Mean Squared Relative Error.

When a forecast of M is produced by two different models, thus yielding two forecast values, the Skill Score (SS) may be used to estimate the improvement of one forecast over another (Murphy, 1988). Choosing one of the forecasts as the reference one, R, the improvement of the second one, F, over R is given by:

$$\text{SS} = 1 - \frac{\text{MSE}_F}{\text{MSE}_R}\,, \quad \text{MSE}_R > 0\,, \tag{4.20}$$

where MSE_F and MSE_R are the Mean Squared Error for F ans R, respectively. This quantity is dimensionless and varies between $-\infty$ and 1. For $\text{SS} < 0$, the forecast F is worse than R and brings no improvement. For $0 < \text{SS} < 1$ the error returned by forecast F is lower than R. If $\text{SS} = 1$ then F is perfect and equal to M. Conversely if $\text{SS} = -\infty$, it is R which is perfect. Although the MSE is the measure commonly used to define the SS, any of the following may be employed instead: MAE, RMSE, MRE, MSRE and RMSRE.

4.3.4.2 Quality of Pinheiro transfer function

In Figure 4.19 are presented polar contour plots for each error measure. As for a wind rose, these are a representation of a quantity, such as the MAE, as function of wind direction (angular axis) and of the wind speed (radial direction). This kind of plot allows to visualize and identify directions and wind speed ranges where errors are higher. Additionally, the number of records was also displayed on Figure 4.19, as this quantity is important to define how much samples were used to compute the errors (BIAS, MAE, RBIAS and MRE). These indicators were computed using the available data from April 2005 to April 2006. This time span was chosen in order to have the maximum amount of continuous data, in a yearly basis, such that the results are representative of a typical year. The month of April was chosen, as the beginning of 2005 has few data on PORT071.

The indicators based on the absolute error were normalized using the wind farm nominal power, Pn, while the ones based on the relative error only consider values where the measurements are $> 5\%$ than the nominal power for the respective turbine. The BIAS is generally low, with absolute values below 5%. For wind speeds at PORT071, V_{71}, between 10 to 16 $\mathrm{m\,s^{-1}}$, there is an increase, generally over-predicting by $20\% \sim 30\%$ for sectors 30° to 150°. This is also shown in the MAE, the later having higher values as it is computed using the square of the differences. For these direction at PORT071, flow maps in Figure 4.15 show few differences between V_{71} and the velocity at the turbines. From the turbine power curve (Figure 4.6), these wind speeds correspond to the zone where the power output approaches its nominal value. Thus, this error may be either to a discrepancy in the power curve, an over-prediction of the wind speed which reflects on the predicted power, or both. From the RBIAS rose the same errors are much higher, 60%, which corresponds to a low value for the measured power. For directions between 180° to 330° the error is lower, with some under-prediction on the north sector.

For $V_{71} > 25\,\mathrm{m\,s^{-1}}$, cut-off effects start and the error increases. From the BIAS, the power is being under-predicted. Turbines that the method considers to be out-of-operation, were still operating. This is associated with the power curve and the difficulty in correctly identify the turbine operational status. These under-predictions are as high as 90%, meaning that the whole park is still operating even for $V_{71} > 25\,\mathrm{m\,s^{-1}}$. These are also zones with very few records (below 10), which hinder the quantification of the error.

The general behaviour is that the power is over-predicted for velocities above $10\,\mathrm{m\,s^{-1}}$, while under-predicting at lower speeds. These velocities correspond to the zone in the power curve where turbine power goes from 0 to its nominal value. In this zone the slope of the power curve is $200\,\mathrm{kJ\,m^{-1}}$. This change of sign in the RBIAS may be due to the slope of the real power curve being less steep than of the manufacturer's curve. Due to the impossibility to measure an unperturbed free wind speed, this hypothesis cannot be tested.

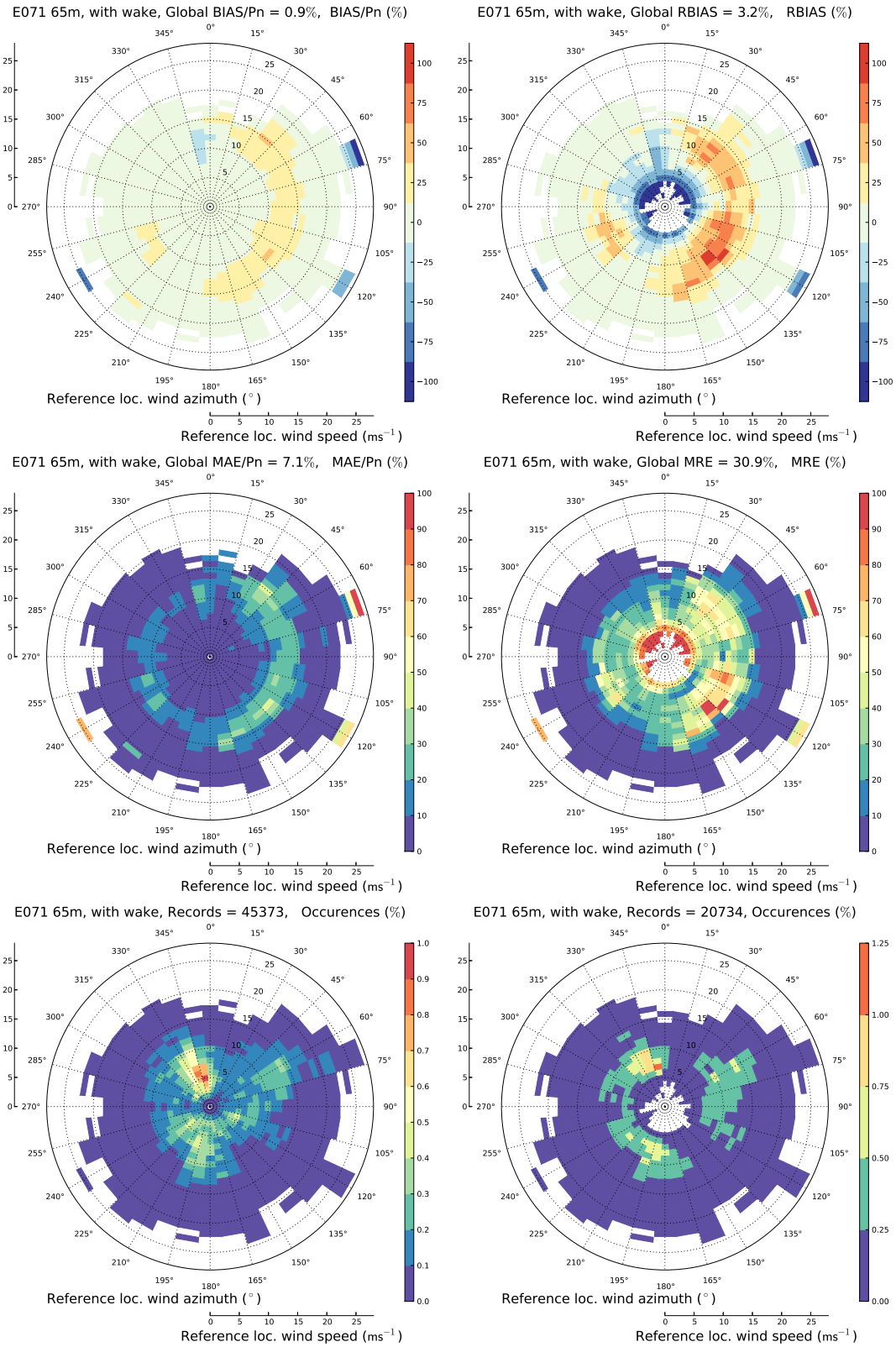

Figure 4.19: Wind power error roses for Pinheiro wind farm, using the velocity measured in the PORT071 mast (ideal forecast) in order to evaluate only the transfer function quality. The quantities are displayed for each class of velocity and direction. The relative error was computed for values where $P > 0.05\,\mathrm{Pn}_t$, using the nominal turbine power, Pn_t. *Left column*: BIAS and the MAE, normalized by the wind farm nominal power Pn. *Right column*: measures based on the relative error, RBIAS and MRE. *Bottom line*: number of records and occurrence frequency.

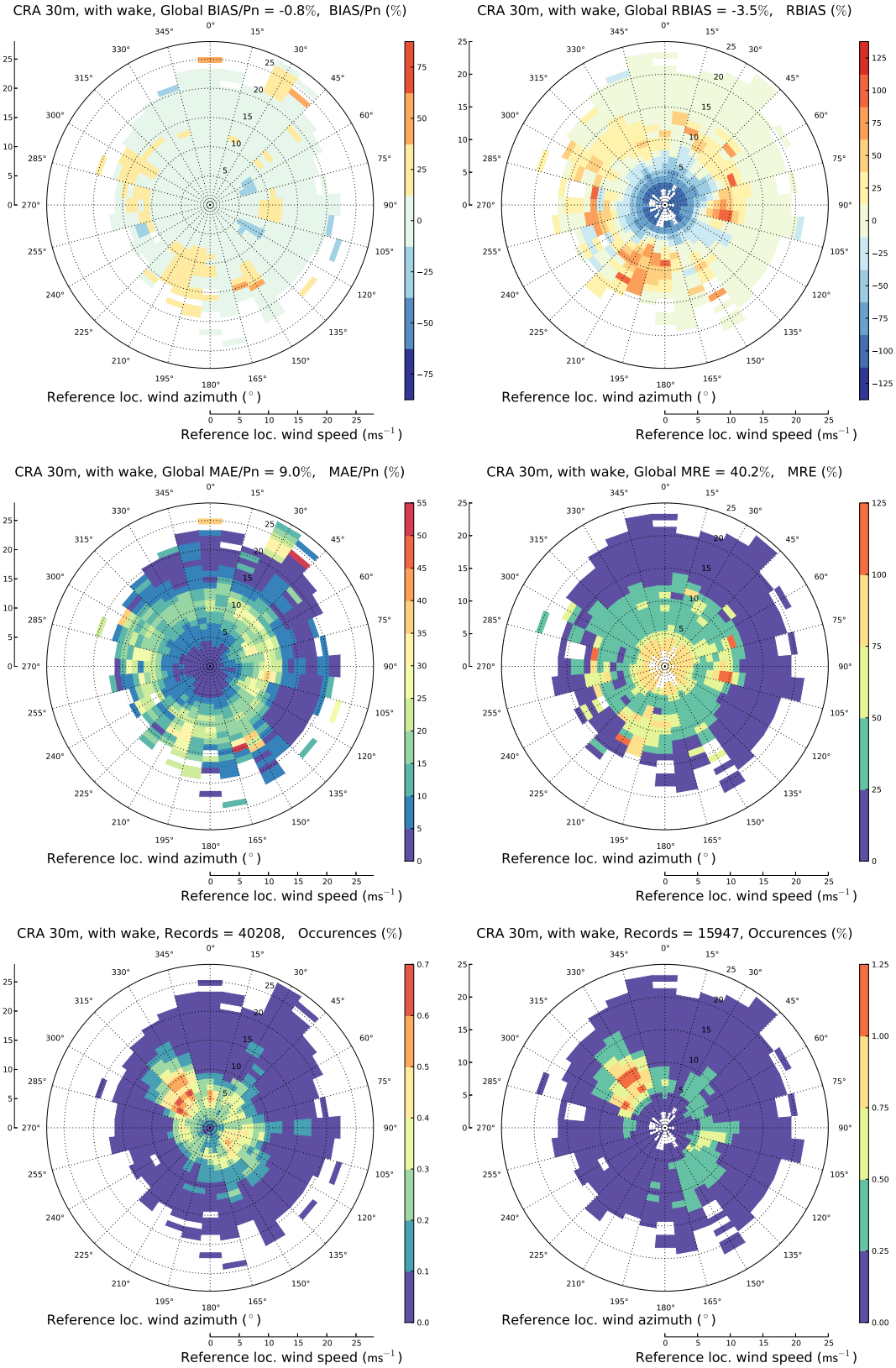

Figure 4.20: Wind power error roses for Cabeço da Rainha wind farm, using the velocity measured in the Ecra mast (ideal forecast), in order to evaluate only the transfer function quality. For a detailed description refer to Figure 4.19.

Table 4.4: Number of turbines under wake effects per directional sector.

	0°	30°	60°	90°	120°	150°	180°	210°	240°	270°	300°	330°
Pinheiro	7	7	4	7	5	5	7	6	5	6	7	8
Rainha	4	16	14	2	0	0	6	8	19	15	2	0

4.3.4.3 Quality of Cabeço da Rainha transfer function

For Cabeço da Rainha the error roses plots are shown in Figure 4.20. These refer to the transfer function generated for the location of mast Ecra, using the available data from October 2004 to October 2005.

The conclusions are similar to the ones found for Pinheiro. For wind speeds at Ecra, V_{cra}, between 7 to 13 m s^{-1} the MAE is 20%. The BIAS and RBIAS show that for $V_{cra} < 8$ m s^{-1} the method consistently under-predicts the power. For the 120° the negative bias persists up to 15 m s^{-1}. In the remaining sectors, the RBIAS changes and consistently over-predicts. Unlike the Pinheiro site, the flow field is much more complex. Small changes in the flow direction have yielded considerable differences in the flow field. From Figure 4.15, V_{cra} is generally lower than the velocities at the turbines, particularly for 50°–90° and 150°–260°. This, together with the power curve for the seventeen E40 turbines, whose slope is steeper, shifts the under and over-prediction power mismatch to lower speeds.

The 150° and 330° sectors required transient simulations, due to lack of convergence for steady RaNS formulation. While the first presents higher MAE and a positive BIAS, the later present lower errors and no significant BIAS.

Cut-off effects exist for wind speeds higher than 20 m s^{-1}, albeit lower than the ones verified in Pinheiro. Firstly, this is due to the storm control mechanism which maintains the seventeen E40 turbines operating, representing 63% of the wind farm nominal power. Secondly, most of the records which present cut-off effects were successfully marked as outlier, by the filter number 6 (§4.3.2, p. 113). Without this condition, the three E66 turbines would return high under-predictions corresponding to 6 MW, 30% of the farm power.

4.3.4.4 Quantification of the improvement gained from the wake model

To know if the wake model introduces improvements and to quantify these, error roses were computed for the original transfer functions without the wake model. The skill score was used to quantify this and the improvement is shown on Figure 4.21.

For the Pinheiro site the results are good. Although the model does not introduces drastic changes, there are several regions where the improvement is above 20%. Up to 7 m s^{-1} the wake model brings no improvement. Although the SS values are mostly above -0.1, at these wind speeds there are several events where turbines are outputting energy but both the model and the nacelle anemometer indicate otherwise. Without further data it is impossible to check if these events are outliers. For speeds around 10 m s^{-1} there is a clear improvement, except for the 210° and 330° sectors. The later

is the sector with more turbines perturbed by wake effects, as shown in Table 4.4. At speeds higher than 15 m s^{-1} the improvement becomes zero.

For Cabeço da Rainha the improvement is much lower. This is expected as the layout of the park is such that wake effects are mainly present in two groups of sectors: [30°, 60°] and [240°, 270°]. According to Table 4.4, these are the ones with most affected turbines. The [180°, 240°] sectors also present wake effects due to the eastern group of turbines (*cf.* Figure 4.8b). From Figure 4.21 these are also the directions where the improvement is higher reaching values above 60% for southwest winds. These sectors also have events where the wake model performs worse, at high wind speeds. From Figure 4.15, the bins where SS < 0 are also characterized by a RBIAS < 0. From the results without wake model (which show also a RBIAS < 0), it was concluded that the real power for some turbines was already at their nominal value, while the predictions were lagging behind, still returning values on the ascending zone of the power curve. The remaining sectors have less than 20% of perturbed turbines and some of the patches where SS < 0 are merely small discrepancies.

Summarizing the several situations that were found in the results:

1. Wake effects on a turbine are characterized by a velocity deficit, as expected.

2. For a given velocity at the reference mast, if the measured power at the turbine was higher than the prediction without the wake model, then there will be more error with the wake model.

3. If the slope of the real power curve is less steep than the manufacturer's power curve, then there will be a zone of low wind speeds of BIAS < 0, followed by another zone with BIAS > 0. Thus, it is expected that the wake model performs worse for the BIAS < 0 zone and yields improvements when BIAS > 0.

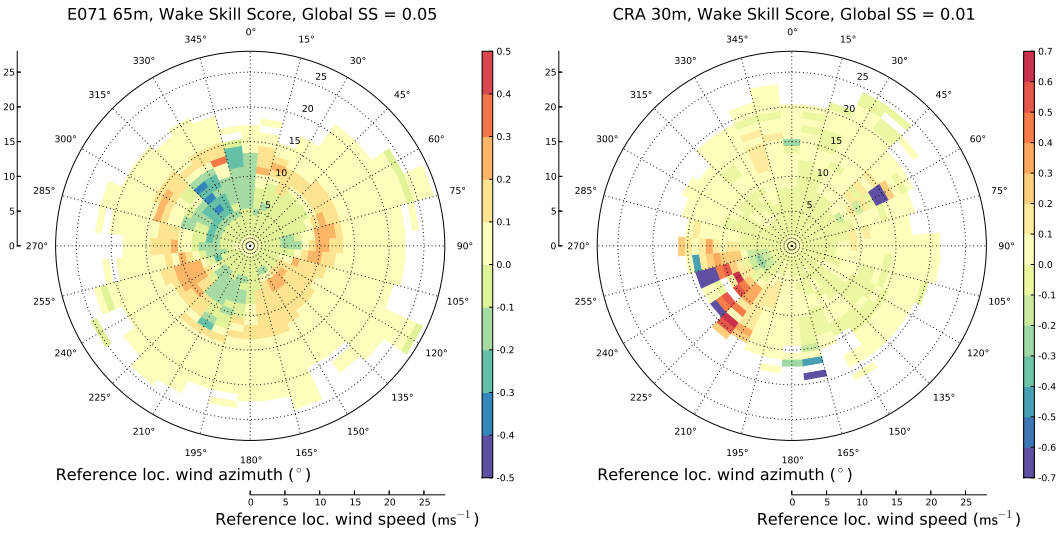

Figure 4.21: Rose with the improvement given by the wake model, evaluated using the skill score of the mean squared error. *Left*: Pinheiro wind farm, PORT071. *Right*: Cabeço da Rainha wind farm, Ecra.

Table 4.5: Assessment of the quality of the transfer functions using the time series at the reference mast (*ideal forecast*), to predict wind power. The BIAS, MAE and RMSE were normalized using the wind farm nominal power. The RBIAS, MRE and RMSRE were computed for values where the measured power was above 1% of the nominal power of the wind turbines. The skill score, SS, is used to show the improvement obtained from the wake model.

	BIAS	MAE	RMSE	RBIAS	MRE	RMSRE	SS wake
Pinheiro, no wake	1.9%	7.2%	12.4%	8.5%	31.7%	45.2%	
Pinheiro, wake	0.9%	7.1%	12.1%	3.2%	30.9%	43.2%	0.05
Rainha, no wake	−0.4%	9.1%	14.8%	−1.6%	40.6%	58.4%	
Rainha, wake	−0.8%	9.0%	14.7%	−3.5%	40.2%	57.3%	0.01

4. As the turbine reaches its nominal power the differences in velocity become unimportant, because the power output remains the same.
5. For a turbine near the cut-off, this velocity deficit may result in a delay, *i.e.*, if there was no wake effect the turbine would be out-of-operation. This may lead to errors if the turbine has been cut-off in the measurements, but not in the prediction.

4.3.4.5 Global errors in the power prediction using transfer functions

Table 4.5 presents the global errors for the power prediction of both wind farms, with and without wake model, using the reference mast measurements as input to the transfer functions. Pinheiro wind farm has lower errors and higher improvements with the inclusion of the wake model. This is justified by the lower complexity of the flow field and the layout of the turbines, where for all directions there are turbines under wake effects. The BIAS is reduced by 1% with the inclusion of the wake model, although this is less noticeable for both MAE and RMSE, with 7% and 12% of error.

For Cabeço da Rainha the error is higher. This is due to the complex topography and flow, which results in a higher sensitivity to wind direction. Despite this and the lower impact of the wake model (SS = 1%), all of the error values decrease with the inclusion of the wake, except the BIAS and the RBIAS. The later increases in magnitude by 2%. This may be explained by the effect that the wake model has on the velocities. At low measured speeds the wake model is increasing under-predictions, reflecting on these values for the RBIAS.

4.4 Power prediction from weather forecasts using transfer functions

4.4.1 Description of the weather forecast time series

The weather forecasts were produced by the Centre of Geophysics of the University of Lisbon at Geophysical Institute of Infante D. Luiz (CGUL/IDL). The results were provided as time series of the wind characteristics at the mast locations of both wind farms. These cover the year 2005 and part of 2006 (May to December), with a NWP run

available for each day, starting at 00:00 Standard Time (ST). As the objective of this work was to supply the wind farm promoters with power predictions up to 72 hours, the weather forecasts are started and left to run until this horizon is reached. Thus there is some overlapping when the forecast time, τ, corresponds to the ST. Hence, the forecast times $\tau = 12$, $\tau = 36$ and $\tau = 60$ all correspond to the 12:00 ST, for the 1st, 2nd and 3rd day of forecast, respectively. Due to the computation time needed to produce the forecast, these are only available 8 hours after the beginning of the process.

The NWP model used was MM5 (Grell *et al.*, 1995), developed by the Pennsylvania State University and the National Center for Atmospheric Research (NCAR). It is a regional mesoscale model, non-hydrostatic and using a terrain-following coordinate system. The results made available by CGUL/IDL used operational analysis from the National Centers for Environmental Prediction (NCEP) to provide the boundary and initial conditions, necessary to drive the model. The spatial resolution of the most refined level was $6 \times 6\,\mathrm{km}^2$. For further details regarding the model set-up and the surface mesh, please refer to Rodrigues *et al.* (2007) and the EPREV project Contract Report (Rodrigues *et al.*, 2008).

To use the forecasts for generating a power forecast with the transfer function method, it is preferable to have the maximum amount of continuous data. It is also desired that the length of the time series is set to one year, so that the results become themselves a fair representation of a typical year. The time span chosen was the whole year of 2005. This decision was subjected to the following considerations:

1. The MM5 forecasts are available from January of 2005 onwards.
2. The first months of 2006 cannot be used as there were no MM5 forecasts available.
3. For Pinheiro, the start of 2005 is hindered due to the lack of data during January and February.
4. Likewise, for Cabeço da Rainha the data is also limited at its end, as there were no valid measurements during December 2005. This is true for both the Ecra mast and the wind farm SCADA, thus, the electrical power measurements.

Pinheiro, PORT071 forecast

A comparison between the measurements and the forecast is made on the several plots in Figure 4.22. Figure 4.22a shows the forecast from MM5 together with the field measurements. Boxcar averaging was employed to make this representation perceptible. At this scale, the wind speed follows the same trends shown by the PORT071 wind speed. This is confirmed by the value of the correlation coefficient, in Figure 4.22b, reaching 0.76 and 0.92, for velocity and direction, using a forecast interval between $[8, 32[$ hours.

The velocity histogram (Figure 4.22c) is well represented, also at high velocities. Even if the instantaneous forecast is off due to magnitude error or phase shifts, the integration over a long period may yield the same values. The wind rose however (Figure 4.22d) predicts 60° winds as the most probable, whereas the measurements show these to be the 330° azimuth. The remaining sectors are well represented though, particularly the 180° and 210° azimuths.

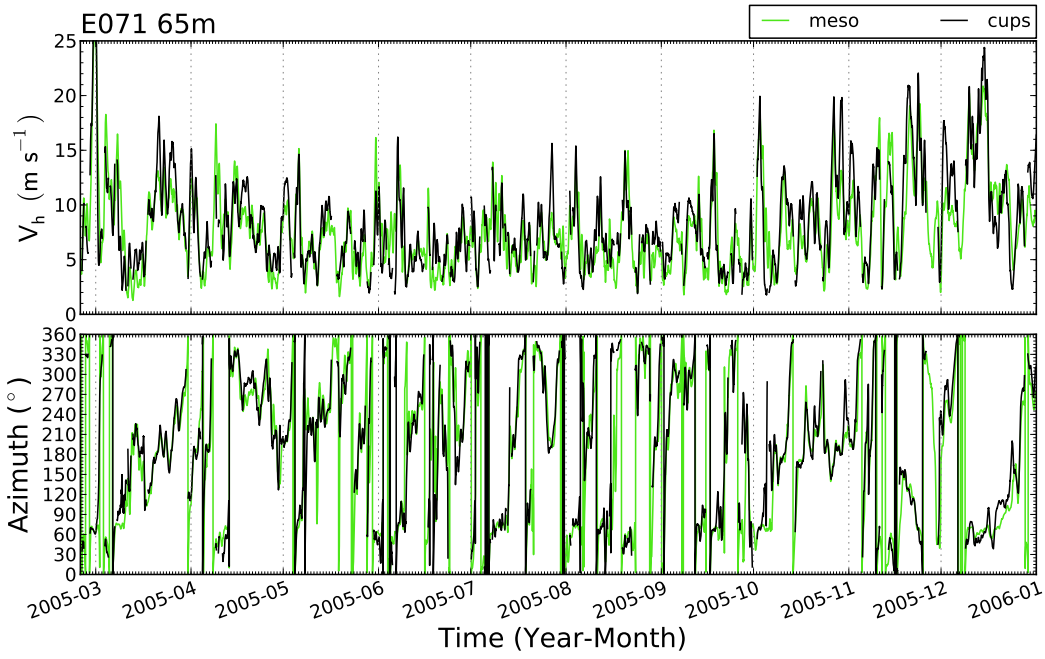

(a) Time series for velocity and direction (smoothed using boxcar averaging).

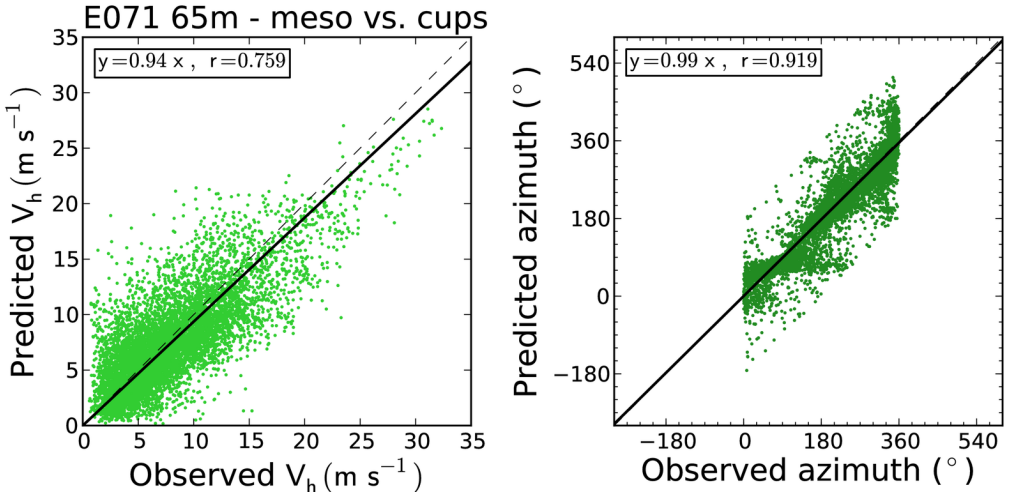

(b) Regression through origin for wind speed and direction (total least squares).

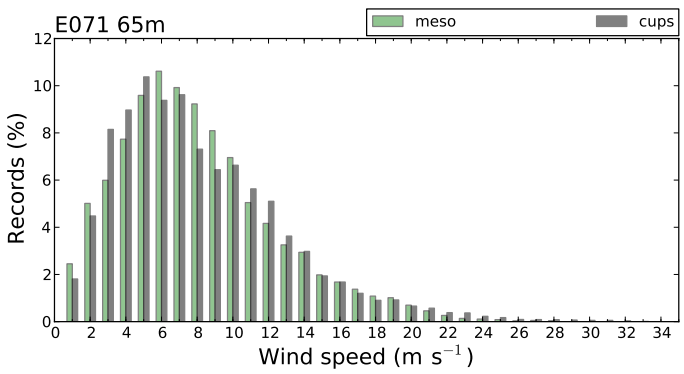

(c) Velocity histogram.

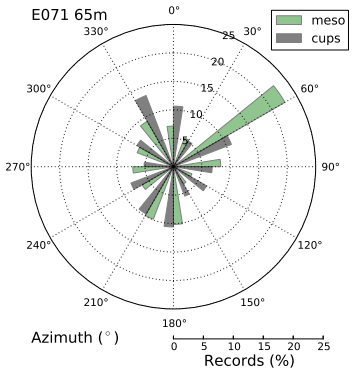

(d) Wind rose.

Figure 4.22: Time series of MM5 forecast for Pinheiro (PORT071) and comparison with the cup anemometers and wind vanes mast measurements. Forecast interval: 8 to 30 hours.

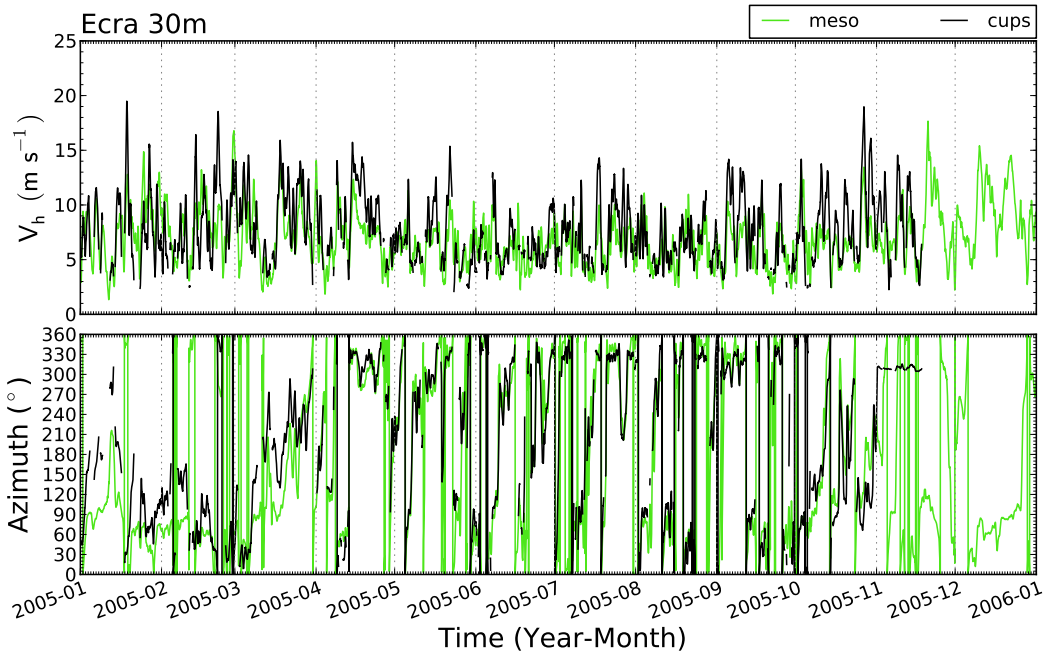

(a) Time series for velocity and direction (smoothed using boxcar averaging).

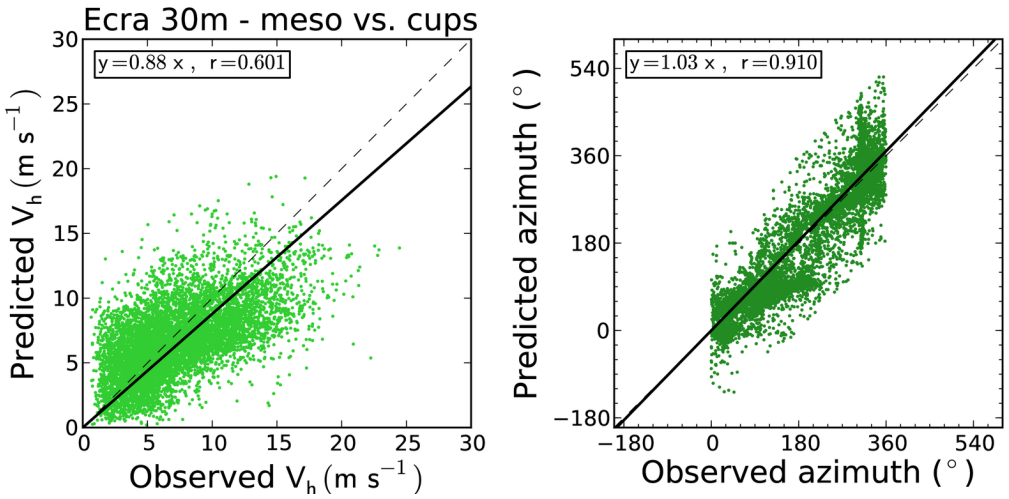

(b) Regression through origin for wind speed and direction (total least squares).

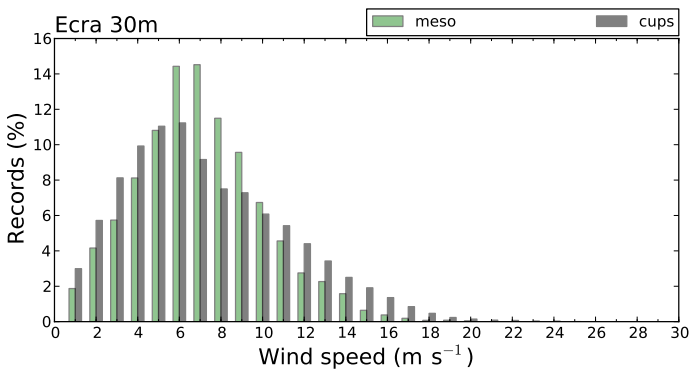

(c) Velocity histogram.

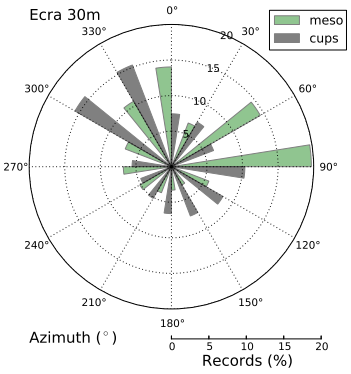

(d) Wind rose.

Figure 4.23: Time series of MM5 forecast for Cabeço da Rainha (Ecra) and comparison with the cup anemometers and wind vanes mast measurements. Forecast interval: 8 to 30 hours.

Cabeço da Rainha, Ecra forecast

Figure 4.23a shows the measurements and the MM5 forecast for the Ecra mast. Qualitatively the forecast is worse than for Pinheiro forecast, as there are several periods where the curves do not coincide. Additionally, the peaks are mostly under-predicted, however this may also be due to the boxcar averaging. While the wind direction is well correlated by the forecast, with a correlation coefficient above 0.9, the velocity correlation is indeed worse, with a value of 0.6 (Figure 4.23b). Although the scatter looks similar to the Pinheiro forecast, the later has more results for speeds above $15\,\mathrm{m\,s^{-1}}$ where the data is still correlated with the observations.

The velocity histogram in Figure 4.23c shows a good match up to $5\,\mathrm{m\,s^{-1}}$. Between this speed and $10\,\mathrm{m\,s^{-1}}$ the wind is being over-predicted, while at higher velocities there is a consistent under-prediction of the observations. This suggest that MM5 has difficulties in predicting peaks in the average wind speed. Additionally, the slope of the total least squares fitting is lower than one (0.88 as shown in Figure 4.23b), which agrees with this particular observation. If this is due to the complex topographic features of the Cabeço da Rainha site, a higher resolution model may introduce some improvement. The wind rose in Figure 4.23d is also worse, as neither of the three main sectors are estimated correctly.

4.4.2 Error analysis of the wind velocity forecast

To quantify the quality of the forecasts, error measures were computed following the description in §4.3.4.1. Because the forecast horizon of each run was 72 hours (more than the 24 hours that separate the start of each forecast run), these overlap such that an event at a particular date and time was simulated by 3 different forecasts. Although the

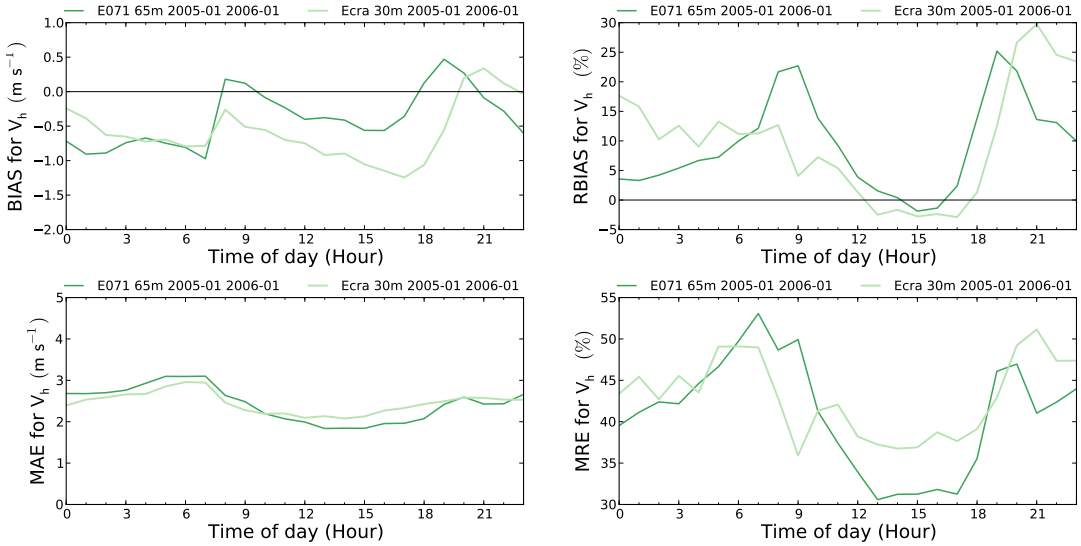

Figure 4.24: Error in MM5 wind speed forecast grouped for each daily hour, to analyse the evolution of the error during a typical day. Two curves are plotted for both Pinheiro and Cabeço da Rainha sites. The measures shown are the BIAS and MAE for absolute errors and RBIAS and MRE for relative errors. Forecast interval: 8 to 30 hours.

Table 4.6: Assessment of the quality of the MM5 forecast time series for several forecast intervals. Description of the quantities in the table: slope a of regression through origin (total least squares); correlation coefficient, r; velocity absolute error measures (BIAS, MAE, RMSE); velocity relative error measures (RBIAS, MRE, RMSRE); azimuth absolute error measures (BIAS(ϕ), MAE(ϕ)). The relative error was computed for velocities $> 1\,\mathrm{m\,s^{-1}}$.

Forecast int. (hour)	slope	r	BIAS ($\mathrm{m\,s^{-1}}$)	MAE ($\mathrm{m\,s^{-1}}$)	RMSE ($\mathrm{m\,s^{-1}}$)	RBIAS (%)	MRE (%)	RMSRE (%)	BIAS(ϕ) (°)	MAE(ϕ) (°)
Pinheiro, MM5 forecast for PORT071										
[8, 20[	0.96	0.791	−0.18	2.11	2.76	9.23	37.38	65.40	−6.8	29.2
[20, 32[	0.92	0.730	−0.60	2.76	3.53	9.26	44.49	82.51	−6.8	30.5
[32, 44[	0.89	0.694	−0.75	2.58	3.35	3.65	43.29	72.79	−8.2	36.5
[44, 56[	0.87	0.646	−0.92	3.14	4.02	9.48	50.54	95.23	−5.4	35.2
[56, 68[	0.86	0.649	−1.00	2.80	3.63	2.35	46.50	79.34	−6.7	38.5
[8, 32[	0.94	0.759	−0.39	2.43	3.17	9.25	40.91	74.39	−6.8	29.8
[32, 56[	0.88	0.672	−0.84	2.86	3.67	7.05	46.89	84.67	−6.8	35.8
[48, 72[	0.86	0.647	−1.00	3.01	3.87	5.59	49.04	87.75	−6.1	37.6
Cabeço da Rainha, MM5 forecast for Ecra										
[8, 20[	0.85	0.658	−0.81	2.26	2.90	2.64	39.13	61.24	−7.3	39.7
[20, 32[	0.90	0.543	−0.35	2.65	3.38	17.20	46.93	77.49	−4.7	43.3
[32, 44[	0.80	0.556	−1.18	2.57	3.32	−0.66	43.1	63.7	−11.5	46.9
[44, 56[	0.87	0.44	−0.50	2.91	3.69	18.28	51.25	83.20	−5.0	47.5
[56, 68[	0.79	0.513	−1.27	2.73	3.50	−0.74	46.36	69.70	−9.8	50.5
[8, 32[	0.88	0.601	−0.58	2.45	3.15	9.82	42.98	69.73	−6.0	41.5
[32, 56[	0.84	0.499	−0.84	2.74	3.51	8.69	47.11	73.97	−8.3	47.2
[48, 72[	0.84	0.480	−0.89	2.82	3.59	8.72	48.91	77.38	−6.9	49.3

time and date of an event is the same, the prediction time differs for the 3 runs, Thus, for a set of N forecast runs, these will be characterized by the time at which the run started, t_n, and by the prediction time, τ, spanning from τ_i to τ_f in N_τ samples, such that $\tau_m = \tau_i + \Delta\tau[m-1], \quad m = 1, \ldots, N_\tau$.

To account for τ in the error measures, these becomes themselves function of τ. Using the same nomenclature as in §4.3.4.1:

$$\mathrm{EA}_{n,m} = F(t_n + \tau_m \,|\, t_n) - M(t_n + \tau_m) \,,$$
$$\mathrm{ER}_{n,m} = \frac{F(t_n + \tau_m \,|\, t_n)}{M(t_n + \tau_m)} - 1 \,, \quad M(t_n + \tau_m) > 0 \,.$$

The averages are afterwards performed over the $\mathrm{EA}_{n,m}$ and $\mathrm{ER}_{n,m}$. Exemplifying on the BIAS and the MAE quantities:

$$\mathrm{BIAS} = \frac{1}{N_t}\sum_{n=1}^{N_t}\frac{1}{N_\tau}\sum_{\tau=1}^{N_\tau}\mathrm{EA}_{n,m} \,, \quad \mathrm{MAE} = \frac{1}{N_t}\sum_{n=1}^{N_t}\frac{1}{N_\tau}\sum_{\tau=1}^{N_\tau}|\mathrm{EA}_{n,m}| \,.$$

The same applies to the MSE and the quantities based on the relative error: RBIAS, MRE and RMSRE.

Whilst the measurements are averages over 10 minutes, the MM5 forecast refers to instantaneous values with a 30 minutes sampling. To reduce the influence from phase errors, these were computed after averaging both time series into an hourly basis. For the mast measurements, as these were already result of a time integration, an arithmetic mean was used. A trapezoidal rule was employed for the MM5 forecast instead.

In Table 4.6 are shown the several error measures as function of several prediction intervals. Besides the error in the velocity magnitude, the BIAS and MAE for the azimuth difference between wind directions is given. Additionally the correlation coefficient, r, was computed, together with the slope for a regression through the origin. A first set has each prediction interval covering a range of 12 hours. As prediction times below 8 hours are neglected, the intervals $[8, 20[$, $[32, 44[$ and $[56, 68[$ hours corresponds to diurnal periods, while $[20, 32[$ and $[44, 56[$ hours correspond to nocturnal periods. The value of r consistently decreases as the prediction time increases, as the forecast becomes less reliable. For Pinheiro however, the worst value is 0.65 which is still a high correlation. In Cabeço da Rainha the values are worse, starting with 0.66 and dropping below 0.5.

The BIAS and MAE values are similar for both sites, around -1 and $2\,\mathrm{m\,s^{-1}}$ respectively. Relative errors are much higher, around 50% for MRE. Consistently for both sites, the MAE and MRE are higher during the nocturnal than the diurnal periods. For Cabeço da Rainha the BIAS is closer to 0 during the nocturnal periods, while for Pinheiro the BIAS does not share this trend, always increasing with the prediction time. Although the MAE for direction increases, the BIAS also follows a daily trend revealing lower values for nocturnal periods. In Figure 4.24 the evolution of the error throughout a typical day is shown. In these, both MAE and MRE show the trend found analysing Table 4.6, where diurnal periods are related to lower errors. While the BIAS is mostly negative, RBIAS is positive for several periods of the day. Considering that for wind speed both the forecast and the measurements always yield positive quantities, to have a BIAS < 0 and a RBIAS > 0 means that the forecast is over-predicting when the observed value is low, while under-predicting when the observed value is high.

Table 4.7: Error in the electrical power for a forecast interval of [8, 32[hours. The relative error was computed for power values higher than 5% of the nominal power of the respective turbine.

	BIAS	MAE	RMSE	RBIAS	MRE	RMSRE	SS wake
Pinheiro, MM5 forecast for PORT071							
65 m, no wake	1.8%	15.5%	23.9%	5.6%	65.8%	104.2%	
65 m wake	0.6%	15.3%	23.6%	0.7%	65.0%	100.9%	0.03
109 m, no wake	2.6%	15.0%	23.3%	10.9%	65.4%	106.3%	
109 m, wake	1.4%	14.7%	22.9%	5.9%	64.4%	102.9%	0.03
Cabeço da Rainha, MM5 forecast for Ecra							
30 m, no wake	−1.1%	15.6%	23.2%	−12.1%	60.9%	85.7%	
30 m, wake	−2.0%	15.3%	22.9%	−15.6%	60.0%	82.6%	0.03
109 m, no wake	−1.0%	14.7%	22.3%	−7.8%	62.3%	90.9%	
109 m, wake	−1.7%	14.6%	22.1%	−10.3%	61.7%	88.9%	0.02

4.4.3 Error analysis of the wind power forecast

The power forecast was first computed using the MM5 time series at the location of the reference mast, at the same height AGL of the cup anemometer. A second set of MM5 forecasts was made available for the same horizontal location, but at 109 m AGL instead. The aim of these was to verify if improvements could be gained by choosing an height where the forecast is less affected by the topography, therefore, of boundary-layer effects. As the microscale model grid has an higher resolution and the $k - \epsilon$ turbulence model is suited to solve small scale problems, it is expected to provide a better description of the boundary-layer flow close to the surface.

The power was predicted by applying the transfer function to the wind speed and direction from the MM5 time series, for each forecast run. These are composed of instantaneous values given every 30 minutes, up to 72 hours of forecast horizon. The measured power in the SCADA data, however, provides the values as 10 minutes averages, with the midpoint of the integration time given at the 5, 15, 25, 35, 45 and 55 minutes of each hour. The SCADA data was averaged to coincide with the 30 minutes sampling, using the two nearest neighbours. The MM5 velocity and direction were interpolated to the previous and preceding 10 minutes. The transfer function was applied to the 3 instants (central, -10 and $+10$ minutes), to obtain the velocity at each turbine location and, afterwards, the power prediction. The power was averaged over those 3 instants, integrated using a trapezoidal rule. Although instantaneous and averaged values are not comparable, this procedure was a way to smooth possible phase errors from both series.

The global errors for both wind farms are shown in Table 4.7. When compared with the errors obtained for the ideal forecasts (Table 4.5) the error increases by a factor of ~ 2. For Pinheiro both the BIAS and RBIAS are positive, indicating a generalized over-prediction. Conversely, for Cabeço da Rainha the BIAS values are negative. This agrees with the previous results for the ideal forecasts. The relative errors are higher, both MRE and RMSRE around 4 times the the MAE and RMSE. This error measure gives more weight for records where the values are lower, thus indicating a mismatch for low

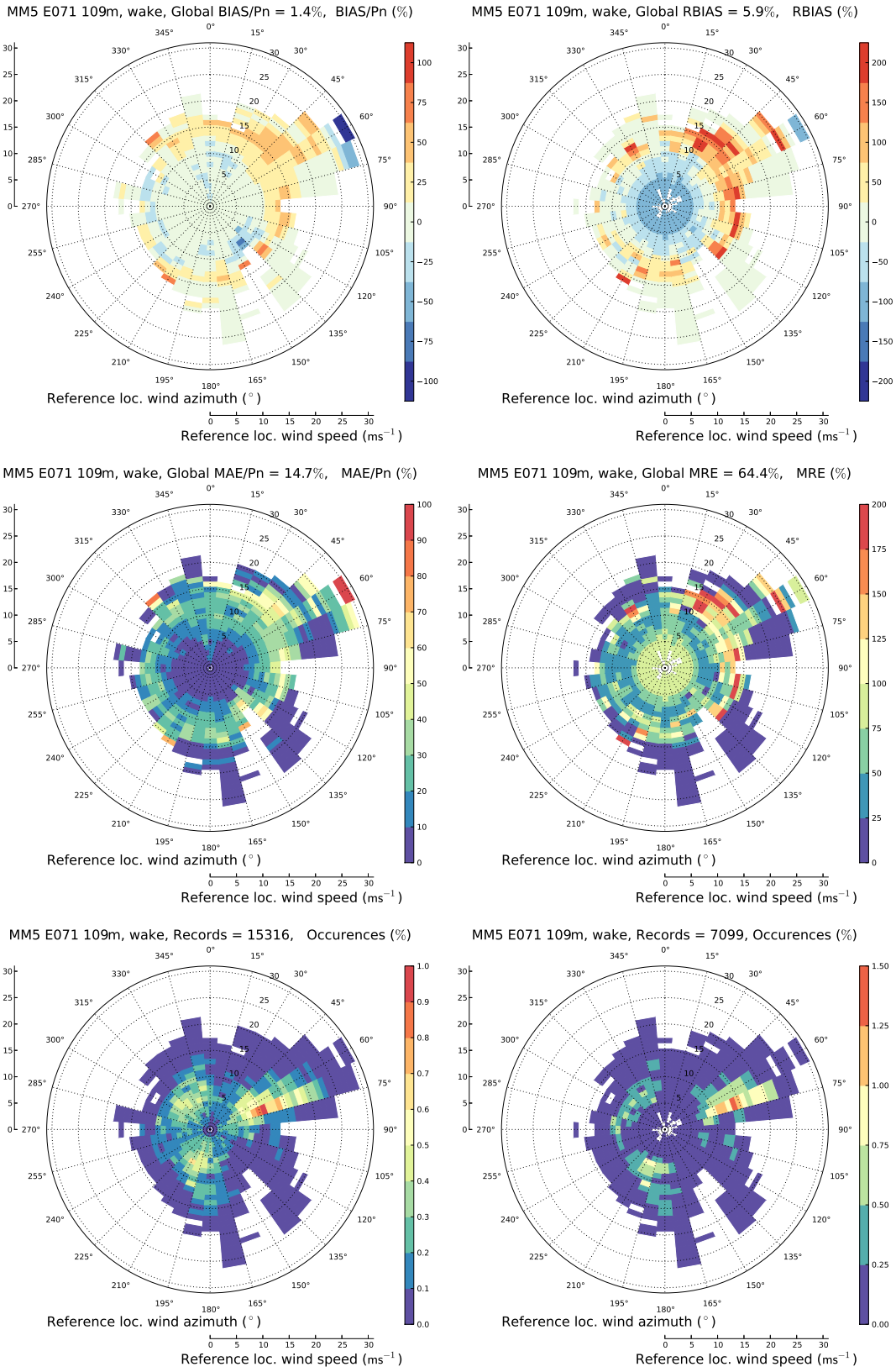

Figure 4.25: Wind power error roses for Pinheiro wind farm using the MM5 wind forecast at the PORT071 mast. The forecast interval is [8, 32[hours. For a detailed description refer to Fig. 4.19.

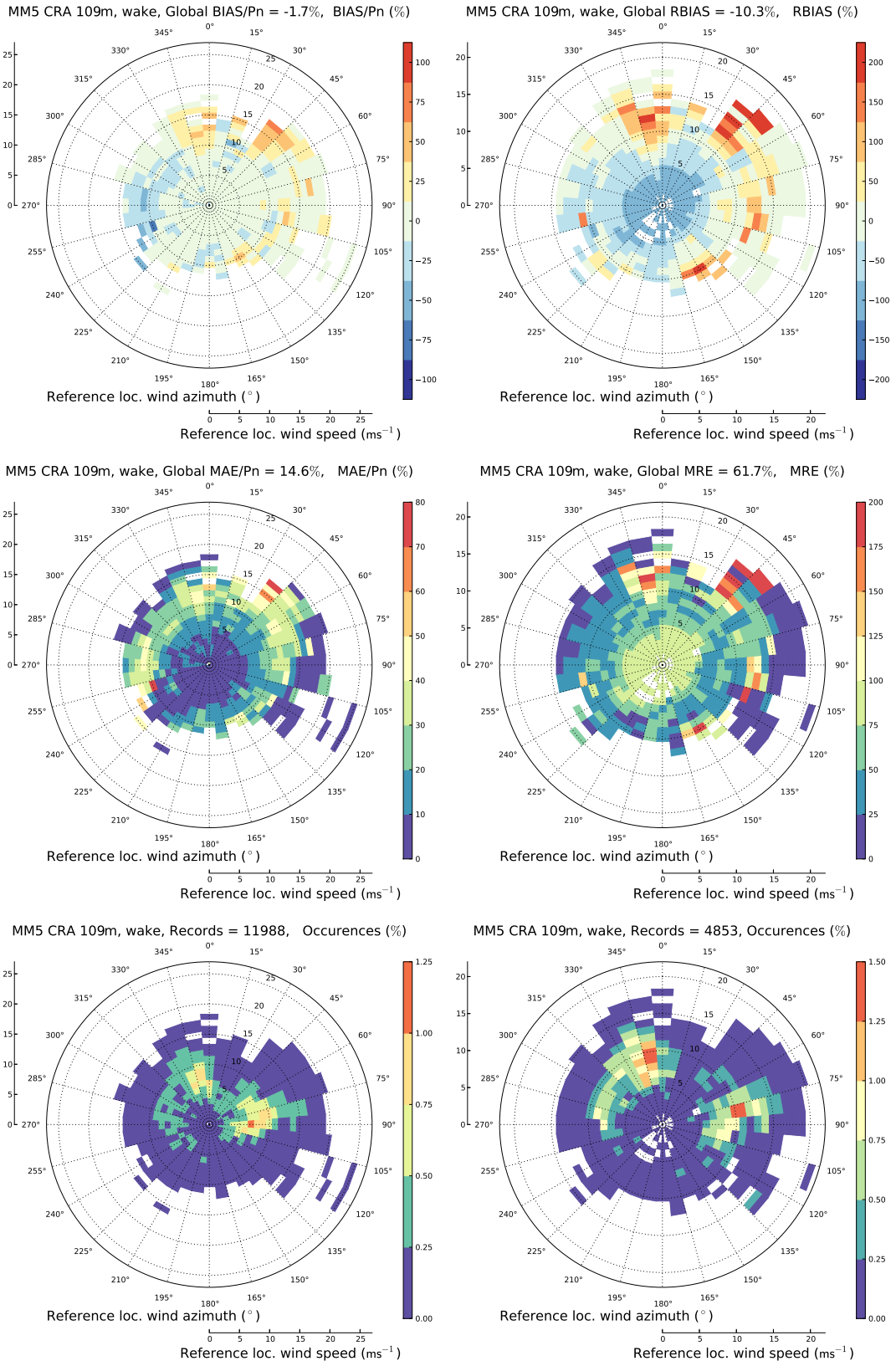

Figure 4.26: Wind power error roses for Cabeço da Rainha wind farm using the MM5 wind forecast at the Ecra mast. For a detailed description refer to Fig. 4.19.

power and velocities. The wake model introduces slight improvements, less than the one obtained in §4.3.4.4. For Cabeço da Rainha the SS value is higher though, similar to the value for Pinheiro, 0.03. There is an improvement when using the MM5 forecast at 109 m than at the original height of the respective reference mast. This is true for both wind farms and for the situations with or without wake model. The change in height brings improvements of roughly 4%.

To better evaluate how the method performs, error roses were computed for a forecast interval between [8, 32[hours, the first useful 24 hours. These are shown in Figure 4.25 for Pinheiro wind. Similar to the ideal forecast results (Figure 4.19), the BIAS is mainly negative below $10\,\mathrm{m\,s^{-1}}$ and positive for higher velocities. As already stated, this may indicate that the real power curve is less steep. For 60° the maximum wind speeds recorded present high under-predictions. These are due to events where the methodology predicts velocities higher than the cut-off wind speed, however the SCADA data does not show this as the wind farm is still in operation. This event is also verified in the results for the ideal forecast. The MAE is $\sim$ 30% for wind speeds between 10 and $15\,\mathrm{m\,s^{-1}}$, being evenly distributed for all the directions.

For Cabeço da Rainha (Figure 4.26), the 270° sector is characterized by a generalized under-prediction of the power. This is opposite to the BIAS sign shown in the ideal forecast (Figure 4.20). Conversely, large over-predictions are found for the 45°-90° sectors, related with the wind direction error found in the MM5 series (*e.g.*, the 60° and 90° sectors in Figure 4.23d). The 230° direction presents low values for MAE, below 10%. On the other directions the MAE is evenly spread, $\sim$ 15% between 5 to $10\,\mathrm{m\,s^{-1}}$ and $\sim$ 30% above. Some of the high error found is also hindered by the low number of available records.

4.4.3.1 Error as function of the forecast time

In Figure 4.27 the error is displayed as a function of the forecast time. The results are compared with a persistence model, which is the same as producing a forecast using the last recorded power value, thus persisting throughout the forecast horizon. For this purpose, the skill score was computed according to eq. (4.20), but using the MAE instead of the MSE.

In both parks, the improvement against persistence is clear. For Pinheiro wind farm this is as high as 50% in the first 16 hours, never dropping below 25% afterwards. For Cabeço da Rainha similar values are found. The use of the MM5 forecasts at 109 m improves both MAE and MRE, although for Cabeço da Rainha it is less significant. For the 109 m series, the Cabeço da Rainha BIAS is more centred but presents higher variance. The MRE errors are around 60%, much lower than the persistence model error. It is seen that the MAE value suffers a slight increase with the forecast time, consequence of the degradation of the MM5 forecast. For both wind farms, this increase was roughly estimated as $\sim$ 3%.

For all error measures there is a cyclic behaviour, with a 24 hours period, where the error achieves its lowest value at 14:00. Afterwards its value increases reaching the maximum value at 06:00. This agrees with the typical day errors in the wind speed

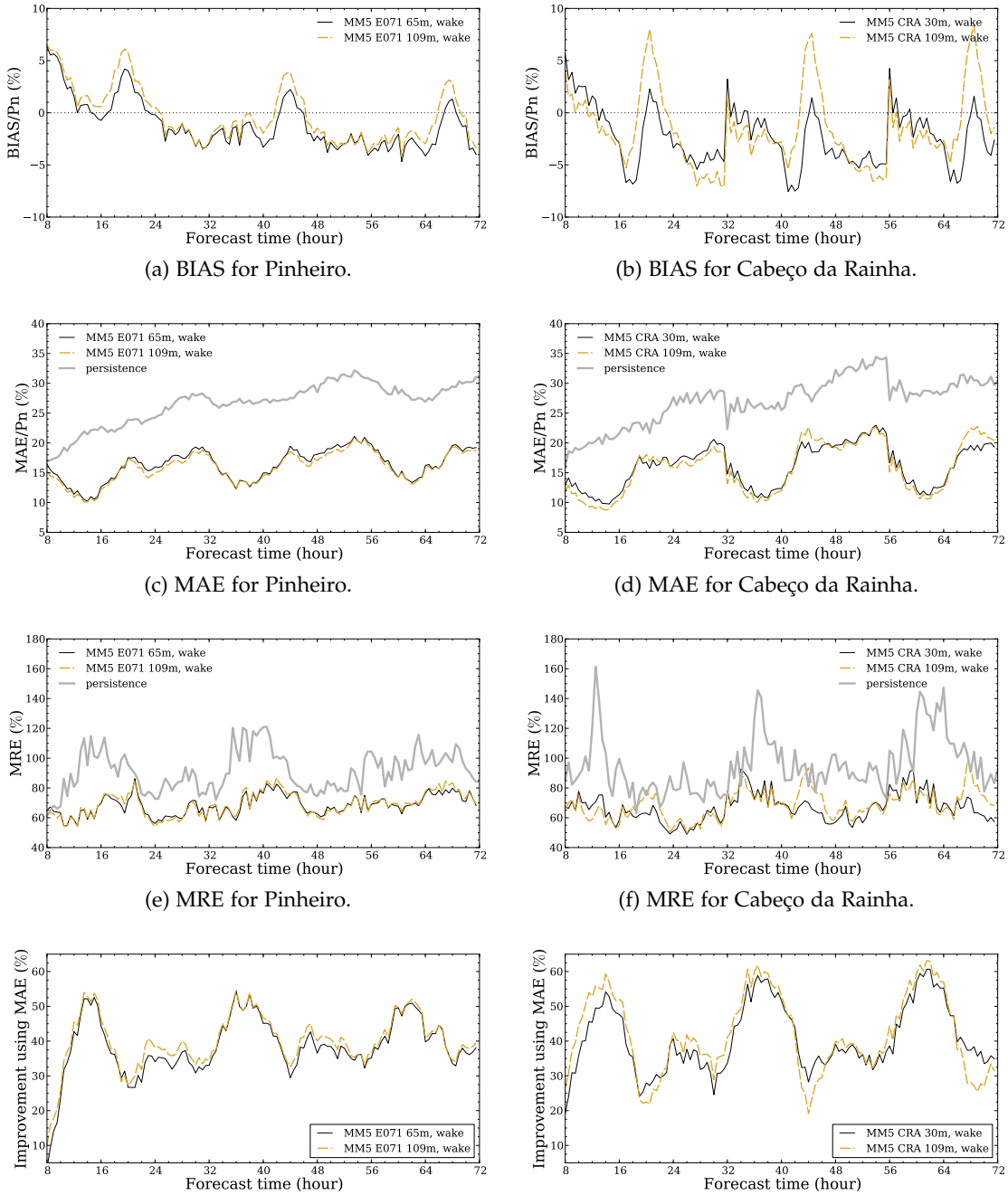

(a) BIAS for Pinheiro.

(b) BIAS for Cabeço da Rainha.

(c) MAE for Pinheiro.

(d) MAE for Cabeço da Rainha.

(e) MRE for Pinheiro.

(f) MRE for Cabeço da Rainha.

(g) Improvement against persistence for Pinheiro.

(h) Improvement against persistence for C. Rainha.

Figure 4.27: Error in power prediction as function of the forecast time. The BIAS and MAE are normalized by the nominal park power. The relative errors were computed for measured power above 5% of the nominal power for each turbine.

(Figure 4.24). It is also similar to the theoretical behaviour of the atmospheric boundary-layer (ABL), where during nocturnal periods the atmosphere is expected to be stable, damping turbulence and decreasing the boundary-layer height. During the day it is expected to be neutral or unstable. As the effect of stratification was not included in the transfer function, it is expected that the results are a compromise between these two states. However, as the neutral and the unstable ABL have similar shape factors, the error arising from the differences between these two situations is expected to be lower than the one between a neutral and a stable situation. There is a second peak less noticeable at each 20:00 hour (τ equal to 20, 44 and 68 hours). This is related with the instants where the BIAS is the highest, possibly being associated with the sunset hour and the change of stability regime.

The persistence was also affected by the daily ABL cycle. Throughout the forecast horizon, the nocturnal periods correspond to a decrease of the error. This is related with the time at which the value of the persistence model was taken, as $\tau = 0$ coincides with 00:00 ST. Thus, it was expected this value agrees better with the power measured at nocturnal periods.

4.4.3.2 Power forecast for the Iberian Electricity Market intraday sessions

The analysis made in the preceding sections scrutinized the error values to short periods of time and for specific direction and velocity classes. However, the purpose of the EPREV project was to predict the power, such that both wind farm promoters and the electrical network were able to participate in the Iberian Electricity Market (MIBEL).

A full description on how MIBEL operates is found in MIBEL (2008). Briefly, the daily electricity market is divided into sessions where the power for the supply day, named as the D day, are negotiated. In Figure 4.28 are shown the time periods which comprehend all these sessions. The MIBEL daily market consists of:

1. Day-ahead market: the market where the energy transaction for the next day are negotiated. The D day and comprehends the 24 hours after 00:00 ST.
2. The intraday market: for the electrical network to manage in case of shortage, there are 6 sessions throughout the D-1 and D day. As the forecasts are only available for 08:00 ST of D day, only the 1st, 4th, 5th and 6th sessions are important. The 1st is included as it also serves to negotiate the last 4 hours of the D-1 Day, besides the next 24 hours.

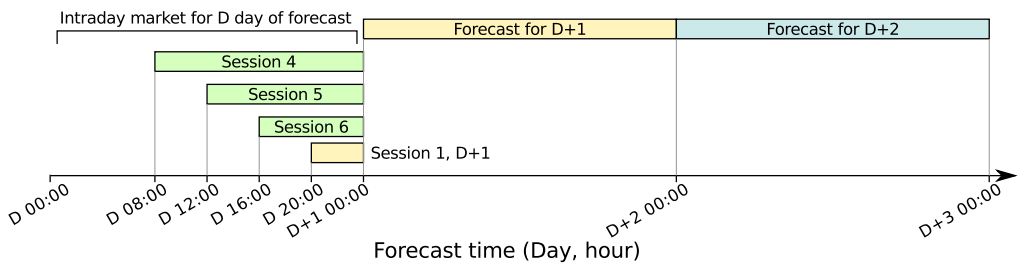

Figure 4.28: Schematic with several sessions that compose the MIBEL, for the intraday market and the following two days, under the 72 hours forecast horizon.

Table 4.8: Error in the power forecast for the periods which compose the intraday sessions of MIBEL. A threshold was applied to the relative errors, such that it were only considered values with and energy output above the correspondent 1 hour power production, with the wind farm at nominal conditions, A linear correction was applied, based on linear least squares regression (the corrected quantities are signalled as such).

Day of forecast	D				D+1	D+2
Interval (hour)	[8, 1, 24[	[12, 24[	[16, 24[	[20, 24[	[24, 48[	[48, 72[
Market session	4th	5th	6th	D+1, 1st		
Pinheiro, MM5 forecast for PORT071, 109 m, with wake						
valid runs	163	182	231	270	141	140
BIAS (MW h)	11.2	8.4	7.7	3.0	4.2	2.0
MAE (MW h)	27.8	22.2	19.3	12.3	52.4	57.3
RBIAS (%)	26.0	27.7	25.3	1.1	13.5	12.8
MRE (%)	69.3	67.2	66.5	51.1	83.9	92.9
r	0.79	0.75	0.70	0.70	0.59	0.54
a_1	0.54	0.52	0.50	0.57	0.42	0.37
a_0 (MW h)	13.9	11.9	10.0	6.2	41.1	45.4
corr. BIAS (MW h)	-9.3	-10.7	-11.9	-13.4	-10.5	-11.5
corr. MAE (MW h)	25.7	23.6	21.3	18.3	38.4	40.5
corr. RBIAS (%)	-2.4	-6.8	-12.8	-25.5	20.9	23.0
corr. MRE (%)	42.2	41.3	40.8	41.5	53.8	58.1
Cabeço da Rainha, MM5 forecast for Ecra, 109 m, with wake						
valid runs	52	77	95	140	35	35
BIAS (MW h)	4.9	5.1	5.6	5.1	14.3	28.6
MAE (MW h)	15.6	13.9	11.8	8.8	28.5	43.1
RBIAS (%)	17.6	24.4	41.2	19.6	43.7	80.4
MRE (%)	67.2	69.6	77.7	56.3	85.6	124.2
r	0.52	0.51	0.54	0.50	0.51	0.39
a_1	0.33	0.30	0.29	0.30	0.29	0.17
a_0 (MW h)	12.6	10.2	7.6	4.8	22.9	26.9
corr. BIAS (MW h)	-8.4	-9.9	-9.5	-10.9	-7.5	-8.8
corr. MAE (MW h)	12.0	12.4	11.5	10.9	16.7	16.8
corr. RBIAS (%)	-17.9	-24.8	-28.9	-42.2	-1.3	-2.7
corr. MRE (%)	33.3	36.0	38.7	42.2	35.3	34.1

To estimate the error between the predicted and measured values of power, in respect to the time periods defined by these market sessions, the total energy outputted by the wind farm was obtained by integration of the power throughout the respective forecast interval. The error was computed from the differences between the energy predicted and the energy actually converted from the wind. These results are shown in Table 4.8. The number of valid runs refers to the number of forecast runs where both the forecast and measured values have 100% availability, for the respective forecast interval. The BIAS and MAE where computed, presented with dimensions as there is no suitable normalization quantity. For both wind farms, the MAE is roughly 1 $\sim$ 2.5 times the energy output of 1 hour of operation at the nominal power (21.8 and 16.2 MW h for Pinheiro and Cabeço da Rainha). Both BIAS and MAE decrease during the D day, consequence of the smaller interval of time and records available, instead of an actual improvement of the forecast. The relative errors are high, around $\sim$ 60%. The forecast for D+1 and D+2 shows an increase of the error, related to the degradation of the forecast as it reaches the horizon.

The coefficient of correlation was computed for each interval, yielding values $\sim$ 0.7 for Pinheiro and $\sim$ 0.5 for Cabeço da Rainha. A 1st degree polynomial was fitted using least squares, relating the energy prediction E_f with the energy measured, E_m. This was used to introduce a correction to the prediction, E_f^{corr}, such that, $E_f^{corr} = a_1 E_f + a_0$. The coefficients of the polynomial, a_1 and a_0, are given in Table 4.8. The error measures were computed using the E_f^{corr} dataset. This lead to an overall improvement of the error, particularly for the MRE which decreases by almost 30%. The values for MAE however, show improvements mainly for the D+1 and D+2 days, while at the 6th and 1st sessions it hinders the forecast. This indicates that such correction is suitable for events where the energy output is low.

4.4.3.3 Histogram of the wind power output

The transfer functions method was developed to provide a forecast of the wind power, thus, the agreement between the measured and predicted power is crucial for this purpose. However, this methodology could also be used for a different goal: the quantification of the energy obtained from the wind farm over a long period of time. To assess this, histograms of the measured and predicted power were produced, shown in Figure

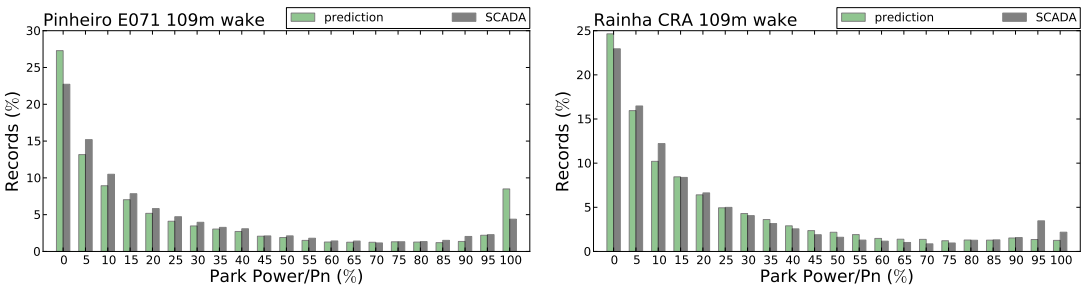

(a) Pinheiro. (b) Cabeço da Rainha.

Figure 4.29: Histogram of the wind farm power output for the forecast and the SCADA measurements. The histogram is normalized by the nominal park power.

4.29 for both wind farms. The overall agreement is good, with discrepancies found only for the bins at the extremes of the scale. The wind power prediction for Pinheiro has more occurrences at the last bin, thus, occurrences where the wind farm is operating at its maximum power. These are ~ 2 times higher than the occurrences actually measured. In Cabeço da Rainha the inverse happens and the power prediction yields less occurrences, at the nominal park power, than what is observed in the measurements. Both of these situations agree with the BIAS sign found in the errors of the wind farms (Figure 4.7), *i.e.*, a overall over-prediction for Pinheiro and under-prediction for Rainha.

These histograms enable us to estimate the wind power for sites where wind measurements were never made. This methodology allows to make power predictions without any information nor measured data at the wind farm, besides the topography and turbines characteristics, *i.e.*, the power curves provided by the manufacturer.

4.5 Conclusions

The power output of two wind farms was predicted using a methodology involving transfer functions. These relate the wind speed at a reference location, forecast by NWP models, with the speed at the location of the wind turbines. The transfer functions were generated from computer simulations of the neutral atmospheric flow, using the non-linear CFD code VENTOS®. The relation between the wind speed and the power output of each turbine was made using a power curve, supplied by the turbine manufacturer.

This methodology is based in the possibility that the wind velocity and direction at two distinct spatial locations can be correlated, solely using these two variables. This relation is afterwards used to convert a velocity value, from a weather forecast or other source, into a velocity magnitude at the location of the turbines. This is the first flaw of the method, as there are other variables that have a severe influence on this correlation. The most important is, perhaps, the atmospheric stability, as it may change significantly the shape factor of the atmospheric boundary-layer.

As the goal of this study was the forecast of wind power, the correlated velocities must be further converted into the power that a wind turbine, at that location, would generate. This is the second flaw in this method, as it cannot describe the whole dynamics of a wind turbine, by using solely a simple power curve.

The method involves a high computational cost, while producing the CFD simulations for the several direction and velocity conditions. This effort however is only needed at an initial stage. In the operational phase, after the transfer function is produced, it is a simple and expedite way to obtain a power prediction. Because the transfer function cannot adapt according to its input, it is a static way to forecast as it relies on a constant correlation for the velocity. If the input velocity and direction have an error associated, the method cannot correct it, propagating it to the power prediction.

The main conclusions found were:

1. The transfer function method, driven by the MM5 weather forecasts, returns MAE around 15% for the electrical power, when normalized by the nominal power of the wind farm. Throughout the forecast horizon, these were always below 25%.

2. Using weather forecasts at the same reference location, but at higher heights (109 m AGL), the overall improvement on the MSE was 6%. With the increase in height, the boundary-layer influence due to the proximity to the wall lessens. As the CFD model has a higher mesh refinement than the regional model, the representation of the topography is improved. Likewise, it was expected an improvement of the boundary-layer depiction.

3. The level of accuracy obtained is better than the one found in Landberg (2001) and similar to the ANEMOS project (Madsen *et al.*, 2004). While Pinheiro wind farm has a similar RIX number to the Golagh and Alaiz test cases, the topography of Cabeço da Rainha shows higher complexity than the published test cases.

4. In order to evaluate the quality of the transfer functions, velocity measurements from meteorological masts were used instead of the weather forecasts. This acted as if an ideal forecast had been produced, ruling out the uncertainty in the weather forecasts. Under these conditions, the MAE was $\leq 9\%$ for both parks.

5. For both parks, the bias changes sign for speeds around $7\,\mathrm{m\,s^{-1}}$: while below this speed the method under-predicts, above it, it over-predicts. This was attributed to the slope of the power curve, as being smoother in reality than what was estimated by the manufacturer.

6. The model of Jensen (Katic *et al.*, 1986) was implemented to estimate the wake effects on the turbines and the consequent power loss. This resulted in improvements as high as 30% for specific wind speeds and directions. However, errors of the same magnitude were introduced at low power values and near the cut-off of the turbines. The overall improvement on the MSE was 3%.

7. The quality of the results degrades at wind speeds close to the turbines cut-off. This is due to the power curve inability to model these effects, but is also consequence of the low number of records available.

8. A proportionality relation was found between the wind speeds at the mast and the each turbine, for results in the same direction group. The coefficient of determination was always higher than 0.998. This relation was exploited to minimize the number of simulations produced.

9. The atmospheric stability could not be determined from the available measurements. In spite of this, both turbulence intensity and shear factor were computed as function of the wind speed for Pinheiro. It was verified that for speeds below $7\,\mathrm{m\,s^{-1}}$, the average of a dataset comprising the summer days deviated from the overall average, yielding higher values. Conversely, the dataset comprising the winter nights yielded values below the overall average. This was related with stratification effects, as these where neglected by the CFD simulations.

10. The histogram of the predicted power was compared with the measurements, yielding an overall good agreement. There was over-prediction for occurrences with power below 5% of the nominal value, as above 95%. Some of these may be due to cut-off effects which are not captured by the outlier conditions. Additionally, there were discrepancies between the nominal power, as given by the sum of the power curves, and the effective maximum power, as measured in the SCADA.

Chapter 5

Wind forecast by one-way coupling between a mesoscale and a microscale model

In this chapter, wind characteristics are forecast and compared with field measurements. Results from weather forecasts with regional models are processed to supply initial and boundary conditions to a microscale model, only solving the physics related to the boundary layer, thermal stratification and atmospheric turbulence. Due to the scarceness of case-studies in the literature, field measurements from wind resource assessment campaigns at four sites are used for validation. A set of time periods of two weeks were chosen and numerical simulations were produced and compared with the experimental results, to quantify the agreement and the benefits in adding the microscale code.

5.1 Introduction

The forecasting of wind conditions at the scales where wind turbines operate is obtained through a model chain, linking global models, regional models operating at the mesoscales and local models, focused in describing the microscale flow. While global models aim to describe the weather for the whole earth, regional models have limited domains, encompassing only part of the globe and require the results of global models as initial and boundary conditions. Microscale models are themselves driven by the regional model results, however these neglect most of the atmospheric phenomena either than the boundary-layer physics and the influence of topography and roughness changes in the flow.

Regional mesoscale models are used to downscale flow conditions from scales $\sim$ 100 km to the microscale $\sim$ 1 km. To decrease the computational requirements these employ nested computational domains (Phillips and Shukla, 1973), each at a different scale, to refine the flow solution at a particular area. The formulation of the vertical discretization in mesoscale models uses terrain following coordinates based on pressure, following the work of Phillips (1957) in establishing the σ coordinate system. The direct use of the vertical height as a coordinate requires either the inclusion of metrics in

the fundamental equations, to accommodate for the topography of the surface, or the use of cut-cells and embedded boundary methods. Additionally, the use of pressure based coordinates allows for simpler forms of the governing equations and uniform meshes, which ease the implementation of nested domains and other numerical techniques. Nonetheless, numerical models using the vertical height as coordinate system have been developed (Clark, 1977; Pielke *et al.*, 1992), using the Gal-Chen and Somerville (1975) coordinate transformation. According to Klemp *et al.* (2003), however, this may originate truncation errors depending on how the metric terms are introduced.

Although pressure based coordinate transformations is preferable for mesoscale modelling, at the microscales the description of the topography becomes essential to describe the surface flow and the turbulence characteristics. Kunz *et al.* (2000) successfully coupled mesoscale and microscale models, MEMO and MIMO, to predict the flow on a urban area in southwest Germany. Both codes used the same staggered arrangement of variables. The microscale was used only to solve the stratified turbulent flow in the surface layer, without other parameterizations. Eidsvik *et al.* (2004) designed a model chain where the microscale model used a finite element discretization, common in engineering fluid dynamics codes. The finite volume and finite element discretization techniques allow the use non-orthogonal computational grids which can describe complex features of steep topography, while correctly handling the required metrics. Recent work from Kristóf *et al.* (2009) focused on coupling mesoscale models with commercial fluid dynamics codes of closed source, typical of engineering studies.

In the present chapter, a model chain was established which uses the VENTOS® computer code as a microscale model. For this purpose, the VENTOS® model was modified in order to use data from a mesoscale model as initial and boundary conditions. The results from both mesoscale and microscale models were compared against measurements from the wind farms used in Chapter 4, together with two other sites with measurements at 7 masts (two height levels), without interference from wind turbines.

5.1.1 Field measurements and data availability

A total of four sites were used in this investigation. The Mendoiro-Bustavade site is located in Serra da Anta, centred at $\{8°25'0''\,W,\ 42°0'8''\,N\}$, at an altitude of 750 m AGL. The topography is displayed in Figure 5.1. It had four measurement masts operating simultaneously from 2004 to 2005, PORT135, PORT136, PORT266 and PORT267, each equipped with cup anemometers and wind vanes at two different heights. At a distance of 15 km to the east lies the Alto do Corisco site, located in Serra da Peneda $\{8°14'44''\,W,\ 42°1'4''\,N\}$, at an altitude of 1200 m. This site had three masts, PORT132, PORT262 and PORT263, also with two measurement heights and operating for the same time span as the ones in Mendoiro site. These measurements were part of a wind resource assessment campaign carried out by Institute of Mechanical Engineering and Industrial Management (INEGI). For the duration of the period of interest, the year of 2005, there were no wind turbines installed.

Additionally, the two sites investigated in Chapter 4, Pinheiro and Cabeço da Rainha, are also studied in the present Chapter. For details regarding the wind farm and the site, refer to §4.3.1. The wind measurements and the dataset structure described in §4.3.2 is

the same for all sites.

5.1.2 Data availability and selection of the time periods for which the forecasts were produced

Figure 5.2 displays the availability of the measurements for Mendoiro and Corisco datasets from the different masts and measurement heights. It was verified that the meso-microscale coupling technique required much higher computational and time resources than the transfer functions method. Thus, the periods to simulate were reduced to two sets, each encompassing 15 days, one during a summer period while the other closer to a winter situation. Another requirement was for the chosen periods to have events of high wind speeds, to see the ability of the microscale in reproducing such occurrences.

The selection of the periods was also constrained by the availability of the wind data and electrical power output, measured at Pinheiro and Cabeço da Rainha. From Figure 4.10, this forced the chosen periods to lie between the year of 2005, as there is no SCADA data for Pinheiro prior to 2005, while for Cabeço da Rainha, the data ends at December. As the availability is worse during winter due to weather hazards, such as cup anemometers freezing, a week during such a period was difficult to find. Subjected to these constrains, two weeks in autumn was chosen near the end of the available data. This is also one of the periods with the highest gusts and wind speeds. Following these considerations, the selected periods were:

1. Two summer weeks, from 2005-07-01 to 2005-07-15.
2. Two autumn weeks from 2005-11-19 to 2005-12-03.

5.2 Simulations of the mesoscale flow with the WRF regional model

5.2.1 Description of the regional model

The Weather Research and Forecast (WRF) is a regional model developed by several institutions from the United States of America, including the National Center for Atmospheric Research (NCAR), the National Oceanic and Atmospheric Administration (NOAA), and the National Center for Environmental Prediction (NCEP). Details on the numerical model and its techniques can be found on the WRF technical description (Skamarock *et al.*, 2008). For information focusing on how to run and produce numerical weather predictions, one should refer to the WRF User's Guide (Wang *et al.*, 2010). A brief description of the WRF model is made throughout the remainder of the present section.

The dynamic solver used was the ARW which is non-hydrostatic and fully compressible, where the primitive equations are formulated using the η coordinate system,

$$\eta = \frac{p_{\mathrm{H}} - p_{\mathrm{H}T}}{p_{\mathrm{H}_{\mathrm{W}}} - p_{\mathrm{H}T}} \,. \tag{5.1}$$

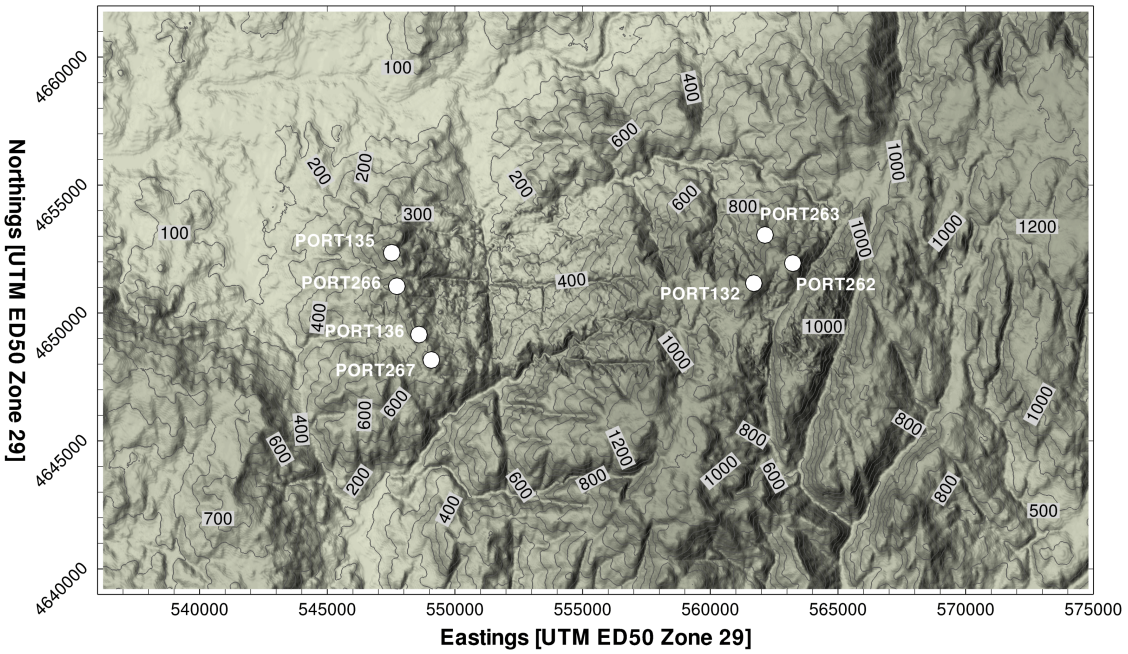

Figure 5.1: Topography for the Mendoiro (left) and Alto do Corisco (right) sites. The masts are represented by the white circles. Contour lines are spaced by 100 m.

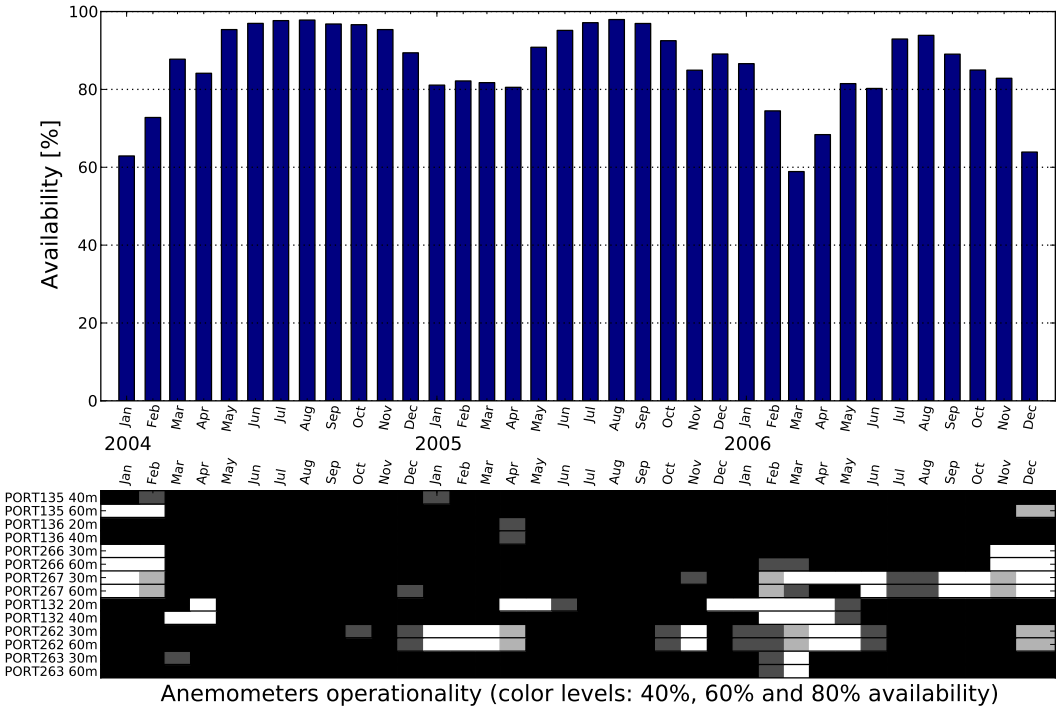

Figure 5.2: Availability of the wind measurements from Mendoiro and Alto do Corisco sites. The topmost plot is the percentage of valid data, for all the measurements combined. In the bottommost plot the availability is given for each dataset, using a colour code where black means $\geq 80\%$, dark grey for $[60\%, 80\%[$, light grey for $[40\%, 60\%[$ and white for $< 40\%$.

This is a pressure based coordinate system which follows the terrain, where $p_{\mathrm{H}T}$ and $p_{\mathrm{H}_\mathrm{W}}$ are the hydrostatic pressure at the top and bottom of the vertical domain, while p_{H} is the hydrostatic pressure for a specific η value. The temporal discretization is split into a 3^{rd} order Runge-Kutta time integration scheme, together with a high-frequency scheme for integration of the acoustic waves. The spatial discretization uses the Arakawa C-grid where the scalars are resolved at grid nodes and the velocity vector components are staggered to the mid-points between the nodes. The convective scheme may be set to 2^{nd}, 4^{th} or 6^{th} order of approximation. The model supports parameterizations for the several physical processes involved, namely:

1. Microphysics processes in clouds involving phase-changes between water vapor, precipitation and ice.
2. Cumulus parameterization for subgrid effects due to convective and shallow clouds.
3. Schemes for modelling the radiation abortion in the atmosphere and the ground heating due to downward longwave and shortwave radiation.
4. Planetary boundary layer and the turbulence kinetic energy in the surface layer.
5. Land-surface model to estimate the heat and moisture surface fluxes.

To reduce the computational load of the model while having zones where the grid resolution is high enough, WRF supports downscaling through nesting. This technique allows to have several domains inside a larger one, forming a hierarchy of domains in which a child domain, nested inside a parent domain, has a finer-resolution. Each child domain is like an independent simulation, except that it receives information on boundary and interior conditions from its parent, in what is designated as one-way nesting. Additionally, a two-way nesting is available where the child can feedback into the coarser parent domain.

As WRF is a limited area model, the initial conditions and the characteristics of the atmosphere at the boundaries are given from a global model. This may be a general circulation model (GCM) or a set of analyses generated from a data assimilation system, usually using both observations and the results from a GCM. The operational analysis from a global model may be described as snapshots of the weather given $4 \sim 8$ times a day. If given only as initial and boundary conditions to drive a regional model, the solution may drift as time evolves, to differ severely from the weather conditions described by latter analyses. The WRF model supports four-dimensional data assimilation (FDDA), commonly known as nudging. This is a technique employed to prevent that the solution given by the regional model drifts too much from the analyses. FDDA employs the following correction:

$$\frac{\partial \phi}{\partial t} = F(\phi) + G_\phi \left[\phi_0 - \phi\right] , \tag{5.2}$$

where for a variable ϕ, obeying a conservation equation whose advection, diffusion and body force terms are represented by $F(\phi)$, a correction towards the field ϕ_0 is forced, weighted by the nudging coefficient G_ϕ. For an *analysis nudging*, ϕ_0 is interpolated from the operational analysis driving the simulation. Alternatively in an *observational nudging*, ϕ_0 is provided from information other than the operational analysis, such as mast measurements.

Table 5.1: Specifications of the WRF domains.

Domain	d1	d2	d3	d4	d5
Parent		d1	d2	d2	d2
Nesting ratio		$1/3$	$1/3$	$1/3$	$1/3$
Resolution (km)	27	9	3	3	3
Grid	24×44	43×61	46×40	34×34	34×34

5.2.2 Description of the WRF simulations

The mesoscale simulations were composed of 5 domains with 3 nesting levels, as represented in Figure 5.3a, with the specifications regarding the grids and nesting presented in Table 5.1. The coarser domain was designed to cover Portugal and allow to have nested domains away from the boundaries. Its central location is the Portuguese geodesic centre in Serra da Melriça $\{8°7'50'' W,\ 39°41'40'' N\}$. The smaller domains, d3, d4 and d5, where chosen to enclose the locations of Mendoiro, Alto do Corisco, Pinheiro and Cabeço da Rainha wind farms. All domains are composed of 49 vertical layers, as represented in Figure 5.3b, with the pressure at the top set to 50 hPa.

The initial and boundary conditions were provided using the final analysis of the Global Data Assimilation System (GDAS) from the National Centers for Environmental Prediction (NCEP FNL ds083.2). These were updated every six hours of each day (00:00,

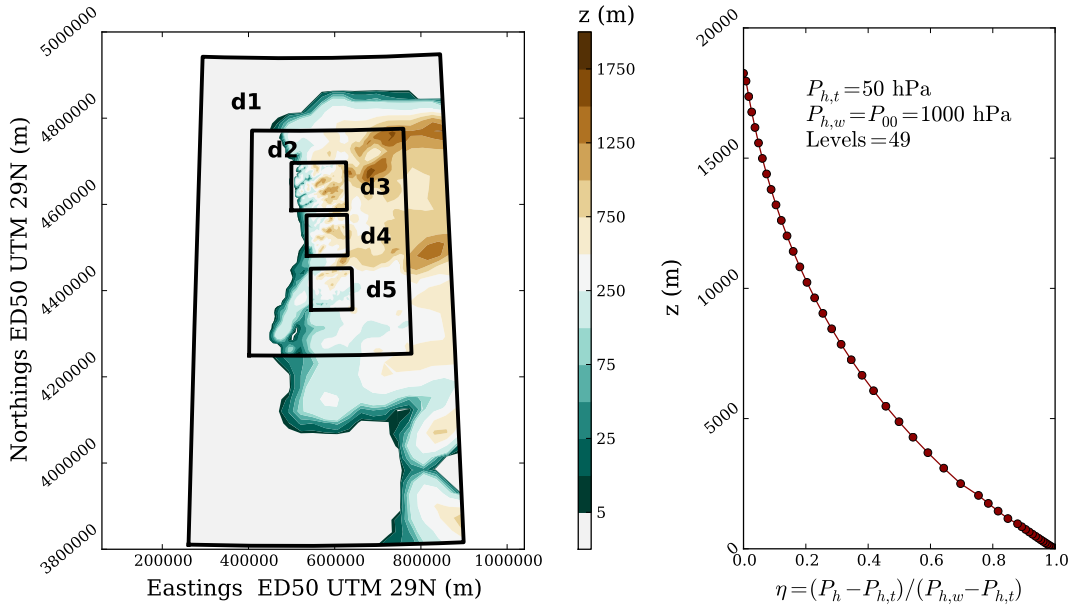

(a) (b)

Figure 5.3: Set-up of the WRF simulations. (a) Domain d2 is nested inside d1, which is the first nesting level. A second nesting level is formed by domains d3, d4 and d5, which are children of d2. The grid resolutions are 27, 9 and 3 km for each nesting level. (b) Distribution of coordinate η in the vertical if the bottom surface is at the mean sea level height.

06:00, 12:00 and 18:00 ST). The respective computational grid is composed of 24 pressure levels (100 kPa to 1 kPa) and has a horizontal resolution of $1° \times 1°$ ($\sim 86 \times 110$ km). The sea surface temperature was given by the real-time global analysis from the National Oceanic and Atmospheric Administration (Thiébaux *et al.*, 2003; NOAA RTG-SST, 2012). This dataset was available in a daily basis, with a spatial resolution of $0.5° \times 0.5°$.

Although reanalysis datasets are expected to provide better boundary conditions, it would solely serve to reconstitute the wind characteristics in the past, with no use for forecasting purposes. Albeit this might be a possible application of the present methodology, it is also an objective to verify if it can be used as a way to improve forecasts. Hence, the analysis datasets were preferred instead of reanalysis ones.

The quality of the results obtained for the first hours of simulation is low, as the initial fields are taken from the coarser GDAS results and the solution is adapting to the new grid. This initial period is regarded as a spin-up time and is discarded. For all WRF simulations the spin-up time was set to 24 hours, *i.e.*, the simulation is started 1 day before the periods defined in §5.1.2.

Following Otte (2008), the nudging coefficients for horizontal wind speed, temperature and water vapor mixing ratio were set to 3×10^{-4}, 3×10^{-4} and 1×10^{-5} s^{-1} respectively. Also, there was no nudging of any scalar inside the ABL.

5.2.3 Selection of parameterizations

The choice on the parameterizations used followed the recommendations in the technical report of Baker *et al.* (2010) for the Ozone Transport Commission, the paper of Hu *et al.* (2010) and other options used by the Centre for Geophysics of Lisbon University (CGUL/IDL). In all simulations, the atmospheric radiation schemes were the Dudhia (1989) and the rapid radiative transfer model (RRTM, Mlawer *et al.* 1997), for modelling shortwave and longwave radiation, respectively. The microphysics of phase-changes was modelled using the WRF Single-Moment 6-Class (WSM6).

The PBL parameterizations may be divided into two categories:

1. Local closure, where a turbulent quantity in a given horizontal and vertical location is function of known variables and gradients at that location. An example is the Mellor-Yamada-Janjic (MYJ) parameterization.

2. Non-local closure, where instead the parameterization uses known variables and gradients at other spatial locations, usually in the vertical direction. An example of such a non-local closure is the ACM2 model by Pleim (2007).

Works such as the dissertation of Carvalho (2009) and the report by Baker *et al.* (2010) tend to favour non-local closures, referring to the ACM2 model. In these, although the RMS error is lower at nocturnal periods for MYJ, it is higher than for the ACM2 at the diurnal periods. Citing Hu *et al.* (2010), the use of the local closure MYJ scheme produces the largest bias at daytime when compared to non-local parameterizations because these are better at predicting the strong vertical mixing.

To evaluate the differences between local and non-local parameterizations, simulations with both were produced. To keep consistency, the change in the PBL model forced

Table 5.2: Parameterizations used in the simulations. The acronyms used refer to: Mellor-Yamada-Janjic scheme (MYJ), Monin-Obukhov Janjic Eta scheme (MOJE), Kain-Fritsch scheme (KF) and Betts-Miller-Janjic scheme (BMJ). Details for the parameterizations are found in the WRF technical description (Skamarock *et al.*, 2008).

Closure	PBL	Surface layer	Land-soil	Cumulus
Local	MYJ	MOJE	Noah	BMJ
Non-local	ACM2	Pleim-Xu	Pleim-Xu	KF

changes in the surface layer and land-soil schemes, creating two set-ups: the *local* and *non-local*. The differences in the parameterizations chosen for both set-ups are in Table 5.2. A different cumulus scheme was also chosen based on the choices among the aforementioned literature, although its importance is lesser than of the other models, considering that the aim is to have a good forecast at heights $\sim 100\,\mathrm{m}$. The cumulus convection scheme is not used for the finer 3 km domains, following the recommendations in the WRF manual (Skamarock *et al.*, 2008).

Table 5.3 shows the global error measures for the two summer weeks. Besides the BIAS, RMSE and SS, all defined in §4.3.4.1, the correlation coefficient, r, is also given for the wind speed. The definition of the SS is the same as in eq. (4.20), so that it measures the improvement of the ACM2 results over those of MYJ. The results using the ACM2 set-up present lower errors than the MYJ closure. This is confirmed in the values of the SS for both wind speed and direction, which are almost all positive. The exceptions are for PORT136 and PORT267 masts, both located at the southern zone of the Mendoiro site. However these negative values are only for the lower heights (20 and 30 meters respectively) and are very close to zero (no improvement). Regarding the wind direction, only the SS for E071 at 30 m is negative. The correlation coefficient is always higher for the ACM2, by a factor 3% to 20%. The wind speed BIAS for ACM2 tends to under-predict more when comparing with MYJ. For the Mendoiro site, both models consistently present a negative BIAS.

The results for the autumn weeks are in Table 5.4. These are consistent in showing that the ACM2 set-up yields a better forecast. The RMSE increases to values $\sim 4\,\mathrm{m\,s^{-1}}$, while for the summer weeks this was $\sim 2.5\,\mathrm{m\,s^{-1}}$. Only for PORT136 and the Lontreira mast (Elnt), the wind direction SS is negative. All of the remainder skill scores show improvements of the ACM2 results against MYJ. The correlation coefficient are much closer though, with fewer discrepancies. The wind speed BIAS is negative for all results, but contrary to the summer period, the MYJ presents higher under-predictions of the mean.

5.2.3.1 Diurnal variation of the WRF forecast error

The error for each mast was computed and grouped according to the hour of the day, to assess its diurnal variation. This is shown in Figures 5.4 and 5.5. In these the green and violet colours are used to represent the ACM2 and MYJ results, respectively. As there are 10 masts and two different model set-ups, this results in 20 lines. For the sake of simplicity, these were condensed in the following way:

Table 5.3: Errors in the 3 km WRF forecast for the period from 2005/07/01 to 2005/07/15. Both local and non-local closures, MYJ and ACM2, are compared. The skill score refers to the improvement of ACM2 over MYJ results, using the mean squared error.

	Speed ($m\,s^{-1}$)							Azimuth (°)				
	MYJ			**ACM2**				**MYJ**		**ACM2**		
Mast	*r*	BIAS	RMSE	*r*	BIAS	RMSE	SS	BIAS	RMSE	BIAS	RMSE	SS
E071 30m	0.77	-0.26	2.26	0.83	-0.76	2.14	0.11	9.03	50.72	-0.59	51.07	-0.01
E071 65m	0.74	0.55	2.61	0.79	-0.07	2.33	0.20	7.09	42.72	-0.56	42.60	0.01
Ecra 30m	0.54	-0.20	2.77	0.60	-0.43	2.65	0.08	20.39	49.56	13.05	40.52	0.33
Elnt 15m	0.45	-1.75	2.69	0.54	-1.81	2.64	0.04	3.97	39.64	0.65	30.38	0.41
Elnt 30m	0.44	-0.84	2.19	0.54	-1.06	2.13	0.05	4.74	41.61	2.04	31.69	0.42
PORT132 20m	0.48	-1.57	2.99	0.69	-1.96	2.87	0.08	2.14	48.55	6.41	46.14	0.10
PORT132 40m	0.55	-0.53	2.67	0.70	-1.04	2.42	0.18	7.11	41.85	12.12	40.49	0.06
PORT262 30m	0.51	0.06	2.22	0.66	-0.45	1.93	0.24	-14.14	47.80	-9.74	41.89	0.23
PORT262 60m	0.55	0.35	2.55	0.68	-0.38	2.17	0.27	-8.27	39.00	-14.47	45.70	0.27
PORT263 30m	0.59	-0.38	2.51	0.73	-0.65	2.20	0.23	-18.52	44.76	-9.87	38.20	0.27
PORT263 60m	0.64	0.75	2.51	0.74	0.18	2.06	0.32	-21.22	47.33	-15.13	39.26	0.31
PORT135 40m	0.78	-1.18	2.61	0.86	-1.73	2.60	0.01	-3.83	47.46	4.87	41.88	0.22
PORT135 60m	0.78	-0.95	2.67	0.87	-1.67	2.63	0.03	-12.82	42.84	-3.86	33.04	0.40
PORT136 20m	0.80	-1.55	2.82	0.84	-1.89	2.87	-0.03	-12.33	61.17	-4.42	55.63	0.17
PORT136 40m	0.81	-0.68	2.28	0.86	-1.17	2.26	0.02	-4.31	50.35	1.35	43.48	0.25
PORT266 30m	0.79	-0.98	2.38	0.86	-1.49	2.38	0.00	-16.16	47.68	-8.74	39.43	0.32
PORT266 60m	0.80	-0.59	2.30	0.88	-1.31	2.23	0.06	-7.53	42.77	0.43	36.92	0.25
PORT267 30m	0.87	-1.39	2.57	0.90	-1.71	2.59	-0.01	-17.00	53.81	-8.42	48.05	0.20
PORT267 60m	0.87	-0.69	2.24	0.91	-1.20	2.20	0.04	-19.80	54.51	-13.83	51.81	0.10

Table 5.4: Errors in the 3 km WRF forecast for the period from 2005/11/19 to 2005/12/03. For details refer to Table 5.3

	Speed ($m\,s^{-1}$)							Azimuth (°)				
	MYJ			**ACM2**				**MYJ**		**ACM2**		
Mast	r	BIAS	RMSE	r	BIAS	RMSE	SS	BIAS	RMSE	BIAS	RMSE	SS
E071 30m	0.84	-2.44	3.92	0.85	-2.44	3.87	0.02	-2.78	15.00	-0.68	13.51	0.19
E071 65m	0.83	-1.82	3.73	0.86	-1.74	3.48	0.13	-3.71	21.36	-1.61	21.30	0.01
Elnt 15m	0.86	-4.89	5.56	0.85	-4.53	5.19	0.13	-10.11	23.67	-7.51	25.04	-0.12
Elnt 30m	0.85	-3.43	4.18	0.85	-3.14	3.87	0.14	-10.28	24.23	-7.42	25.43	-0.10
PORT132 20m	0.72	-6.14	7.47	0.73	-6.09	7.38	0.02	0.34	17.97	0.27	17.51	0.05
PORT132 40m	0.80	-3.75	5.36	0.81	-3.53	5.12	0.09	5.53	26.79	6.62	20.36	0.42
PORT262 30m	0.79	-1.83	3.51	0.81	-1.63	3.30	0.12	1.49	33.81	4.19	30.52	0.18
PORT262 60m	0.78	-1.73	3.75	0.80	-1.66	3.56	0.10	-8.56	25.14	-7.77	20.54	0.33
PORT263 30m	0.69	-1.67	3.81	0.72	-1.44	3.60	0.11	-4.97	26.30	-1.29	25.72	0.04
PORT263 60m	0.73	-0.28	3.47	0.75	-0.24	3.36	0.06	-15.86	26.60	-12.02	24.35	0.16
PORT135 40m	0.65	-2.61	4.22	0.68	-2.30	3.93	0.13	-2.26	40.56	4.85	40.54	0.00
PORT135 60m	0.69	-2.53	4.35	0.71	-2.28	4.10	0.11	-11.23	40.83	-4.17	38.00	0.13
PORT136 20m	0.67	-2.31	3.66	0.65	-1.76	3.41	0.14	-18.89	57.64	-8.64	54.11	0.12
PORT136 40m	0.69	-1.76	3.43	0.67	-1.16	3.28	0.09	-3.42	46.42	5.53	47.18	-0.03
PORT266 30m	0.66	-2.60	4.02	0.69	-2.17	3.66	0.17	-16.13	45.25	-4.61	40.96	0.18
PORT266 60m	0.68	-2.29	3.97	0.70	-1.90	3.69	0.14	-2.48	39.68	3.74	36.85	0.14
PORT267 30m	0.79	-2.83	3.98	0.77	-2.14	3.59	0.18	-13.45	51.20	-7.62	45.16	0.22
PORT267 60m	0.81	-2.22	3.55	0.79	-1.51	3.27	0.15	-18.54	48.65	-13.46	46.20	0.10

1. For a specific hour the average value of the error measure is computed. This was plotted as a solid line.
2. To have an idea of the variation of the error in that specific hour, the maximum and minimum value are also displayed. This is shown using a patch of the same colour as the solid line, delimited by the maximum and minimum.

Summer period

In Figures 5.4a and 5.4c the BIAS and RMSE is shown for wind speed forecast by the 3 km nesting. Both models have a negative BIAS, apart from the afternoon period where MYJ shows positive values. The RMSE trend is similar for both models, increasing in the nocturnal periods to $3\,\mathrm{m\,s^{-1}}$. The ACM2 performs better in the period between 9:00 and 15:00, showing almost less 40% of error than the MYJ forecast. This suggests that a non-local closure responds faster to the morning heating, as it allows convective motions to rise faster. Although this agrees with the conclusions of Hu *et al.* (2010), the magnitude of the BIAS at daytime is similar for both ACM2 and MYJ forecasts, only differing in the sign. In the RMSE results for the 9 km nesting (Figure 5.4g) the trend is the same in showing higher errors for the nocturnal period. However no improvement is seen for the ACM2, even for the morning hours. Thus, the ACM2 closure appears to be dependent on the resolution, being ineffective for coarser grids.

The azimuth error is shown in Figure 5.4d. The RMSE increases during the diurnal periods, although the trend is less noticeable with an average error around 40°. The results for 9 km (Figure 5.4h) yield better agreement with the observations. To analyse this, wind roses for the several masts are presented in §E.1.1.1 of the Appendix E, for the 3 km nesting. For both Alto do Corisco and Mendoiro the wind direction was mainly from the northeast. The Pinheiro and Cabeço da Rainha sites have a broader range, with stronger components from the northwest. When these were compared with the roses for the 9 km nest results (not shown), none of the main directions change or shift. Regarding the wind roses, for some masts the 3 km nesting provided better results. It was concluded that the finer resolution grid introduces more variability in the wind direction, which returns higher errors due to lags in predicting the instants where shifts occur in the wind direction.

Autumn period

The results for the autumn weeks are shown in Figures 5.5a and 5.5c. Both BIAS and RMSE of the wind speed are similar, with ACM2 providing a slightly better agreement with the observations for both 3 km and 9 km nesting levels. Both models show small variations throughout the day, with some increase in the late afternoon. Regarding the wind direction, the RMSE is higher during the morning but is lower than for the summer week, around $\sim 30°$. The wind roses (Appendix E, §E.1.2.1) show different directions for all sites. For Mendoiro the northeast winds were predominant, with a good agreement except for PORT136 and PORT267, with the 0° sector over-predicted. In Corisco and Cabeço da Rainha it is the southeast sectors which had most occurrences. These were well represented by the simulations, with the MYJ model returning a slightly better

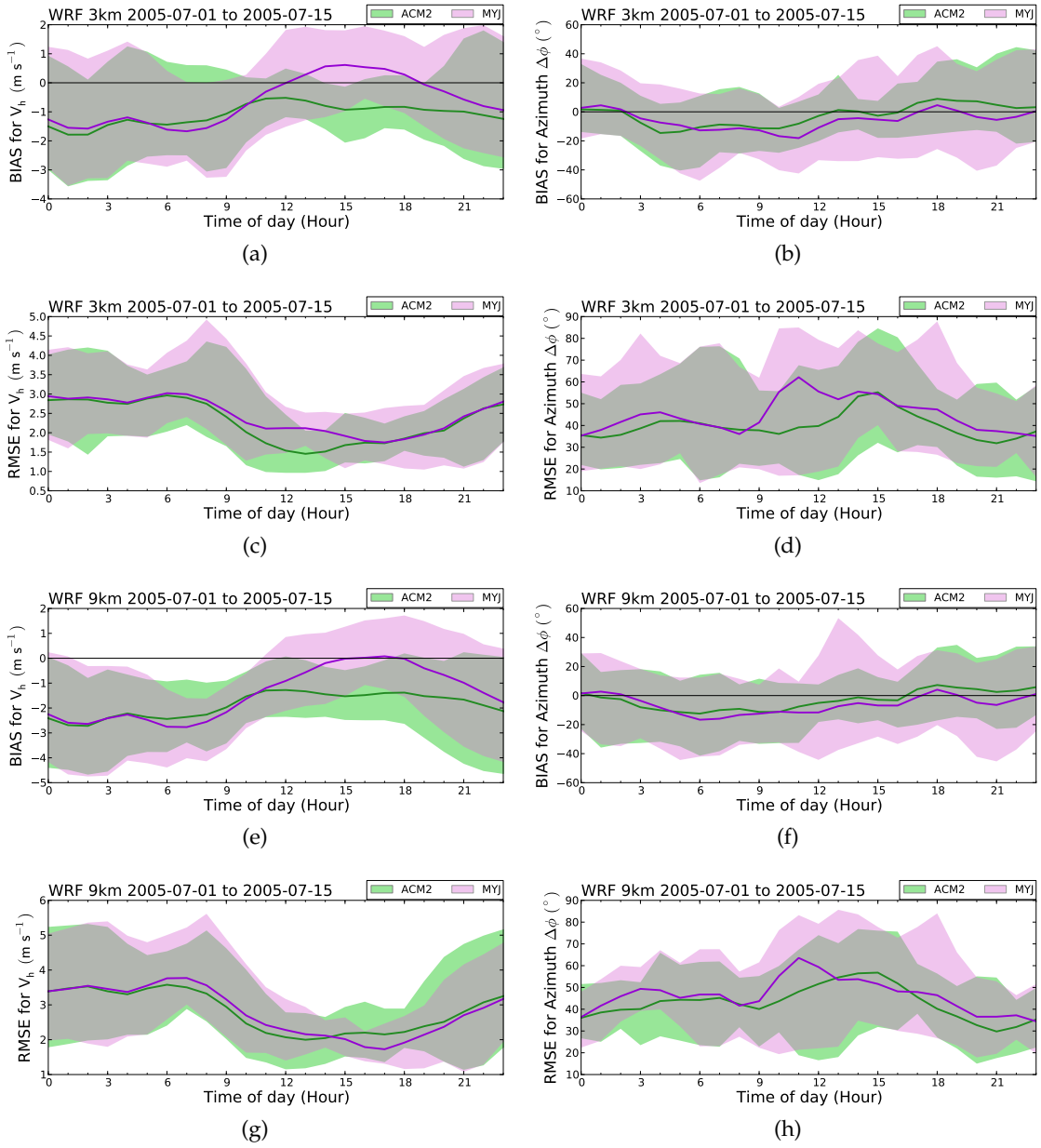

Figure 5.4: Error in the WRF forecast for the period 2005/07/01 to 2005/07/15. The plots show the evolution of the error as function of the diurnal cycle. This is achieved considering all records that fall within a specific hour of the day. The measures are based on errors using hourly averages. To condense the curves from all 10 masts analysed, the patch is obtained from the minimum and maximum values found, while the centre curve is an average of all of the 10 lines. The different colours refer to the PBL parameterization used: green for ACM2 nonlocal closure, purple for the Mellor-Yamada-Janjic. The first four figures (a), (b), (c), (d); refer to the 3 km nestings; while the remaining to the 9 km nesting. Figures in the left column (a), (c), (e), (g): BIAS and RMSE for the wind speed. Figures in the right column (b), (d), (f), (h): BIAS and RMSE for the wind direction.

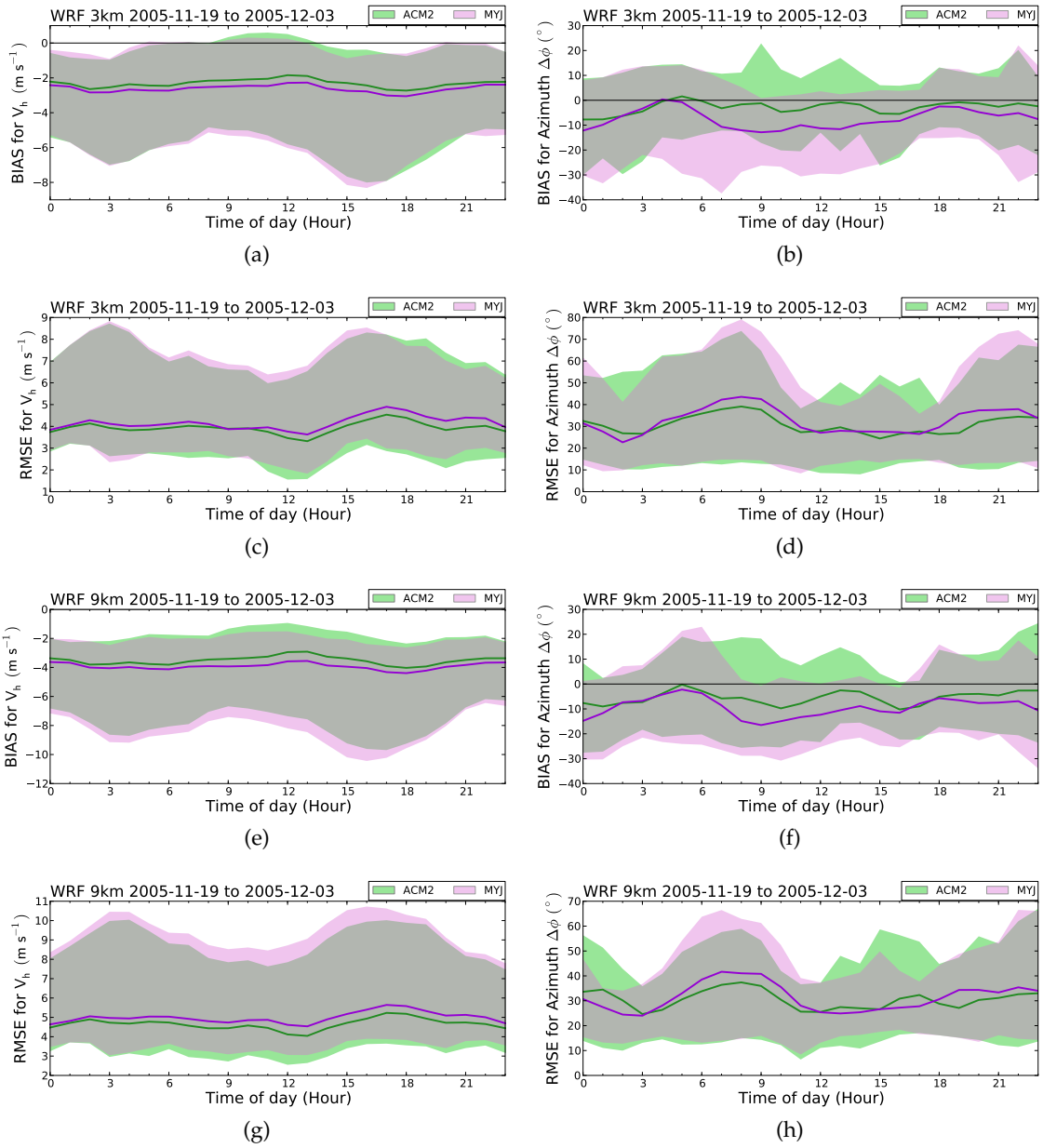

Figure 5.5: Error in the WRF forecast for the period 2005/11/19 to 2005/12/03. The meaning and organization of the plots is the same that in Figure 5.4

forecast. The Pinheiro site has no predominant direction, with all quadrants sharing the same frequency of occurrence. The main bins are in agreement except for some over-prediction of the 270° sector.

5.2.3.2 Summary

The main considerations that were drawn from the comparison of the mesoscale simulations with ACM2 and MYJ parameterization set-ups are summarized as follows:

1. For both periods considered, the ACM2 set-up yielded lower error than the MYJ, in both wind speed and direction. The ACM2 correlation is higher, particularly in the summer weeks.
2. The wind speed bias is mostly negative for both forecasts. While for the summer the ACM2 shows higher bias magnitude, in autumn it favours the ACM2 set-up.
3. The differences in bias and quadratic error between the two forecasts happen mainly during the diurnal rather than the nocturnal hours. For the summer weeks these differences were more pronounced than for the autumn weeks, the latter being less dependent on the diurnal cycle.

5.3 Microscale model set-up

In this section are outlined the details and changes made to the VENTOS® computer code in order to use the mesoscale results from WRF. The model was changed to consider buoyancy effects as described in §2.5, requiring an additional transport equation for the potential temperature and different surface boundary conditions.

To have consistency between the mesoscale and the microscale surface grids, the latter was generated such that the resolution near its boundaries matches the WRF mesh. The several grids used and their resolution near the locations of the meteorological masts are characterized.

The procedure used to interpolate both initial and boundary conditions from the WRF results is explained. In zones where the vertical resolution near the surface is higher than in WRF, profiles of velocity and temperature were fitted to be consistent with Monin-Obukhov similarity theory. The WRF data used were the results with the ACM2 non-local closure, as it yielded the best agreement with the field measurements.

5.3.1 Topography and grid generation for the microscale model

The geographic latitude and longitude were converted to Universal Transverse Mercator (UTM), using a set of FORTRAN routines written by Daly (1999) of the Ocean Acoustics Group from MIT (Massachusetts Institute of Technology). As the coordinates of the Portuguese site were given in a different geodetic datum (European Datum 1950), the conversion could yield errors in the order of the 100 meters. To correct for this, a standard Molodensky transformation was implemented on the code, described in §7 of

NIMA (2000). The three parameters used for this correction were the ones recommended by the Portuguese Geographic Institute, namely 87.987 m, 108.639 m and 121.593 m. With these, the mismatch in the coordinates of the masts was reduced to less than 1 m.

The surface grid was generated by choosing a centre location and expanding the mesh from that point to the domain edges. The expansion was made using a geometric progression applied on the control volumes length. The centre location for a site was obtained by computing the geometrical centre of the respective masts.

High-resolution maps were provided by INEGI for all sites. The microscale grid is obtained through bi-linear interpolation from these maps, except near the boundaries. Below a specified distance from the boundary, the mesh was forced to agree with the

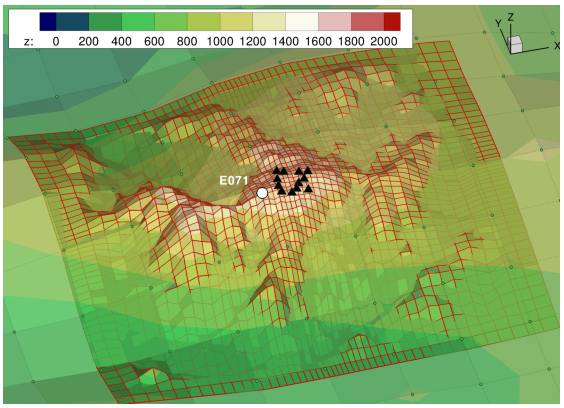

(a) Pinheiro wind farm.

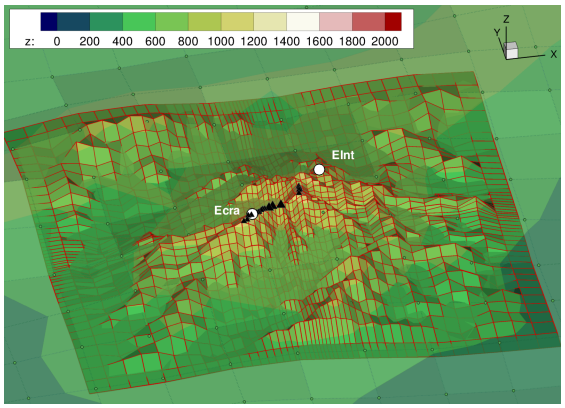

(b) Cabeço da Rainha wind farm.

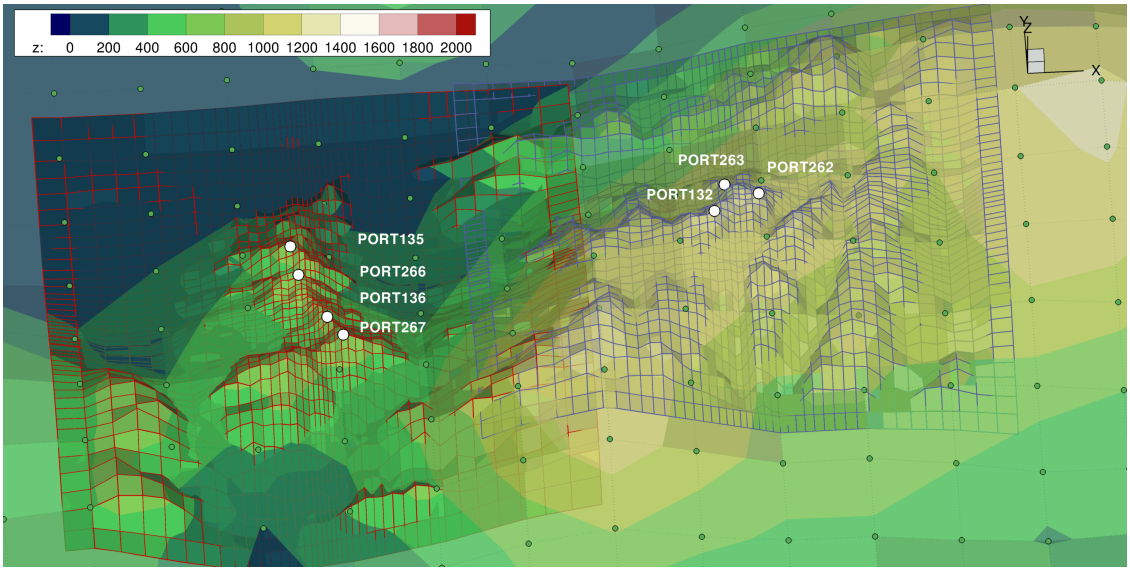

(c) Mendoiro (red) and Corisco (blue) sites.

Figure 5.6: Surface grid used in the microscale simulations, with the mesoscale grid points (mass centres), for the four topographies investigated. The 3 km grid used in the regional model is show for comparison (un-staggered), with the horizontal location of each node represented by the green circles. Symbols: ○ - measurement masts, ▲ - turbines. The vertical scale was exagerated by a factor of 4.

Table 5.5: Characteristics of the computational domain used in the microscale simulations. For the horizontal plane are shown: the domain size, minimum and maximum resolution, and the expansion factor. For the vertical direction: height of the surface mesh (min. and max.), distance between the top and surface boundaries (min. and max.), maximum expansion factor f_z, minimum and maximum control volume height.

	Pinheiro	Rainha	Corisco	Mendoiro
Grid	$50 \times 47 \times 44$	$49 \times 47 \times 44$	$47 \times 47 \times 44$	$42 \times 49 \times 44$
Length x (km)	19	21	18	18
Length y (km)	18	20	18	21
$\min(\Delta x, \Delta y)$ (m)	200	150	200	150
$\max(\Delta x, \Delta y)$ (m)	684	957	665	984
$\max(f_x, f_y)$	1.06	1.09	1.06	1.10
Surface height (m)	[261, 1355]	[341, 1059]	[115, 1322]	[26, 1150]
$z_{top} - z_{surf}$ (m)	[6054, 7147]	[6343, 7060]	[5826, 7033]	[5891, 7015]
$\max(f_z)$	1.15			
$\min(\Delta z)$ (m)	3			
$\max(\Delta z)$ (m)	942	925	922	919

WRF surface grid using a smoothing function to interpolate from the high-resolution to the mesoscale topography. An interpolation coefficient α is obtained from the absolute distance x to the nearest boundary and the distance Δx through which the smoothing function acts, such that:

$$\alpha = \frac{\tanh(C\,X)}{2\,\tanh(C)} + \frac{1}{2}\,, \quad X = \max\left(-1,\, \min\left(1,\, \frac{2\,x}{\Delta x} - 1\right)\right)\,, \tag{5.3}$$

where C is a smoothing coefficient with a value set to $\tanh^{-1}(0.9999)$. The microscale surface height, z_{w}, is then obtained from the high-resolution and WRF grids, z_{hr} and z_{wrf} respectively:

$$z_{\mathrm{w}} = z_{\mathrm{hr}}\,\alpha + z_{\mathrm{wrf}}\,[1-\alpha]\,.$$

In Figure 5.6 are shown the microscale and mesoscale surface grids for each of the four sites. The distance Δx where the smoothing function acts was set to 2.5 km, which represents $3 \sim 5$ elements in the edges of the domain. Other characteristics of the grids generated are given in Table 5.5. For each direction, the horizontal size of the domain was set to ensure that the boundaries are 8 km away from any mast or turbine. The resolution at the domain centre was chosen to meet the following criteria: (i) to reduce the number of elements; (ii) keep a resolution at the locations of the masts and turbines similar and below ~ 300 m; (iii) to have a ratio between the spacing of a regular mesh and the minimum resolution < 3. The grids have horizontal expansion factors below 1.1, with the elements near the boundaries having maximum lengths ~ 1 km, lower than the resolution of the WRF mesh. The resolutions at the locations of interest, masts and turbines, are shown in Table 5.6.

The vertical grid was generated with a height of 3 m for the first elements, expanding up to ~ 7 km using a geometric progression with factors below 1.15. This resulted in a mesh with, at least, 13 elements inside the first 100 m AGL.

Table 5.6: Microscale grid resolution near the masts and turbines.

Pinheiro	E71	Turbines min.	Turbines max.	
Resolution in x (m)	248	200	248	
Resolution in y (m)	224	211	236	
Rainha	Ecra	Elnt	Turbines min.	Turbines max.
Resolution in x (m)	286	310	163	310
Resolution in y (m)	270	293	163	293
Corisco	PORT132	PORT262	PORT263	
Resolution in x (m)	236	236	224	
Resolution in y (m)	250	211	250	
Mendoiro	PORT135	PORT136	PORT266	PORT267
Resolution in x (m)	223	166	202	223
Resolution in y (m)	310	243	207	310

5.3.2 Hydrostatic reference state

To keep consistency, the same hydrostatic thermodynamic reference state that is implemented in WRF was used in the microscale model. This is based on the following relation between the temperature and pressure profiles:

$$T_{\mathrm{H}} = T_0 + A \ln\left(\frac{p_{\mathrm{H}}}{p_0}\right) , \tag{5.4}$$

where A is a measure of the temperature lapse rate between the pressure levels of p_{H} and $p_{\mathrm{H}} \cdot e^{-1}$, defined as 50 K. Applying the equation of state (2.11) and the definition of hidrostatic equilibrium in eq. (2.4), the vertical profile for p_{H} is derived:

$$p_{\mathrm{H}} = p_0 \exp\left(-\frac{T_0}{A} + \sqrt{\left[\frac{T_0}{A}\right]^2 - \frac{2\,g\,z}{A\,R_d}}\right) . \tag{5.5}$$

This allows to define both p_{H}, T_{H} and ρ_{H}. By applying the definition of θ in eq. (2.15), a profile for θ_{H} is obtained.

5.3.3 Procedure to generate initial and time-dependent boundary conditions from the mesoscale results

After the conclusion of the mesoscale simulations and the microscale grid is generated, the surface heat flux, q_{w}, surface skin temperature and the boundary-layer height, δ, are obtained through bi-linear interpolation. For the microscale grid elements whose centre is above the first vertical level of the WRF mesh, the components of the velocity vector, $\overline{\vec{u}}$, and potential temperature, $\overline{\theta}$, are computed using tri-linear interpolation.

For nodes which are below the first vertical level, wall functions are used to estimate both $\overline{u}$, $\overline{v}$ and $\overline{\theta}$, while $\overline{w}$ is tri-linearly interpolated. This requires that $\mathcal{L}$ is estimated,

to know both u_* and θ_*. From the definition of the bulk Richardson number, $\mathrm{Ri_b}$, the Obukhov Length in eq. (2.90), and the velocity and temperature logarithmic profiles, eqs. (2.96) and (2.97):

$$\mathrm{Ri_b} = \frac{g}{\Theta}\frac{\Delta z\,\Delta\overline{\theta}}{\left[\overline{u}^2+\overline{v}^2\right]} = \frac{\Delta z}{\mathcal{L}}\frac{\left[\ln\left(\frac{\Delta z}{z_{\mathrm{h0}}}+1\right)-\psi_h\left(\frac{\Delta z+z_{\mathrm{h0}}}{\mathcal{L}}\right)+\psi_h\left(\frac{z_{\mathrm{h0}}}{\mathcal{L}}\right)\right]}{\left[\ln\left(\frac{\Delta z}{z_{\mathrm{m0}}}+1\right)-\psi_m\left(\frac{\Delta z+z_{\mathrm{m0}}}{\mathcal{L}}\right)+\psi_m\left(\frac{z_{\mathrm{m0}}}{\mathcal{L}}\right)\right]^2}\,, \tag{5.6}$$

where $\overline{u}$, $\overline{v}$ and $\Delta\overline{\theta}$ at height Δz are known, as these are given by the solution from the mesoscale simulation at the first vertical level above the wall. $\mathcal{L}$ is computed by numerically solving eq. (5.6) using a bisection root-finding method. Afterwards the velocity and temperature diabatic profiles are used to compute $\overline{u}$, $\overline{v}$ and $\overline{\theta}$ at the vertical height of the microscale grid nodes.

For fields of density and velocity that respect mass conservation,

$$\dot{m}_w - \dot{m}_e + \dot{m}_s - \dot{m}_n - \dot{m}_t = 0\,,$$

where $\dot{m}$ is the mass flow through each of the computational domain boundaries where flow may occur, hence labelled as w, e, s, n and t. As the interpolated fields from the regional model may not conserve mass, a residual $\mathcal{R}$ may exist:

$$\mathcal{R} = \dot{m}_w - \dot{m}_e + \dot{m}_s - \dot{m}_n - \dot{m}_t\,, \tag{5.7}$$

The easiest way to enforce mass conservation is attained by choosing and modifying one of the domain boundaries. This is done by scaling the velocity values, normal to the chosen boundary, by a factor $\mathcal{F}$, such that:

$$\mathcal{F} = \frac{\dot{m}_f - s\,\mathcal{R}}{\dot{m}_f}\,, \qquad s = \begin{cases} -1, & \text{for } f = e,n,t \\ +1, & \text{for } f = w,s \end{cases}\,,$$

with the subscript f indicating the location of the domain boundary, while s merely changes the sign to be consistent with mass flow entering or exiting the domain.

This approach was attempted in several numerical tests. The top boundary was chosen as the one where the values would be changed, as this boundary is generally wider than the lateral boundaries. This led to satisfactory results at most of the times because the vertical velocity values would not change drastically. However, in some rare situations this procedure originated unreasonable values which resulted in numerical problems. To tackle this, the velocities at all the domain boundaries were changed by a factor $\mathcal{F}_f$, weighted by the ratio between the mass flow through that specific boundary and the total mass flow, represented by $\widehat{\mathcal{F}}$. Thus,

$$\widehat{\mathcal{F}}_f = \frac{|\dot{m}_f|}{\sum_j |\dot{m}_j|} \quad\Rightarrow\quad \mathcal{F}_f = \frac{\dot{m}_f - s\,\widehat{\mathcal{F}}_f\,\mathcal{R}}{\dot{m}_f}\,, \qquad s = \begin{cases} -1, & \text{for } f = e,n,t \\ +1, & \text{for } f = w,s \end{cases}\,,$$

Although this approach changes all of the inflow and outflow velocities, as the imbalance is distributed over all boundaries, the effect was unperceived as the resulting factors, $\mathcal{F}$, would differ from unity only after the 3$^{\mathrm{rd}}$ decimal place.

5.3.4 Treatment of the turbulence production terms in the $k-\epsilon$ model

The microscale code uses the $k-\epsilon$ turbulence model following some of the changes proposed in Duynkerke (1988), described in §2.2.3. The set of coefficients are the ones presented in eq. (2.76). If the buoyancy production term $\mathcal{G}$ is negative, its value is neglected from the ϵ equation production, $\mathcal{P}_\epsilon$, as shown in eq. (2.79).

Fundamentally the $k-\epsilon$ model assumes that the flow is turbulent and it is not appropriate when flow laminarization happens. Such may occur if the Richardson number is higher than a critical value, $\mathrm{Rf} > \mathrm{Rf_c}$, estimated to lie between 0.2 and 1 (Businger, 1969; Galperin *et al.*, 2007). Using the modified $\mathcal{P}_\epsilon$ production term in eq. (2.79), Duynkerke (1988) deduced that:

$$\mathrm{Rf_c} = 1 - {C_{\epsilon 1}}\Big/{C_{\epsilon 2}} \approx 0.2\,. \tag{5.8}$$

To avoid numerical problems and retain the flow turbulence even under very stable conditions, eq. (5.8) is used to keep the turbulence production balance positive. Thus:

$$\mathcal{P}_k = \max\left(\mathcal{P}+\mathcal{G},\, \mathcal{P}\left[1-\mathrm{Rf_c}\right]\right)\,, \tag{5.9}$$

where $\mathcal{P}_k$ is the sum of the production terms due to mechanical shear and buoyancy, $\mathcal{P}$ and $\mathcal{G}$, which are accounted in the k equation (2.66).

5.3.5 Prescribed heat flux condition at the bottom surface

The WRF model provides fields for both surface temperature and sensible heat flux. Although a prescribed temperature is straightforward to implement, *e.g.*, using eq. (5.6), it could introduce severe discrepancies due to the sensitivity of the temperature to the vertical height. If the microscale and mesoscale grids show different elevations for the same location, due to the coarseness of the latter, the surface temperature will not correspond between them. Instead, as the heat flux within the surface layer is nearly constant with height, it becomes preferable to use it in the microscale to estimate the stratification level at the bottom surface.

This boundary condition may yield two solutions of the Obukhov length, $\mathcal{L}$, for the same surface heat flux, q'_{w}. This is known as the duality problem (Taylor, 1971; van de Wiel *et al.*, 2007) making it necessary to choose one of the possible solutions. As one of these leads to a collapse of turbulence, such that both turbulent and laminar states are possible, a limitation was imposed on the maximum value of $\zeta = \Delta z/\mathcal{L}$ to force a continuous turbulent regime. This limit arises from the minimum value which is possible for q'_{w} to attain:

$$\min\left(q'_{\mathrm{w}}\right) = \frac{-4\,\kappa^2\,\rho_{\mathrm{w}}\,c_p\,u_\tau^3}{27\,\dfrac{g}{\Theta}\,b_{ms}\left[\Delta z - z_{\mathrm{m0}}\right]\ln\left(\dfrac{\Delta z}{z_{\mathrm{m0}}}\right)^2}\,,\quad \max\left(\zeta\right) = \frac{\ln\left(\dfrac{\Delta z}{z_{\mathrm{m0}}}\right)}{2\,b_{ms}\left[1-\dfrac{z_{\mathrm{m0}}}{\Delta z}\right]}\,. \tag{5.10}$$

In this equation, u_τ is the magnitude of the velocity tangent to the wall, $\|\vec{u}_\tau\|$, located at the centre of the first control volume. The other variables are defined in §2.3.

Table 5.7: Computational details of the microscale simulations.

Site	Simulation period	Partitions	CPU time (days)	Speed-up
Pinheiro	2005-07-01 – 2005-07-15	6	4.3	3.2
	2005-11-19 – 2005-12-03		2.7	5.1
Rainha	2005-07-01 – 2005-07-15	4	5.6	2.5
	2005-11-19 – 2005-12-03		3.6	3.9
Corisco	2005-07-01 – 2005-07-15	6	3.5	4.0
	2005-11-19 – 2005-12-03		3.7	3.8
Mendoiro	2005-07-01 – 2005-07-15	4	4.5	3.1
	2005-11-19 – 2005-12-03		2.7	5.2

The Obukhov length is computed from the known values of u_τ and ${q'}_{\mathrm{w}}$. The velocity is related with u_* by the momentum bulk transfer coefficient, as defined in eq. (2.162):

$$u_* = u_\tau \, C_m \; . \tag{5.11}$$

Note that coefficient $C_m = C_m(\zeta)$. From the definition of $\mathcal{L}$ in eq. (2.90), the following implicit relation is found:

$$\zeta = -\frac{\kappa \, \Delta z \, g \, {q'}_{\mathrm{w}}}{\rho_{\mathrm{w}} \, c_p \, \Theta \, {u_*}^3} = -\frac{\kappa \, \Delta z \, g \, {q'}_{\mathrm{w}}}{\rho_{\mathrm{w}} \, c_p \, \Theta} \; [u_\tau \, C_m]^{-3} \; . \tag{5.12}$$

Besides itself, ζ becomes function of u_τ and ${q'}_{\mathrm{w}}$. A value for ζ is obtained by numerically solving eq. (5.12). This was done using a fixed point iteration, where ζ is made explicit by using the value of $\mathcal{L}$ in the previous time-step. The method was verified to converge in the range of ζ for which the stability functions are valid, considering the limit imposed by eq. (5.10).

5.3.6 Computational details

The simulations were run on a Dell™ Precision™ T7500 workstation with a quad-core Intel® Xeon® CPU, model W5580 at 3.20 GHz clock speed, 8 MB cache and 64 bit instruction set, allowing eight threads. The compiler used was the Intel® Fortran Compiler 11.1. The parallelization was achieved using the Open MPI 1.4.3 implementation of the Message Passing Interface (MPI) standard. Details regarding the parallelization technique are described in Castro *et al.* (2008).

5.4 Analysis of the forecast results

Throughout this section the results for the microscale forecast are analysed and compared with the mesoscale. This is done separately for the two time periods considered: the summer and autumn weeks.

The results in Tables 5.8 and 5.9 comprise the several global measures for the summer and autumn weeks. Each line in the tables refers to the measurements at a specific mast and height AGL. These are ordered according to the respective site: Pinheiro, Cabeço da

Rainha, Alto do Corisco and Mendoiro. The errors are also shown both for the mesoscale and microscale. The skill score uses the mesoscale results as reference, thus it measures the improvement of the microscale over the mesoscale, if it is > 0. In Figures 5.7 and 5.13 is variation of the RMSE over a typical day for each site, to verify any dependency on the diurnal cycle.

For each site a mast was chosen, regarded as representative of the wind conditions at that area. The time series of the forecast and measurements are shown for each of the selected masts in Figures 5.8 and 5.14, while in Figures 5.9 and 5.15 are shown histograms of wind speed and direction. These were important not for the forecasting purposes but for wind resource assessment and to verify the quality of the results without the influence of phase errors.

To identify patterns and trends related to the diurnal cycle, a detailed analysis is made using Figures 5.11 and 5.17. These are Hovmöller diagrams which show the variation of the histograms of wind speed and direction, over a typical day.

On the overall, there are improvements of the microscale over the mesoscale in the forecast of the wind speed. These are generally higher at lower heights. Although the summer period returns lower error values, the improvements are higher for the autumn weeks. For the wind direction, the mesoscale forecast provides a better agreement during the summer.

5.4.1 Results for the summer weeks: 2005-07-01 to 2005-07-15

5.4.1.1 Global errors

For the summer weeks, the microscale shows improvements in the wind speed forecast for 11 of the 19 locations. In Mendoiro the results are very good, with the $SS > 0.15$ except for one location. At PORT136 (40 m) the SS is ~ 0 and the correlation coefficient r is the worst, equal to 0.83. For the other locations r is always above 0.87. The BIAS is similar for all locations, positive and below $1\,\mathrm{m\,s^{-1}}$ for the microscale results. The mesoscale results show negative BIAS with values between -1 and $-2\,\mathrm{m\,s^{-1}}$. The PORT136 (40 m) has lower RMSE than most of the other masts, nearly 10% less than the average error. The negative result in the SS is due both to an inferior microscale forecast against a superior mesoscale forecast. The forecast of wind direction is better for the mesoscale, which has less BIAS and less 10% of error, equivalent to less $\sim 5°$. Following the order in Figure 5.6c, the northern masts gather the lowest scores and the largest microscale bias. For the mesoscale the inverse trend is observed.

In Alto do Corisco the microscale velocity BIAS is also closer to 0. The RMSE values are close to the ones found in Mendoiro, but the scores are worse and half of these are negative. PORT263 is the worst location with $SS = -0.2$ at 60 m and a smaller but negative SS for 30 m. This is the northernmost mast and is located lower than the others, outside of the mountain top. For the several simulations which were produced for this site, the score was always negative. PORT262 also yields negative SS at 30 m, albeit the microscale RMSE is the lowest for this site. PORT132 shows better results with an $SS \sim 0.4$ at its highest height. The r is ~ 0.7 for the microscale with small deviations,

Table 5.8: Comparison of the errors in the mesoscale (WRF 3 km ACM2) and microscale forecasts, for the period from 2005/07/01 to 2005/07/15. The skill score refers to the improvement of the microscale over the mesoscale results, using the mean squared error.

	Speed ($m\,s^{-1}$)							Azimuth (°)				
	Mesoscale			Microscale				Mesoscale		Microscale		
Mast	r	BIAS	RMSE	r	BIAS	RMSE	SS	BIAS	RMSE	BIAS	RMSE	SS
Pinheiro												
E071 30m	0.83	-0.76	2.14	0.75	-0.36	2.43	-0.30	-0.59	51.07	3.13	53.23	-0.09
E071 65m	0.79	-0.07	2.33	0.72	-0.57	2.69	-0.33	-0.56	42.60	2.85	46.90	-0.21
Cabeço da Rainha												
Ecra 30m	0.60	-0.43	2.65	0.59	-0.55	2.71	-0.05	13.05	40.52	10.76	43.50	-0.15
Elnt 15m	0.54	-1.81	2.64	0.33	-0.33	2.44	0.14	0.65	30.38	-1.50	59.65	-2.85
Elnt 30m	0.54	-1.06	2.13	0.40	-0.10	2.23	-0.10	2.04	31.69	0.56	56.42	-2.17
Alto do Corisco												
PORT132 20m	0.69	-1.96	2.87	0.71	-0.41	2.24	0.39	6.41	46.14	-1.12	57.89	-0.57
PORT132 40m	0.70	-1.04	2.42	0.72	-0.18	2.32	0.08	12.12	40.49	8.21	50.58	-0.56
PORT262 30m	0.66	-0.45	1.93	0.69	0.23	2.03	-0.10	-9.74	41.89	-0.83	45.85	-0.20
PORT262 60m	0.68	-0.38	2.17	0.71	-0.18	2.16	0.01	-8.27	39.00	0.91	45.33	-0.35
PORT263 30m	0.73	-0.65	2.20	0.71	-0.06	2.23	-0.03	-9.87	38.20	-0.06	61.40	-1.58
PORT263 60m	0.74	0.18	2.06	0.71	0.23	2.24	-0.19	-15.13	39.26	-0.51	60.64	-1.39
Mendoiro												
PORT135 40m	0.86	-1.73	2.60	0.87	0.89	2.23	0.26	4.87	41.88	15.92	56.03	-0.79
PORT135 60m	0.87	-1.67	2.63	0.89	0.64	2.13	0.34	-3.86	33.04	7.10	51.87	-1.46
PORT136 20m	0.84	-1.89	2.87	0.83	0.31	2.26	0.38	-4.42	55.63	5.49	52.77	0.10
PORT136 40m	0.86	-1.17	2.26	0.84	0.52	2.29	-0.02	1.35	43.48	15.38	49.39	-0.29
PORT266 30m	0.86	-1.49	2.38	0.89	0.88	2.05	0.25	-8.74	39.43	8.61	43.32	-0.21
PORT266 60m	0.88	-1.31	2.23	0.89	0.69	2.05	0.16	0.43	36.92	15.86	44.16	-0.43
PORT267 30m	0.90	-1.71	2.59	0.87	0.19	1.96	0.42	-8.42	48.05	8.99	47.92	0.01
PORT267 60m	0.91	-1.20	2.20	0.88	0.28	1.99	0.18	-13.83	51.81	-0.37	45.66	0.22

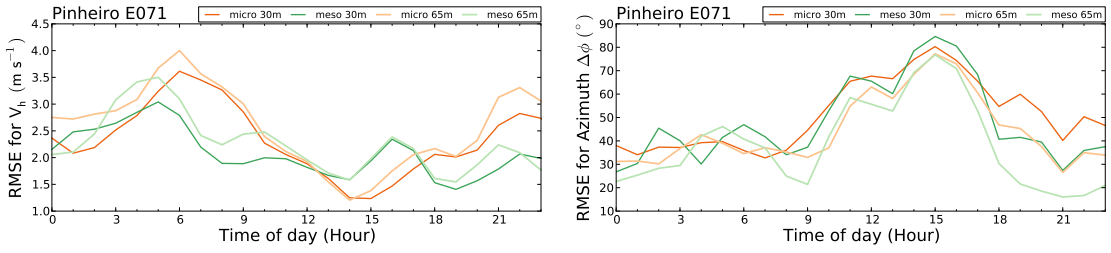

(a) Meteorological masts in Pinheiro.

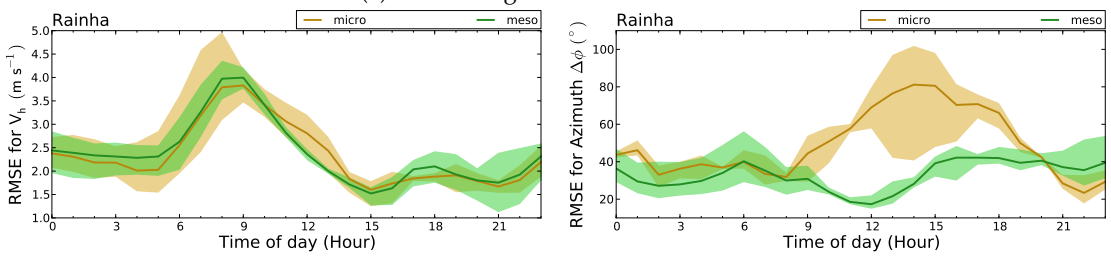

(b) Meteorological masts in Cabeço da Rainha.

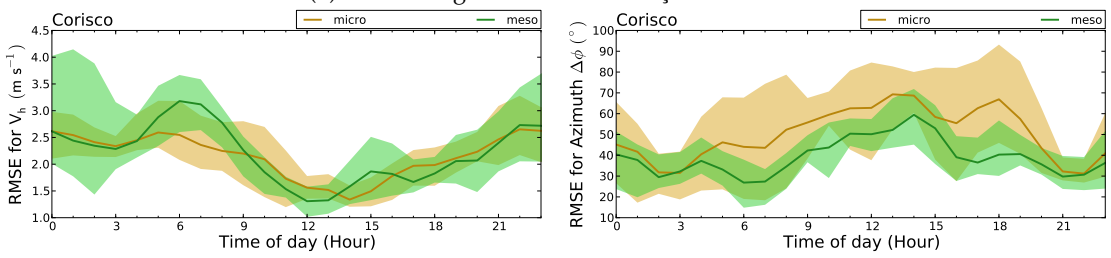

(c) Meteorological masts in Alto do Corisco.

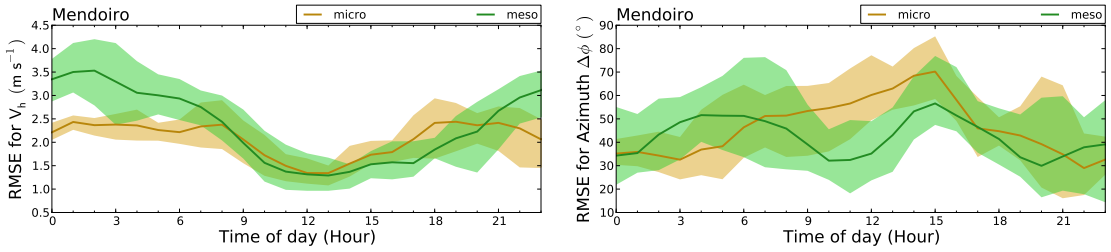

(d) Meteorological masts in Mendoiro.

Figure 5.7: Diurnal variation of the RMSE in the period between 2005-07-01 to 2005-07-15. The green and yellow colours refer to the mesoscale and microscale forecasts. For sites with more than two operational masts, to condense the results the average of the several errors was computed, shown in the solid line. The patch is delimited by the minimum and maximum RMSE found for all the masts. The leftmost and rightmost figures refer to the RMSE in the wind speed and direction, respectively.

with more differences in the mesoscale results and higher values at PORT263, where the forecast is better. The mesoscale was able to provide a better wind direction forecast in terms of the quadratic error. The scores are negative with the worst result found for PORT263. The microscale average increase in the RMSE is around 12°, however it manages to return a direction BIAS closer to 0.

The forecasts of Pinheiro and Cabeço da Rainha show better results in the mesoscale than the microscale time series. The worst values for r are obtained in Rainha, reaching $0.4 \sim 0.5$, Despite this, the scores are better than for Pinheiro, the latter reaching -0.3. The direction forecast at Lontreira mast has a low BIAS and a RMSE similar to other locations, however the score is the lowest, below -2. The low score is due to an histogram bias which is not evidenced by the BIAS measure due to phase errors.

5.4.1.2 Diurnal variation of the RMSE

Figure 5.7 shows the diurnal variation of the RMSE for all sites, for both wind speed and direction azimuth. In sites with more than 2 locations the errors are displayed using the same representation as in §5.2.3.1: a solid line showing the average value for the respective masts together with a patch of colour delimited by the minimum and maximum RMSE.

The variation in the RMSE throughout the day is generally higher for the microscale forecast. The average error in wind speed, however, is similar for both forecasts. The hours where the errors are lower is in the afternoon, prior to the sunset, which happens near 20:00 ST. The same is not true for the wind direction, where the best agreement is generally observed during the nocturnal periods.

In Pinheiro the mesoscale shows better results on the periods near the sunrise and sunset. In the afternoon the microscale yields better agreement. For the wind direction forecast the differences appear mainly between 18:00 to 1:00, when the mesoscale has lower error.

In Cabeço da Rainha the velocity RMSE is similar for both predictions, with higher dispersion by the microscale during daytime. The microscale wind direction error comes mainly from the time between 10:00 and 18:00, where the RMSE increases to much higher values, more than 2 times larger than the mesoscale RMSE. The mesoscale error is roughly constant throughout the diurnal cycle.

For Alto do Corisco, the mesoscale patch shows higher dispersion. On average the velocity RMSE is smoother for the microscale, which shows better agreement on the hours after the sunrise (5:00 to 9:00). The wind direction forecast is better for the mesoscale, which shows less 15° of difference in the average error.

In the Mendoiro site, the microscale velocity forecast outperforms the mesoscale by $\sim 30\%$, during the nocturnal period. There is an increase in the RMSE in the afternoon and a better agreement by the mesoscale, yielding 10% less of error. The wind direction shows higher dispersion in the mesoscale RMSE. The average error is similar except for the period between 8:00 and 15:00 where the mesoscale error decreases by 40%, trend which is not followed by the microscale prediction.

5.4.1.3 Time series of the wind speed and direction

In Figure 5.8 are shown time series of velocity and direction for the mesoscale, microscale and the measurements. For each site a mast was chosen and displayed on the respective sub-figure. Similar plots for each of the other masts may be found in Appendix E, §E.2.1. The measurements and the microscale time series are values of time integrations over 10 minutes, while the mesoscale are instantaneous snapshots with a 30 minutes sampling. To compare the three results, each of the time series was resampled to have values representing 1 hour averages.

On the overall, the microscale curve shows more variability and predicts higher wind speeds than the mesoscale. This is evident in Figure 5.8d, where the microscale provides a good agreement for wind speeds above $12\,\mathrm{m\,s^{-1}}$ which the mesoscale is unable to reproduce. Additionally, although the microscale follows most of the trends imposed by the mesoscale, it is not merely a noisier version of it as the magnitude in both curves is clearly different. However, the increase in variance may yield more error. As observed in Figures 5.8a and 5.8b, there are peaks where the forecast over and under-shoots, producing high mismatches in the squared deviations.

Regarding phase errors, these are mostly verified for Pinheiro and Cabeço da Rainha. Also, if a delay is observed at a particular event it may be a local phenomena and is not shown by the time series at other sites. When comparing the wind speed forecasts for July 4^{th} to 5^{th} for Figures 5.8b and 5.8d, there is a clear phase error at Lontreira which does not appears to exist at PORT135. Conversely, it is difficult to perceive any similar time lapse in the mesoscale curve.

The wind direction plots show variations which mostly occur in a daily basis, thus closely related to the diurnal cycle. The nocturnal winds are characterized as having directions between north and northeast, exhibiting small variations. During the day the main oscillations in the direction are observed. In the period which starts after July 7^{th}, there are regular counter-clockwise shifts which cover the whole range of directions. The typical wind regime during summer is characterized by northwest winds which result from the interaction between the synoptic wind (mainly northeast) and a sea breeze effect (from west). Such events are probable to occur in the afternoon, which coincides with the part of the day when most direction shifts happen. However there is a southern component which, although small, is present due to the counter-clockwise veer. This may be explained by valley breezes, happening in periods where the magnitude of the regional-scale sea breeze is low enough to allow for these local circulations to appear. An analysis of the existence of such phenomena and their interaction is made in §5.4.1.6.

Both direction forecasts are generally close to the measurements. When a shift in direction is observed the microscale response has some overshoot, unlike the mesoscale prediction. This accounts for the higher error verified in Table 5.8. When present, the phase errors are generally related to the forecast of events before these take place. For example, in Cabeço da Rainha the higher discrepancies occur in the period between day 7^{th} to 13^{th}. These are mainly due to the large lag which results from the forecast in advance of the direction shifts which happen during daytime. Additionally, the lag observed in the wind direction prediction is larger than the one from the velocity time series.

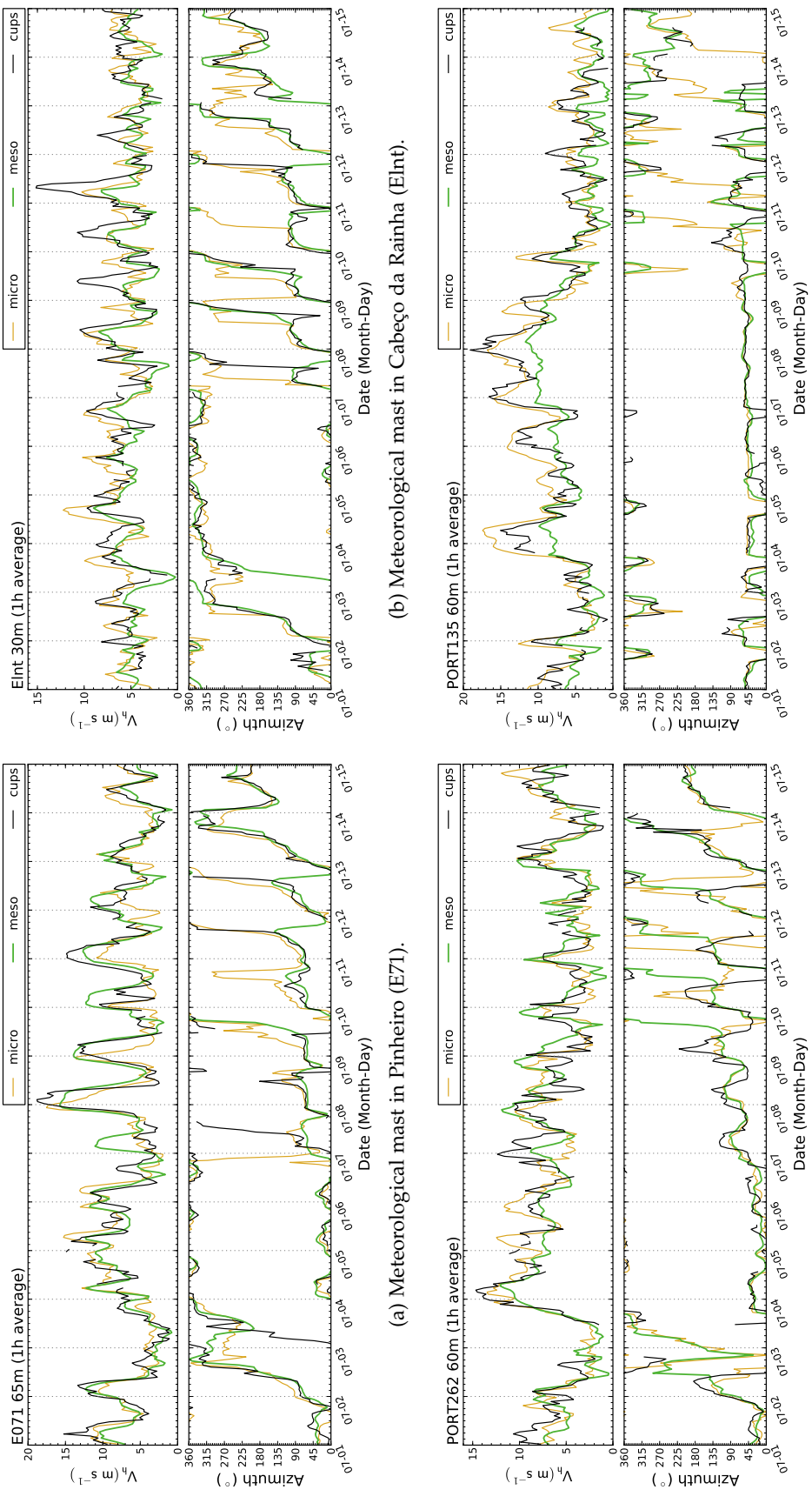

Figure 5.8: Time series of wind speed and direction of the mesoscale and microscale forecasts, together with the field measurements. The results refer to the period between 2005-07-01 to 2005-07-15.

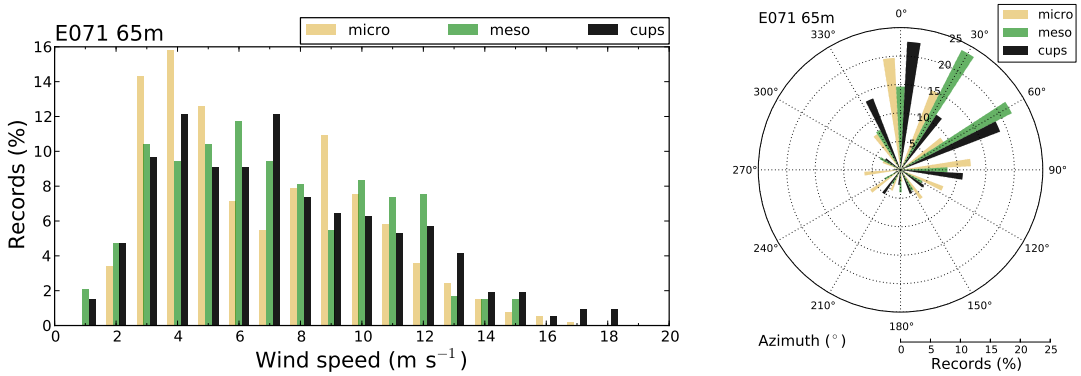

(a) Meteorological mast in Pinheiro.

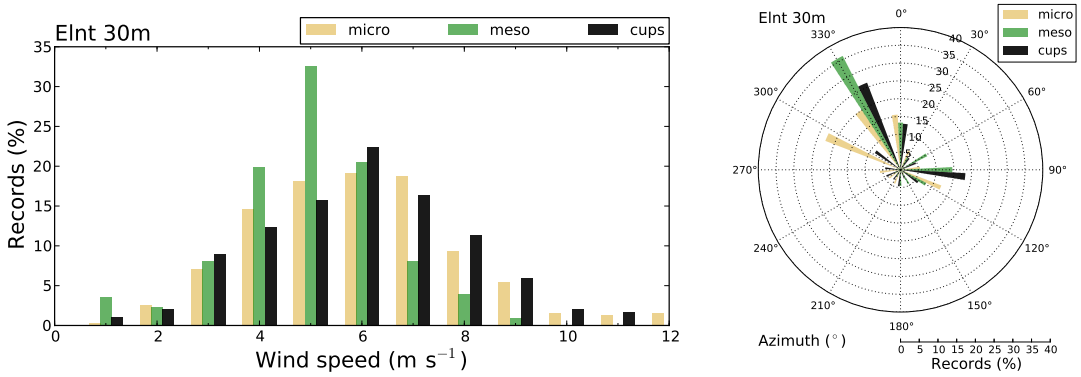

(b) Meteorological mast in Cabeço da Rainha.

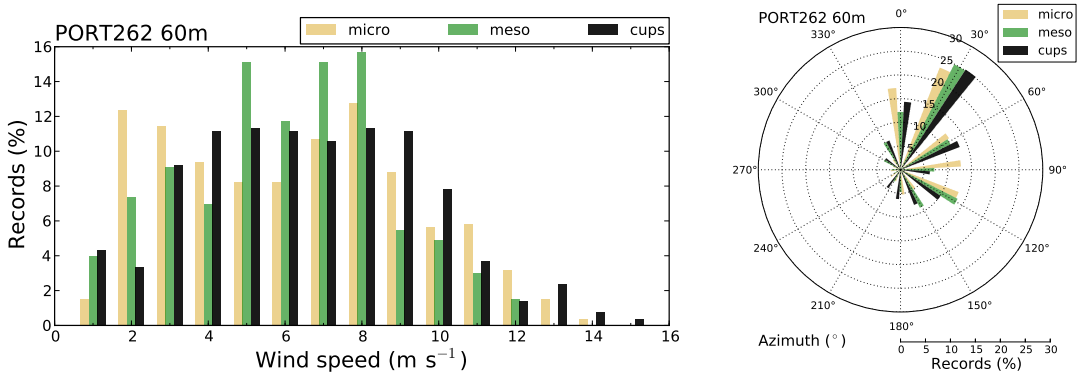

(c) Meteorological mast in Alto do Corisco.

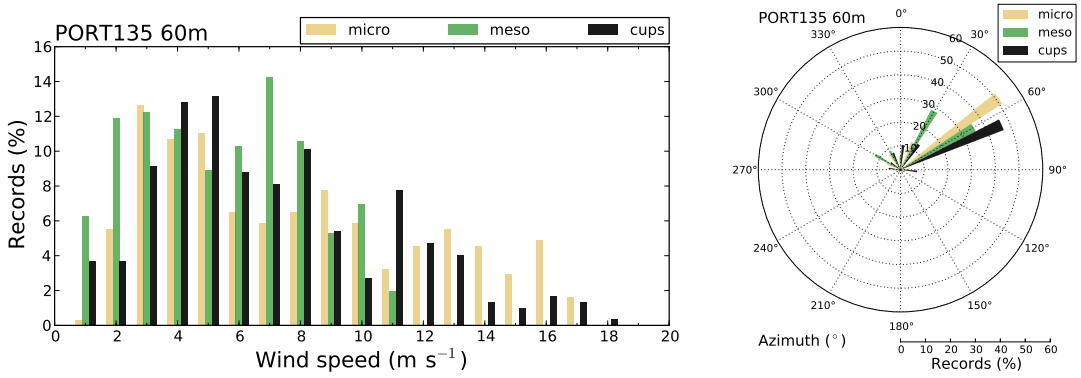

(d) Meteorological mast in Mendoiro.

Figure 5.9: Histograms and wind roses for the mesoscale and microscale results, in the period between 2005-07-01 to 2005-07-15.

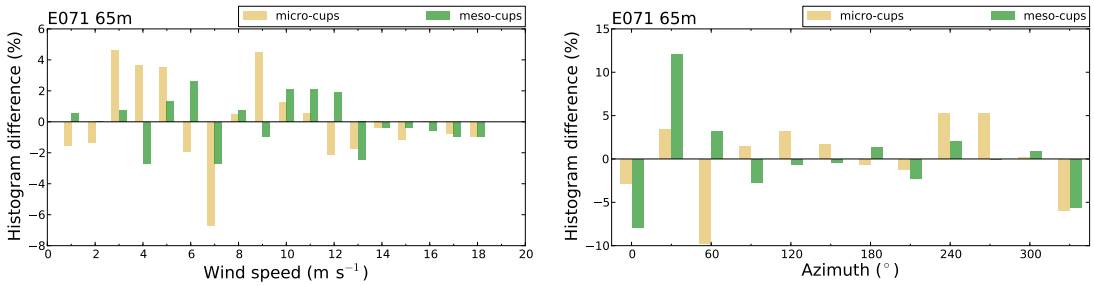

(a) Meteorological mast in Pinheiro.

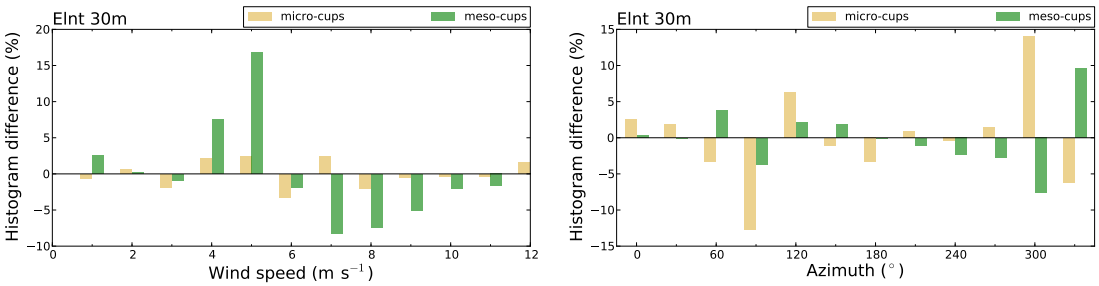

(b) Meteorological mast in Cabeço da Rainha.

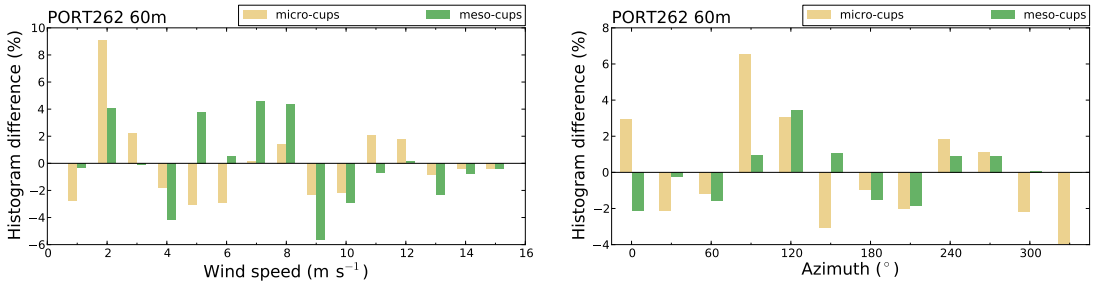

(c) Meteorological mast in Alto do Corisco.

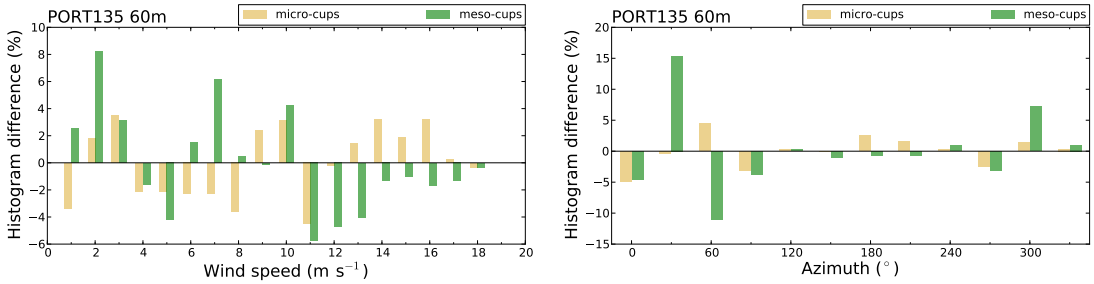

(d) Meteorological mast in Mendoiro.

Figure 5.10: Differences in the histograms and wind roses between the forecasts and the measurements, in the period between 2005-07-01 to 2005-07-15.

5.4.1.4 Histograms of the wind speed and direction

In Figure 5.9 are shown histograms and wind roses for the selected masts. The remaining plots may be found in Appendix E, §E.2.1.1. The ability to reproduce an histogram is of particular interest in wind resource assessment and the prediction of the energy potential of a site. Even if the results from a simulation are unsatisfactory for short-term forecasting, due to phase errors or mismatches arising from an high variance, the histogram may yield a very good agreement. As an example, if the measurements and forecast curves would have the same shape, but with a large phase error, this could result in high error but the histogram would be perfect.

To explicit how both models perform against each other, in Figure 5.10 are shown the differences between the histogram of each forecast to the histogram of the measurements. This figure structure is the same as Figure 5.9, *i.e.*, the leftmost plots show the differences in the velocity histogram and the rightmost plots show the same for the direction azimuth.

As it was observed in the analysis of the time series (Figure 5.8), the velocity range in the microscale time series is higher than in the mesoscale forecast. Apart from some discrepancies, the agreement at this high range is good. The histogram for the Lontreira mast is very good (Figure 5.9b), correcting the mesoscale over-predictions below $5\,\mathrm{m\,s^{-1}}$ bin and under-predictions above $7\,\mathrm{m\,s^{-1}}$. For the other sites there is some over-prediction by the microscale of the bins below $4\,\mathrm{m\,s^{-1}}$, while under-predicting the $5 \sim 8\,\mathrm{m\,s^{-1}}$ bins. On the overall the microscale yields better results on both Mendoiro and Cabeço da Rainha. For Alto do Corisco the results are also better for velocities above $3\,\mathrm{m\,s^{-1}}$.

Regarding the wind roses, the microscale performs better at Mendoiro (Figure 5.9d). In Alto do Corisco both forecasts yield similar results. In Pinheiro there are mixed results: the microscale shows a better agreement for the 0°, 30° and 90°, however for the 2^{nd} most important sector, 60°, there is a severe under-prediction while the mesoscale nearly yields the same value. In Cabeço da Rainha (Figure 5.9b), the microscale results are worse as there is an excessive number of records which fall under the 300°, instead of 330°. This suggests an bias which is not completely perceived from the respective time series (5.8b). To verify if such bias exists, a wind rose with 5° bins was produced (not shown) which allowed to estimate a shift by $-15°$ affecting the northwest sectors only.

5.4.1.5 Hovmöller diagrams of wind speed and direction

To refine the analysis from the histograms in Figure 5.9, the results were grouped according to the daily hour. This results in a contour plot where for each hour which composes the diurnal cycle, the histogram is represented by a colour scale to observe its variation throughout a typical day. This representation, known as an Hovmöller diagram, was made for both wind speed and direction and is shown in Figure 5.11. Each sub-figure is composed by six plots. The Hovmöller diagrams for wind speed and direction are shown in the topmost and bottommost line respectively. The three columns refer to the measurements, mesoscale and microscale results.

For Pinheiro (Figure 5.11a), the mesoscale shows a well defined cyclic variation of the wind speed where the maximum speeds are more frequent to occur at 5:00 and the minimum at 16:00 ST. The low variance histogram predicted by the mesoscale is not observed in the measurements, particularly in the range between 21:00 up to 10:00. Instead, the dispersion is such that it is difficult to define the mean value. The microscale was able to capture some of this increase in variance from 0:00 to 10:00. On the wind direction forecast, the mesoscale agreement with the measurements is better. The microscale has more dispersion in the histograms than what was observed. The northwest winds observed during the afternoon (14:00 to 23:00) are predicted by the mesoscale to occur after 17:00, while for the microscale these start at 10:00. The events between 22:00 and 9:00 are well described by both micro and mesoscale, however the microscale predicts the bimodal pattern that is present in the measurements, although with decreased magnitude.

For Cabeço da Rainha (Figure 5.11b), the patterns in the velocity histograms are similar. The mesoscale has frequency peaks of higher magnitude. Conversely, the observations occasionally show higher dispersion through the form of a positive skewness, which is natural as the velocity scale is limited by 0. The microscale was able to capture some of this dispersion in the afternoon period, ranging from 6:00 to 18:00, although with some lag. The highest wind speeds where measured around 9:00 but are predicted to occur at 17:00. The wind direction patterns at Lontreira are also similar but the mesoscale predicts a high occurrence of 345° winds from 21:00 to 3:00 which does not match with the observations. The mesoscale also over-predicts these northwest winds but with lower magnitude and higher dispersion, however it anticipates from 16:00 to 13:00 the start of this pattern. The bias of $-15°$ discussed in §5.4.1.4 is also discernible. The agreement is similar for the forecast of the $\sim 100°$ winds during the morning.

In Alto do Corisco (Figure 5.11c) the wind speed histograms have a large velocity range, reaching $17\,\mathrm{m\,s^{-1}}$ at 4:00. The mesoscale under-predicts the dispersion in the observations during the nocturnal period, which the microscale was able to capture. The wind direction forecast by the meso and microscale does not match completely with the observations. During the morning, between 0:00 and 9:00, both forecasts predict the $120° \sim 150°$ winds, the mesoscale with higher magnitudes and the microscale with increased variance. There is also some bias in the mesoscale prediction, particularly during the afternoon where instead of $\sim 345°$ winds, the forecast returns $\sim 300°$. This difference is concealed in the wind rose (Figure 5.8c). The microscale is able to predict the 345° winds for the same period.

For Mendoiro (Figure 5.11d) the microscale shows a better agreement both on the wind speed and wind direction histograms. The range in the wind speed mesoscale prediction has a maximum of $11\,\mathrm{m\,s^{-1}}$ while the microscale and the observations reach $17\,\mathrm{m\,s^{-1}}$. There is some lag between the microscale and the measurements, namely in the time that these high speeds occur, respectively 4:00 and 0:00. However most of the other patterns are similar in magnitude and the time at which they occur: the bimodal histograms during the morning and the persistent $4\,\mathrm{m\,s^{-1}}$ winds during the afternoon. The wind direction measurements and forecasts shows a strong persistence of 50° winds throughout all day, with almost no cyclic behaviour. The histograms are unimodal except during 15:00 to 19:00, where weak northwest winds appear. Although the mesoscale was able to capture these winds, the forecast shows a higher magnitude.

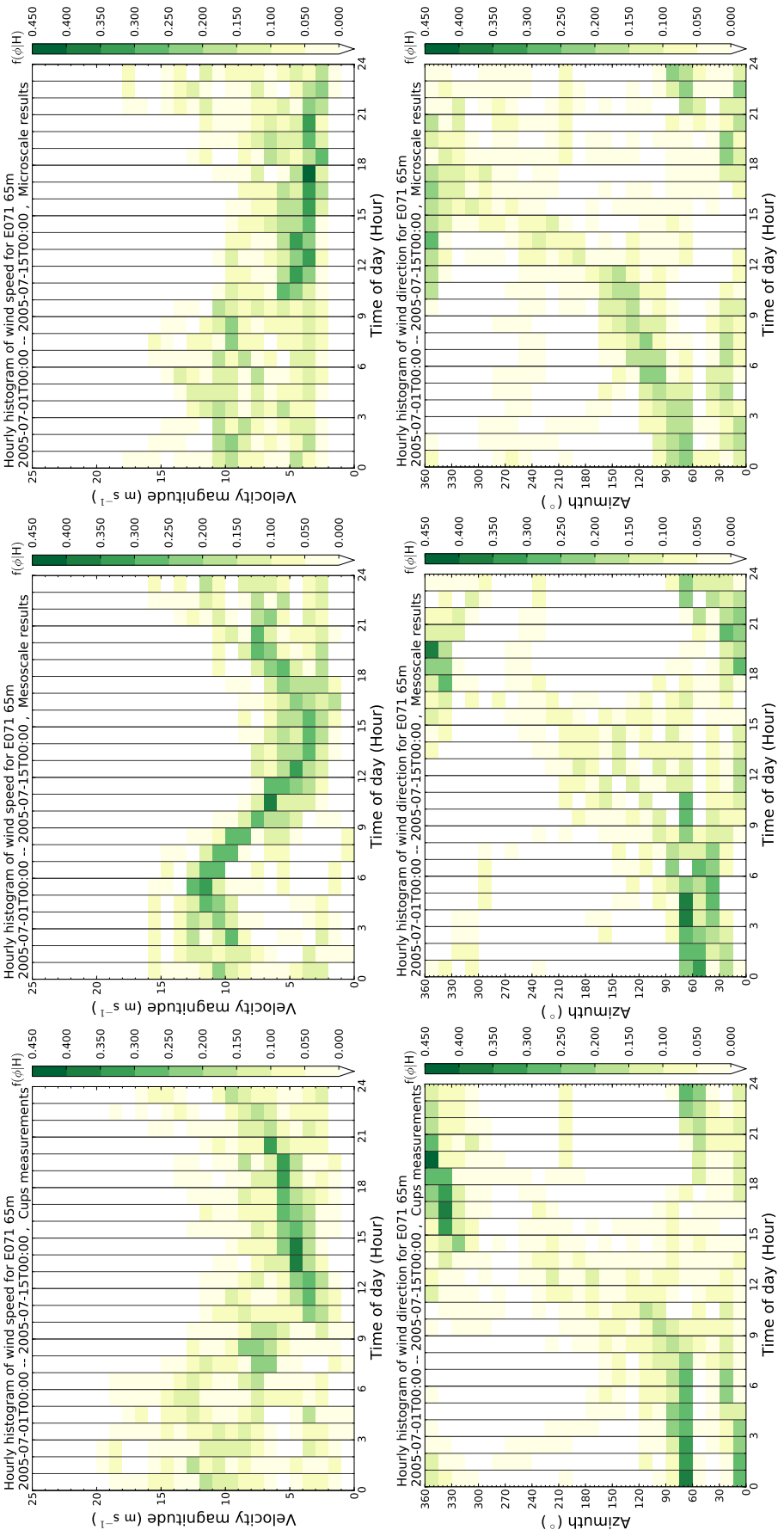

(a) Meteorological mast in Pinheiro (E71).

Figure 5.11: *Caption in page 188.*

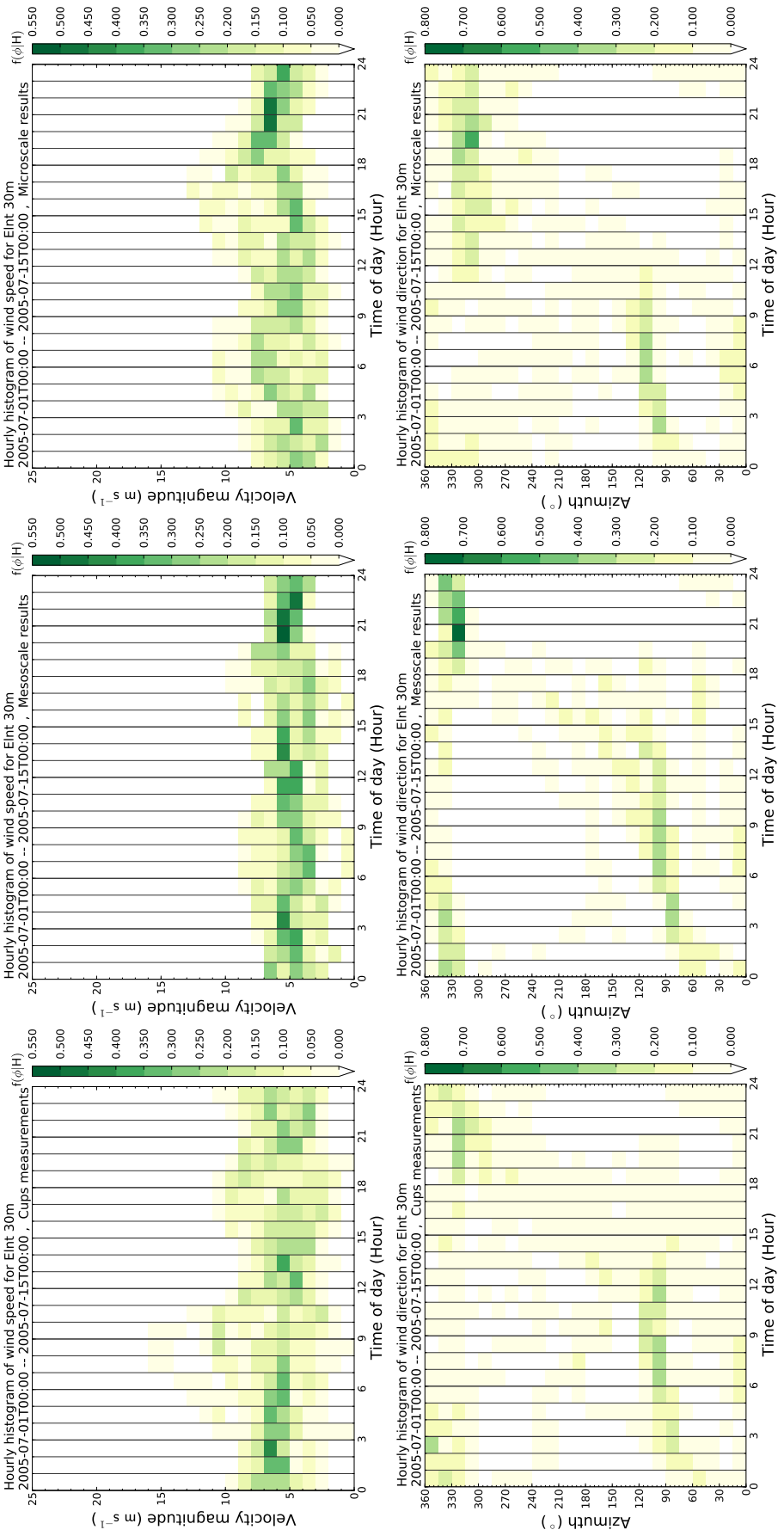

(b) Meteorological mast in Cabeço da Rainha (Elnt).

Figure 5.11: *Caption in page 188.*

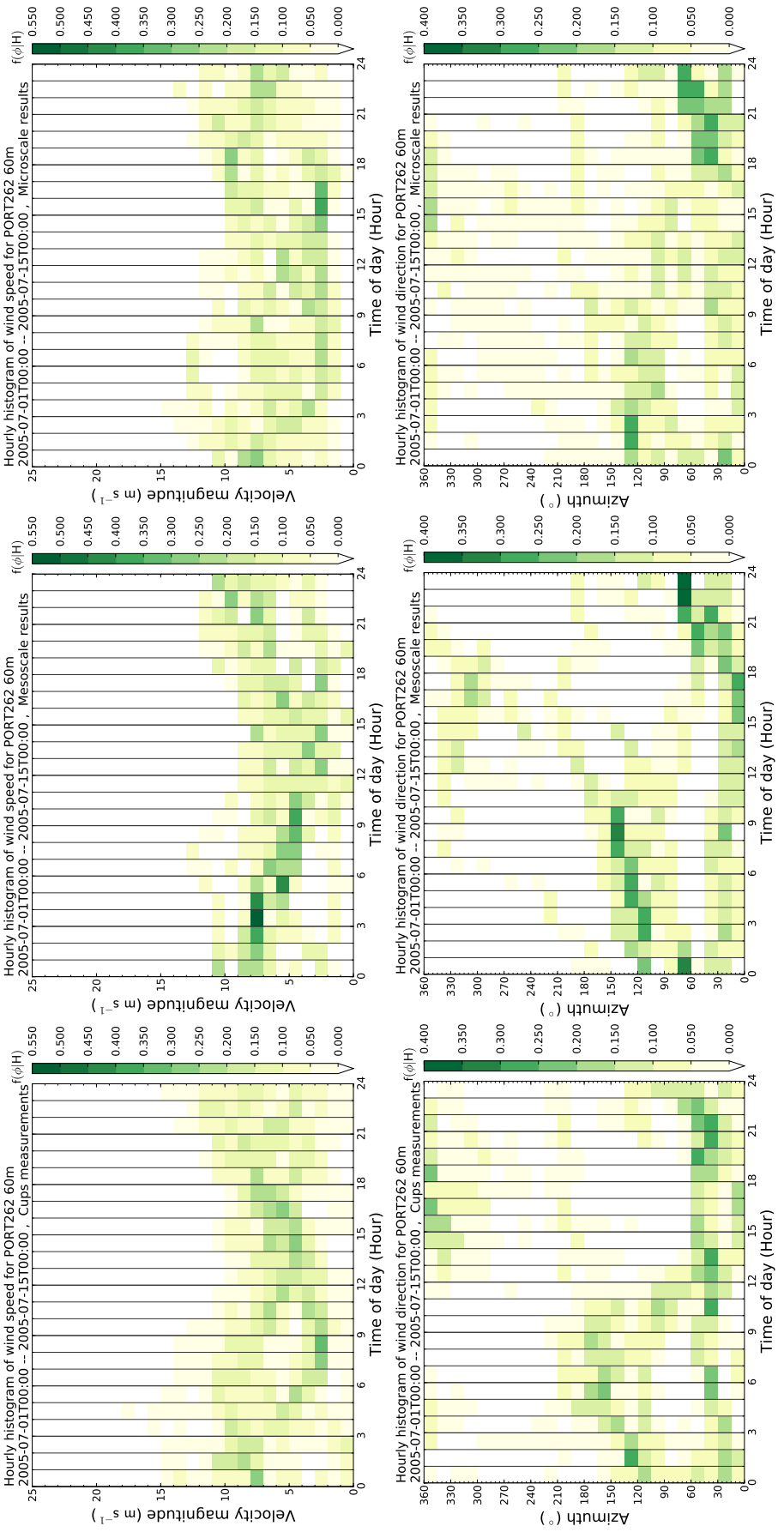

(c) Meteorological mast in Alto do Corisco (PORT262).

Figure 5.11: *Caption in page 188.*

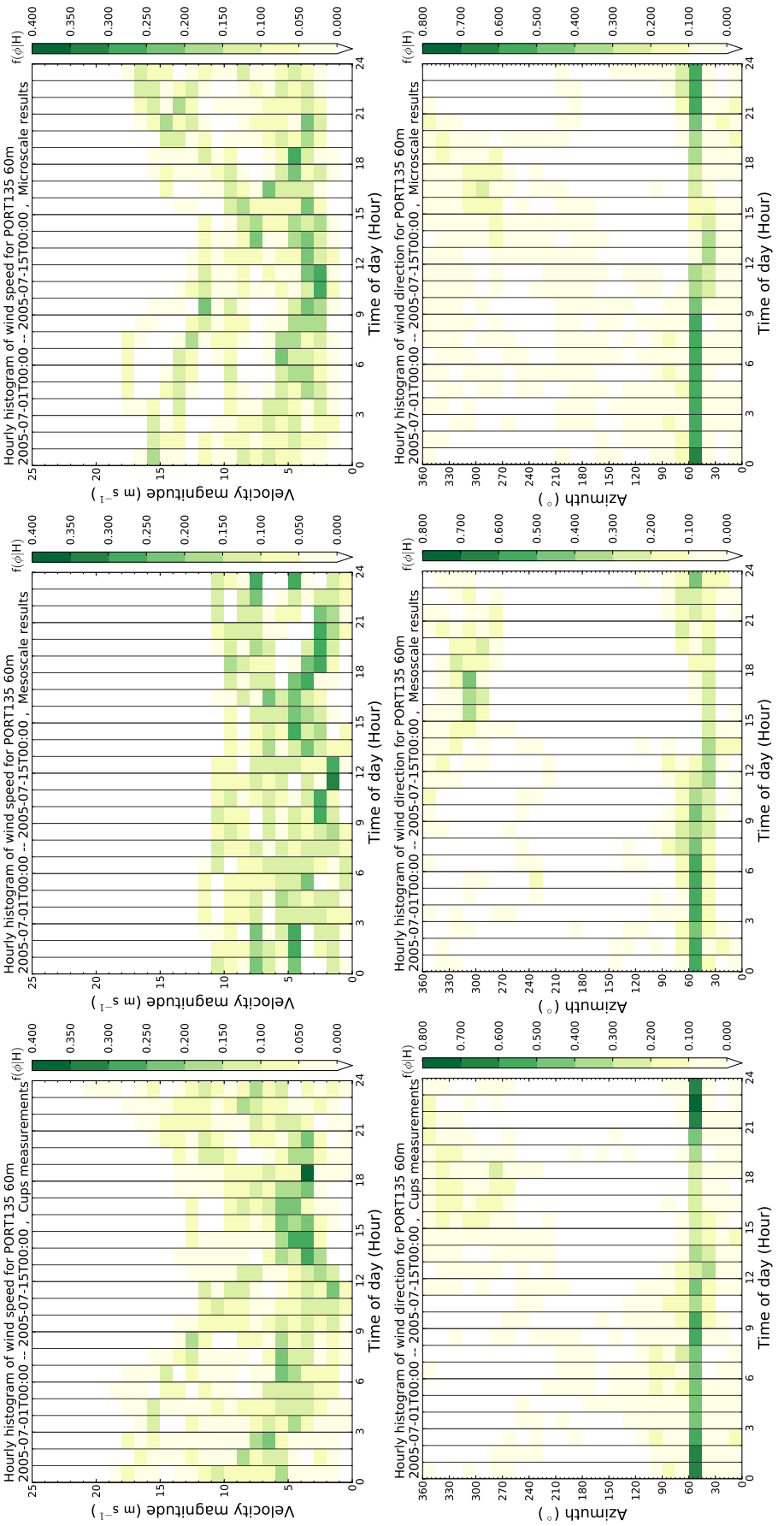

(d) Meteorological mast in Mendoiro (PORT135).

Figure 5.11: Hovmöller plots of wind speed (topmost) and direction (bottommost) for the period between 2005-07-01 to 2005-07-15.

The microscale prediction was able to provide a better agreement of these events. It has a higher dispersion however, although with very low magnitude, for several directions where no occurrences where measured. This is the cause for the errors found in the azimuth deviations and the negative skill scores in Table 5.8.

5.4.1.6 Thermal circulations predicted by the simulations

The strong cyclic changes in the wind direction observed in the time series (Figure 5.8), reflect a dependency on phenomena related with the solar diurnal cycle. The Portuguese typical wind regime during summer is characterized by sea breeze. Additionally, typical wind systems over complex terrain include valley and mountain breezes, the former related to the heating of valley air faster than the mountain air, the latter to the faster cooling of mountain air (Whiteman, 2000). Figure 5.12 shows the flow patterns for several times during July 2nd, 2005. This is visualized with streamline plots in several domains of the mesoscale simulation results. The aim is to distinguish between the several wind systems which are typical of the summer period, how these interact and to verify to what extent the wind direction is influenced.

Starting with the 00:00 plot, the coastline flow is less complex than in the mountainous areas. The existence of mountain breeze is evident because the wind originates from the ridges and mountain peaks, as most of the attachment nodes are therein located. The wind is katabatic, flowing over the downslopes into the nearby valleys. Land breezes happen only on the north part and are much weaker than mountain breezes.

At 06:00 the land breeze is more intense. At the latitude of 41°, the eastern winds penetrate 40 km into the sea, forming a vortex as the wind pushes into the north winds which prevail over the ocean. The flow in the mountain regions is similar, the extension and magnitude of the mountain breezes remains unchanged.

For 09:00 the wind over the mountainous areas changes. The mountain breeze has ceased and, over land, the prevailing wind direction is the east. The flow moves towards the coastline, concentrating on the valleys and circumventing terrains of higher altitude. Over sea, the northern wind is mainly unaffected, albeit there are vortices near the coast of the same scale as for 06:00. This is a period where there is still some land breeze but the mountain breezes have stopped and valley breezes are forming. This process is completed at 12:00, where the flow characteristics are the opposite to the 00:00 plot: (i) over the sea the wind is deflected from the north to the west, moving into land and starting the sea breeze which is typical of the Portuguese wind regime; (ii) over the mountains there are local flows with anabatic wind originating from the valleys, climbing the mountain slopes.

The plot for 15:00 is representative of the typical flow during the remainder of the afternoon. The local flow in the mountains is still characterized by valley breezes, however these are completely dominated by the sea breeze. The streamlines which flow through the valleys are deflected towards the ridges and mountain tops. This, however, happens in the mountain slopes which are upstream, facing the direction of the wind from the sea breeze. The streamlines do not end on the summits and mountain peaks. Instead, on the lee side the flow is katabatic, falling to the valleys and plains which lie

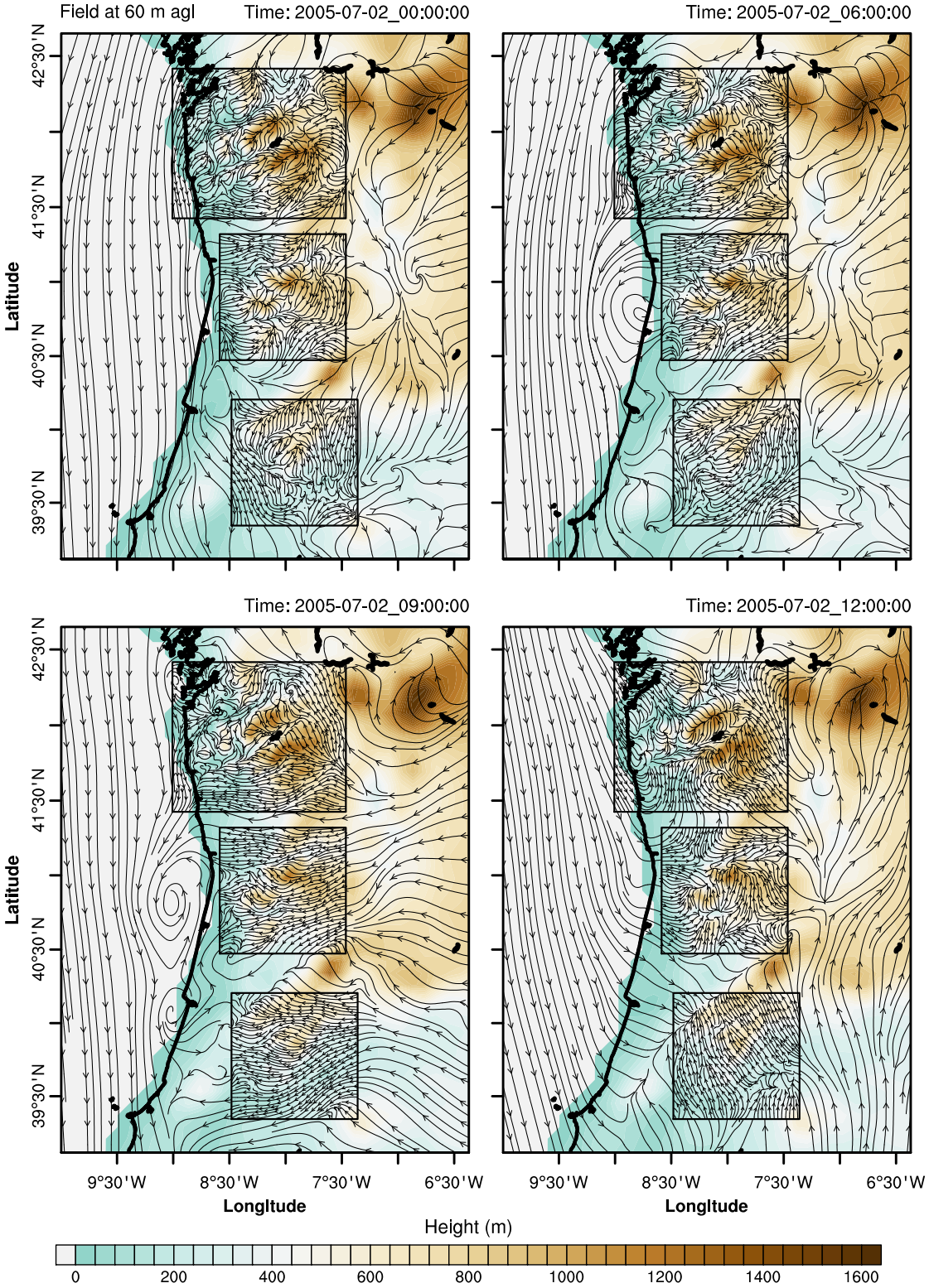

Figure 5.12: *Caption in page 191.*

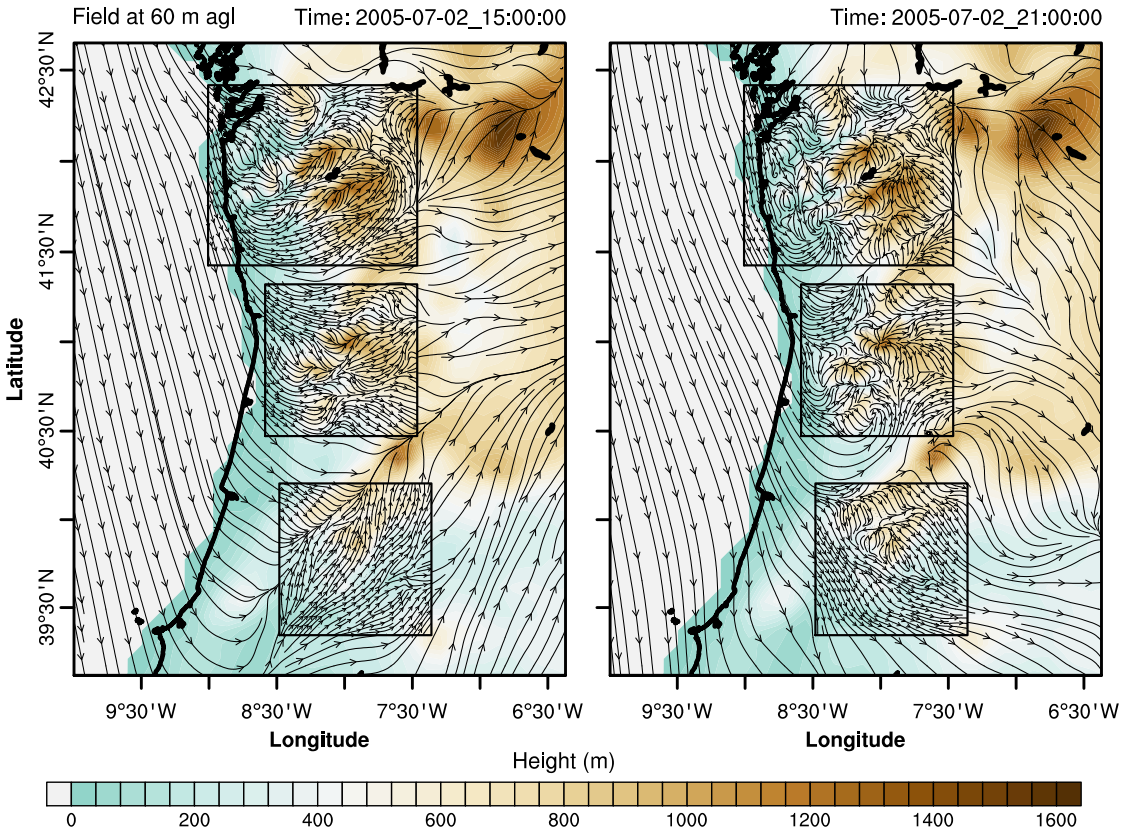

Figure 5.12: Streamline plots of the 60 m AGL wind for the mesoscale results of July 2nd, 2005. Each plot refers to a specific time during the day, according to which both sea-land and valley-mountain breezes may be observed. The contour map refers to the topography, as modelled in the computational domain.

to the east (beyond 7°30′ W). Up to the end of the domain, the wind direction is extensively influenced by the sea breeze, which is able to travel 100 km inland without being deflected.

At 21:00, characteristics of the afternoon wind regime still persist. The sea breeze is still present and the seashore winds are directed inland, closing from the north-west. On the highland the local flows are katabatic, having already formed mountain breezes alike the 00:00 plot. To the east the flow direction is mainly from the northwest, being deflected by the local orography.

The wind direction which is measured at the masts changes considerably over the day (Figure 5.8). According to the mesoscale results, these changes throughout the diurnal cycle are consequence of the interaction between two kinds of thermal circulation phenomena: sea (or land) breeze and valley (or mountain) breeze. The former act on a regional scale while the latter is related to local features of the flow. Comparatively, the sea breeze is more intense than the land breezes, as these are able to change the whole inland flow. Although having lower magnitude, mountain and valley breezes establish themselves much faster than the sea and land breeze. The latter have higher inertia, thus, a larger settling time relative to the sunrise and sunset hours.

5.4.1.7 Summary

The main conclusions from the analysis of the summer weeks forecast were:

1. The microscale velocity forecast shown lower error in 11 of the 19 available locations. The average microscale RMSE was $2.25\,\mathrm{m\,s^{-1}}$, lower than that of the mesoscale, $2.38\,\mathrm{m\,s^{-1}}$.

2. The Mendoiro site showed improvements for 7 of the 8 anemometers, with positive SS between 0.16 to 0.42 and an average bias around $0.5\,\mathrm{m\,s^{-1}}$. The mesoscale performs better at Pinheiro wind farm with improvements of 0.24 for both anemometers and negative bias, around $-0.4\,\mathrm{m\,s^{-1}}$.

3. The wind speed RMSE showed diurnal variations, being higher near the sunrise hour. The main differences between the mesoscale and microscale error were observed during night, where the latter generally performs better.

4. The mesoscale was better to forecast the wind direction, with an average RMSE of 42° on the azimuth differences against 51° for the microscale. This difference was mainly due to phase errors which were observed in the time series.

5. The best agreement in the wind direction RMSE was found for the nocturnal period. The differences between the mesoscale and microscale error were more evident during the afternoon hours, the latter with higher values.

6. Regular cyclic patterns were observed in the wind direction, matching the diurnal cycle. These were characterized as a slow veer throughout the day, from the predominant nocturnal northeast wind to the afternoon west and northwest wind. On some days the direction shift is such that a full revolution is completed, with the wind occurring from the east in the morning and south near noon. These were related with regional scale sea (or land) breeze and their interaction with local circulations induced by the topography, particularly valley (or mountain) breezes.

7. The velocity range in the microscale forecast was higher than in the mesoscale. This resulted in a better agreement of the microscale histogram.

8. The Hovmöller charts showed that the mesoscale velocity forecast has less dispersion than the measurements. Also, the maximum magnitude of the wind speed was under-predicted. Conversely, the microscale was able to mimic the dispersion and skewness found in the observations, albeit with lag errors, in some events higher than 4 hours.

9. The microscale wind direction forecast showed higher dispersion than the mesoscale, occasionally more than the one found in the measurements. Despite this, it was able to correct some discrepancies in the mesoscale histograms, where the frequency magnitude was being over-predicted.

5.4.2 Results for the autumn weeks: 2005-11-19 to 2005-12-03

5.4.2.1 Global errors

The results in Table 5.9 show results where the microscale is generally superior to the mesoscale, particularly on the wind speed. There are improvements on 13 of the 18 locations and the positive scores vary between 0.1 and 0.7. The wind direction also shows positive scores for 9 locations with a maximum of 0.3. Disregarding the Pinheiro site, the negative scores are above -0.6 (which correspond to an improvement of 0.4 by the mesoscale).

As for the summer weeks, Mendoiro shows the best results having only one mast with negative skill score: PORT267 at 60 m. Excluding this mast, the correlation of the microscale data with the measurements is higher, with values near 0.8. The BIAS is positive for the microscale and is closer to 0 than the values obtained for the mesoscale forecast, which are negative. This is in agreement with the results during the summer weeks. The RMSE is higher, however, between 2.6 and 3.5 m s^{-1}. For the wind direction the microscale returns less error but higher bias, 12° on average. As for the summer period the northernmost mast shows the worst results, PORT135, however it is PORT136 which has the highest RMSE. The mesoscale values for the RMSE are similar to those found in the summer.

In Alto do Corisco half of the locations show improvements, as in the summer period. Both correlation coefficients and the positive scores are higher, reaching 0.6, but the RMSE also increases by 70%. For the microscale, the BIAS sign is negative for the locations with both higher r and $SS > 0$. The most problematic mast for this period is the PORT262, whereas PORT263 continues to yield a poor result at 60 m. Despite this, when comparing the RMSE values these two masts yield better results than the PORT132, where the SS is positive and high. A conclusion may be drawn from the meso and microscale RMSE values: the difference in the error when the mesoscale is better is not as large as the differences when the microscale returns improvements. Additionally, the RMSE values of the microscale results show fewer differences between themselves. Regarding the wind direcion, the northernmost mast shows the worse results as in the summer weeks, however the RMSE values are 2 times lower and the skill scores improve. The PORT132 shows positive scores around 0.1.

In Cabeço da Rainha the microscale forecast for Lontreira shows low RMSE values and the highest improvements over the mesoscale, around 0.6 for both height levels. The correlation coefficients are above 0.8. The wind direction prediction is also characterized by low RMSE and positive scores, with $SS = 0.1$ for the 30 m vane. This is the opposite of the prediction during the summer weeks, where this was one of the locations with negative scores. Although the microscale wind speed RMSE is similar, around 2.5 m s^{-1}, the azimuth RMSE reduces by a factor of 2.3.

For the Pinheiro site the results are slightly better for the wind speed but worse for the direction. At 30 m height the microscale prediction is better, having a positive score, albeit at 65 m it remains negative. The wind direction skill score becomes much worse, however the microscale RMSE improves as the values are 2 times lower than those obtained in the summer forecast. When this RMSE value is compared with the

ones obtained for the other sites, it is similar and even lower than all values obtained in Mendoiro.

5.4.2.2 Diurnal variation of the RMSE

The diurnal variation of the error, shown in Figure 5.13, is significantly different between the autumn and summer periods. The strong diurnal cycle which was observed for the summer (Figure 5.7) is greatly reduced in the autumn weeks. The improvements in the microscale results are not restrained to the nocturnal periods as for the summer, instead are observed throughout the day.

For Pinheiro the velocity predictions are similar, showing a similar trend with low error at night, starting to increase with the sunrise (around 7:30 for this period) reaching values which are higher by 80%. This large error lasts until mid-afternoon, decreasing afterwards. The microscale curves show an higher increase in the hours prior to the sunrise, 15% higher than the mesoscale. At night the 30 m microscale forecast shows improvements while the 65 m yields an RMSE near 40% higher than that of the mesoscale. The microscale forecast of the wind direction shows more error, around 20% higher throughout most of the day. Near noon, between 10:00 to 13:00, the RMSE for the 65 m height level becomes 2 times higher. The same happens for the mesoscale prediction at that same height, but the increase is of less magnitude and for a shorter time span. This is the major contribution to the negative skill score observed in Table 5.9.

The forecast in Cabeço da Rainha show n microscale error similar for both height levels. The mesoscale RMSE is always higher, showing more 50% for the 30 m prediction. The errors are generally constant throughout the day, except after 16:00 where these gradually decrease. The direction forecast shows lower error by the mesoscale during the morning and the late afternoon, around 25% lower than the microscale values. However the mesoscale error increases around noon, becoming almost 3 times higher than the microscale values. The better results observed during this time period may be related to the higher terrain complexity of Cabeço da Rainha and the finer resolution of the microscale grid. During the summer period the variation of temperature throughout the diurnal cycle is higher. The microscale model lacks a soil parameterization to estimate the surface heat flux. Instead it interpolates from the heat flux predicted by the mesoscale, thus both surface velocity and temperature are computed using a field coarser than the respective mesh. This mismatch of resolutions and terrain heights for the micro and mesoscale grids may result in an inaccurate description of the heat flux, at the microscales, affecting the velocity and temperature fields. As the thermal variations in the autumn diurnal cycle lessens, the inaccuracies in the heat flux field loose importance which leads to improvements by the microscale forecast, especially in complex terrains.

In Alto do Corisco, the mesoscale shows a large dispersion which is not observed in the microscale prediction. This is mainly due to the large error in the PORT132 forecast, whereas PORT262 sets the minimum RMSE values. The largest RMSE in the microscale prediction happens around the sunrise. The lowest errors are observed in the afternoon and during early morning, after midnight. The wind direction shows large dispersion in both forecasts. Most of the microscale error is observed during the

Table 5.9: Comparison of the errors in the mesoscale (WRF 3 km ACM2) and microscale forecasts, for the period from 2005/11/19 to 2005/12/03. The structure is the same as of Table 5.8

	Speed ($m\,s^{-1}$)							Azimuth (°)				
	Mesoscale			Microscale				Mesoscale		Microscale		
Mast	r	BIAS	RMSE	r	BIAS	RMSE	SS	BIAS	RMSE	BIAS	RMSE	SS
Pinheiro												
E071 30m	0.85	-2.44	3.87	0.75	0.06	3.66	0.11	-0.68	13.51	5.82	21.12	-1.45
E071 65m	0.86	-1.74	3.48	0.74	-0.44	4.10	-0.39	-1.61	21.30	-1.96	29.45	-0.91
Cabeço da Rainha												
Elnt 15m	0.85	-4.53	5.19	0.81	-1.04	2.75	0.72	-7.51	25.04	0.43	24.87	0.01
Elnt 30m	0.85	-3.14	3.87	0.83	-0.14	2.53	0.57	-7.42	25.43	0.17	24.14	0.10
Alto do Corisco												
PORT132 20m	0.73	-6.09	7.38	0.76	-0.66	4.64	0.60	0.27	17.51	2.79	16.39	0.12
PORT132 40m	0.81	-3.53	5.12	0.81	-0.31	4.04	0.38	6.62	20.36	5.38	19.43	0.09
PORT262 30m	0.81	-1.63	3.30	0.77	0.48	3.57	-0.17	4.19	30.52	8.45	31.42	-0.06
PORT262 60m	0.80	-1.66	3.56	0.75	0.05	3.94	-0.23	-7.77	20.54	-4.03	23.06	-0.26
PORT263 30m	0.72	-1.44	3.60	0.73	-0.76	3.36	0.13	-1.29	25.72	-2.94	31.92	-0.54
PORT263 60m	0.75	-0.24	3.36	0.72	0.19	3.78	-0.27	-12.02	24.35	-13.75	30.97	-0.62
Mendoiro												
PORT135 40m	0.68	-2.30	3.93	0.80	1.12	3.11	0.37	4.85	40.54	26.59	49.02	-0.46
PORT135 60m	0.71	-2.28	4.10	0.80	0.79	3.15	0.41	-4.17	38.00	16.30	40.67	-0.15
PORT136 20m	0.65	-1.76	3.41	0.79	0.62	2.60	0.42	-8.64	54.11	3.71	50.24	0.14
PORT136 40m	0.67	-1.16	3.28	0.79	0.67	2.78	0.28	5.53	47.18	18.01	46.53	0.03
PORT266 30m	0.69	-2.17	3.66	0.78	1.22	3.15	0.26	-4.61	40.96	10.66	34.08	0.31
PORT266 60m	0.70	-1.90	3.69	0.77	1.01	3.33	0.19	3.74	36.85	17.07	37.44	-0.03
PORT267 30m	0.77	-2.14	3.59	0.74	0.36	3.33	0.14	-7.62	45.16	5.20	43.27	0.08
PORT267 60m	0.79	-1.51	3.27	0.76	0.51	3.53	-0.16	-13.46	46.20	-1.96	41.80	0.18

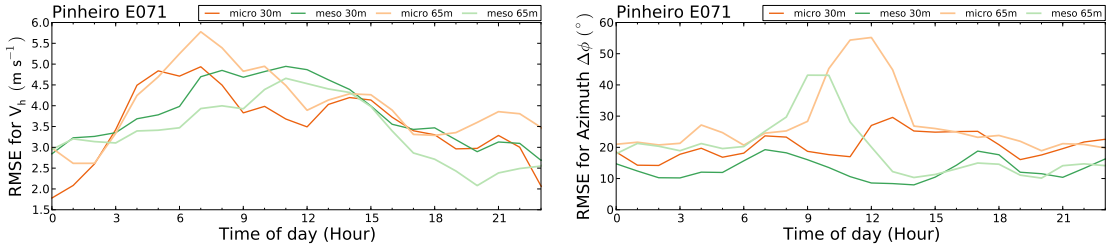

(a) Meteorological masts in Pinheiro.

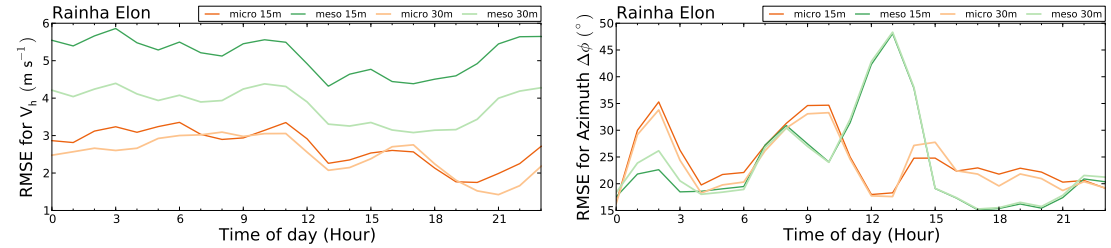

(b) Meteorological masts in Cabeço da Rainha.

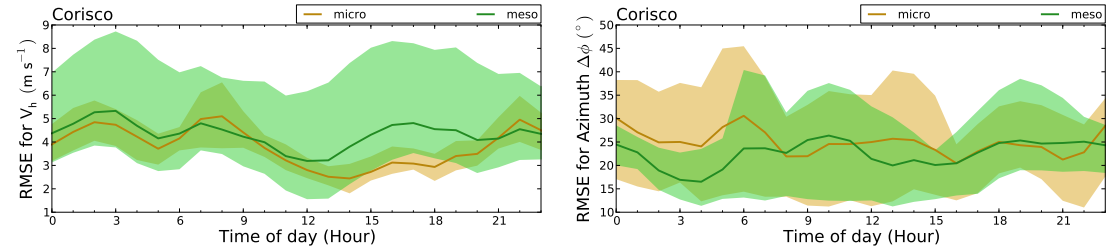

(c) Meteorological masts in Alto do Corisco.

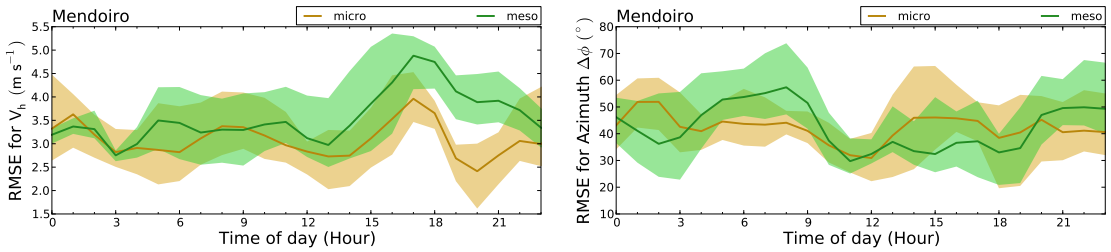

(d) Meteorological masts in Mendoiro.

Figure 5.13: Diurnal variation of the RMSE in the period between 2005-11-19 to 2005-12-03. The green and yellow colours refer to the mesoscale and microscale forecasts. For further details refer to the legend of Figure 5.7.

morning, between 0:00 and the sunrise, where the average error is 25% higher than the mesoscale. Throughout the rest of the day both forecasts yield similar error.

In Mendoiro the forecasts shows similar RMSE in the wind speed from 0:00 up to 9:00. Afterwards the microscale shows better results, yielding errors 10% to 60% lower than those of the mesoscale. The average RMSE is around $3\,\mathrm{m\,s^{-1}}$ except during the sunset (17:10) where it increases to $4\,\mathrm{m\,s^{-1}}$. Regarding the wind direction, the microscale shows improvements over the mesoscale during the morning and after sunset, where it yields around 25% less RMSE.

5.4.2.3 Time series of the wind speed and direction

In Figure 5.14 are shown time series for selected masts of the several sites, the same which were chosen in §5.4.1. The respective plots for the remaining masts are referred in Appendix E, §E.2.2. The autumn weeks are affected by some lack of data due to the harsher weather conditions to which the masts are subjected to. This is seen in both Pinheiro and Alto do Corisco for the period between 26 to 29 of November.

In the autumn weeks there were three events of high wind speeds which were of particular interest: (i) the first 2 days of simulation, (ii) the 23$^{\mathrm{rd}}$ to 25$^{\mathrm{th}}$ November, (iii) the last 2 days. The wind direction shows the same trend for all sites. At the start of the forecast the wind flows mainly from the southeast, gradually changing direction to the east, north, until its direction reaches west. This direction shift is continuous and happens throughout the first 9 days. Only after November 28$^{\mathrm{th}}$ there is a new trend which is characterized by winds varying between the north and the west.

In Pinheiro (Figure 5.14a) the microscale curve is able to reproduce the high wind speeds, contrary to the mesoscale forecast. However, there are important mismatches in the 23$^{\mathrm{rd}}$ November where the microscale prediction suffers both from a time lag and lower magnitude. The microscale also shows disagreements in the last day, where it predicts a decrease in the wind speed which does not occur. As for the summer period (Figure 5.8), there appears to be no deterioration of the forecast with the increase of the simulation time. Regarding the wind direction, although it was verified less error in the mesoscale prediction, the curves for both forecasts show small differences and are much closer to the measurements than in the summer period.

The conclusions are similar for the masts in the other sites. The microscale is able to successfully predict most of the high velocities, while the mesoscale consistently under-predicts the several peaks. This is well observed in Figure 5.14b and 5.14d. Although PORT262 of Alto do Corisco does not show it that clearly, the time series for masts PORT132 and PORT263 in Appendix E (Figure E.9a) show the microscale capturing $25\,\mathrm{m\,s^{-1}}$ in the extreme events of 19 to 20 November and December 1$^{\mathrm{st}}$. For this last day, the microscale forecasts for all masts of Alto do Corisco and Mendoiro was able to capture the high wind speeds, despite being the 13$^{\mathrm{th}}$ day of continuous forecast.

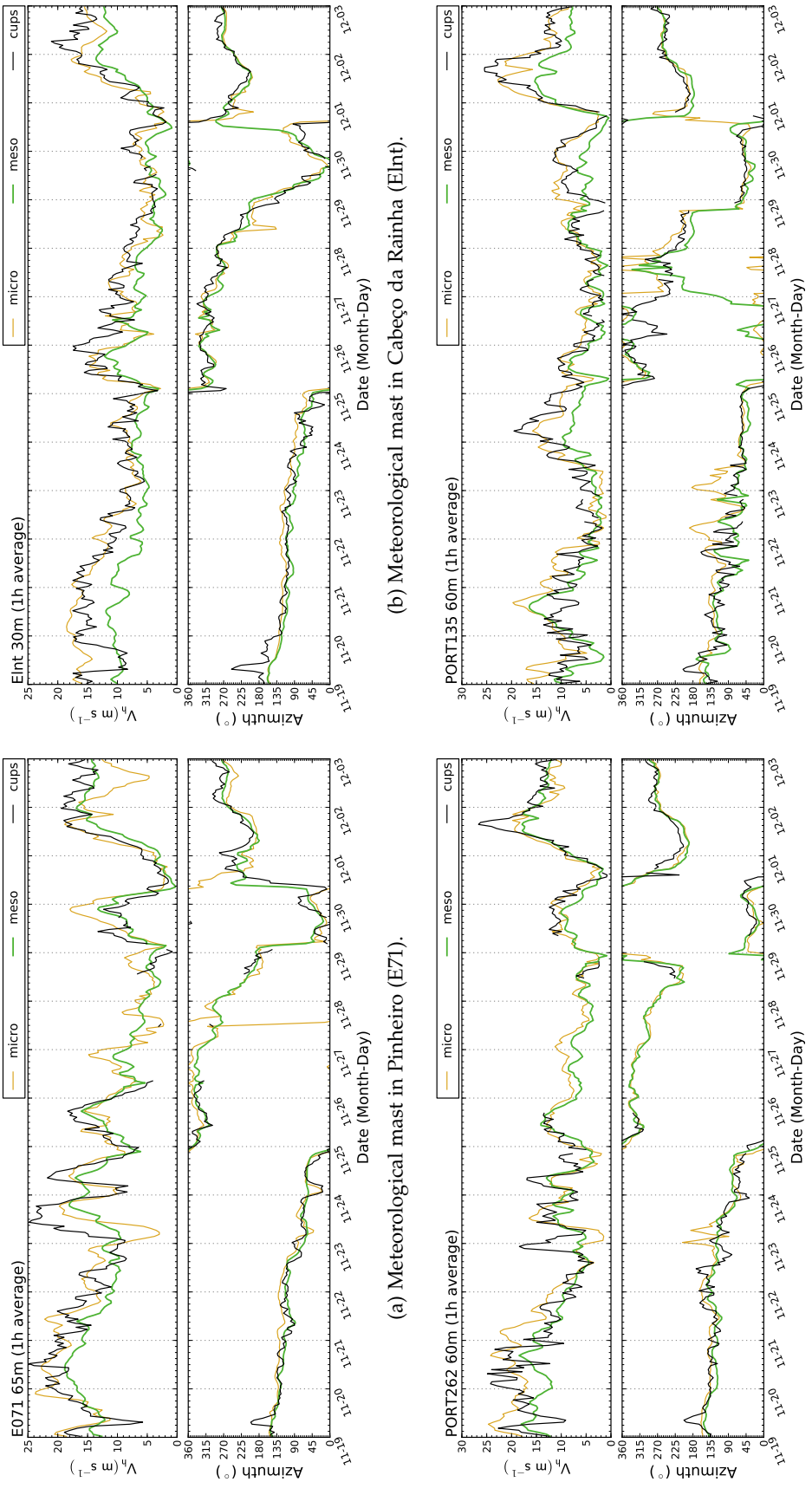

Figure 5.14: Time series of wind speed and direction of the mesoscale and microscale forecasts, together with the field measurements. The results refer to the period between 2005-11-19 to 2005-12-03.

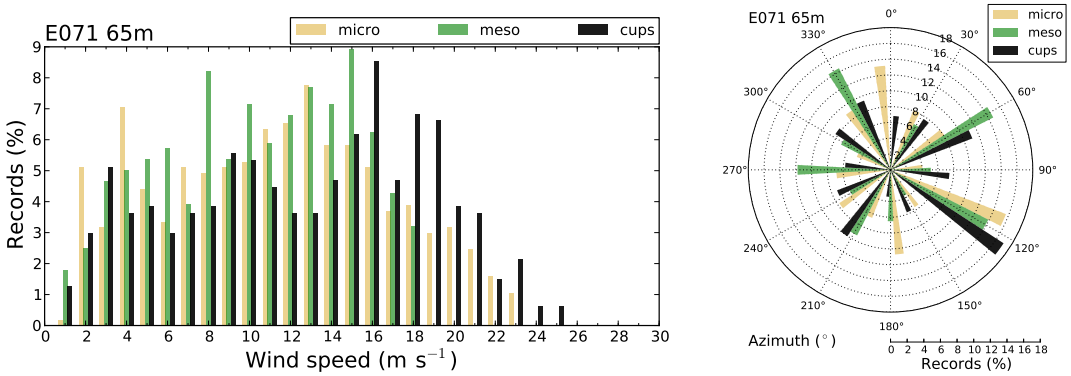

(a) Meteorological mast in Pinheiro.

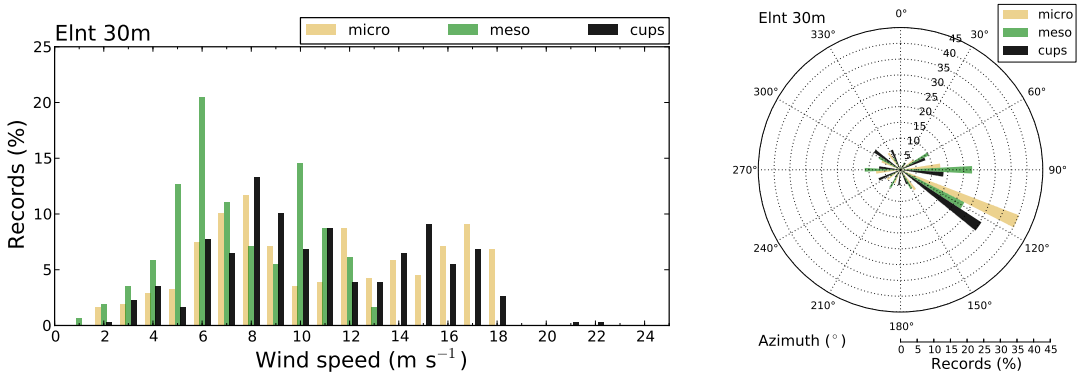

(b) Meteorological mast in Cabeço da Rainha.

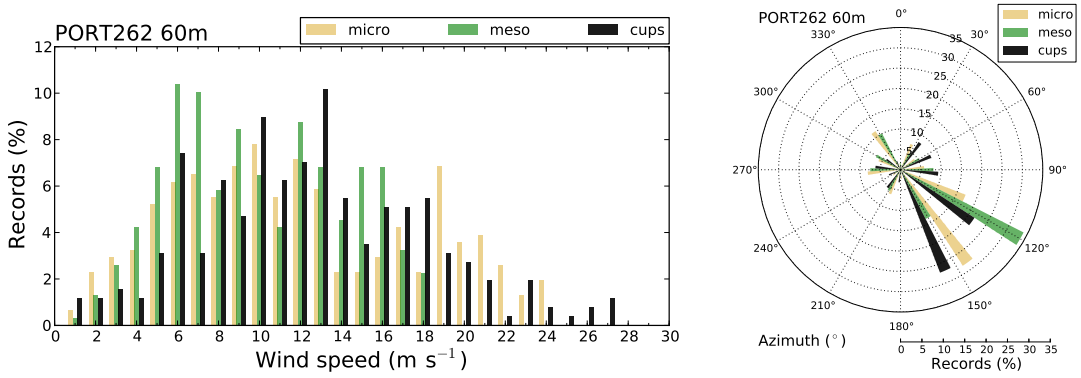

(c) Meteorological mast in Alto do Corisco.

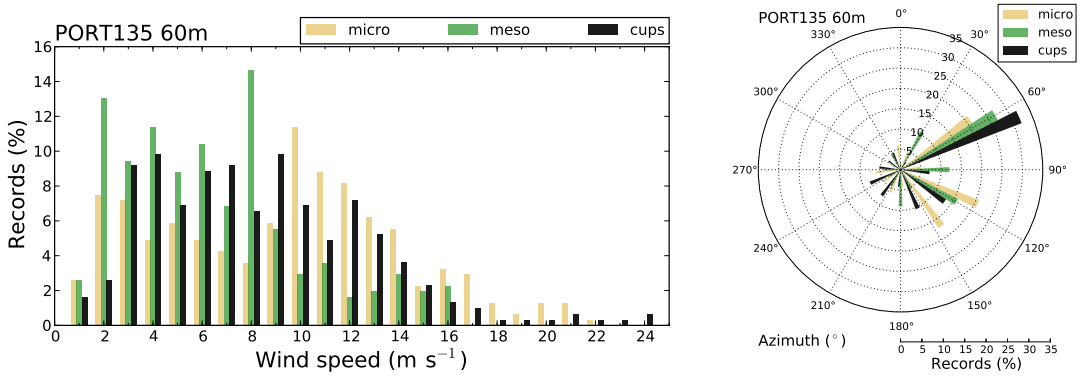

(d) Meteorological mast in Mendoiro.

Figure 5.15: Histograms and wind roses for the mesoscale and microscale results, in the period between 2005-11-19 to 2005-12-03.

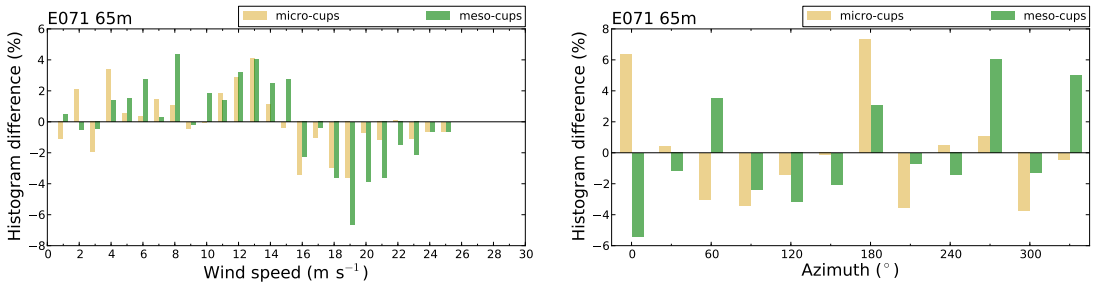

(a) Meteorological mast in Pinheiro.

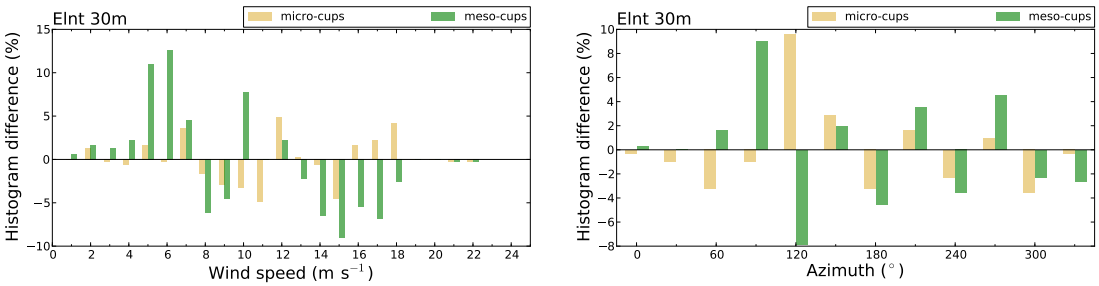

(b) Meteorological mast in Cabeço da Rainha.

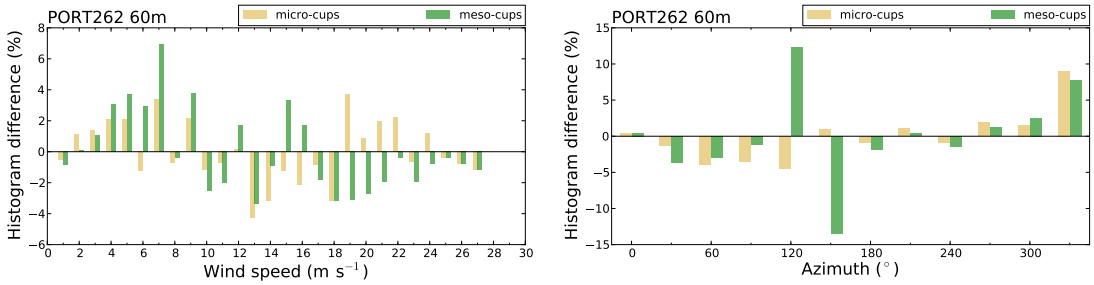

(c) Meteorological mast in Alto do Corisco.

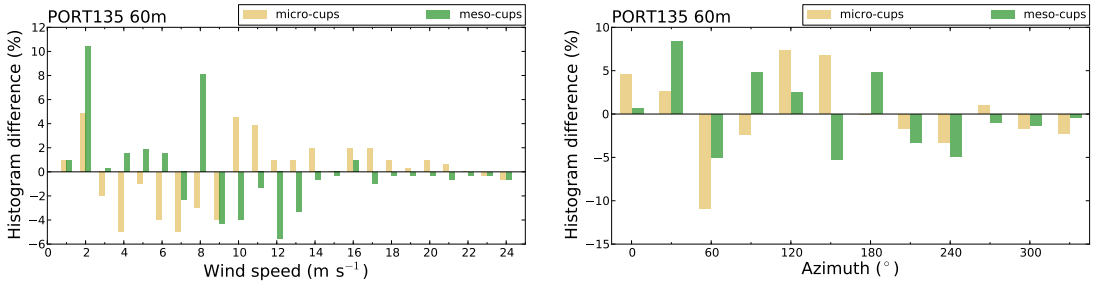

(d) Meteorological mast in Mendoiro.

Figure 5.16: Differences in the histograms and wind roses between the forecasts and the measurements, in the period between 2005-11-19 to 2005-12-03.

5.4.2.4 Histograms of the wind speed and direction

In Figure 5.15 are displayed the histograms of wind speed and wind direction. This information is complemented by Figure 5.16 which shows the differences between the histograms of each forecast to the histogram of the measurements.

As it was already observed in the analysis of the time series (Figure 5.14), the mesoscale forecast was unable to predict wind speeds above $18\,\mathrm{m\,s^{-1}}$. The microscale increases the range up to $24\,\mathrm{m\,s^{-1}}$, although there are measurements of $27\,\mathrm{m\,s^{-1}}$. Aside from some disparity in Pinheiro, the magnitude of the bins at such high speeds is in agreement with the measurements. On overall, there is some over-prediction in the occurrence of speeds below $4\,\mathrm{m\,s^{-1}}$ and under-prediction for $6\,\mathrm{m\,s^{-1}}$ to $10\,\mathrm{m\,s^{-1}}$. As for the summer weeks, the microscale histogram for Lontreira is very good when compared to that of the mesoscale, both in the velocity range and in the magnitude of the bins. (Figure 5.15b).

For the wind direction the microscale results are better than in the summer. In Alto do Corisco and Cabeço da Rainha the microscale is able to correctly predict the most important sectors, whereas the mesoscale fails to do so. In PORT135 the mesoscale provides a better agreement, as the microscale shows few differences between the 60°, 120° and 150° sectors. The wind roses from PORT136 and PORT267, however, show a superior prediction by the microscale (Figure E.10b from the Appendix E). In Pinheiro the distribution of directions over the bins is more homogeneous than of the other sites. Dismissing the north and south bins, the microscale shows a better agreement on most of the sectors which compose the wind rose.

5.4.2.5 Hovmöller diagrams of wind speed and direction

In Figure 5.17 are shown the Hovmöller diagrams for wind speed and direction for each of the masts representative of the four sites. For details on this kind of plot refer to the discussion in §5.4.1.5.

When displayed as function of the diurnal cycle, the results in autumn show higher dispersion in the histograms for both wind speed and direction. Regarding wind speed alone, this is a natural consequence of the higher velocity range which was verified for this period. The scatter in the wind direction is mainly due to the lack of sensitivity to the diurnal cycle itself. The predominant azimuths refer to the east and northeast, as that was main wind direction for nearly week, as observed in the time series.

For Pinheiro (Figure 5.17a) the patterns in the sequence of histograms are unclear. There is a tendency for velocities $\sim 16\,\mathrm{m\,s^{-1}}$ between 9:00 and 23:00. This is also present in the microscale results, but for $\sim 14\,\mathrm{m\,s^{-1}}$ and only in the afternoon. The mesoscale over-predicts the magnitudes in the histograms frequency, caused by the lack of wind speeds above $18\,\mathrm{m\,s^{-1}}$. Regarding the wind direction, the measurements show that the main occurrences lie either around the 60° or the 120° directions, in a faint bimodal pattern. The mesoscale tends to show higher magnitudes on the former while the microscale accentuates the latter. Both results, however, over-predict the frequency magnitude and show some time lag. Additionally, both forecasts show some northwest winds

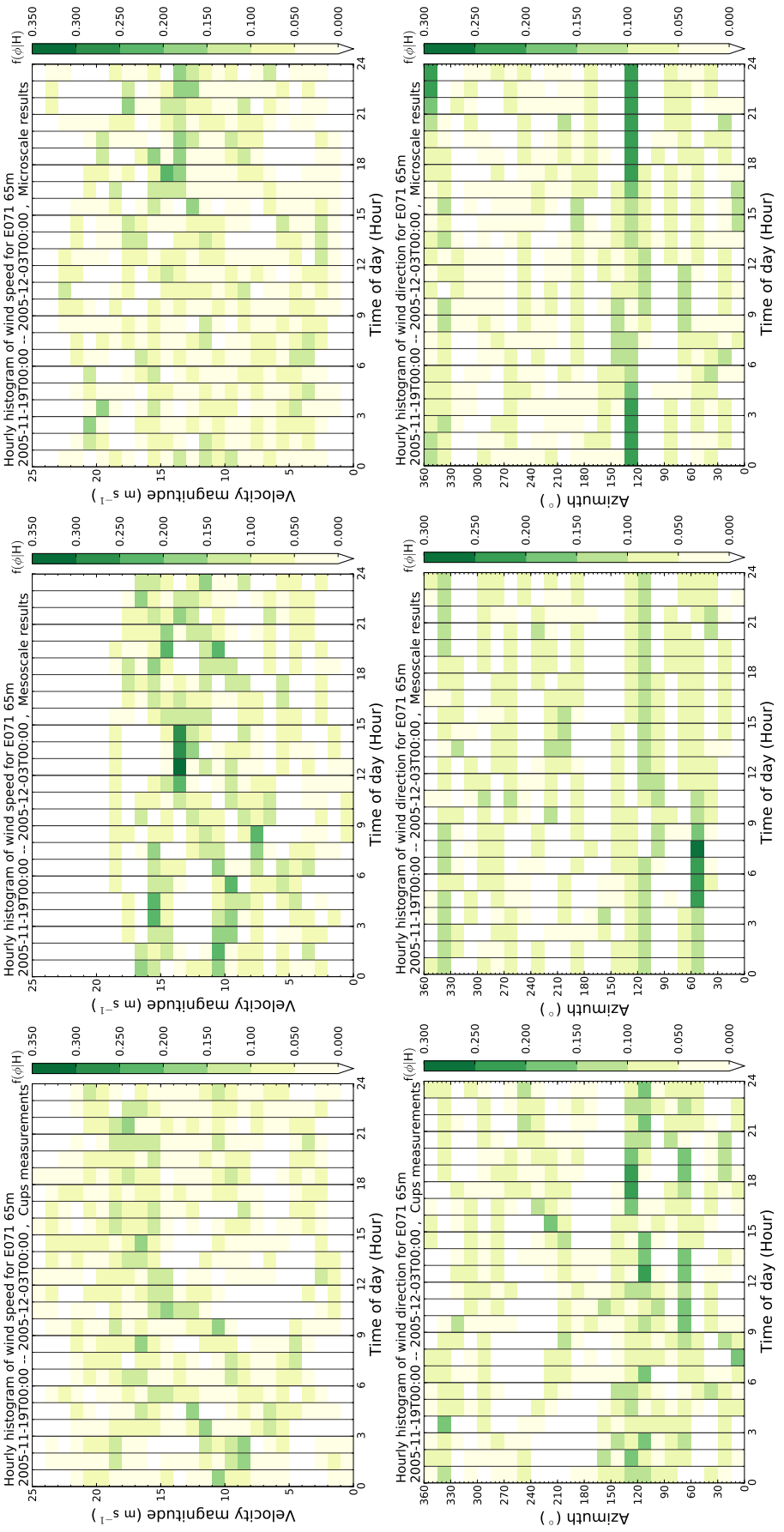

(a) Meteorological mast in Pinheiro (E71).

Figure 5.17: *Caption in page 205.*

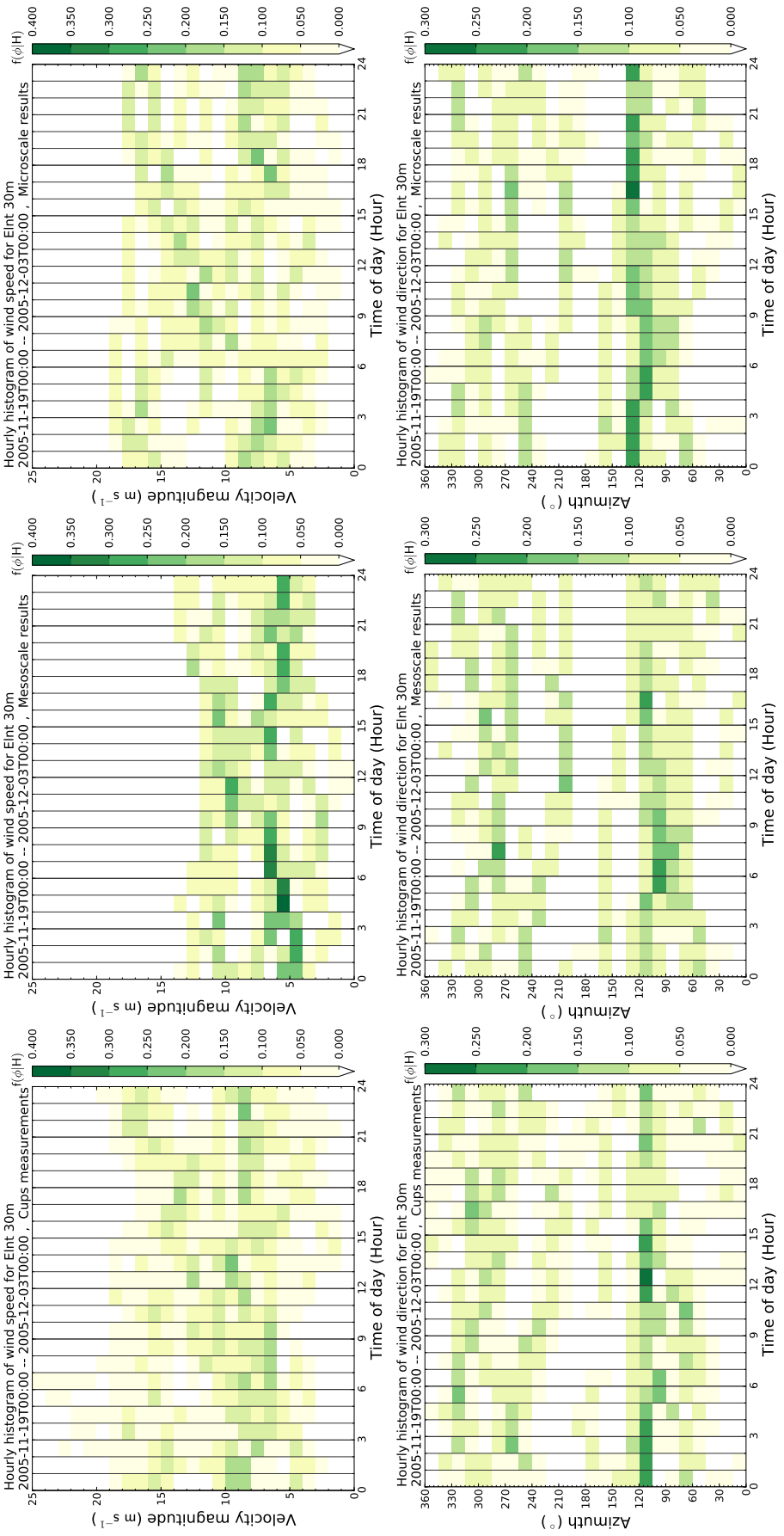

(b) Meteorological mast in Cabeço da Rainha (Elnt).

Figure 5.17: *Caption in page 205.*

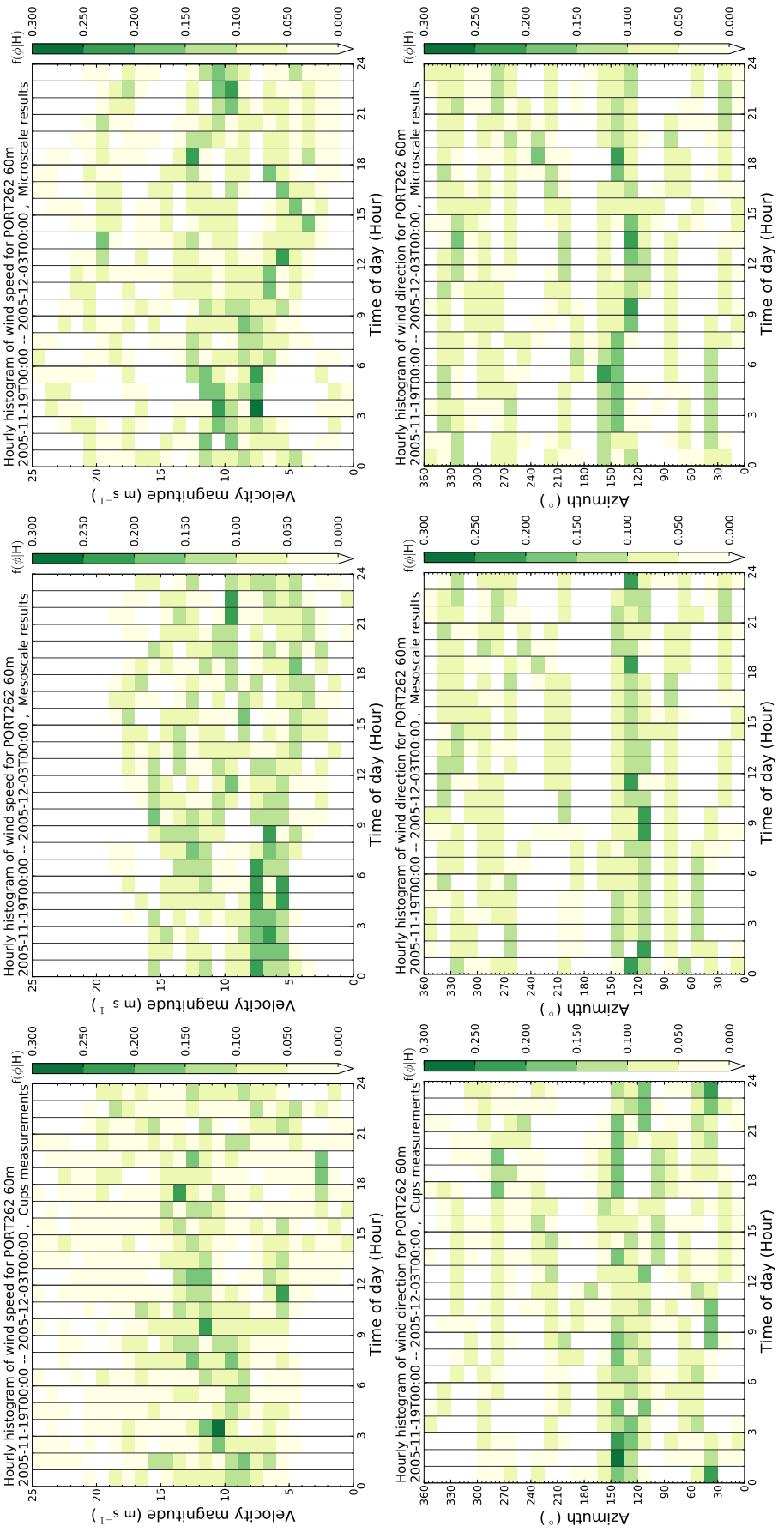

(c) Meteorological mast in Alto do Corisco (PORT262).

Figure 5.17: *Caption in page 205.*

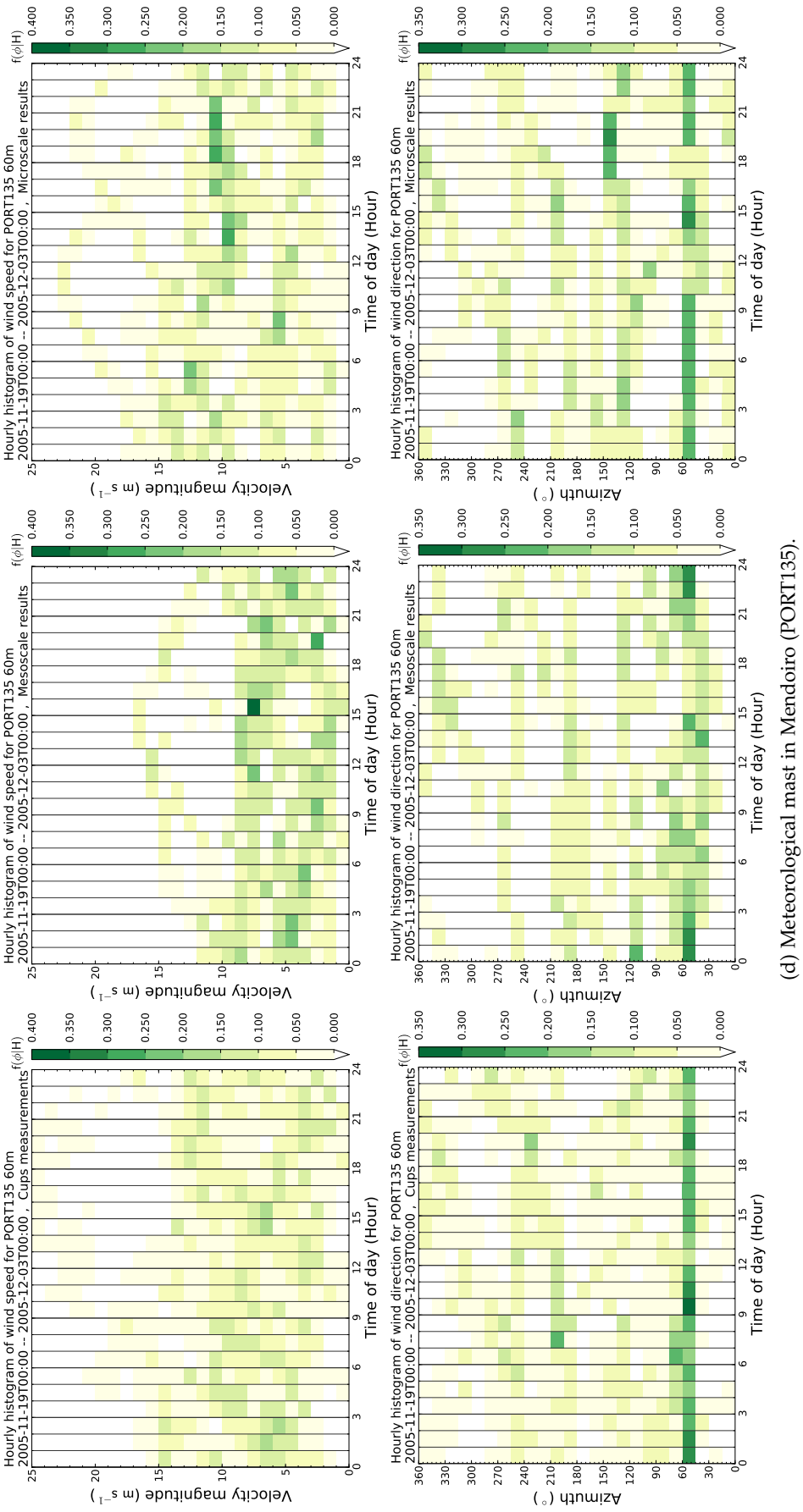

(d) Meteorological mast in Mendoiro (PORT135).

Figure 5.17: Hovmöller plots of wind speed (topmost) and direction (bottommost) for the period between 2005-11-18 to 2005-12-03.

which are weaker in the measurements. This effect becomes worse in the microscale near 23:00.

For Lontreira (Figure 5.17b) the results are similar. The mesoscale over-predicts the magnitude of the mode due to the lack of high wind speeds. The measurements show a trend where the wind speed increases from $7\,m\,s^{-1}$ at 3:00 to $15\,m\,s^{-1}$ at 0:00. The nocturnal result is bimodal as there are also histogram peaks for $10\,m\,s^{-1}$. Although the microscale mode is over-predicting between 8:00 and 12:00, it was able to capture this trend of increasing wind speed, as well as the bimodal pattern from 18:00 onwards. There is a large dispersion in the wind direction, thus it is difficult to find a clear trend. However the 110° winds are predominant throughout the day, also gathering the highest magnitude in the number of occurrences. While the mesoscale under-predicts the magnitudes for those directions, the microscale over-predicts.

At Alto do Corisco (Figure 5.17c) the velocity measurements also show an increase in the mode throughout the day, from $8\,m\,s^{-1}$ to $14\,m\,s^{-1}$. This is accompanied by an increase in the dispersion of the histogram, saw by the lack of records below $4\,m\,s^{-1}$ for the whole morning. In the mesoscale there is an increase in the dispersion and the lack of low velocities during morning is also in agreement. However the predictions are limited to $18\,m\,s^{-1}$ speeds and the increase in the mode is not perceptible. The microscale was able to increase the values by $\sim 2\,m\,s^{-1}$, which is in agreement with the BIAS values found in Table 5.9. There are disagreements regarding some low speeds in the early morning and som over-prediction in the occurrence of high velocities. The main direction has a southern component, around 120° to 150°, aside from the high dispersion similar to the other sites. These azimuths are reproduced by the mesoscale, although with an over-prediction of northwest winds. The microscale shows similar results to the mesoscale, however with a bias of 15° on the value of the mode.

For Mendoiro (Figure 5.17d) the conclusions are similar as for Alto do Corisco. The microscale wind speed patterns are similar to those of the mesoscale, but scaled up by ~ 1.4. The microscale also reproduces some of the dispersion found in the histograms from the measurements, however for speeds above $15\,m\,s^{-1}$ the number of records is being over-predicted. The predominant winds arrive from the 50° azimuth. For this direction the microscale shows some improvements over the mesoscale, as it reduces some dispersion and provides a better agreement. However there was some southeastern component which, although also present in the measurements, is over-predicted in the forecasts.

5.4.2.6 Summary

The main conclusions for the autumn weeks were:

1. In respect to the summer results, the wind speed RMSE increases for both forecasts. However, the microscale results are generally superior to those of the mesoscale. There are improvements on 13 of the 18 locations and the positive SS varies between 0.1 and 0.7. The average RMSE was $3.4\,m\,s^{-1}$ for the microscale and $4\,m\,s^{-1}$ for the mesoscale.

2. Similarly to the summer, the Mendoiro site showed improvements for 7 of the 8

anemometers, with positive SS between 0.14 to 0.42 and an average bias around $0.2\,\mathrm{m\,s^{-1}}$. Likewise, the mesoscale was better at Pinheiro wind farm but only for the highest anemometer, with improvements of 0.28 and a bias of $-0.2\,\mathrm{m\,s^{-1}}$.

3. Conversely to the summer, the microscale prediction agreement was best at Cabeço da Rainha wind farm. The average velocity RMSE is similar, $2.6\,\mathrm{m\,s^{-1}}$, however the correlation coefficient greatly improved returning 0.8, as opposed to 0.4 during summer. The skill scores were the highest, with values of 0.6 and 0.7.

4. The forecast of wind direction greatly improves. The average RMSE is 33°, less 35% than of the microscale in the summer period. The skill scores show improvements on 9 of the 18 locations available, with the highest values near 0.3.

5. In respect to the summer period, the diurnal variation of the RMSE is reduced. The improvements observed, either of the microscale over the mesoscale or otherwise, are not specific to one particular period or set of hours.

6. Several events of high wind speeds were observed in all of the available time series. In most of these events, the microscale was able to reproduce the velocity magnitude and provide a good agreement. Although the mesoscale could capture the variations and slopes in the wind speed signal, it was unable to get the amplitude, under-predicting the observations.

7. The ability for the microscale to reproduce high wind speeds allowed to increase the velocity histogram by 30% in respect to the mesoscale. On overall, the microscale histogram has higher agreement with the measurements.

8. The wind roses are better reproduced by the microscale for Alto do Corisco and Cabeço da Rainha sites. In Mendoiro and Pinheiro the microscale under-predicts the most important sectors.

9. Time shifts of 3 to 6 hours happened in both forecasts, without predefined sign (lag or lead in time). When such shifts occurs, it seldom occurs in both forecasts simultaneously.

10. The time series show that the wind direction was insensitive to the diurnal cycle. This is the contrary to what was observed in the summer weeks. Instead of strong variations within 24 hours, azimuth changes happen over time periods lengthier than a week. The same pattern was observed in all four sites, namely the constant change from southern winds to the east, north and northwest.

11. The Hovmöller diagrams consistently showed histograms of wind speed and direction with higher dispersion than those of the summer weeks. For velocity this was a consequence of the higher range of speeds which were observed in this period. Additionally, there was no apparent trend, in agreement with the time series regarding the independence of the wind conditions on the diurnal cycle.

5.4.3 Effect of thermal stratification on the forecast accuracy

The analysis in §5.4.1 and 5.4.2 allowed to distinguish different behaviour in the forecasts for the summer and autumn periods. Both wind speed and direction appear to

be insensitive to the diurnal cycle in autumn, as concluded from Figure 5.17. Although there is an increase of the dispersion of the histograms and of the velocity RMSE, the microscale forecast in autumn is better than the mesoscale at more masts than in summer. Additionally the direction RMSE improves in both its magnitude and the skill score.

It is expected that the variation of the surface heat flux, q'_w, has an higher amplitude in summer than in autumn. Because the microscale lacks a land-surface model, it is unable to reproduce the surface heating due to solar radiation. Its main link to the diurnal cycle due to q'_w, supplied as a boundary condition from the mesoscale. As such, in periods where the wind conditions become less sensitive to q'_w and its diurnal cycle, the lack of a land-surface model is mitigated. The expectation is for the microscale to deliver better results under such conditions.

In Figure 5.18 is shown the error as function of the stability parameter, $z/\mathcal{L}$, together with time series of q'_w and $z/\mathcal{L}$. The Lontreira mast from Cabeço da Rainha was chosen because it is the one where the amplitude in q'_w is the highest during summer, at least 50% greater than in all other masts. Similar plots for the other masts are shown in §E.2.3 of the Appendix E.

As expected, the variation of q'_w is much lower in the autumn, as shown in Figure 5.18a. Even so, the heat flux is characterized by oscillations that match with the diurnal cycle. This dependency becomes much lower on the parameter $z/\mathcal{L}$ (Figure 5.18b). Conversely to the summer, in autumn $z/\mathcal{L}$ and q'_w do not appear to be linearly correlated. This is due to the dependency of $\mathcal{L}$ on both the heat flux and the shear stress, the later predicted by the microscale code. The higher the shear, u_* increases and the influence of q'_w decreases.

Figures 5.18c and 5.18d show the RMSE of speed and direction as function of $z/\mathcal{L}$. The average error was computed using bins containing at least 10 records. There is a gradual increase of the error with higher values of $|z/\mathcal{L}|$, particularly for the wind direction. As in autumn the range of $z/\mathcal{L}$ is much lower than for the summer and the values are concentrated near neutral stability, the error tends to become smaller. As already stated, as the amplitude of stratification itself decreases, the influence of the diurnal cycle is lower and the agreement yielded by the microscale forecast improves.

5.4.4 Forecast of the electrical power output

In Chapter 4 was discussed the forecast of wind power using a methodology based on transfer functions. For a wind farm, the wind speed at each turbine was estimated from a weather forecast at a reference location within the wind farm, by the use of a transfer function. This transfer function was produced from numerical simulations results, mapping several possible conditions at the reference location, namely the wind speed and direction. Afterwards, a prediction of the power output of each turbine was made by using a power curve supplied by the respective manufacturer. Due to the limitations of this method, the numerical simulations considered only the neutral flow. As such, two main characteristics of the flow field were missing: unsteady effects and thermal stratification.

To evaluate how a methodology based on a model chain performs in producing wind

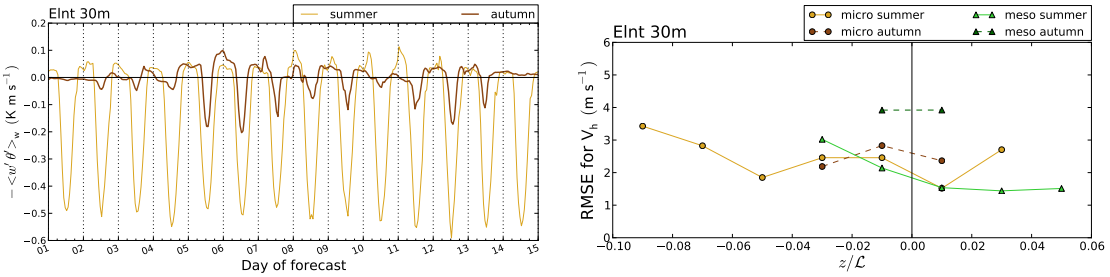

(a) Time series of the surface heat flux.

(c) Velocity RMSE *v.* stability parameter $z/\mathcal{L}$.

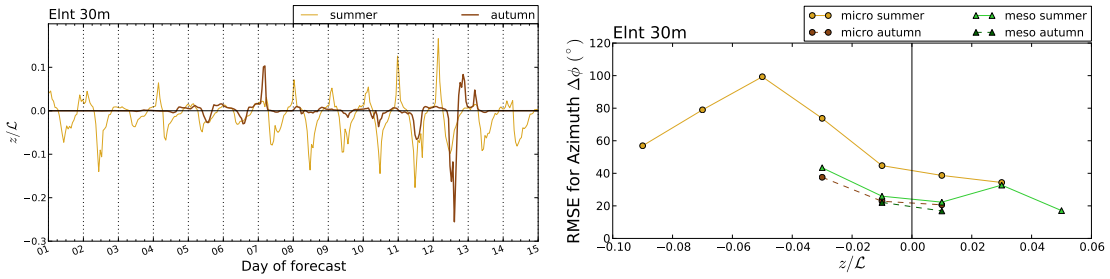

(b) Time series of the stability parameter $z/\mathcal{L}$.

(d) Direction RMSE *v.* stability parameter $z/\mathcal{L}$.

Figure 5.18: Influence of atmospheric stability on the prediction error in Cabeço da Rainha wind farm. The green lines refer to the mesoscale, the yellow and red lines to the microscale.

power forecasts, the mesoscale and microscale results were used to obtain time series for the turbines of Pinheiro and Cabeço da Rainha wind farms. As for the forecast with transfer functions, the manufacturer power curve was used to estimate the power output from the wind speed prediction. The transfer functions used in Chapter 4 were applied to the time series at the respective reference locations for the wind farms: E71 and Ecra masts. It was verified in §4.4.3 that using wind speed predictions at higher heights for the reference location, 109 m, yielded better results. As such, the respective transfer functions were used to estimate the velocity at the turbines and a power prediction was produced, hereafter designated as TF.

In Table 5.10 is shown the error found in the power forecast, together with the respective skill scores in Table 5.11, for four different predictions methods:

1. The transfer function methodology applied to the mesoscale forecast alone.
2. The transfer function methodology applied to the microscale forecast.
3. The direct use of the mesoscale forecast at the turbines location, using the respective turbine manufacturer power curve.
4. Likewise, the direct forecast at the turbines location using the microscale results, together with the respective turbine manufacturer power curve.

All of these four predictions are made for the two time periods simulated: the two summer weeks and the two autumn weeks. The measures based on the absolute error, the BIAS, MAE and RMSE, are all normalized using the nominal wind farm power. The RBIAS, MRE and RMSRE are measures based on the relative error, thus any record where the measured power is low will have an increased weight. To prevent floating-point exception due to a power measurement equal to 0, as well as an excessive influence

Table 5.10: Error in the power forecast, for both mesoscale and microscale results. The prediction using transfer functions was also produced, using the wind velocity at the reference location (E71 for Pinheiro and Ecra for Rainha, both at 109 m). Those results are marked with TF (transfer function). For the definition of the error measures, refer to §4.3.4.1.

	BIAS	MAE	RMSE	RBIAS	MRE	RMSRE
Pinheiro, 2005/07/01 to 2005/07/15						
meso TF 109 m	0.4%	12.1%	18.3%	10.2%	76.3%	106.6%
micro TF 109 m	−7.5%	15.5%	24.1%	−32.8%	80.0%	94.6%
meso at turbines	3.6%	11.4%	17.3%	30.8%	80.0%	119.3%
micro at turbines	0.6%	12.3%	18.7%	6.3%	73.4%	99.3%
Cabeço da Rainha, 2005/07/01 to 2005/07/15						
meso TF 109 m	−1.7%	13.1%	18.6%	11.5%	67.6%	101.6%
micro TF 109 m	−9.1%	13.8%	20.6%	−24.7%	63.7%	84.3%
meso at turbines	−4.7%	12.1%	17.4%	−2.1%	52.5%	79.1%
micro at turbines	−3.6%	12.4%	18.8%	5.7%	64.7%	100.4%
Pinheiro, 2005/11/19 to 2005/12/03						
meso TF 109 m	1.8%	11.1%	19.9%	9.4%	34.6%	83.7%
micro TF 109 m	1.5%	18.2%	29.6%	12.1%	49.9%	94.2%
meso at turbines	2.4%	11.0%	18.2%	13.4%	35.3%	83.2%
micro at turbines	5.2%	16.6%	26.1%	26.7%	46.5%	86.9%
Cabeço da Rainha, 2005/11/19 to 2005/12/03						
meso TF 109 m	−3.0%	13.8%	20.2%	−28.0%	38.0%	50.8%
micro TF 109 m	6.1%	12.3%	19.3%	−2.8%	30.1%	47.7%
meso at turbines	−3.9%	14.0%	20.7%	−25.6%	39.5%	53.0%
micro at turbines	9.4%	13.5%	20.2%	12.9%	37.4%	60.6%

Table 5.11: Skill score for the several results shown in Table 5.10. The $\{a, b\}$ nomenclature refers to the improvement of forecast a over b, using the mean squared error.

	{micro TF, meso TF}	{micro, meso}	{meso, meso TF}	{micro, micro TF}
2005/07/01 to 2005/07/15				
Pinheiro	-0.74	-0.17	0.11	0.40
CRainha	-0.22	-0.17	0.12	0.16
2005/11/19 to 2005/12/03				
Pinheiro	-1.22	-1.05	0.16	0.22
CRainha	0.08	0.05	-0.05	-0.09

of records of very low magnitude, a threshold was set to consider only the values above 2% of the wind turbine nominal power.

On the overall, the mesoscale forecast shows the best agreement. In Pinheiro the microscale performs worse. The increase in the microscale MAE relative to the mesoscale is 8% for the summer and 50% in autumn. In the summer, the MRE is 8% lower though, related with the lower BIAS value. Conversely, the autumn forecast in Pinheiro is unsatisfactory with higher MAE and MRE than the mesoscale. Comparing the MAE during summer and autumn, there is an increase by 35% for the microscale in autumn and a decrease of 4% for the mesoscale. Regarding the relative measures, for all forecast methods these decrease in autumn becoming as low as $\sim 50\%$.

The power prediction for Cabeço da Rainha is worse during the summer but improves in the autumn period. However for the later there is only 39% of valid measurements by the wind farm SCADA. In July, while the microscale MAE is similar to the mesoscale, the MRE increases by 23%. Although during the autumn weeks there are improvements of the microscale over the mesoscale, the absolute error measures are higher than for July. As it was verified for Pinheiro, the relative measures show values $40\% \sim 50\%$ lower. Also, the methods using TF show better agreement than the direct forecasts at the turbines locations. From the skill scores displayed in Table 5.11, this is the opposite to Pinheiro and the July weeks, where the TF return worse results.

To further analyse the power predictions, each of Figures 5.19, 5.20, 5.21 and 5.22 show two plots: the histogram of the park power and the power curve, relating the power and the velocity at a reference location. Each plot shows the SCADA observations together with the microscale and mesoscale results. The power curve makes use of box-plots to represent the data. As referred in §4.3.3.3, the limits of the box-plot do not include the records above and below $^3/_2$ of the interquartile range, considered to be outliers. Any extreme values outside of the box-plots are represented by dots. Additionally, if the sample size is less than 9 records for a bin, the raw data is shown instead of the box-plot. It should be noted that the wind speed used to plot the power curve is related to the respective dataset, *i.e.*, the microscale park power is displayed as function of the microscale wind speed at the reference location. Thus the power curve representation minimizes the influence of the error in the velocity forecast on the power prediction.

Regarding the Pinheiro wind farm, the histogram (Figure 5.19a) shows few differences between the mesoscale and microscale. The mismatches in both forecasts are independent of the respective park power. The power curve (Figure 5.19b) shows that there is a consistent over-prediction of both microscale and mesoscale. This is related with wake effects which are not modelled in the microscale and mesoscale results. In the autumn weeks the results are similar but with higher wind speeds, leading to more events where the wind farm was operating at maximum power (Figure 5.21). The respective park power curve also exhibits over-predictions due to the lack of a wake model, for wind speeds where the park power was below the maximum.

With higher wind speeds there is an increase in the scatter of the measurements, until the rated power for all turbines in the wind farm is reached. Considering two distinct locations, if the average wind speed at one location is made function of the average speed at the other location, for a specific velocity value at the first location it is expected that the speed at the second spot varies, instead of showing a constant

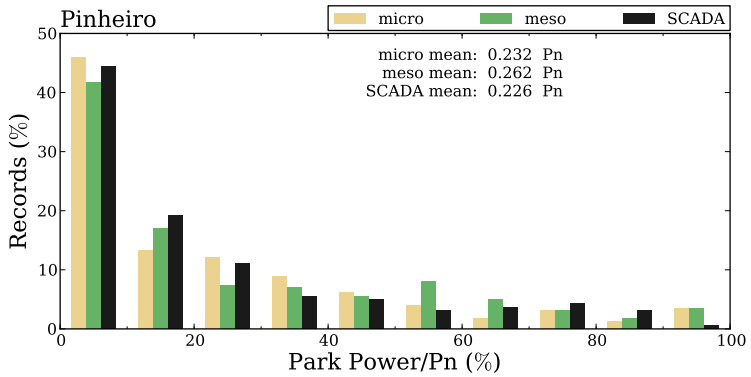

(a) Histograms of the park power.

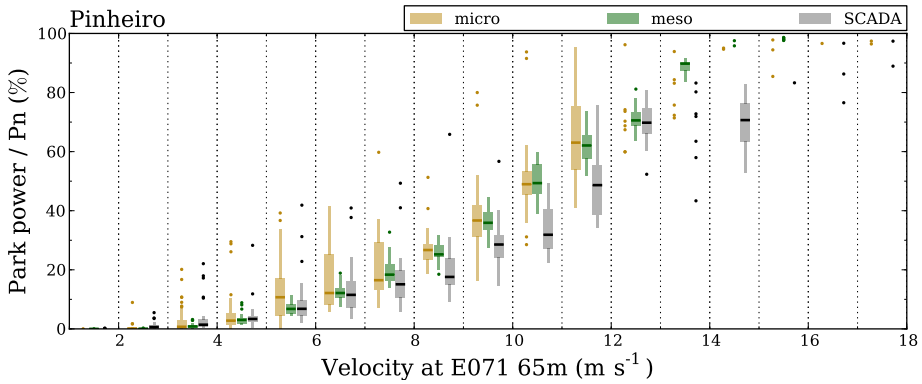

(b) Power curve.

Figure 5.19: Power prediction for the Pinheiro wind farm in the period between 2005-07-01 and 2005-07-15 (*for details refer to Figure 5.22*).

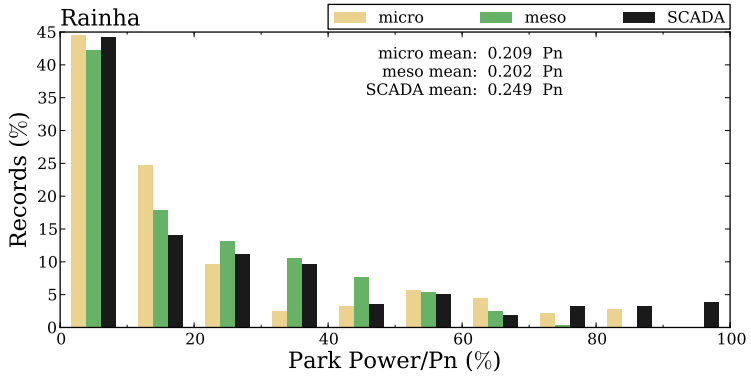

(a) Histograms of the park power.

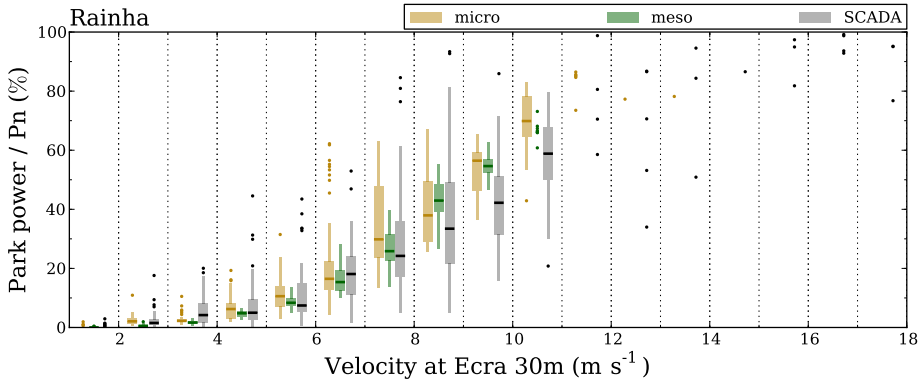

(b) Power curve.

Figure 5.20: Power prediction for theCabeço da Rainha wind farm in the period between 2005-07-01 and 2005-07-15 (*for details refer to Figure 5.22*).

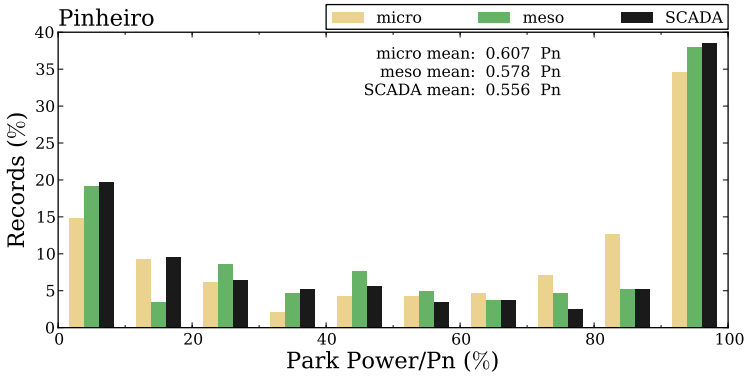

(a) Histograms of the park power.

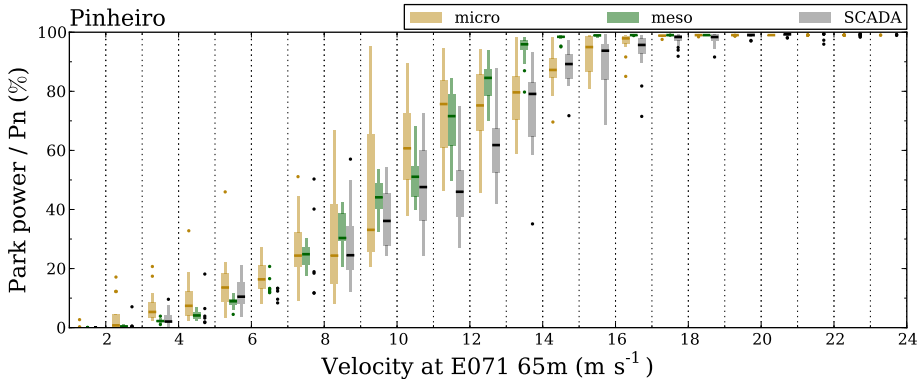

(b) Power curve.

Figure 5.21: Power prediction for the Pinheiro wind farm, in the period between 2005-11-18 and 2005-12-03 (*for details refer to Figure 5.22*).

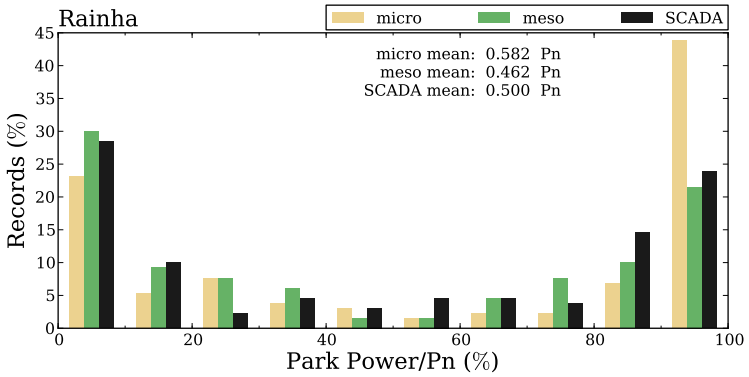

(a) Histograms of the park power.

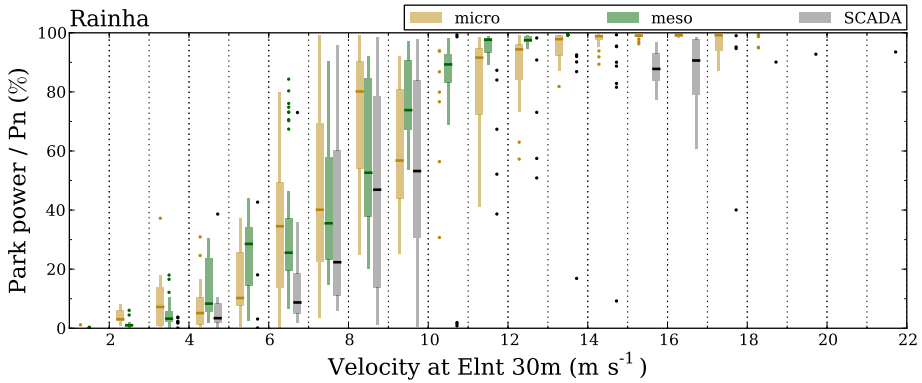

(b) Power curve.

Figure 5.22: Power prediction for the Cabeço da Rainha wind farm in the period between 2005-11-18 and 2005-12-03. The leftmost plot shows the histogram of the power predictions and the SCADA measurements. The rightmost plot shows the wind farm power curve, *i.e.*, the power predictions and SCADA measurements organized as function of the wind speed at a reference location. The data is represented using box-plots instead of the raw values. The power is normalized using the wind farm nominal power, Pn.

value. Even if both speeds are well correlated, the velocity at the second location is better described by a probability distribution, due to unsteady phenomena, stratification effects, among others. The same is expected to happen when the velocity at a turbine location is observed as function of the velocity at a reference location (used to plot the wind farm power curve in the figures). As such, for a specific turbine, the blending between the velocity variance at the turbine location and the shape of the turbine power curve results in a higher dispersion of the respective power output. For a wind farm, as the power of each individual turbine is summed up to form the park power, the more significant become this effect.

The analysis regarding the increase of the power variance is similar to the one used in the influence of the wind speed variance within a integration time, referred in §4.2.5. For a specific bin of the wind speed at the reference location, even if the probability distribution of the wind speed at the turbine is symmetric, the same asymmetry observed in Figure 4.7 is verified in the probability distribution of the power. For wind speeds near the cut-in, the skewness in the power distribution is expected to be positive. The variance of the power becomes higher for wind speeds between the cut-in and the rated output speed, where the power curve derivative is more steep. When the speed at the turbines is close to the rated output, it will be limited by the nominal turbine power and the skewness becomes negative. For higher values of the wind speed, above the rated output, the power values will be close to the nominal power with very little dispersion. Such is the case for some events in the autumn weeks (Figure 5.21b), where due to the higher wind speeds the agreement is particularly good for velocities above $17\,\mathrm{m\,s^{-1}}$. For these speeds all turbines are operating at the rated power output.

These remarks regarding the large dispersion found in the park power curve may be extended to both microscale and mesoscale results. Because unsteady and thermal stratification effects are considered, the wind characteristics near a turbine may be different from the reference location. Additionally the relation between both locations may change over time, depending on the diurnal cycle and the boundary conditions from the respective driving model (either the GCM or the mesoscale model). Additionally the mesoscale is seen to show a smaller interquartile range than the microscale. This is due to the coarser grid resolution, which is higher than the distances between the wind farm turbines. As such, the wind characteristics in the wind farm area show higher correlation, resulting in a power curve with less variance. This is shown in Figure 5.23 for turbine 1 of both wind farms. Similar plots for the each of the other turbines exhibited the same characteristics, thus were not included in the text.

In Cabeço da Rainha the histogram (Figure 5.20a) shows events where the wind farm was operating at full capacity but both microscale and mesoscale were unable to predict this. From the power curve (Figure 5.20b) it is concluded that such events happen in a wide range of wind speeds, starting at $12\,\mathrm{m\,s^{-1}}$, but for very few records. The measurements are characterized by a large dispersion, *e.g.*, for $8\,\mathrm{m\,s^{-1}}$ one finds power outputs ranging from 10% to 80%. This is due to the higher number of turbines that compose the wind farm. The interaction of the seventeen 600 kW together with the output from the three 2 MW turbines (representing 35% of the maximum park power), result in a system very difficult to predict.

The Cabeço da Rainha forecast for the autumn weeks shows different results from all

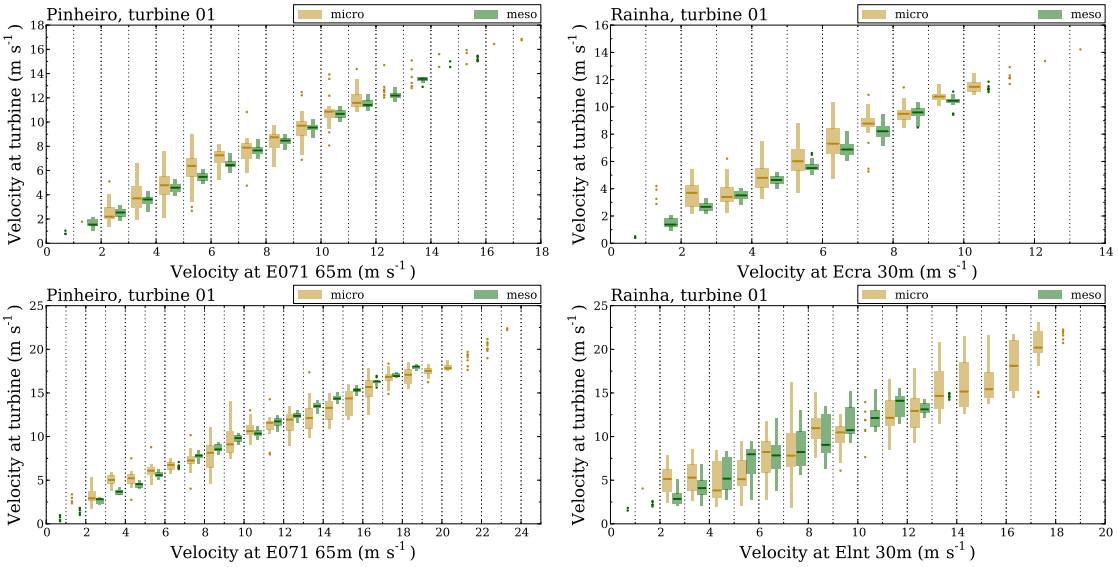

Figure 5.23: Variation of the wind speed near a turbine as function of the wind speed at the reference location, for the Pinheiro and Cabeço da Rainha wind farms in the summer (*topmost*) and autumn period (*bottommost*).

others. The histogram (Figure 5.22a) presents a high over-prediction of the microscale for events where the wind farm was operating above 90% of the rated output, near 2 times higher than for the measurements and mesoscale. Hence, there is an overall deficit of the remaining histogram bins, albeit much smaller. As it was previously referred, this period was hindered by a data availability of only 39%, of a total of 336 hourly averaged records. The power curve in Figure 5.22b reflects the lack of data, as the variance is much higher than for the other periods analysed. This is also consequence of the need to use the Lontreira mast as the reference location, as the Rainha mast was out of operation. The microscale results have records reaching the maximum wind farm production for wind speeds above $7\,\mathrm{m\,s^{-1}}$ at the Lontreira mast. Such events were also due to the higher wind speeds which the microscale was able to predict. As showed in Figure 5.23, for the same wind speeds above $7\,\mathrm{m\,s^{-1}}$ at Lontreira there were records above $12\,\mathrm{m\,s^{-1}}$ at turbine 1, which represent 90% of the respective rated power of 600 kW.

5.4.5 Turbulence intensity predicted by the microscale model

In Chapter 4, due to the impossibility to estimate the atmospheric stability from the available measurements, the turbulence intensity, TI, was shown as function of the wind speed at the measurement masts. The data from the measurements exhibited a trend similar to an exponential decay. The measurements were organized in a summer days and winter nights dataset, to find the differences in both trends, as these are probably related with stratification effects on the wind turbulence. The numerical simulations of the neutral flow were unable to reproduce this, showing instead a constant value.

In Figures 5.24 and 5.25 the same kind of plots are made for both July and autumn weeks, being the counterpart to the neutral flow results in Figure 4.17. The purpose is to perceive if the presence of stratification in the simulations is enough to obtain the

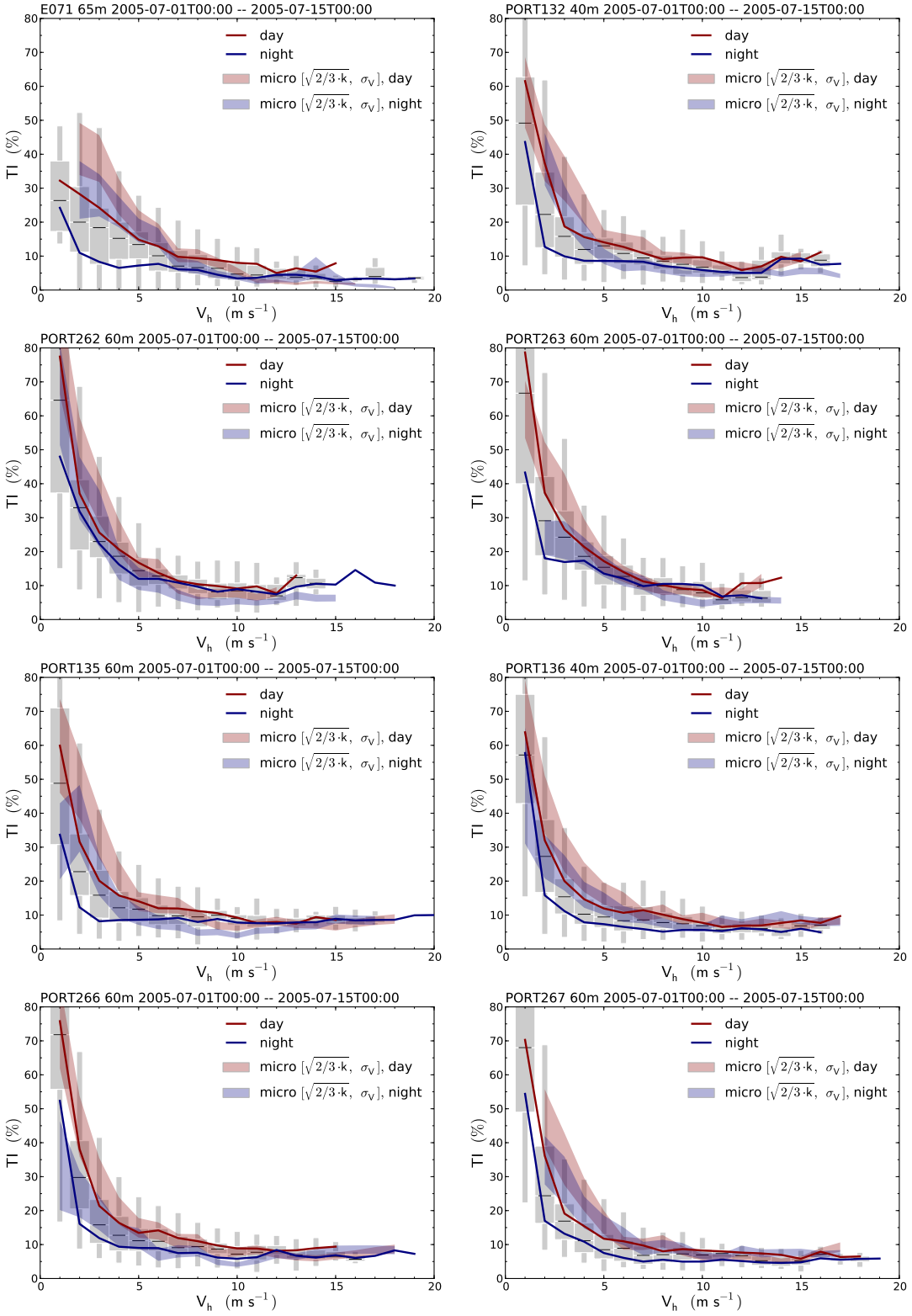

Figure 5.24: Turbulence intensity, TI, as function of the wind speed, in the period between 2005-07-01 to 2005-07-15. The raw data is displayed using box plots (see text). The red and blue colours refer to diurnal and nocturnal events, respectively. The TI average at each bin is shown in the solid curves. The results from the microscale simulations are shown by the coloured patches, using two different measures for the standard deviation of the horizontal velocity magnitude.

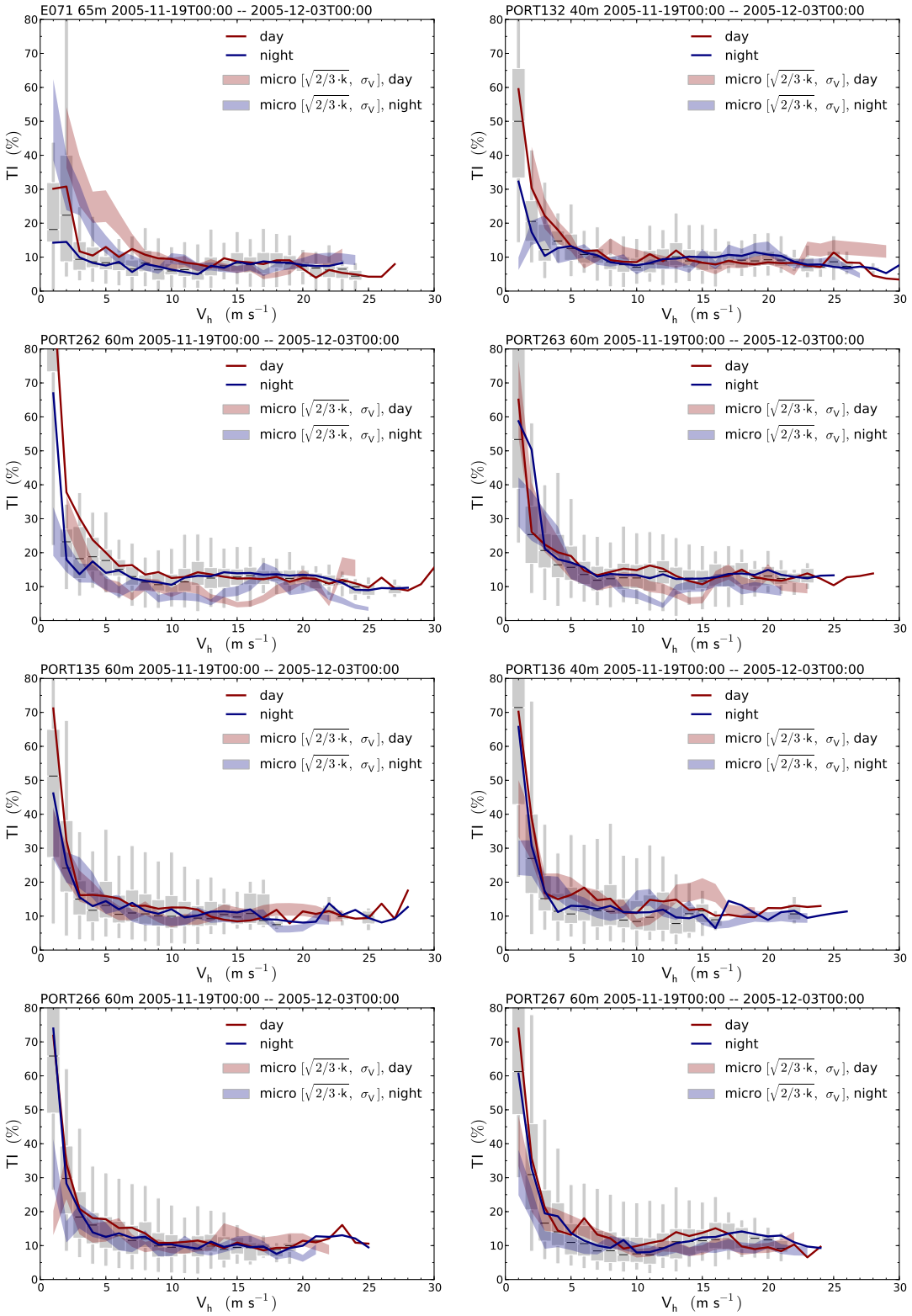

Figure 5.25: Turbulence intensity, *TI*, as function of the wind speed, in the period between 2005-11-19 to 2005-12-03. For details refer to Figure 5.24.

same trend found in the measurements. The data was also separated into a diurnal and nocturnal period and, instead of splitting into azimuth bins, the several measurements from the masts of Alto do Corisco and Mendoiro are also shown. For the July weeks the sunrise and sunset were approximately at 5:00 and 20:00 ST. The diurnal and nocturnal periods were characterized using the events that happened between [7:00, 18:00] and [21:00, 4:00], respectively. Similarly for the autumn weeks, as the sunrise and sunset happened around 7:30 and 17:15, the equivalent periods were between [9:00, 16:00] for the day and [19:00, 6:00] for the night.

Because the WRF simulations were obtained using the ACM2 non-local closure (as referred in §5.3), it provides no turbulence kinetic energy fields. Thus, only the TI predicted by the microscale was used to compared with the observations. The microscale output contains both the turbulence kinetic energy, k, and the variance of the horizontal velocity, σ_V^2, computed accordingly to the definitions in Appendix D, Table D.1. These allowed to have two estimates for TI:

$$\frac{\sqrt{\frac{2}{3}k}}{V} \leq TI \leq \frac{\sigma_V}{V}\,, \tag{5.13}$$

where V is the average magnitude of the horizontal velocity. The value of TI may vary between these limits, depending on the value of the average velocities and variances in the longitudinal and spanwise directions, as discussed in §4.3.3.3.

All of the results in Figure 5.24 show a decay trend in both the measurements and the microscale. For high velocities, both diurnal and nocturnal curves converge to the same asymptotic value, showing fewer differences between them. This is similar to the neutral results in §4.3.3.3 and the conclusion is the same. As the Reynolds number increases, the production of turbulence due to shear becomes higher. Conversely, the influence of buoyancy effects decreases.

For low velocities the diurnal and nocturnal curves differ, being the latter characterized by lower TI. This follows the expected behaviour for the typical diurnal and nocturnal boundary layers. In a convective ABL, buoyancy contributes to turbulence production, increasing TI. Conversely, the nocturnal ABL is characterized by stable stratification where turbulence is dampened by buoyancy. The trend showed by the measurements is well reproduced by the simulations. This is contrary to the neutral results in §4.3.3.3, indicating that stratification effects are paramount to reproduce the TI decay. Despite of the good agreement in the trend, the discrepancies are higher for low velocities. Even with buoyancy production being accounted, the $k-\epsilon$ model always assumes that the flow has a high Reynolds number. These disagreements might be attributed to the failure of this requirement.

On overall, the diurnal period shows better agreement than the nocturnal period. The simulations over-predict the turbulence during the night. This is both due to the wall boundary condition of imposed heat flux and also the higher difficulty in modelling the turbulence damping under stable conditions. As described in §5.3.4, limits are imposed on the turbulence production due to buoyancy, $\mathcal{G}$, to prevent flow laminarization due to very stable conditions. Additionally, the stability parameter $\zeta = z/\mathcal{L}$ is bounded by the upper limit in eq. (5.10). As stated in §5.3.5, a wall boundary condition based on a prescribed heat flux leads to two solutions when the stratification is

stable, *i.e.*, the duality problem. Both of these conditions restrain the microscale model to reproduce phenomena in moderately to extreme stable conditions, where turbulence is characterized by intermittency.

These conclusions are similar for all of the sites and masts in both Figures 5.24 and 5.25. The agreement is worse for masts E071 and PORT267 in the July weeks, and PORT262 for the autumn weeks. There are, however, further differences between these two periods. Althoug the trends are the same, the autumn weeks show a steeper decay. As the events where the ABL is convective are less and of lower intensity, due to the decreased temperature range and diurnal hours, the results will be more similar to the ones found in the July weeks for the nocturnal period. The autumn weeks are also characterized by more oscillations and mismatches at high wind speeds, as shown in the PORT262 and PORT136 results. This behaviour is influenced by the lack of data at high velocities

5.4.6 Shear factor predicted by the mesoscale and microscale results

In Figures 5.26 and 5.27 is shown the variation shear factor as function of the wind speed. The shear factor, α, already defined in eq. 4.14, is a measure of the velocity profile steepness. An higher value corresponds to a steeper gradient. The plots presented in this section are the counterpart to the results of the neutral flow simulations in Figure 4.18. Analogous to the results in §5.4.5, the data was divided into nocturnal and diurnal periods. In these plots, besides the measurements and the microscale data, the mesoscale results are shown as α could be computed for all datasets.

Besides the higher wind speeds observed during autumn, the results are similar for both periogs considered in Figures 5.26 and 5.27. For higher wind speeds both measurements and simulation results tend to a constant value, although with much more spurious oscillations than in the TI results. On overall there is a good agreement in this high speed range between the microscale results and the measurements. The mesoscale generally over-predicts, particularly in the nocturnal periods. As in these it is expected that the ABL is stably stratified, the α should have higher values. The exception is the Alto do Corisco masts, PORT135, PORT262 and PORT263, whose results shows better agreement for the mesoscale. The PORT262 mast is particularly interesting as both measurements and mesoscale show α around 0.25 during night and 0.1 during day, while the microscale curves are both under-predicting. In the remaining masts the microscale is better, especially in the range between $5\,\mathrm{m\,s^{-1}}$ to $15\,\mathrm{m\,s^{-1}}$.

For low wind speeds, below $5\,\mathrm{m\,s^{-1}}$, the agreement vanishes as the values of α shoot into values of high magnitudes, generally of negative sign. Although some events of nocturnal jets might exist, these inverted profiles are merely due to the noise introduced by the higher variance in the velocity measurements. This is confirmed in the results of §5.4.5, as the TI is saw to increase at low wind speeds. Also, following the same arguments given in the analysis of the TI results, the numerical models are not suited for low Reynolds number flows, both due to the turbulence model characteristics and, regarding the mesoscale, the coarser grid resolution.

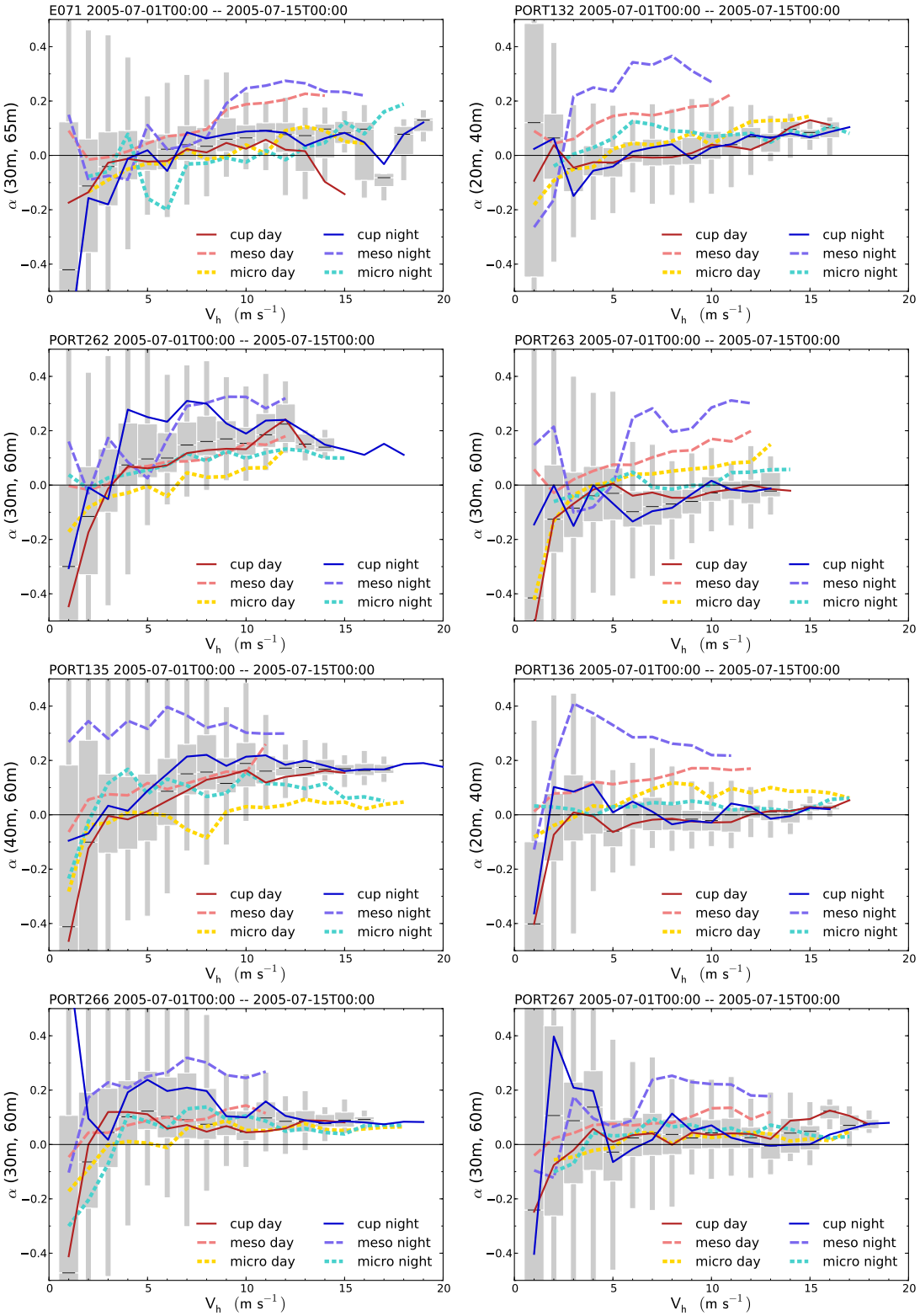

Figure 5.26: Shear factor, α, as function of the wind speed, in the period between 2005-07-01 to 2005-07-15. The raw data is displayed using box plots (see text). The red and blue colours refer to diurnal and nocturnal events, respectively. The α average at each bin is shown in the solid curves. The results from the mesoscale model are shown by the dashed curves. The results from the microscale simulations are shown also by dashed curves, with smaller gaps, using the yellow and cyan colours.

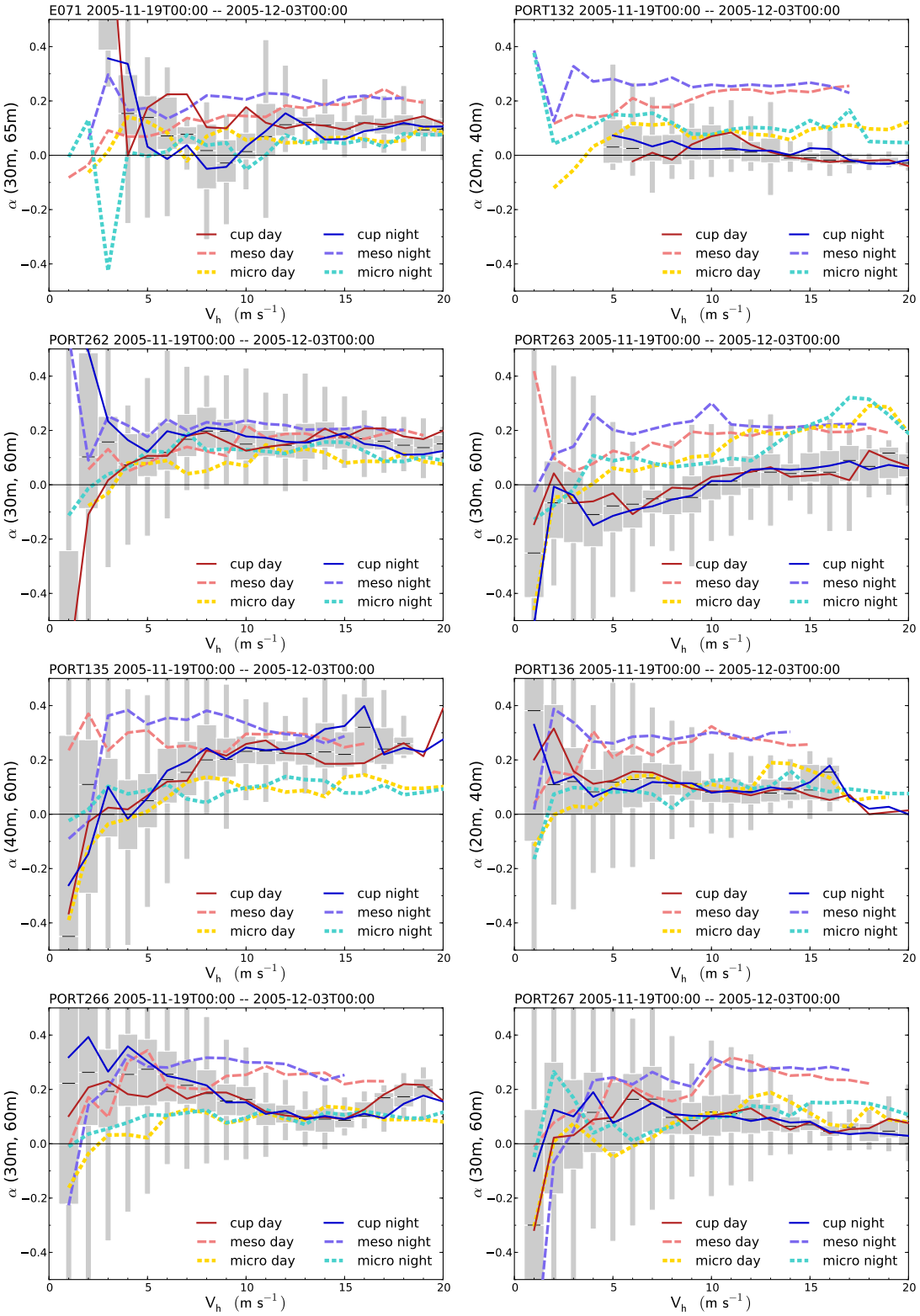

Figure 5.27: Shear factor, α, as function of the wind speed, in the period between 2005-11-19 to 2005-12-03. For details refer to Figure 5.26.

5.5 Conclusions

The atmospheric flow at four distinct sites was simulated to reproduce the wind conditions for two specific periods in time. The mesoscale flow was first forecast using the regional model WRF. The result was a dataset, consisting of time-dependent fields which characterize the flow. A procedure was devised to interpolate these results into a more refined grid, requiring special care of the surface flow and changes to ensure mass conservation without severe modifications to the data. These results were used as initial and boundary conditions to drive the VENTOS® model, in order to characterize the microscale flow. Several changes were made in VENTOS® such that thermal stratification was modelled and for it to work under this one-way coupling.

Regarding the sites, there were a total of 10 measurement masts with a wind vane and two anemometers at different heights. The selected periods consisted of two weeks during the month of July and two weeks in autumn, covering November and December.

The mesoscale simulations consisted of two sets, differing in the parameterization of turbulent quantities: one using a local closure (MYJ) and the other a non-local closure (ACM2). The non-local closure was chosen as it was verified to produce results with higher agreement with the measurements. The microscale simulations were run and their output consisted on fields averaged to the same time integration as that of the measurements. The general conclusions of the analysis of the results were:

1. The summer observations showed variations of the wind conditions which were dependent on the daily cycle of solar heating. The wind direction was characterized by patterns of wind veer between the nocturnal northeast wind and the afternoon western winds, periodically repeating each day. This behaviour was induced by two different thermal circulation systems: sea and valley breezes during the day; land and mountain breezes at night.

2. The summer forecasts showed good agreement and correlation values. The microscale brought improvements in the wind speed prediction for most of the masts of Alto do Corisco and Mendoiro. Conversely, the microscale wind direction agreement was poor due to lag error and the scatter in the time series. Despite this, the quality of the wind roses matched that of the mesoscale forecast.

3. The measurements in the autumn weeks are characterized by a lack of patterns happening with a daily recurrence. Instead, events such as direction veer happen over larger time periods, on the week scale or higher.

4. The autumn forecasts have shown correlation values similar to those of the summer, albeit with higher bias and quadratic error on the wind speed. This was due to the range of wind speed values, as it was 30% higher in autumn. The wind direction, however, greatly improved, particularly for the microscale forecast. Both the lower surface heat flux and higher wind speeds observed reduce the magnitude of the stratification regimes, resulting in a better performance by the mesoscale and microscale models in forecasting direction.

5. The mesoscale forecast is characterized as reproducing less of the dispersion found in the measurements, as observed in the histograms. The microscale is able to

partly reproduced it, however at the expense of higher error due to mismatches.

6. A forecast of the electrical power output was established for the Pinheiro and Cabeço da Rainha wind farms. For both mesoscale and microscale results, the methodology using transfer functions was compared against the direct wind speed forecast for each turbine. The mesoscale gave the best agreement using both methodologies. Additionally, the use of forecasts of the wind speed at the turbine is preferable over the transfer functions. Despite this, the histograms for both microscale and mesoscale power predictions were similar. Regarding the wind farm power curve, both forecasts over-predicted the measurements for wind speeds below the wind farm rated power output. This was mainly attributed to the bias and scatter in the reference wind speed (used as the abscissa for the power curve), but also to the lack of a turbine wake model in these results.

7. The microscale prediction of the turbulence intensity was compared against the measurements. Conversely to the neutral flow results in §4.3.3.3, all results showed a realistic decay trend with the wind speed increase, in agreement with the measurements. The values to which the decay curves converged was coincident for both microscale and the measurements. The agreement was better for the diurnal periods. This was attributed to some limitations imposed on the microscale model when working under conditions where the flow is stably stratified, necessary to prevent flow laminarization to occur.

8. The variation of the shear factor as function of the wind speed was compared for the measurements and both forecasts. These were able to successfully reproduce the trends showed by the measurements. Regarding the convergence values of the shear factors in high wind speeds, the microscale gave a better agreement for most masts. For low wind speeds the agreement vanishes, as the scatter of the measured values of the shear factor sharply increases.

Chapter 6

Conclusions

6.1 Conclusions

In the present work, numerical models were developed and used to predict the wind conditions near wind farms. This was achieved using methodologies where the results from weather predictions (mesoscales) were downscaled to the microscales which characterize the local flow. These predictions are most useful in two different situations: (i) the real-time forecast for the management of the electrical network and (ii) the hindcast of past events, thus building a database for wind resource assessment. Regarding the former, the focus is mainly on the electrical power output. For the later, such knowledge would guide the selection of sites with wind energy potential. The ultimate goal is the wind resource evaluation with the fewer field measurements as possible. The interest is not solely on the energy potential, but also on the wind shear and turbulence intensity, as both are crucial in the selection of the locations where wind turbines should be installed.

A methodology was proposed in Chapter 4 where the atmospheric flow over a site was described by performing steady-state simulations, covering the full range of wind directions at different wind speeds. From these results, a transfer function was obtained relating the wind conditions at a reference location and every wind turbine location. The application of this transfer function to a weather forecast time series at the reference location, yielded a forecast at the turbines. Such approach provided a fast way to obtain a forecast for the wind turbines, instead of resolving the flow at scales smaller than 1 km, which would require a finer computational mesh for the weather model, better topographic input and higher computational resources.

The predicted wind speed at each turbine was related to its power output through the power curve specified by the manufacturer. The far wake effects between the turbines were estimated with the model of Jensen (Katic *et al.*, 1986). Although the turbines possess anemometers, the measured wind speed is severely affected by the near wake of the turbine and cannot be compared with the flow solver results. Hence, the forecast error was solely computed for the difference in the power output, rather than for the wind speed. The error in the forecasts was decomposed into two sources: the one already in the weather forecast and the error in the transfer function together with that of the power curve. The later was evaluated by feeding a time series of field measurements at the reference location, instead of a weather forecast, yielding mean absolute errors

below 9%.

This methodology requires a low error forecast at the reference location, which is difficult when this location is close to the surface. The best results were obtained with a forecast farther from the ground, at 110 m instead of 30 $\sim$ 60 m, as the vertical gradient in the wind speed due to the boundary-layer was lower. When applied to one year of data, this methodology returned mean absolute errors of 15%, never surpassing 25% throughout a three day forecast horizon.

From an engineering application perspective this method gave comparable results to other procedures in the literature based on physical methodologies and statistical techniques (Madsen *et al.*, 2004). However, this method does not reproduce time-dependent phenomena which might exist at the microscales. Additionally, only neutral stratification was considered both due to the lack of detailed field measurements and the complexity it would require to accommodate these effects in the transfer function.

The alternative to numerical weather prediction with very fine grids and the transfer function method was to downscale the mesoscale forecasts, trough the coupling with a microscale model. The four-dimensional results from the mesoscale model provided boundary and initial conditions for the microscale model, producing a time-dependent solution which includes the combined effects of turbulence, rough complex topography variations and thermal stratification. The inclusion of stratification in the previously neutral numerical model required developments to the model and a validation process, in order to gain confidence in the results of the new model.

Among the phenomena related to stratified flow over complex topography, the ability to reproduce mountain lee waves is a paramount requirement for any numerical model. However, most analytical solutions available in the literature assume inviscid flow (Smith, 1980). Additionally, several numerical results that consider turbulent diffusion are described in the literature using a frictionless bottom surface, thus unable to reproduce the boundary-layer. The test case chosen was a tri-dimensional idealized axisymmetric mountain with a stably stratified air flow, to generate internal waves.

An inviscid version of the numerical model was developed and its results were compared with both linear theory and other numerical results. The relevant parameters were modified to have a set of solutions encompassing several wave regimes. The simulations successfully reproduced both the linear regime and non-linear phenomena, namely wave breaking and flow splitting. The results agreed with the reference numerical results, both qualitatively and quantitatively. The same conditions were repeated considering turbulent flow and surface-friction, for a constant boundary-layer depth of $0.2\,U/N$. The overall result was the dampening of the internal waves amplitude. Although flow splitting occurred for equivalent mountain heights, in both the inviscid and turbulent cases, wave breaking did not, happening only in the first time-steps after the start of the turbulent flow simulations. Also, the inclusion of surface-friction produced a streamwise pressure gradient to balance the wall shear stress. This rendered the pressure drag to become unrelated with the wave drag for low hills, hindering the quantitative comparison between the inviscid and turbulent cases.

Another set of turbulent flow simulations were performed to compare with experimental and numerical results (Hunt and Snyder, 1980; Eidsvik, 2008), where surface-

friction was considered. These used a mountain with a smaller width inducing non-hydrostatic lee waves and resonance, generating a trail of wave crests downstream of the obstacle. A reasonable agreement was obtained with the experimental results, mostly explained by the differences between the laboratory experiment and the conditions used in the simulation. Up to 10 dimensionless time units the flow features were very similar. For longer time, the leeward wake continued growing, becoming significantly larger throughout the simulation, in agreement with the numerical results of Eidsvik (2008).

Having ensured that the numerical model was able to reproduce stratified flow phenomena, it was adapted to use the results from a mesoscale model. Pre-processing routines were established to interpolate the regional model output into the microscale computational grid, enforce mass conservation and adapt the surface variables to the finer topographic representation. To simulate the mesoscale flow, two different sets of parameterizations were selected for the regional model, based on the use of local and non-local quantities to estimate turbulent stresses. The later employed the model of Pleim (2007) and gave a better agreement.

The downscaling methodology was applied to two wind farms and two sites with data available from 7 meteorological masts. As the computational requirements of the downscaling are more demanding, only two periods of 15 days were chosen: one in July and the other near the end of autumn. The summer results showed variations in the wind conditions closely matching the diurnal cycle. The results showed both sea and valley breezes interacting during the day, while at night the mountain flows were dominated by mountain and land breeze. For the autumn period, while the wind speed showed some daily variations, the direction was independent of the diurnal cycle. The inclusion of the microscale model in the model chain yielded improvements to the wind speed on more than half of the locations. In the July weeks, the skill scores varied between 0.08 and 0.42 on 10 of the 19 masts. A similar analysis for autumn shows a score range between 0.11 and 0.72 on 13 of the 18 available locations. The wind direction was generally better predicted by the mesoscale, particularly during summer.

For the two wind farms the power output was predicted using both the transfer function method and the direct forecast at the location of the turbines, together with the power curve of the manufacturer. The downscaling method was preferable to the transfer functions, albeit yielding comparable values. The agreement showed by the mesoscale was better than that of the microscale, with improvements of 14% in the mean squared error during summer. This result was affected by the short time span used, especially during autumn where most turbines were not operational for a considerable amount of time. While the mesoscale model resembles a smoother version of the measurements, the microscale model was able to add some of the variance which characterizes the wind time series. Quantitatively, this introduced error as more mismatches happen between the measurements and the simulation results.

Both the predicted turbulence intensity and wind shear were compared with the measurements, to attain the performance of the method as a hindcast. The agreement was good for both quantities. Contrary to similar results with neutral flow, the predicted turbulence intensity was inversely proportional to the average wind speed, following the trend shown by the measurements. The wind shear predicted by the microscale showed a superior agreement to that of the mesoscale.

6.2 Topics for further research

Throughout the work described in this dissertation, several subjects appeared that, while deemed important, had to be overlooked in favour of the previously established paths and the results which were accomplished. The following topics are proposals for further research which would continue the development of the work presented in this thesis, namely the numerical model for stratified flow and the mesoscale-microscale coupling.

1. Due to bottom surface friction and the stress-free condition at the top, turbulent flow simulations had a streamwise pressure gradient which contributed to the overall pressure drag. For low mountain heights this contribution was severe, resulting in high drag values unrelated with the wave drag. Under such conditions it is difficult to determine what is the proper value of the wave drag. A naive approach would use a similar simulation, but with a flat terrain, to compute a streamwise pressure gradient. This approach, however, would neglect that the mountain itself interacts with the flow such that the wall shear stress would differ, even in a neutral case without buoyancy effects. The wall shear stress will vary according to the effect of the mountain on the flow and, additionally, due to streamwise boundary-layer growth. Regarding this topic, further work is required to understand how much is the contribution of the pressure gradient to the pressure drag, in order to solely estimate the wave drag.

2. Develop analytical expressions for the inlet profiles of turbulent kinetic energy and dissipation, k and ϵ, under convective and stably-stratified situations. Besides the analytical work involved, this requires experimental results, either from laboratory or field measurements. The difficulty lies in establishing the vertical profiles for quantities that are not directly measurable, such as ϵ and μ_t.

3. Conduct several parametric studies to optimize the parameters of the mesoscale-microscale coupling. Firstly, the configuration of the Rayleigh damping layer, namely its size, coefficients and variable fields to which these should be applied. Secondly, investigate the behaviour of the mesoscale-microscale coupling for different resolutions, regarding both the regional and local model. Such would include an assessment on how the regional model would perform at resolutions below 1 km. Lastly, check for the impact on the speed and performance that could be obtained by an increase of the nesting resolution ratio and the decrease of the nesting levels.

4. Development of modifications to the turbulence model to improve its performance under moderate and very stable regimes. The $k-\epsilon$ model always assumes that the flow is turbulent. Under the neutral and convective boundary-layer this assumption is largely met, however, in stably stratified flow turbulence is dampened. For very stable regimes the Richardson number is above its critical value and flow laminarization may occur, as turbulence becomes characterized by intermittency. Insight might be gained from the modifications which are commonly employed in two-equation turbulence models for operation under low Reynolds numbers (Patel *et al.*, 1985).

Appendices

Appendix A

Pressure correction equation for non-orthogonal collocated grids

A.1 Discretized equations for the conservation of momentum

The equations for the conservation of momentum (2.58), integrated over a CV (control volume) using the finite volume method (following §2.4.3) become:

$$A_P^u\, u_P + \sum_F A_F^u\, u_F = -\beta_{x,e}^1\, p_e + \beta_{x,w}^1\, p_w - \beta_{x,n}^2\, p_n + \beta_{x,s}^2\, p_s - \beta_{x,t}^3\, p_t + \beta_{x,b}^3\, p_b + S^u \;,$$

$$A_P^v\, v_P + \sum_F A_F^v\, v_F = -\beta_{y,e}^1\, p_e + \beta_{y,w}^1\, p_w - \beta_{y,n}^2\, p_n + \beta_{y,s}^2\, p_s - \beta_{y,t}^3\, p_t + \beta_{y,b}^3\, p_b + S^v \;,$$

$$A_P^w\, w_P + \sum_F A_F^w\, w_F = -\beta_{z,e}^1\, p_e + \beta_{z,w}^1\, p_w - \beta_{z,n}^2\, p_n + \beta_{z,s}^2\, p_s - \beta_{z,t}^3\, p_t + \beta_{z,b}^3\, p_b + S^w \;.$$

The index P is used to represent the CV and refers to its centre, while the index F is used to represent the control volumes neighbouring P, *i.e.*, $F = W, E, S, N, B, T$. Additionally, the index f will be employed to represent the centre of a face connecting P to a neighbour CV: $f = w, e, s, n, b, t$. The non-orthogonal grid and its metrics are described in §2.4.1.

To represent these equations in a compact form, the following symbols will be used:

$$\oplus = \begin{cases} +1\,, & \text{if} \quad f = e, n, t \\ -1\,, & \text{if} \quad f = w, s, b \end{cases} \;, \tag{A.1}$$

$$\triangle = \begin{cases} 1 \equiv \xi\,, & \text{if} \quad f = e, w \\ 2 \equiv \eta\,, & \text{if} \quad f = n, s \\ 3 \equiv \zeta\,, & \text{if} \quad f = t, b \end{cases} \;. \tag{A.2}$$

The discretized equations can thus be written as:

$$A_P^i\, u_{i,P} + \sum_F A_F^i\, u_{i,F} = -\sum_f \oplus\, \beta_{i,f}^{\triangle}\, p_f + S^i \;, \tag{A.3}$$

A.1.1 Guessed and correction velocity and pressure fields

When solving the system of equations in (A.3), the pressure field at the faces will be an approximation obtained by an arbitrary interpolation method, instead of the true pressure field. To distinguish between these, p will be used to represent the correct pressure field, p^* the guessed field and p^c the correction to be applied such that:

$$p = p^* + p^c \,, \tag{A.4}$$

Similarly the velocity field will also have a true, guessed and a correction, both at the nodes as at the faces of each control volume:

$$u_i = u_i^* + u_i^c \,, \tag{A.5}$$

In the beginning of an iteration, p is unknown at the faces. By using p^* instead of p, when solving the discretized system in (A.3), what is being computed is u_i^* instead of u_i:

$$A_P^i \, u_{i,P}^* + \sum_F A_F^i \, u_{i,F}^* = -\sum_f \oplus \beta_{i,f}^{\triangle} \, p_f^* + S^i \,, \tag{A.6}$$

By subtracting (A.6) from (A.3), one obtains:

$$\begin{aligned} & A_P^i \, \left[u_{i,P} - u_{i,P}^*\right] + \sum_F A_F^i \, \left[u_{i,F} - u_{i,F}^*\right] = -\sum_f \oplus \beta_{i,f}^{\triangle} \, \left[p_f - p_f^*\right] \quad \Leftrightarrow \\ \Leftrightarrow \quad & A_P^i \, u_{i,P}^c + \sum_F A_F^i \, u_{i,F}^c = -\sum_f \oplus \beta_{i,f}^{\triangle} \, p_f^c \,, \end{aligned} \tag{A.7}$$

It is important to notice that in this equation, any source or sink term gathered in S^i vanishes. In the SIMPLE algorithm (semi-implicit method for pressure-linked equations, Patankar, 1980) the following approximation is used:

$$\sum_F A_F^i \, u_{i,F}^c \approx 0 \,, \tag{A.8}$$

allowing to explicit the correction variables:

$$A_P^i \, u_{i,P}^c = -\sum_f \oplus \beta_{i,f}^{\triangle} \, p_f^c \qquad \Rightarrow \quad u_{i,P} = u_{i,P}^* - \sum_f \oplus \frac{\beta_{i,f}^{\triangle}}{A_P^i} \, p_f^c \,. \tag{A.9}$$

It is important to refer that, albeit the pressure correction field will be computed, the correction at a face location p_f^c is interpolated from the pressure correction at the CV centres, p_F^c.

Discretizing the mass conservation equation (2.56) using the finite volume method:

$$\iiint_\Omega \nabla \cdot (\rho \, \vec{u}) \; d\Omega \;=\; \iint_S \rho_S \, \vec{u}_S \cdot \hat{\mathbf{n}} \, dS \;=\; 0 \,, \tag{A.10}$$

$$\begin{aligned} \Rightarrow \quad & \rho_e \left[\, u_e \, \beta_{x,e}^1 + v_e \, \beta_{y,e}^1 + w_e \, \beta_{z,e}^1 \, \right] - \rho_w \left[u_w \, \beta_{x,w}^1 + v_w \, \beta_{y,w}^1 + w_w \, \beta_{z,w}^1 \right] \ldots \\ \ldots & + \rho_n \left[u_n \, \beta_{x,n}^2 + v_n \, \beta_{y,n}^2 + w_n \, \beta_{z,n}^2 \right] - \rho_s \left[\, u_s \, \beta_{x,s}^2 + v_s \, \beta_{y,s}^2 + w_s \, \beta_{z,s}^2 \, \right] \ldots \\ \ldots & + \rho_t \left[\, u_t \, \beta_{x,t}^3 + v_t \, \beta_{y,t}^3 + w_t \, \beta_{z,t}^3 \, \right] - \rho_b \left[\, u_b \, \beta_{x,b}^3 + v_b \, \beta_{y,b}^3 + w_b \, \beta_{z,b}^3 \, \right] = 0 \,, \end{aligned} \tag{A.11}$$

or alternatively:

$$\sum_f \oplus \rho_f \left[u_f \, \beta^{\triangle}_{x,f} + v_f \, \beta^{\triangle}_{y,f} + w_f \, \beta^{\triangle}_{z,f} \right] = 0 \, . \tag{A.12}$$

Following Rhie and Chow (1983), instead of using the Cartesian velocity components one can define the contravariant velocities as:

$$G_1 = u \, \beta^1_x + v \, \beta^1_y + w \, \beta^1_z \, , \quad G_2 = \sum_i u_i \, \beta^2_i \, , \quad G_3 = \sum_i u_i \, \beta^3_i \, . \tag{A.13}$$

Note that the dimensions of G_1, G_2 and G_3 are in fact velocity times area, *i.e.*, the area of the surface to which the corresponding line of constant ξ, η or ζ is perpendicular to. Although the contravariant components are usually defined at the CV faces, they may be defined also at the centres:

$$\begin{aligned} G_{1,P} &= G^*_{1,P} - \sum_f \oplus p^c_f \left[\frac{\beta^1_{x,P} \, \beta^{\triangle}_{x,f}}{A^u_P} + \frac{\beta^1_{y,P} \, \beta^{\triangle}_{y,f}}{A^v_P} + \frac{\beta^1_{z,P} \, \beta^{\triangle}_{z,f}}{A^w_P} \right] \ldots \\ \ldots &= G^*_{1,P} - \sum_f \sum_i \oplus \frac{\beta^1_{i,P} \, \beta^{\triangle}_{i,f}}{A^i_P} \, p^c_f \, , \end{aligned} \tag{A.14}$$

or, in a compact form:

$$G_{j,P} = G^*_{j,P} - \sum_f \sum_i \oplus \frac{\beta^j_{i,P} \, \beta^{\triangle}_{i,f}}{A^i_P} \, p^c_f \, . \tag{A.15}$$

A.1.2 Formulation using the volume integral of the pressure gradient

One cannot proceed without deducing eqs. (A.3) and (A.9) with the pressure gradient being expressed as a volume integral instead of a surface integral, as well as the relation between the results obtained from both ways. Exemplifying for the x direction, the surface integral is obtained by applying Green's theorem:

$$\iiint_\Omega \frac{\partial p}{\partial x} \, d\Omega \equiv \iiint_\Omega \nabla \cdot (p \, \hat{\boldsymbol{\imath}}) \, d\Omega = \iint_S p \, \hat{\boldsymbol{\imath}} \cdot \hat{\mathbf{n}} \, dS \approx \sum_f \oplus \beta^{\triangle}_{x,f} \, p_f \, . \tag{A.16}$$

However, if the volume integral is directly discretized:

$$\begin{aligned} \iiint_\Omega \frac{\partial p}{\partial x} \, d\Omega &= \left. \frac{\partial p}{\partial x} \right|_P \Delta\Omega_P \ldots \\ \ldots &= \left[\beta^1_{x,P} \left. \frac{\partial p}{\partial \xi} \right|_P + \beta^2_{x,P} \left. \frac{\partial p}{\partial \eta} \right|_P + \beta^3_{x,P} \left. \frac{\partial p}{\partial \zeta} \right|_P \right] \frac{\Delta\Omega_P}{J_P} \ldots \\ \ldots &= \sum_j \beta^j_{x,P} \left. \frac{\partial p}{\partial \xi^j} \right|_P \, . \end{aligned} \tag{A.17}$$

As both are equivalent, thus:

$$\sum_j \beta^j_{x,P} \left.\frac{\partial p}{\partial \xi^j}\right|_P = \sum_f \oplus \beta^{\triangle}_{x,f}\, p_f \,. \tag{A.18}$$

Generalizing, for the index i related to direction x_i:

$$\sum_j \beta^j_{i,P} \left.\frac{\partial p}{\partial \xi^j}\right|_P = \sum_f \oplus \beta^{\triangle}_{i,f}\, p_f \,. \tag{A.19}$$

Considering the relation given by eq. (A.19), eq. (A.3) can be expressed as:

$$A^i_P\, u_{i,P} + \sum_F A^i_F\, u_{i,F} = S^i - \sum_j \beta^j_{i,P} \left.\frac{\partial p}{\partial \xi^j}\right|_P \,, \tag{A.20}$$

with the correction equation for u_i, eq. (A.9), changing accordingly:

$$A^i_P\, u^c_{i,P} = -\sum_j \beta^j_{i,P} \left.\frac{\partial p^c}{\partial \xi^j}\right|_P \quad \Rightarrow \quad u_{i,P} = u^*_{i,P} - \sum_j \frac{\beta^j_{i,P}}{A^i_P} \left.\frac{\partial p^c}{\partial \xi^j}\right|_P \,. \tag{A.21}$$

A.2 Pressure correction equation

The objective now is to substitute the correct velocities u_i by the guessed fields u^*_i into the mass conservation eq. (A.12). However in eq. (A.9) the u^*_i are defined at the centres of the CV instead of the faces. By using equation (A.21) instead of (A.9), this task becomes simpler. Exemplifying for the east face:

$$u_e = u^*_e - \frac{\beta^1_{x,e}}{A^u_{P/e}} \left.\frac{\partial p^c}{\partial \xi}\right|_e - \frac{\beta^2_{x,e}}{A^u_{P/e}} \left.\frac{\partial p^c}{\partial \eta}\right|_e - \frac{\beta^3_{x,e}}{A^u_{P/e}} \left.\frac{\partial p^c}{\partial \zeta}\right|_e \,, \tag{A.22}$$

where $A^u_{P/e}$ is the A^u_P coefficient for a control volume with location e as its centre. Although the derivative in ξ can be computed directly, the others will always require an interpolating technique. For the sake of simplicity, an interpolation will be represented by the symbol $\overset{\text{loc}\leftarrow}{\{\ldots\}}$, such that:

$$\phi_e = \overset{e\leftarrow}{\{\phi_P\,,\, \phi_E\}} \,, \tag{A.23}$$

where ϕ_e the quantity ϕ at location e, obtained through interpolation from the values of ϕ at locations P and E.

Rewriting equation (A.21) in face e:

$$u_e = u^*_e - \frac{\beta^1_{x,e}}{A^u_{P/e}} \left.\frac{\partial p^c}{\partial \xi}\right|_e - \frac{\beta^2_{x,e}}{A^u_{P/e}} \overset{e\leftarrow}{\left\{ \left.\frac{\partial p^c}{\partial \eta}\right|_P , \left.\frac{\partial p^c}{\partial \eta}\right|_E \right\}} - \frac{\beta^3_{x,e}}{A^u_{P/e}} \overset{e\leftarrow}{\left\{ \left.\frac{\partial p^c}{\partial \zeta}\right|_P , \left.\frac{\partial p^c}{\partial \zeta}\right|_E \right\}} \,, \tag{A.24}$$

with,

$$\frac{1}{A^u_{P/e}} = \overset{e\leftarrow}{\left\{ \frac{1}{A^u_{P/P}}, \frac{1}{A^u_{P/E}} \right\}}, \quad \frac{1}{A^u_{P/w}} = \overset{w\leftarrow}{\left\{ \frac{1}{A^u_{P/W}}, \frac{1}{A^u_{P/P}} \right\}} \,. \tag{A.25}$$

Conversely for the north face, u_n becomes:

$$u_n = u_n^* - \frac{\beta^1_{x,n}}{A^u_{P/n}} \overleftarrow{\left\{ \left.\frac{\partial\, p^c}{\partial\, \xi}\right|_P , \left.\frac{\partial\, p^c}{\partial\, \xi}\right|_N \right\}}^{n} - \frac{\beta^2_{x,n}}{A^u_{P/n}} \left.\frac{\partial\, p^c}{\partial\, \eta}\right|_n - \frac{\beta^3_{x,n}}{A^u_{P/n}} \overleftarrow{\left\{ \left.\frac{\partial\, p^c}{\partial\, \zeta}\right|_P , \left.\frac{\partial\, p^c}{\partial\, \zeta}\right|_N \right\}}^{n}, \tag{A.26}$$

and for the top face:

$$u_t = u_t^* - \frac{\beta^1_{x,t}}{A^u_{P/t}} \overleftarrow{\left\{ \left.\frac{\partial\, p^c}{\partial\, \xi}\right|_P , \left.\frac{\partial\, p^c}{\partial\, \xi}\right|_T \right\}}^{t} - \frac{\beta^2_{x,t}}{A^u_{P/t}} \overleftarrow{\left\{ \left.\frac{\partial\, p^c}{\partial\, \eta}\right|_P , \left.\frac{\partial\, p^c}{\partial\, \eta}\right|_T \right\}}^{t} - \frac{\beta^3_{x,t}}{A^u_{P/t}} \left.\frac{\partial\, p^c}{\partial\, \zeta}\right|_t . \tag{A.27}$$

Substituting the face velocities $u_{i,f}$ for $u^*_{i,f}$ in the mass conservation eq. (A.12):

$$\begin{aligned}
&\rho_e \left[u^*_e\, \beta^1_{x,e} + v^*_e\, \beta^1_{y,e} + w^*_e\, \beta^1_{z,e} \right] - \rho_w \left[u^*_w\, \beta^1_{x,w} + v^*_w\, \beta^1_{y,w} + w^*_w\, \beta^1_{z,w} \right] \ldots \\
&\ldots + \rho_n \left[u^*_n\, \beta^2_{x,n} + v^*_n\, \beta^2_{y,n} + w^*_n\, \beta^2_{z,n} \right] - \rho_s \left[u^*_s\, \beta^2_{x,s} + v^*_s\, \beta^2_{y,s} + w^*_s\, \beta^2_{z,s} \right] \ldots \\
&\ldots + \rho_t \left[u^*_t\, \beta^3_{x,t} + v^*_t\, \beta^3_{y,t} + w^*_t\, \beta^3_{z,t} \right] - \rho_b \left[u^*_b\, \beta^3_{x,b} + v^*_b\, \beta^3_{y,b} + w^*_b\, \beta^3_{z,b} \right] \ldots \\
&\ldots - \rho_e \left[\frac{\beta^1_{x,e}\, \beta^1_{x,e}}{A^u_{P/e}} + \frac{\beta^1_{y,e}\, \beta^1_{y,e}}{A^v_{P/e}} + \frac{\beta^1_{z,e}\, \beta^1_{z,e}}{A^w_{P/e}} \right] \left.\frac{\partial\, p^c}{\partial\, \xi}\right|_e \ldots \\
&\ldots - \rho_w \left[\frac{\beta^1_{x,w}\, \beta^1_{x,w}}{A^u_{P/w}} + \frac{\beta^1_{y,w}\, \beta^1_{y,w}}{A^v_{P/w}} + \frac{\beta^1_{z,w}\, \beta^1_{z,w}}{A^w_{P/w}} \right] \left.\frac{\partial\, p^c}{\partial\, \xi}\right|_w \ldots \\
&\ldots - \rho_n \left[\frac{\beta^2_{x,n}\, \beta^2_{x,n}}{A^u_{P/n}} + \frac{\beta^2_{y,n}\, \beta^2_{y,n}}{A^v_{P/n}} + \frac{\beta^2_{z,n}\, \beta^2_{z,n}}{A^w_{P/n}} \right] \left.\frac{\partial\, p^c}{\partial\, \eta}\right|_n \ldots \\
&\ldots - \rho_s \left[\frac{\beta^2_{x,s}\, \beta^2_{x,s}}{A^u_{P/s}} + \frac{\beta^2_{y,s}\, \beta^2_{y,s}}{A^v_{P/s}} + \frac{\beta^2_{z,s}\, \beta^2_{z,s}}{A^w_{P/s}} \right] \left.\frac{\partial\, p^c}{\partial\, \eta}\right|_s \ldots \\
&\ldots - \rho_t \left[\frac{\beta^3_{x,t}\, \beta^3_{x,t}}{A^u_{P/t}} + \frac{\beta^3_{y,t}\, \beta^3_{y,t}}{A^v_{P/t}} + \frac{\beta^3_{z,t}\, \beta^3_{z,t}}{A^w_{P/t}} \right] \left.\frac{\partial\, p^c}{\partial\, \zeta}\right|_t \ldots \\
&\ldots - \rho_b \left[\frac{\beta^3_{x,b}\, \beta^3_{x,b}}{A^u_{P/b}} + \frac{\beta^3_{y,b}\, \beta^3_{y,b}}{A^v_{P/b}} + \frac{\beta^3_{z,b}\, \beta^3_{z,b}}{A^w_{P/b}} \right] \left.\frac{\partial\, p^c}{\partial\, \zeta}\right|_b \ldots \\
&\ldots - \rho_e \left[\frac{\beta^1_{x,e}\, \beta^2_{x,e}}{A^u_{P/e}} + \frac{\beta^1_{y,e}\, \beta^2_{y,e}}{A^v_{P/e}} + \frac{\beta^1_{z,e}\, \beta^2_{z,e}}{A^w_{P/e}} \right] \overleftarrow{\left\{ \left.\frac{\partial\, p^c}{\partial\, \eta}\right|_P , \left.\frac{\partial\, p^c}{\partial\, \eta}\right|_E \right\}}^{e} \quad \ldots \\
&\ldots - \rho_e \left[\frac{\beta^1_{x,e}\, \beta^3_{x,e}}{A^u_{P/e}} + \frac{\beta^1_{y,e}\, \beta^3_{y,e}}{A^v_{P/e}} + \frac{\beta^1_{z,e}\, \beta^3_{z,e}}{A^w_{P/e}} \right] \overleftarrow{\left\{ \left.\frac{\partial\, p^c}{\partial\, \zeta}\right|_P , \left.\frac{\partial\, p^c}{\partial\, \zeta}\right|_E \right\}}^{e} \quad \ldots \\
&\ldots - \rho_w \left[\frac{\beta^1_{x,w}\, \beta^2_{x,w}}{A^u_{P/w}} + \frac{\beta^1_{y,w}\, \beta^2_{y,w}}{A^v_{P/w}} + \frac{\beta^1_{z,w}\, \beta^2_{z,w}}{A^w_{P/w}} \right] \overleftarrow{\left\{ \left.\frac{\partial\, p^c}{\partial\, \eta}\right|_W , \left.\frac{\partial\, p^c}{\partial\, \eta}\right|_P \right\}}^{w} \quad \ldots \\
&\ldots - \rho_w \left[\frac{\beta^1_{x,w}\, \beta^3_{x,w}}{A^u_{P/w}} + \frac{\beta^1_{y,w}\, \beta^3_{y,w}}{A^v_{P/w}} + \frac{\beta^1_{z,w}\, \beta^3_{z,w}}{A^w_{P/w}} \right] \overleftarrow{\left\{ \left.\frac{\partial\, p^c}{\partial\, \zeta}\right|_W , \left.\frac{\partial\, p^c}{\partial\, \zeta}\right|_P \right\}}^{w} \quad \ldots \\
&\ldots - \rho_n \left[\frac{\beta^2_{x,n}\, \beta^1_{x,n}}{A^u_{P/n}} + \frac{\beta^2_{y,n}\, \beta^1_{y,n}}{A^v_{P/n}} + \frac{\beta^2_{z,n}\, \beta^1_{z,n}}{A^w_{P/n}} \right] \overleftarrow{\left\{ \left.\frac{\partial\, p^c}{\partial\, \xi}\right|_P , \left.\frac{\partial\, p^c}{\partial\, \xi}\right|_N \right\}}^{n} \quad \ldots \\
&\ldots - \rho_n \left[\frac{\beta^2_{x,n}\, \beta^3_{x,n}}{A^u_{P/n}} + \frac{\beta^2_{y,n}\, \beta^3_{y,n}}{A^v_{P/n}} + \frac{\beta^2_{z,n}\, \beta^3_{z,n}}{A^w_{P/n}} \right] \overleftarrow{\left\{ \left.\frac{\partial\, p^c}{\partial\, \zeta}\right|_P , \left.\frac{\partial\, p^c}{\partial\, \zeta}\right|_N \right\}}^{n} \quad \ldots
\end{aligned}$$

$$
\begin{aligned}
\ldots - \rho_s \left[\frac{\beta^2_{x,s}\,\beta^1_{x,s}}{A^u_{P/s}} + \frac{\beta^2_{y,s}\,\beta^1_{y,s}}{A^v_{P/s}} + \frac{\beta^2_{z,s}\,\beta^1_{z,s}}{A^w_{P/s}} \right]^{s\leftarrow} \left\{ \left.\frac{\partial\, p^c}{\partial\, \xi}\right|_S , \left.\frac{\partial\, p^c}{\partial\, \xi}\right|_P \right\} \quad \ldots \\
\ldots - \rho_s \left[\frac{\beta^2_{x,s}\,\beta^3_{x,s}}{A^u_{P/s}} + \frac{\beta^2_{y,s}\,\beta^3_{y,s}}{A^v_{P/s}} + \frac{\beta^2_{z,s}\,\beta^3_{z,s}}{A^w_{P/s}} \right]^{s\leftarrow} \left\{ \left.\frac{\partial\, p^c}{\partial\, \zeta}\right|_S , \left.\frac{\partial\, p^c}{\partial\, \zeta}\right|_P \right\} \quad \ldots \\
\ldots - \rho_t \left[\frac{\beta^3_{x,t}\,\beta^1_{x,t}}{A^u_{P/t}} + \frac{\beta^3_{y,t}\,\beta^1_{y,t}}{A^v_{P/t}} + \frac{\beta^3_{z,t}\,\beta^1_{z,t}}{A^w_{P/t}} \right]^{t\leftarrow} \left\{ \left.\frac{\partial\, p^c}{\partial\, \xi}\right|_P , \left.\frac{\partial\, p^c}{\partial\, \xi}\right|_T \right\} \quad \ldots \\
\ldots - \rho_t \left[\frac{\beta^3_{x,t}\,\beta^2_{x,t}}{A^u_{P/t}} + \frac{\beta^3_{y,t}\,\beta^2_{y,t}}{A^v_{P/t}} + \frac{\beta^3_{z,t}\,\beta^2_{z,t}}{A^w_{P/t}} \right]^{t\leftarrow} \left\{ \left.\frac{\partial\, p^c}{\partial\, \eta}\right|_P , \left.\frac{\partial\, p^c}{\partial\, \eta}\right|_T \right\} \quad \ldots \\
\ldots - \rho_b \left[\frac{\beta^3_{x,b}\,\beta^1_{x,b}}{A^u_{P/b}} + \frac{\beta^3_{y,b}\,\beta^1_{y,b}}{A^v_{P/b}} + \frac{\beta^3_{z,b}\,\beta^1_{z,b}}{A^w_{P/b}} \right]^{b\leftarrow} \left\{ \left.\frac{\partial\, p^c}{\partial\, \xi}\right|_B , \left.\frac{\partial\, p^c}{\partial\, \xi}\right|_P \right\} \quad \ldots \\
\ldots - \rho_b \left[\frac{\beta^3_{x,b}\,\beta^2_{x,b}}{A^u_{P/b}} + \frac{\beta^3_{y,b}\,\beta^2_{y,b}}{A^v_{P/b}} + \frac{\beta^3_{z,b}\,\beta^2_{z,b}}{A^w_{P/b}} \right]^{b\leftarrow} \left\{ \left.\frac{\partial\, p^c}{\partial\, \eta}\right|_B , \left.\frac{\partial\, p^c}{\partial\, \eta}\right|_P \right\} \quad = \quad 0 \,.
\end{aligned}
\tag{A.28}
$$

This equation can be decomposed in three parts:

1. the net mass flux obtained from the guesse velocity field,

$$
\sum_f \dot{m}^*_f = \sum_f \sum_i \rho_f \, u^*_{i,f} \, \beta^{\triangle}_{i,f} \,, \tag{A.29}
$$

2. the p^c derivatives tangent to the coordinate lines (normal to the faces),

$$
\sum_f \sum_i \rho_f \, \frac{\beta^{\triangle}_{i,f}\,\beta^{\triangle}_{i,f}}{A^i_{P/f}} \left.\frac{\partial\, p^c}{\partial\, \xi^{\triangle}}\right|_f \,, \tag{A.30}
$$

3. the remainder pressure correction cross-derivatives.

These last cross derivatives make eq. (A.28) difficult to solve, as it would require a matrix with 9 diagonals for a 2D grid and 19 diagonals for a 3D grid (P, W, E, S, N, B, T, SW, NW, SE, NE, BW, TW, BE, TE, BS, TS, BN, TN). However for most problems the importance of these terms is much less than the derivatives tangent to coordinate lines, provided that the non-orthogonality of the grid is not too severe. Perić (1990) showed that the inclusion of the cross derivatives is only necessary when the angles formed by each of the coordinates lines, ξ, η and ζ, is between 45° and 135°. Neglecting the cross derivatives, eq. (A.28) becomes:

$$
\sum_f \sum_i \rho_f \, \frac{\beta^{\triangle}_{i,f}\,\beta^{\triangle}_{i,f}}{A^i_{P/f}} \left.\frac{\partial\, p^c}{\partial\, \xi^{\triangle}}\right|_f = \sum_f \dot{m}^*_f \,,
$$

expanding the derivatives:

$$
\left.\frac{\partial\, p^c}{\partial\, \xi}\right|_e = p^c_E - p^c_P \,, \quad \left.\frac{\partial\, p^c}{\partial\, \eta}\right|_n = p^c_N - p^c_P \,, \quad \left.\frac{\partial\, p^c}{\partial\, \zeta}\right|_t = p^c_T - p^c_P \,,
$$

$$
\begin{aligned}
\Rightarrow \quad & \rho_e \left[\frac{\beta^1_{x,e}\,\beta^1_{x,e}}{A^u_{P/e}} + \frac{\beta^1_{y,e}\,\beta^1_{y,e}}{A^v_{P/e}} + \frac{\beta^1_{z,e}\,\beta^1_{z,e}}{A^w_{P/e}} \right] [p^c_E - p^c_P] \ldots \\
\ldots & + \rho_w \left[\frac{\beta^1_{x,w}\,\beta^1_{x,w}}{A^u_{P/w}} + \frac{\beta^1_{y,w}\,\beta^1_{y,w}}{A^v_{P/w}} + \frac{\beta^1_{z,w}\,\beta^1_{z,w}}{A^w_{P/w}} \right] [p^c_P - p^c_W] \ldots \\
\ldots & + \rho_n \left[\frac{\beta^2_{x,n}\,\beta^2_{x,n}}{A^u_{P/n}} + \frac{\beta^2_{y,n}\,\beta^2_{y,n}}{A^v_{P/n}} + \frac{\beta^2_{z,n}\,\beta^2_{z,n}}{A^w_{P/n}} \right] [p^c_N - p^c_P] \ldots \\
\ldots & + \rho_s \left[\frac{\beta^2_{x,s}\,\beta^2_{x,s}}{A^u_{P/s}} + \frac{\beta^2_{y,s}\,\beta^2_{y,s}}{A^v_{P/s}} + \frac{\beta^2_{z,s}\,\beta^2_{z,s}}{A^w_{P/s}} \right] [p^c_P - p^c_S] \ldots \\
\ldots & + \rho_t \left[\frac{\beta^3_{x,t}\,\beta^3_{x,t}}{A^u_{P/t}} + \frac{\beta^3_{y,t}\,\beta^3_{y,t}}{A^v_{P/t}} + \frac{\beta^3_{z,t}\,\beta^3_{z,t}}{A^w_{P/t}} \right] [p^c_T - p^c_P] \ldots \\
\ldots & + \rho_b \left[\frac{\beta^3_{x,b}\,\beta^3_{x,b}}{A^u_{P/b}} + \frac{\beta^3_{y,b}\,\beta^3_{y,b}}{A^v_{P/b}} + \frac{\beta^3_{z,b}\,\beta^3_{z,b}}{A^w_{P/b}} \right] [p^c_P - p^c_B] = \textstyle\sum_f \dot{m}^*_f \,,
\end{aligned}
\tag{A.31}
$$

which results in the septa-diagonal linear system:

$$
A^p_P\, p^c_P + A^p_W\, p^c_W + A^p_E\, p^c_E + A^p_S\, p^c_S + A^p_N\, p^c_N + A^p_B\, p^c_B + A^p_T\, p^c_T = S^p \,, \tag{A.32}
$$

with a dominant centre term because: $A^p_P = -A^p_W - A^p_E - A^p_S - A^p_N - A^p_B - A^p_T$.

For consistency, if the cross derivatives are neglected, the same happens for the correction of the face velocities in eq. (A.22), thus:

$$
u_{i,f} \;=\; u^*_{i,f} - \frac{\beta^{\triangle}_{i,f}}{A^i_{P/f}} \left. \frac{\partial\, p^c}{\partial\, \xi^i} \right|_f \,. \tag{A.33}
$$

This also serves to set the boundary conditions for the system of equations (A.32). As the mass flux at the boundaries is known, the cell face velocity correction is null and the derivative $\partial p^c / \partial \xi^i$ normal to the boundary is zero. Thus, a zero gradient boundary condition is used to solve eq. (A.32).

A.2.1 Algorithm to solve both pressure and velocity fields

At the start of the iterative process, an initial condition is provided for the velocity and pressure fields. From the discretized momentum conservation equations (eq. (A.6)), the guessed fields for each velocity component, $u^*_{i,P}$, are obtained at the CV centres. From these, the guessed velocities at each CV face, $u^*_{i,f}$, are estimated by interpolation from the CV centres. The coefficients $\left(\beta^j_{i,f} \Big/ A^i_{P/f}\right)$ are estimated, also by interpolation. The pressure correction equation (A.28) is solved and the pressure correction field, p^c, is used to correct both pressure and velocity components at the CV centres and faces, applying eqs. (A.4), (A.9) and (A.33).

After solving for other equations, passive or active scalars, turbulence model or any other parameterizations, if the convergence criteria for the solution are not met, a new iteration starts using the computed fields as new guesses. This iterative process is represented in the flowchart at Figure A.1.

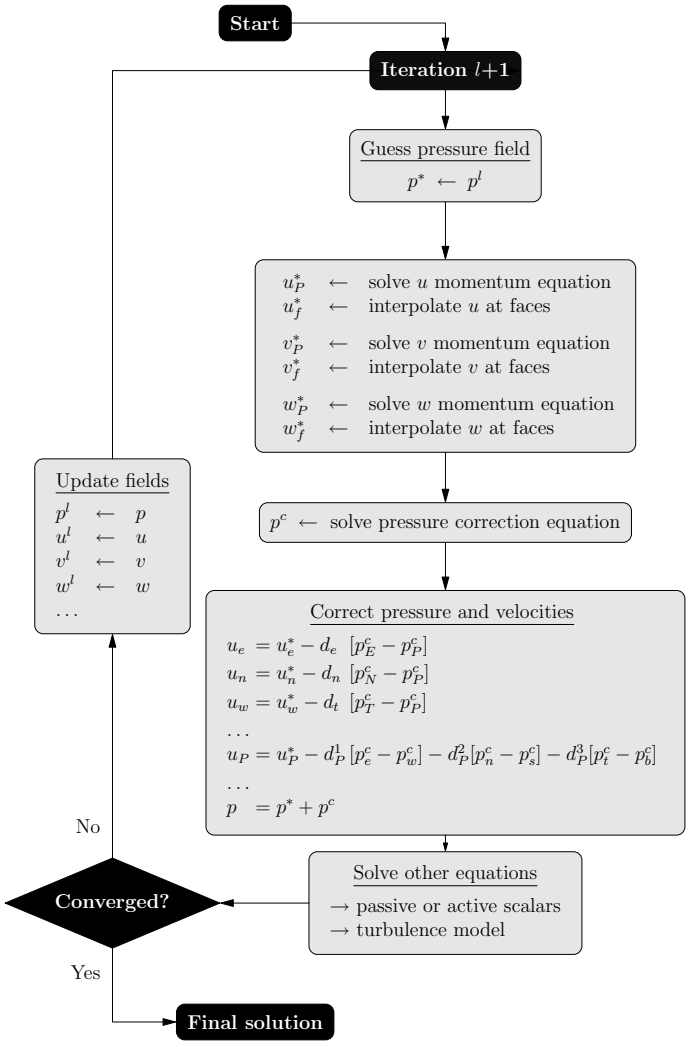

Figure A.1: Flowchart of the SIMPLE algorithm.

A.2.2 Extension to include under-relaxation

It is common to relax the velocity field, such that the solution of the momentum equations is only allowed to change by a fraction α. This leads to the following expression:

$$u_{i,P}^* = \alpha\, \widetilde{u}_{i,P}^* + [1-\alpha]\, u_{i,P}^l \,, \tag{A.34}$$

where l is an iteration index, α is the under-relaxation factor, u_i^l is the velocity field at the previous iteration, $\widetilde{u}_i^*$ is the guessed velocity field at the current iteration and u_i^* is the guessed velocity field for the pressure correction equation, but under-relaxed by α. Thus, without under-relaxation, eq. (A.6) is:

$$A_P^i\, \widetilde{u}_{i,P}^* + \sum_F A_F^i\, \widetilde{u}_{i,F}^* = -\sum_f \oplus \beta_{i,f}^{\triangle}\, p_f^* + S^i \,.$$

Dividing by A_P^i and substituting for $\widetilde{u}_{i,P}^*$ in eq. (A.34) leads to:

$$u_{i,P}^* = \frac{\alpha}{A_P^i}\left[-\sum_F A_F^i\,\widetilde{u}_{i,F}^* - \sum_f \oplus\, \beta_{i,f}^{\triangle}\, p_f^* + S^i\right] + [1-\alpha]\, u_{i,P}^l \,,$$

$$\Rightarrow \quad \frac{A_P^i}{\alpha}\, u_{i,P}^* + \sum_F A_F^i\,\widetilde{u}_{i,F}^* = -\sum_f \oplus\, \beta_{i,f}^{\triangle}\, p_f^* + S^i + \frac{A_P^i}{\alpha}[1-\alpha] u_{i,P}^l \,. \tag{A.35}$$

For the sake of simplicity, the velocities at the neighbouring nodes $\widetilde{u}_{i,F}^*$ are written as $u_{i,F}^*$ instead. The central diagonal term of the new linear system to be solved becomes:

$${}^{\alpha}A_P^i = \frac{A_P^i}{\alpha} \,.$$

A.2.3 Extension for unsteady flows

For unsteady flows, the conservation equations are integrated in time which results in additional transient terms. Approximating the time derivative in the conservation equations using a three time-level implicit scheme (3FTI scheme in Fletcher (1991)):

$$\frac{\partial}{\partial t}\left(\iiint_\Omega \rho\, u_i\, d\Omega\right) \;\approx\; \left[\frac{3}{2}\, u_{i,P}^{n+1} - 2\, u_{i,P}^n + \frac{1}{2}\, u_{i,P}^{n-1}\right] \frac{\rho_P\, \Delta\Omega_P}{\Delta t} \,, \tag{A.36}$$

with index n referring to the time vector discretized with evenly spaced Δt intervals. The field of u_i at time t^{n+1} is computed from the values at the two previous time-steps. Other terms in the conservation equation, *i.e.*, advection, diffusion, pressure gradient, buoyancy and other body forces, are evaluated at time t^{n+1}.

At the beginning of an time iteration neither the velocity and pressure fields are known for time-step t^{n+1}. Following the SIMPLE algorithm, the velocity and pressure at the current time-step are guessed as in §A.1.1, thus:

$$u_i^{n+1} \equiv u_i^* \,, \qquad p^{n+1} \equiv p^* \,.$$

Thus the linear system in eq. (A.6) becomes:

$$\left[A_P^i + \frac{3}{2}\frac{\rho_P\, \Delta\Omega_P}{\Delta t}\right] u_{i,P}^* + \sum_F A_F^i\,\widetilde{u}_{i,F}^* = \;\ldots$$

$$\ldots\; - \sum_f \oplus\, \beta_{i,f}^{\triangle}\, p_f^* + S^i + \frac{\rho_P\, \Delta\Omega_P}{\Delta t}\left[2\, u_{i,P}^n - \frac{1}{2}\, u_{i,P}^{n-1}\right] \,, \tag{A.37}$$

where the central diagonal of the new linear system to be solved is:

$$\widetilde{A}_P^i = A_P^i + \frac{3}{2}\frac{\rho_P\, \Delta\Omega_P}{\Delta t} \,. \tag{A.38}$$

A.2.4 Extension for unsteady flows with under-relaxation

Under-relaxation can be interpreted as an unsteady simulation where the time-step is dependent on the mass and A_P coefficient of the CV at location P,

$$\Delta t \equiv \frac{\alpha}{[1-\alpha]} \frac{\rho_P \, \Delta\Omega_P}{A_P} \, .$$

If the objective of a simulation is to obtain a steady state solution, using either under-relaxation or an unsteady formulation may be equivalent. However for a simulations where the objective is to characterize the time evolution, rather than an asymptotic steady state, the pressure-velocity coupling algorithm may introduce constrains on the time-step that go beyond the Courant-Friedrichs-Lewy condition. In these situations it may be necessary to under-relax the time dependent velocity field.

Starting with the unsteady system in eq. (A.37), the guessed fields correspond to the latest time-step without relaxation:

$$u_i^{n+1} \equiv \widetilde{u}_i^* \, , \qquad p^{n+1} \equiv p^* \, .$$

The under-relaxed field is thus given by:

$$u_{i,P}^* = \alpha \, \widetilde{u}_{i,P}^* + [1-\alpha] \, u_{i,P}^l \, ,$$

which is the same as eq. (A.34), but now the l index refers to the u_i field of the previous iteration, while solving for time t^{n+1}. For the time integration scheme in eq. (A.36), the central diagonal coefficient of the linear system becomes the same as in eq. (A.38). Following the reasoning that lead to eq. (A.35), the new linear system becomes:

$$\begin{aligned} &\frac{\widetilde{A}_P^i}{\alpha} \, u_{i,P}^* + \sum_F A_F^i \, \widetilde{u}_{i,F}^* = \; \ldots \\ &\ldots \; - \sum_f \oplus \beta_{i,f}^{\triangle} \, p_f^* + S^i + \frac{\widetilde{A}_P^i}{\alpha} [1-\alpha] u_{i,P}^l + \frac{\rho_P \, \Delta\Omega_P}{\Delta t} \left[2 \, u_{i,P}^n - \frac{1}{2} \, u_{i,P}^{n-1} \right] \, . \end{aligned} \tag{A.39}$$

A.3 PWIM: Pressure weighted interpolation method

To compute the pressure correction through eq. (A.31), a velocity field at the CV faces must be guessed. A naive approach would simply use an interpolation method such as linear interpolation to get $u_{i,f}^*$. Exemplifying for the east face:

$$u_{i,e}^* = \overset{e\leftarrow}{\left\{ u_{i,P}^* \, , \; u_{i,E}^* \right\}} \, . \tag{A.40}$$

For the north and top faces, the values at the respective centres, $u_{i,N}^*$ and $u_{i,T}^*$, would be used instead of $u_{i,E}^*$. The west, south and bottom faces can be viewed as the east, north and top faces of the adjacent CV with centre values $u_{i,P/W}^*$, $u_{i,P/N}^*$, $u_{i,P/T}^*$, respectively.

In order to reduce pressure oscillations due to the checkerboard problem, Rhie and Chow (1983) use a different formulation that improves the interpolation by removing

the interpolated pressure gradient and substituting it by the correct pressure gradient at the respective face. Expliciting $u_{i,P}$ from eq. (A.20):

$$u^*_{i,P} = \frac{-\sum_F A^i_F\, u^*_{i,F} + S^i_P}{A^i_P} - \sum_j \frac{\beta^j_{i,P}}{A^i_P} \left.\frac{\partial\, p^*}{\partial\, \xi^j}\right|_P . \tag{A.41}$$

Taking the east face as example, computing $u_{i,e}$ by linear interpolation alone would be equivalent to:

$$\begin{aligned} \overleftarrow{\{u^*_{i,e}\}}^{e} &= \overleftarrow{\{u^*_{i,P},\, u^*_{i,E}\}}^{e} \ \dots \\ \dots &= \overleftarrow{\left\{\frac{-\sum_{F/P} A^i_{F/P}\, u_{i,F/P} + S^i_{P/P}}{A^i_{P/P}},\, \frac{-\sum_{F/E} A^i_{F/E}\, u_{i,F/E} + S^i_{P/E}}{A^i_{P/E}}\right\}}^{e} \ \dots \\ \dots &- \overleftarrow{\sum_j \left\{\frac{\beta^j_{i,P}}{A^i_{P/P}} \left.\frac{\partial\, p^*}{\partial\, \xi^j}\right|_P,\, \frac{\beta^j_{i,E}}{A^i_{P/E}} \left.\frac{\partial\, p^*}{\partial\, \xi^j}\right|_E\right\}}^{e} . \end{aligned} \tag{A.42}$$

The proposed method to estimate $u_{i,e}$, evaluating the pressure gradient with the values at P and E is:

$$u^*_{i,e} = \overleftarrow{\{u^*_{i,e}\}}^{e} + \overleftarrow{\left\{\frac{\beta^1_{i,P}}{A^i_{P/P}} \left.\frac{\partial\, p^*}{\partial\, \xi}\right|_P,\, \frac{\beta^1_{i,E}}{A^i_{P/E}} \left.\frac{\partial\, p^*}{\partial\, \xi}\right|_E\right\}}^{e} - \overleftarrow{\left\{\frac{\beta^1_{i,P}}{A^i_{P/P}},\, \frac{\beta^1_{i,E}}{A^i_{P/E}}\right\}}^{e} \left.\frac{\partial\, p^*}{\partial\, \xi}\right|_e , \tag{A.43}$$

where the new pressure gradient is evaluated using the guessed pressure values at P and E. For the sake of simplicity, the terms H will be used, defined as:

$$\begin{aligned} H^i_e = &\overleftarrow{\left\{\frac{-\sum_{F/P} A^i_{F/P}\, u_{i,F/P} + S^i_{P/P}}{A^i_{P/P}},\, \frac{-\sum_{F/E} A^i_{F/E}\, u_{i,F/E} + S^i_{P/E}}{A^i_{P/E}}\right\}}^{e} \ \dots \\ \dots &- \overleftarrow{\left\{\frac{\beta^2_{i,P}}{A^i_{P/P}} \left.\frac{\partial\, p^*}{\partial\, \eta}\right|_P,\, \frac{\beta^2_{i,E}}{A^i_{P/E}} \left.\frac{\partial\, p^*}{\partial\, \eta}\right|_E\right\}}^{e} - \overleftarrow{\left\{\frac{\beta^3_{i,P}}{A^i_{P/P}} \left.\frac{\partial\, p^*}{\partial\, \zeta}\right|_P,\, \frac{\beta^3_{i,E}}{A^i_{P/E}} \left.\frac{\partial\, p^*}{\partial\, \zeta}\right|_E\right\}}^{e} , \end{aligned} \tag{A.44}$$

$$\begin{aligned} H^i_n = &\overleftarrow{\left\{\frac{-\sum_{F/P} A^i_{F/P}\, u_{i,F/P} + S^i_{P/P}}{A^i_{P/P}},\, \frac{-\sum_{F/N} A^i_{F/N}\, u_{i,F/N} + S^i_{P/N}}{A^i_{P/N}}\right\}}^{n} \ \dots \\ \dots &- \overleftarrow{\left\{\frac{\beta^1_{i,P}}{A^i_{P/P}} \left.\frac{\partial\, p^*}{\partial\, \xi}\right|_P,\, \frac{\beta^1_{i,N}}{A^i_{P/N}} \left.\frac{\partial\, p^*}{\partial\, \xi}\right|_N\right\}}^{n} - \overleftarrow{\left\{\frac{\beta^3_{i,P}}{A^i_{P/P}} \left.\frac{\partial\, p^*}{\partial\, \zeta}\right|_P,\, \frac{\beta^3_{i,N}}{A^i_{P/N}} \left.\frac{\partial\, p^*}{\partial\, \zeta}\right|_N\right\}}^{n} , \end{aligned} \tag{A.45}$$

$$\begin{aligned} H^i_t = &\overleftarrow{\left\{\frac{-\sum_{F/P} A^i_{F/P}\, u_{i,F/P} + S^i_{P/P}}{A^i_{P/P}},\, \frac{-\sum_{F/T} A^i_{F/T}\, u_{i,F/T} + S^i_{P/T}}{A^i_{P/T}}\right\}}^{t} \ \dots \\ \dots &- \overleftarrow{\left\{\frac{\beta^1_{i,P}}{A^i_{P/P}} \left.\frac{\partial\, p^*}{\partial\, \xi}\right|_P,\, \frac{\beta^1_{i,T}}{A^i_{P/T}} \left.\frac{\partial\, p^*}{\partial\, \xi}\right|_T\right\}}^{t} - \overleftarrow{\left\{\frac{\beta^2_{i,P}}{A^i_{P/P}} \left.\frac{\partial\, p^*}{\partial\, \eta}\right|_P,\, \frac{\beta^2_{i,T}}{A^i_{P/T}} \left.\frac{\partial\, p^*}{\partial\, \eta}\right|_T\right\}}^{t} . \end{aligned} \tag{A.46}$$

With these, the method can also be represented in the following alternative form:

$$
\begin{aligned}
u^*_{i,e} &= H^i_e - \overleftarrow{\left\{ \frac{\beta^1_{i,P}}{A^i_{P/P}}, \frac{\beta^1_{i,E}}{A^i_{P/E}} \right\}}^{e} \frac{\partial p^*}{\partial \xi}\bigg|_e \,, \\
u^*_{i,n} &= H^i_n - \overleftarrow{\left\{ \frac{\beta^2_{i,P}}{A^i_{P/P}}, \frac{\beta^2_{i,N}}{A^i_{P/N}} \right\}}^{n} \frac{\partial p^*}{\partial \eta}\bigg|_n \,, \\
u^*_{i,t} &= H^i_t - \overleftarrow{\left\{ \frac{\beta^3_{i,P}}{A^i_{P/P}}, \frac{\beta^3_{i,T}}{A^i_{P/T}} \right\}}^{t} \frac{\partial p^*}{\partial \zeta}\bigg|_t \,.
\end{aligned}
\tag{A.47}
$$

A.3.1 Inclusion of under-relaxation for steady flows

If under-relaxation is used, one should consider the extra term that appears in eq. (A.35). Because the relaxation factor α is constant,

$$
\overleftarrow{\left\{ \frac{\alpha}{A^i_{P/P}}, \frac{\alpha}{A^i_{P/E}} \right\}}^{e} = \alpha \overleftarrow{\left\{ \frac{1}{A^i_{P/P}}, \frac{1}{A^i_{P/E}} \right\}}^{e} ,
$$

The PWIM in eq. (A.47) is changed to:

$$
\begin{aligned}
u^*_{i,e} &= \alpha\, H^i_e - \alpha \overleftarrow{\left\{ \frac{\beta^1_{i,P}}{A^i_{P/P}}, \frac{\beta^1_{i,E}}{A^i_{P/E}} \right\}}^{e} \frac{\partial p^*}{\partial \xi}\bigg|_e + [1-\alpha]\, u^l_{i,e} \,, \\
u^*_{i,n} &= \alpha\, H^i_n - \alpha \overleftarrow{\left\{ \frac{\beta^2_{i,P}}{A^i_{P/P}}, \frac{\beta^2_{i,N}}{A^i_{P/N}} \right\}}^{n} \frac{\partial p^*}{\partial \eta}\bigg|_n + [1-\alpha]\, u^l_{i,n} \,, \\
u^*_{i,t} &= \alpha\, H^i_t - \alpha \overleftarrow{\left\{ \frac{\beta^3_{i,P}}{A^i_{P/P}}, \frac{\beta^3_{i,T}}{A^i_{P/T}} \right\}}^{t} \frac{\partial p^*}{\partial \zeta}\bigg|_t + [1-\alpha]\, u^l_{i,t} \,.
\end{aligned}
\tag{A.48}
$$

In order for the PWIM to be consistent, the values at the CV faces from the previous iteration, $u^l_{i,f}$, should be used.

A.3.2 PWIM for unsteady flows with under-relaxation

For unsteady flows, the traditional change in the PWIM is to modify the H^i_f terms to have the transient $\widetilde{A}^i_p$ coefficients of eq. (A.38), instead of A^i_p. Thus,

$$
\begin{aligned}
\widetilde{H}^i_e = & \overleftarrow{\left\{ \frac{-\sum_{F/P} A^i_{F/P}\, u_{i,F/P} + S^i_{P/P}}{\widetilde{A}^i_{P/P}}, \frac{-\sum_{F/E} A^i_{F/E}\, u_{i,F/E} + S^i_{P/E}}{\widetilde{A}^i_{P/E}} \right\}}^{e} \cdots \\
& \cdots - \overleftarrow{\left\{ \frac{\beta^2_{i,P}}{\widetilde{A}^i_{P/P}} \frac{\partial p^*}{\partial \eta}\bigg|_P, \frac{\beta^2_{i,E}}{\widetilde{A}^i_{P/E}} \frac{\partial p^*}{\partial \eta}\bigg|_E \right\}}^{e} - \overleftarrow{\left\{ \frac{\beta^3_{i,P}}{\widetilde{A}^i_{P/P}} \frac{\partial p^*}{\partial \zeta}\bigg|_P, \frac{\beta^3_{i,E}}{\widetilde{A}^i_{P/E}} \frac{\partial p^*}{\partial \zeta}\bigg|_E \right\}}^{e} ,
\end{aligned}
\tag{A.49}
$$

which results in the following scheme,

$$u^*_{i,e} = \alpha\, H^i_e - \alpha \overleftarrow{\left\{ \frac{\beta^1_{i,P}}{\widetilde{A}^i_{P/P}}, \frac{\beta^1_{i,E}}{\widetilde{A}^i_{P/E}} \right\}_e} \left.\frac{\partial\, p^*}{\partial\, \xi}\right|_e + [1-\alpha]\, u^l_{i,e} \;\ldots$$
$$\ldots + \frac{\alpha}{\Delta t} \overleftarrow{\left\{ \frac{\rho_P\, \Delta\Omega_P}{\widetilde{A}^i_{P/P}}, \frac{\rho_E\, \Delta\Omega_E}{\widetilde{A}^i_{P/E}} \right\}_e} \left[2\, u^n_{i,e} - \frac{1}{2}\, u^{n-1}_{i,e} \right] . \tag{A.50}$$

Although easy to implement, recent work by Pascau (2011) shows that this methodology does not ensure that the PWIM is independent of the time-step nor the under-relaxation factor. To achieve this, interpolation should be made such that the divisor in H^i_f is done with A^i_P, without the transient term present in $\widetilde{A}^i_P$. Defining variable d as:

$$d^i_P = \frac{\rho_P\, \Delta\Omega_P}{A^i_P\, \Delta t} , \tag{A.51}$$

and starting from eq. (A.39),

$$\frac{\widetilde{A}^i_P}{\alpha}\, u^*_{i,P} = -\sum_F A^i_F\, u_{i,F} + S^i_P - \sum_j \beta^j_{i,P} \left.\frac{\partial\, p^*}{\partial\, \xi^j}\right|_P + \frac{\widetilde{A}^i_P}{\alpha}[1-\alpha]\, u^l_{i,P} \;\ldots$$
$$\ldots + A^i_P\, d^i_P \left[2\, u^n_{i,P} - \frac{1}{2}\, u^{n-1}_{i,P} \right] . \tag{A.52}$$

Applying the substitution $\alpha^{-1} = 1 + [1-\alpha]\,\alpha^{-1}$:

$$\Rightarrow\; \widetilde{A}^i_P\, u^*_{i,P} = -\sum_F A^i_F\, u_{i,F} + S^i_P - \sum_j \beta^j_{i,P} \left.\frac{\partial\, p^*}{\partial\, \xi^j}\right|_P \;\ldots$$
$$\ldots + \frac{\widetilde{A}^i_P}{\alpha}[1-\alpha] \left[u^l_{i,P} - u^*_{i,P} \right] + A^i_P\, d^i_P \left[2\, u^n_{i,P} - \frac{1}{2}\, u^{n-1}_{i,P} \right] \;\Leftrightarrow$$

$$\Leftrightarrow\; A^i_P\, u^*_{i,P} = -\sum_F A^i_F\, u_{i,F} + S^i_P - \sum_j \beta^j_{i,P} \left.\frac{\partial\, p^*}{\partial\, \xi^j}\right|_P \;\ldots$$
$$\ldots + \frac{\widetilde{A}^i_P}{\alpha}[1-\alpha] \left[u^l_{i,P} - u^*_{i,P} \right] + A^i_P\, d^i_P \left[-\frac{3}{2}\, u^*_{i,P} + 2\, u^n_{i,P} - \frac{1}{2}\, u^{n-1}_{i,P} \right] \;\Leftrightarrow$$

$$\Leftrightarrow\; u^*_{i,P} = \frac{-\sum_F A^i_F\, u_{i,F} + S^i_P}{A^i_P} - \sum_j \frac{\beta^j_{i,P}}{A^i_P} \left.\frac{\partial\, p^*}{\partial\, \xi^j}\right|_P \;\ldots$$
$$\ldots + \frac{\widetilde{A}^i_P}{A^i_P} \frac{[1-\alpha]}{\alpha} \left[u^l_{i,P} - u^*_{i,P} \right] + d^i_P \left[-\frac{3}{2}\, u^*_{i,P} + 2\, u^n_{i,P} - \frac{1}{2}\, u^{n-1}_{i,P} \right] . \tag{A.53}$$

From the relation between $\widetilde{A}^i_P$ and A^i_P,

$$\widetilde{A}^i_P = A^i_P + \frac{3}{2}\frac{\rho_P\, \Delta\Omega_P}{\Delta t} \quad \Rightarrow \quad \frac{\widetilde{A}^i_P}{A^i_P} = 1 + \frac{3}{2} d^i_P . \tag{A.54}$$

Making $u^*_{i,P}$ explicit,

$$u^*_{i,P}\left[1+\frac{3}{2}d^i_P+\frac{[1-\alpha]}{\alpha}\left[1+\frac{3}{2}d^i_P\right]\right]=u^*_{i,P}\,\frac{1}{\alpha}\left[1+\frac{3}{2}d^i_P\right]\,.$$

$$\Rightarrow\; u^*_{i,P}\left[1+\frac{3}{2}d^i_P\right]=\alpha\,\frac{-\sum_F A^i_F\,u_{i,F}+S^i_P}{A^i_P}-\alpha\sum_j\frac{\beta^j_{i,P}}{A^i_P}\,\frac{\partial\,p^*}{\partial\,\xi^j}\bigg|_P\;\ldots$$

$$\ldots+\left[1+\frac{3}{2}d^i_P\right][1-\alpha]\,u^l_{i,P}+\alpha\,d^i_P\,\left[2\,u^n_{i,P}-\frac{1}{2}\,u^{n-1}_{i,P}\right]\,. \tag{A.55}$$

Defining the following interpolated quantities,

$$d^i_e=\overleftarrow{\left\{d^i_P\,,\,d^i_E\right\}}^{\,e}\,,\quad d^i_n=\overleftarrow{\left\{d^i_P\,,\,d^i_N\right\}}^{\,n}\quad d^i_t=\overleftarrow{\left\{d^i_P\,,\,d^i_T\right\}}^{\,t}\,,$$

a PWIM which ensures independence from both the time-step and under-relaxation is,

$$u^*_{i,e}=\frac{\alpha}{1+\frac{3}{2}d^i_e}\left[H^i_e\;-\overleftarrow{\left\{\frac{\beta^1_{i,P}}{A^i_{P/P}}\,,\,\frac{\beta^1_{i,E}}{A^i_{P/E}}\right\}}^{\,e}\frac{\partial\,p^*}{\partial\,\xi}\bigg|_e+d^i_e\left[2\,u^n_{i,e}-\frac{1}{2}\,u^{n-1}_{i,e}\right]\;\right]+[1-\alpha]\,u^l_{i,e}\,,$$

$$u^*_{i,n}=\frac{\alpha}{1+\frac{3}{2}d^i_n}\left[H^i_n-\overleftarrow{\left\{\frac{\beta^2_{i,P}}{A^i_{P/P}}\,,\,\frac{\beta^2_{i,N}}{A^i_{P/N}}\right\}}^{\,n}\frac{\partial\,p^*}{\partial\,\eta}\bigg|_n+d^i_n\left[2\,u^n_{i,n}-\frac{1}{2}\,u^{n-1}_{i,n}\right]\right]+[1-\alpha]\,u^l_{i,n}\,,$$

$$u^*_{i,t}=\frac{\alpha}{1+\frac{3}{2}d^i_t}\left[H^i_t\;-\overleftarrow{\left\{\frac{\beta^3_{i,P}}{A^i_{P/P}}\,,\,\frac{\beta^3_{i,T}}{A^i_{P/T}}\right\}}^{\,t}\frac{\partial\,p^*}{\partial\,\zeta}\bigg|_t+d^i_t\left[2\,u^n_{i,t}-\frac{1}{2}\,u^{n-1}_{i,t}\right]\;\right]+[1-\alpha]\,u^l_{i,t}\,, \tag{A.56}$$

named as proper interpolation for a colocated treatment of the unsteady Reynolds-averaged equations (PICTURE).

A.4 Definition of the pressure at domain boundaries

When the SIMPLE algorithm is applied for a computational grid with a staggered arrangement of variables, the pressure correction field is computed and used to correct the velocities at the faces. The pressure at the boundary surfaces is not needed for this procedure, thus it may remain unknown. For a collocated arrangement, the same applies when correcting for the velocities at the faces, but not at the CV centres.

The standard practice is to extrapolate the pressure at the boundaries from the inner p^c field. Following Perić (1990), this may be achieved considering $\partial p/\partial n = 0$ at the boundary, where n is the direction normal to the boundary. The argument is the same used to specify the boundary conditions used to solve the pressure correction equation (A.31), in which the mass flux at the boundary is known, thus, the correction is null. An alternative is to use a 1st order polynomial, where $\partial p/\partial n$ is considered constant.

These techniques work for the RaNS equations for incompressible and neutral stratification flows, both in steady and unsteady formulation. When buoyancy terms are introduced but the flow is considered inviscid, the application of the momentum equations (2.58) to a location at the bottom boundary shows that the vertical pressure gradient balances the buoyancy term, thus it should not be considered zero. As such, for inviscid flow with stratification the pressure was linearly extrapolated at both bottom and the top boundaries, while employing a null pressure gradient at the other boundaries. When diffusion terms are considered, linear extrapolation is used at all boundaries, similar to standard procedure used in the simulation of incompressible turbulent flows.

Appendix B

Idealized inlet conditions

B.1 Introduction

In the simulation of atmospheric flows, to solve the system of equations governing its physics, one needs to prescribe boundary conditions and initial conditions. In problems regarding incompressible turbulent flows dominated by roughness, one expects the solution is dominated by the boundary conditions. The higher the Péclet number, *i.e.* the advection compared to the diffusion, the less dependent the flow is from conditions downstream (Patankar, 1980). Due to this the conditions at the outflow may be extrapolated from the interior of the computational domain, not needing any *a priori* prescription. However the conditions at the domain inlet need to be known and prescribed in order to compute a solution. Even in analytical linearized models (*e.g.* Hunt *et al.*, 1988), the shape of the profile for the approaching flow must be known.

The easiest way to set a condition for the inflow is to know, by field measurements or from other numerical model, the profiles for the mean velocity and the turbulence quantities. However, this is not known for the majority of problems and the inlet conditions must be idealized. To minimize the influence of the inlet on the solution, the common practice is to position it in the computational domain such that it is far from the zone of interest. The logical conditions to use are simplified solutions of the governing equations, such as the logarithmic law in eqs. (2.93) and (2.96), according to the stability of the ABL. Likewise the potential temperature $\overline{\theta}$ may be set using eq. (2.97), for the stratified ABL.

B.2 Inlet profiles of turbulence quantities for neutral flow

Considering the turbulence quantities, k and ϵ, it becomes difficult to find consensus on the literature regarding what inlet conditions should be used. The starting point is to derive the conditions near the surface, considering the characteristics of the surface layer. As discussed in §2.3, the logarithmic profiles of the mean quantities are itself derived from assuming constant turbulent fluxes with height. Considering a flow aligned in the x direction with relevant gradients only in the vertical direction, no vertical velocity, and

constant pressure in both vertical and streamwise directions:

$$\begin{cases} \mathcal{P} \approx \rho\,\epsilon \\ \mathcal{P} = \mu_t \left[\dfrac{\partial \overline{u}}{\partial z}\right]^2 \\ \mu_t = \rho\, C_\mu \dfrac{k^2}{\epsilon} \end{cases} \quad \Rightarrow \quad \begin{cases} k_\mathrm{w} = {u_*}^2\, {C_\mu}^{-\frac{1}{2}} \\ \epsilon_\mathrm{w} = \dfrac{{u_*}^3}{l_*} \\ l_* = \kappa\, \min(z, \delta) \end{cases} , \tag{B.1}$$

where these relations would be valid at the wall (as indicated by the $()_\mathrm{w}$ subscript). Richards and Hoxey (1993) proposed to extend these values to the whole boundary layer, implying a constant shear-stress up to the boundary layer height, δ. It would also return a profile of k constant in z. Although being a doubtful approximation, it is commonly found on the recent literature (*e.g.* Hargreaves and Wright, 2007; Griffiths and Middleton, 2010).

Another approach is to use different formulations for the mixing-length: besides l_*, the scale representative of the surface layer, a local scale $l_\wedge$ is defined, representative of the turbulence characteristics at height z. Defining the local scales, $u_\wedge$ and $l_\wedge$ in the same way as the surface scales:

$$u_\wedge = f(z)\,, \qquad u_\wedge^2 = -\left.\overline{(u'\,w')}\right|_z\,, \qquad \frac{\partial \overline{u}}{\partial z} = \frac{u_\wedge}{l_\wedge}\,, \qquad \nu_t = u_\wedge\, l_\wedge\,.$$

From these, a profile for k may be obtained by assuming again a balance between turbulence production and dissipation, yielding:

$$\begin{aligned} &\mathcal{P} \approx \rho\,\epsilon \quad \Leftrightarrow \quad {\nu_t}^2 \left[\frac{\partial \overline{u}}{\partial z}\right]^2 = C_\mu\, k^2 \quad \Leftrightarrow \quad k\, {C_\mu}^{\frac{1}{2}} = \nu_t \frac{\partial \overline{u}}{\partial z} = -\left.\overline{(u'\,w')}\right|_z\,, \\ &-\left.\overline{(u'\,w')}\right|_z = u_\wedge^2 = \left[l_\wedge \frac{\partial \overline{u}}{\partial z}\right]^2 \quad \Rightarrow \quad k\,(z) = {u_*}^2\, {C_\mu}^{-\frac{1}{2}} \left[\frac{l_\wedge}{l_*}\right]^2\,. \end{aligned} \tag{B.2}$$

An equation for ϵ is directly obtained by applying eq. (2.71):

$$\epsilon\,(z) = C_\mu \frac{k\,(z)^2}{\nu_t} = \frac{C_\mu\, k\,(z)^2}{u_\wedge l_\wedge} = \frac{{C_\mu}^{\frac{3}{4}}\, k\,(z)^{\frac{3}{2}}}{l_\wedge} \equiv \frac{{u_*}^3}{l_*} \left[\frac{l_\wedge}{l_*}\right]^2\,. \tag{B.3}$$

This formulation is found in works such as Utnes and Eidsvik (1996), Eidsvik (2008) and Palma *et al.* (2008). In these, $l_\wedge$ is based on the expression proposed by Blackadar (1962):

$$\frac{1}{l_\wedge} = \frac{1}{l_*} + \frac{1}{l_\delta}\,, \qquad \text{where:} \quad l_\delta = \kappa\,\delta \quad \vee \quad l_\delta = \kappa\,[\delta - z]\,, \tag{B.4}$$

where δ is the boundary layer height or other typical scale. Depending on the choice for l_δ one may have different results. If:

$$l_\delta = \kappa\,\delta \quad \Rightarrow \quad \frac{l_\wedge}{l_*} = \frac{\delta}{\delta + \min(z, \delta)}\,, \tag{B.5}$$

named as the `Blackadar 1962` inlet in the remainder of the text. If the formulation of Eidsvik (2008) is used instead:

$$l_\delta = \kappa\,[\delta - \min(z, 0.99\,\delta)] \quad \Rightarrow \quad \frac{l_\wedge}{l_*} = 1 - \frac{\min(z, 0.99\,\delta)}{\delta}\,. \tag{B.6}$$

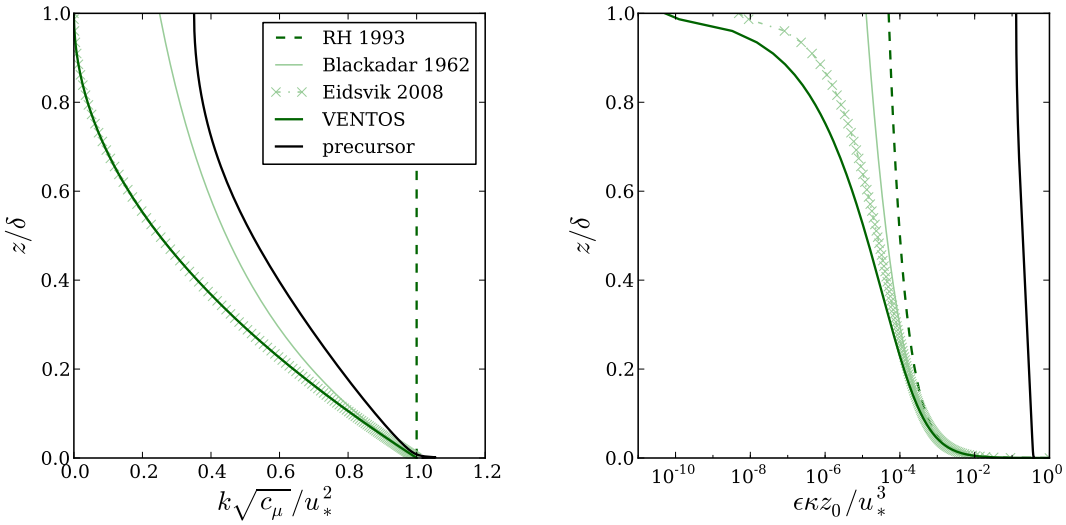

Figure B.1: Comparison of inlet profiles for k and ϵ between several analytical formulations and a precursor simulation updated such that u_* remains constant. In the legend, `RH 1993` refers to Richards and Hoxey (1993); `Blackadar 1962` to a formulation using $l_\delta = \kappa\,\delta$, `Eidsvik 2008` to a formulation with $l_\delta = \kappa\,[\delta - z]$ and `VENTOS` to the formulation with eq. (B.8) for ϵ.

The formulation in VENTOS® uses the same mixing-length formulation stated above, $l_\delta = \kappa\,[\delta - \min(z, 0.99\,\delta)]$, but assuming that the vertical shear stress decreases linearly with height,

$$-\left.\overline{(u'\,w')}\right|_z = {u_*}^2\,\left[\frac{l_\wedge}{l_*}\right] = {u_*}^2\,\left[1 - \min(z, 0.99\,\delta)/\delta\right]\,. \tag{B.7}$$

This yields a slight difference in the equation for ϵ:

$$\epsilon\,(z) = \frac{{u_*}^3}{l_*}\,\left[\frac{l_\wedge}{l_*}\right]^3\,, \tag{B.8}$$

Simulations of the neutral ABL over a flat plate where realized using these analytical formulations to set-up the inlet conditions. It was verified that the velocity profile changes along the computational domain, with the larger variations occurring in the elements near the inlet. Boundary-layer growth is expected as there are no artefacts in the simulations to stop it. Additionally, it is also due to the lack of equilibrium between the mean field and the turbulence quantities. To obtain profiles that are in equilibrium, a 2D simulation was realized such that at each iteration the $\vec{u}$, $\widehat{p}$, k and ϵ fields are shifted in the flow direction. For the u_* to remain constant throughout the simulation, the variables were scaled according to their respective physical dimensions:

$$f = u_*\,\left[\frac{|\tau_w|}{\rho}\right]^{-\frac{1}{2}}\,, \qquad \overline{u}^n_{i,k} = \overline{u}^{n-1}_{i+1,k}\,f^2\,, \qquad \overline{w}^n_{i,k} = \overline{u}^{n-1}_{i+1,k}\,f^2\,, \qquad \overline{w}^n_{1,k} = 0\,,$$

$$k^n_{i,k} = k^{n-1}_{i+1,k}\,f^2\,, \qquad \epsilon^n_{i,k} = \epsilon^{n-1}_{i+1,k}\,f^3\,,$$

where f is the scaling factor, n is the iteration index and the grid indexes, i and k, refer to the streamwise and vertical direction. To ensure conservation the outflow boundary

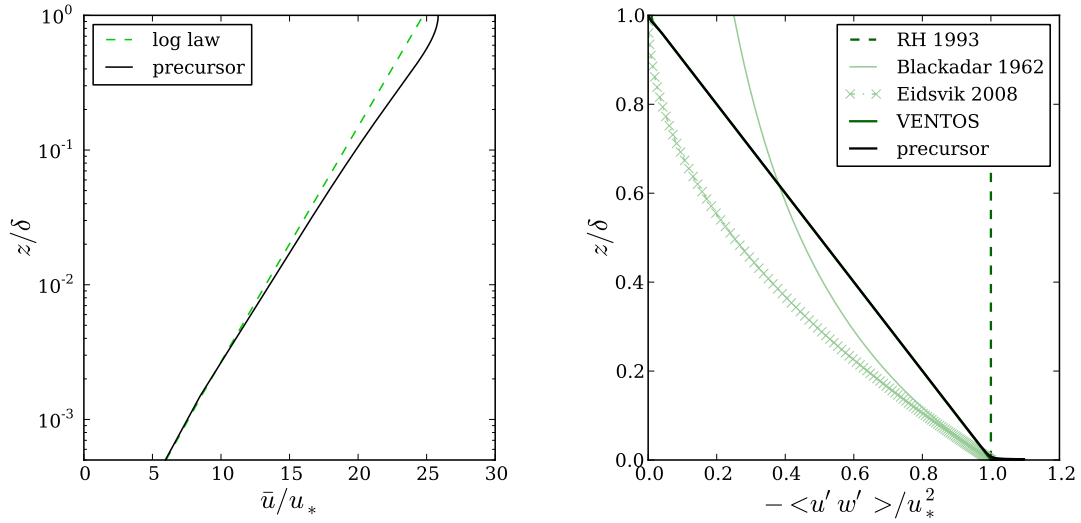

Figure B.2: (*left*) Comparison between the neutral logarithmic law and the velocity profile obtained for the precursor simulation; (*right*) same as Figure B.1 but for the vertical shear stress.

is extrapolated from the adjacent nodes and scaled to the same mass flow that was set at the inlet. The computational domain was composed of 16×128 elements, extending up to a height of 1000 m (set equal to δ). The simulation was stopped after 2×10^4 iterations, when the normalized pressure residual was below 2×10^{-7} and all the remaining residuals were $< 7 \times 10^{-5}$.

In Figure B.1 the several analytical formulations are compared with the results from the precursor simulation. For all, u_* is set to 0.3 m s^{-1} and δ to 1000 m. The k profile lies in between the `RH 1993` and `Blackadar 1962` profiles, being higher than both Eidsvik (2008) and VENTOS®. There is a peak in the vicinity of the wall that is caused by the boundary condition for the turbulence production due to shear, $\mathcal{P}$, which obliges that the hypothesis of local equilibrium between production and dissipation is respected. For ϵ, all of the analytical formulations under-predict the computed profile. The precursor simulation returns values of ϵ which vary little with height, except at the wall where the value is 1 order of magnitude higher. In Figure B.2 are shown both the logarithmic law and the precursor simulation streamwise velocity, as well as the vertical shear stress. Although the VENTOS® profiles under-predicted both k and ϵ, the agreement for $\overline{(u'\,w')}$ is very good, better thant the other formulations. This indicates that the turbulence viscosity is being well estimated and the discrepancies in both k and ϵ compensate for this.

B.3 Extension to account for stratification

As for the neutral case, a balance between production and dissipation is assumed. However, production due to buoyancy must be considered, thus eq. (2.66) becomes:

$$\mathcal{P} + \mathcal{G} \approx \rho\,\epsilon \quad \Leftrightarrow \quad \mathcal{P}\,[1 - \mathrm{Rf}] = \rho\,\epsilon \quad \Leftrightarrow \quad C_\mu\,k^2 = {\nu_t}^2 \left[\frac{\partial\,\overline{u}}{\partial\,z}\right]^2 \left[1 - \frac{\zeta}{\phi_m}\right], \tag{B.9}$$

where Rf is the Richardson flux number, $\zeta = z/\mathcal{L}$ and ϕ_m is the momentum stability function as defined in §2.3.1. The velocity gradient is represented either by the surface layer scales, u_* and l_*, or the local scales, $u_\wedge$ and $l_\wedge$, thus:

$$\frac{\partial\,\overline{u}}{\partial\,z} = \frac{u_*}{l_*}\,\phi_m = \frac{u_\wedge}{l_\wedge}\,. \tag{B.10}$$

Additionally the following quantities are defined locally as:

$$-\,\overline{(u'\,w')}\Big|_z = u_\wedge^2\,, \qquad \nu_t = u_\wedge\,l_\wedge\,.$$

An expression for k is obtained from the equations stated above:

$$k\,(z) = \frac{{u_*}^2}{\sqrt{C_\mu}} \left[1 - \frac{\zeta}{\phi_m}\right]^{\frac{1}{2}} \left[\frac{l_\wedge}{l_*}\right]^2\,. \tag{B.11}$$

As for the neutral case, the definition chosen for $l_\wedge$ will result in different profiles. However this becomes more complex as different profiles for ϵ may be obtained. For example, direct application of equations (B.10) and (B.11) on (2.71) yields:

$$\begin{aligned} &\epsilon = C_\mu\,\frac{k^2}{\nu_t} = \frac{{u_*}^4}{\nu_t}\left[1 - \frac{\zeta}{\phi_m}\right]\left[\frac{l_\wedge}{l_*}\right]^4 = \frac{{u_*}^4}{l_*\,u_\wedge}\left[1 - \frac{\zeta}{\phi_m}\right]\left[\frac{l_\wedge}{l_*}\right]^3\,, \\ &u_\wedge = u_*\,\frac{l_\wedge}{l_*}\,\phi_m \quad \Rightarrow \quad \epsilon = \frac{{u_*}^3}{l_*\,\phi_m}\left[1 - \frac{\zeta}{\phi_m}\right]\left[\frac{l_\wedge}{l_*}\right]^2\,. \end{aligned} \tag{B.12}$$

The same expressions applied on eq. (B.9) return instead:

$$\epsilon = \nu_t \left[\frac{\partial\,\overline{u}}{\partial\,z}\right]^2 \left[1 - \frac{\zeta}{\phi_m}\right] \quad \Rightarrow \quad \epsilon = \frac{{u_*}^3\,{\phi_m}^3}{l_*}\left[1 - \frac{\zeta}{\phi_m}\right]\left[\frac{l_\wedge}{l_*}\right]^2\,. \tag{B.13}$$

To resolve these inconsistencies either the profile of ν_t or $-\overline{(u'\,w')}$ should be given. By adopting a profile similar to the neutral Eidsvik (2008) inlet:

$$-\overline{(u'\,w')} = {u_*}^2\left[\frac{l_\wedge}{l_*}\right]^2 \quad \Rightarrow \quad \begin{cases} \epsilon(z) = \dfrac{{u_*}^3}{l_*}\,[\phi_m - \zeta]\left[\dfrac{l_\wedge}{l_*}\right]^2\,, \\ \nu_t(z) = \dfrac{u_*\,l_*}{\phi_m}\left[\dfrac{l_\wedge}{l_*}\right]^2\,, \end{cases} \tag{B.14}$$

Adopting a linear decrease of $-\overline{(u'\,w')}$ akin to the neutral VENTOS®,

$$-\overline{(u'\,w')} = {u_*}^2 \left[\frac{l_\wedge}{l_*}\right] \quad \Rightarrow \quad \begin{cases} \epsilon(z) = \dfrac{{u_*}^3}{l_*}\,[\phi_m - \zeta] \left[\dfrac{l_\wedge}{l_*}\right]^3 , \\ \nu_t(z) = \dfrac{u_*\, l_*}{\phi_m} \left[\dfrac{l_\wedge}{l_*}\right] , \end{cases} \tag{B.15}$$

Brost and Wyngaard (1978) realized simulations of the stably stratified boundary layer with a 2nd order closure model. Their results show that the profile of ν_t is well described by:

$$\nu_t(z) = \frac{u_*\,\kappa\, z}{1 + b_{ms}\dfrac{z}{\delta}\dfrac{\delta}{\mathcal{L}}} \left[1 - \frac{z}{\delta}\right]^{\frac{3}{2}} = \frac{u_*\, l_*}{\phi_m} \left[\frac{l_\wedge}{l_*}\right]^{\frac{3}{2}} , \tag{B.16}$$

which lies in between the expressions presented in (B.14) and (B.15). Using it with the profile already defined for k in eq. (B.11) returns:

$$\begin{cases} \epsilon(z) = \dfrac{{u_*}^3}{l_*}\,[\phi_m - \zeta] \left[\dfrac{l_\wedge}{l_*}\right]^{\frac{5}{2}} , \\ -\overline{(u'\,w')} = {u_*}^2 \left[\dfrac{l_\wedge}{l_*}\right]^{\frac{3}{2}} . \end{cases} \tag{B.17}$$

Although these profiles may be better suited for the stably stratified case, for the convective boundary-layer a linear profile for the momentum flux is preferred (*e.g.*, Figure 9 in Wyngaard *et al.*, 1974).

For consistency with the neutral case, the profiles in eq. (B.15) could be adopted. However the inconsistencies found suggest that more information is needed, both from from experimental and numerical investigations, to settle on a correct formulation.

Appendix C

Outflow boundary conditions

C.1 Introduction

In the numerical simulation of stratified atmospheric flow over idealized topography, boundary conditions at the outflow have to be specified. These should allow for the fluid patterns developed in the simulation to exit, while reducing inward reflections to a minimum. Several types of boundary conditions were tested, from simple zero gradient to radiation conditions based on the work of Orlansky (1976).

C.2 Mathematical description

In this section the conditions tested at the outflow boundary are presented. For the sake of comprehension, throughout this appendix code words were given for each boundary condition, these being described in Table C.1.

Table C.1: Code words for the outflow boundary conditions used.

Boundary condition	code word
Zero gradient	`e0`
Unsteady convective condition	`adv`
Miller and Thorpe (1981)	`mt`
Durran and Klemp (1983)	`dk`
Raymond and Kuo (1984)	`rk`
Miranda and James (1992)	`mj`
Marchesiello, McWilliams and Shchepetkin (2001)	`mms`
Implicit 3 time-level scheme based on Durran and Klemp	`dk3t`

C.2.1 Zero gradient condition (e0)

The simplest boundary condition to have is a zero gradient extrapolation at the boundary node:

$$\frac{\partial \phi}{\partial x} = 0 \quad \Rightarrow \quad \phi_b = \phi_{b-1} \,. \tag{C.1}$$

with ϕ as the variable being computed, x as the direction normal to the boundary and b representing the index of the boundary node. Even being the most stable condition at an outflow, it may produces reflections that propagate into the computational domain.

A 1st order extrapolation could also be used:

$$\frac{\partial \phi}{\partial x} = \text{constant} \quad \Rightarrow \quad \phi_b = \phi_{b-1} + [x_b - x_{b-1}] \left[\frac{\phi_{b-1} - \phi_{b-2}}{x_{b-1} - x_{b-2}} \right] \,. \tag{C.2}$$

With variables were positiveness must be maintained, specifically turbulence model variables like the turbulence kinetic energy k and its dissipation ϵ, this condition should not be used unless a clipping exists, enforcing $\phi_b = \max(0, \phi_b)$.

C.2.2 Radiation boundary condition according to Orlansky

More elaborate outflow conditions are based on the Sommerfeld radiation equation:

$$\frac{\partial \phi}{\partial t} = -C \frac{\partial \phi}{\partial x} \,, \tag{C.3}$$

where t represents time and C the phase velocity of an outgoing wave. Klemp and Wilhelmson (1978) prescribe C using twice the domain height and the wavelength of vertically propagating gravity waves:

$$C = u + C_* = u + \frac{z_{\text{top}}\, N}{\pi} \,.$$

Another alternative is to set C as the average inflow velocity, commonly used in the simulation of neutral incompressible flow (Ferziger and Perić, 2002). Such technique is designated as adv throughout this text, following the code words in Table C.1.

Orlansky (1976) proposed to estimate C locally, for each nodal point at the boundary. Following his work, eq. (C.3) is integrated in time using the leap-frog method,

$$\frac{\partial \phi}{\partial t} = f(t, \phi(t)) \quad \Leftrightarrow \quad \int_{t_{n-1}}^{t_{n+1}} \frac{\partial \phi}{\partial t} \mathrm{d}t = \int_{t_{n-1}}^{t_{n+1}} f(t, \phi(t))\, \mathrm{d}t \quad \Leftrightarrow$$

$$\Leftrightarrow \quad \phi_i^{n+1} - \phi_i^{n-1} = f(t_n, \phi_i^n)\, 2\,\Delta t \,, \tag{C.4}$$

where indices n and i refer to a discrete instant in the time domain and x direction, respectively. The spatial derivative in eq. (C.3) is approximated using a backward-difference scheme and the DuFort-Frankel method, *i.e.*, stabilized with central differencing in time:

$$\left.\frac{\partial \phi}{\partial x}\right|_i^n = \frac{\phi_i^n - \phi_{i-1}^n}{x_i - x_{i-1}} = \frac{\phi_i^{n+1} + \phi_i^{n-1} - 2\,\phi_{i-1}^n}{2\,\Delta x_i} \,,$$

where $\Delta x_i = x_i - x_{i-1}$. Substituting in eq. (C.4), an expression for ϕ_b^{n+1} is obtained:

$$\begin{aligned} f\left(t_n, \phi_b^n\right) = -C_b^n \left.\frac{\partial \phi}{\partial x}\right|_b^n \quad \Leftrightarrow \\ \Leftrightarrow \quad \phi_b^{n+1} - \phi_b^{n-1} = -C_b^n \frac{\Delta t}{\Delta x_b}\left[\phi_i^{n+1} + \phi_i^{n-1} - 2\,\phi_{i-1}^n\right] \quad \Leftrightarrow \\ \Leftrightarrow \quad \phi_b^{n+1} = \left[\frac{1-r}{1+r}\right]\phi_b^{n-1} + \left[\frac{2\,r}{1+r}\right]\phi_{b-1}^n\,, \end{aligned} \tag{C.5}$$

with $r = C\,\Delta t/\Delta x_b$. To satisfy the convexity property, *i.e.*, the extrapolated value is a weighted sum of the values at neighbouring time and nodes, all weighting coefficients should sum to one. Thus, the value of C should lie between:

$$C = \begin{cases} 0\,, & \text{if} \quad C < 0 \\ C\,, & \text{if} \quad 0 < C < \dfrac{\Delta x_b}{\Delta t} \\ \dfrac{\Delta x_b}{\Delta t}\,, & \text{if} \quad C > \dfrac{\Delta x_b}{\Delta t} \end{cases}\,. \tag{C.6}$$

This condition also implies the satisfaction of the CFL (Courant-Friedrichs-Lewy) condition.

To estimate C, Orlansky proposes to extrapolate the value from the one at the previous time and spatial step, assuming that the changes are small. Thus,

$$C_b^n \approx C_{b-1}^{n-1} = -\frac{\Delta x_{b-1}}{\Delta t}\left[\frac{\phi_{b-1}^n - \phi_{b-1}^{n-2}}{\phi_{b-1}^n + \phi_{b-1}^{n-2} - 2\,\phi_{b-2}^{n-1}}\right]\,. \tag{C.7}$$

The bounds in eq. (C.6) may be enforced by applying:

$$C_b^n = \min\left(\frac{\Delta x_b}{\Delta t}, \max\left(0, C_b^n\right)\right)\,. \tag{C.8}$$

C.2.3 Miller and Thorpe outflow condition (`mt`)

Miller and Thorpe (1981) proposed the same method as Orlansky (1976), changing however the discretization of the derivatives in eq. (C.3) to a 1st order forward time difference and an upstream spatial difference:

$$\left.\frac{\partial \phi}{\partial t}\right|_b^n = \frac{\phi_b^{n+1} - \phi_b^n}{\Delta t}\,, \qquad \left.\frac{\partial \phi}{\partial x}\right|_b^n = \frac{\phi_b^n - \phi_{b-1}^n}{\Delta x_b}\,.$$

These changes yield a simpler expression to extrapolate the boundary value:

$$\phi_b^{n+1} = \left[1 - r\right]\phi_b^{n-1} + r\,\phi_{b-1}^n\,, \tag{C.9}$$

with $r = C\,\Delta t/\Delta x_b$. The computation of the velocity C is similar to eqs. (C.7) and (C.8):

$$C_b^n \approx C_{b-1}^{n-1} \quad \Rightarrow \quad C_b^n = \min\left(\frac{\Delta x_b}{\Delta t}, \max\left(0, -\frac{\Delta x_{b-1}}{\Delta t}\left[\frac{\phi_{b-1}^n - \phi_{b-1}^{n-1}}{\phi_{b-1}^{n-1} - \phi_{b-2}^{n-1}}\right]\right)\right)\,. \tag{C.10}$$

C.2.4 Durran and Klemp outflow condition (dk)

Durran and Klemp (1983) proposed changes to the Orlansky outflow condition where eq. (C.3) was integrated as in Miller and Thorpe (1981), such that:

$$\phi_b^{n+1} = \phi_b^n - \overline{C}\,\frac{\Delta t}{\Delta x_b}\,\left[\phi_b^n - \phi_{b-1}^n\right]\,. \tag{C.11}$$

A value for a local velocity C_b^n is computed as in eq. (C.10). The difference in this formulation is that C is surface averaged for the whole boundary, instead of being used locally. Thus:

$$\overline{C} \approx \frac{\sum_{j=1}^{Nj}\sum_{k=1}^{Nk} \min\left(\frac{\Delta x_b}{\Delta t},\, \max\left(0,\, -\frac{\Delta x_{b-1}}{\Delta t}\left[\frac{\phi_{b-1}^n - \phi_{b-1}^{n-1}}{\phi_{b-1}^{n-1} - \phi_{b-2}^{n-1}}\right]\right)\right)\Delta S_{b-1,j,k}}{\sum_{j=1}^{Nj}\sum_{k=1}^{Nk}\Delta S_{b-1,j,k}}\,, \tag{C.12}$$

with ΔS as the area of the eastern boundary face of the respective control volume.

C.2.5 Raymond and Kuo outflow condition (rk)

Raymond and Kuo (1984) proposed to improve the Sommerfeld radiation equation (C.3) by expanding it to three dimensions:

$$\frac{\partial \phi}{\partial t} = -\,\overrightarrow{C}\cdot\nabla\phi = -C_x\frac{\partial\phi}{\partial x} - C_y\frac{\partial\phi}{\partial y} - C_z\frac{\partial\phi}{\partial z}\,, \tag{C.13}$$

where $\overrightarrow{C}$ is a vector phase velocity and its components, C_x, C_y, C_z, are the projection in each spatial direction. In this nomenclature, direction x is normal to the boundary while y and z are co-planar. The phase velocities are computed as:

$$C_x = -\frac{\partial\phi}{\partial t}\frac{\partial\phi}{\partial x}\,G^{-1}\,,\quad C_y = -\frac{\partial\phi}{\partial t}\frac{\partial\phi}{\partial y}\,G^{-1}\,,\quad C_z = -\frac{\partial\phi}{\partial t}\frac{\partial\phi}{\partial z}\,G^{-1}\,, \tag{C.14}$$

with,

$$G = \left(\frac{\partial\phi}{\partial x}\right)^2 + \left(\frac{\partial\phi}{\partial y}\right)^2 + \left(\frac{\partial\phi}{\partial z}\right)^2\,.$$

This implies that the relationship between C_x, C_y and C_z is given by the cross product,

$$\overrightarrow{C}\times\nabla\phi = 0\,.$$

Using a leap-frog time integration scheme with the DuFort-Frankel method,

$$\left.\frac{\partial\phi}{\partial t}\right|_{b,j,k}^{n} = \frac{\phi_{b,j,k}^{n+1} - \phi_{b,j,k}^{n-1}}{\Delta t}\,,\qquad \left.\frac{\partial\phi}{\partial x}\right|_{b,j,k}^{n} = \frac{\phi_{b,j,k}^{n+1} + \phi_{b,j,k}^{n-1} - 2\phi_{b-1,j,k}^{n}}{2\,\Delta x_b}\,,$$

$$\left.\frac{\partial\phi}{\partial y}\right|_{b,j,k}^{n} = \frac{\phi_{b,j+1,k}^{n} - \phi_{b,j-1,k}^{n}}{y_{b,j+1,k} - y_{b,j-1,k}}\,,\quad \left.\frac{\partial\phi}{\partial z}\right|_{b,j,k}^{n} = \frac{\phi_{b,j,k+1}^{n} - \phi_{b,j,k-1}^{n}}{z_{b,j,k+1} - z_{b,j,k-1}}\,,$$

an equation for $\phi_{b,j,k}^{n+1}$ is obtained:

$$\phi_{b,j,k}^{n+1} = \left[\frac{1-r_x}{1+r_x}\right]\phi_{b,j,k}^{n-1} + \left[\frac{2r_x}{1+r_x}\right]\phi_{b-1,j,k}^{n} \quad \cdots$$
$$\cdots - \left[\frac{r_y}{1+r_x}\right]\left[\phi_{b,j+1,k}^{n} - \phi_{b,j-1,k}^{n}\right] - \left[\frac{r_z}{1+r_x}\right]\left[\phi_{b,j,k+1}^{n} - \phi_{b,j,k-1}^{n}\right], \tag{C.15}$$

where,

$$r_x = C_x\frac{\Delta t}{\Delta x_b}, \quad r_y = C_y\frac{\Delta t}{\Delta y}, \quad r_z = C_z\frac{\Delta t}{\Delta z}. \tag{C.16}$$

The discrete grid distances are the same as in the finite differences: $\Delta y = y_{b,j+1,k} - y_{b,j-1,k}$ and $\Delta z = z_{b,j,k+1} - z_{b,j,k-1}$. Limits to the values of $\overrightarrow{C}$ are imposed to satisfy the CFL condition, thus:

$$\begin{cases} C_x = \min\left(\dfrac{\Delta x_b}{\Delta t}, \max\left(0, C_{x_b}^{n}\right)\right), \\ C_y = \min\left(\dfrac{\Delta y}{\Delta t}, \max\left(-\dfrac{\Delta y}{\Delta t}, C_{y_b}^{n}\right)\right), \\ C_z = \min\left(\dfrac{\Delta z}{\Delta t}, \max\left(-\dfrac{\Delta z}{\Delta t}, C_{z_b}^{n}\right)\right). \end{cases} \tag{C.17}$$

Following the Orlansky methodology, the phase velocities are estimated from the previous time step and spatial node, thus:

$$C_{x}{}_{b,j,k}^{n} \approx C_{x}{}_{b-1,j,k}^{n-1}, \quad C_{y}{}_{b,j,k}^{n} \approx C_{y}{}_{b-1,j,k}^{n-1}, \quad C_{z}{}_{b,j,k}^{n} \approx C_{z}{}_{b-1,j,k}^{n-1}.$$

C.2.6 Miranda and James outflow condition (mj)

In the work of Miranda and James (1992), the same formulation as Raymond and Kuo is used except in the computation of the phase velocity at the previous time-step, $\overrightarrow{C}_{b-1,j,k}^{n-1}$. A central-differencing scheme for the longitudinal derivative is used instead, thus:

$$\left.\frac{\partial\phi}{\partial t}\right|_{b-1,j,k}^{n-1} = \frac{\phi_{b-1,j,k}^{n} - \phi_{b-1,j,k}^{n-2}}{2\,\Delta t}, \qquad \left.\frac{\partial\phi}{\partial x}\right|_{b-1,j,k}^{n-1} = \frac{\phi_{b,j,k}^{n-1} - \phi_{b-2,j,k}^{n-1}}{x_{b,j,k} - x_{b-2,j,k}},$$

$$\left.\frac{\partial\phi}{\partial y}\right|_{b-1,j,k}^{n-1} = \frac{\phi_{b-1,j+1,k}^{n-1} - \phi_{b-1,j-1,k}^{n-1}}{y_{b-1,j+1,k} - y_{b-1,j-1,k}}, \qquad \left.\frac{\partial\phi}{\partial z}\right|_{b-1,j,k}^{n-1} = \frac{\phi_{b-1,j,k+1}^{n-1} - \phi_{b-1,j,k-1}^{n-1}}{z_{b-1,j,k+1} - z_{b-1,j,k-1}}$$

C.2.7 Marchesiello *et al.* outflow condition (mms)

Marchesiello *et al.* (2001) reimplements the Raymond and Kuo scheme, introducing three important changes: (i) implicit formulation in the derivative normal to the boundary,

(ii) upwind scheme in the formulation of the tangential derivatives, (iii) the phase speed is computed at the current time. With these changes, the equation for $\phi^{n+1}_{b,j,k}$ becomes:

$$\phi^{n+1}_{b,j,k} = \frac{1}{1+r_x}\left[\phi^{n}_{b,j,k} + r_x\,\phi^{n+1}_{b-1,j,k} - r_y\ \Delta_y\phi\big|^n - r_z\ \Delta_z\phi\big|^n\right]\,, \tag{C.18}$$

where the differences in the directions tangential to the wall become dependent on the direction of the flow:

$$\Delta_y\phi\big|^n = \begin{cases} \phi^n_{b,j,k} - \phi^n_{b,j-1,k}\,, & r_y > 0 \\ \phi^n_{b,j+1,k} - \phi^n_{b,j,k}\,, & r_y < 0 \end{cases}\,,$$

$$\Delta_z\phi\big|^n = \begin{cases} \phi^n_{b,j,k} - \phi^n_{b,j,k-1}\,, & r_z > 0 \\ \phi^n_{b,j,k+1} - \phi^n_{b,j,k}\,, & r_z < 0 \end{cases}\,.$$

The coefficients r_x, r_y and r_z are the dimensionless forms of $\overrightarrow{C}$, obtained from eq. (C.16). The latter is computed as in eq. (C.14). Conversely to the other formulations, the value of $\overrightarrow{C}$ is estimated for the current time-step for the derivatives in time and the direction normal to the boundary. Thus:

$$\Delta\phi_t = \phi^{n+1}_{b-1,j,k} - \phi^n_{b-1,j,k}\,, \qquad \left.\frac{\partial\phi}{\partial x}\right|^{n+1}_{b-1,j,k} = \frac{\phi^{n+1}_{b-1,j,k} - \phi^{n+1}_{b-2,j,k}}{x_{b-1,j,k} - x_{b-2,j,k}}\,.$$

Regarding the tangential derivatives, although evaluated from the ϕ field at the previous time, the fact that these are computed through an upwind scheme must be considered, yielding:

$$\left.\frac{\partial\phi}{\partial y}\right|^{n}_{b-1,j,k} = \begin{cases} \dfrac{\phi^n_{b-1,j,k} - \phi^n_{b-1,j-1,k}}{y_{b-1,j,k} - y_{b-1,j-1,k}}\,, & \Delta\phi_t\left[\phi^n_{b-1,j+1,k} - \phi^n_{b-1,j-1,k}\right] > 0\,, \\ \dfrac{\phi^n_{b-1,j+1,k} - \phi^n_{b-1,j,k}}{y_{b-1,j+1,k} - y_{b-1,j,k}}\,, & \Delta\phi_t\left[\phi^n_{b-1,j+1,k} - \phi^n_{b-1,j-1,k}\right] < 0\,, \end{cases}$$

$$\left.\frac{\partial\phi}{\partial z}\right|^{n}_{b-1,j,k} = \begin{cases} \dfrac{\phi^n_{b-1,j,k} - \phi^n_{b-1,j,k-1}}{z_{b-1,j,k} - z_{b-1,j,k-1}}\,, & \Delta\phi_t\left[\phi^n_{b-1,j,k+1} - \phi^n_{b-1,j,k-1}\right] > 0\,, \\ \dfrac{\phi^n_{b-1,j,k+1} - \phi^n_{b-1,j,k}}{z_{b-1,j,k+1} - z_{b-1,j,k}}\,, & \Delta\phi_t\left[\phi^n_{b-1,j,k+1} - \phi^n_{b-1,j,k-1}\right] < 0\,. \end{cases}$$

C.2.8 Implicit outflow condition based on Durran and Klemp (`dk3t`)

One of the outflow conditions tested in this work was based on the Durran and Klemp (1983) formulation, with the following difference: the differentiation scheme should match the one used by the unsteady solver (3FTI scheme in Fletcher, 1991). As this is an implicit formulation, the spatial derivative is evaluated at the current time-step. Thus:

$$\left.\frac{\partial\phi}{\partial t}\right|^{n+1}_{b,j,k} = \frac{3\,\phi^{n+1}_{b,j,k} - 4\,\phi^n_{b,j,k} + \phi^{n-1}_{b,j,k}}{2\,\Delta t}\,, \qquad \left.\frac{\partial\phi}{\partial x}\right|^{n+1}_{b,j,k} = \frac{\phi^{n+1}_{b,j,k} - \phi^{n+1}_{b-1,j,k}}{\Delta x_b}\,.$$

The value of $\phi_{b,j,k}^{n+1}$ is computed from:

$$\phi_{b,j,k}^{n+1} = \frac{1}{1+\overline{r}\,\frac{2}{3}} \left[\frac{4}{3}\,\phi_{b,j,k}^{n} - \frac{1}{3}\,\phi_{b,j,k}^{n-1} + \overline{r}\,\frac{2}{3}\,\phi_{b-1,j,k}^{n+1} \right] , \tag{C.19}$$

where the coefficient $\overline{r}$ is the dimensionless form of the surface averaged phase velocity, $\overline{C}\,\Delta t/\Delta x_b$. The computation of $\overline{C}$ is similar to eq. (C.12):

$$\overline{C} \approx \frac{\sum_{j=1}^{Nj}\sum_{k=1}^{Nk} \min\left(\frac{\Delta x_b}{\Delta t},\, \max\left(0,\, -\frac{\Delta x_{b-1}}{\Delta t}\,\frac{\Delta \phi_t}{\Delta \phi_x}\right)\right) \Delta S_{b-1,j,k}}{\sum_{j=1}^{Nj}\sum_{k=1}^{Nk} \Delta S_{b-1,j,k}} , \tag{C.20}$$

with:

$$\Delta\phi_t = \frac{1}{2}\left[3\,\phi_{b-1,j,k}^{n} - 4\,\phi_{b-1,j,k}^{n-1} + \phi_{b-1,j,k}^{n-2}\right] , \qquad \Delta\phi_x = \phi_{b-1,j,k}^{n} - \phi_{b-2,j,k}^{n} \,.$$

C.3 Performance of the outflow conditions

C.3.1 Description of the test case

The test case used to verify the performance of the several outflow conditions is similar to the problem of Chapter 3, described in §3.1.2. Regarding the simulation:

1. The flow is inviscid and stably stratified.
2. The velocity at the inlet, U_∞, was set constant and equal to $5\,\mathrm{m\,s^{-1}}$.
3. The value of the Brunt-Väisälä frequency, N, was $0.01\,\mathrm{s^{-1}}$.
4. The surface topography is an Agnesi shaped mountain, described by eq. (3.1).
5. The mountain height, h, was 250 m.
6. The characteristic mountain length, a, was 5 km.
7. The height of the computational domain was set to 12 km, roughly the same as $4\,\lambda_z$.

Other parameters describing the computational domain are shown in Table C.2. The main difference from the other simulations made in Chapter 3 is the coarser resolution in both horizontal and vertical directions, leading to a lower number of nodes.

All of the outflow conditions referred in §C.2 were tested, except for the Orlansky condition which, due to its similarity with the Miller and Thorpe formulation, was not included. When a phase velocity is computed, it is done using the longitudinal velocity field, normal to the outlet boundary. The outflow condition is applied only to the velocity field. For scalar variables the outlet value is always extrapolated using a zero gradient. Independently of the outflow condition used, the outlet velocity field is rescaled to ensure mass conservation. As such, the outflow conditions affect the profile of the velocity field at the outlet, but not on its average magnitude.

Table C.2: Description of the computational domain of the simulations performed. $\min(\Delta x)$ and $\min(\Delta z)$ refers to the minimum horizontal length and vertical height of the elements that compose the grid. The parameters $\max(f_x)$ and $\max(f_z)$ are the maximum expansion factors for the geometric progression used, in the horizontal and vertical.

h^*	a^*	Grid	x/a	y/a	$\min(\Delta x)$	$\max(f_x)$	$\min(\Delta z)$	$\max(f_z)$
0.5	10	$80 \times 62 \times 60$	$[-10, 15]$	$[-10, 10]$	$0.2\,a$	1.0272	$0.02\dfrac{U_\infty}{N}$	1.079

The simulation with the Raymond and Kuo outflow condition was run up to a dimensionless time of $t^* = 37$, having been stopped due to numerical problems which severely affected convergence. All other simulations were run successfully to a dimensionless time of $t^* = 100$.

C.3.2 Results

Figure C.1 shows the time evolution of the Courant number for the several outflow conditions tested. For a control volume, the Courant number was computed by summing the magnitude of the contravariant velocities at the faces:

$$\mathrm{Cr} = \left[\left| \sum_i u_{i,e}\, \beta^1_{i,e} \right| + \left| \sum_i u_{i,n}\, \beta^2_{i,n} \right| + \left| \sum_i u_{i,t}\, \beta^3_{i,t} \right| \right] \frac{\Delta t}{\Delta \Omega_P} \,,$$

where Cr is the Courant number, $\Delta\Omega_P$ is the volume, $u_{i,f}$ the velocity component in the i direction at face f and $\beta^n_{i,f}$ is the cofactor of the matrix of transformation, defined in eq. (2.111). For each time-step, Cr was computed near the outlet and the maximum value was recorded.

The outflow conditions which attempt to prescribe a local value for the advection velocity have Cr numbers which are higher than the methods which prescribe a constant

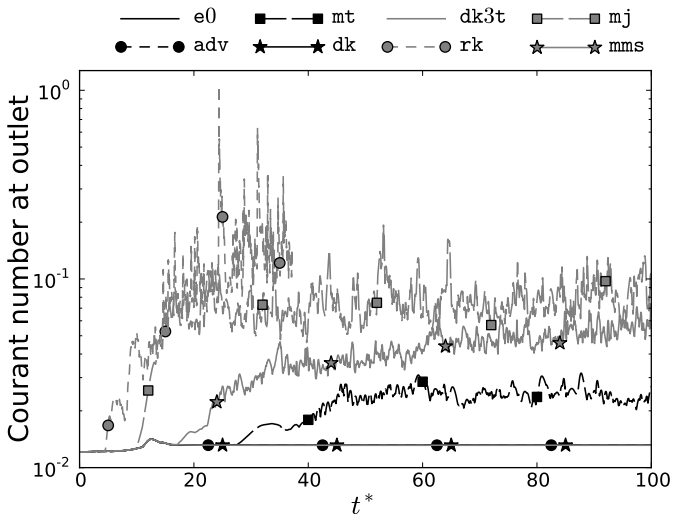

Figure C.1: Evolution in time of the maximum Courant number at the outlet for the outflow conditions tested.

Table C.3: Difference between maximum and minimum values of the extrapolated outflow speed, in the $y = 0$ surface: maximum value observed and value at last time-step.

	Boundary condition							
	`e0`	`adv`	`mt`	`dk`	`dk3t`	`rk`	`mj`	`mms`
$\max\left(\frac{\Delta u}{U_\infty}\right)$	5.24%	5.34%	324%	5.31%	5.30%	783%	513%	502%
$\left.\frac{\Delta u}{U_\infty}\right\|_{\text{tmax}}$	2.78%	2.77%	13.3%	2.77%	2.77%	683%	269%	428%

value instead and the `e0`. The latter methods do not show significant differences between themselves. The differences between the methods are also negligible up to $t^* = 10$. The `mt` is the last condition to diverge (for $t^* > 30$), showing lower values comparatively to `mms` and `mj`. The `rk` condition is the least stable. Although the values are below the unity, these become two orders of magnitude higher near $t^* = 20$.

For the test case used in this comparison, it is expected that the mountain produces some wake which decreases the further the flow is downstream of the summit. As the simulations are inviscid, in the limit the velocity at the outlet surface would resemble the inlet, with a constant value equal to U_∞. The velocity range of the vertical profile at the outlet was computed for each time-step, at the centre place $y = 0$:

$$\Delta u(t) = \max(u(t,\, x = x_b,\, y = 0)) - \min(u(t,\, x = x_b,\, y = 0))\,.$$

In Table C.3 are shown the maximum value of Δu found in the simulation and the value at the last recorded time-step. Both are normalized by U_∞. Again, the methods which are based on constant values for C return maximum variations around 5% and values at $t^* = 100$ around 3%. The other methods have velocity ranges which are unreasonable. The `mt` formulation lies in between, with a value at the last time-step of 13%.

In Figure C.2 are shown Hovmöller plots of the vertical velocity profile at the outlet centre place ($y = 0$), for the whole simulation time span. The `e0`, `adv`, `dk` and `dk3t` conditions yielded similar plots. These show a smooth evolution of the velocity at the outflow, converging to a steady result for $t^* > 40$. The oscillations observed near $t^* = 15$ are produced by the exit of a soliton wave, generated at the simulation start due to the initial conditions used (constant field set to U_∞). This soliton wave is observed for all simulations except `rk`, as the patterns up to $t^* = 15$ show similar features. The differences between the several methods are observed after this event. As already discussed, the methods which assign a value for C locally have a unsatisfactory interaction with the pressure solver, leading to the degeneration of the velocity field. Albeit the `mt` method (Figure C.2c) shows less severe variations in the outlet velocity, it does not converges to a steady result.

C.3.3 Conclusion

A survey of the outflow boundary conditions commonly used in the numerical simulation of atmospheric flows was made. Besides the zero gradient extrapolation, the other

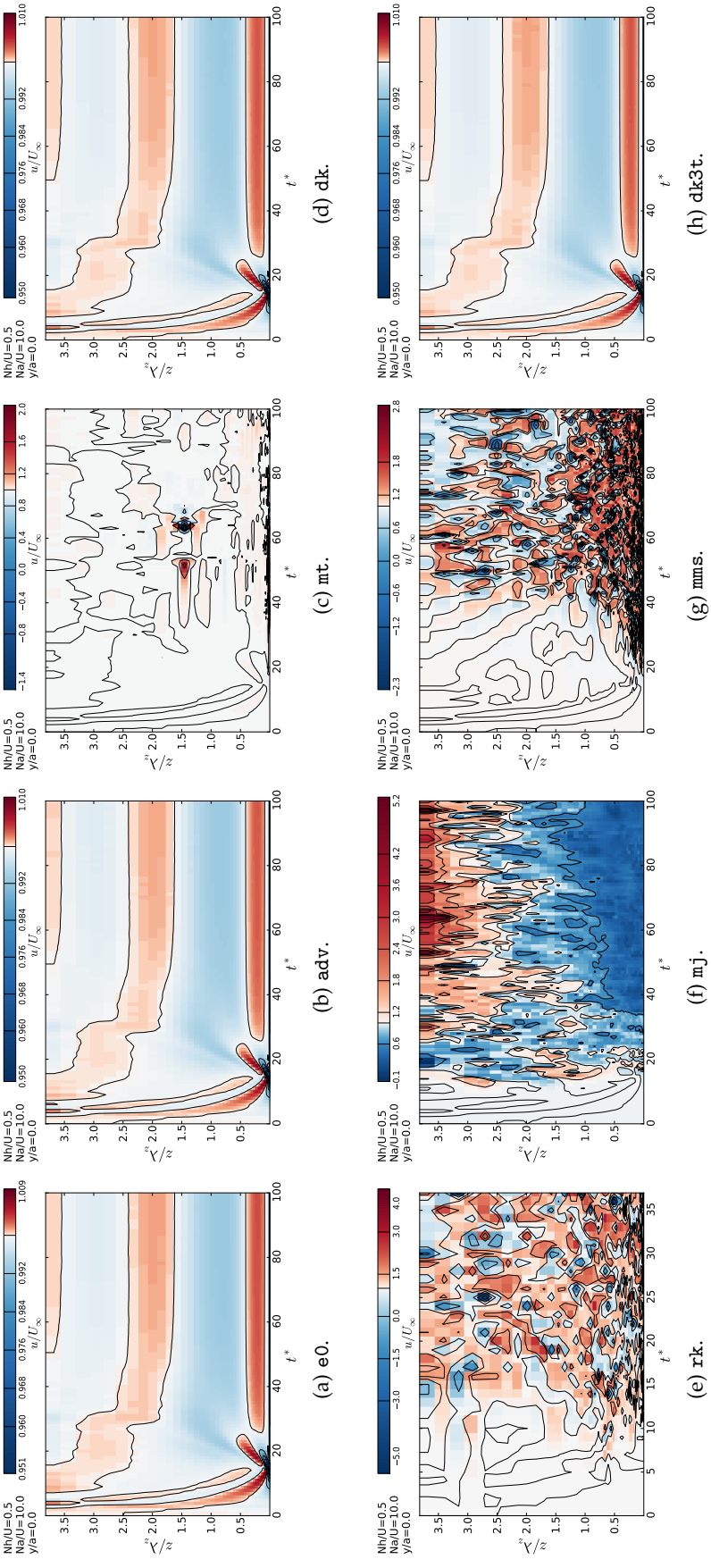

(a) e0. (b) adv. (c) mt. (d) dk.

(e) rk. (f) mj. (g) mms. (h) dk3t.

Figure C.2: Hovmöller plots of the velocity profile at the outlet ($y = 0$ surface), for several outflow boundary conditions. The bold contour line refers to the value where $u = U_\infty$. For the kind of outflow condition which corresponds to the code word, refer to Table C.1.

methods are based on the Sommerfeld radiation equation. This is a pure advection condition which, after integration, yields an equation that can be used to extrapolate the boundary value. The main concern becomes to estimate the advection velocity for the Sommerfeld equation.

These methods may be divided into two categories:

1. The advective velocity is prescribed as constant for the whole outlet boundary.
2. A local prescription of the advective velocity, resulting in different values along the outlet surface.

The methods based on type 1 performed substantially better than the type 2 conditions. The latter are suitable only in simulations for short dimensionless time range, as for $t^* > 20$ a significative degeneration of the flow field was observed. No conclusion regarding why such happens was obtained. Similar difficulties with type 2 conditions and improvements in using a zero gradient condition instead were reported also by Jorge (2006).

There is an interaction with the pressure field where the gradients increase, particularly near the outlet. However it is difficult to diagnose if the degeneration of the flow field is due to an inability of the SIMPLE solver to cope with the type 2 conditions, or is the opposite. Most of the type 2 conditions where developed using numerical models employing a staggered arrangement of variables and an explicit formulation. The use of collocated variables might be an factor of instability, as it requires that pressure boundary conditions are defined at the outlet. Another hypothesis would be that the use of some outflow conditions with a semi-implicit solver might introduce numerical instability, depending on how the implicit part of the code is implemented.

For the numerical model used in Chapter 3 to simulate stably stratified flow, either inviscid or turbulent, the `dk3t` condition was used, described in §C.2.8. Although its results are very similar to the other type 1 conditions, the implicit three-time level scheme is more consistent with the unsteady solver from the numerical model.

Appendix D

Statistics for uRaNS results to compare with cup anemometers measurements

The unsteady Reynolds averaged Navier-Stokes equations (uRaNS) are derived by applying the Reynolds decomposition to each variable. For the x component of velocity:

$$u\left(t,\vec{x}\right) \;=\; \left\langle\, u \,\right\rangle\left(t,\vec{x}\right) + u'\left(t,\vec{x}\right) \;, \tag{D.1}$$

where $()'$ refers to a turbulent fluctuation and the operator $\left\langle\ \right\rangle$ is the ensemble average, *i.e.*, for a number N of hypothetical statistically independent experiments:

$$\left\langle\, u \,\right\rangle\left(t,\vec{x}\right) \equiv \lim_{N\to\infty} \frac{1}{N} \sum_{m=1}^{N} u\left(m,t,\vec{x}\right) \quad , \quad m = 1,2,\ldots,N \;. \tag{D.2}$$

When applying the Reynolds decomposition to the Navier-Stokes equations to simulate a stationary process, it is assumed that turbulence is homogeneous and that time, spatial and ensemble averages converge to the same value, *i.e.*, the ergodic hypothesis. Unsteady atmospheric flows do not converge to a stationary state because these respond to external inputs. However it is assumed that the mean and turbulent quantities are quasi-stationary. This means that, albeit the mean and turbulent components evolves with time, the turbulent time scale is assumed to be much smaller than the mean flow time scale. Thus, at the integration scale Δt, turbulence fluctuations becomes null when averaged:

$$\overline{u'}\left(t,\vec{x}\right) = \frac{1}{\Delta t} \int_{0}^{\Delta t} u'\, dt = 0 \quad \wedge \quad \left\langle\, u' \,\right\rangle\left(t,\vec{x}\right) = 0 \;. \tag{D.3}$$

A sketch showing how such a process would evolve with time is displayed in Figure D.1. According to Lee *et al.* (2005), although its impossible to replicate an experiment for the same meteorological conditions, an evidence of the ergodic hypothesis in the ABL is the success of the Monin-Obukhov Similarity Theory, at least in a weak sense (for the mean and variances).

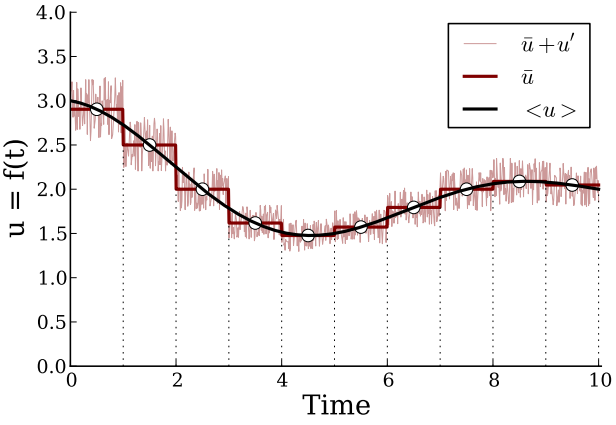

Figure D.1: Reynolds decomposition for an unsteady, quasi-stationary flow.

Time series from field measurements are given as statistics with integration times ΔT of 10 minutes, higher than a common simulation time-step Δt which is in the order of seconds. Knowing the mean and the variance, $\langle u \rangle$ and $\langle u' u' \rangle$, of velocity component u at each time-step of a uRaNS simulation, the mean at an integration time ΔT is given by:

$$\overline{u}(t) = \frac{1}{\Delta T}\int_0^{\Delta T} u\,dt = \frac{1}{\Delta T}\sum_{n=1}^{N_T}\left[\int_{(n-1)\Delta t}^{n\Delta t} u\,dt\right] = \frac{1}{\Delta T}\sum_{n=1}^{N_T}\Delta t\,\langle u \rangle_n \quad \Leftrightarrow$$

$$\Leftrightarrow \quad \overline{u}(t) = \frac{1}{N_T}\sum_{n=1}^{N_T}\langle u \rangle_n = \overline{\langle u \rangle}\,. \tag{D.4}$$

In this derivation, ΔT is divided into $N_T \Delta t$ evenly spaced intervals, where at each of these the time average is approximated by the ensemble average predicted by the simulation. The variance is obtained from:

$$\begin{aligned}
\sigma_u^2(t) &= \frac{1}{\Delta T}\int_0^{\Delta T}[u-\overline{u}]^2\,dt = \frac{1}{\Delta T}\int_0^{\Delta T}\left[u^2 - 2\,u\,\overline{u} + \overline{u}^2\right]dt \\
&= \frac{1}{\Delta T}\sum_{n=1}^{N_T}\left[\int_{(n-1)\Delta t}^{n\Delta t} u^2\,dt\right] - \frac{2\,\overline{u}}{\Delta T}\sum_{n=1}^{N_T}\left[\int_{(n-1)\Delta t}^{n\Delta t} u\,dt\right] + \overline{\left(\overline{u}^2\right)} \\
&= \frac{1}{\Delta T}\sum_{n=1}^{N_T}\left[\int_{(n-1)\Delta t}^{n\Delta t}\left(\langle u \rangle_n + u'\right)^2 dt\right] - 2\overline{\langle u \rangle}^2 + \overline{\langle u \rangle}^2 \\
&= \frac{1}{\Delta T}\sum_{n=1}^{N_T}\left[\int_{(n-1)\Delta t}^{n\Delta t}\left(\langle u \rangle_n^2 + 2\,\langle u \rangle_n\,u' + \left(u'\right)^2\right)dt\right] - \overline{\langle u \rangle}^2\,,
\end{aligned}$$

Assuming that the turbulence fluctuations are uncorrelated with the motions of the

mean flow, thus $\overline{(\langle u \rangle\ u')} \approx 0$,

$$\Rightarrow \int_{(n-1)\Delta t}^{n\Delta t} \left(\langle u \rangle_n^2 + 2 \langle u \rangle_n\ u' + (u')^2 \right) dt = \Delta t \left[\langle u \rangle_n^2 + 2\ \langle u \rangle_n \underbrace{\langle u' \rangle_n}_{=0} + \langle u'\, u' \rangle_n \right]$$
$$= \Delta t \left[\langle u \rangle_n^2 + \langle u'\, u' \rangle_n \right]$$

Thus, the variance is given by the sum of the variance of the mean flow and the turbulence fluctuations:

$$\sigma_u^2 = \frac{1}{N_T} \sum_{n=1}^{N_T} \left[\langle u \rangle_n^2 + \langle u'\, u' \rangle_n \right] - \overline{\langle u \rangle}^2 = \overline{\langle u'\, u' \rangle} + \overline{\langle u \rangle^2} - \overline{\langle u \rangle}^2 . \tag{D.5}$$

Measurements with a cup anemometer returns the horizontal magnitude of the wind velocity and its variance, integrated over ΔT, while the simulations results return the average components of the velocity vector at a Δt timescale, as well as the turbulence kinetic energy, k. Averaging $\langle u \rangle$ and $\langle v \rangle$ over ΔT and computing the magnitude will not yield the same value as computing the average of the magnitude directly:

$$m = \sqrt{u^2 + v^2} \quad \Rightarrow \quad \begin{cases} \overline{m} = \overline{\sqrt{u^2 + v^2}}\,, \\ \overline{m^2} = \overline{u^2} + \overline{v^2}\,, \end{cases}$$

where m represents the horizontal velocity magnitude and u and v the horizontal components of the velocity vector. As the variances are given by:

$$\sigma_m^2 = \overline{(m - \overline{m})^2} = \overline{m^2} - \overline{m}^2\,, \quad \sigma_u^2 = \overline{u^2} - \overline{u}^2\,, \quad \sigma_v^2 = \overline{v^2} - \overline{v}^2\,,$$

an expression can be derived which relates the means and the variances, such that:

$$\overline{m^2} = \overline{u^2 + v^2} = \overline{u^2} + \overline{v^2} \quad \Rightarrow \quad \sigma_m^2 + \overline{m}^2 = \sigma_u^2 + \overline{u}^2 + \sigma_v^2 + \overline{v}^2\,. \tag{D.6}$$

By applying eq. (D.6), the variance of the magnitude σ_m^2 can be computed from the known values of $\overline{m}$, $\overline{u}$, $\overline{v}$, σ_u^2 and σ_v^2. For the time-step Δt of a uRaNS the ensemble average of the magnitude, $\langle m \rangle$, is not know, only $\langle u \rangle$ and $\langle v \rangle$. The best assumption is:

$$\langle m \rangle \approx \sqrt{\langle u \rangle^2 + \langle v \rangle^2}\,. \tag{D.7}$$

The value for the variance given by eq. (D.6) becomes:

$$\langle m \rangle^2 \approx \langle u \rangle^2 + \langle v \rangle^2 \quad \Rightarrow \quad \langle m'm' \rangle \approx \langle u'u' \rangle + \langle v'v' \rangle\ . \tag{D.8}$$

To estimate the variances of turbulence fluctuations, the turbulence-viscosity hypothesis is used (§2.2.2, eq. (2.61)):

$$\langle u'u' \rangle = -\frac{\tau_{11}}{\rho} = -\nu_t\, 2\, \frac{\partial \langle u \rangle}{\partial x} + \frac{2}{3} k\,,$$
$$\langle v'v' \rangle = -\frac{\tau_{22}}{\rho} = -\nu_t\, 2\, \frac{\partial \langle v \rangle}{\partial y} + \frac{2}{3} k\,. \tag{D.9}$$

Table D.1: Summary of the expressions used to compute the statistics from the time series returned by a uRaNS simulation.

$\langle u'u' \rangle = -\nu_t 2 \dfrac{\partial \langle u \rangle}{\partial x} + \dfrac{2}{3} k$	
$\langle v'v' \rangle = -\nu_t 2 \dfrac{\partial \langle v \rangle}{\partial y} + \dfrac{2}{3} k$	
$\langle w'w' \rangle = -\nu_t 2 \dfrac{\partial \langle w \rangle}{\partial z} + \dfrac{2}{3} k$	
$\overline{u} = \dfrac{1}{N_T} \sum_{n=1}^{N_T} \langle u \rangle_n$	$\sigma_u^2 = \dfrac{1}{N_T} \sum_{n=1}^{N_T} \langle u \rangle_n^2 + \langle u'u' \rangle_n - (\overline{u})^2$
$\overline{v} = \dfrac{1}{N_T} \sum_{n=1}^{N_T} \langle v \rangle_n$	$\sigma_v^2 = \dfrac{1}{N_T} \sum_{n=1}^{N_T} \langle v \rangle_n^2 + \langle v'v' \rangle_n - (\overline{v})^2$
$\overline{w} = \dfrac{1}{N_T} \sum_{n=1}^{N_T} \langle w \rangle_n$	$\sigma_w^2 = \dfrac{1}{N_T} \sum_{n=1}^{N_T} \langle w \rangle_n^2 + \langle w'w' \rangle_n - (\overline{w})^2$
$\langle m \rangle = \sqrt{\langle u \rangle^2 + \langle v \rangle^2}$	$\langle m'm' \rangle = \langle u'u' \rangle + \langle v'v' \rangle$
$\overline{m} = \dfrac{1}{N_T} \sum_{n=1}^{N_T} \langle m \rangle_n$	$\sigma_m^2 = \dfrac{1}{N_T} \sum_{n=1}^{N_T} \langle m \rangle_n^2 + \langle m'm' \rangle_n - (\overline{m})^2$
$\widetilde{u} = \dfrac{1}{N_T} \sum_{n=1}^{N_T} \dfrac{\langle u \rangle_n}{\langle m \rangle_n}$	$\widetilde{v} = \dfrac{1}{N_T} \sum_{n=1}^{N_T} \dfrac{\langle v \rangle_n}{\langle m \rangle_n}$
$\overline{\phi} = \begin{cases} \text{arctan2}\,(\widetilde{u},\widetilde{v}) + \pi\,, & \text{arctan2}\,(\widetilde{u},\widetilde{v}) < \pi \\ \text{arctan2}\,(\widetilde{u},\widetilde{v}) - \pi\,, & \text{arctan2}\,(\widetilde{u},\widetilde{v}) \geq \pi \end{cases}$	

The wind direction is computed from the horizontal velocity vector:

$$\phi = \begin{cases} \text{arctan2}\,(u,v) + \pi\,, & \text{arctan2}\,(u,v) < \pi \\ \text{arctan2}\,(u,v) - \pi\,, & \text{arctan2}\,(u,v) \geq \pi \end{cases}\,, \tag{D.10}$$

where the function arctan2 is defined as:

$$\text{arctan2}\,(u,v) = \begin{cases} 2 \arctan\left(\dfrac{\sqrt{u^2+v^2}-v}{u}\right), & u \neq 0 \\ 0 \qquad\qquad\qquad\qquad\quad , & u = 0 \ \wedge \ v > 0 \\ \pi \qquad\qquad\qquad\qquad\quad , & u = 0 \ \wedge \ v \leq 0 \end{cases}\,. \tag{D.11}$$

These expressions are compliant with the meteorological definition for the azimuth angle, *i.e.*, measured clockwise with 0 pointing to the north. To obtain the mean wind direction, at each time-step both components from the horizontal vector are normalized by its magnitude. The angle is computed using the normalized components averaged over ΔT.

The expressions presented in this section are summarized in Table D.1.

Appendix E

Results from the mesoscale-microscale coupling

E.1 WRF forecasts errors for the 3km domain

E.1.1 Period from 2005-07-01 to 2005-07-15

E.1.1.1 Wind speed histograms and wind roses

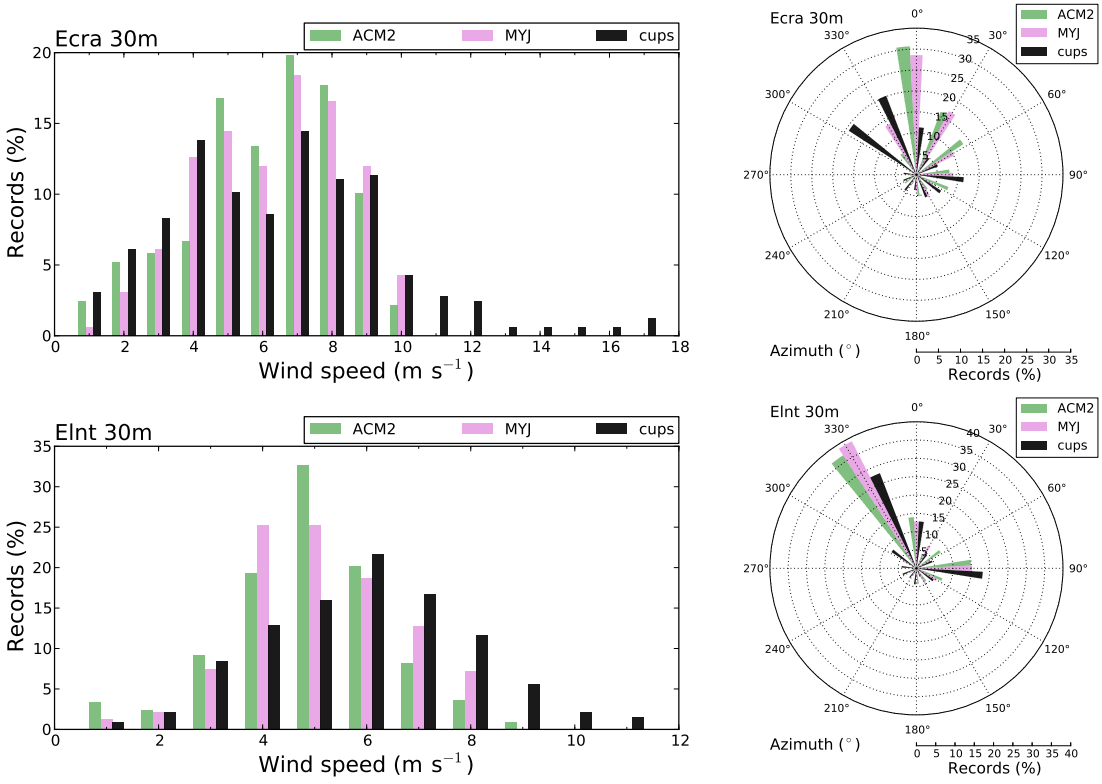

(a) Meteorological masts in Cabeço da Rainha.

Figure E.1: *Caption in page 271.*

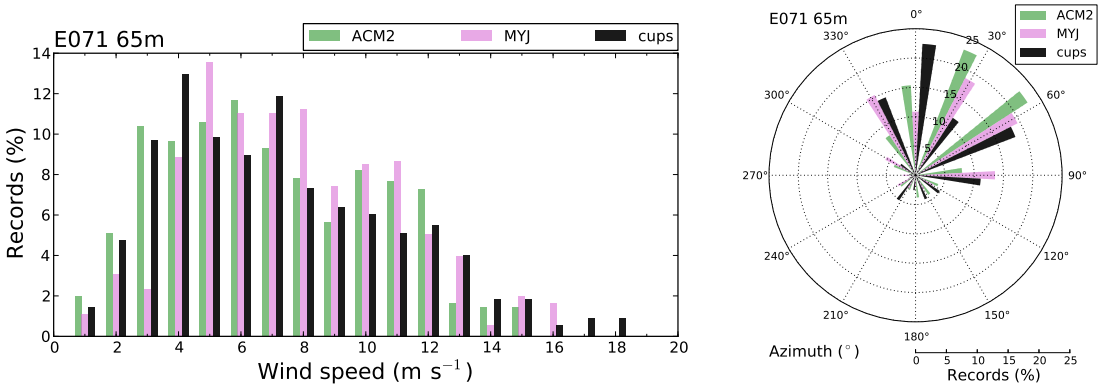

(b) Meteorological mast in Pinheiro.

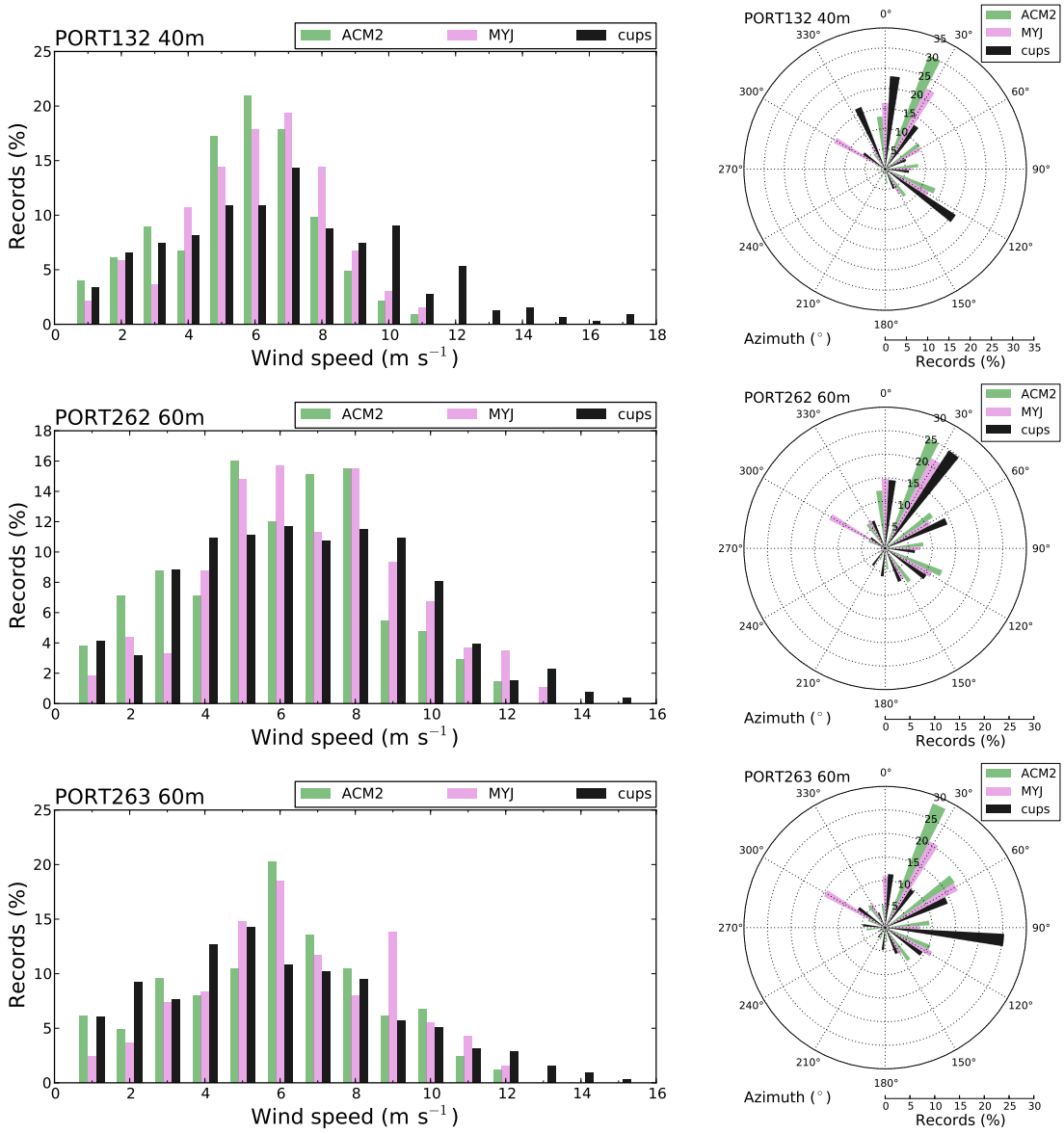

(c) Meteorological masts in Alto do Corisco.

Figure E.1: *Caption in page 271*.

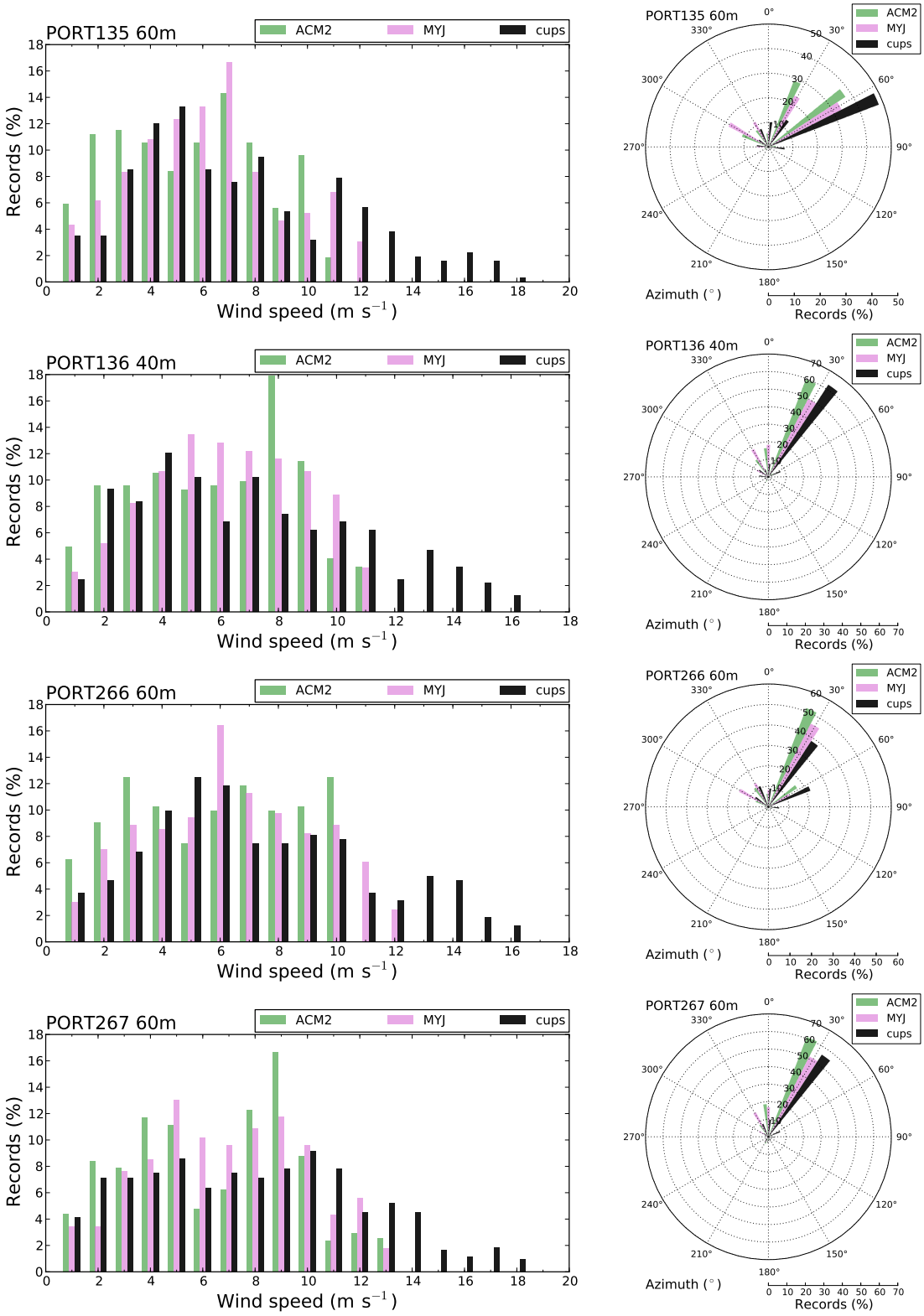

(d) Meteorological masts in Mendoiro.

Figure E.1: Histograms and wind roses for the WRF simulations using the ACM2 and MYJ parameterizations for the PBL.

E.1.1.2 Scatter plots and correlation coefficients for the ACM2 results

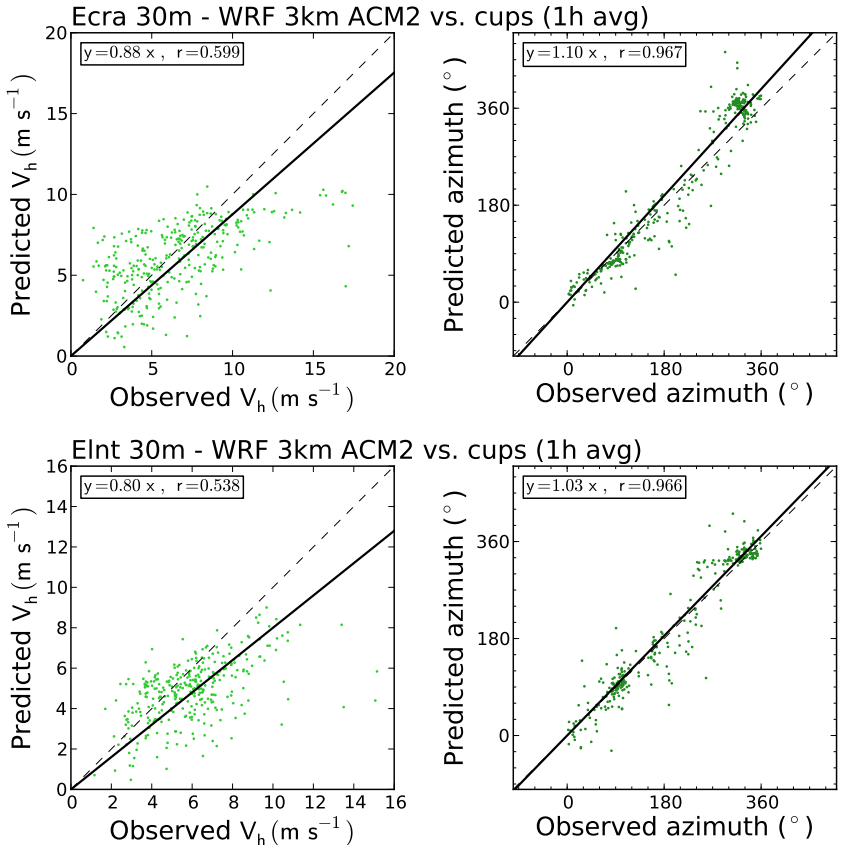

(a) Meteorological masts in Cabeço da Rainha.

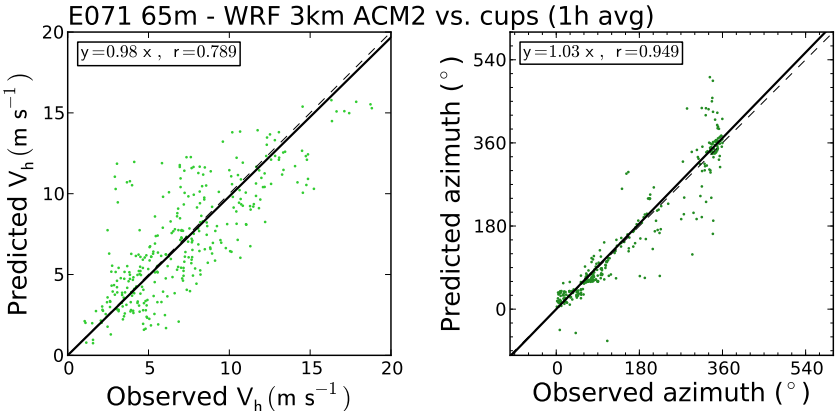

(b) Meteorological masts in Pinheiro.

Figure E.2: Scatter plots of wind speed and azimuth for the WRF simulations using the nonlocal PBL parameterization ACM2. The black continuous line represents a linear regression forced through the origin, where its coefficient is given by the expression at the top left corner, together with the Pearson's correlation coefficient.

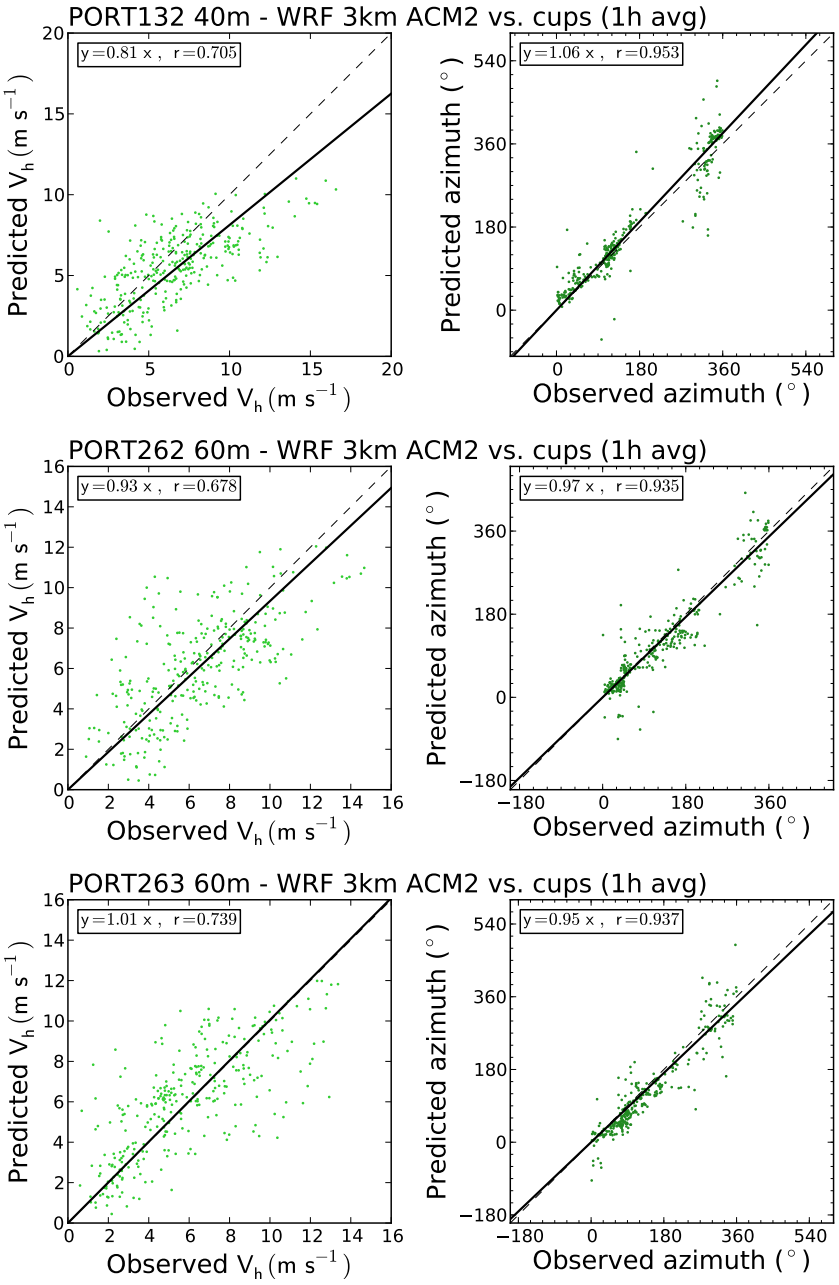

(c) Meteorological masts in Alto do Corisco.

Figure E.2: *Caption in page 272*.

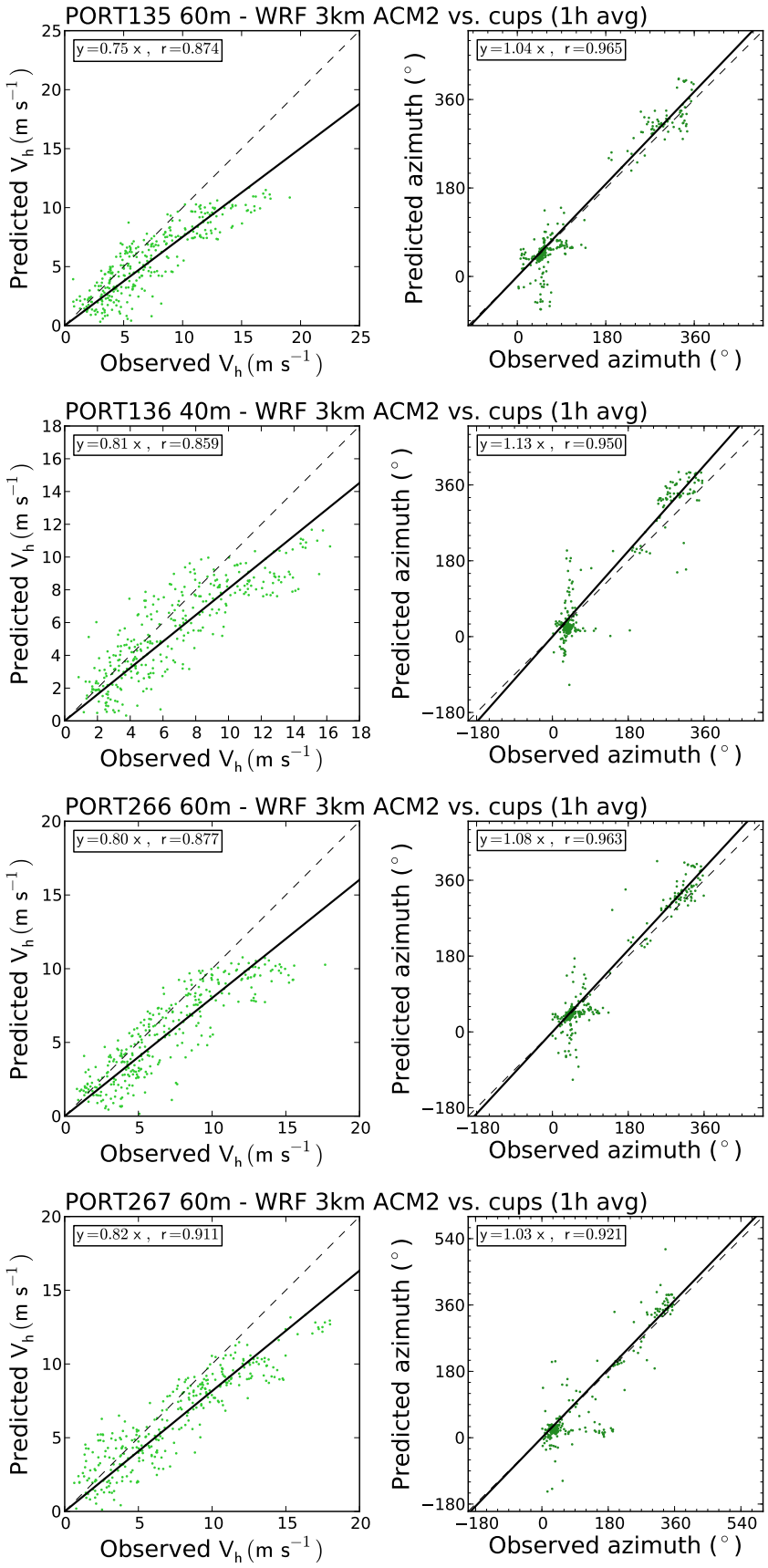

(d) Meteorological masts in Mendoiro.

Figure E.2: *Caption in page 272.*

E.1.2 Period from 2005-11-19 to 2005-12-3

E.1.2.1 Wind speed histograms and wind roses

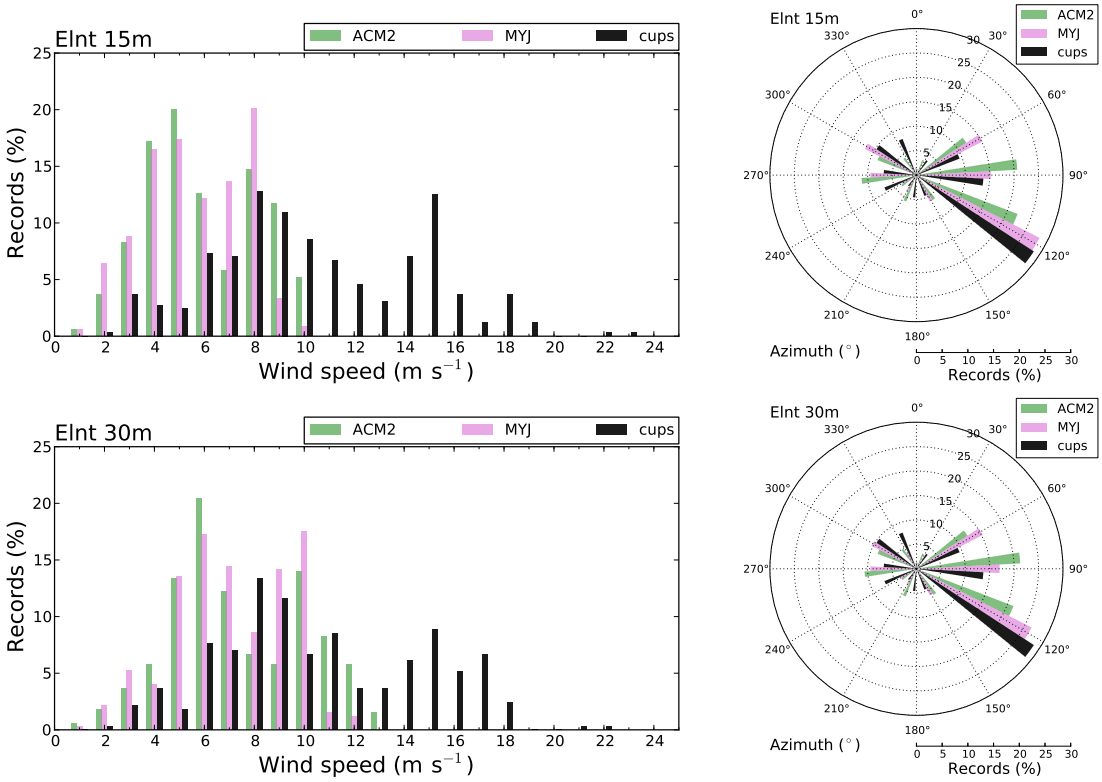

(a) Meteorological masts in Cabeço da Rainha.

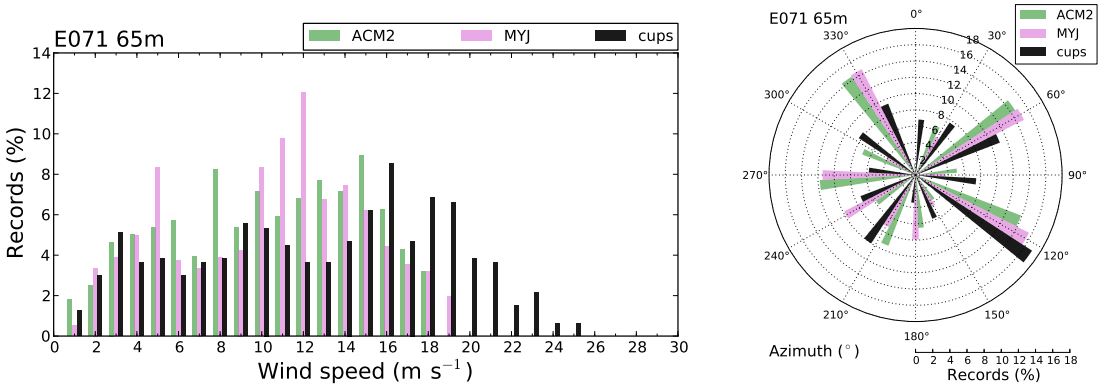

(b) Meteorological masts in Pinheiro.

Figure E.3: *Caption in page 277*.

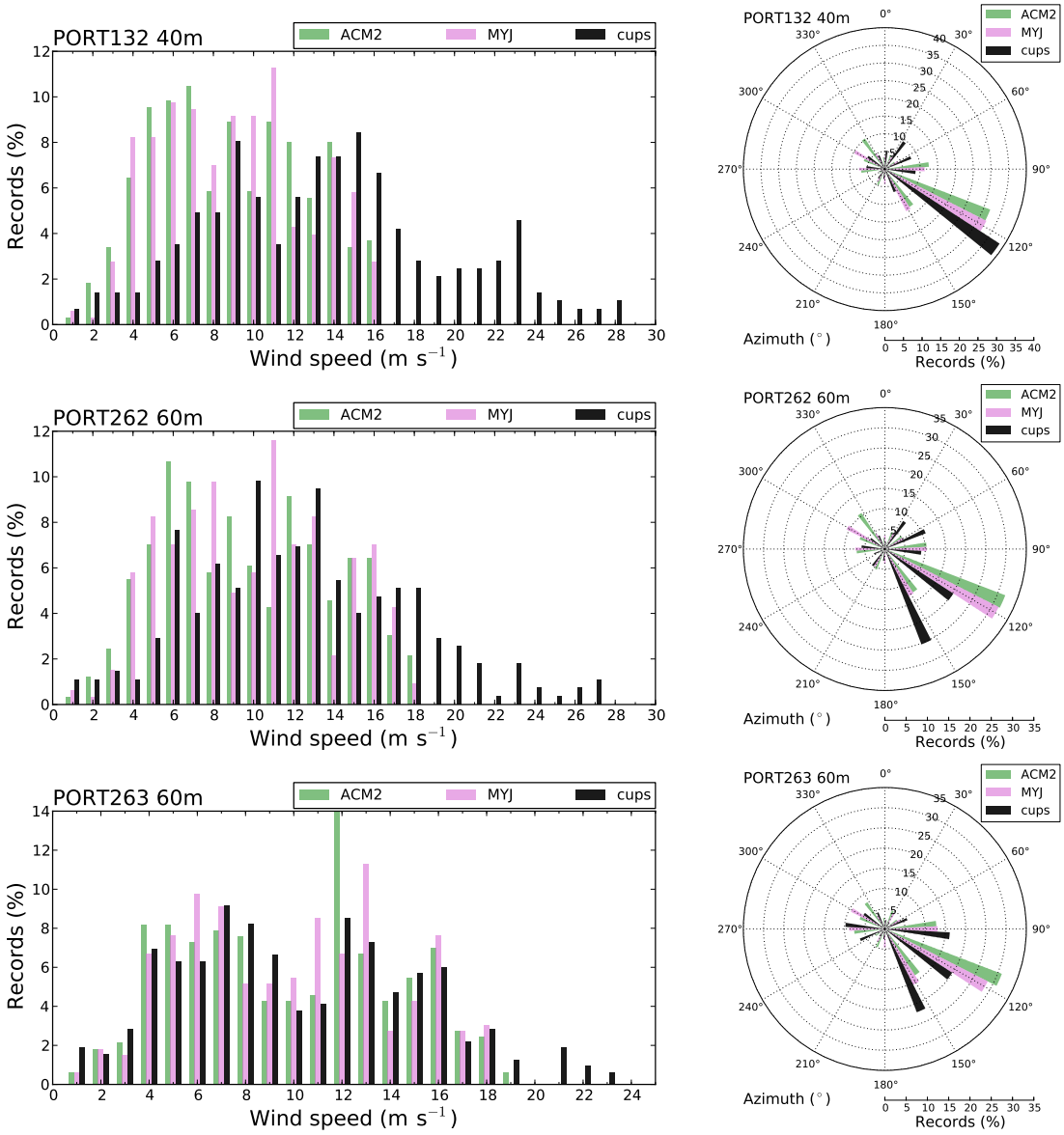

(c) Meteorological masts in Alto do Corisco.

Figure E.3: *Caption in page 277.*

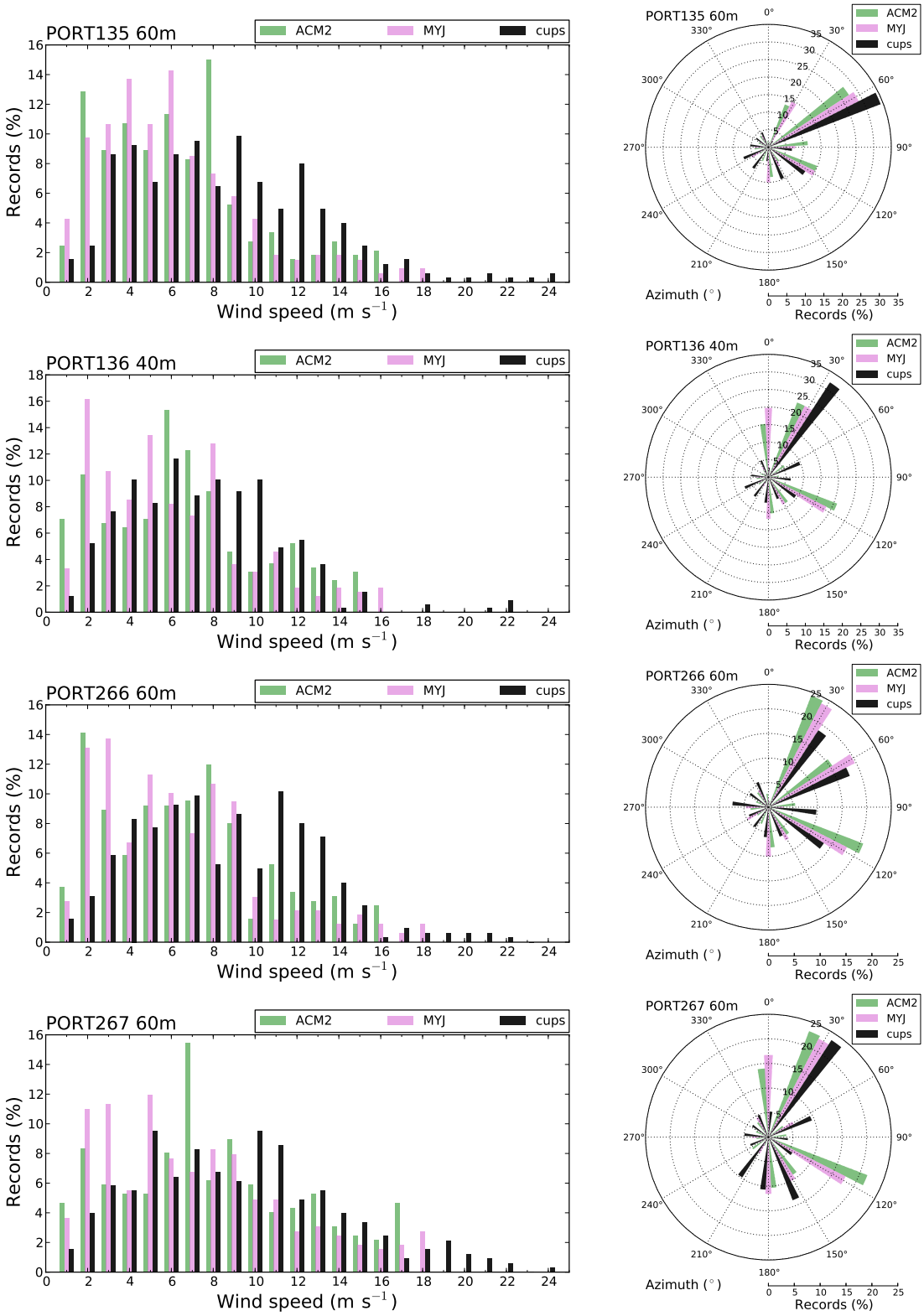

(d) Meteorological masts in Mendoiro.

Figure E.3: Histograms and wind roses for the WRF simulations using the ACM2 and MYJ parameterizations for the PBL.

E.1.2.2 Scatter plots for the ACM2 results

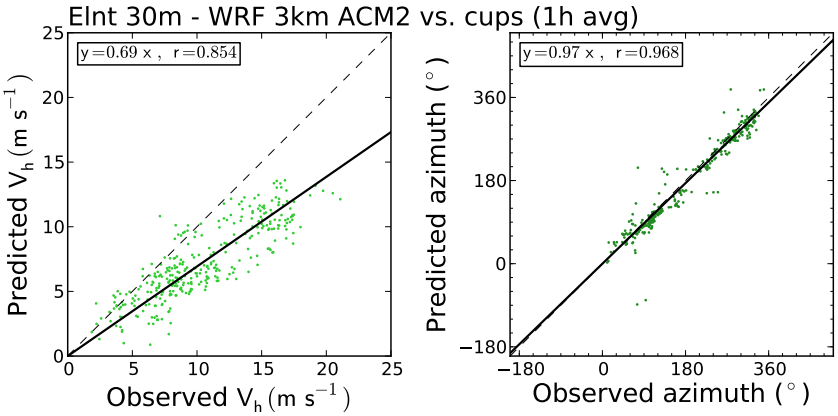

(a) Meteorological masts in Cabeço da Rainha.

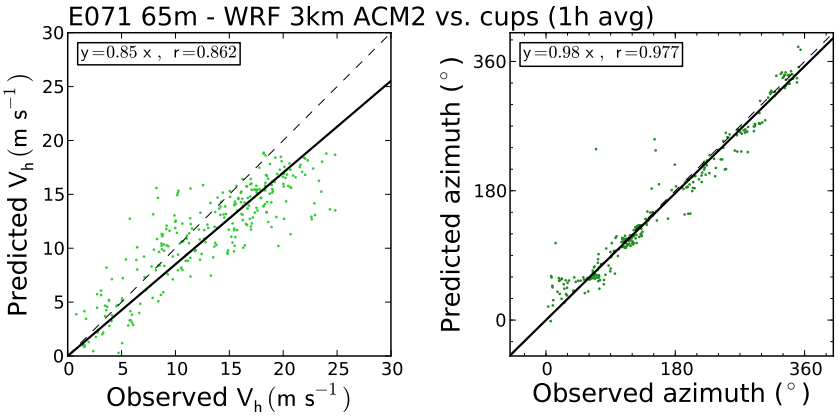

(b) Meteorological masts in Pinheiro.

Figure E.4: Scatter plots of wind speed and azimuth for the WRF simulations using the nonlocal PBL parameterization ACM2. For details refer to Figure E.2.

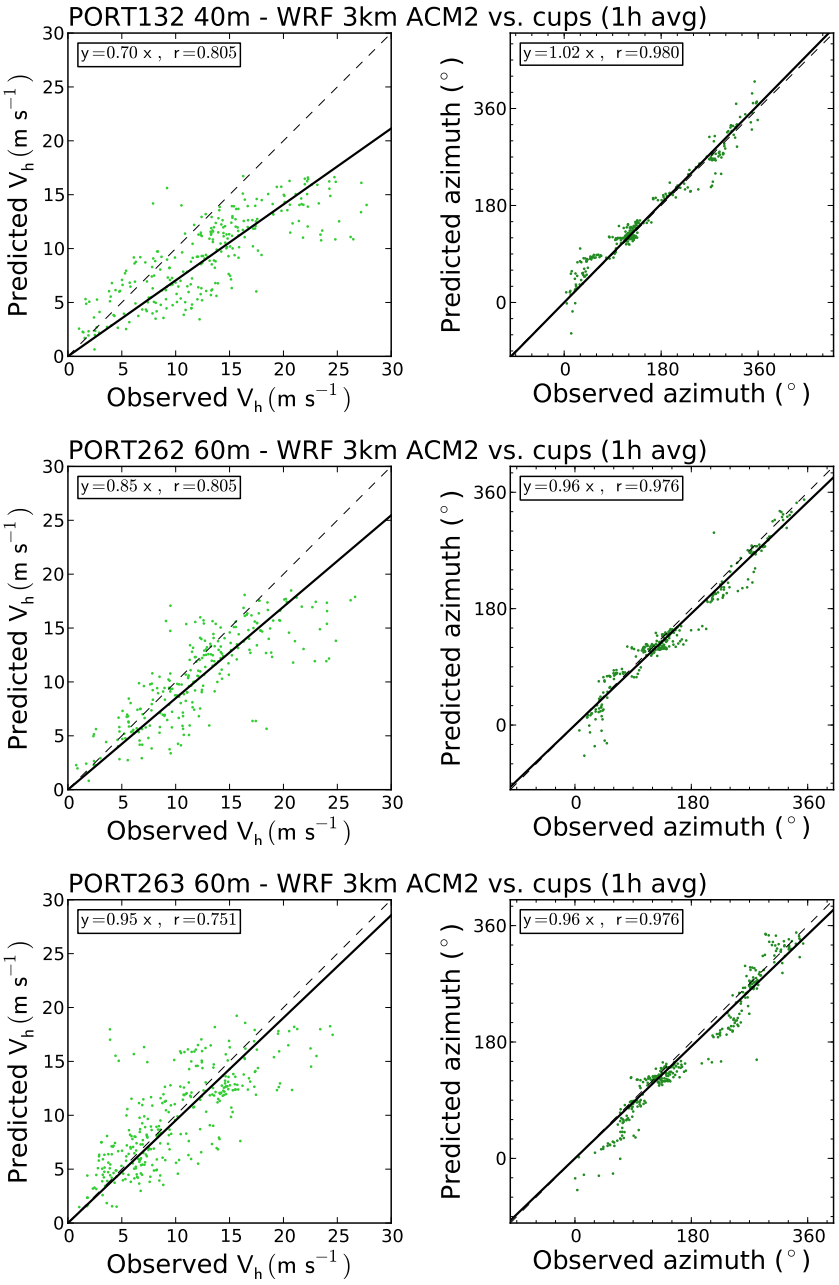

(c) Meteorological masts in Alto do Corisco.

Figure E.4: *Caption in page 278*.

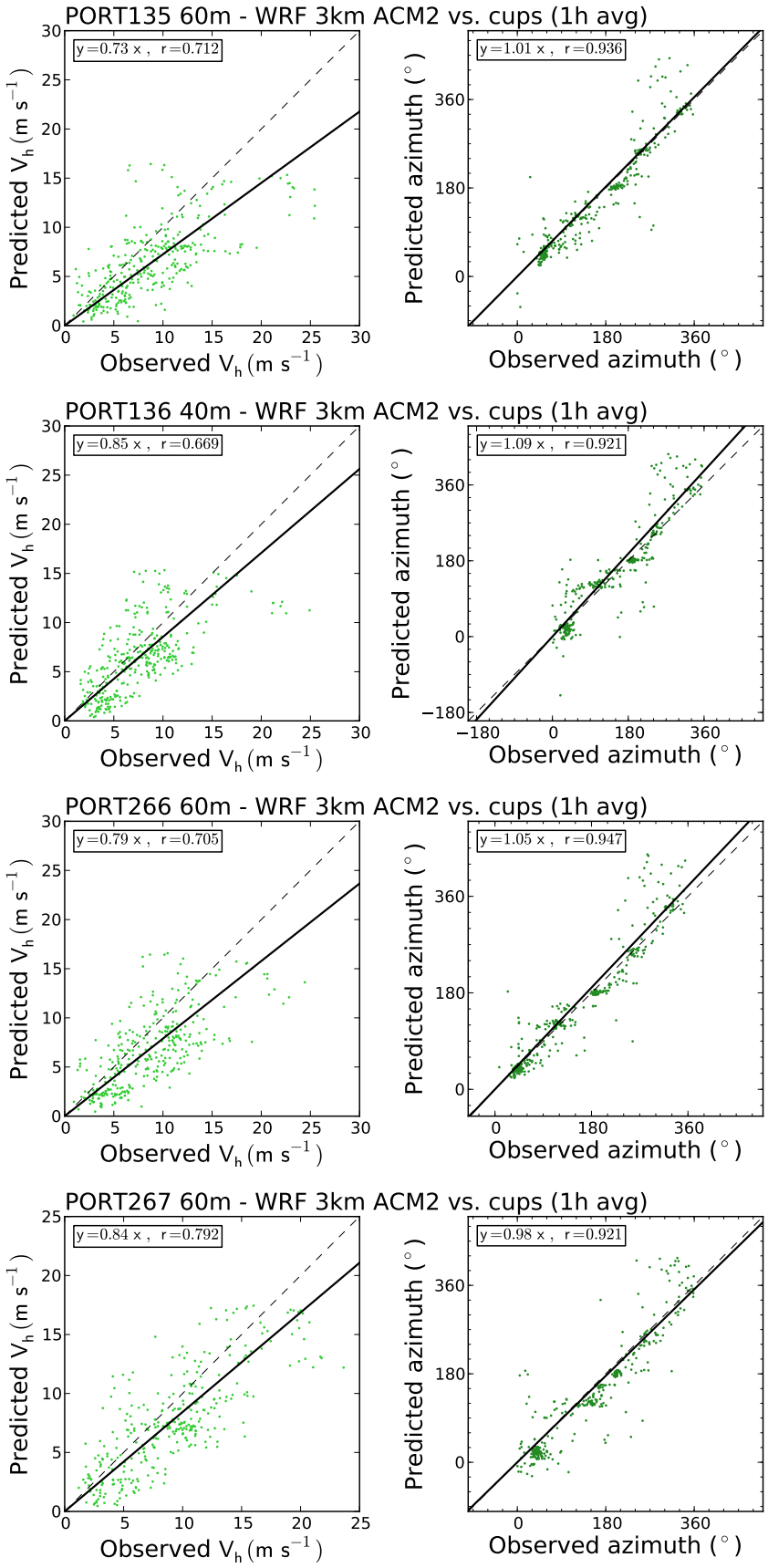

(d) Meteorological masts in Mendoiro.

Figure E.4: *Caption in page 278.*

E.2 Mesoscale and microscale results

E.2.1 Period from 2005-07-01 to 2005-07-15

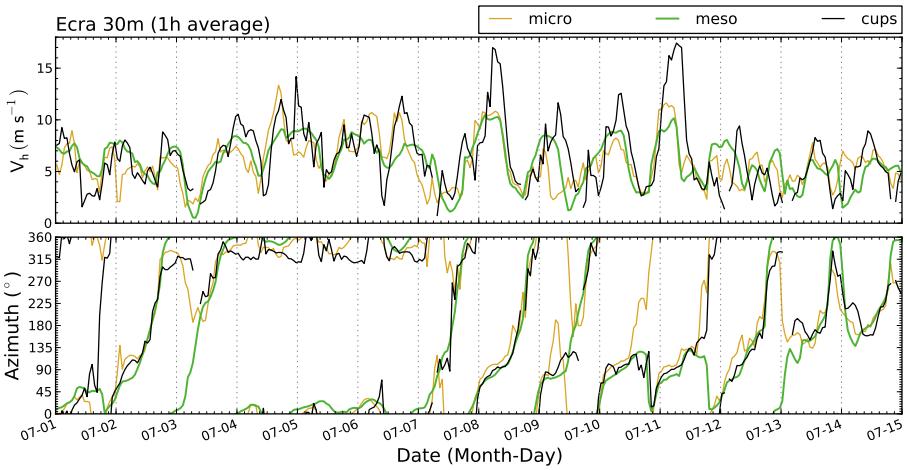

(a) Meteorological mast in Cabeço da Rainha (Ecra).

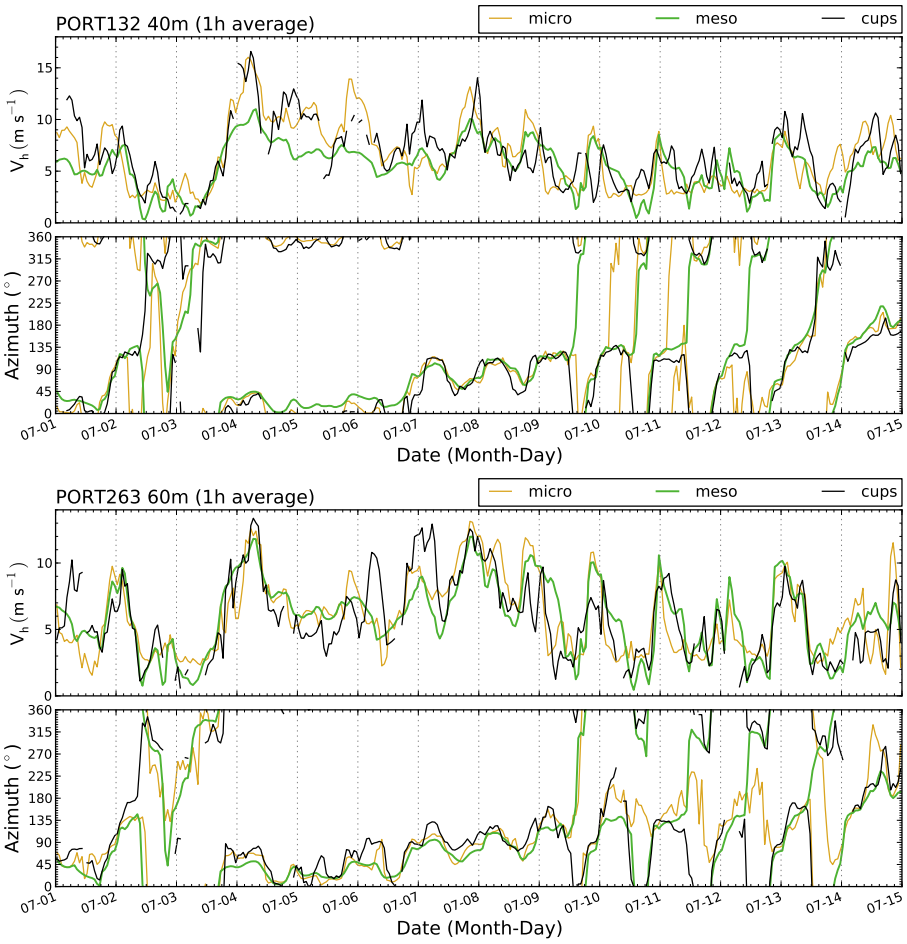

(b) Meteorological masts in Alto do Corisco.

Figure E.5: *Caption in page 282.*

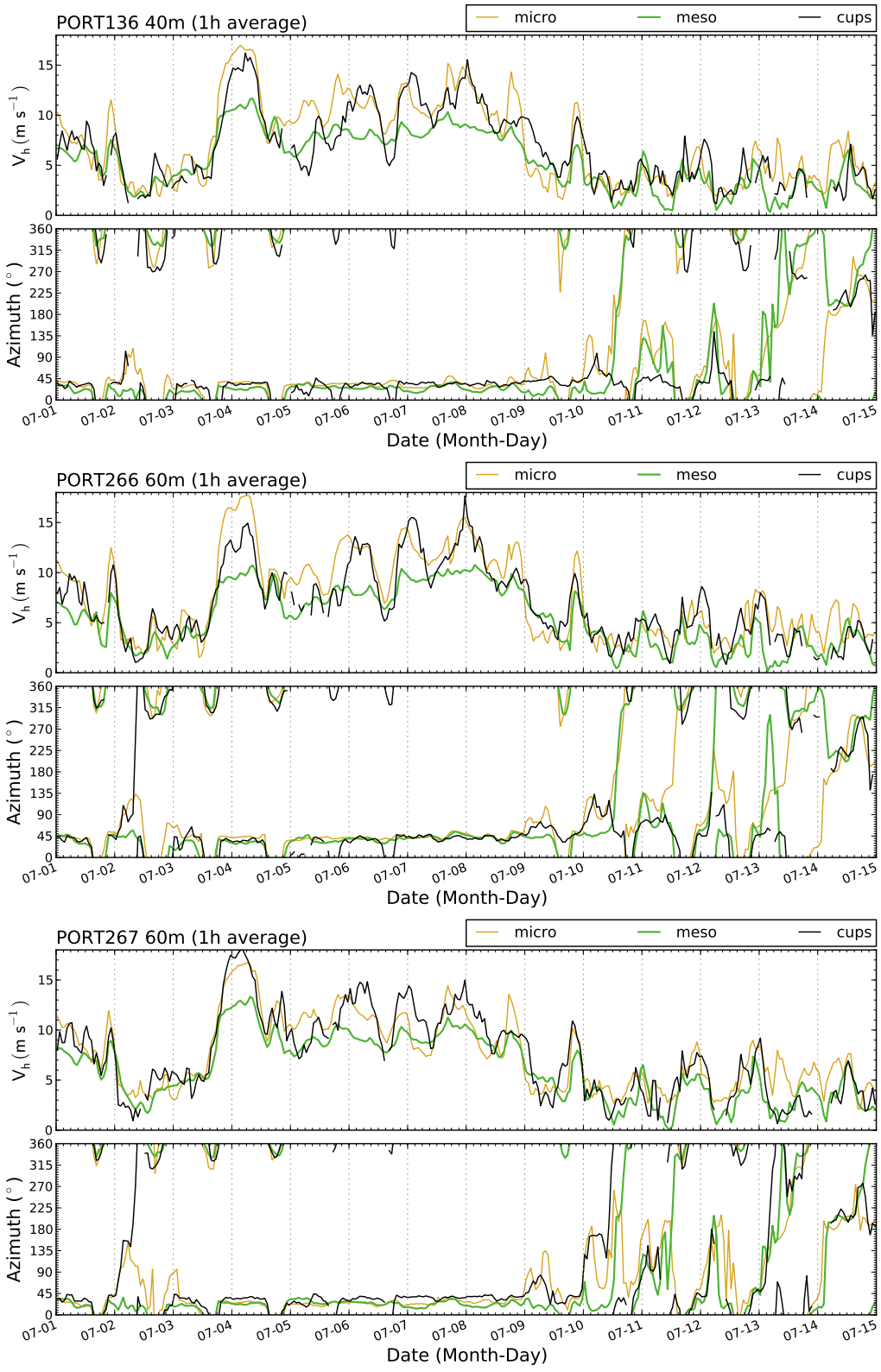

(c) Meteorological masts in Mendoiro.

Figure E.5: Time series of wind speed and direction of the mesoscale and microscale forecasts, together with the field measurements. The results refer to the period between 2005-07-01 to 2005-07-15.

E.2.1.1 Wind speed histograms and wind roses

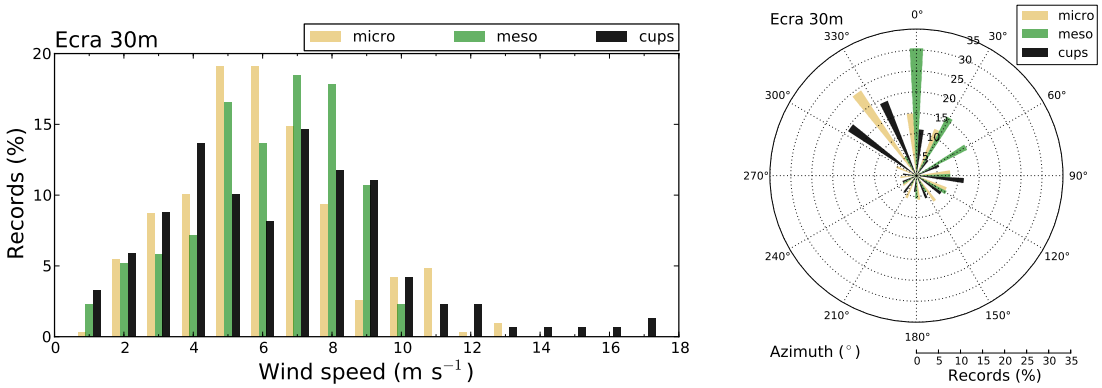

(a) Meteorological mast in Cabeço da Rainha.

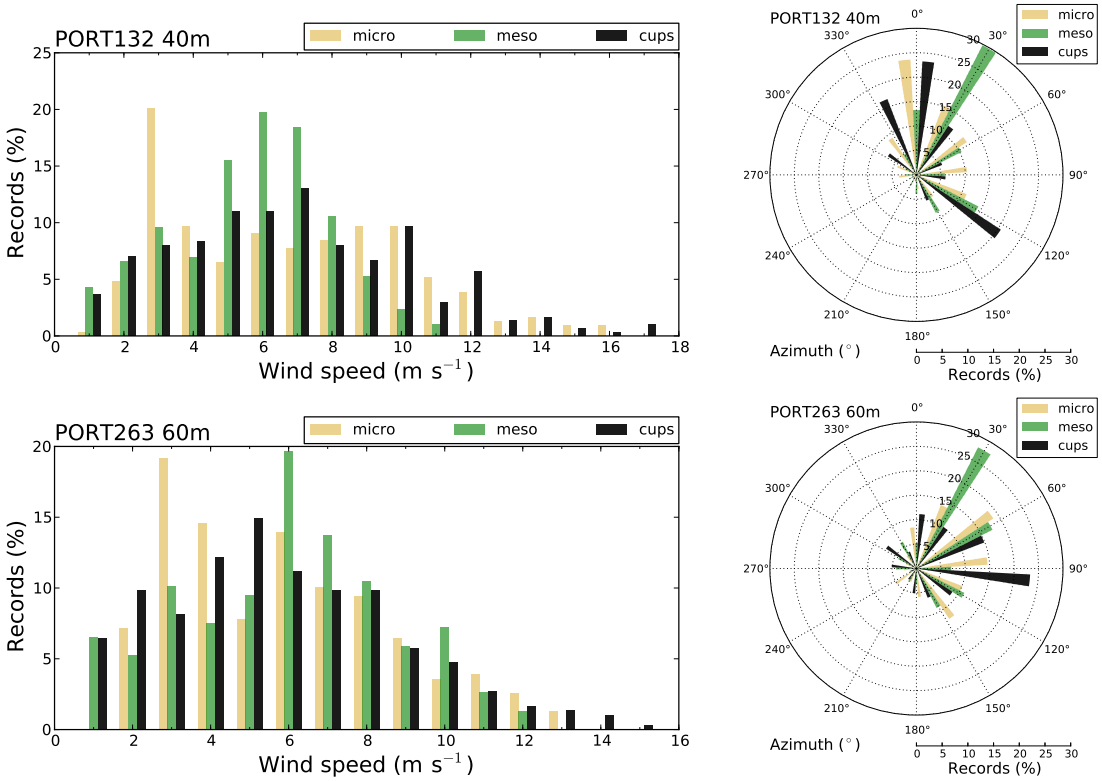

(b) Meteorological mast in Alto do Corisco.

Figure E.6: *Caption in page 284*.

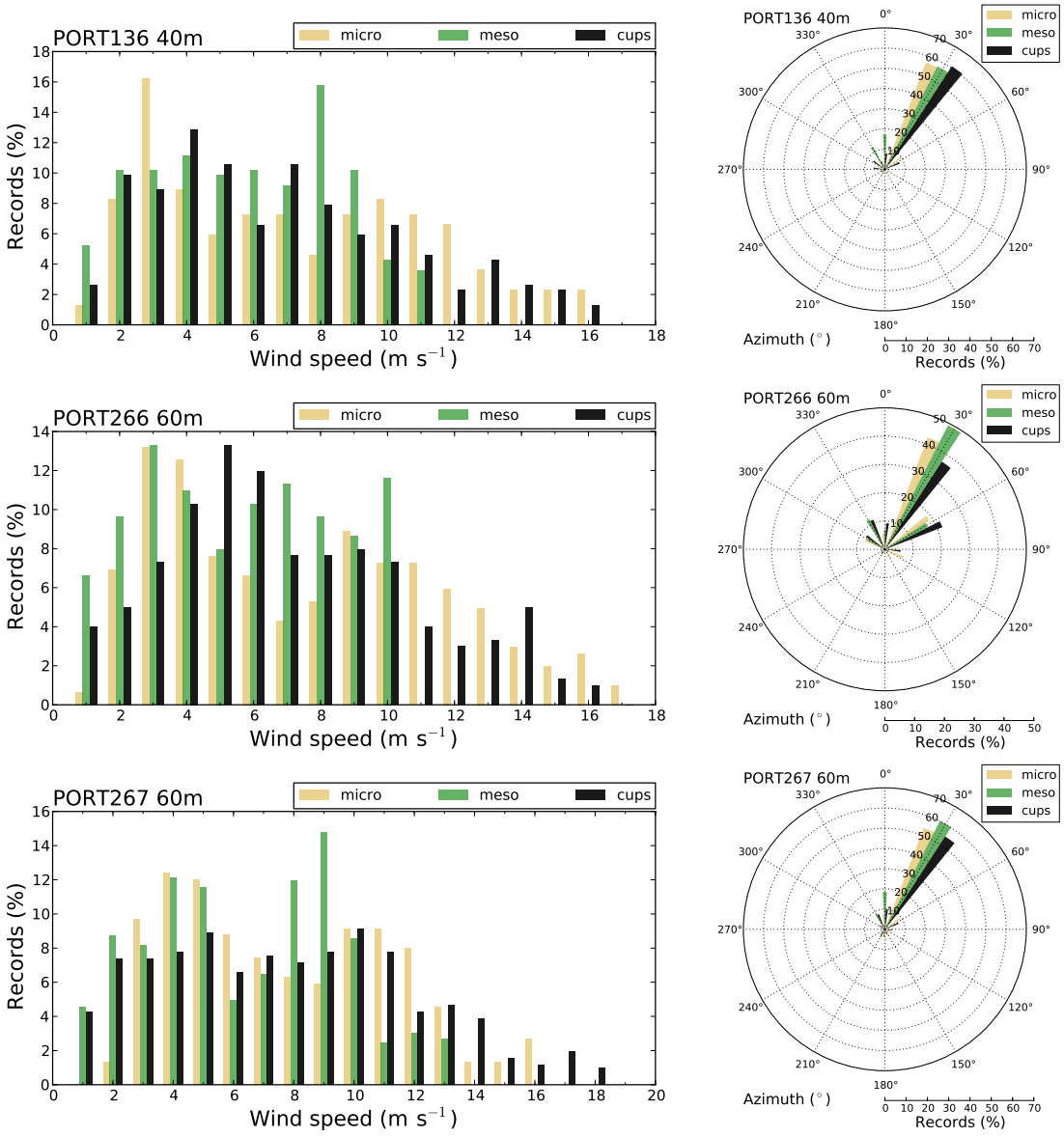

(c) Meteorological mast in Mendoiro.

Figure E.6: Histograms and wind roses for the mesoscale and microscale results, in the period between 2005-07-01 to 2005-07-15.

E.2.1.2 Hovmöller plots of wind speed and direction

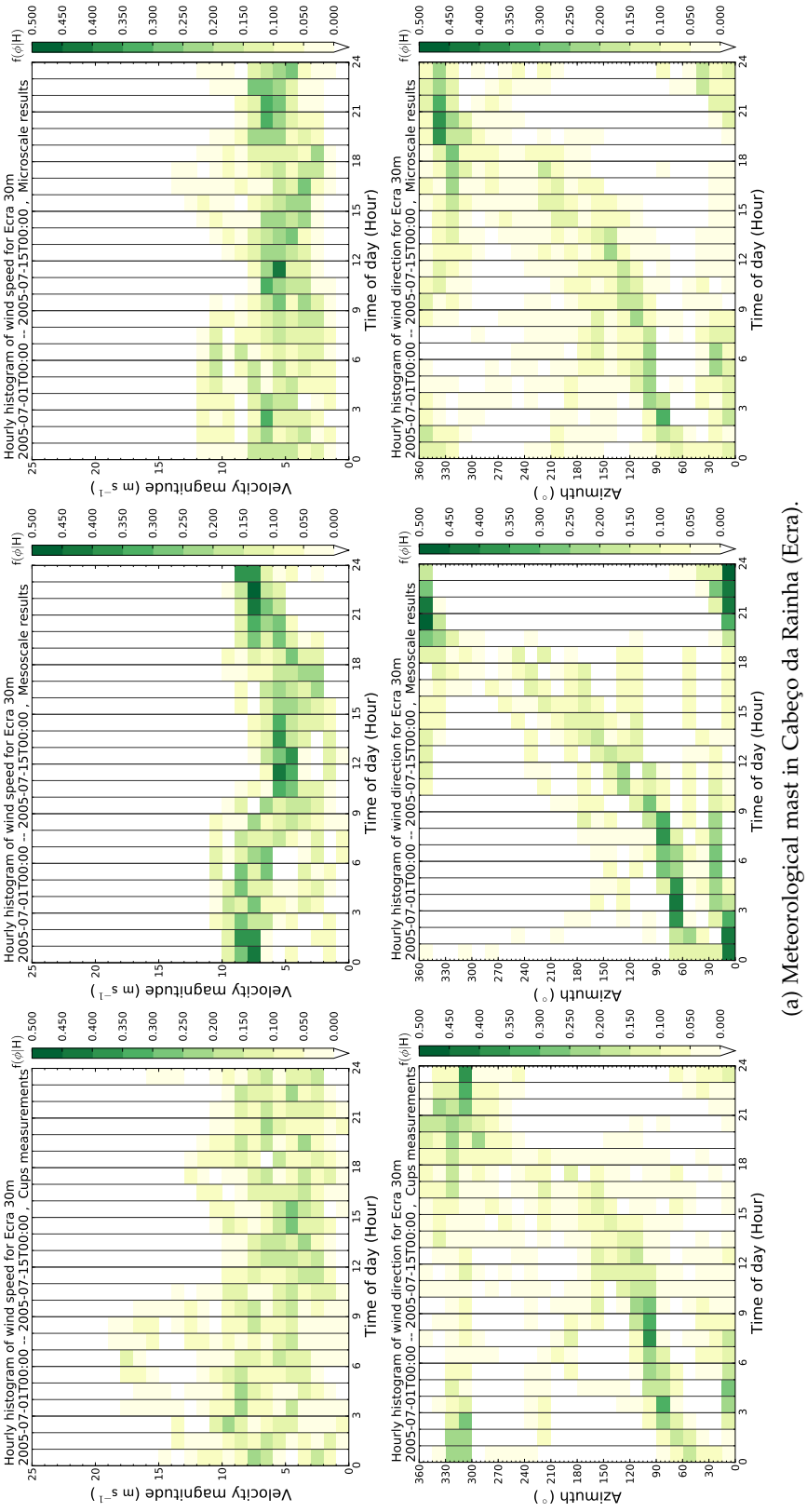

(a) Meteorological mast in Cabeço da Rainha (Ecra).

Figure E.7: *Caption in page 290.*

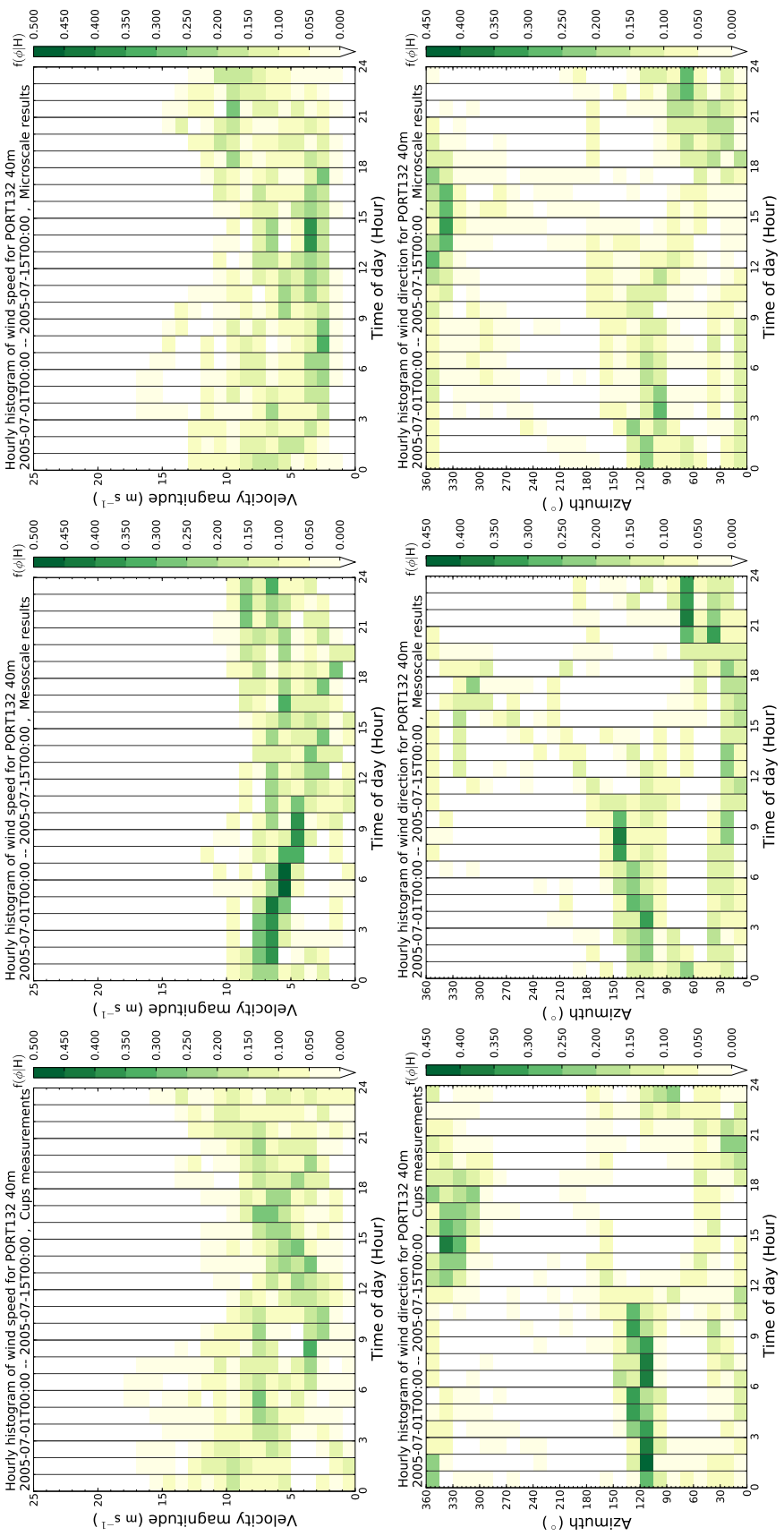

(b) Meteorological mast in Alto do Corisco (PORT132).

Figure E.7: *Caption in page 290.*

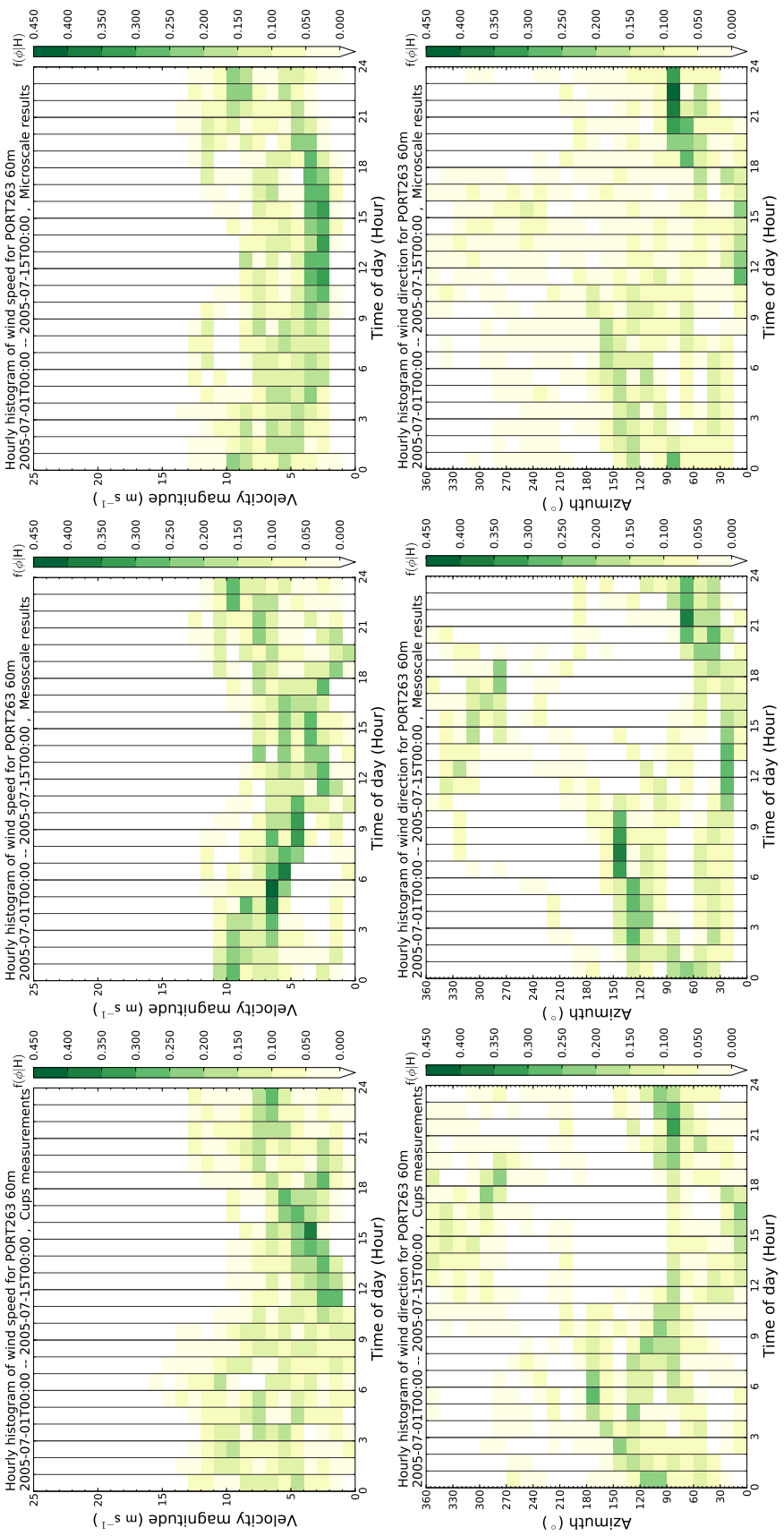

(c) Meteorological mast in Alto do Corisco (PORT263).

Figure E.7: *Caption in page 290.*

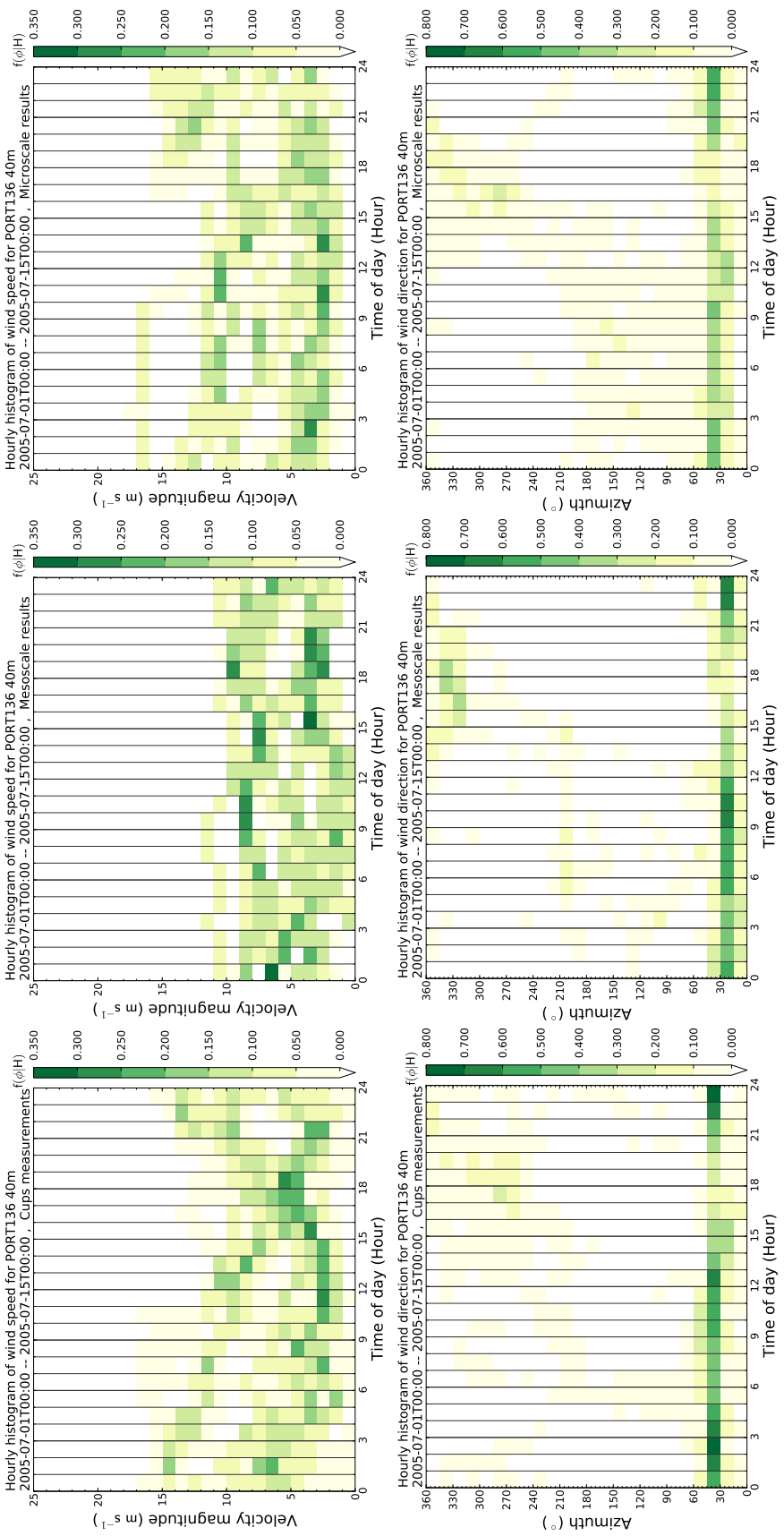

(d) Meteorological mast in Mendoiro (PORT136).

Figure E.7: *Caption in page 290.*

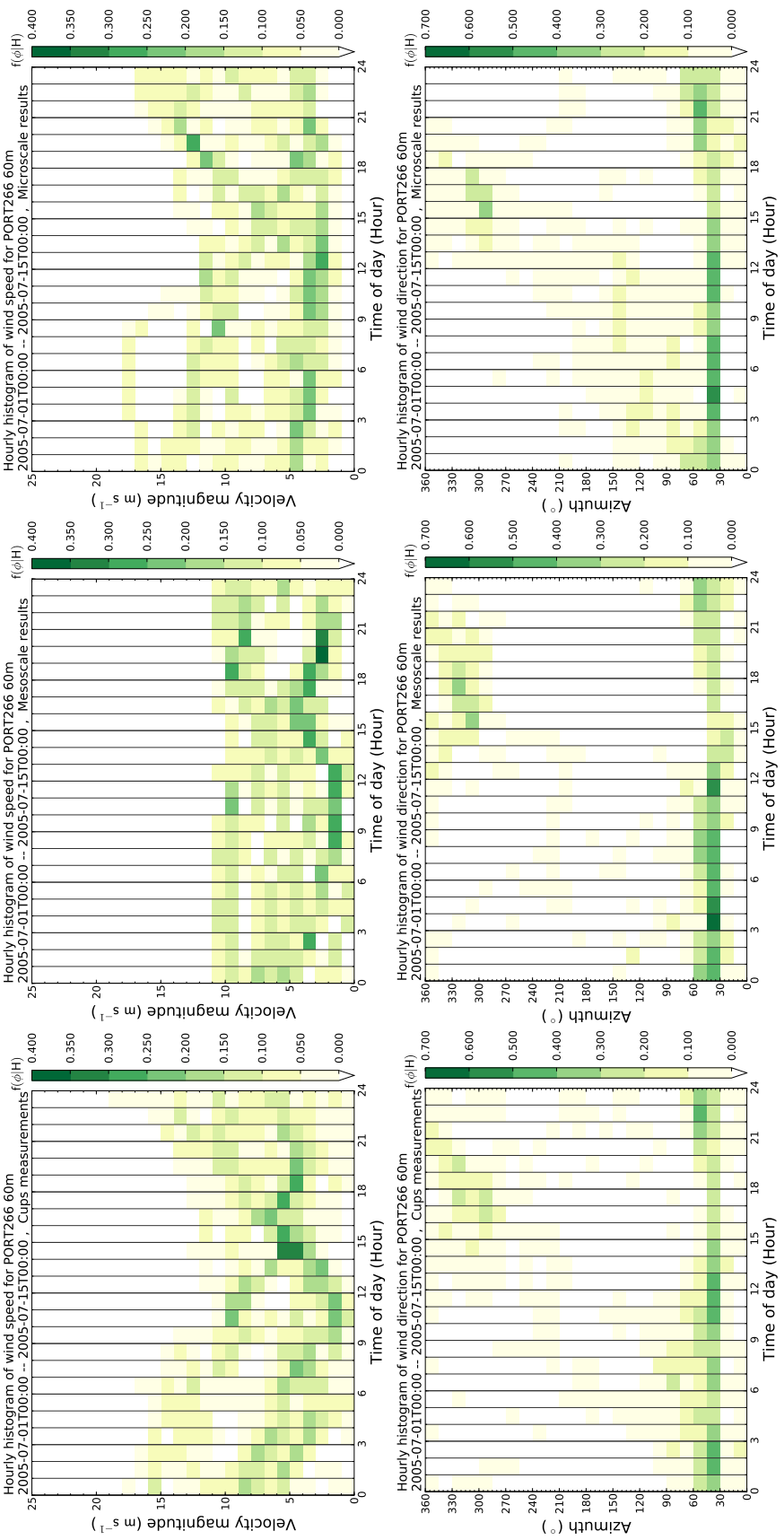

(e) Meteorological mast in Mendoiro (PORT266).

Figure E.7: *Caption in page 290.*

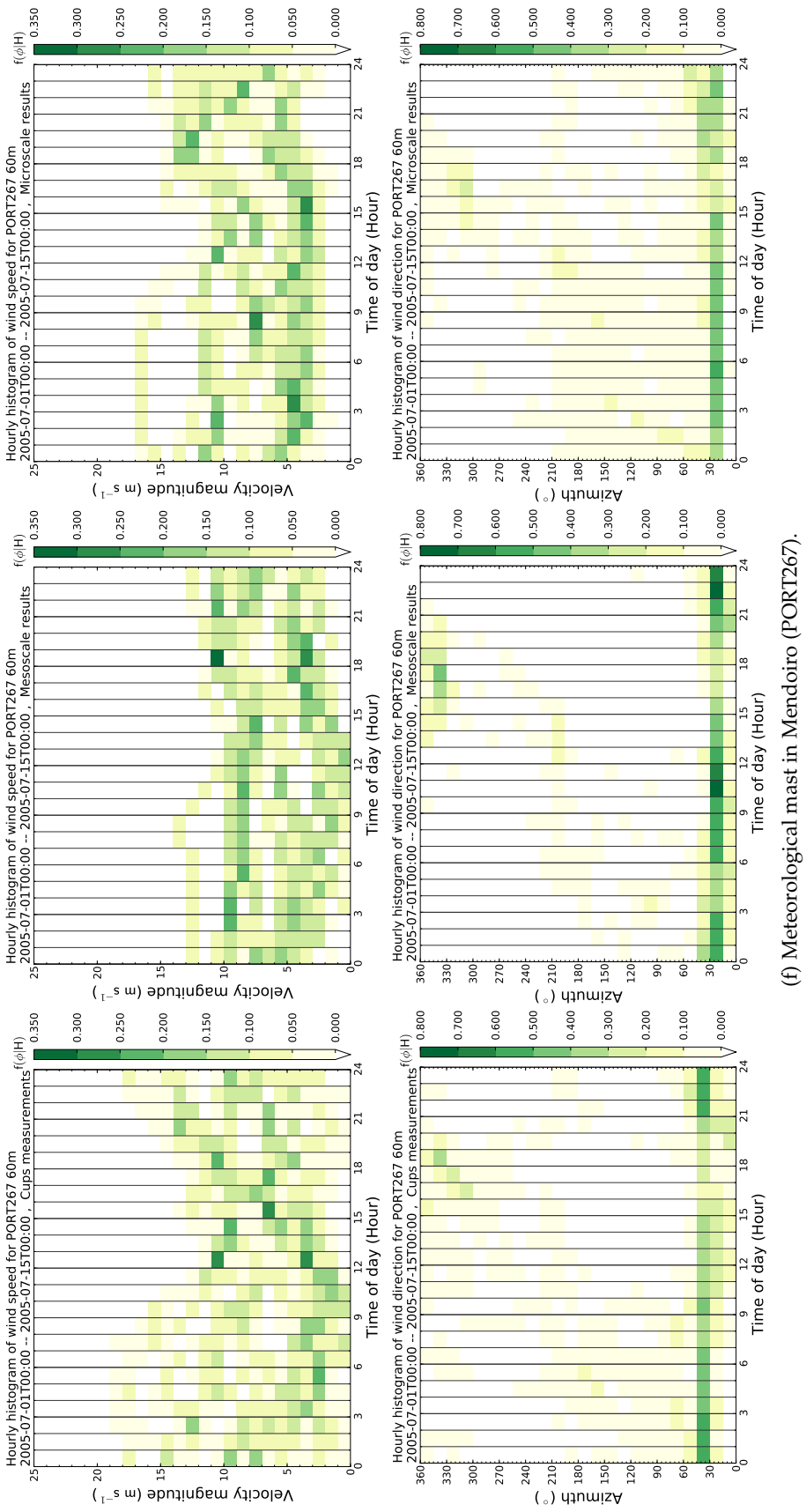

(f) Meteorological mast in Mendoiro (PORT267).

Figure E.7: Hovmöller plots of wind speed (topmost) and direction (bottommost) for the period between 2005-07-01 to 2005-07-15.

E.2.1.3 Scatter plots for the microscale results

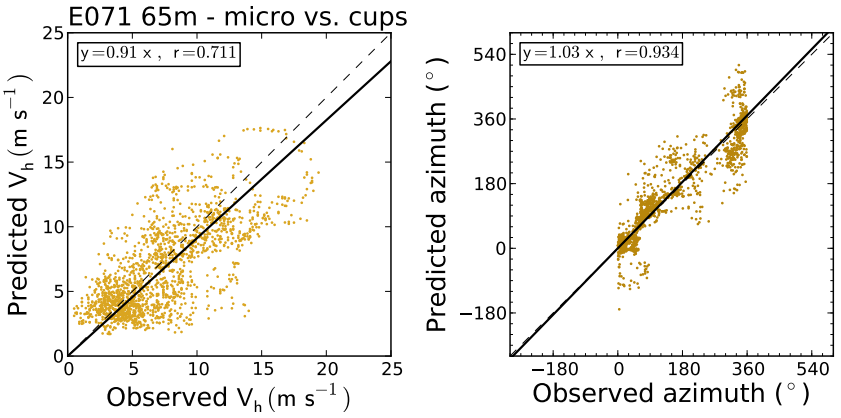

(a) Meteorological mast in Pinheiro.

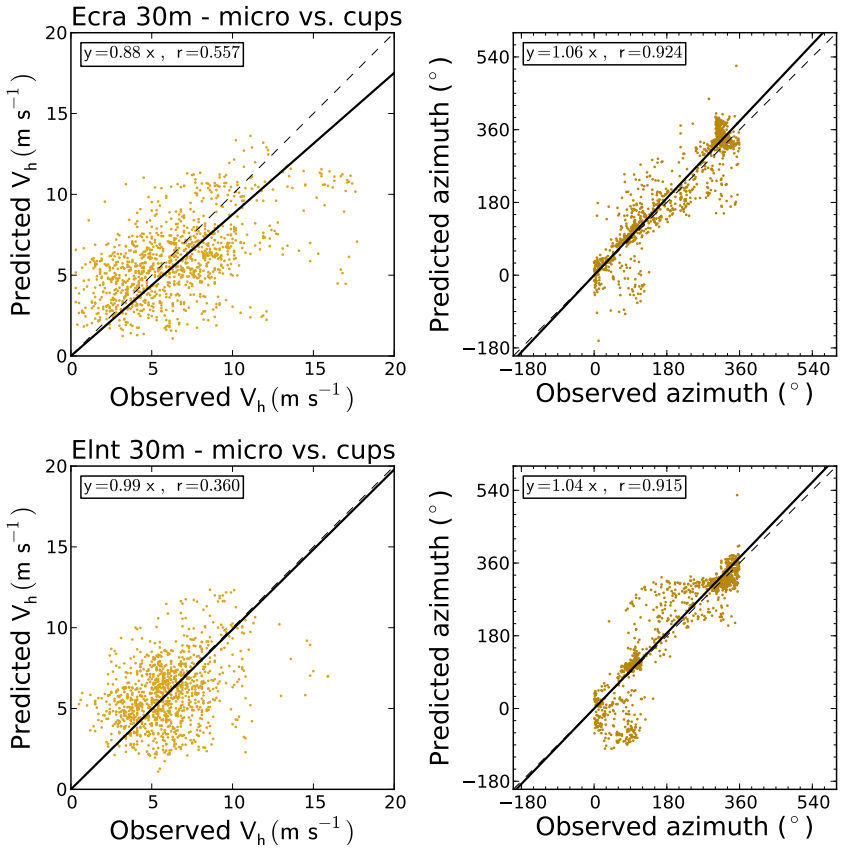

(b) Meteorological mast in Cabeço da Rainha.

Figure E.8: Scatter plots of wind speed and azimuth for the microscale results, in the period between 2005-07-01 to 2005-07-15 (refer to Figure E.2 for a detailed description).

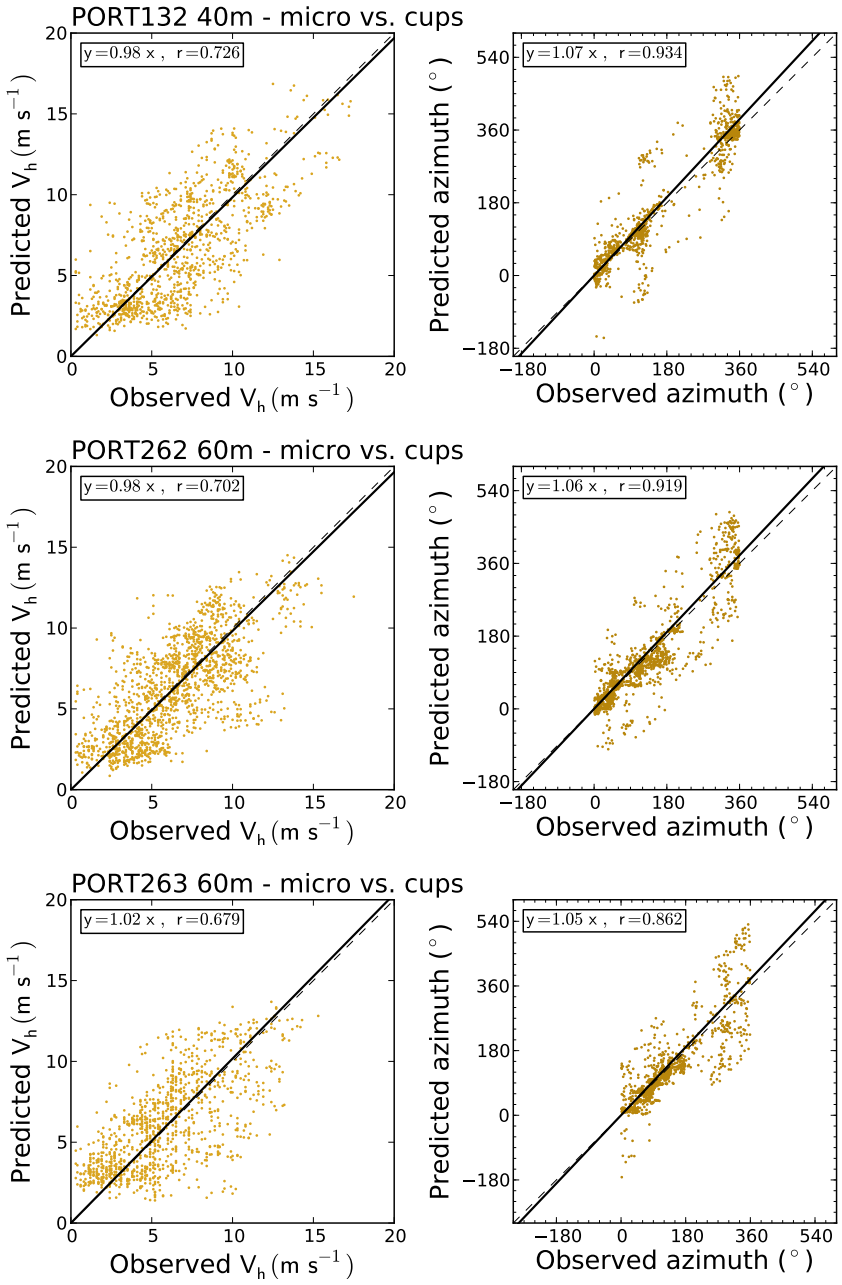

(c) Meteorological mast in Alto do Corisco.

Figure E.8: *Caption in page 291*.

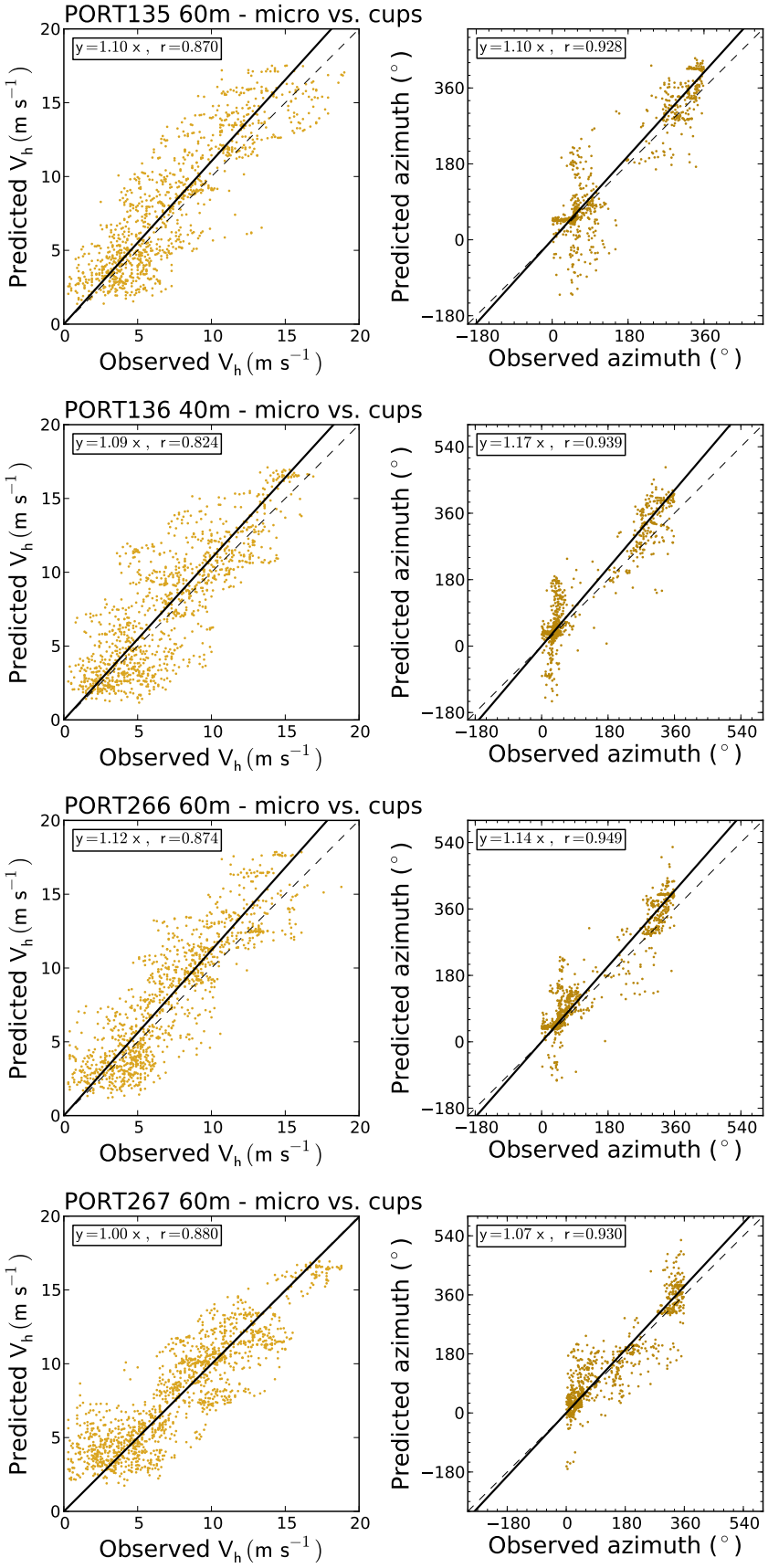

(d) Meteorological mast in Mendoiro.

Figure E.8: *Caption in page 291*.

E.2.2 Period from 2005-11-19 to 2005-12-03

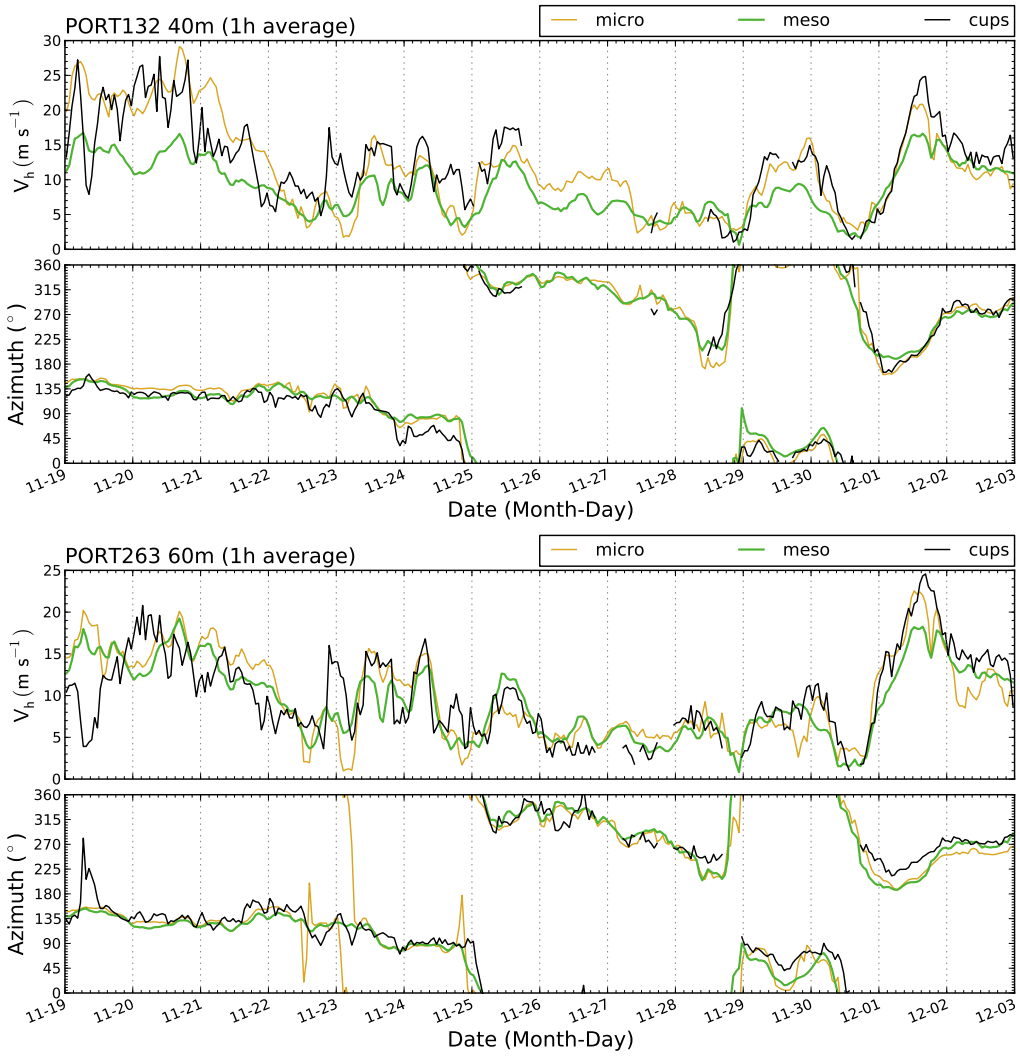

(a) Meteorological masts in Alto do Corisco.

Figure E.9: *Caption in page 295*.

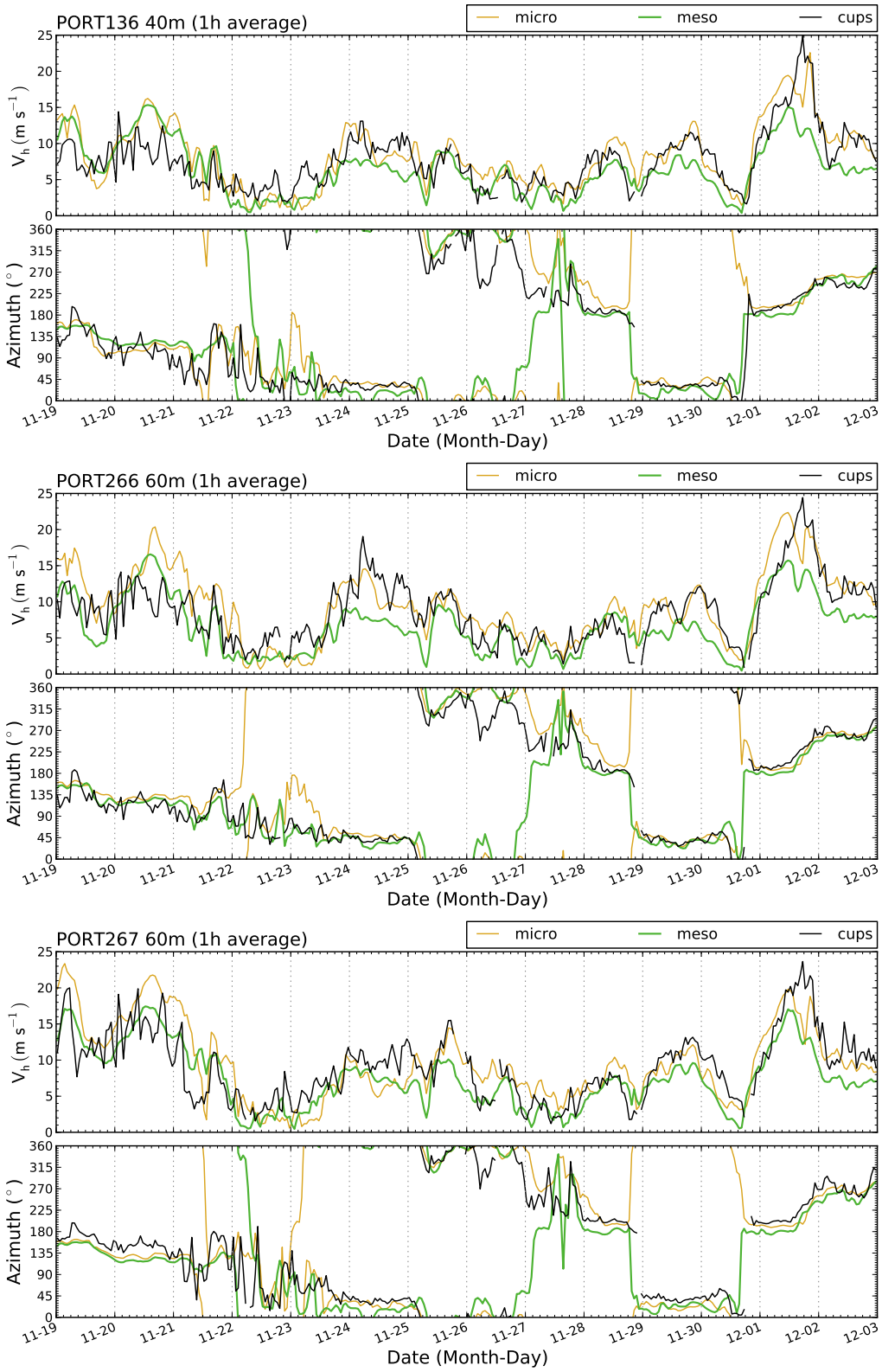

(b) Meteorological masts in Mendoiro.

Figure E.9: Time series of wind speed and direction of the mesoscale and microscale forecasts, together with the field measurements. The results refer to the period between 2005-11-19 to 2005-12-03.

E.2.2.1 Wind speed histograms and wind roses

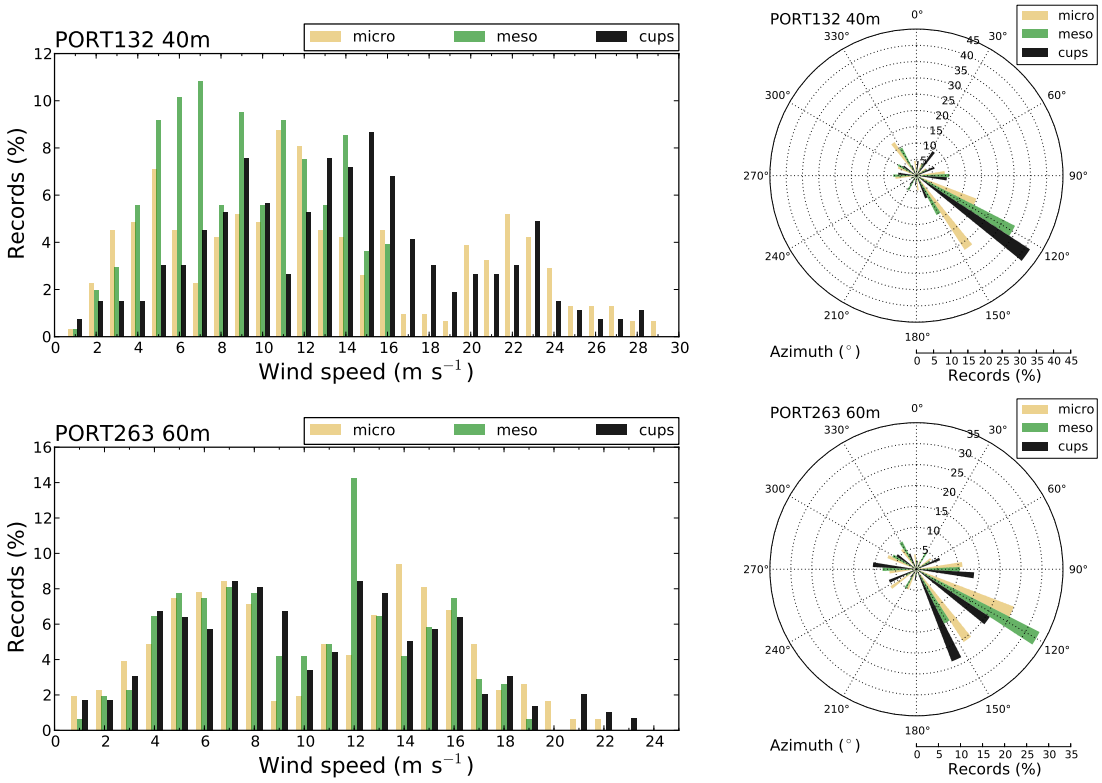

(a) Meteorological mast in Alto do Corisco.

Figure E.10: *Caption in page 297*.

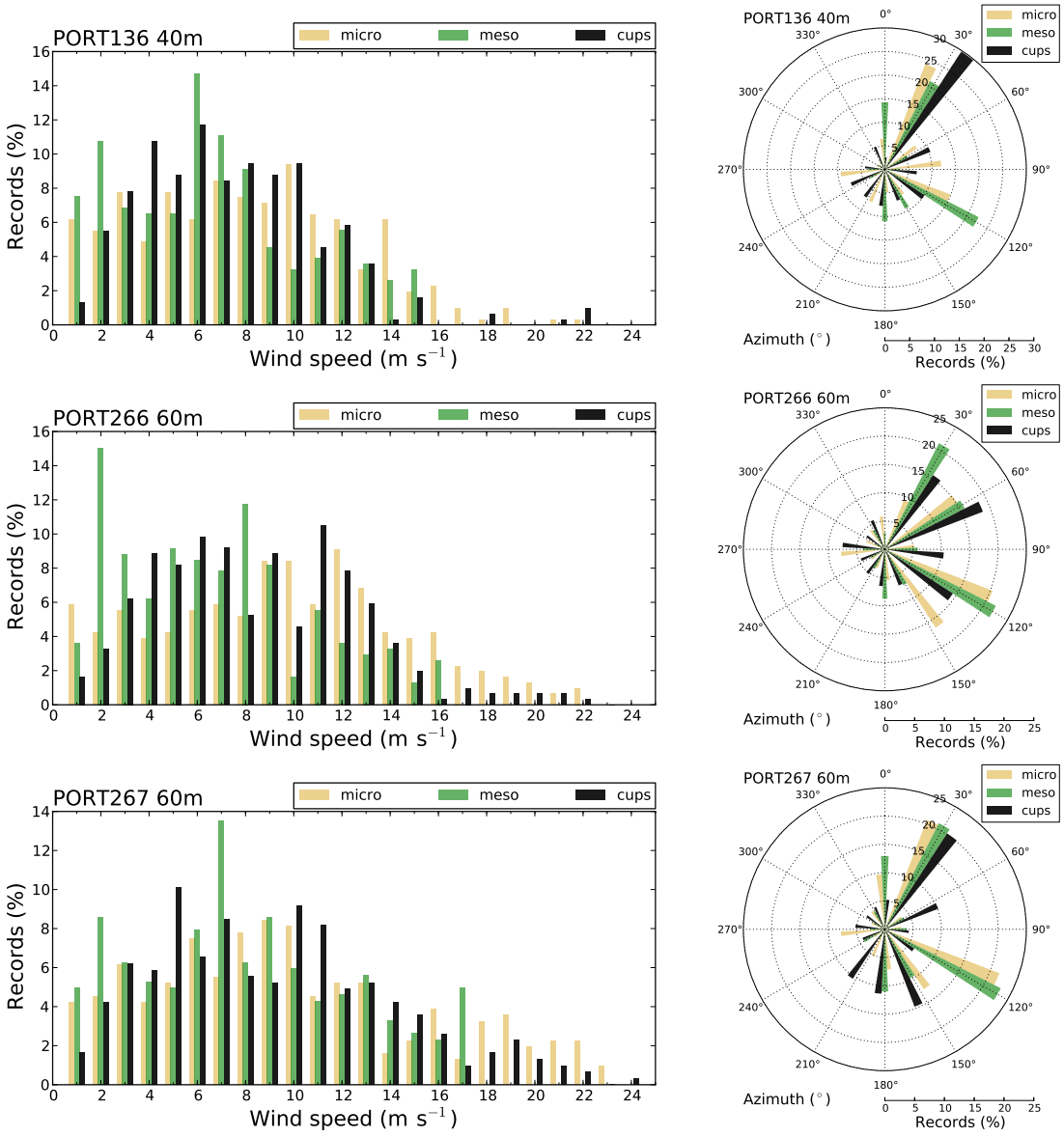

(b) Meteorological mast in Mendoiro.

Figure E.10: Histograms and wind roses for the mesoscale and microscale results, in the period between 2005-07-19 to 2005-12-03.

E.2.2.2 Hovmöller plots of wind speed and direction

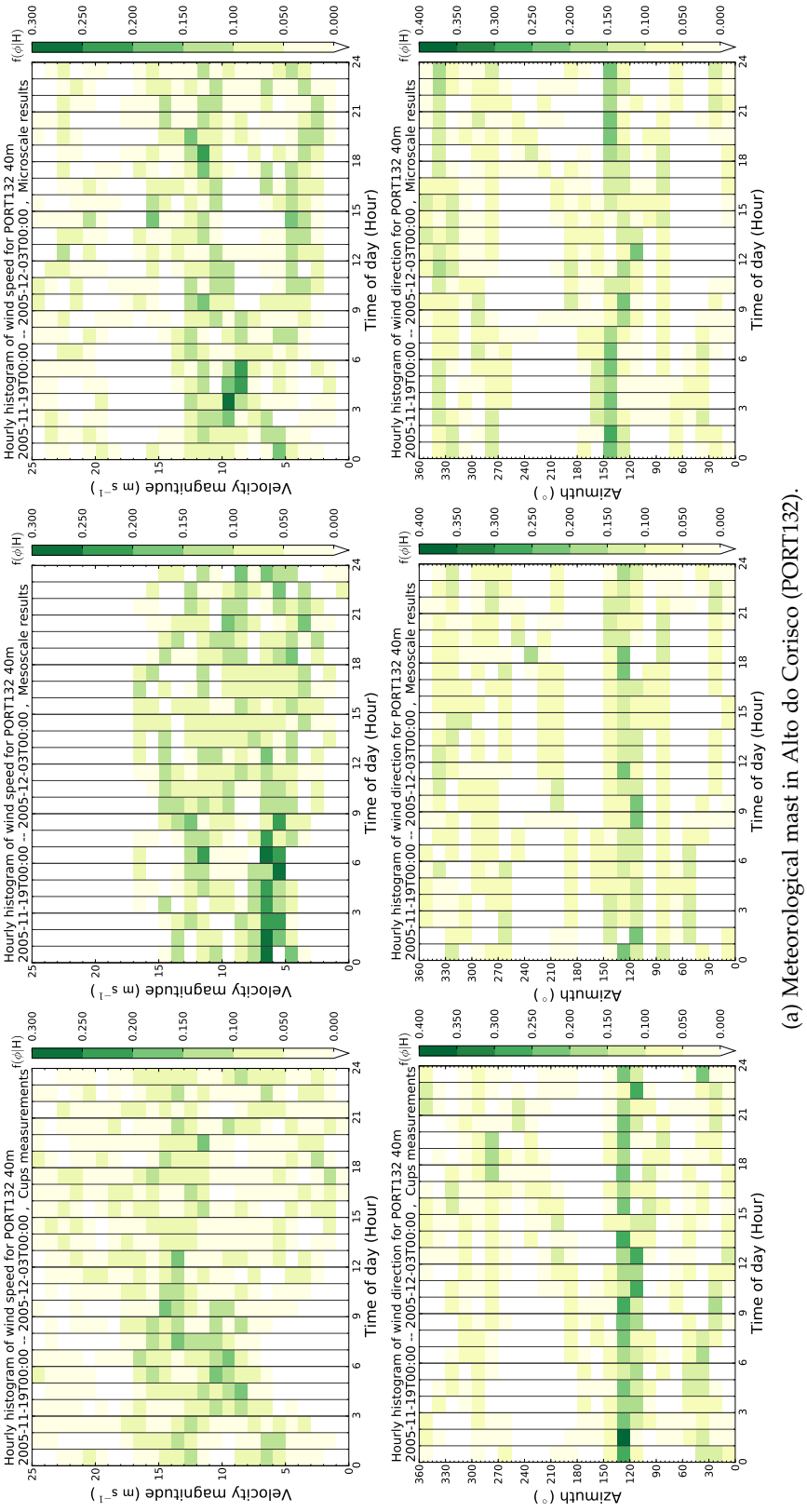

(a) Meteorological mast in Alto do Corisco (PORT132).

Figure E.11: *Caption in page 302.*

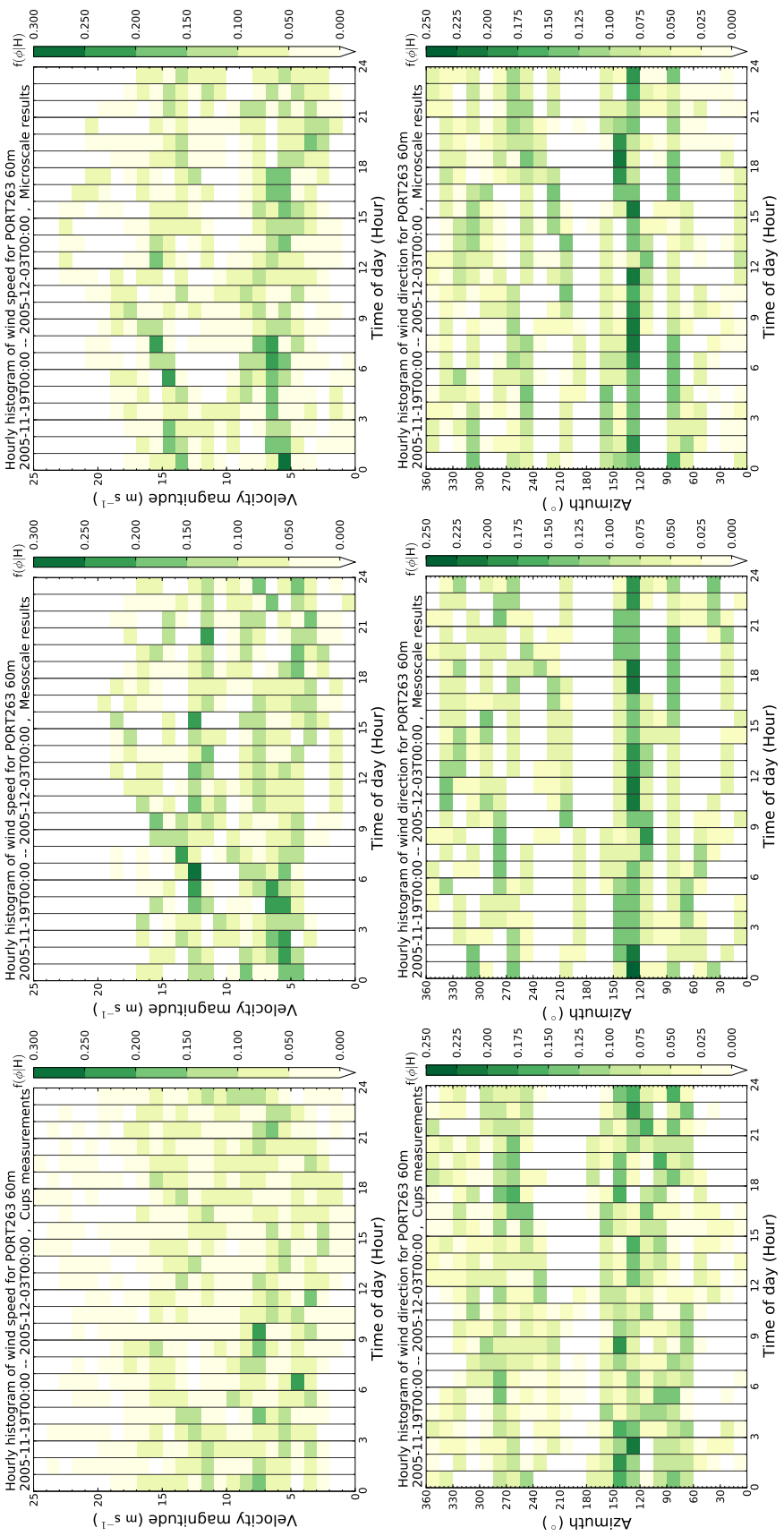

(b) Meteorological mast in Alto do Corisco (PORT263).

Figure E.11: *Caption in page 302.*

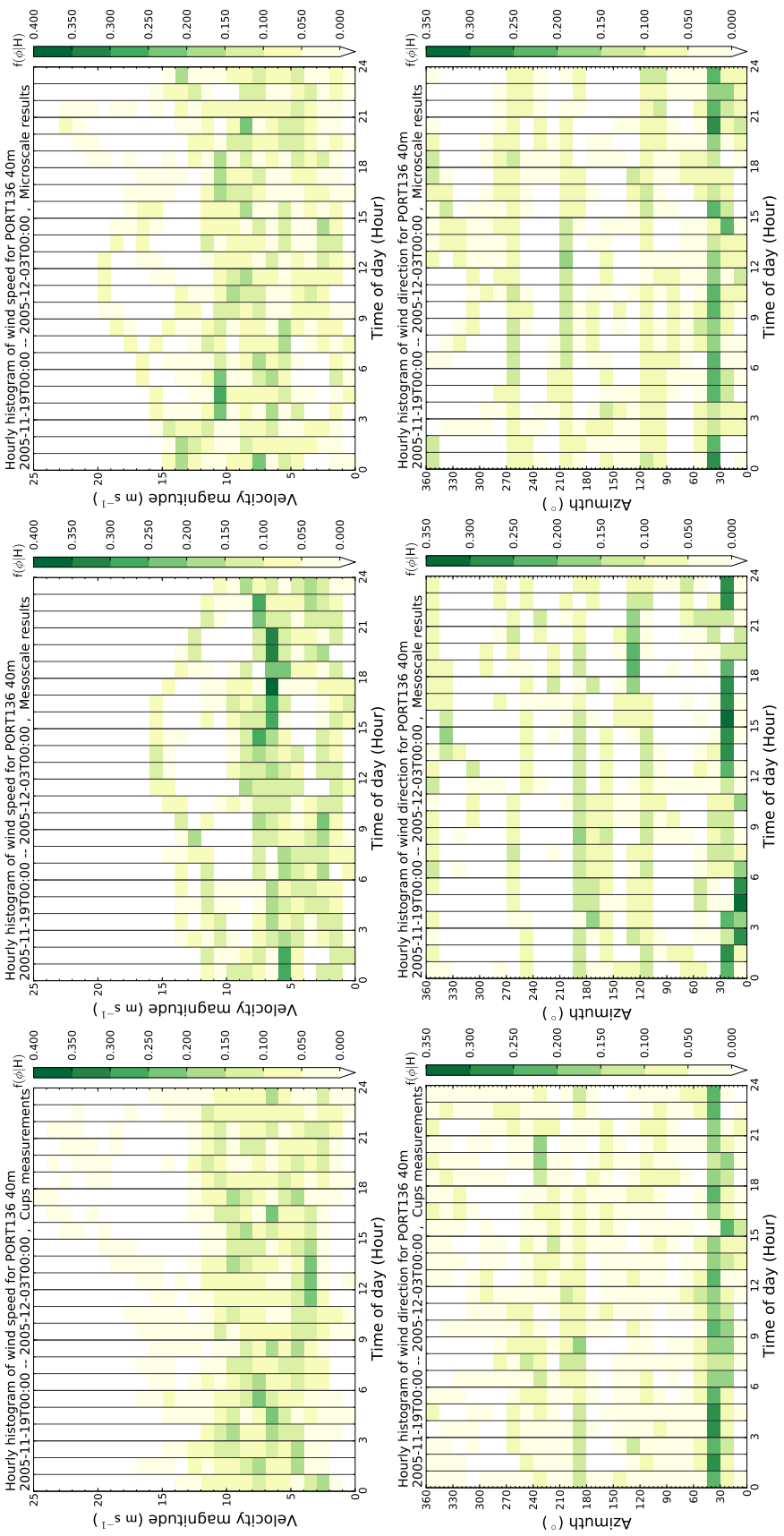

(c) Meteorological mast in Mendoiro (PORT136).

Figure E.11: *Caption in page 302.*

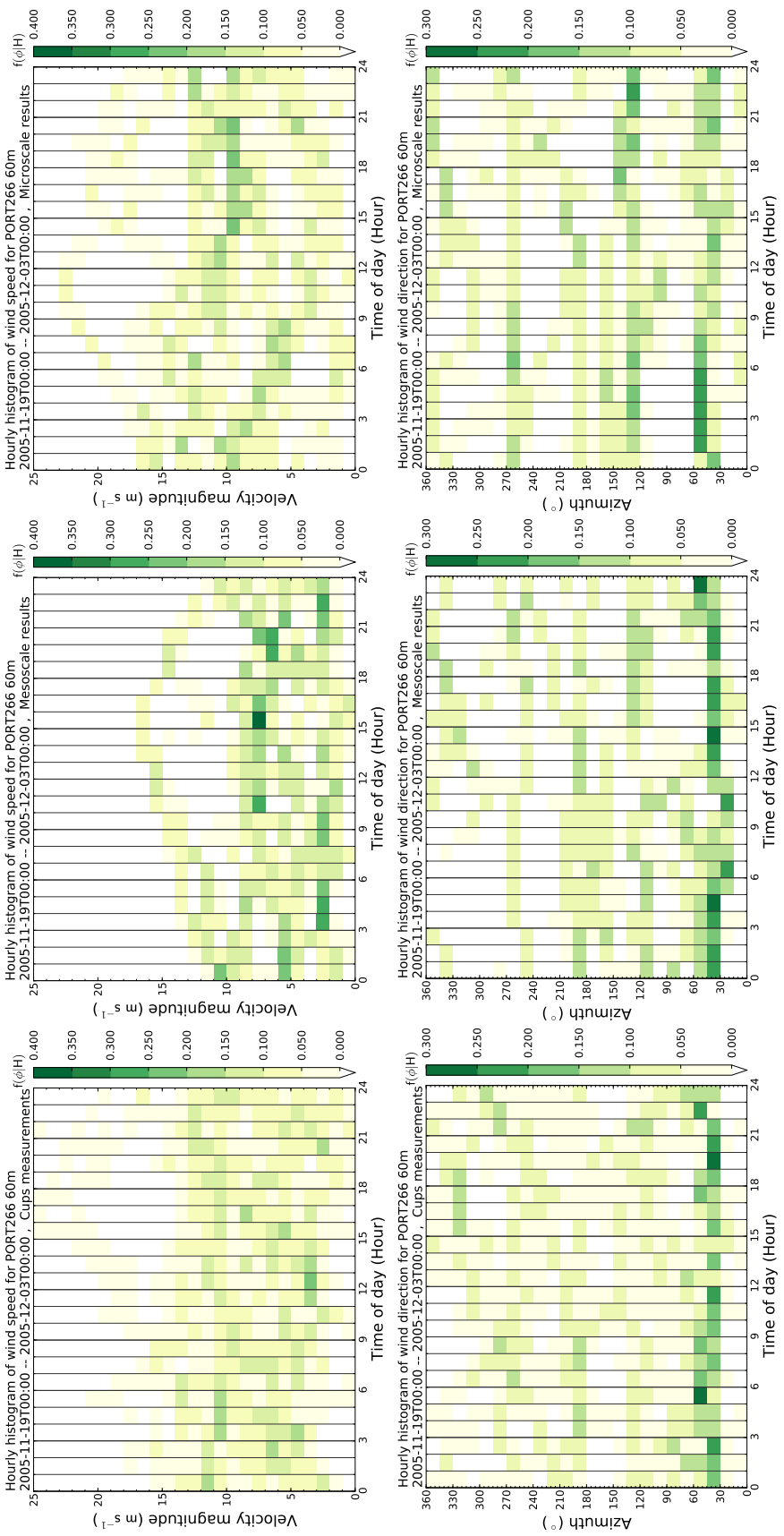

(d) Meteorological mast in Mendoiro (PORT266).

Figure E.11: *Caption in page 302.*

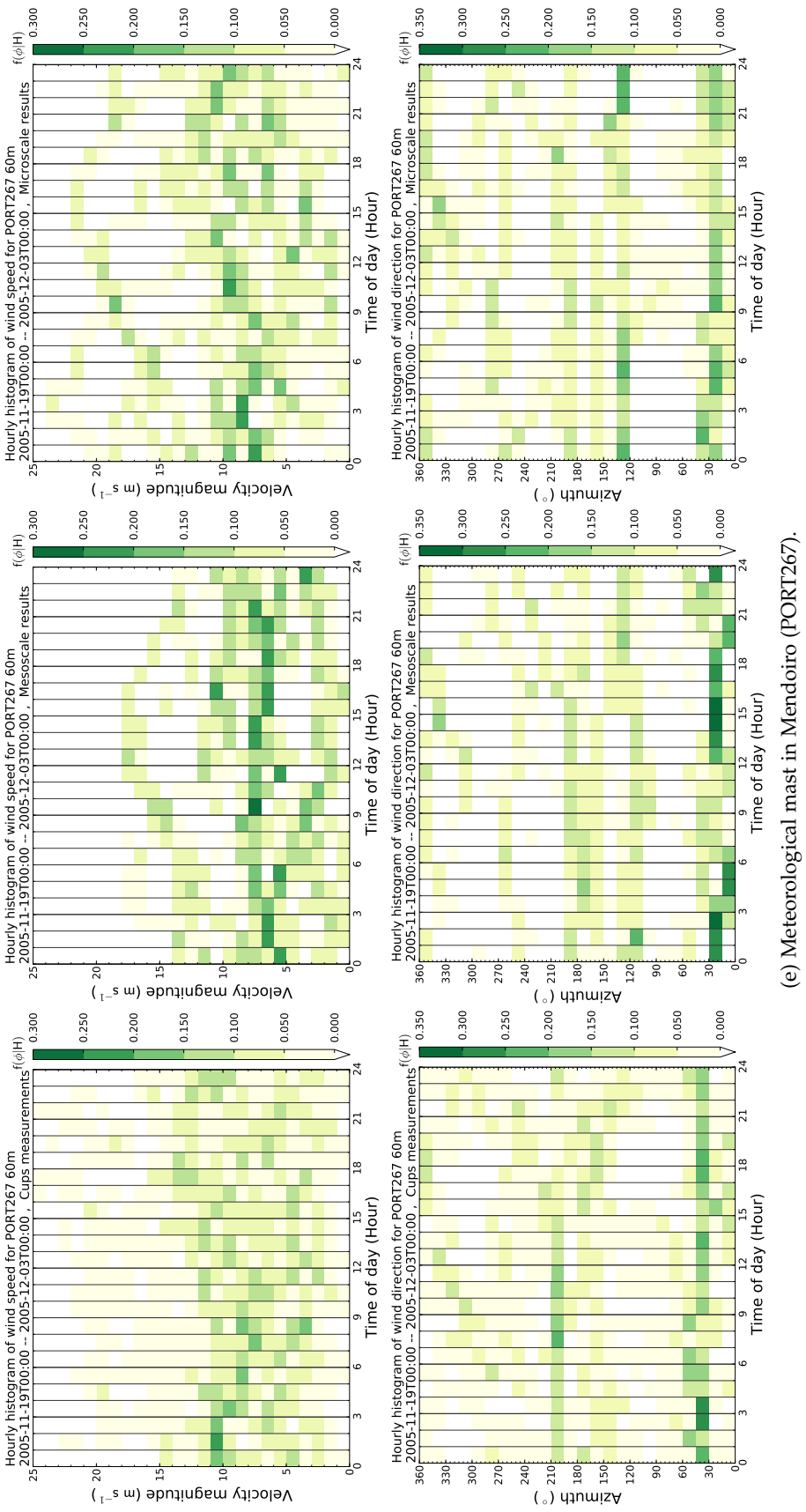

(e) Meteorological mast in Mendoiro (PORT267).

Figure E.11: Hovmöller plots of wind speed (topmost) and direction (bottommost) for the period between 2005-11-18 to 2005-12-03.

E.2.2.3 Scatter plots for the microscale results

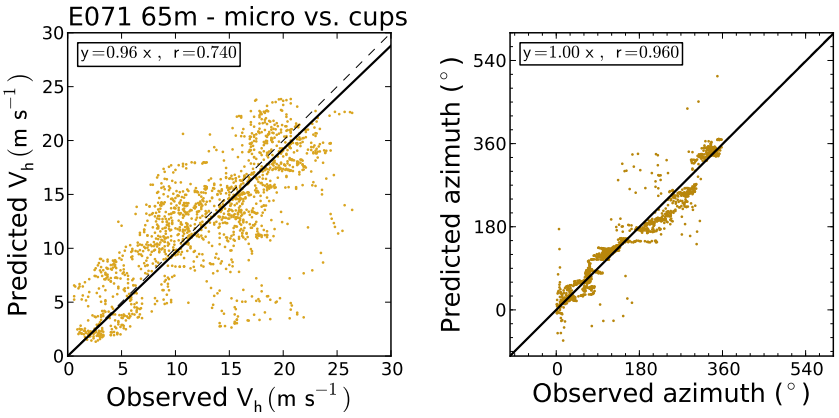

(a) Meteorological mast in Pinheiro.

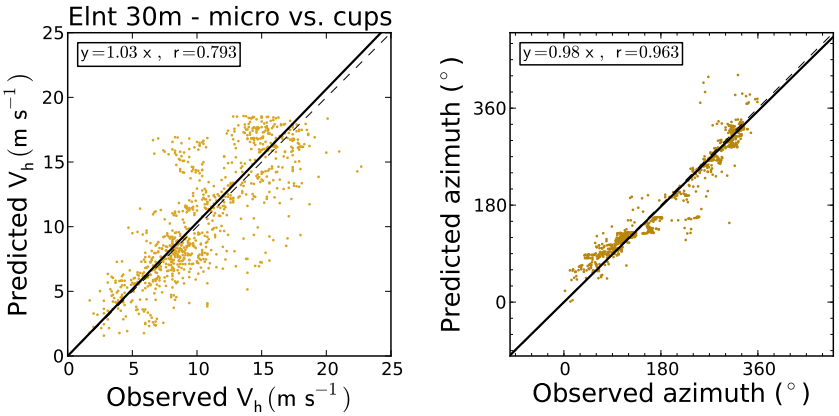

(b) Meteorological mast in Cabeço da Rainha.

Figure E.12: Scatter plots of wind speed and azimuth for the microscale results, in the period between 2005-07-19 to 2005-12-03 (refer to Figure E.4 for a detailed description).

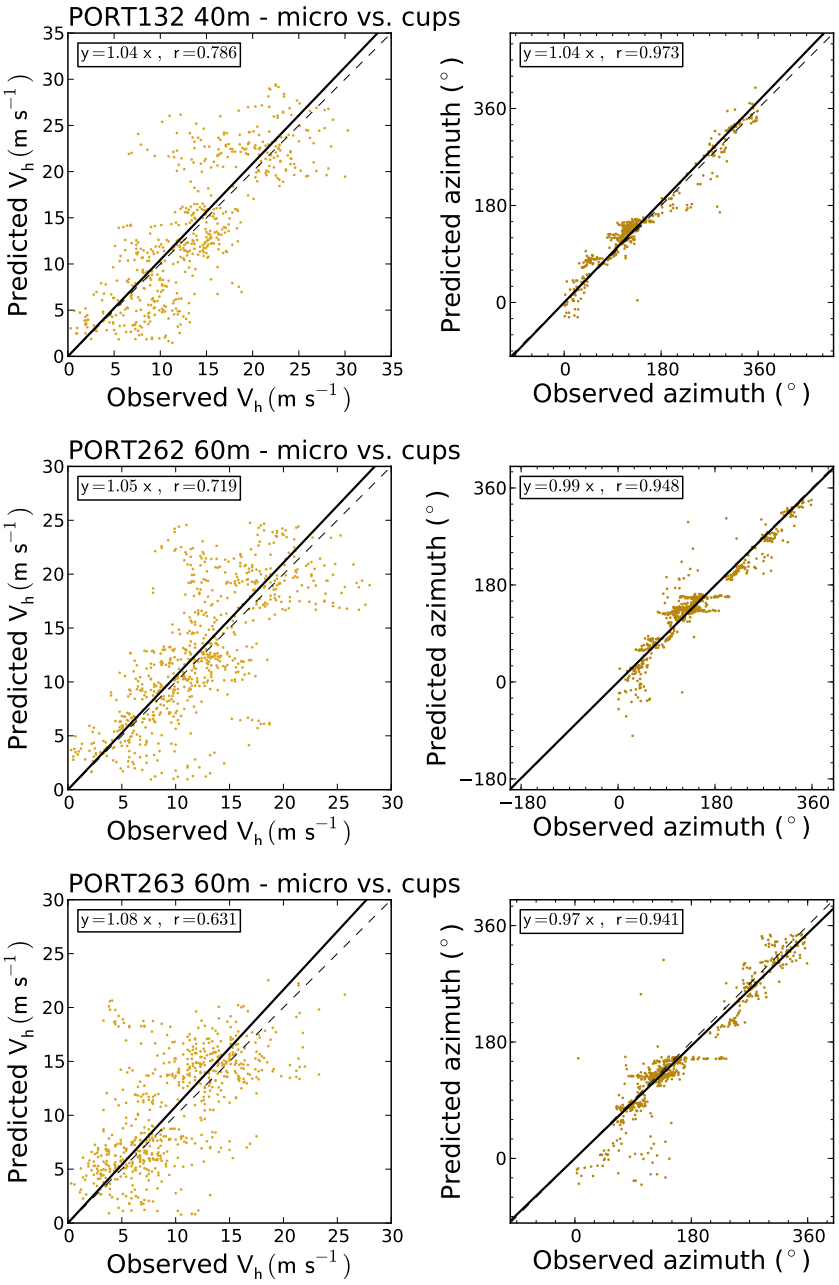

(c) Meteorological mast in Alto do Corisco.

Figure E.12: *Caption in page 303.*

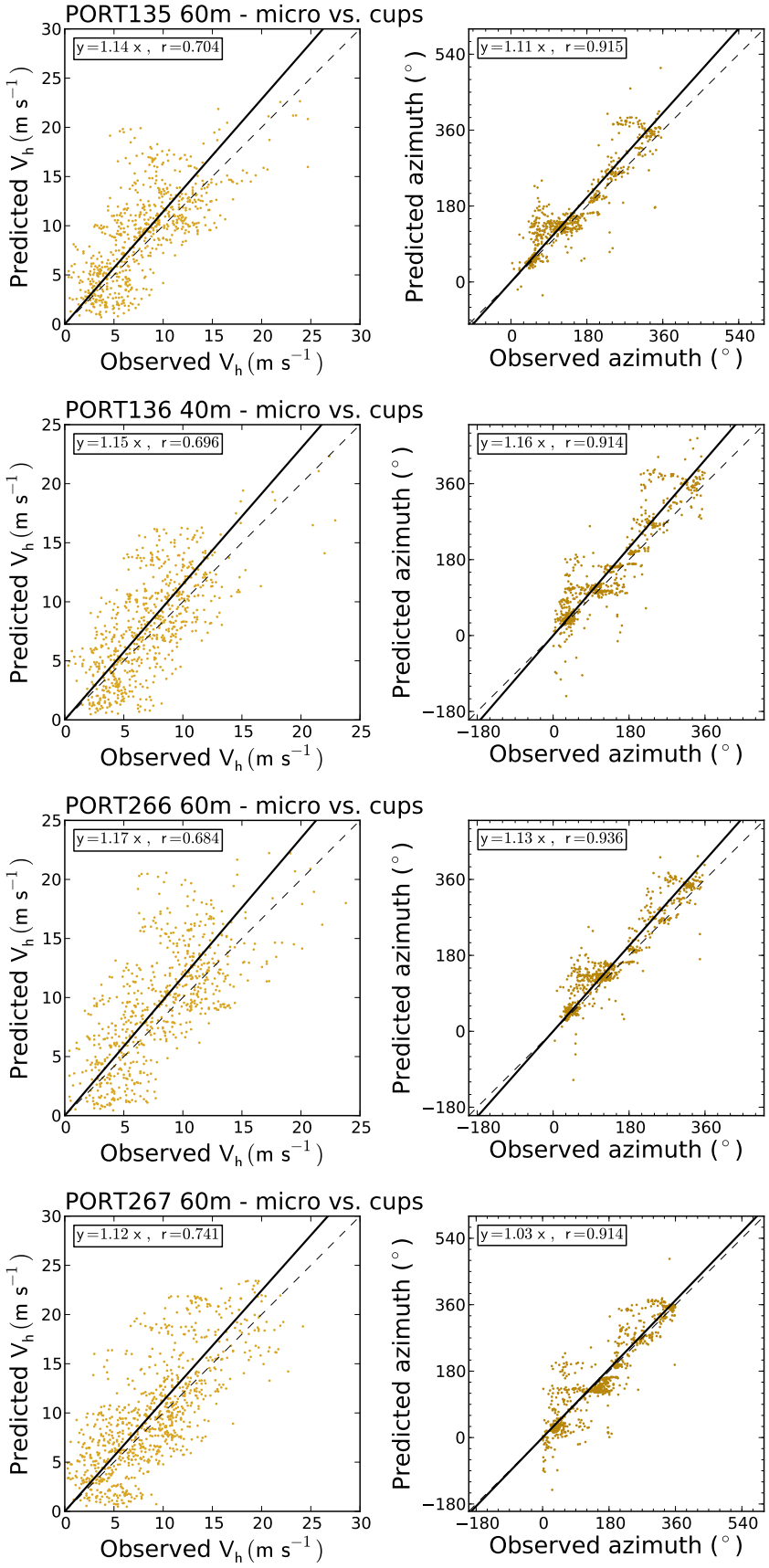

(d) Meteorological mast in Mendoiro.

Figure E.12: *Caption in page 303.*

E.2.3 Influence of thermal stratification on the forecast accuracy

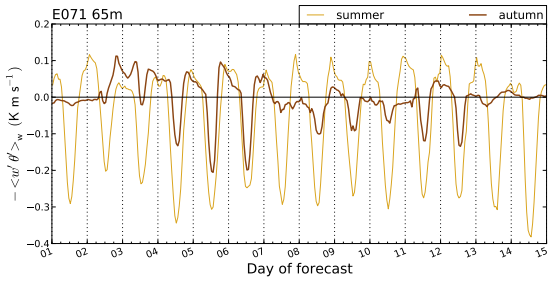

(a) Time series of the surface heat flux.

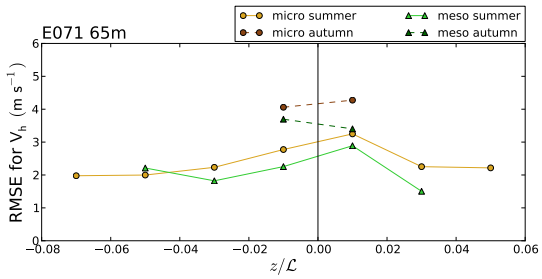

(b) Velocity RMSE *v.* stability parameter $z/\mathcal{L}$.

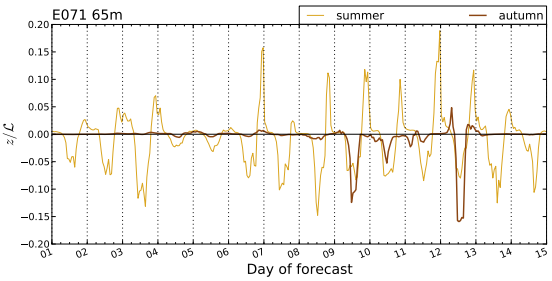

(c) Time series of the stability parameter $z/\mathcal{L}$.

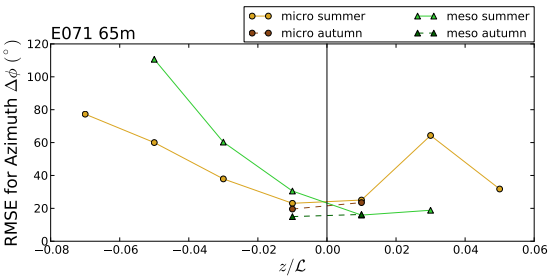

(d) Direction RMSE *v.* stability parameter $z/\mathcal{L}$.

Figure E.13: Influence of atmospheric stability on the prediction error in Pinheiro wind farm.

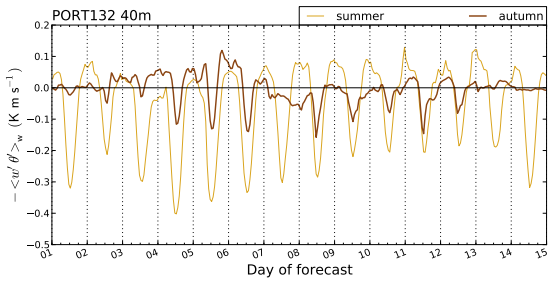

(a) Time series of the surface heat flux.

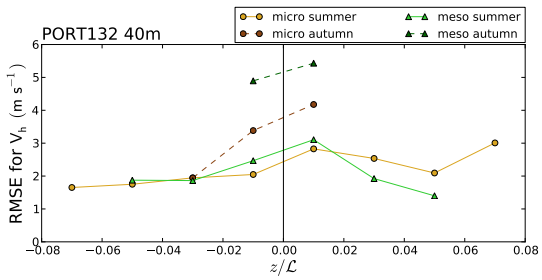

(b) Velocity RMSE *v.* stability parameter $z/\mathcal{L}$.

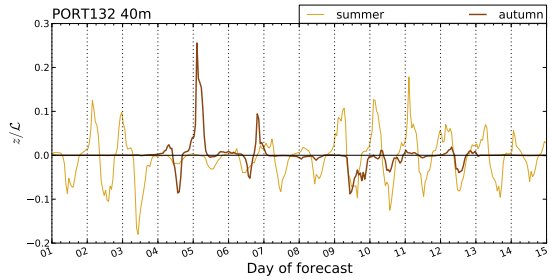

(c) Time series of the stability parameter $z/\mathcal{L}$.

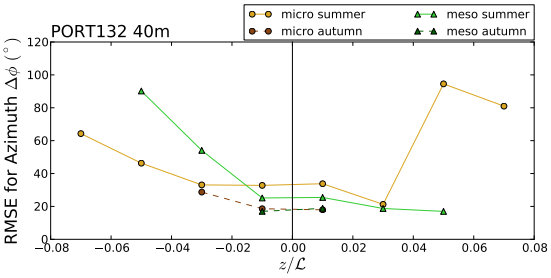

(d) Direction RMSE *v.* stability parameter $z/\mathcal{L}$.

Figure E.14: Alto do Corisco site, mast PORT132 (*Caption in page 307*).

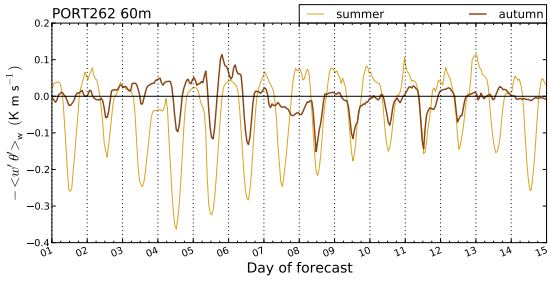

(e) Time series of the surface heat flux.

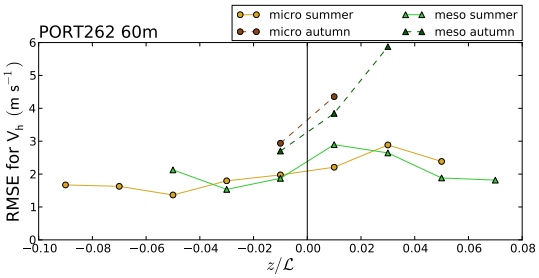

(f) Velocity RMSE *v.* stability parameter $z/\mathcal{L}$.

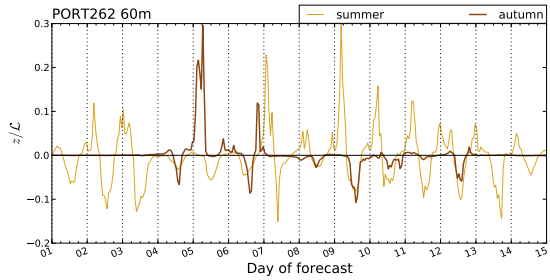

(g) Time series of the stability parameter $z/\mathcal{L}$.

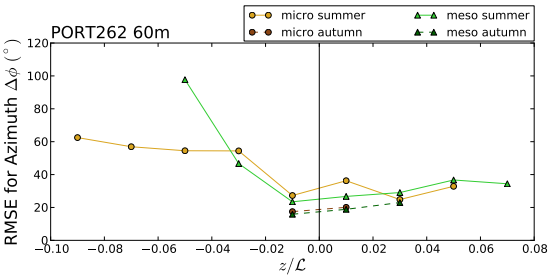

(h) Direction RMSE *v.* stability parameter $z/\mathcal{L}$.

Figure E.14: Alto do Corisco site, mast PORT262 (*Caption in page 307*).

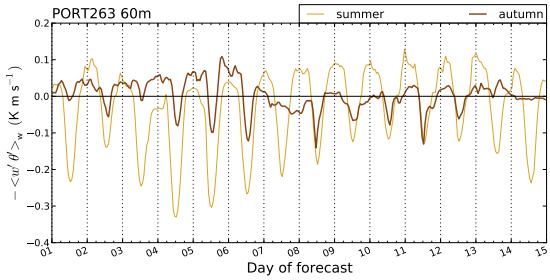

(i) Time series of the surface heat flux.

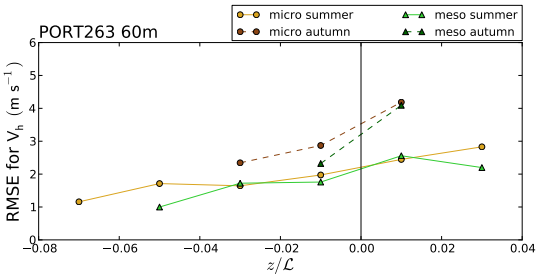

(j) Velocity RMSE *v.* stability parameter $z/\mathcal{L}$.

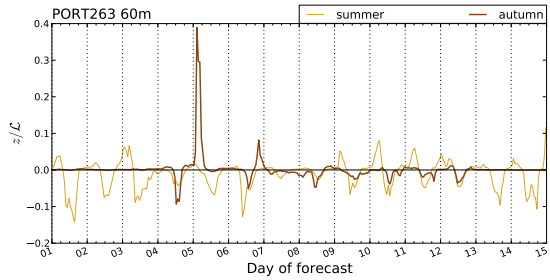

(k) Time series of the stability parameter $z/\mathcal{L}$.

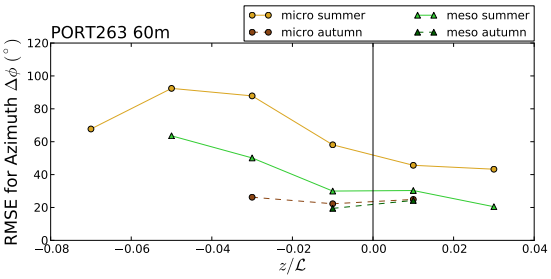

(l) Direction RMSE *v.* stability parameter $z/\mathcal{L}$.

Figure E.14: Influence of atmospheric stability on the prediction error in Alto do Corisco wind farm, mast PORT263.

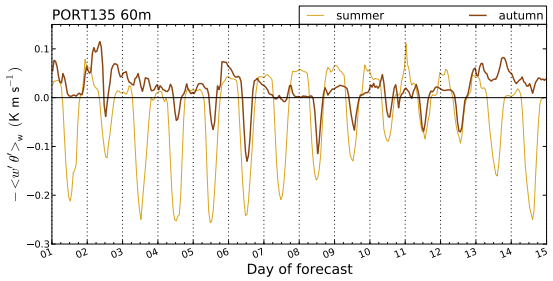

(a) Time series of the surface heat flux.

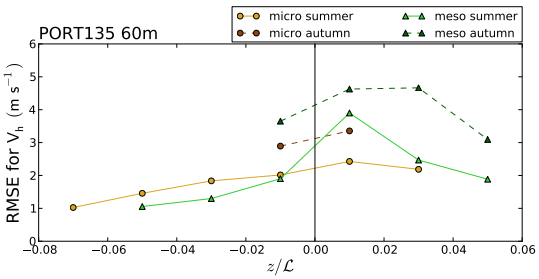

(b) Velocity RMSE *v.* stability parameter $z/\mathcal{L}$.

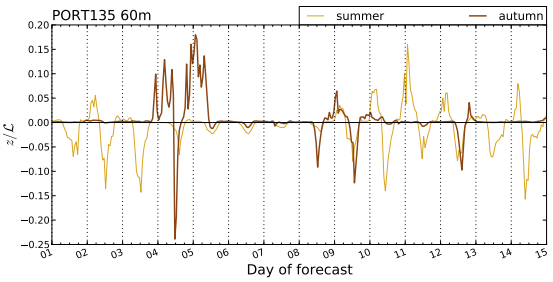

(c) Time series of the stability parameter $z/\mathcal{L}$.

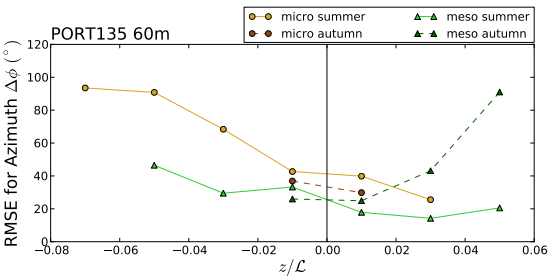

(d) Direction RMSE *v.* stability parameter $z/\mathcal{L}$.

Figure E.15: Mendoiro site, mast PORT135 (*Caption in page 309*).

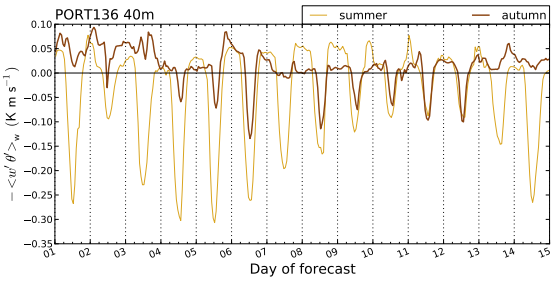

(e) Time series of the surface heat flux.

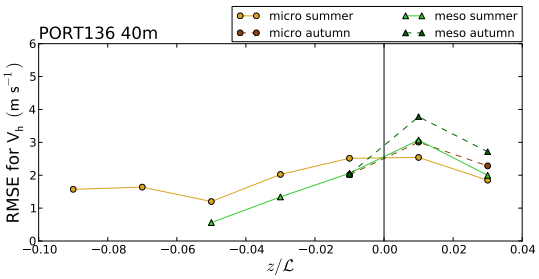

(f) Velocity RMSE *v.* stability parameter $z/\mathcal{L}$.

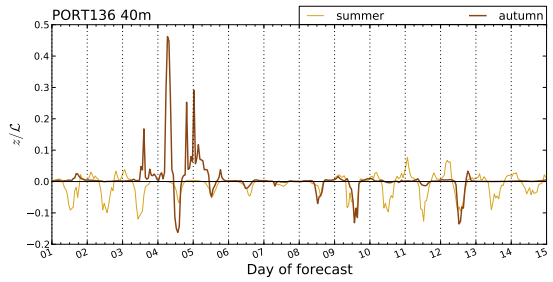

(g) Time series of the stability parameter $z/\mathcal{L}$.

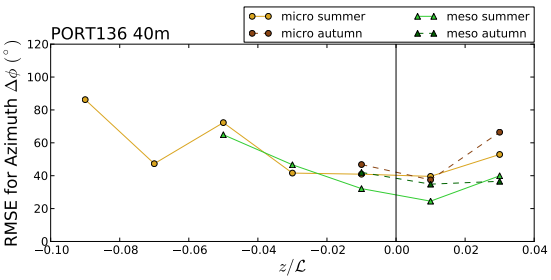

(h) Direction RMSE *v.* stability parameter $z/\mathcal{L}$.

Figure E.15: Mendoiro site, mast PORT136 (*Caption in page 309*).

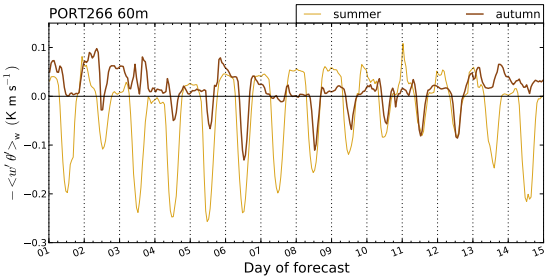

(i) Time series of the surface heat flux.

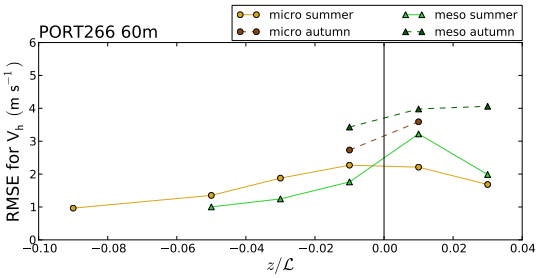

(j) Velocity RMSE *v.* stability parameter $z/\mathcal{L}$.

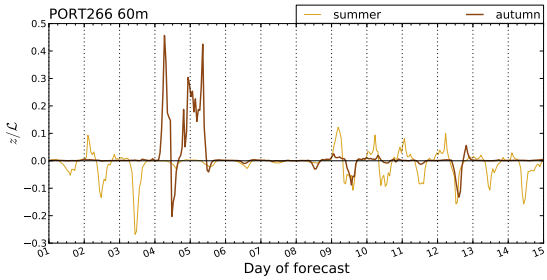

(k) Time series of the stability parameter $z/\mathcal{L}$.

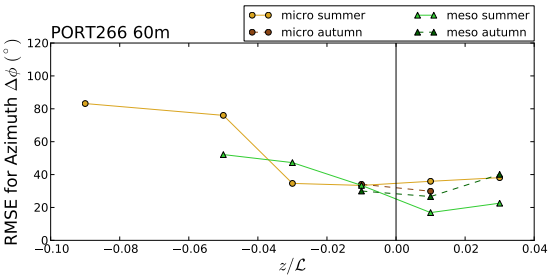

(l) Direction RMSE *v.* stability parameter $z/\mathcal{L}$.

Figure E.15: Mendoiro site, mast PORT266 (*Caption in page 309*).

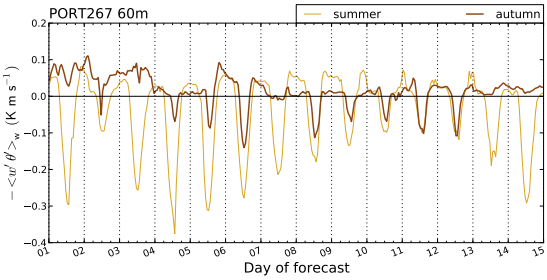

(m) Time series of the surface heat flux.

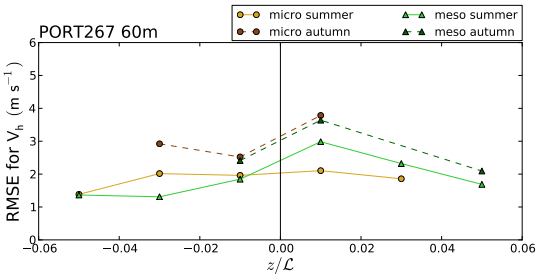

(n) Velocity RMSE *v.* stability parameter $z/\mathcal{L}$.

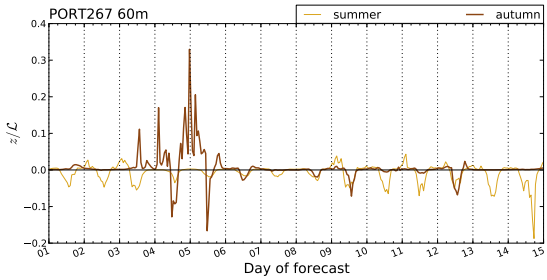

(o) Time series of the stability parameter $z/\mathcal{L}$.

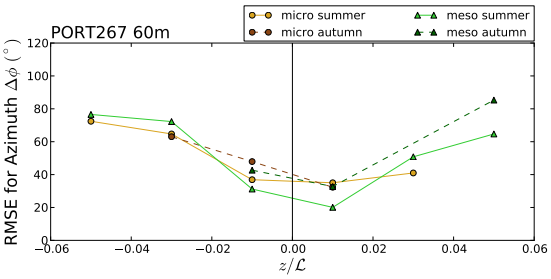

(p) Direction RMSE *v.* stability parameter $z/\mathcal{L}$.

Figure E.15: Influence of atmospheric stability on the prediction error in Mendoiro wind farm, mast PORT267.

Bibliography

Ainslie JF. 1988. Calculating the flowfield in the wake of wind turbines. *J. Wind Eng. Ind. Aerodyn.* **27**(1-3): 213–224, doi: 10.1016/0167-6105(88)90037-2.

Alinot C, Masson C. 2005. $k-\epsilon$ Model for the Atmospheric Boundary Layer Under Various Thermal Stratifications. *J. Sol. Energy Eng.* **127**: 438–443, doi: 10.1115/1.2035704.

Apsley DD, Castro IP. 1997. A Limited-Length-Scale $k-\epsilon$ Model for the Neutral and Stably-Stratified Atmospheric Boundary Layer. *Bound.-Layer Meteor.* **83**: 75–98, doi: 10.1023/A:1000252210512.

Arya SP. 2001. *Introduction to Micrometeorology*, *International Geophysics Series*, vol. 79. Academic Press, 2nd edn, ISBN 0-12-059354-8.

Baker D, Downs T, Ku M, Hao W, Sistia G, Kiss M, Johnson M, Brown D. 2010. Sensitivity Testing of WRF Physics Pparameterizations for Meteorological Modeling and Protocol in Support of Regional SIP Air Quality Modeling in the OTR. Technical report, Ozone Transport Commission, Modeling Committee, Washington, D.C., USA. 73 pp.

Barthelmie RJ, Folkerts L, Larsen GC, Rados K, Pryor S, Frandsen S, Lange B, Schepers G. 2006. Comparison of Wake Model Simulations with Offshore Wind Turbine Wake Profiles Measured by Sodar. *J. Atmos. Oceanic Technol.* **23**: 888–901, doi: 10.1175/JTECH1886.1.

Batchelor GK. 1953. The conditions for dynamical similarity of motions of a frictionless perfect-gas atmosphere. *Quart. J. Roy. Meteor. Soc.* **79**: 224–235, doi: 10.1002/qj.49707934004.

Bauer MH, Mayr GJ, Vergeiner I, Pichler H. 2000. Strongly Nonlinear Flow over and around a Three-Dimensional Mountain as a Function of the Horizontal Aspect Ratio. *J. Atmos. Sci.* **57**: 3971–3991, doi: 10.1175/1520-0469(2001)058⟨3971:SNFOAA⟩2.0.CO;2.

Beljaars ACM, Walmsley JL, Taylor PA. 1987. A Mixed Spectral Finite-Difference Model for Neutrally Stratified Boundary-Layer Flow over Roughness Changes and Topography. *Bound.-Layer Meteor.* **38**: 273–303, doi: 10.1007/BF00122448.

Benoit R. 1977. On the Integral of the Surface Layer Profile-Gradient Functions. *J. Appl. Meteor.* **16**: 859–860, doi: 10.1175/1520-0450(1977)016⟨0859:OTIOTS⟩2.0.CO;2.

Blackadar AK. 1962. The Vertical Distribution of Wind and Turbulent Exchange in a Neutral Atmosphere. *J. Geophys. Res.* **67**(8): 3095–3102, doi: 10.1029/JZ067i008p03095.

Boussinesq J. 1877. Essai sur la théorie des eaux courantes. *Mémoires présentés par divers savants à l'Académie des Sciences* **23**: 1–680.

Bowen AJ, Mortensen NG. 2004. WAsP prediction errors due to site orography. Technical Report Risø-R-995(EN), Risø National Laboratory, Roskilde, Denmark.

Brost RA, Wyngaard JC. 1978. A Model Study of the Stably Stratified Planetary Boundary Layer. *J. Atmos. Sci.* **35**: 1427–1440, doi: 10.1175/1520-0469(1978)035⟨1427:AMSOTS⟩2.0.CO;2.

Businger JA. 1969. Note on the critical Richardson number(s). *Quart. J. Roy. Meteor. Soc.* **95**(405): 653–654, doi: 10.1002/qj.49709540519.

Businger JA. 1988. A Note on the Businger-Dyer Profiles. *Bound.-Layer Meteor.* **42**: 145–151, doi: 10.1007/BF00119880.

Businger JA, Wyngaard JC, Izumi Y, Bradley EF. 1971. Flux-Profile Relationships in the Atmospheric Surface Layer. *J. Atmos. Sci.* **28**: 181–189, doi: 10.1175/1520-0469(1971)028⟨0181:FPRITA⟩2.0.CO;2.

Carl DM, Tarbell TC, Panofsky HA. 1973. Profiles of Wind and Temperature from Towers Over Homogeneous Terrain. *J. Atmos. Sci.* **30**: 788–794, doi: 10.1175/1520-0469(1973)030⟨0788:POWATF⟩2.0.CO;2.

Carvalho DJdS. 2009. Optimização do modelo numérico de Previsão do Tempo WRF no Contexto de Previsão e Produção de Energia Eólica. Master's thesis, Universidade de Aveiro (in portuguese).

Castro FA. 1997. Métodos Numéricos para a Simulação de Escoamentos Atmosféricos sobre Topografia Complexa. PhD thesis, Universidade do Porto (in portuguese).

Castro FA, Palma JMLM, Silva Lopes A. 2003. Simulation of the Askervein Flow. Part 1: Reynolds Averaged Navier-Stokes Equations ($k-\epsilon$ Turbulence Model). *Bound.-Layer Meteor.* **107**: 501–530, doi: 10.1023/A:1022818327584.

Castro FA, Silva Santos CM, Palma JMLM. 2008. Parallelisation of the CFD Code of a CFD-NWP Coupled System for the Simulation of Atmospheric Flows over Complex Terrain. In: *High Performance Computing for Computational Science - VECPAR 2008*. Springer, pp. 27–38, doi: 10.1007/978-3-540-92859-1_4.

Choi H, Moin P. 2012. Grid-point requirements for large eddy simulation: Chapman's estimates revisited. *Phys. Fluids* **24**(1): 011 702, doi: 10.1063/1.3676783.

Chow FK, Street RL. 2009. Evaluation of Turbulence Closure Models for Large-Eddy Simulation over Complex Terrain: Flow over Askervein Hill. *J. Appl. Meteor. Clim.* **48**: 1050–1065, doi: 10.1175/2008JAMC1862.1.

Clark TL. 1977. A Small-Scale Dynamic Model Using a Terrain-Following Coordinate Transformation. *J. Comput. Phys.* **24**: 186–215, doi: 10.1016/0021-9991(77)90057-2.

Daly P. 1999. `utm2ll.f90`: Fortran routines for utm to lat/longitude conversion. URL `http://acoustics.mit.edu/sbcx/saic/software/utm2ll.f90`. Version 1.2, Copyright © 1998 Massachusetts Institute of Technology, Ocean Acoustics Group.

Davies-Jones R. 2003. An Expression for Effective Buoyancy in Surroundings with Horizontal Density Gradients. *J. Atmos. Sci.* **60**: 2922–2925, doi: 10.1175/1520-0469(2003)060⟨2922:AEFEBI⟩2.0.CO;2.

Detering HW, Etling D. 1985. Application of the E-e Turbulence Model to the Atmospheric Boundary Layer. *Bound.-Layer Meteor.* **33**: 113–133, doi: 10.1007/BF00123386.

Doswell III CA, Markowski PM. 2004. Is Buoyancy a Relative Quantity? *Mon. Wea. Rev.* **132**: 853–863, doi: 10.1175/1520-0493(2004)132⟨0853:IBARQ⟩2.0.CO;2.

Dudhia J. 1989. Numerical Study of Convection Observed during the Winter Monsoon Experiment Using a Mesoscale Two-Dimensional Model. *J. Atmos. Sci.* **46**(20): 3077–3107, doi: 10.1175/1520-0469(1989)046⟨3077:NSOCOD⟩2.0.CO;2.

Durran DR. 1989. Improving the Anelastic Approximation. *J. Atmos. Sci.* **46**(11): 1453–1461, doi: 10.1175/1520-0469(1989)046⟨1453:ITAA⟩2.0.CO;2.

Durran DR. 2002. Lee Waves and Mountain Waves. In: *Encyclopedia of Atmospheric Sciences*, Holton JR, Curry JA, Pyle JA (eds), Elsevier Science Ltd., ISBN 978-0-12-227090-1, pp. 1161–1169.

Durran DR, Klemp JB. 1983. A Compressible Model for the Simulation of Moist Mountain Waves. *Mon. Wea. Rev.* **111**(12): 2341–2361, doi: 10.1175/1520-0493(1983)111⟨2341:ACMFTS⟩2.0.CO;2.

Dutton JA, Fichtl GH. 1969. Approximate Equations of Motion for Gases and Liquids. *J. Atmos. Sci.* **26**: 241–254, doi: 10.1175/1520-0469(1969)026⟨0241:AEOMFG⟩2.0.CO;2.

Duynkerke PG. 1988. Application of the $E-\epsilon$ Turbulence Closure Model to the Neutral and Stable Atmospheric Boundary Layer. *J. Atmos. Sci.* **45**: 865–880, doi: 10.1175/1520-0469(1988)045⟨0865:AOTTCM⟩2.0.CO;2.

Dyer AJ. 1974. A Review of Flux-Profile Relationships. *Bound.-Layer Meteor.* **7**: 363–372, doi: 10.1007/BF00240838.

Dyer AJ, Bradley EE. 1982. An Alternative Analysis of Flux-Gradient Relationships at the 1976 ITCE. *Bound.-Layer Meteor.* **22**: 3–19, doi: 10.1007/BF00128053.

Dyer AJ, Hicks BB. 1970. Flux-Gradient Relationships in the Constant Flux Layer. *Quart. J. Roy. Meteor. Soc.* **96**: 715–721, doi: 10.1002/qj.49709641012.

Eidsvik KJ. 2008. Prediction Errors Associated with Sparse Grid Estimates of Flows over Hills. *Bound.-Layer Meteor.* **127**: 153–172, doi: 10.1007/s10546-007-9247-9.

Eidsvik KJ, Holstad A, Lie I, Utnes T. 2004. A prediction system for local wind variations in mountainous terrain. *Bound.-Layer Meteor.* **112**: 557–586, doi: 10.1023/B:BOUN.0000030561.25252.9e.

El Kasmi A, Masson C. 2008. An extended $k-\epsilon$ model for turbulent flow through horizontal-axis wind turbines. *J. Wind Eng. Ind. Aerodyn.* **96**(1): 103–122, doi: 10.1016/j.jweia.2007.03.007.

Ely A, Stuart P, Zhu M, Donnet V, Feeney S, Palma JMLM, Veiga Rodrigues C, Chertovskih R. 2013a. Comparisons of Coupled Mesoscale-CFD Model Predictions with Atmospheric Stability Measurements. In: *Proceedings of the EWEA annual Conference and Exhibition*. European Wind Energy Association: Vienna, Austria. 11 pp.

Ely A, Stuart P, Zhu M, Palma JMLM, Veiga Rodrigues C, Chertovskih R. 2012. Mesoscale and CFD Coupling: An Improved Technique for Predicting Microscale Wind. In: *Proceedings of the EWEA annual Conference and Exhibition*. European Wind Energy Association: Copenhagen, Denmark. 10 pp.

Ely A, Stuart P, Zhu M Chertovskih R, Palma JMLM, Veiga Rodrigues C. 2013b. Mesoscale and CFD coupling: an improved technique for predicting microscale wind. *Wind Energy* (submitted).

EWEA. 2013. Wind in Power, 2012 European statistics. Institutional report, EWEA (European Wind Energy Association), Rue d'Arlon 80, 1040 Brussels, Belgium. 14 pp.

Fermi E. 1956. *Thermodynamics*. Dover Publications, ISBN 978-0486603612.

Ferziger JH, Perić M. 2002. *Computational Methods for Fluid Dynamics*. Springer, 3rd revised edn, ISBN 3-540-42074-6.

Fletcher CAJ. 1991. *Computational Techniques for Fluid Dynamics 1. Fundamental and General Techniques*. Springer series in Computational Physics, Springer, 2nd edn, ISBN 0-387-53058-4.

Frandsen S, Barthelmie R, Pryor S, Rathmann O, Larsen S, Højstrup J, Thøgersen M. 2006. Analytical Modelling of Wind Speed Deficit in Large Offshore Wind Farms. *Wind Energy* **9**: 39–53, doi: 10.1002/we.189.

Frank HP, Landberg L. 1997. Modelling the Wind Climate of Ireland. *Bound.-Layer Meteor.* **85**: 359–378, doi: 10.1023/A:1000552601288.

Gal-Chen T, Somerville RCJ. 1975. On the Use of a Coordinate Transformation for the Solution of the Navier-Stokes Equations. *J. Comput. Phys.* **14**: 209–228, doi: 10.1016/0021-9991(75)90037-6.

Galperin B, Sukoriansky S, Anderson PS. 2007. On the critical Richardson number in stably stratified turbulence. *Atmos. Sci. Letters* **8**(3): 65–69, doi: 10.1002/asl.153.

Garrat JR. 1992. *The Atmospheric Boundary Layer*. Cambridge Atmospheric and Space Science series, Cambridge University Press, ISBN 0-521-38052-9.

Germano M, Piomelli U, Moin P, Cabot WH. 1991. A dynamic subgrid-scale eddy viscosity model. *Phys. Fluids A* **3**(7): 1760–1765, doi: 10.1063/1.857955.

Gough DO. 1969. The Anelastic Approximation for Thermal Convection. *J. Atmos. Sci.* **26**: 448–456, doi: 10.1175/1520-0469(1969)026⟨0448:TAAFTC⟩2.0.CO;2.

Grell AG, Dudhia J, Stauffer DR. 1995. A Description of the Fifth-Generation Penn State/NCAR Mesoscale Model (MM5). NCAR Technical Note NCAR/TN-398+STR, National Center for Atmospheric Research, Boulder, Colorado, USA. 122 pp.

Griffiths AD, Middleton JH. 2010. Simulations of separated flow over two-dimensional hills. *J. Wind Eng. Ind. Aerodyn.* **98**(3): 155–160, doi: 10.1016/j.jweia.2009.10.011.

GWEC. 2013. Global Wind Statistics 2012. Institutional report, GWEC (Global Wind Energy Council), Rue d'Arlon 80, 1040 Brussels, Belgium. 4 pp.

Gyalistras D. 2003. Development and validation of a high-resolution monthly gridded temperature and precipitation data set for Switzerland. *Clim. Res.* **25**: 55–83, doi: 10.3354/cr025055.

H PK, C SN, S PU, Morfiadakis E. 2001. Effects of Turbulence and Flow Inclination on the Performance of Cup Anemometers in the Field. *Bound.-Layer Meteor.* **101**: 77–107, doi: 10.1023/A:1019254020039.

Hargreaves DM, Wright NG. 2007. On the use of the $k-\epsilon$ model in commercial CFD software to model the neutral atmospheric boundary layer. *J. Wind Eng. Ind. Aerodyn.* **95**(2): 355–369, doi: 10.1016/j.jweia.2006.08.002.

Hicks BB. 1976. Wind Profile Relationships from the Wangara Experiment. *Quart. J. Roy. Meteor. Soc.* **102**: 535–551, doi: 10.1002/qj.49710243304.

Högström U. 1988. Non-Dimensional Wind and Temperature Profiles in the Atmospheric Surface Layer: A Re-evaluation. *Bound.-Layer Meteor.* **42**: 55–78, doi: 10.1007/BF00119875.

Högström U. 1996. Review of Some Basic Characteristics of the Atmospheric Surface Layer. *Bound.-Layer Meteor.* **78**: 215–246, doi: 10.1007/BF00120937.

Holton JR. 2004. *An Introduction to Dynamic Meteorology*, *International Geophysics series*, vol. 88. Elsevier Academic Press, 4th edn, ISBN 0-12-354015-1.

Hu XM, Nielsen-Gammon JW, Zhang F. 2010. Evaluation of Three Planetary Boundary Layer Schemes in the WRF Model. *J. Appl. Meteor. Climatol.* **49**: 1831–1844, doi: 10.1175/2010JAMC2432.1.

Hunt JCR, Abell CJ, Peterka JA, Woo H. 1978. Kinematical Studies of the Flows Around Free or Surface-Mounted Obstacles; Applying Topology to Flow Visualization. *J. Fluid Mech.* **86**: 179–200, doi: 10.1017/S0022112078001068.

Hunt JCR, Leibovich S, Richards KJ. 1988. Turbulent shear flows over low hills. *Quart. J. Roy. Meteor. Soc.* **114**: 1435–1470, doi: 10.1002/qj.49711448405.

Hunt JCR, Snyder WH. 1980. Experiments on Stably and Neutrally Stratified Flow Over a Model Three-Dimensional Hill. *J. Fluid Mech.* **96**: 671–704, doi: 10.1017/S0022112080002303.

IEC. 1998. Wind turbine generator systems - Part 12: Wind turbine power performance testing. International Standard IEC 61400-12:1998, 1st edn., Int. Electrotechnical Commission, Geneva, Switzerland.

Jackson PS, Hunt JCR. 1975. Turbulent wind flow over a low hill. *Quart. J. Roy. Meteor. Soc.* **101**: 929–955, doi: 10.1002/qj.49710143015.

Jiang QF, Doyle JD, Smith RB. 2006. Interaction between Trapped Waves and Boundary Layers. *J. Atmos. Sci.* **63**: 617–633, doi: 10.1175/JAS3640.1.

Jorge DF. 2006. Transporte de Escalares Passivos em Escoamentos Turbulentos Sujeitos a Curvatura e Corte Uniforme. PhD thesis, Universidade do Porto (in portuguese).

Kaimal JC, Finnigan JJ. 1994. *Atmospheric Boundary Layer Flows. Their Structure and Measurement*. Oxford University Press, ISBN 0-19-506239-6.

Katic I, Højstrup J, Jensen NO. 1986. A Simple Model for Cluster Efficiency. In: *Proceedings of the European Wind Energy Conference and Exhibition*, vol. 1. European Wind Energy Association: Rome, Italy, pp. 407–410.

Klein R. 2010. Scale-Dependent Models for Atmospheric Flows. *Annu. Rev. Fluid Mech.* **42**: 249–274, doi: 10.1146/annurev-fluid-121108-145537.

Klemp JB, Skamarock WC, Fuhrer O. 2003. Numerical Consistency of Metric Terms in Terrain-Following Coordinates. *Mon. Wea. Rev.* **131**: 1229–1239, doi: 1520-0493(2003)131⟨1229:NCOMTI⟩2.0.CO;2.

Klemp JB, Wilhelmson RB. 1978. The Simulation of Three-Dimensional Convective Storm Dynamics. *J. Atmos. Sci.* **35**: 1070–1096, doi: 10.1175/1520-0469(1978)035⟨1070:TSOTDC⟩2.0.CO;2.

Kristóf G, Rácz N, Balogh M. 2009. Adaptation of Pressure Based CFD Solvers for Mesoscale Atmospheric Problems. *Bound.-Layer Meteor.* **131**(1): 85–103, doi: 10.1007/s10546-008-9325-7.

Kunz R, Khatib I, Moussiopoulos N. 2000. Coupling of Mesoscale and Microscale Models – An Approach to Simulate Scale Interaction. *Environ. Model. Software* **15**(6-7): 597–602, doi: 10.1016/S1364-8152(00)00055-4.

Lafore JP, Stein J, Asencio N, Bougeault P, Ducrocq V, Duron J, Fisher C, Héreil P, Mascart P, Masson V, Pinty JP, Redelsperger JL, Richard E, Vilà-Guerau de Arellano J. 1998. The Meso-NH Atmospheric Simulation System. Part I: adiabatic formulation and control simulations. *Annales Geophysicae* **16**: 90–109, doi: 10.1007/s00585-997-0090-6.

Landberg L. 1999. Short-term Prediction of the Power Production from Wind Farms. *J. Wind Eng. Ind. Aerodyn.* **80**: 207–220, doi: 10.1016/S0167-6105(98)00192-5.

Landberg L. 2001. Short-term Prediction of Local Wind Conditions. *J. Wind Eng. Ind. Aerodyn.* **89**: 235–245, doi: 10.1016/S0167-6105(00)00079-9.

Landberg L, Myllerup L, Rathmann O, Petersen EL, Jørgensen BH, Badger J, Mortensen NG. 2003. Wind resource estimation – An overview. *Wind Energy* **6**: 261–271, doi: 10.1002/we.94.

Landberg L, Watson SJ. 1994. Short-Term Prediction of Local Wind Conditions. *Bound.-Layer Meteor.* **70**: 171–195, doi: 10.1007/BF00712528.

Larsén XG, Mann J, Berg J, Göttel H, Jacob D. 2010. Wind climate from the regional climate model REMO. *Wind Energy* **13**(4): 279–296, doi: 10.1002/we.337.

Launder BE, Spalding DB. 1974. The Numerical Computation of Turbulent Flows. *Comp. Meth. in Appl. Mech. Eng.* **3**: 269–289, doi: 10.1016/0045-7825(74)90029-2.

Lee X, Massman W, Law B (eds). 2005. *Handbook of Micrometeorology. A Guide for Surface Flux Measurement and Analysis*. Atmospheric and Oceanographic Sciences Library, Springer, ISBN 1-4020-2265-4.

Leonard BP. 1979. A stable and accurate convection modelling procedure based on quadratic upstream interpolation. *Com. Meth. Applied Mech. Eng.* **19**(1): 59–98, doi: 10.1016/0045-7825(79)90034-3.

Lions PL. 1996. *Mathematical Topics in Fluid Mechanics. Vol. 1, Incompressible Models*. Oxford lecture series in mathematics and its applications, Clarendon Press, Oxford, ISBN 0-19-851487-5.

Lopes da Costa JC, Castro FA, Palma JMLM, Stuart P. 2006. Computer simulation of atmospheric flows over real forests for wind energy resource evaluation. *J. Wind Eng. Ind. Aerodyn.* **94**: 603–620, doi: 10.1016/j.jweia.2006.02.002.

Lynch AH, Cassano JJ. 2006. *Applied Atmospheric Dynamics*. John Wiley & Sons, ISBN 0-470-86172-X.

Madsen H, Kariniotakis G, Nielsen HA, Nielsen TS, Pinson P. 2004. A Protocol for Standardizing the Performance Evaluation of Short-Term Wind Power Prediction Models. Technical report of the project ANEMOS (European Commision contract No. ENK5-CT-2002-00665) D2.3, IMM, Technical University of Denmark, Ricard Petesens Plads, Bld. 321, 2800 Lyngby, Denmark. 16 pp.

Madsen H, Pinson P, Kariniotakis G, Nielsen HA, Nielsen TS. 2005. Standardizing the Performance Evaluation of Short-Term wind Power Prediction Models. *Wind Eng.* **29**(6): 475–489, doi: 10.1260/030952405776234599.

Marchesiello P, McWilliams JC, Shchepetkin A. 2001. Open boundary conditions for long-term integration of regional oceanic models. *Ocean Modelling* **3**(1-2): 1–20, doi: 10.1016/S1463-5003(00)00013-5.

MIBEL. 2008. Descrição do funcionamento do mibel. Technical report, MIBEL Board of Regulators: CMVM, ERSE, CNMV, CNE.

Miller MJ, Thorpe AJ. 1981. Radiation conditions for the lateral boundaries of limited-area numerical models. *Quart. J. Roy. Meteor. Soc.* **107**: 615–628, doi: 10.1002/qj.49710745310.

Miranda PMA, James IN. 1992. Non-linear Three-Dimensional Effects on Gravity-wave Drag: Splitting Flow and Breaking Waves. *Quart. J. Roy. Meteor. Soc.* **118**: 1057–1081, doi: 10.1002/qj.49711850803.

Mlawer EJ, Taubman SJ, Brown PD, Iacono MJ, Clough SA. 1997. Radiative Transfer for Inhomogeneous Atmospheres: RRTM, a Validated Correlated-k Model for the Longwave. *J. Geophys. Res.* **102**(D14): 16 663–16 682, doi: 10.1029/97JD00237.

Mortensen NG, Petersen EL. 1997. Influence of Topographical Input Data on the Accuracy of Wind Flow Modeling in Complex Terrain. In: *Proceedings of the European Wind Energy Conference and Exhibition*. European Wind Energy Association: Dublin, Ireland, pp. 317–320.

Murphy AH. 1988. Skill Scores Based on the Mean Square Error and Their Relationships to the Correlation Coefficient. *Mon. Wea. Rev.* **116**: 2417–2424, doi: 10.1175/1520-0493(1988)116⟨2417:SSBOTM⟩2.0.CO;2.

NCEP FNL ds0832. 1999–2012. National Centers for Environmental Prediction (NCEP), FNL Operational Model Global Tropospheric Analyses, ID: ds083.2. URL http://rda.ucar.edu/datasets/ds083.2/.

NIMA. 2000. Department of Defense World Geodetic System 1984: Its Definition and Relationships with Local Geodetic Systems. Technical Report NIMA TR8350.2, National Imagery and Mapping Agency, St. Louis, Missouri, USA. 174 pp.

NOAA RTG-SST. 2001–2012. Real-time, global, sea surface temperature (RTG SST) analysis. URL http://polar.ncep.noaa.gov/sst/oper.

Ogura Y, Phillips NA. 1962. Scale Analysis of Deep and Shallow Convection in the Atmosphere. *J. Atmos. Sci.* **19**: 173–179, doi: 10.1175/1520-0469(1962)019⟨0173:SAODAS⟩2.0.CO;2.

Ólafsson H, Bougeault P. 1996. Nonlinear Flow Past and Elliptic Mountain Ridge. *J. Atmos. Sci.* **53**(17): 2465–2489, doi: 10.1175/1520-0469(1996)053⟨2465:NFPAEM⟩2.0.CO;2.

Ólafsson H, Bougeault P. 1997. The Effect of Rotation and Surface Friction on Orographic Drag. *J. Atmos. Sci.* **54**: 193–210, doi: 10.1175/1520-0469(1997)054⟨0193:TEORAS⟩2.0.CO;2.

Orlansky I. 1976. A Simple Boundary Condition for Unbounded Hyperbolic Flows. *J. Comput. Phys.* **21**(3): 251–269, doi: 10.1016/0021-9991(76)90023-1.

Otte TL. 2008. The Impact of Nudging in the Meteorological Model for Retrospective Air Quality Simulations. Part I: Evaluation against National Observation Networks. *J. Appl. Meteor. Climatol.* **47**: 1853–1867, doi: 10.1175/2007JAMC1790.1.

Paiva LT, Veiga Rodrigues C, Palma JMLM. 2013. Determining a wind turbine power curve based on operating conditions. *Wind Energy* (manuscript ID: WE-10-0113.R6, in press).

Palma JMLM, Castro FA, Ribeiro LF, Rodrigues AH, Pinto AP. 2008. Linear and Nonlinear Models in Wind Resource Assessment and Wind Turbine Micro-Siting in Complex Terrain. *J. Wind Eng. Ind. Aerodyn.* **96**: 2308–2326, doi: 10.1016/j.jweia.2008.03.012.

Panofsky HA. 1963. Determination of Stress From Wind and Temperature Measurements. *Quart. J. Roy. Meteor. Soc.* **89**: 85–94, doi: 10.1002/qj.49708937906.

Pascau A. 2011. Cell face velocity alternatives in a structured colocated grid for the unsteady Navier-Stokes equations. *Int. J. Num. Methods in Fluids* **65**(7): 812–833, doi: 10.1002/fld.2215.

Patankar SV. 1980. *Numerical Heat Transfer and Fluid Flow*. Series in Computational Methods in Mechanics and Thermal Sciences, McGraw–Hill, ISBN 0-07-048740-5.

Patel VC, Rodi W, Scheuerer G. 1985. Turbulence Models for Near-Wall and Low Reynolds Number Flows: A Review. *AIAA Journal* **23**(9): 1308–1319, doi: 10.2514/3.9086.

Paulson CA. 1970. The Mathematical Representation of Wind Speed and Temperature Profiles in the Unstable Atmospheric Surface Layer. *J. Appl. Meteor.* **9**: 857–861, doi: 10.1175/1520-0450(1970)009⟨0857:TMROWS⟩2.0.CO;2.

Perić M. 1990. Analysis of Pressure-Velocity Coupling on Nonorthogonal Grids. *Num. Heat Transfer B* **17**: 63–82, doi: 10.1080/10407799008961733.

Phillips DS. 1984. Analytical Surface Pressure and Drag for Linear Hydrostatic Flow over Three-Dimensional Elliptical Mountains. *J. Atmos. Sci.* **41**(6): 1073–1084, doi: 10.1175/1520-0469(1984)041⟨1073:ASPADF⟩2.0.CO;2.

Phillips NA. 1957. A Coordinate System having some special advantages for Numerical Forecasting. *J. Meteor.* **14**: 184–185, doi: 10.1175/1520-0469(1957)014⟨0184:ACSHSS⟩2.0.CO;2.

Phillips NA, Shukla J. 1973. On the Strategy of Combining Coarse and Fine Grid Meshes in Numerical Weather Prediction. *J. Atmos. Meteor.* **12**: 763–770, doi: 10.1175/1520-0450(1973)012⟨0763:OTSOCC⟩2.0.CO;2.

Pielke RA. 2002. *Mesoscale Meteorological Modeling*, *International Geophysics Series*, vol. 78. Academic Press, 2nd edn, ISBN 0-12-554766-8.

Pielke RA, Cotton WR, Walko RL, Tremback CJ, Lyons WA, Grasso LD, Nicholls ME, Moran MD, Wesley DA, Lee TJ, H CJ. 1992. A Comprehensive Meteorological Modeling System-RAMS. *Meteorol. Atmos. Phys.* **49**(1–4): 69–91, doi: 10.1007/BF01025401.

Pleim JE. 2007. A Combined Local and Nonlocal Closure Model for the Atmospheric Boundary Layer. Part I: Model Description and Testing. *J. Appl. Meteor. Climatol.* **46**: 1383–1395, doi: 10.1175/JAM2539.1.

Pope SB. 2000. *Turbulent Flows*. Cambridge University Press, ISBN 0-521-59886-9.

Raithby GD, Stubley GD, Taylor PA. 1987. The Askervein Hill Project: A Finite Control Volume Prediction of Three-Dimensional Flows Over the Hill. *Bound.-Layer Meteor.* **39**: 247–267, doi: 10.1007/BF00116121.

Raymond WH, Kuo HL. 1984. A Radiation Boundary Condition for Multi-Dimensional Flows. *Quart. J. Roy. Meteor. Soc.* **110**: 535–551, doi: 10.1002/qj.49711046414.

Réthoré PEM, Sørensen N, Bechmann A, Zahle F. 2009. Study of the atmospheric wake turbulence of a CFD actuator disc model. In: *Proceedings of the European Wind Energy Conference and Exhibition*. European Wind Energy Association: Marseille, France. 9 pp.

Reynolds O. 1895. On the Dynamical Theory of Incompressible Viscous Fluids and the Determination of the Criterion. *Philos. Trans. Roy. Soc. London A* **186**: 123–164, doi: 10.1098/rsta.1895.0004.

Rhie CM, Chow WL. 1983. Numerical Study of the Turbulent Flow Past an Airfoil with Trailing Edge Separation. *AIAA Journal* **21**(11): 1525–1532, doi: 10.2514/3.8284.

Richard E, Mascart P, Nickerson EC. 1989. The Role of Surface Friction in Downslope Windstorms. *J. Appl. Meteorol.* **28**: 241–251, doi: 10.1175/1520-0450(1989)028⟨0241:TROSFI⟩2.0.CO;2.

Richards PJ, Hoxey R. 1993. Appropriate boundary conditions for computational wind engineering models using the $k-\epsilon$ turbulence model. *J. Wind Eng. Ind. Aerodyn.* **46–47**: 145–153, doi: 10.1016/0167-6105(93)90124-7.

Rodi W. 1984. *Turbulence Models and Their Application in Hydraulics – A State of the Art Review*. IAHR, International Association for Hydraulic Research, 2nd revised edn, ISBN 9-021-27002-1.

Rodrigues AH, Lopes JA, Miranda PMA, Palma JMLM, Monteiro C, Sousa JN, Bessa RJ, Veiga Rodrigues C, Matos JC. 2007. EPREV – A Wind Power Forecasting Tool for Portugal. In: *Proceedings of the European Wind Energy Conference and Exhibition*. European Wind Energy Association: Milan, Italy. 10 pp.

Rodrigues AH, Matos JC, Bessa RJ, Sousa JN, Monteiro C, Lopes JA, Veiga Rodrigues C, Silva Santos C, Castro FA, Palma JMLM, Dutra E, Martins JPA, Tomé R, Miranda PMA. 2008. *EPREV - Previsão da Produção Eléctrica de Base Eólica*. Contract report for the EPREV companies consortium, INEGI, INESC-Porto, CEsA, CGUL/IDL. 339 pp.

Sánchez I. 2006. Short-Term Prediction of Wind Energy Production. *Int. J. of Forecasting* **22**: 43–56, doi: 10.1016/j.ijforecast.2005.05.003.

Schär C, Durran DR. 1997. Vortex Formation and Vortex Shedding in Continuously Stratified Flows past Isolated Topography. *J. Atmos. Sci.* **54**: 534–554, doi: 10.1175/1520-0469(1997)054⟨0534:VFAVSI⟩2.0.CO;2.

Schlichting H, Gersten K. 2000. *Boundary-Layer Theory*. Springer, 8th revised edn, ISBN 978-3-540-66270-9. Originally published by McGraw Hill, New York.

Skamarock WC, Klemp JB, Dudhia J, Gill DO, Barker DM, Duda MG, Huang XY, Wang W, Powers JG. 2008. A Description of the Advanced Research WRF Version 3. Technical Note NCAR/TN-475+STR, National Center for Atmospheric Research, Boulder, Colorado, USA. 113 pp.

Smagorinsky J. 1963. General Circulation Experiments with the Primitive Equations. *Mon. Wea. Rev.* **91**(3): 99–164, doi: 10.1175/1520-0493(1963)091⟨0099:GCEWTP⟩2.3.CO;2.

Smith RB. 1980. Linear Theory of Stratified Hydrostatic Flow Past an Isolated Mountain. *Tellus* **32**(4): 348–364, doi: 10.1111/j.2153-3490.1980.tb00962.x.

Smith RB. 1989. Hydrostatic Airflow Over Mountains. *Adv. Geophys.* **31**: 1–41, doi: 10.1016/S0065-2687(08)60052-7.

Smith RB. 2007. Interacting Mountain Waves and Boundary Layers. *J. Atmos. Sci.* **64**: 594–607, doi: 10.1175/JAS3836.1.

Smolarkiewicz PK, Rotunno R. 1989. Low Froude Number Flow Past Three-Dimensional Obstacles. Part i: Bariclinically Generated Lee Vortices. *J. Atmos. Sci.* **46**(8): 1154–1164, doi: 10.1175/1520-0469(1989)046⟨1154:LFNFPT⟩2.0.CO;2.

Stull RB. 1988. *An introduction to Boundary Layer Meteorology*. Atmospheric Sciences Library, Springer, ISBN 9-027-72769-4.

Taylor PA. 1971. A note on the log-linear velocity profile in stable conditions. *Quart. J. Roy. Meteor. Soc.* **97**: 326–329, doi: 10.1002/qj.49709741308.

Thiébaux J, Rogers E, Wang W, Katz B. 2003. A new high-resolution blended real-time global sea surface temperature analysis. *Bull. Amer. Meteor. Soc.* **84**: 645–656.

Thompson JF, Warsi ZUA, Mastin CW. 1985. *Numerical Grid Generation. Foundations and Applications*. North Holland, ISBN 0-444-00985-X.

Tukey JW. 1977. *Exploratory Data Analysis*. Addison Wesley, ISBN 978-0201076165.

Turner JS. 1973. *Buoyancy Effects in Fluids*. Cambridge monographs on mechanics & applied mathematics, Cambridge University Press, ISBN 0-521-08623-X.

Utnes T, Eidsvik KJ. 1996. Turbulent Flows Over Mountainous Terrain Modelled by the Reynolds Equations. *Bound.-Layer Meteor.* **79**: 393–416, doi: 10.1007/BF00119406.

van de Wiel BJH, Moene AF, Steeneveld GJ, Hartogensis OK, Holtslag AAM. 2007. Predicting the Collapse of Turbulence in Stably Stratified Boundary Layers. *Flow Turbulence Combust* **79**: 251–274, doi: 10.1007/s10494-007-9094-2.

Veiga Rodrigues C, Matos JC, Paiva LT, Palma JMLM. 2010. Analysis of the Similarity in Turbulence Intensity and Wind Shear as Function of the Wind Velocity: Field Measurements and Numerical Results. In: *Proceedings of the European Wind Energy Conference and Exhibition*. European Wind Energy Association: Warsaw, Poland, ISBN 978-1-61782-310-7, pp. 2742–2751.

Veiga Rodrigues C, Silva Santos CM, Palma JMLM, Castro FA, Miranda PMA, Rodrigues AH. 2008. Short-term Forecasting of a Wind Farm Output using CFD. In: *Proceedings of the European Wind Energy Conference and Exhibition*. European Wind Energy Association: Brussels, Belgium, ISBN 978-1-61567-115-1, pp. 675–684.

Wang W, Bruyère C, Duda MG, Dudhia J, Gill DO, Lin HC, Michalakes J, Rizvi S, Zhang X, Beezley JD, Coen JL, Mandel J. 2010. ARW Version 3 Modeling System User's Guide. User guide, National Center for Atmospheric Research, Boulder, Colorado, USA. 351 pp.

Warner TT. 2011. *Numerical Weather and Climate Prediction*. Cambridge University Press, ISBN 9780521513890.

Whiteman CD. 2000. *Mountain Meteorology: Fundamentals and Applications*. Oxford University Press, ISBN 0-19-513271-8.

Wilcox DC. 1994. *Turbulence Modelling for CFD*. DCW Industries: La Cañada, California, ISBN 0-9636051-0-0.

WMO. 2008. Guide to Meteorological Instruments and Methods of Observation. WMO Technical Regulations WMO-No. 8, 7th ed., World Meteorological Organization, Geneva, Switzerland. 680 pp.

Wyngaard JC. 1975. Modeling the Planetary Boundary Layer – Extension to the Stable Case. *Bound.-Layer Meteor.* **9**: 441–460, doi: 10.1007/BF00223393.

Wyngaard JC, Coté OR, Rao KS. 1974. Modeling the Atmospheric Boundary Layer. *Adv. Geophys.* **18A**: 193–212, doi: 10.1016/S0065-2687(08)60461-6.

Yaglom AM. 1977. Comments on Wind and Temperature Flux-Profile Relationships. *Bound.-Layer Meteor.* **11**: 89–102, doi: 10.1007/BF00221826.

Acknowledgements

"Exhibit *sapere vivere* in all circunstances. (...)
The only article Lady Fortuna has no control
over is your behavior. Good luck."

Nassim Taleb (1960–), Fooled by Randomness

I express my gratitude to Prof. Laginha Palma for its supervision and support throughout this work, as well as in the painful review process. I also thank him for the opportunity to work in CEsA (Centre for Wind Energy and Atmospheric Flows) with the VENTOS® code and team.

I would like to thank Prof. Fernando Aristides Castro for all of the support and teachings, which I hope were well learned. Also, I must thank Dr. Carlos Silva Santos for all of the guidance, in addition to some patience, even stoicism. More important, to both I thank not only for the camaraderie, but also the friendship.

I would like to thank RES (Renewable Energy Systems Ltd.) and NP (Natural Power consultants) for all the cooperation in the development of the VENTOS®/M model, as well as the satisfaction for seeing it being used in an engineering/technological context. I also would like to thank the people I have met, namely Alice Ely, Claude Abiven, Peter Stuart and Oisin Brady.

This work has been funded by the Portuguese Foundation for Science and Technology, under the SFRH/BD/30309/2006 doctoral grant, and by Prof. Laginha Palma through CEsA, under a research grant by University of Porto. I am frankly grateful for all the support.

The EPREV project (Previsão de Produção Eléctrica de Base Eólica), was made in cooperation with CGUL/IDL (Centre for Geophysics of Lisbon University), INEGI (Institute of Mechanical Engineering and Industrial Management) and INESC-Porto (Institute for Systems and Computer Engineering). It was sponsored by a consortium of wind power promoters involving: Enernova–Novas Energias, S.A.; Finerge–Gestão de Projectos Energéticos, S.A.; Galp Power, S.A.; Grupo GENERG; EDF EN Portugal Unipessoal, Lda.; Tecneira, S.A.; and Telener–Serviços de Telecomunicações, S.A.. I whish to express my gratitude to these companies for making their measurements available, namelly the resource assessment campaigns and wind farm data. I am thankful for having been given the chance to work in this project and with the people involved, namely Prof. Álvaro Rodrigues, Eng. Bruno Silva, Prof. Cláudio Monteiro, Eng. Fernando Junça, Eng. João Sousa, Eng. José Matos, and Eng. Miguel Marques.

I also thank the people I have met from the Centre for Geophysics (CGUL/IDL) whose contact, unfortunately brief, was always helpful: Dr. Miguel Teixeira, Prof. Pedro Soares, Prof. Pedro Miranda and Ricardo Tomé.

I cannot forget some of my former professors which, perhaps unawarely, helped me in my work through their knowledge and inspiration: Eng. Campos Costa, Prof. Carlos Pinho, Prof. Dias Rodrigues, Prof. Farinha Mendes, Dr. Javier Sanz Rodrigo, Prof. José Novais and Prof. Jeroen van Beeck.

A special greet to friends and fellows from FEUP and nearby, namely Alexandre Lopes, António Oliveira, Catarina Ribeiro, David Carvalho, Elisabete Mota, José Carlos Lopes da Costa, José Carlos Ribeiro, Luís Tiago Paiva, Pedro Areal and Rui Gomes.

I am also deeply grateful for some of the colleagues who I had the pleasure of knowing throughout my academic life: Erinç Erdem, João Cunha, Jorge Silva, Henrique Pinto, Michel Rasquin, Nicolas Bastin, Ogus Dayi, Peter Vass, Sophie Herpin, Tamás Bányai, Tiago Quintino and Youri Elkouch.

A cheerful "*Salvé!*" to my former comrades from IMPE and all the people I have met there, whose influence on me was paramount. I also would like to thank Dinis for is friendship and support.

I cannot forget João Henriques and the cheerful times in Lisbon and Cartaxo, namely the ramblings which eventually emerged regarding the nature of life, the universe and everything.

I apologise to those I have inevitably missed to refer. I also apologise for those who, because of work and life, I have made myself distant. I hope such will be amended in the future.

Finally I would like to thank my family. I wish to deeply acknowledge my mother whose support was unmeasurable. Last but surely not the least, I would like to show my deepest gratitude to Joana for all the perserverance, companionship and for the amazing person she is.